THE PHYSICS AND CHEMISTRY OF SOLIDS

AN INTERNATIONAL JOURNAL

VOLUME 15 1960

VOL. 15 1960

Editor-in-Chief HARVEY BROOKS, *Cambridge, Mass*

Associate Editors H. B. G. CASIMIR, *Eindhoven*; G. J. DIENES, *Brookhaven*; JACQUES FRIEDEL, *Paris*; E. M. LIFSHITZ, *Moscow*

Editorial Advisory Board

U.S.A.

E. N. Adams, Pittsburgh
D. Alpert, Illinois
L. Apker, Schenectady
J. Bardeen, Illinois
D. S. Billington, Oak Ridge
R. G. Breckenridge, Cleveland
Leo Brewer, Berkeley, Calif.
E. Burstein, Penn.
J. A. Burton, New Jersey
N. Cabrera, Virginia
G C. Danielson, Iowa
I. Estermann, Washington, D.C.
J. C. Fisher, Schenectady
F. Herman, Princeton
Conyers Herring, New Jersey
A. R. von Hippel, Cambridge, Mass
J. H. Hollomon, Schenectady
W. V. Houston, Houston
H. B. Huntington, Troy
H. M. James, Purdue
C. Kittel, Berkeley, Calif.
W. Kohn, Pittsburgh
J. A. Krumhansl, Cleveland
A. W. Lawson, Chicago
H. W. Leverenz, Princeton
O. T. Marzke, Pittsburgh
B. T. Matthias, New Jersey
L. R. Maxwell, Silver Spring
Joseph E. Mayer, Chicago
E. W. Montroll, Maryland
David Pines, Princeton
George T. Rado, Washington, D.C.
H. Reiss, New Jersey
J. R. Reitz, Cleveland
A. Rose, Princeton
O. C. Simpson, Argonne
R. Smoluchowski, Pittsburgh
F. H. Spedding, Iowa
D. Turnbull, Schenectady
J. H. Van Vleck, Harvard
B. E. Warren, Cambridge, Mass.
Eugene P. Wigner, Princeton
B. H. Zimm, Schenectady

Canada

R. E. Burgess, Vancouver
D. K. C. MacDonald, Ottawa
W. B. Pearson, Ottawa

United Kingdom

A. Charlesby, Shrivenham, Berks.
W. J. Dunning, Bristol
F. C. Frank, Bristol
H. K. Henisch, Reading
H. Jones, London
J. W. Mitchell, Bristol
A. B. Pippard, Cambridge
M. H. L. Pryce, Bristol
R. A. Smith, Malvern
K. W. H. Stevens, Nottingham
F. C. Tompkins, London

France

E. F. Bertaut, Grenoble
A. Guinier, Orsay
Louis Néel, Grenoble
Louis Weil, Grenoble

Germany

M. Born, Bad Pyrmont
Ulrich Dehlinger, Stuttgart
R. Hilsch, Göttingen
G. Leibfried, Aachen
E. Mollwo, Erlangen
H. Pick, Stuttgart
M. von Laue, Berlin
H. Welker, Erlangen

Italy

F. G. Fumi, Pavia

Czechoslovakia

J. Tauc, Praha

Japan

Toshinosuke Muto, Tokyo

The Netherlands

A. Michels, Amsterdam
G. W. Rathenau, Amsterdam

Sweden

J. O. Linde, Stockholm
Per-Olov Löwdin, Uppsala

Switzerland

G. Busch, Zurich
P. Scherrer, Zurich

U.S.S.R.

G. S. Zhdanov, Moscow

PERGAMON PRESS NEW YORK · LONDON · PARIS · LOS ANGELES

NOTES FOR CONTRIBUTORS

I. GENERAL

1. Submission of a paper to the *Journal of the Physics and Chemistry of Solids* will be taken to imply that it represents original research not previously published (except in the form of an abstract or preliminary report), that it is not being considered for publication elsewhere, and that if accepted, it will not be published elsewhere in the same form, in any language, without the consent of the editor-in-chief. It should deal with original research work in the field of the physics and chemistry of solids.

2. Papers should be submitted to the appropriate regional editor (all English-language papers to be sent to the U.S. editor).

3. Papers will be published as quickly as possible after acceptance, and, subject to space being available, should appear in the following issue, if this is due for publication not earlier than three months after the acceptance date. Short communications under the heading of "Letters to the Editor" will receive priority for publication, and will be published in the issue following receipt, if accepted not later than the beginning of the month preceding publication.

4. Fifty free reprints of each paper are supplied. Additional copies can be obtained at a reasonable cost if ordered when proofs are returned. A reprint order form will accompany first proofs.

II. SCRIPT REQUIREMENTS

1. Papers submitted should be concise and written in a readily understandable style. Scripts should be typed and double spaced and submitted in duplicate to facilitate refereeing.

It will be appreciated if authors clearly indicate any special characters used. An abstract, not exceeding 200 words, should be provided in the language of the paper. French and German papers should be submitted with English abstract and titles, but if this is not possible the abstract will be translated by the publishers. To conserve space, authors are requested to mark less important parts of the paper, such as details of experimental technique, methods, mathematical derivations, etc. for printing in small type. The technical description of methods should be given in detail only when such methods are new. Authors will receive proofs for correction when their papers are first set; page proofs will be sent only when the amount of alteration makes it advisable.

2. Illustrations should not be included in the typescript of the paper, and legends should be typed on a separate sheet. Line drawings which require redrawing should include all relevant details and clear instructions for the draughtsman. If figures are already well drawn it may be possible to reproduce them direct from the originals, or from good photo-prints if these can be provided. It is not possible to reproduce from prints with weak lines. Illustrations for reproduction should normally be about twice the final size required. The lettering should be sufficiently large and bold to permit this reduction. Photographs should only be included where they are essential.

3. Tables and figures should be so constructed as to be intelligible without reference to the text. Every table and column should be provided with an explanatory heading. Units of measure must always be clearly indicated. The same data should not be published in both tables and figures. The following standard symbols should be used on line drawings since they are easily available to the printers: ○, ●, +, ×, □, ■, △, ▲, ◇, ◆, ▽, ▼.

4. References are indicated in the text by superior numbers in parentheses, and the full reference should be given in a list at the end of the paper in the following form:

1. HILL R., *J. Iron St. Inst* **158**, 177 (1948).
2. PEARSON C., *The Extrusion of Metals*, p. 137. Chapman and Hall, London (1944).

Abbreviations of journal titles should follow those given for *Physics Abstracts*. It is particularly requested that authors' initials, and appropriate volume and page numbers, should be given in every case.

Footnotes, as distinct from literature references should be indicated by the following symbols—*, †, ‡, ‡‡, commencing anew on each page; they should *not* be included in the numbered reference system.

5. Due to the international character of the journal no rigid rules concerning notation and spelling will be observed, but each paper should be consistent within itself as to symbols and units.

CONTENTS LISTS FOR VOLUME 15, NOS. 1–4

Volume 15 Numbers 1/2

page

P. Cossee and A. E. van Arkel: Magnetic properties of Co^{2+} ions in tetrahedral interstices of an oxide lattice 1
W. Desorbo: Quenched-in defects in tin and the super-conducting transition temperature 7
J. R Wiese and L. Muldawer: Lattice constants of Bi_2Te_3–Bi_2Se_3 solid solution alloys 13
N. S. Rasor and J. D. McClelland: Thermal properties of graphite, molybdenum and tantalum to their destruction temperatures 17
J. C. Woolley and B. Ray: Effects of solid solution of In_2Te_3 with $A^{II}B^{VI}$ tellurides 27
J. H. Apfel and A. M. Portis: Exciton-induced photoconductivity in Cu_2O 33
J. R. Hardy: A theoretical study of point defects in the rocksalt structure substitutional K^+ in NaCl . . 39
H. B. Rosenstock: Infrared absorption by one-dimensional ionic lattices 50
I. S. Jacobs: High field magnetization study of ferrimagnetic arrangements in chromite spinels. . . . 54
E. J. Murphy: The temperature dependence of the conductivity of dry cellulose 66
M. T. Beal: Sur la résistivité électrique des alliages métalliques en fonction de l'ordre 72
D. Haneman and E. W. J. Mitchell: The analysis of spectral yield and accelerating field characteristics of the photoelectric emission from semiconductors 82
D. G. Thomas: The exciton spectrum of zinc oxide 86
J. J. Hopfield: Fine structure in the optical absorption edge of anisotropic crystals. 97
C. Haas: The diffusion of oxygen in silicon and germanium. 108
R. A. Eppler and H. G. Drickamer: The effect of pressure on the absorption spectra of alkali halide phosphors 112
D. A. Young: Surface heterogeneity in irradiated solids 119
F. A. Cunnell and C. H. Gooch: Diffusion of zinc in gallium arsenide 127
J. W. Allen: The diffusion of ionised impurities in semiconductors 134
A. D. Brailsford and A. W. Overhauser: Theory of the resistance minimum in dilute paramagnetic alloys . 140
R. J. Elliott and R. Loudon: Group theory of scattering processes in crystals 146
R. J. Arnott and A. Wold: The preparation and crystallography of FeNiN and the series $Fe_{4-x}Ni_xN$. 152
D. M. Speros and L. J. Schupp: Surface phenomena during the interaction between MgO(s) and various gases at elevated temperatures 157
Roland Aléonard: Etude paramagnétique des ferrites d'yttrium et de terres rares de formule $5Fe_2O_3 . 6M_2O_3$ 167

Letter to the Editor:
G. E. Gottlieb, W. M. Kane, J. F. Walsh and C. Wood: Electrical properties of Ag_2Te . . . 183

Book Review:
"General Crystallography: A brief Compendium", by W. F. DeJong (reviewed by C. S. Hurlbut, Jr.) . 183

Erratum:
J. A. Hofmann, A. Paskin, K. J. Tauer and R. J. Weiss: Analysis of ferromagnetic and antiferromagnetic second order transitions 187
Papers to be published in future issues 188

Volume 15 Numbers 3/4

P. A. Flinn, G. M. McManus and J. A. Rayne: Elastic constants of ordered and disordered Cu_3Au from 4·2 to 300°K. 189
R. J. Elliott and R. Loudon: Theory of the absorption edge in semiconductors in a high magnetic field . 196
E. M. Conwell and A. L. Brown: Scattering of hot carriers in germanium 208
J. Forten and E. R. Johnson: The radiation induced decomposition of potassium nitrate 218
A. G. Chynoweth and W. L. Feldman: Ferroelectric domain delineation in triglycine sulphate and domain arrays produced by thermal shocks 225
R. I. Beecroft and C. A. Swenson: On the existence of a critical point for the phase transition in cerium . 234
D. L. Weinberg and N. Bloembergen: Nuclear resonance study of electronic magnetism in copper–nickel . 240
D. L. Weinberg: Nuclear magnetic resonance intensities in alloys 249

page

H. G. Heal and J. P. S. Pringle: Colour centres in X-irradiated alkali metal azides 261
P. F. Schmidt, F. Huber and R. F. Schwarz: Ion size effect and mechanism of electrolytic rectification. . . 270
M. Sachs: Rotational properties of paramagnetic resonance spectra of non-cubic crystals 291
W. Albers, C. Haas and F. van der Maesen: The preparation and the electrical and optical properties of SnS crystals 306
J. Hornstra: Dislocations, stacking faults, and twins in the spinel structure 311
J. J. Lander: Reactions of lithium as a donor and an acceptor in ZnO 324
J. C. Slonczewski: Origin of magnetoelastic effects in cobalt–iron ferrite 335

Letters to the Editor:

I. T. Steinberger: Further experimental evidence on majority carrier injection in CdS single crystals . 354
M. P. Klein and W. D. Knight: Nuclear magnetic resonance in metallic potassium 355
E. C. McIrvine: Phenomenology of impurity conduction in semiconductors 356

Book Review:

"Electrons and Phonons", by J. M. Ziman (reviewed by E. N. Adams) 359

Tôme 15 Nos 1/2

P. Cossee et A. E. van Arkel: Propriétés magnétiques des ions interstitiels Co^{2+} dans un environnement tétraédrique dans un réseau d'oxyde 1
W. Desorbo: Défauts trempés dans l'étain et température de transition supraconductrice 7
J. R. Wiese et L. Muldawer: Paramètres de réseau des alliages solutions solides de Bi_2Te_3–Bi_2Se_3 . . 13
N. S. Rasor et J. D. McClelland: Propriétés thermiques du graphite, du tantale et du molybdène à leur température de destruction 17
J. C. Woolley et B. Ray: Effets de la formation de solutions solides de In_2Te_3 dans les tellurers $A^{II}B^{VI}$. 27
J. H. Apfel et A. M. Portis: Photoconductivité induite dans Cu_2O par les excitons 33
J. R. Hardy: Etude théorique des défauts ponctuels dans la structure du sel gemme : K^+ substitué dans NaCl. 39
H. B. Rosenstock: Absorption infra-rouge par les réseaux ioniques unidimensionnels 50
I. S. Jacobs: Etude à grand champ magnétique des arrangements ferrimagnétiques dans les spinelles de chrome 54
E. J. Murphy: La dépendance en température de la conductibilité de la cellulose sèche 66
M. T. Beal: Sur la résistivité électrique des alliages métalliques en fonction de l'ordre 72
D. Haneman et E. W. J. Mitchell: Analyse de la répartition spectrale et des caractéristiques du champ accélérateur pour l'émission photoélectrique dans les semi-conducteurs 82
D. G. Thomas: Spectre d'excitons dans l'oxyde de zinc 86
J. J. Hopfield: Structure fine dans la limite d'absorption optique des cristaux anisotropes 97
C. Haas: Diffusion de l'oxygène dans le silicium et dans le germanium 108
R. A. Eppler et H. G. Drickamer: Effet de la pression sur le spectre d'absorption des halogénures alcalins luminescents 112
D. A. Young: Hétérogénéité de surface dans les solides irradiés 119
F. A. Cunnell et C. H. Gooch: Diffusion du zinc dans l'arseniure de gallium 127
J. W. Allen: Diffusion des impuretés ionisées dans les semi-conducteurs 134
A. D. Brailsford et A. W. Overhauser: Théorie du minimum de résistance dans les alliages paramagnétiques dilués 140
R. J. Elliott et R. Loudon: La theorie des ensembles pour les procèdes de diffusion en cristaux. . . . 146
R. J. Arnott et A. Wold: Préparation et étude cristallographique de FeNiN et de la série $Fe_{4-x}Ni_xN$. . 152
D. M. Speros et L. J. Schupp: Phénomènes de surface au cours des interactions de MgO(s) et de divers gaz à températures élevées 157
R. Aléonard: Etude paramagnétique des ferrites d'yttrium et de terres rares de formule $5Fe_2O_3$, $6M_2O_3$. 167

Lettre aux éditeurs:

G. E. Gottlieb, W. M. Kane, J. F. Walsh et C. Wood: Propriétés électriques de Ag_2Te . . . 183

Revue de Livre:

"General Crystallography: A Brief Compendium", par W. F. DeJong (revu par C. S. Hurlbut, Jr.). . 186

Erratum: *page*

J. A. Hofmann, A. Paskin, K. J. Tauer et R. J. Weiss: Analyse des transitions ferromagnétiques et antiferromagnétiques du derniere order 187

Articles à publier dans les prochaines numéros 188

Tôme 15 Nos 3/4

P. A. Flinn, G. M. McManus et J. A. Rayne: Constantes élastiques de Cu_3Au ordonnée et désordonnée de 4,2 à 300°K 189

R. J. Elliott et R. Loudon: Théorie de a limite d'absorption dans les semi-conducteurs soumis à un champ magnétique intense 196

E. M. Conwell et A. L. Brown: Diffusion des porteurs chauds dans le germanium 208

J. Forten et E. R. Johnson: Décomposition du nitrate de potassium induite par les radiations. . . . 218

A. G. Chynoweth et W. L. Feldmann: Mise en évidence des domaines ferroélectriques dans le sulfate de triglycine et arrangements des domaines créés par les "chocs" thermiques 225

R. I. Beecroft et C. A. Swenson: Sur l'existence d'un point critique pour le changement de phase du cerium 234

D. L. Weinberg et N. Bloembergen: Etude par résonance nucléaire du magnétisme électronique des cuivre–nickel 240

D. L. Weinberg: Intensités de résonance magnétique nucléaire dans les alliages 249

H. G. Heal et J. P. S. Pringle: Centres colorés dans les nitrures alcalins irradiés aux Rayons X . . . 261

P. F. Schmidt, F. Huber et R. F. Schwarz: Effet de la taille des ions et mécanisme du redressement électrolytique 270

M. Sachs: Influence des rotations sur les spectres de résonance paramagnétique des cristaux non cubiques . 291

W. Albers, C. Haas et F. van der Maesen: Préparation et propriétés électriques et optiques des cristaux de SnS 306

J. Hornstra: Dislocations, fautes d'empilement et macles dans la structure des spinelles 311

J. J. Lander: Comportement du lithium comme donneur et comme accepteur dans ZnO. 324

J. C. Slonczewski: L'origine des effets magnetoelastiques dans la ferrite cobalt–fer 335

Lettres au Rédacteur:

I. T. Steinberger: Nouvelles preuves expérimentales de l'injection de porteurs majoritaires dans les monocristaux de GdS 354

M. P. Klein et W. D. Knight: Résonance magnétique nucléaire dans le potassium métallique . . 355

E. C. McIrvine: Etude phénoménologique de la conduction par impuretés dans les semi-conducteurs . 356

Revue de Livre: "Electrons and Phonons" par J. M. Ziman (revu par E. N. Adams) 359

Band 15 Nr. 1/2

P. Cossee und A. E. van Arkel: Magnetische Eigenschaften des Co^{2+}-Ions bei tetragonaler Zwischengitteratomlage in Oxyd–Gittern 1

W. Desorbo: Abgeschreckte Fehlstellen in Zinn und die Übergangstemperatur zur Supraleitung. . . . 7

J. R. Wiese und L. Muldawer: Gitterkonstanten der Legierungen fester Lösungen von Bi_2Te_3—Bi_2Se_3 . 13

N. S. Rasor und J. D. McClelland: Thermische Eigenschaften von Graphit, Molybdän und Tantal bei ihren Umwandlungstemperaturen 17

J. C. Woolley und B. Ray: Effekte fester Lösungen von In_2Te_3 mit $A^{III}B^{VI}$-Telluriden 27

J. H. Apfel und A. M. Portis: Durch Exzitonen hervorgerufene Photoleitfähigkeit in Cu_2O 33

J. R. Hardy: Eine theoretische Untersuchung punktförmiger Fehlstellen der Steinsalzstruktur mit K^+ als Substitutionsatom in NaCl 39

H. B. Rosenstock: Infrarote Absorption durch eindimensionale Ionengitter 50

I. S. Jacobs: Untersuchungen ferrimagnetischer Anordnungen in Chromitspinellen mit Magnetisierungen bei hohen Feldstärken 54

E. J. Murphy: Die Temperaturabhängigkeit der Leitfähigkeit trockener Zellulose 66

M. T. Beal: Über den elektrischen Widerstand metallischer Legierungen in Abhängigkeit von der Ordnung 72

D. Haneman und E. W. J. Mitchell: Die Analyse der spektralen Ausbeute und die Charakteristiken des beschleunigenden Feldes der photoelektrischen Emission bei Halbleitern. 82

D. G. Thomas: Das Exzitonenspektrum von Zinkoxyd 82

J. J. Hopfield: Die Feinstruktur bei der optischen Absorptionskante in anisotropen Kristallen 97

VOL. 15 1960

page

C. Haas: Die Diffusion des Sauerstoffs in Silizium und Germanium 108
R. A. Eppler und H. G. Drickamer: Die Druckabhängigkeit der Absorptionsspektren von Alkalihalogenid-phosphoren 112
D. A. Young: Die Heterogenität der Oberfläche bei bestrahlten Festkörpern 117
F. A. Cunnell und C. H. Gooch: Diffusion von Zink in Galliumarsenid 127
J. W. Allen: Die Diffusion von ionisierten Verunreinigungen in Halbleitern 134
A. D. Brailsford und A. W. Overhauser: Eine Theorie des Widerstandsminimums in verdünnten paramagnetischen Legierungen 140
R. J. Elliott und R. Loudon: Die Gruppentheorie der Streuprozesse in Kristallen 146
R. J. Arnott und A. Wold: Herstellung und Kristallographie von FeNiN und der Verbindungen $Fe_{4-x}NiN$. 152
D. M. Speros und L. J. Schupp: Oberflächeneffekte während der Wechselwirkung zwischen MgO(s) und verschiedenen Gasen bei erhöhten Temperaturen 157
R. Aleonard: Untersuchung des Paramagnetismus von Yttriumferriten und der seltenen Erden mit der Konstitutionsformel $5Fe_2O_3 . 3M_2O_3$ 167

Brief an den Herausgeber:
G. E. Gottlieb, W. M. Kane, J. F. Walsh und C. Wood: Elektrische Eigenschaften von Ag_2Te . . 183

Büchbesprechung:
W. F. DeJong: "General Crystallography: A Brief Compendium" (besprochen von C. S. Hurlbut, Jr.) . 186

Erratum:
J. A. Hofmann, A. Paskin, K. J. Tauer und R. J. Weiss: Eine Analyse der ferromagnetischen und antiferromagnetischen Übergangsgruppen der zweiten Ordnung 187
Arbeiten zur Veröffentlichung in zukünftigen Heften 188

Band 15 Nr. 3/4

P. A. Flinn, G. M. McManus und J. A. Rayne: Die elastischen Konstanten von geordnetem und ungeordnetem Cu_3Au von 4,2° bis 300°K 189
R. J. Elliott und R. Loudon: Die Theorie der Absorptionskante bei Halbleitern in einem hohen Magnetfeld 196
E. M. Conwell und A. L. Brown: Streuung heisser Ladungsträger in Germanium 208
J. Forten und E. R. Johnson: Die durch Bestrahlung hervorgerufene Zersetzung von Kaliumnitrat . . 218
A. G. Chynoweth und W. L. Feldmann: Beschreibung ferroelektrischer Domänen in Triglyzinsulfat, und Domänenanordnungen, welche durch thermischen Schock erzeugt werden. 225
R. I. Beecroft und G. A. Swenson: Über die Existenz eines kritischen Punktes für die Phasenumwandlung in Cer 234
D. L. Weinberg und N. Bloembergen: Kernmagnetische Resonanzstudien des Elektronenmagnetismus in Kupfer–Nickel. 240
D. L. Weinberg: Intensität der Kernmagnetischen Resonanz in Legierungen. 249
H. G. Heal und J. P. S. Pringle: Farbzentren in röntgenbestrahlten Alkalimetallaziden 261
P. F. Schmidt, F. Huber und R. F. Schwarz: Einfluss der Ionengrösse und der Mechanismus der elektrolytischen Gleichrichtung 270
M. Sachs: Rotationseigenschaften paramagnetischer Resonanzspektren nichtkubischer Kristalle. . . . 291
W. Albers, C. Haas und F. van der Maesen: Die Herstellung, elektrische und optische Eigenschaften von ZnS-Kristallen 306
J. Hornstra: Versetzungen, Stapelfehler und Zwillinge in der Spinellstruktur 311
J. J. Lander: Reaktionen des Lithiums als Donator und Akzeptor in ZnO 324
J. C. Slonczewski: Der Ursprung magnetoelastischer Effekte in Kobalt–Eisen-Ferriten 335

Briefe an den Herausgeber:
I. T. Steinberger: Weitere experimentelle Beweise für die Impfung von Überschussladungen in GdS-Einkristallen 354
M. P. Klein und W. D. Knight: Kernmagnetische Resonanz in metallischem Kalium 355
E. C. McIrvine: Die Phänomenologie der Fremdleitung in Halbleitern 356

Buchbesprechung:
J. M. Ziman: "Electrons and Phonons" (besprochen von E. N. Adams) 359

VOL. 15 1960

Том 15 На. 1/2

page

П. Коссее, А. Е. ван Аркель: Магнитные свойства ионов Co^{2+} в тетраэдрических положениях в окисных решетках 1
В. Дезорбо: Закаленные дефекты в олове и температура сверхпроводящего перехода . . 7
Дж. Р. Визе, Л. Мулдавер: Постоянные решетки сплавов Bi_2Te_3 — Bi_2Se_3 13
Н. С. Резор, Дж. МкКлелланд: Тепловые свойства графита, молибдена и тантала вплоть до их температуры разрушения 17
Дж. Вулей, Б. Рей: Эффекты растворения In_2Te_3 с теллуридами $A^{II}B^{VI}$ 27
Дж. Апфель, А. М. Портис: Фотопроводимость Cu_2O , индуцированная экситонами . . 33
Дж. Харди: Теоретическое исследование точечных дефектов при введении атомов замещения K^+ в структуру каменной соли 39
Г. Б. Розеншток: Инфракрасное поглощение в одномерных ионных решетках 50
И. С. Джекобс: Изучение ферримагнитных структур в хромовых шпинелях в высоких полях 54
Е. Мерфи: Температурная зависимость проводимости сухой целлюлозы 66
М. Т. Бил: Об электрическом сопротивлении металлических сплавов как функции упорядочения 72
Д. Ханеман, Е. В. Митчелл: Анализ спектрального выхода и характеристик в ускоряющем поле для фотоэлектрической эмиссии из полупроводников 82
Д. Г. Томас: Экситонный спектр окиси цинка 86
Дж. Дж. Гопфилд: Тонкая структура края поглощения в анизотропных кристаллах . . 97
К. Хааз: Диффузия кислорода в кремнии и германии 108
Р. А. Эпплер, Г. Дрикамер: Влияние давления на спектры поглощения в щелочных фосфорах . 112
Д. А. Юнг: Поверхностная неоднородность в облученных твердых телах 119
Ф. А. Куннелл, К. Гух: Диффузия цинка в мышьяковистом галлии 127
Дж. В. Аллен: Диффузия ионизированных примесей в полупроводниках 134
А. Д. Брейлсфорд, А. В. Оверхаузер: Теория минимума сопротивления в разведенных парамагнитных сплавах 140
Р. Эллиот, Р. Лоудон: Применение теории групп к процессам рассеяния в кристаллах . . 146
Р. Дж. Арнотт, А. Волд: Изготовление и кристаллография FeNiN и серии $Fe_{4-x}Ni_xN$ . . 152
Д. М. Сперос, Л. Шапп: Поверхнотные явления при взаимодействии между MgO(s) и различными газами при повышенных температурах 157
Р. Алеонар: Парамагнитное исследование ферритов иттрия и редких земель состава 5 $Fe_2O_3 . 3M_2O_3$ 167

Письмо в редакцию:
Г. Готтлиб, В. Кейн, Дж. Велш, К. Вуд: Электрические свойства Ag_2Te . . . 183

Рецензия на книгу:
В. Ф. Деджонг: "Общая кристаллография: краткое Руководство" (Рецензент С. С. Гурибут) 186
Объявление: Дж. А. Гофманн, А. Паскин, К. Дж. Тауер и Р. Дж. Вейсс: Анализ Ферро-магнитных и Анти-Ферромагнитных Переходов 187
Статьи Издаваемые v предстоящих выпусках 188

Том 15 На. 3/4

П. А. Флинн, Г. М. Масманус, Дж. А. Рейн: Упругие постоянные упорядоченного и неупорядоченного Cu_3Au при температурах от 4,2 до 300°К. 189
Р. Эллиотт и Р. Лоудон: Теория края поглощения в полупроводниках в сильном магнитном поле 196
Е. М. Конвелл, А. Л. Броун: Рассеяние горячих носителей в германии 208
Дж. Фортен и Е. Р. Джонсон: Разложение нитрата калия, индуцированное излучением . 218
А. Г. Чиновет, В. Л. Фельдманн: Делинеация ферроэлектрических доменов в триглицин-сульфате и системы доменов, производимые термическим ударом 225
Р. Биикрофт и К. А. Свенсон: О существовании критической точки для фазового перехода в церии 234
Д. Л. Вейнберг и Н. Блумберген: Исседование электронного магнетизма в сплавах меди с никкелем посредством ядерного резонанса 240

page

Л. Вейнберг: Интенсивности ядерного магнитного резонанса в сплавах 249
Г. Гил и Дж. П. С. Прингл: Центры окраски в X-облученных азидах щелочных металлов . 261
П. Ф. Шмидт, Ф. Губер и Р. Ф. Шварц: Влияние размеров ионов и механизм электролитического выпрямления 270
М. Сакс: Ротационные свойства спектров парамагнитного резонанса не-кубических кристаллов 291
В. Альберс, К. Хааз, Ф. ван дер Мэзен: Приготовление и электрические и оптические свойства кристаллов SnS 306
Дж. Хорнстра: Дислокации, дефекты упаковки и двойники в структуре шпинеля . . 311
Дж. Ландер: Реакции лития как акцептора и донора в ZnO 324
Дж. Слончевский: Происхождение магнитоупругих эффектов в Co–Fe-ферритах . . . 335

Письма в Редакцию:
Письмо в редакцию. Г. Ремо, Дж. Венник, А. Амелинкс: Дальнейшие экспериментальные свидетельства об инжекции носителей в монокристаллы GdS 354
В. Д. Найт: Ядерный магнитный резонанс в металлическом калии 355
Письмо в редакцию. Е. Мак Ирвин: Феноменологическое поведение примесной проводимосви в полупроводниках 356

Рецензия на книгу:
Дж. М. Зиман: "Электроны и фононы" (рецензент И. Н. Адамс) 359

AUTHOR INDEX TO VOLUME 15

(B) denotes book review (E) denotes erratum

Adams, E. N. 359 (B)
Aleonard, R. 167
Albers, W. 306
Allen, J. W. 134
Apfel, J. H. 33
van Arkel, A. E. 1
Arnott, R. J. 152
Beal, M. T. 72
Beecroft, R. I. 234
Bloembergen, N. 240
Brailsford, A. D. 140
Brown, A. L. 208
Chynoweth, A. G. 255
Conwell, E. M. 208
Cossee, P. 1
Cunnell, F. A. 127
Desorbo, W. 7
Drickamer, H. G. 112
Elliott, R. J. 146, 196
Eppler, R. A. 112
Feldman, W. L. 225
Flinn, P. A. 189
Forten, J. 218
Gooch, C. H. 127
Gottlieb, G. E. 183
Haas, C. 108, 306
Haneman, D. 82
Hardy, J. R. 39
Heal, H. G. 261
Hofmann, J. A. 187 (E)
Hopfield, J. J. 97
Hornstra, J. 311
Huber, F. 270
Hurlbut, C. S., Jr. 186 (B)
Jacobs, I. S. 54
Johnson, E. R. 218
Kane, W. M. 183
Klein, M. P. 355
Knight, W. D. 355
Lander, J. J. 324
Loudon, R. 146, 196
van der Maesen, F. 306
McClelland, J. D. 17
McIrvine, E. C. 356
McManus, G. M. 189
Mitchell, E. W. J. 82
Muldawer, L. 13
Murphy, E. J. 66
Overhauser, A. W. 140
Paskin, A. 187 (E)
Portis, A. M. 33
Pringle, J. P. S. 261
Rasor, N. S. 17
Ray, B. 27
Rayne, J. A. 189
Rosenstock, H. B. 50
Sachs, M. 291
Schmidt, P. F. 270
Schupp, L. J. 157
Schwartz, R. F. 270
Slonczewski, J. C. 335
Speros, D. M. 157
Steinberger, I. T. 354
Swenson, C. A. 234
Tauer, K. J. 187 (E)
Thomas, D. G. 86
Walsh, J. F. 183
Weinberg, D. L. 240, 249
Weiss, R. J. 187 (E)
Wiese, J. R. 13
Wold, A. 152
Wood, C. 183
Woolley, J. C. 27
Young, D. A. 119

VOL.
15
1960

VOL
15
196

J. Phys. Chem. Solids Pergamon Press 1960. Vol. 15. pp. 1–6. Printed in Great Britain.

MAGNETIC PROPERTIES OF Co^{2+} IONS IN TETRAHEDRAL INTERSTICES OF AN OXIDE LATTICE

P. COSSEE* and A. E. VAN ARKEL

Laboratorium voor Anorganische en Physische Chemie, Rijks-Universiteit, Leiden

(*Received* 21 *September* 1959)

VOL. 15 1960

Abstract—The magnetic properties of Co^{2+} ions in tetrahedral environment are discussed in relation to published optical data. It appears that the singlet ground state $^4F(\Gamma_2)$ is responsible for a magnetic moment close to the spin-only value, while the $^4F(\Gamma_5)$ level about 4000 cm^{-1} above this singlet gives rise to a temperature-independent paramagnetic term of $\approx 0{\cdot}5 \times 10^{-3}$ erg. G^{-2} . $mole^{-1}$. The expected departure from the Curie–Weiss law is demonstrated by susceptibility measurements on mixed crystals of CoO with ZnO, $CoAl_2O_4$ with $ZnAl_2O_4$ and $CoAl_2O_4$ with $MgAl_2O_4$ between 300° and 1200°K. The magnetic properties of Co^{2+} in tetrahedral interstices are compared with those of Co^{2+} ions in octahedral surroundings.

1. INTRODUCTION

Co^{2+} IONS in the tetrahedral interstices of an oxide lattice may exhibit interesting magnetic properties.†

In a crystalline field of four negative ions in tetrahedral arrangement the seven-fold orbitally degenerate ^4F ground state of Co^{2+} is split into two triplets and a singlet. The singlet level Γ_2 is the lowest, while the two triplets Γ_5 and Γ_4 are at distances of about 4000 and 7000 cm^{-1}, respectively, above this singlet ground state.

In first approximation only this singlet will be of importance for the magnetic properties and one may expect that the orbital contribution is nearly completely quenched. As a consequence of the fairly small energy differences between the singlet (Γ_2) and the lower triplet (Γ_5) the second-order perturbation treatment will reveal the presence of a temperature-independent or so-called Van Vleck paramagnetism.

A rough calculation shows that its value is not negligible and departure from the ideal Curie–Weiss behaviour may be expected.

Such a departure has already been found by GREENWALD *et al.*[3] They obtained a $1/\chi$ vs. T curve concave towards the T-axis for $CoAl_2O_4$, but interpreted the results by assuming a gradual transfer of Co^{2+} ions from the tetrahedral interstices of the spinel structure to the octahedral interstices as the temperature is raised.

In the present investigation χ-measurements were made on mixed crystals of CoO with ZnO between 300 and 1200°K. Provided the CoO content is less than 25 per cent, the Co^{2+} ions exclusively occupy tetrahedral interstices of the hexagonal Wurtzite structure.[4] In this case deviations from an ideal Curie–Weiss behaviour, if any, cannot be due to a transfer of Co^{2+} ions to other lattice positions.

These mixed crystals thus seem to be very suitable for studying the magnetic properties of Co^{2+} in tetrahedral surroundings.

In addition, χ-measurements were also carried out on $CoAl_2O_4$ and on mixed crystals of this compound with $ZnAl_2O_4$ and $MgAl_2O_4$, respectively.

All these compounds showed the same characteristic $1/\chi$ vs. T plot concave towards the T-axis which is now interpreted as to be due to temperature-independent paramagnetism.

2. EXPERIMENTAL

(a) *Preparation of samples*

Accurately known volumes of standard solutions of the metal nitrates were combined into a

* Present address: Koninklijke/Shell-Laboratorium, Amsterdam.

† For a study of Co^{2+} ions in octahedral interstices see Ref. (1); for Co^{3+} in octahedral interstices see Ref. (2).

weighed porcelain crucible, evaporated to dryness over infrared lamps and preheated at 300 to 350°C in air in order to decompose the nitrates. The resulting black mass was ground in an agate mortar and fired in a platinum boat at 1100°C. Debye–Scherrer photographs were taken to check the homogeneity of the products.

The whole preparation procedure was carried out quantitatively. Whenever the sample was transferred from one container into an other, the loss-factor was determined by weighing. In this way were prepared:

(Co,Zn)O mixed crystals with 20, 10, 5 and 2·5 mole per cent CoO;
pure $CoAl_2O_4$;
(Co,Zn)Al_2O_4 mixed crystals with 75, 50, 40, 20, 17, 10, 5 and 3·3 mole per cent $CoAl_2O_4$ and (Co,Mg)Al_2O_4 with 50, 20 and 10 mole per cent $CoAl_2O_4$.

The magnetic susceptibility measurements on these series of samples showed a very regular behaviour on dilution of the magnetic ions. The Curie temperatures, originally negative, tended to approximately zero as dilution increased. Therefore we shall only discuss the results of the magnetic measurements on $CoAl_2O_4$ and on one representative of the three types of mixed crystals each.

The complete results of this investigation may be found in Ref. (5).

(b) *Susceptibility measurements*

Magnetic measurements were carried out with a Faraday torsion balance.* The instrument was calibrated with $NiSO_4 . (NH_4)_2SO_4 . 6H_2O$. For the susceptibility of this salt the following formula was used:

$$\chi_g = \left(\frac{3174}{T+2{\cdot}5} - 0{\cdot}30\right) \times 10^{-6} \text{ erg. } G^{-2} . g^{-1}.$$

This formula was derived from JACKSON's data.[6]

Gd_2O_3 was used as a secondary standard for calibrating the balance in the high-temperature region.

(c) *Diamagnetic corrections*

The diamagnetic susceptibilities of ZnO,

* The authors gratefully acknowledge that both torsion balance and magnet were put at their disposal by the management of N.V. Philips Research Laboratories, Eindhoven.

Table 1. *Susceptibilities per gramatom of* Co^{2+} *corrected for diamagnetic contributions*

$Co_{0{\cdot}11}Zn_{0{\cdot}89}O$		$CoAl_2O_4$		$Co_{0{\cdot}20}Zn_{0{\cdot}80}Al_2O_4$		$Co_{0{\cdot}20}Mg_{0{\cdot}80}Al_2O_4$	
T °K	$\chi_M \times 10^3$ erg . G^{-2} . mole^{-1}	T °K	$\chi_M \times 10^3$ erg . G^{-2} . mole^{-1}	T °K	$\chi_M \times 10^3$ erg . G^{-2} . mole^{-1}	T °K	$\chi_M \times 10^3$ erg . G^{-2} . mole^{-1}
290	7·07	291	6·67	288	7·30	292	7·94
291	7·02	380	5·35	288	7·25	412	5·79
414	5·27	409	5·10	424	5·03	568	4·34
519	4·34	530	4·04	575	3·78	702	3·57
644	3·65	684	3·28	686	3·21	862	2·98
779	3·13	779	2·95	734	3·04	990	2·63
914	2·80	850	2·74	893	2·55	1096	2·42
1095	2·40	996	2·40	991	2·33	1193	2·26
1195	2·24	1085	2·27	1050	2·24		
		1130	2·19	1195	2·04		
		1192	2·10				
$a \times 10^3 = 0{\cdot}58$		$a \times 10^3 = 0{\cdot}46$		$a \times 10^3 = 0{\cdot}38$		$a \times 10^3 = 0{\cdot}35$	
θ	$= -30$°K	θ	$= -35$°K	θ	$= +6$°K	θ	$= -10$°K
μ	$= 4{\cdot}07$ B.M.	μ	$= 4{\cdot}02$ B.M.	μ	$= 3{\cdot}94$ B.M.	μ	$= 4{\cdot}28$ B.M.

a = temperature-independent paramagnetism (erg . G^{-2} . mole^{-1})
θ = Curie–Weiss temperature μ = magnetic moment

VOL. 15 1960

$ZnAl_2O_4$ and $MgAl_2O_4$ were determined by direct measurement with the same balance.

The following values were found:

ZnO	—	$0{\cdot}026\times10^{-3}$ erg G^{-2} $mole^{-1}$
$ZnAl_2O_4$	—	$0{\cdot}076\times10^{-3}$ erg G^{-2} $mole^{-1}$
$MgAl_2O_4$	—	$0{\cdot}057\times10^{-3}$ erg G^{-2} $mole^{-1}$

These values were used to calculate the diamagnetic corrections for the mixed crystals.

3. RESULTS

In all cases the temperature dependence of the susceptibility could be represented by

$$\chi_M = a + \frac{C}{T-\theta}.$$

a and θ can be evaluated is not very large as their values are small in comparison with χ and T, respectively.

In Fig. 1 the $1/\chi$ vs. T plots are given for three of the four substances under consideration (the fourth has been omitted for reasons of clarity) and the results of a calibration with Gd_2O_3 for comparison. The Gd_2O_3-plot is given on another scale in order to obtain a comparable slope of the line. The Gd_2O_3 points show no greater departure from the straight line than 0·5 per cent, which gives an indication of the accuracy of the high-temperature measurements.

Compared to this straight line, the plots for the Co-containing compounds clearly show a deviation from a Curie–Weiss behaviour.

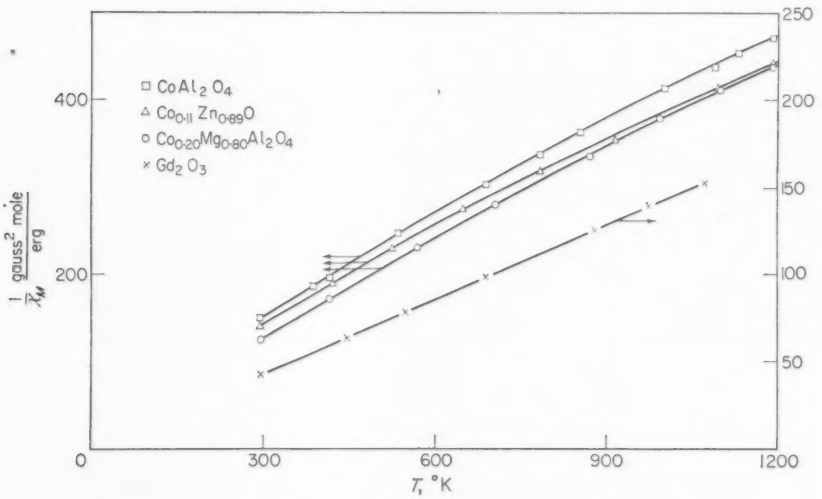

FIG. 1. $1/\chi$ as a function of T for various compounds containing Co^{2+} in tetrahedral interstices. For comparison a calibration with Gd_2O_3 is drawn on another scale, which is placed at the right-hand side of the figure.

The experimental results are summarized in Table 1, where for each substance the susceptibility per gramatom of Co, corrected for the diamagnetic contribution has been given as a function of absolute temperature, together with the values of $\mu = \sqrt{(8C)}$, a and θ, which were calculated to give the best fit to the experimental points. For practically all points the difference between calculated and experimental values is less than 1 per cent. It may be noted that the accuracy with which

4. DISCUSSION

(a) *Optical data*

The distances between the energy levels which are of importance for the calculation of magnetic properties may be estimated from optical data.

The detailed analysis of the absorption spectrum of Co^{2+} ions in MgO by Low[7] shows that the crystal-field parameter in the octahedral interstices of an oxygen lattice $\Delta_{oct.} = 9600\ cm^{-1}$ and the ^4F–^4P distance, $E_P = 12500\ cm^{-1}$.

Table 2. Optical data for various mixed crystals (Energy values in cm^{-1})

Compound		First absorption band cm^{-1}			Second absorption band cm^{-1}		
(Co,Zn)O	*	6000	7000	7600	15400	16400	17600
(Co,Zn)O	†	—	—	—	15240	16300	17540
(Co,Zn)Al_2O_4	†	—	—	—	16000	16850	18200
(Co,Mg)Al_2O_4	†	—	—	—	15950	17050	18200

* Measurements by McCLURE[8]. † Measurements by SCHMITZ-DU MONT *et al.*[9].

A value for the crystal-field parameter in tetrahedral interstices of an oxide lattice may be estimated by taking

$$\Delta_{\text{tetr.}} \approx \frac{4}{9}\Delta_{\text{oct.}}$$

With $\Delta_{\text{tetr.}} = 4000$ cm^{-1} and $E_P = 12500$ cm^{-1} one calculates three absorption bands for Co^{2+} in tetrahedral interstices at approximately 4000, 7000 and 17000 cm^{-1}. The second and third of the predicted bands are in good agreement with measurements, summarized in Table 2, by McCLURE[8] and SCHMITZ-DU MONT[9]. Unfortunately no extensive data are known in the infrared region. We have

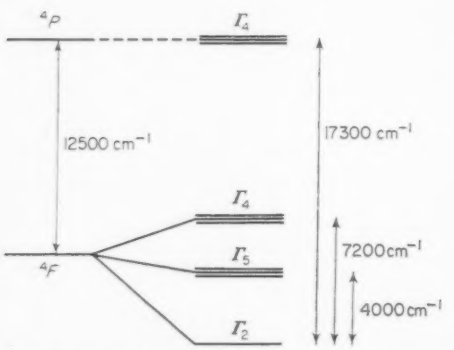

FIG. 2. Reconstruction of the energy-level diagram of Co^{2+} in tetrahedral interstices based on $\Delta_{\text{tetr.}} = 4000$ cm^{-1}.

thus made the assumption that in the slightly distorted tetrahedra of the (Co,Zn)O mixed crystals, $\Delta_{\text{tetr.}} \approx 4000$ cm^{-1} will not be far from the truth. For the aluminates of Co^{2+}, Zn^{2+} and Mg^{2+}, which according to X-ray analysis are normal spinels[10], it is assumed that the same value may be applied. A reconstruction of the energy-level diagram is given in Fig. 2, in which second-order effects like mutual repulsion of the two Γ_4 levels and spin-orbit coupling have not been taken into account.

(b) *Magnetic moment*

We are now able to make a prediction about the magnetic properties. In first approximation the magnetic moment due to the orbital singlet Γ_2 has the spin-only value. According to SCHLAPP and PENNEY[11] the inclusion of the spin-orbit interaction introduces a correction factor $(1-4\lambda')/\Delta$, where λ' is the spin-orbit coupling constant in the crystal. Regarding this constant it may be noted that generally a reduction of about 20 per cent with respect to the free-ion value is found for first-row bivalent transition elements in six-fold coordination.[1,12]

If λ' is taken equal to -150 cm^{-1} for Co^{2+} ions in tetrahedral surroundings (free-ion value $\lambda_{Co} = -180$ cm^{-1}) the magnetic moment

$$\mu = \sqrt{[4S(S+1)]}\left(1 - \frac{4\lambda'}{\Delta}\right)$$

becomes 4·4 Bohr magnetons.

It may be seen from Table 3 that the experimental magnetic moments are generally lower than this calculated value. It will be of great importance to have a more reliable value of the crystal-field parameter in order to estimate the reduction of the spin-orbit interaction in tetrahedral interstices.

(c) *Temperature-independent paramagnetism*

The temperature-independent paramagnetism

VOL. 15 1960

Table 3. Experimental values of magnetic moment and temperature-independent paramagnetism for various mixed crystals, with the theoretical estimates for Co^{2+} in tetrahedral interstices of a close-packed oxygen lattice.

Compound	μ (B.M.)	$a \times 10^3$ erg . G^{-2} $mole^{-1}$
$Co_{0.11}Zn_{0.89}O$	4·07	0·58
$CoAl_2O_4$	4·02	0·46
$Co_{0.20}Zn_{0.80}Al_2O_4$	3·94	0·38
$Co_{0.20}Mg_{0.80}Al_2O_4$	4·28	0·35
$Co^{2+}_{tetr.}$ (theor.)	4·4	0·5

has been given in first approximation by VAN VLECK[13]

$$a = \frac{N\beta^2}{3} \frac{2L(L+1)}{h\nu(\Gamma_5, \Gamma_2)}.$$

The formula is derived assuming a cubic tetrahedron and neglecting spin–orbit interaction. With $L = 3$ and $h\nu(\Gamma_5,\Gamma_2) = 4000\ cm^{-1}$ a becomes $0{\cdot}5 \times 10^{-3}$ erg . G^{-2} . $mole^{-1}$. It is seen from Table 3 that the agreement with experiment is very satisfactory.

(d) *The position of Co^{2+} in spinel structures*

The results obtained for the aluminates strongly support the statements, based on X-ray analysis, that these spinels have the normal arrangement of the cations. A comparison of our measurements on (Co,Zn)O with those on $CoAl_2O_4$ demonstrate that the bending of the $1/\chi$ vs. T curves towards the T-axis, which was also observed by GREENWALD *et al.*[3] for $CoAl_2O_4$ is due to the temperature-independent paramagnetism and not to a gradual transfer of Co^{2+} ions to octahedral interstices as was proposed by the latter authors.

(e) *Comparison with Co^{2+} in octahedral surroundings*

The interesting magnetic properties of Co^{2+} ions in tetrahedral interstices may finally be compared with the behaviour of Co^{2+} ions in octahedral interstices.[1] In the latter case the triplet level Γ_4 is the lowest, which gives rise to a magnetic moment that is slightly temperature dependent.[1] Consequently, another deviation from the normal Curie–Weiss behaviour must occur at elevated temperatures. This is demonstrated in Fig. 3, where $1/\chi$ is given as a function of T for $Co_{0.11}Zn_{0.89}O$ and for $Co_{0.196}Mg_{0.804}O$ together with the tangents to these curves in the room-temperature region. The curve for Co^{2+} in tetrahedra is concave

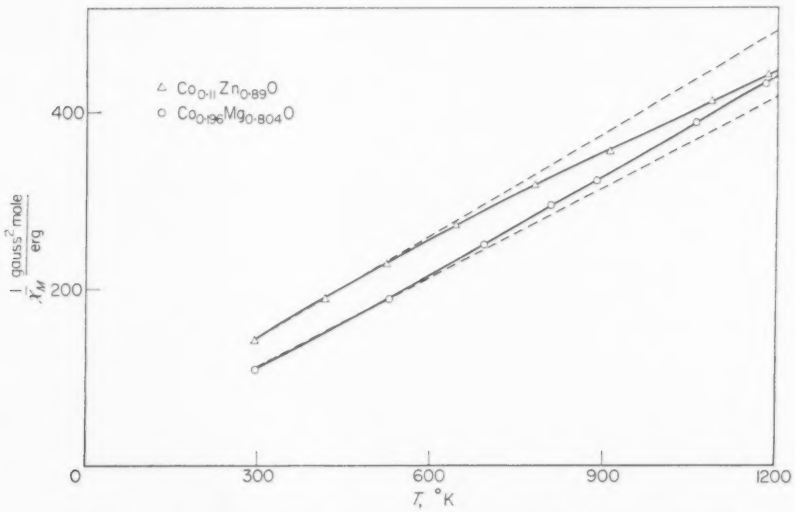

FIG. 3. Comparison of magnetic behaviour of Co^{2+} in octahedral and tetrahedral interstices. Dotted lines are tangents to the curves at room temperature.

towards the T-axis owing to temperature-independent paramagnetism, whereas that for Co^{2+} in octahedra is slightly S-shaped and convex towards the T-axis in the lower part owing to a temperature dependent magnetic moment.

Acknowledgements—The authors wish to thank Prof. J. H. VAN VLECK for his interest and for his written comments and Dr. Ir. E. L. MACKOR for valuable discussions.

REFERENCES

1. COSSEE P., *Mol. Phys.*, to be published.
2. COSSEE P., *J. Inorg. Nucl. Chem.* **8**, 483 (1958).
3. GREENWALD S., PICKART J. and GRANNIS F. H., *J. Chem. Phys.* **22**, 1597 (1954).
4. ROBIN J., *C.R. Acad. Sci. Paris* **235**, 1301 (1952).
5. COSSEE P., Thesis, Leiden (1956).
6. JACKSON L. C., *Phil. Trans. Roy. Soc.* A**224**, 1 (1924).
7. LOW W., *Phys. Rev.* **109**, 256 (1958).
8. MCCLURE D. S., *J. Phys. Chem. Solids* **3**, 311 (1957).
9. SCHMITZ-DU MONT O., BROKOPF H. and BURKHARDT K., *Z. anorg. Chem.* **295**, 7 (1958).
10. ROMEYN F. C., *Philips Res. Rep.*, **8**, 304 (1953).
11. SCHLAPP R. and PENNEY W. G., *Phys. Rev.* **42**, 666 (1932).
12. OWEN J., *Proc. Roy. Soc.* A**227**, 183 (1955).
13. VAN VLECK J. H., private communication.

J. Phys. Chem. Solids Pergamon Press 1960. Vol. 15. pp. 7–12. Printed in Great Britain.

QUENCHED-IN DEFECTS IN TIN AND THE SUPER-CONDUCTING TRANSITION TEMPERATURE

W. DESORBO

General Electric Research Laboratory, Schenectady, New York

(*Received* 10 *July* 1959; *revised* 14 *October* 1959)

VOL. 15 1960

Abstract—Wire specimens of tin quenched from a temperature T_Q ($370°K < T_Q < T_{m.p.}$), exhibit a resistivity component, $\Delta\rho_0$, which disappears on annealing at lower temperatures. It is inferred that this increase in resistivity is the result of quenched-in defects. The activation energy of motion of the defects, $E_m = 0{\cdot}68 \pm 0{\cdot}06$ eV; while the activation energy of formation, $E_f = 0{\cdot}51 \pm 0{\cdot}05$ eV. The sum of these values, $E_f + E_m = Q$, is in fair agreement with the measured value of Q, the activation energy of diffusion suggesting that the imperfections are vacancies. These defects depress the resistive super-conducting transition temperature by a measurable amount. The effect depends on the chemical purity of the specimen.

1. INTRODUCTION

RECENTLY it has been shown that the addition of small amounts of chemical impurity to a relatively pure super-conductor has a rather sharp effect on the super-conducting transition temperature.[1–3] However, information on the effect of a physical or structural impurity *per se* on super-conducting properties has been practically non-existent. Investigations that have been reported on lattice imperfections and super-conductivity include the introduction of inhomogeneous strains by compression and tension[4], by cold work[5, 6] and by condensation of thin films on cold substrates.[7] These techniques undoubtedly introduce, simultaneously, a complexion of lattice defects, dislocations, vacancies and interstitials. The problem of distinguishing experimentally what influence each of these physical impurities has on the super-conducting behavior, such as critical temperature, critical field or critical current, is a most difficult one. It is further complicated by the possibility of mutual interaction between the lattice imperfections as well as by their interplay with impurity solute atoms.

An experimental method that offers an opportunity for studying the effect of a particular type of lattice imperfection on super-conducting properties is that presented by investigations concerned with quenched-in defects in metals. It is generally supposed that these imperfections, originating at a high temperature and retained on rapidly quenching the metal to some lower temperature, are point lattice defects. It has been shown that their presence is accompanied by an increase in electrical resistivity,[8] in volume[8] and in internal energy[9] of the lattice. These results, and the corresponding recovery kinetic data, can be explained most satisfactorily in terms of lattice vacancies.[10–13]

In this work an attempt has been made to quench-in defects in tin and to study their effect on the resistive super-conductive transition temperature. This paper presents these results and in addition some evidence for believing that the defects are probably lattice vacancies.

2. EXPERIMENTAL

The tin specimens consisted of wires drawn from ingots which had been previously etched in a mixture of concentrated nitric acid (1 part by volume), concentrated acetic acid (3 parts by volume), and glycerol (5 parts by volume). Information pertaining to the chemical purity of the five specimens studied is presented in Table 1. The impurities listed for each were those provided by the supplier except for specimens 1 and 5 whose source was unknown. Specimen 2 was made from an ingot obtained from Allied Chemical & Dye

Table 1. The resistivity increase at 4·2°K and the change in the resistive super-conductive transition temperature due to quenched-in defects in tin*

Specimen	Diameter of wire (10^{-3} in.)	Analysis %	$R_{273°K}/R_{4·2°K}$		$\Delta\rho_0.10^{-9}\Omega$-cm	$-\Delta T_c$°K
			Annealed	Quenched		
1	19·5	As<0·005 Cu<0·0005 Fe<0·004 Pb 0·002 Zn<0·005 Ag<0·0001 Bi<0·001 Cd<0·003 Co<0·0005 In<0·0005 Ni 0·005 Sb 0·007	1 413	447†	22·3	0·0030
2	19·5	As 0·001 Cu 0·002 Fe 0·01 Pb 0·005 Zn 0·005	1 464	522†	13·7	0·0024
3	17·5	Pb 0·0011 Fe 0·00005	9 208	8 290†	0·152	0·0010
4	10·0	Pb 0·00002 Fe 0·00001	12 750	11 230†	0·149	0·0008
5(a)	19·5	From same bulk	1 316	467‡	16·7	0·0026
5(b)	19·5	stock as spec. 1	1 325	611‡	10·6	0·0020

* Arbitrarily defined as the mid point of the normalized resistive transition.
† Cooling rate ≅ 1900°C/sec
‡ Cooling rate ≅ 550°C/sec

Corporation (New York, N.Y.); ingots for specimen 3 and 4 were obtained from the Vulcan Detinning Co. (Sewaren, N.J.). The impurities listed for specimen 1 were determined for a wire sample by Ledoux & Co. using quantitative spectroscopic analysis (report-Ledoux No. 774205). The reciprocal residual resistance ratios ($\delta = R_{273°K}/R_{4·2°K}$) were determined for each specimen both in the annealed and quenched states (see Table 1). Six to 7 ft of wire were mounted strain free on a mica cross. The resistance measurement procedure and the technique for rapidly quenching the specimens have already been described.[14] Because of the relatively low melting point of tin, a suitable quenching medium (see below) was found to be a mixture of pentene-1 and methylcyclohexane maintained at a temperature of about −160°C.

3. RESULTS AND DISCUSSION

The total increase in resistivity, $\Delta\rho_0$, due to the quenched-in defect (for the temperature range 100–160°C) can be described by the equation:

$$\Delta\rho_0 = A \exp(-E_f/kT_Q) \qquad (1)$$

as shown in Fig. 1.* A is a constant, T_Q is the temperature from which the sample was quenched (injection temperature), k the Boltzmann constant and E_f is inferred to be the activation energy of formation of the defect responsible for the

* For $T_Q > 160$°C, the experimental points fall somewhat below the straight line plot of ln $\Delta\rho_0$ vs. $1/T_Q$. This implies that for these higher injection temperatures not all of the defects are retained during the quench, see for example Ref. (8).

VOL. 15 1960

resistivity increase.* Based on a least square fit to the data, $A = (4{\cdot}1 \pm 1{\cdot}0) \times 10^3$ μ-ohm cm and $E_f = 0{\cdot}51 \pm 0{\cdot}05$ eV.

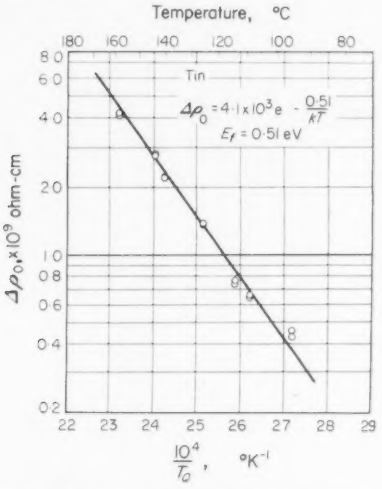

FIG. 1. Logarithm of the resistivity component, $\Delta\rho_0$, due to the "quenched-in" defect, as a function of reciprocal temperature, T_Q, immediately before quench.

The activation energy of motion, E_m, of the defects may be evaluated from data obtained on annealing the specimen isothermally. A convenient method is that proposed by KAUFFMAN and KOEHLER[16] and is illustrated in Fig. 2. In this procedure the thermal activation probability enters the rate equation for annealing as follows:

$$\frac{dc}{dt} = k' \exp(-E_m/kT_a)c \qquad (2)$$

where c is the concentration of the defect, k' is the rate constant, E_m the activation energy of motion, and T_a the annealing temperature. It is assumed that the fractional part of the quenched-in resistivity remaining at time, t, is proportional to the concentration of quenched-in defects at that time, i.e. $(\Delta\rho/\Delta\rho_0)_t \sim c_t$. The activation energy may be evaluated from plots $[\Delta\dot{\rho}(t)]/[\Delta\rho(t)] \sim t$ immediately before and after an abrupt change in the annealing temperature during a single recovery. The value for E_m evaluated by this method is $0{\cdot}68 \pm 0{\cdot}06$ eV.†

For isotropic solids, a possible mechanism for self-diffusion is through the migration of lattice vacancies. The diffusion coefficient is[17]

$$D = D_0 \exp(-Q/kT) \qquad (3)$$

The activation energy for self-diffusion, $Q = E_f + E_m$. The constant, $D_0 = a^2\nu \exp(\Delta S/k)$, where a is the lattice constant, ν is the frequency of atomic vibration and ΔS is the sum of the entropy of formation of the defect and entropy change due to the jump of an atom from one lattice site into an adjacent site. The tin structure, however, is anisotropic and is body-centered tetragonal with atoms at the (0, 0, 0), (1/2, 1/2, 1/2), (1/2, 0, 1/4), (0, 1/2, 3/4) positions and c/a equals 0·5455.[18] Although the activation energy of formation of the defect, E_f, is expected to be independent of lattice anisotropy, the activation energy of motion, E_m, should be structure sensitive.[17] However, KLOKHOLM and MEAKIN[19] have recently shown that for tin, the activation energy of self diffusion both along the a and c axis is of the same order of magnitude and in general agreement with the value predicted from a vacancy model for diffusion. These results pre-suppose that the activation energy of motion, E_m, for tin is not too structure dependent and hence $Q \simeq E_f + E_m$. Therefore, the activation energy for self-diffusion in tin,

$$Q \simeq E_f + E_m = 1{\cdot}19 \pm 0{\cdot}11 \text{ eV} \qquad (4)$$

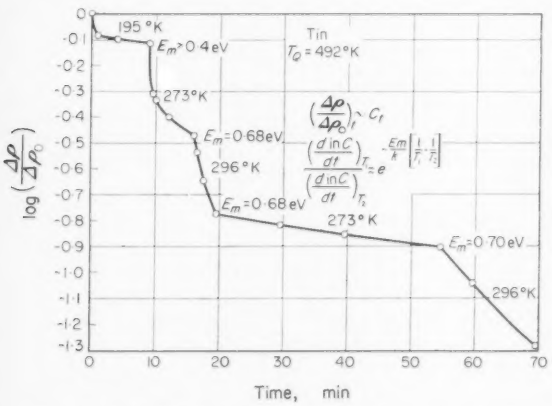

FIG. 2. Activation energy of motion of "quenched-in" defects determined from the ratio of slopes of log $\Delta\rho/\Delta\rho_0$ vs. t at identical concentration.

* Derivable from statistical mechanics, see for example Ref. (15).

† The data used for evaluating E_f and E_m, respectively, were obtained on a specimen similar to specimen 1 (see Table 1).

This is in fair agreement with the measured value $Q = 1{\cdot}04 \pm 0{\cdot}05$ eV obtained by MEAKIN and KLOKHOLM[19].

Figure 3(a) presents a typical result showing the influence of quenched-in defects on the residual resistivity and super-conducting transition temperature for tin (α = 1413). This is illustrated by comparing the resistivity vs. temperature curve for the sample in quenched state and for the sample subsequently annealed for a couple of hours at room temperature. The effect on the super-conducting temperature (arbitrarily defined as T_c at $R_T/R_{4.2} = 0{\cdot}5$ where $T < 4{\cdot}2$°K) is more clearly illustrated in Fig. 3(b) where the resistance ratio ($R_T/R_{4.2°K} \cong \rho_T/\rho_{4.2°K}$), is plotted as a function of temperature. The decrease in the super-conducting transition temperature, ΔT_c, amounts to $-3{\cdot}0 \pm 0{\cdot}2$ millidegrees for $\Delta\rho_0 = 2{\cdot}23 \times 10^{-8}\Omega$-cm. Fig. 4(a) shows the variation in resistivity with temperature in the vicinity of the super-conducting transition for a higher purity tin specimen (α = 9208) both in the quenched and the annealed state. Fig. 4(b) shows the corresponding $R_T/R_{4.2}$ vs. T curve. In this case $\Delta\rho_0 = 0{\cdot}152 \times 10^{-9}\,\Omega$-cm and $\Delta T_c = -1{\cdot}0 \pm 0{\cdot}2$ millidegrees.

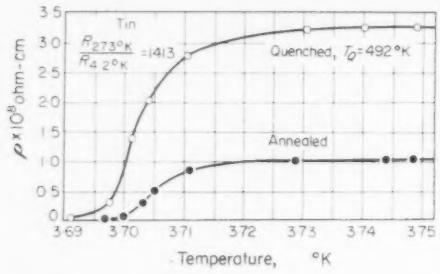

(a)

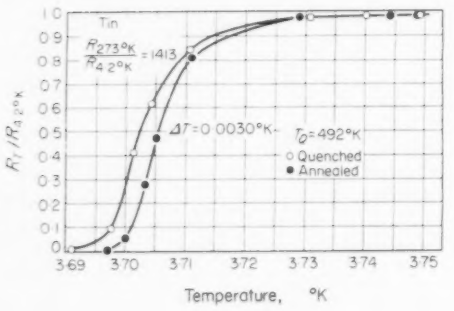

(b)

FIG. 3. (a) The influence of quenched-in defects on (i) the residual resistivity and (ii) the super-conducting transition for tin specimen 1 (α = 1413, $\Delta\rho_0 = 22{\cdot}3 \times 10^{-9}\,\Omega$ cm, $\Delta T_c = -0{\cdot}0030$°K) (b) Resistance ratio $R_T/R_{4.2°K}$ vs. temperature °K showing the influence of the quenched-in defects on the super-conducting transition temperature (α = 1413, $\Delta\rho_0 = 22{\cdot}3 \times 10^{-9}\Omega$-cm, $\Delta T_c = -0{\cdot}0030$°K).

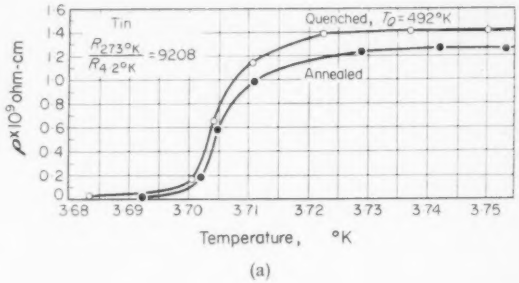

(a)

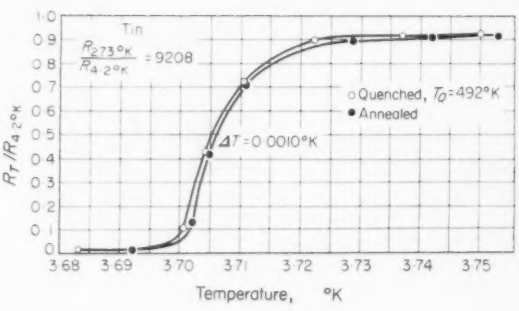

(b)

FIG. 4. (a) The influence of quenched-in defects on the residual resistivity and on the super-conducting transition for a tin specimen (α = 9208, $\Delta\rho_0 = 0{\cdot}152 \times 10^{-9}$ Ω-cm, $\Delta T_c = -0{\cdot}0010$°K). (b) Resistance ratio $R_T/R_{4.2°K}$ vs. temperature °K showing the influence of the quenched-in defects on the super-conducting transition temperature (α = 9208, $\Delta\rho_0 = 0{\cdot}152 \times 10^{-9}\Omega$-cm., $\Delta T_c = -0{\cdot}0010$°K.)

Table 1 summarizes the various increases in resistivity, $\Delta\rho_0$, due to quenched-in defects and the change in the resistive super-conductive transition temperature ΔT_c for the different specimens investigated. The injection temperature, T_Q, was the same for each specimen and equal to 219 ± 2°C. Specimens 1 through 4 were cooled in the hydrocarbon mixture mentioned above at rates equal to approximately 1900°C/sec. Two

runs listed for specimen 5 were cooled at rates equal to approximately 550°C/sec. The measuring current through each wire was kept constant at approximately 230 mA.

It is noteworthy to point out that the total increase in resistivity due to the quenched-in defects ($\Delta\rho_0$) for a given cooling rate is markedly dependent on the concentration of chemical impurities in tin. This may indicate that in quenching from a temperature, such as 492°K, more defects anneal out during the quench-in case of the high purity sample than for the less pure material (compare Figs. 3(a) and 4(a)). If this is the case, then the variation in $\Delta\rho_0$ with chemical purity suggests a possible stabilization of the vacancies during the quench in the less pure specimen. This difference between the two samples in the retentivity of vacancies during the quench could be accounted for by any one of several possible ways. There can exist an interaction (elastic and/or electrical) between the vacancies and impurity atoms. LOMER and COTTRELL[20] have discussed the possible important role that vacancies may play in trapping impurity atoms. Some possible evidence for a vacancy–solute association has recently been cited in studies on annealing defects in small concentrations of Mg in aluminum[21] and in dilute Al–Cu alloys.[22] A second method for preventing the loss of vacancies could be that due to the adsorption of impurity atoms on dislocations inhibiting their climb causing fewer vacancies to be annihilated. Some evidence for this has been cited from data on annealing kinetics of vacancies in aluminum.[13] Here the impurity–dislocation adsorption hypothesis inhibiting the dislocation climb seems to be in better agreement with observations than the vacancy–impurity interaction. A third possible mechanism for conserving the number of vacancies is that brought about by a decrease of dislocation loops with increase in the concentration of the solute atoms. THOMAS[23] has recently observed this after quenching thin foils of Al–Ag and Al–Cu specimens having various concentrations of solute atoms.

We have not made any attempt to elucidate the role that chemical impurities (substitutional or interstitials) play in the annealing kinetics of quenched-in defects in Sn. Further experimentation on the recovery behavior of quenched-in defects in tin specimens of varying impurity would be appropriate as well as their effect on the critical magnetic field and critical current (SILSBEE's hypothesis) in the superconductive region.

LYNTON *et al.*[1] have reported on the effect of addition of various metallic impurities (0·04–2·0 at. %) to the superconductive critical temperature T_c in Sn by threshold magnetic field measurements. For impurity concentrations less than approximately 0·3 at. %, ΔT_c was found to decrease linearly with the increase in residual resistance ratio.* The change has been correlated with the decrease in the electronic mean free path in the normal state.† A direct comparison of the influence on T_c by chemical impurities in tin as reported by LYNTON *et al.*[1] and by quenched-in defects *per se* is not feasible at this time. For a given cooling procedure (and rate), ΔT_c and $\Delta\rho_0$ due to the quenched-in defects in tin are dependent on the nature and concentration of chemical impurities already present in the specimen. To resolve this problem, further studies should be made on the effect on ΔT_c by a systematic variation in the concentration of quenched-in imperfections for a tin specimen having a low and constant level of chemical impurities. Furthermore, these results should be corroborated by threshold magnetic field studies.

SUMMARY

It has been shown that upon heating tin wire specimens below the melting point, there appears, upon rapid quenching, a resistivity component that disappears upon holding the samples at some lower temperature. It is inferred that this increase in resistivity is due to lattice vacancies having an activation energy of formation, $E_f = 0{\cdot}51$ eV, and an activation energy of motion, $E_m = 0{\cdot}68$ eV. These structural defects lower the resistive super-conductive transition temperature by a measurable amount depending on the chemical purity of the specimen.

Acknowledgements—The author is grateful to D. TURNBULL for discussions and for reviewing the manuscript. For the latter he also thanks J. C. FISHER and R. W. SCHMITT. G. E. NICHOLS assisted in the experimental work.

* A similar behavior has recently been reported for isoelectronic tin alloys by WIPF and COLES[24].

† See also Refs. (25–27).

VOL. 15 1960

REFERENCES

1. LYNTON E. A., SERIN B. and ZUCKER M., *J. Phys. Chem. Solids* **3**, 165 (1957); CHANIN G., LYNTON E. A. and SERIN B., Superconductivity Conf., Roy. Soc. Mond. Lab., Cambridge, 30 June to 3 July, 1959.
2. ITTNER W. B. III, *Trans. New York Acad. Sci.* **21**, 406 (1959); See also ITTNER W. B. III and SERAPHIM D. P., *Bull. Amer. Phys. Soc.* **4**, 224 (1959).
3. MATTHIAS B. T., SUHL H. and CORENZWIT E., *Phys. Rev. Letters* **1**, 92 (1958).
4. LASAREW B. and GALKIN A., *J. Exp. Theor. Phys. (URSS)* **8**, 371 (1944).
5. BUCKEL W. and HILSCH R., *Z. Phys.* **132**, 420 (1952).
6. BUCKEL W., HILSCH R. and MINNIGERODE G. V., *Acta. Phys. Acad. Sci.* **8**, 5 (1957).
7. BUCKEL W. and HILSCH R., *Z. Phys.* **138**, 109 (1954).
8. BAUERLE J. E. and KOEHLER J. S., *Phys. Rev.* **107**, 1493 (1957).
9. DESORBO W., *Phys. Rev. Letters* **1**, 238 (1958).
10. KOEHLER J. S., SEITZ F. and BAUERLE J. E., *Phys. Rev.* **107**, 1499 (1957).
11. KIMURA H., MADDIN R. and KUHLMANN-WILSDORF D., *Acta Met.* **7**, 145 (1959), see also *J. Metals N.Y.* **10**, 93 (1958).
12. SILCOX J. and HIRSCH P. B., *Phil. Mag.* **4**, 72 (1959).
13. DESORBO W. and TURNBULL D., *Phys. Rev.* **115**, 560 (1959).
14. DESORBO W., *Phys. Rev.* **111**, 810 (1958).
15. BROOKS H., *Lattice Vacancies and Interstitials in Metals, Impurities and Imperfections*. American Society for Metals, Cleveland, Ohio (1955).
16. KAUFFMAN J. W. and KOEHLER J. S., *Phys. Rev.* **97**, 555 (1955).
17. ZENER C., *Theory of Diffusion, Imperfections in Nearly Perfect Crystals*, Symposium held at Pocono Manor, Oct. 12–14, 1950. Wiley, New York (1952).
18. WYCKOFF R. W. G., *Crystal Structure*, Sect. II, Interscience Publishers, New York (1948).
19. KLOKHOLM E. and MEAKIN J. D., *Bull. Amer. Phys. Soc.* **4**, 171 (1959), also MEAKIN J. D. and KLOCKHOLM E., *Symposium on Diffusion*, AIME Meeting, Oct. 30 (1958). Abstract in *J. Metals, N.Y.* **10**, (9), 587 (1958).
20. LOMER W. M. and COTTRELL A. H., *Phil. Mag.* **46**, 71 (1955).
21. PANSERI G., GATTO F. and FEDERIGHI T., *Acta Met.* **6**, 198 (1958).
22. HART E., *Acta Met.* **6**, 553 (1958).
23. THOMAS G., private communication to D. TURNBULL.
24. WIPF S. and COLES B. R., Superconductivity Conf., Roy. Soc. Mond Lab., Cambridge, 30 June to 3 July, 1959.
25. PIPPARD A. B., *J. Phys. Chem. Solids* **3**, 175 (1957).
26. ANDERSON P. W., *Bull. Amer. Phys. Soc.* (ser. 2), **4**, 148 (1959); *J. Phys. Chem. Solids* **12**, 41 (1959).
27. ABRAHAMS E. and WEISS P. R., Superconductivity Conf., Roy. Soc. Mond Lab., Cambridge, 30 June to 3 July, 1959.

J. Phys. Chem. Solids Pergamon Press 1960. Vol. 15. pp. 13–16. Printed in Great Britain.

LATTICE CONSTANTS OF Bi_2Te_3–Bi_2Se_3 SOLID SOLUTION ALLOYS

J. R. WIESE and L. MULDAWER

The Franklin Institute Laboratories, Philadelphia 3, Pennsylvania

(*Received* 23 *January* 1959; *revised* 12 *November* 1959)

VOL. 15 1960

Abstract—The Bi_2Te_3–Bi_2Se_3 quasi-binary system is rhombohedral for all compositions. Lattice constants a_0 and c_0 (based on a hexagonal lattice) for the entire range were determined using powder pattern film techniques. The constant a_0 follows Vegard's Rule over the entire range of compositions, while the constant c_0 exhibits a positive deviation over the range from 40 mol% Bi_2Se_3 to Bi_2Se_3. Bi_2Te_3 has a layered structure with planes of atoms of a single type parallel to the basal plane. The lattice constant data can be explained in terms of Se-atom substitution in preferred planes for the range Bi_2Te_3–Bi_2Te_2Se. Interlayer spacings for Bi_2Te_3 and Bi_2Te_2S are given and discussed.

1. INTRODUCTION

TILLER and MCHUGH[1] have shown by thermal analysis that Bi_2Te_3 is soluble in Bi_2Se_3 in all proportions. The structures of Bi_2Te_3 and Bi_2Se_3 have been established as rhombohedral[2, 3] which, for convenience of indexing, can be referred to a hexagonal unit cell. It was also shown that planes perpendicular to the c-axis contain atoms of the same type. This structure is shown in Fig. 1, with the rhombohedron outlined.

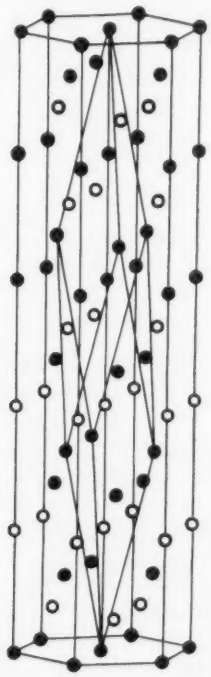

FIG. 1. Crystal Structure of Bi_2Te_3.

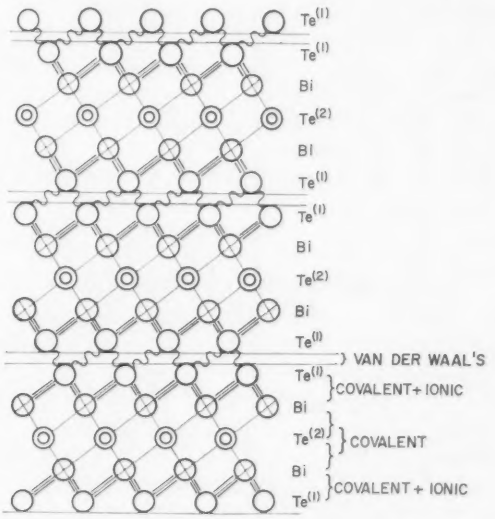

FIG. 2. Bonding Scheme of Bi_2Te_3.

DRABBLE and GOODMAN[4] have proposed a model for the bonding in Bi_2Te_3, and the bonding model is shown schematically in Fig. 2. In this

model the stacking consists of "quintuple layer" leaves where, in each leaf, the layers occur in the order $Te^{(I)}$–Bi–$Te^{(II)}$–Bi–$Te^{(I)}$, with the bond lengths of the $Te^{(I)}$–Bi atoms approximately 0·1 Å shorter than those of the $Te^{(II)}$–Bi bond lengths. The superscripts (I) and (II) are here used to distinguish the Te atoms with different surroundings and with different type bonding with their nearest Bi neighbors. As seen in Fig. 2 the $Te^{(II)}$–Bi bond is covalent, and the $Te^{(I)}$–Bi bond is mixed covalent and ionic; the $Te^{(I)}$–$Te^{(I)}$ (intermolecular bond) is of the van der Waal type. DRABBLE and GOODMAN suggest that when Se atoms are substituted for Te in Bi_2Te_3, they first replace tellurium atoms in the $Te^{(II)}$ layers, after which the Se atoms randomly replace the $Te^{(I)}$ atoms. Optical[5] and electrical[6] measurements indicate that energy gap, thermoelectric power and electrical conductivity values change sharply at a composition near 30 mol% Bi_2Se_3–70 mol% Bi_2Te_3 ($Bi_2Te_{2\cdot1}$ $Se_{0\cdot9}$). This would indicate a change in the nature of the Se substitution. If we assume that the DRABBLE and GOODMAN suggestion[4] is correct, then the new substitution mechanism must be one of replacing tellurium atoms in $Te^{(I)}$ layers.

Evidence for the ordered structure for Bi_2Te_2Se may be found by comparing with the analogous substance Bi_2Te_2S (Tetradymite). HARKER[7] has shown that tetradymite is ordered with layers of atoms in the following order: Te–Bi–S–Bi–Te. Thus, it would seem probable in our alloy that we would obtain a layering of atoms similar in every way except that Se replaces S.

2. EXPERIMENTAL PROCEDURE

All of the alloys in this investigation were prepared in the same way. Stoichiometric amounts of the elements involved were weighed and capsulated in evacuated Vycor tubes. After heating to approximately 50°C above their liquidus temperatures, the alloys were shaken vigorously several times to insure thorough mixing, then quenched into water.

Initially the prepared powders were rolled into "rat-tails", but it was found that the powders cold-worked during this process. The selected technique was to coat very thin (0·3 mm) fibres of glass with diluted Duco cement, then dip the fibres into the annealed powders. This process was repeated until the diameter of the specimen was approximately 0·8 mm. The X-ray diffraction photographs were taken with a 114 mm diameter Debye-Scherrer camera using CoKα radiation.

The reflections for Bi_2Te_3 were indexed on the basis of a hexagonal lattice and this led to values for c and a of 30·45 Å and 4·384 Å, respectively. FRANCOMBE[8] recently obtained values of 30·487Å and 4·3835 Å, in good agreement with our values. Because of the difficulty in indexing some lines, a cleaved single crystal of Bi_2Te_3 was studied with a diffractometer in order to definitely establish the (00l) reflections. The c constant obtained with the diffractometer was 30·51 Å. Since we were interested in an alloy series, we used the X-ray photographs because only Bi_2Te_3 single crystals were available. The film reflections—uniquely (00l)—were (00·6), (00·15) and (00·30). The (00·15) and (00·30) c values were plotted against the extrapolation function $1/2\ (\cos^2\theta/\sin\theta+\cos^2\theta/\theta)$ and an extrapolated value of c was obtained. a was similarly obtained using the (hk0) lines: (110), (300) and (220). c and a constants for the other alloys of the series were obtained by utilizing corresponding X-ray diffraction lines.

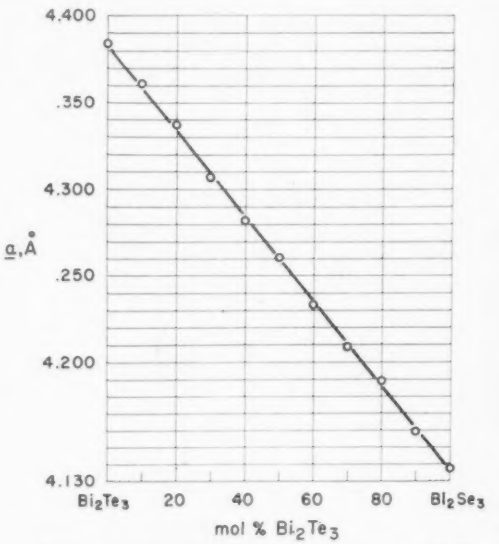

FIG. 3. Constant a as a Function of composition Bi_2Te_3–Bi_2Se_3 system.

3. RESULTS AND DISCUSSIONS

Figure 3 shows the variation of the a constant with

composition, and Fig. 4 the variation of *c*. We see from the figures that both constants decrease as the composition goes from Bi_2Te_3 to Bi_2Se_3 and that the *a* value follows Vegard's Law. The deviation from Vegard's Law values for the lattice

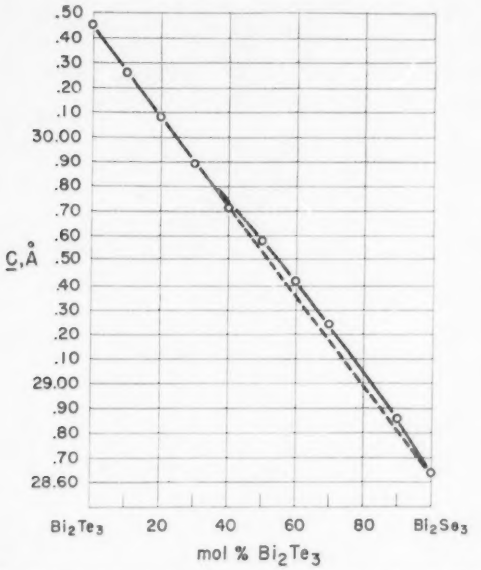

FIG. 4. Constant *c* as a Function of composition Bi_2Te_3–Bi_2Se_3 system.

constant *c* is shown in Fig. 5. It is recalled that *a* is the interatomic distance of atoms in the basal plane of our structure. It seems clear that the main

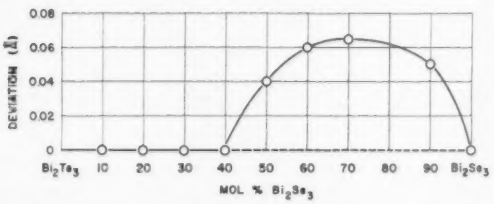

FIG. 5. Constant *c* deviation from Vegard's Law, Å.

cause of the decrease in *a* is that Te atoms are replaced by the smaller Se atoms. The ionic radius for Te is 2·21 Å and for Se is 1·98 Å.[9] As has been indicated previously, these Se atoms at first go into $Te^{(II)}$ layers.

A somewhat different effect on the *c* constant due to Se substitution is shown in Figs. 4 and 5. The decrease is linear to approximately 40% Bi_2Se_3, beyond which there is a positive deviation from Vegard's Law. This deviation implies that effects other than size are acting within the lattice. In general, it is expected that substitution of Se for Te would lead to smaller *c* values for the reason that the Se atom is smaller than Te.

There is a kind of van der Waal's interaction which is stronger between identical systems than between non-identical systems.[10] These are specific charge fluctuation forces which have been utilized to explain phenomena such as polymerization and biological replication. So long as the $Te^{(I)}$ sites are all occupied by one atomic species—either all Te or all Se—one of the five-layer molecules is bounded on each side by its identical twin and the specific forces increase the van der Waal's attraction. When the $Te^{(I)}$ sites are partially replaced by Se, the adjacent five-layer molecules are no longer identical and the van der Waal's interaction is weakened. Thus we believe that up to about 33 per cent Se, the Se atoms would all go into the $Te^{(II)}$ layers in order to have maximum binding. The specificity effect then could explain the positive deviation of the *c* constant from Vegard's Law beyond 33 per cent Se. The adjoining five-layer molecules will be most unlike at $67\frac{2}{3}$% Bi_2Se_3 and we see from Fig. 5 that, near this composition, the greatest deviation from Vegard's Law occurs. We do not understand why there is no positive deviation from Vegard's Law at 40% Bi_2Se_3 for *c*.

In his publication, HARKER gives the lattice constants and parameters for rhombohedral tetradymite.[7] From these values interplanar spacings can be calculated; these are given in Table 1. Also in Table 1 are values obtained from interatomic distances in Bi_2Te_3 as given by AIRAPETIANTS and EFIMOVA[11].

Table 1

	Bi_2Te_3 (this work)	Bi_2Te_3 (from Russian data)	Bi_2Te_2S (after HARKER)
$Te^{(I)}$–$Te^{(I)}$	2·60$_4$	2·73	2·73
Bi–$Te^{(I)}$	1·73$_9$	1·69	1·86
Bi–$Te^{(II)}$	2·03$_8$	2·02	
or Bi–S			1·77

Our values of the Bi_2Te_3 lattice parameters were obtained utilizing a single crystal. Intensity data from (00*l*) reflections, up to (00·10), were obtained on a diffractometer using CuKα radiation. A one dimensional Fourier synthesis of electron density was carried out for a reduced hexagonal unit cell (1/3 of the true cell in *c*), using signs which were the same as those of the corresponding tetradymite terms. The space group for Bi_2Te_3 is the same as that of tetradymite, $R\bar{3}m$.[12] The electron density was projected onto the *c* axis and initially trial parameters of $\mu = 0{\cdot}401$ and $\nu = 0{\cdot}208$ were obtained. The refinement was carried out utilizing the fact that the third and fourth order reflections were experimentally zero. Since single crystals and a sensitive counter were used, we feel that these zero values are highly significant. The limiting factor is the atomic structure factor. The standard Thomas–Fermi values corrected for dispersion[13] were used. Parameters $\mu = 0{\cdot}400_1$ and $\nu = 0{\cdot}209_5$ were obtained. An *R* factor of 0·46 was obtained for the limited set of reflections. The values computed from the Russian data are $\mu = 0{\cdot}399$ and $\nu = 0{\cdot}211$. These parameters are close to the values we obtained by refinement using atomic scattering factors without the dispersion correction; $\mu = 0{\cdot}399_5$ and $\nu = 0{\cdot}212_4$. AIRAPETIANTS and EFIMOVA do not state how or from what source their data are obtained. We feel that our data are probably the better.

The difference between the $Te^{(I)}$–$Te^{(I)}$ spacings for the two alloys is expected to be small; an idea of the magnitude of the error ($\cong 0{\cdot}1$ Å) may be obtained from the difference. Again, the Bi–$Te^{(I)}$ distances are expected to be similar in magnitude and, within experimental error, they are. The smaller size of the sulphur ion (1·74 Å) leads to the 1·77 Å spacing for Bi–S versus 2·07 Å for Bi–$Te^{(II)}$ The important numbers to be observed are these: (i) the large spacings for $Te^{(I)}$–$Te^{(I)}$ in both cases; (ii) the smaller value for Bi–$Te^{(I)}$ when compared with Bi–$Te^{(II)}$. Both of these features are in keeping with the bonding scheme of DRABBLE and GOODMAN, namely, that the "quintuple layer" leaves are bonded by weak $Te^{(I)}$–$Te^{(I)}$ homopolar forces and that the mixed covalent and ionic Bi–$Te^{(I)}$ bond length is shorter than the purely covalent Bi–$Te^{(II)}$ bond length.

Acknowledgements—This work was done under the sponsorship of The Thermoelectric Effects Cooperative Program. The authors wish to thank Dr. F. DONAHOE for his stimulating discussions and valuable suggestions and R. PYLE for his valuable help in experimental procedures.

REFERENCES

1. McHUGH J. P. and TILLER W. A., *Trans. Amer. Inst. Min. (Metall.) Engrs.* **215**, 651 (1959).
2. DONGES E., *Z. anorg. Chem.* **265**, 56 (1951).
3. SCHUBERT K., ANDERKO K., KLUGE M., BUSKOW H., ILSCHNER M., DORRE E. and ESSLINGER P., *Naturwissenschaften*, **40**, 269 (1953).
4. DRABBLE J. R. and GOODMAN C. H. L., *J. Phys. Chem. Solids* **5**, 142 (1958).
5. AUSTIN I. G. and SHEARD A., *J. Electron.* **3**, 236 (1957).
6. FUSCHILLO N., BIERLY J. and DONAHOE F., *J. Phys. Chem. Solids* **8**, 430 (1959).
7. HARKER D., *Z. Kristallogr.* **89**, 175 (1934).
8. FRANCOMBE M. H., *Brit. J. Appl. Phys.* **9**, 415 (1958).
9. *Handbook of Chemistry and Physics*, 33rd Ed. (edited by HODGMAN C. D.). Chemical Rubber Publ. Co., Cleveland, Ohio. (1951–1952).
10. JEHLE H., YOS J. M. and BADE W. L., *Phys. Rev.* **110**, 793 (1958); YOS J. M., *Phys. Rev.* **110**, 800 (1958).
11. AIRAPETIANTS S. V. and EFIMOVA B. A., *J. Tech. Phys., Moscow* **8**, 1632 (1958).
12. LANGE P. W., *Naturwissenschaften* **27**, 133 (1939).
13. DAUBER C. H. and TEMPLETON D. H., *Acta Cryst., Camb.* **8**, 841 (1955).

J. Phys. Chem. Solids Pergamon Press 1960. Vol. 15. pp. 17–26. Printed in Great Britain.

THERMAL PROPERTIES OF GRAPHITE, MOLYBDENUM AND TANTALUM TO THEIR DESTRUCTION TEMPERATURES*

N. S. RASOR and J. D. McCLELLAND

Atomics International, A Division of North American Aviation, Inc., Canoga Park, California

(*Received* 9 *November* 1959)

VOL. 15 1960

Abstract—Thermal expansion, specific heat and thermal conductivity have been determined from 1000°C to near the destruction temperature of molybdenum (m.p. 2620°C), tantalum (m.p. 3000°C) and four types of graphite (sublimes at 3650°C). The thermal expansion data for the materials investigated show no grossly unusual features except those due to impurity evolution. The specific heat of the metals, particularly that of molybdenum, appreciably exceeds the Dulong–Petit value. However, their thermal conductivities follow closely the Lorenz (Wiedemann–Franz) relation for free electrons. At intermediate temperatures (1000–2800°C) the thermal conductivity and specific heat of graphite show no unusual features. At higher temperatures, however, large and rapid increases in specific heat and thermal resistivity appear, which are consistent with the occurrence of thermally produced lattice defects, presumably vacant lattice sites. A defect concentration of about 0·5 atomic per cent at the sublimation temperature, and a formation energy in the vicinity of 7·7 eV, are indicated.

1. INTRODUCTION

LITTLE information exists concerning the thermal properties of materials above 1500°C. In addition, considerable disagreement may be found in the results reported by various workers in the temperature region immediately below 1500°C, making confident extrapolation of the properties to higher temperatures difficult or impossible. This void in the technical literature is due partially to the rapidly increasing experimental difficulty at higher temperatures, and partially to the relatively limited utilization of the higher temperatures in industrial technology in the past. Recent engineering requirements for materials which can function at very high temperatures demand that data for engineering evaluation be obtained in this region. Such data will also permit extension of the physics of solids into the temperature domain which distinguishes refractory solids as a unique class of materials.

In the present work, thermal expansion, specific heat and thermal conductivity have been determined from 1000°C to near the destruction temperature of molybdenum (melting point 2620°C) tantalum (melting point 3000°C) and graphite (sublimation point 3650°C). Although the data were obtained primarily for use in engineering evaluation, many of the effects observed can be interpreted in the light of existing theories of the solid state.

2. METHODS AND SPECIMEN MATERIALS

Thermal expansion and specific-heat determinations were carried out in a specially designed carbon-tube furnace. Thermal expansion was determined by measuring the distance between fiducial marks on the specimen, using filar telescopes with micrometer eyepieces. Specific heat was determined from the rate of temperature increase resulting from uniform electrical heat dissipation in the specimen.

Thermal conductivity was determined between 1000 and 2700°C by passing heat from an external heater through a cylindrical shell specimen to a heat sink along its axis. Conductivity was calculated from the radial temperature drop across the specimen and the heat flow into the heat sink. A carbon helix furnace was constructed especially

* Supported by the United States Air Force under Contract AF33(616)–2909.

Table 1. Impurity content of metal specimens

Sample	Analysis time	Impurity content (p.p.m.)											
		Si	Cr	Cu	Al	Ca	Ni	Zr	Co	Fe	Mn	Ti	C
Ta	Before	200	47	7300	170	33	900	7300	700	2100	300	0	800
	After	130	23	19	0	0	0	0	0	0	0	0	150
Mo	Before	730	3	130	0	0	0	0	0	2500	0	210	70
	After	630	3	130	0	0	0	0	0	2500	0	210	80

for this method. At temperatures above 2700°C thermal conductivity was determined from the center-to-surface radial temperature drop resulting from uniform electrical heat dissipation in a specimen rod placed in the carbon-tube furnace.

Purified argon or helium was used throughout as the furnace atmosphere. Optical and photoelectric pyrometers were used for temperature measurement. Details of the construction and operation of the experimental apparatus are given elsewhere.[1, 2]

Arc-melted unalloyed molybdenum for property determinations was obtained from Climax Molybdenum Company in the form of swaged rods 2 in. and $\frac{3}{8}$ in. diameter, having the theoretical maximum density (10·22 g/cm³.). The tantalum used was obtained from Fansteel Metallurgical Corporation, which manufactured the bulk metal by pressing and sintering powder. The sintered bar was then swaged to $\frac{3}{8}$ in. dia. rods or rolled to $\frac{1}{4}$ in. thick plates whose density (16·66 g/cm³) approached the theoretical maximum density. Table 1 gives the results of a chemical and spectroscopic analysis of the impurity content of the metal specimens as received, and after heating to near their melting temperatures in the course of the thermal property determinations.

These results are typical for all specimens used in the various property determinations. It may be seen that the composition of the molybdenum was not changed significantly as a result of heating to near its melting temperature. However, the heating substantially reduced or completely removed the impurities initially present in the tantalum.

Property determinations were made on four types of graphite with the characteristics listed in Table 2. Since the behavior of the Speer Carbon Company types is representative of the group, some of the data on the National Carbon Company types will not be presented here, but may be found elsewhere.[2] The manufacturers coöperated by delivering material only from specified locations in the bulk graphite forms, and a record was kept of the orientation of each specimen. To avoid

Table 2. Characteristics of graphite types

Manufacturer	Type	Method of forming	Anisotropy ratio*	Specific Gravity	Structure
Speer Carbon Company	3474D	extruded	1·08	1·67	Very fine-grained and uniform.
	7087	extruded	1·19	1·63	Coarse-grained with small voids and fissures.
National Carbon Company	GBH	molded	0·780	1·77	Very fine-grained and uniform.
	GBE	extruded	1·18	1·57	Extremely coarse-grained and fragile. Voids and fissures up to $\frac{1}{8}$ in. dia.

* Ratio of electrical resistivity normal and parallel to the extrusion axis or molding pressure.

VOL. 15 1960

density and orientation variations which occur near the surface of the bulk forms, specimens were taken from the center regions only.

3. THERMAL EXPANSION

The thermal expansion results obtained for molybdenum and tantalum are given in Fig. 1.

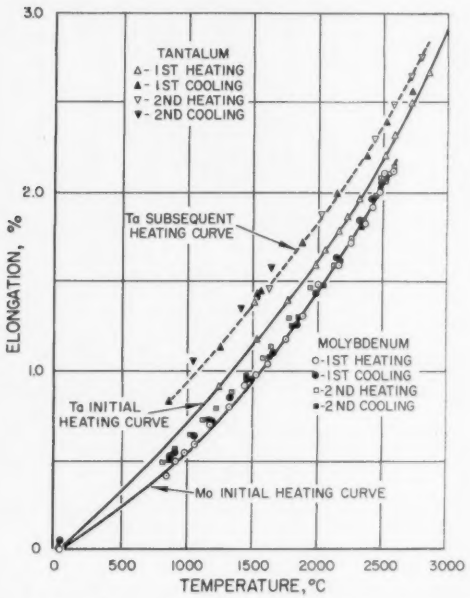

FIG. 1. Thermal expansion of molybdenum and tantalum.

Both metals show a small permanent elongation as a result of the initial heating, but no further permanent elongation was observed upon heating a second time. Measurements on an additional specimen of each metal confirmed the data shown in Fig. 1 within the experimental error. The precision of the elongation determinations was limited by refraction effects introduced by temperature variations in the sight tubes. However, readings could be consistently reproduced to within $\pm$ 0·0003 in. (0·003 per cent of the specimen length).

Above 1000°C, the solid curves in Fig. 1 representing thermal expansion upon initial heating are plots of the equation:

$$\epsilon = \frac{L-L_0}{L_0} = A+BT_e+CT_e^2 \qquad (1)$$

where L is the specimen length at temperature T, $T_e = T-20$°C (i.e. the difference between test and room temperature); L_0 is the room-temperature length; and A, B and C are constants determined from the experimental data. The coefficient of thermal expansion α may be obtained by differentiation of equation (1), yielding:

$$\alpha = \frac{d\epsilon}{dT} = B+2CT_e.$$

The values of A, B and C are tabulated in Table 3.

The thermal expansion results for two types of graphite in directions both normal and parallel to the crystallographically preferred orientation are

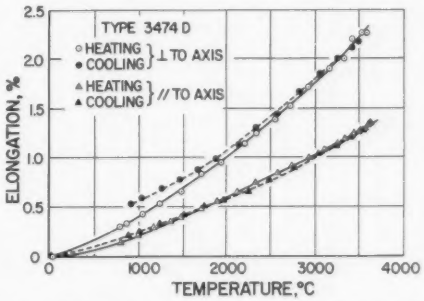

FIG. 2. Thermal expansion of type-3474D graphite.

given in Figs. 2 and 3. All types showed a slightly different behavior upon initial heating than during subsequent cooling and heating. The data above

Table 3. Expansion equation coefficients for initial heating of molybdenum and tantalum above 1000°C

	A	B (°C^{-1})	C (°C^{-2})
Molybdenum	$6{\cdot}00\times10^{-4}$	$2{\cdot}95\times10^{-6}$	$2{\cdot}00\times10^{-9}$
Tantalum	$8{\cdot}97\times10^{-4}$	$4{\cdot}80\times10^{-6}$	$1{\cdot}44\times10^{-9}$

1000°C for the direction normal to the forming pressure* upon initial heating were found to be accurately represented by the relationship:

$$\epsilon = D + ET_e + FT_e^{3/2} \qquad (2)$$

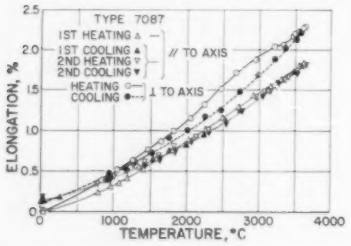

FIG. 3. Thermal expansion of type-7087 graphite.

It was not possible to represent the curves for the parallel direction by a simple analytical expression. The coefficient of thermal expansion obtained from equation (2) is:

$$\alpha = E + \frac{3}{2} FT_e^{3/2} \qquad (3)$$

Values of the constants D, E and F are tabulated in Table 4.

For a more convenient comparison of the expansion coefficient α, equation (3) is plotted in Fig. 4 for the initial heating curves, using the constants in Table 4.

* This pressure is normal to extrusion axis or parallel to molding pressure.

The metal specimens generally appeared bright and untarnished after being heated. No visible change was generally observed in the appearance

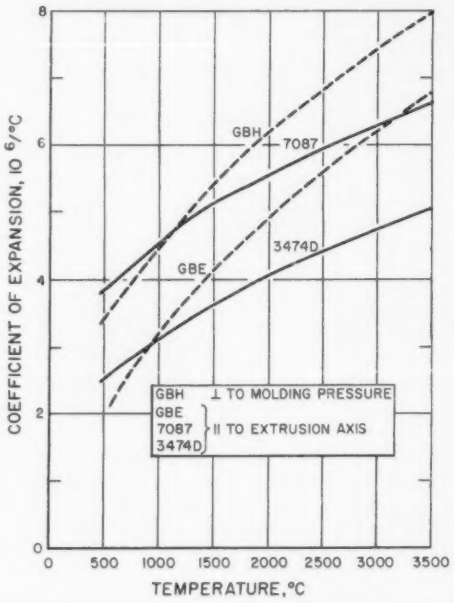

FIG. 4. Coefficient of thermal expansion of four types of graphite.

of the graphite specimens even after several excursions to the vicinity of 3650°C.

The results in Fig. 1 generally agree with the empirical rule that metals expand approximately

Table 4. Expansion equation coefficients for graphite normal to forming pressure above 1000°C

Graphite type	History	D (10^{-3})	E (10^{-7}/°C)	F (10^{-8}/°C$^{3/2}$)
7087*	Initial heating	0	21·7	4·98
3474D*		0	9·47	4·59
GBE†		0	−8·27	8·56
GBH†		0	6·95	8·18
7087*	Subsequent cooling	1·29	−2·47	8·40
3474D*		0·11	4·20	5·44
GBE†		1·10	−3·38	7·26
GBH†		1·64	4·53	7·79

* National Carbon Company types.
† Speer Carbon Company types.

VOL. 15 1960

2 per cent before melting. The smooth character of the curves and the conformity to the usual quadratic-expansion relation indicates that no major change of structure has taken place in these metals in the temperature range covered.

The *c*-axis of the graphite crystallites tends to be oriented preferentially parallel to the forming pressure in the manufactured forms. The observed larger expansion in these directions is to be expected, since this is the direction of smallest elastic modulus in graphite. It may be seen in Fig. 3 that, parallel to the forming pressure, type 7087 exhibits a curious "hump" in the expansion curve during initial heating, centered at about 2700°C. Repeat tests on different specimens confirmed the existence of such a hump in both types 7087 and GBH and indicated that the magnitude of the effect depended on the time–temperature history of the specimen during the test. Since the effect occurs in a temperature region close to or above the temperature at which the graphite was manufactured, it is likely that it is due to further graphitization (or purification) taking place as the temperature is increased above this value. The absence of the effect in the cooling portion of the data indicates that graphitization (or purification) is indeed the cause of the effect in the heating portion.

The failure of the effect to appear in types 3474D and GBE is probably due to their being subjected to a higher temperature during manufacture, resulting in graphitization being carried to completion. The absence of the hump in the expansion data for the other directions in types 7087 and GBH (specimen axis normal to the preferred orientation of the *c*-axis) is consistent with the hump being due to an irreversible change in the *c*-axis spacing. Indeed, X-ray analysis[3] showed a 0·23, 0·06, 0·04 and 0·00 per cent reduction in the *c*-axis spacing for types 7087, GBH, GBE and 3474D, respectively, due to the heating cycle. This is approximately the same magnitude as the humps in the respective expansion curves. A thermally induced change in the number of interstitial atoms between the graphitic planes could readily account for such a change.

It should be stated here that, upon heating, all specimens of type 7087 graphite evolved a considerable amount of odorous vapor, which partially condensed as a lacy white deposit. Much smaller amounts were observed for types GBH and GBE, and none for type 3474D. This correlation with the above effects therefore strongly suggests that the interstitial atoms giving rise to the above effects are impurities.

4. SPECIFIC HEAT

The specific-heat values obtained for molybdenum and tantalum are shown in Fig. 5. The

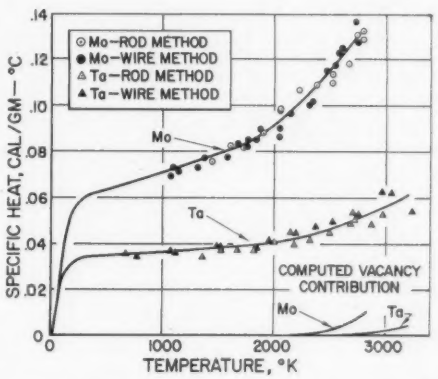

FIG. 5. Specific heat of molybdenum and tantalum.

results for the four types of graphite described in Table 2 are shown in Fig. 6. The heating cycle was repeated for the original specimen of 7087 and for an additional specimen of all types except GBE.

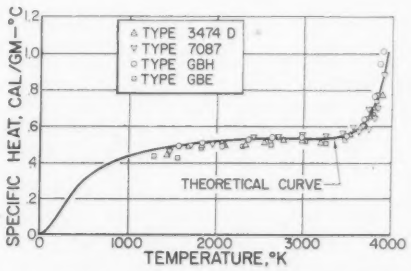

FIG. 6. Specific heat of four types of graphite.

The results agreed well with those shown in Fig. 6. The specific-heat curves obtained are estimated to be accurate to within ±5 per cent.

Due to plastic flow, all specimens sagged somewhat under their own weight near their destruction temperatures. This was only a relatively

small effect for graphite at 3700°C and molybdenum at 2600°C. However, sagging of the tantalum specimens above 2500°C was so severe as to prevent reliable data from being obtained at higher temperatures by the pulse method. A continuous-heating method,[4] using 0·040 in. dia. wires, was used to extend and confirm the data obtained on the rods, and the results are included in Fig. 5.

The curves below 1600°K in Fig. 5, and below 1100°K in Fig. 6, represent previously published experimental data[5] and may be seen to be in satisfactory agreement with the present results. However, the present results are in serious disagreement with published values obtained[6] by extrapolation into the previously unexplored high-temperature region.

According to the Dulong–Petit law, the specific heat at high temperatures should approach a fairly constant value of ~6 cal/mole°C (~0·062 cal/g °C for molybdenum, 0·033 for tantalum and 0·50 for graphite). The amount by which molybdenum and tantalum exceed this value is much larger than can be explained by the difference in specific heats at constant pressure and volume. Large deviations, such as are observed here, are commonly attributed to an electronic contribution to the specific heat, which should be linearly dependent on temperature for a uniform distribution of electronic energy states. A large, rapidly increasing specific-heat behavior, similar to that observed here for molybdenum, has been reported[7] for chromium, which has an electronic structure quite similar to that of molybdenum. The non-linearity occurring at the higher temperatures in Fig. 5 may be due in part to the thermal formation of lattice imperfections, to be discussed later.

It may be clearly seen from Fig. 6 that the specific heats of the four graphite specimens investigated are identical within the experimental error. The fact that the values obtained for type GBE appear consistently lower than those for the other types is probably due to the large inhomogeneity of this type. The local density at the point of property determination was probably different from the average density as determined from the bulk sample.

The conformity among the various types and the approach to a saturation value above 2200°C (the higher Debye temperature for graphite) are in excellent agreement with the Dulong–Petit law, indicating little electronic contribution.

The most striking feature of the data is the abrupt but reversible rise in specific heat above 3300°C. Analysis of the temperature dependence of the specific heat in excess of the observed saturation value indicates that it is due to a thermally activated process; i.e. it is proportional to $\exp(-E/kT)$, where k is the Boltzmann constant. The activation energy E appears to be in the vicinity of 7·7 eV/atom, which leads to two possible interpretations of the effect. Since 7·7 eV is approximately equal to the heat of vaporization for graphite, it is possible that the effect may be spurious and related to the rapid rise in vapor pressure that occurs at these temperatures. However, a detailed analysis of the transient diffusion of carbon vapor from the specimen surface during the heating interval indicates that heat is not removed by vaporization at a rate sufficiently large to account for the observed effect. Alternatively, the effect may be due to the reversible thermal formation of lattice defects that must exist in an equilibrium concentration characterized by an activation energy equal to their energy of formation. Since the activation energy observed is approximately the heat of vaporization of monatomic carbon[8] (7·4 eV), elementary considerations suggest that the defects produced are vacant lattice sites (vacancies).

An effect similar to the one observed here has been reported[9] in the specific heat of sodium, lead and aluminum near their melting temperatures and ascribed to vacancy formation. Since the vacancy formation energy in these metals is in the vicinity of only 1 eV, the effect is much smaller in magnitude and spread over a proportionately larger temperature interval than in the case of graphite. The excess area under the specific-heat curve resulting from the present effect is equal to an energy which is assumed to be the total energy stored in the vacancies at a given temperature. Therefore, using the known formation energy per vacancy and the magnitude of this excess area, the vacancy concentration may be computed. For lead and aluminum, the concentration reported was 0·2 atomic per cent at the melting temperatures, which is quite reasonable according to the vacancy theory of melting. If the excess area under the present specific-heat curve for graphite is divided

VOL. 15 1960

by 7·7 eV, the concentration obtained is 0·5 atomic per cent at the sublimation temperature, 3650°C. Thus, if it can be assumed that sublimation is equivalent to melting as an indication of the instability of the solid phase, this result is strong confirmation that vacancy formation is responsible for the observed abrupt increase in the specific heat. The equation which includes an exponential vacancy formation contribution to the heat content, assuming a 7·7 eV formation energy and 0·5 atomic per cent vacancies at 3650°C, is:

$$C_p = 0{\cdot}52 + \frac{(4{\cdot}7\times 10^{16})}{T^2} \times$$

$$\times \exp[-8{\cdot}9\times 10^4/T]\text{cal/g-°C}, \qquad (4)$$

where T is in °K. The curve in Fig. 6 above 2200°C is a plot of this equation and may be seen to represent the observed data adequately.

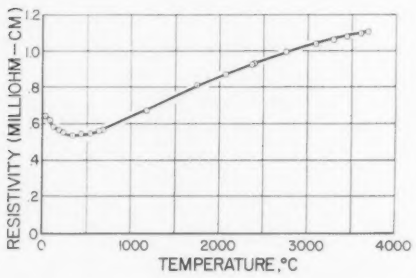

FIG. 7. Electrical resistivity of type-3474D graphite parallel to extrusion axis.

Vacancy formation should also contribute to the specific heat of molybdenum and tantalum. However, theoretical computations using reasonable formation energies for these metals (between 2 and 3 eV) and vacancy concentrations (0·3 per cent at melting points) indicate that vacancy formation could account for only a small part of the observed excess specific heat, as may be seen in Fig. 5. Thus, except possibly for the slight non-linearity at the higher temperatures, the high values observed are probably due principally to the electronic specific-heat contribution.

Electrical resistivity of the specimens was determined as a by-product of the specific-heat determinations. The resistivities obtained for tantalum and molybdenum were in satisfactory agreement with published values[10] and thus will not be repeated here. The resistivity observed for type-3474D graphite, shown in Fig. 7, is typical of that observed for the other types.

It should be emphasized, however, that the few per cent deviation from a linear extrapolation above 2800°C may result from spurious thermionic-emission effects. The resistivity data are presented here primarily because of their significance in relation to the interpretation of the specific-heat and thermal conductivity data. Thus, the smooth character of the resistivity curve indicates that the large abrupt changes observed in the thermal properties above 3000°C are not the result of a spurious change in electrical power input to the specimen.

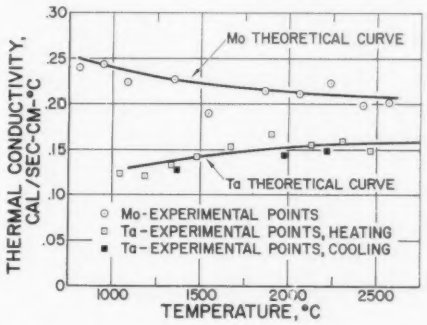

FIG. 8. Thermal conductivity of molybdenum and tantalum.

5. THERMAL CONDUCTIVITY

The thermal conductivities of molybdenum and tantalum to 2500°C, obtained by the external-heating method, are shown in Fig. 8. The thermal conductivities of two types of graphite are given in Figs. 9 and 10. For comparison, data obtained[11] from the observation of the temperatures at the bottom of small cavities in a carbon arc electrode were normalized to the present data at 3300°C and are shown in Fig. 9.

The thermal-conductivity curves obtained by means of the external-heating method have been estimated to be accurate to within ±5 per cent, while those obtained by the direct-heating method have an estimated accuracy of ±8 per cent. However, it should be emphasized that the time available for completion of the project did not allow

adequate development of the direct-heating method. The data presented are those for which the required experimental conditions were indeed

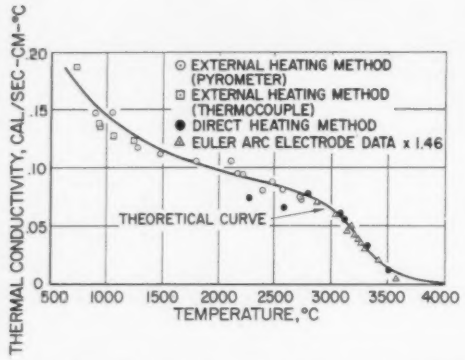

FIG. 9. Thermal conductivity of type-3474D graphite normal to extrusion axis.

achieved. Nevertheless, time did not permit repeat measurements to be made to obtain the same degree of confidence that characterizes the other

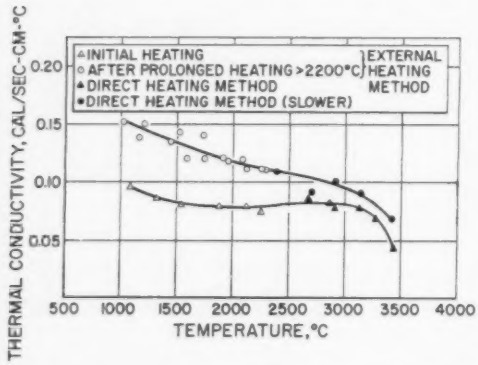

FIG. 10. Thermal conductivity of type-7087 graphite normal to extrusion axis.

data reported here. Therefore, the thermal conductivity values for graphite above 2700°C need confirmation by further work.

The theoretical curves in Fig. 8 were computed from the Lorenz (Wiedemann–Franz) relationship:

$$K = A\frac{T}{\rho} \qquad (5)$$

using the free-electron value for the constant $A = \pi^2k^2/3e^2 = 2{\cdot}45 \times 10^{-8}\ \mathrm{W\Omega/(^\circ C)^2}$, and the published[10] dependence of the electrical resistivity ρ on the absolute temperature T. As may be seen in Fig. 8, the experimentally determined thermal conductivities of molybdenum and tantalum quite accurately obey this relationship over this temperature region. This allows a fairly confident extrapolation of the data for tantalum to higher temperatures.

Since methods requiring radial heat flow were used, the thermal conductivity of graphite was determined only in the direction normal to the extrusion axis or molding pressure. However, the anisotropy ratio for the electrical resistivity is approximately the same as that for the thermal conductivity. Thus, the thermal conductivity in the direction normal to that reported may be estimated by multiplying the reported conductivities by the anisotropy ratio listed under the corresponding type in Table 2.

The Lorenz relation cited above is based on the conduction of heat by electrons and is generally valid only for good metals. Graphite, on the other hand, like most non-metals, conducts heat principally by elastic lattice waves.[12] The elementary theory of lattice conduction predicts that at high temperatures, where thermal conduction is limited principally by the mutual scattering of lattice waves, the thermal resistivity (reciprocal conductivity) should show a linear temperature dependence. The curve below 2700°C in Fig. 9 is based on this prediction and corresponds qualitatively with the observed behavior of types 3474D and GBE in this region. However, types 7087 and GBH show an irreversible increase in conductivity upon initial heating (Fig. 10). It should be recalled that these are the types which showed impurity or graphitization effects in the thermal expansion data. Since lattice thermal conductivity is sensitive to lattice imperfection, the removal of imperfections and impurities is probably responsible for the observed irreversible increase. Thus the thermal conductivity of types GBH and 7087 at temperatures above 1600°C depends on the thermal history of these materials. Since such irreversible behavior was not observed in types GBE and 3474D, their conductivities are probably unique and represent the intrinsic behavior of polycrystalline graphite at these temperatures.

VOL. 15 1960

Above 2700°C the conductivity may be seen to decrease rapidly, falling by about an order of magnitude in a relatively small temperature interval. Analysis of the temperature dependence of this very large increase in thermal resistivity indicates that it is a thermally activated process again characterized by an activation energy in the vicinity of 7·7 eV/atom. As discussed previously in relation to the very similar effect in the specific-heat data, this leads to two possible interpretations of the cause of the effect: vaporization or vacancy formation. However, in this case vaporization effects would cause the radial temperature drop to appear too small, which is in the wrong direction to explain the observed effect. On the other hand, lattice imperfections introduced by radiation damage have been observed[13] to increase the thermal resistivity of graphite by as much as several orders of magnitude, due to increased scattering of lattice waves. It is logical, therefore, to expect the thermal formation of vacancies postulated to explain the specific-heat anomaly to be accompanied by a proportionate increase in thermal resistivity such as is indeed observed. Thus, combining the linear low-temperature thermal resistivity behavior and the exponential contribution due to vacancy formation with a 7·7 eV formation energy, the following theoretical equation is obtained to fit the experimental data for type 3474D:

$$\frac{1}{K} = 2{\cdot}4+(3{\cdot}46\times 10^{-3})\,T+(8{\cdot}5\times 10^{11})\times \times \exp\left[-8{\cdot}9\times 10^{4}/T\right]\frac{\text{cm-sec-°C}}{\text{cal}} \qquad (6)$$

where T is in °K. The curve in Fig. 9 is a plot of this equation and may be seen to represent adequately the experimental data. The thermal resistivity per vacancy, r, may readily be computed from the observed heat capacity and conductivity data to be:

$$r \simeq \frac{bE^2}{fR} = 2{\cdot}4\times 10^{4}\ \frac{\text{cm-sec-°C}}{\text{cal}}$$

per mole fraction of vacancies, where b and f are the coefficients of the exponential terms in equations (6) and (4), respectively, and R is the gas constant. The thermal resistivity per vacancy may also be estimated from the observed[13] initial rate of change of thermal resistivity of graphite with radiation damage (~0·4 cm-sec-°C/cal per MW-day), and the corresponding theoretical value[14] of the fraction of atoms displaced by a given irradiation (~$0{\cdot}5\times 10^{-4}$ mole fraction per MW-day). The value thus obtained from radiation-damage data is estimated to be approximately:

$$r \simeq 0{\cdot}8\times 10^{4}\ \frac{\text{cm-sec-°C}}{\text{cal}}$$

per mole fraction of vacancies. However, since this value is the change in room-temperature resistivity, the change in resistivity at elevated temperatures should be somewhat larger, as is indeed observed above, due to the more efficient scattering of lattice waves at shorter average wavelengths. The magnitude of this correction probably does not exceed the combined uncertainty in the approximations, so that further analysis does not seem warranted. Nevertheless, the agreement, within an order of magnitude, of the thermal resistivity change values computed from entirely independent considerations again provides strong confirmation that the thermal formation of lattice defects is responsible for the observed abrupt changes in heat capacity and conductivity above 2700°C.

The behavior of the thermal conductivity of graphite above 2700°C obtained by EULER[11], using a carbon arc method, is in excellent agreement with that observed by the present method. This is strong confirmation that the rapid drop in conductivity is not spurious, since the methods used are entirely different. The expansion data obtained at these temperatures (Section 3) indicate that the large irreversible drop in density, postulated by EULER to explain the effect, does not occur. Also, direct bulk-density determinations by weighing after heating showed that no detectable change had occurred.

The absence of a corresponding decrease in both the thermal and the electrical conductivities of the metals near their melting points indicates that thermal scattering of conduction electrons predominates over scattering by thermally produced vacancies. The same conclusion is reached concerning the absence of a corresponding decrease in the electrical conductivity of graphite (Fig. 7).

6. CONCLUSIONS

The thermal expansion data for most of the materials investigated show no grossly unusual features. An exception is the irreversible behavior of two types of graphite near 2700°C in a direction suggesting the removal of interlayer impurity atoms from the graphite lattice.

The specific heat of the metals, particularly molybdenum, has been found to exceed the Dulong–Petit value by a large amount as the melting temperature is approached. The thermal conductivities of tantalum and molybdenum have been found to obey the Lorenz (Wiedemann–Franz) relation closely to near their melting temperatures.

Up to 2700°C the specific heat of graphite saturates near the Dulong–Petit value and, except for irreversible graphitization effects, the thermal conductivity behaves in accordance with simple lattice-conduction theory. However, at higher temperatures the specific heat and thermal resistivity experience large and abrupt increases which may be both qualitatively and quantitatively described as due to thermal formation of vacant lattice sites. The changes in both properties are consistent with an energy of formation of $7{\cdot}7 \pm 0{\cdot}5$ eV for the vacancies and a vacancy concentration of about 0·5 atomic per cent at the sublimation temperature (3650°C). This behavior may be of critical engineering significance, since, if volume-heated electrically or by nuclear fuel, graphite may be unstable as a heat-transfer medium above 3000°C. An increase in temperature leads to a large drop in thermal conductivity and diffusivity, possibly leading to further increase in temperature and so on until the vapor pressure causes disintegration. The observed effects of vacancy formation on the thermal properties of graphite should also appear in other lattice heat conductors having high vacancy-formation energies.

The results obtained show the general character of the observed properties of graphite, molybdenum and tantalum to the accuracy required for engineering analysis. The existence of large, previously unknown effects in these materials has been established, and further work is indicated to achieve the detailed understanding required for their complete description. Nevertheless, the apparent agreement between the observed data and contemporary theories of the solid state is gratifying and gives an indication of the reliability of the data.

Acknowledgements—The following personnel contributed directly to the technical effort: R. C. DAHLEEN, E. H. ZEHMS, W. E. WALTERS, D. R. WARNER and C. BOTKER. The writers gratefully acknowledge the interest and helpful suggestions of the members of the Solid State Physics Group headed by D. BOWEN.

This report covers work conducted from March 1955 to June 1956 administered under the direction of the Materials Laboratory, Directorate of Research, Wright Air Development Center, with Captain S. V. ZALESKI and Lt. MYRON W. BELAGA of the Materials Laboratory, Research Division, acting as project engineers.

REFERENCES

1. RASOR N. S. and MCCLELLAND J. D., *Rev. Sci. Instrum.* **31**, 595 (1960).
2. RASOR N. S. and MCCLELLAND J. D., *Wright Air Development Center Tech. Rep.* 56–400, Part I (Nov. 1956).
3. WALKER P. L. and IMPERIAL G., *Nature, Lond.* **180**, 1184 (1957).
4. AVRAMESCU A., *Z. techn. Phys.* **20**, 213 (1939).
5. SIMON F. and ZEIDLER W., *Z. phys. Chem.* **123**, 383 (1926); JAEGER F. M. and VEENSTRA W. A., *Rev. Trav. Chim. Pays-Bas* **53**, 677 (1934); CLUSIUS K. and LOSA C. G., *Z. Naturf.* **10A**, 939 (1955); MAGNUS A., *Ann. Phys., Lpz.* **70**, 303 (1923).
6. STULL D. R. and SINKE G. C., *Thermodynamic Properties of the Elements*, American Chemical Society, Washington D.C. (1956).
7. ARMSTRONG L. D. and GRAYSON-SMITH H., *Canad. J. Res.* **28A**, 51 (1950).
8. THORN R. J. and WINSLOW G. H., *J. Chem. Phys.* **26**, 186 (1957).
9. POCHAPSKY T. E., *Acta Met.* **1**, 747 (1953).
10. WORTHING A. G., *Phys. Rev.* **28**, 190 (1926); MALTER L. and LANGMUIR D. B., *Phys. Rev.* **55**, 745 (1939).
11. EULER J., *Naturwissenschaften* **39**, 568 (1952).
12. TYLER W. W. and WILSON A. C., Jr., *Phys. Rev.* **89**, 870 (1953).
13. SMITH A. W. and RASOR N. S., *Phys. Rev.* **104**, 885 (1956).
14. HENNIG G. R. and HOVE J. E., *Proc. Internat. Conf. Peaceful Uses of Atomic Energy* **7**, 666 (1956).

J. Phys. Chem. Solids Pergamon Press 1960. Vol. 15. pp. 27–32. Printed in Great Britain.

EFFECTS OF SOLID SOLUTION OF In_2Te_3 WITH $A^{II}B^{VI}$ TELLURIDES

J. C. WOOLLEY and B. RAY

Department of Physics, University of Nottingham, England

(*Received* 20 *October* 1959)

Abstract—Alloys have been produced for the three systems In_2Te_3–CdTe, In_2Te_3–ZnTe and In_2Te_3–HgTe and annealed to obtain equilibrium conditions. The ranges of solid solution, the variation of lattice parameter with composition and the ranges and types of ordering that occur have been investigated for each system. For the systems In_2Te_3–CdTe and In_2Te_3–ZnTe, the variation of optical energy gap, E_g, with composition have been determined by infrared transmission measurements, and the effects on E_g of solid solution and ordering have been observed.

VOL. 15 1960

1. INTRODUCTION

As In_2Te_3 possesses a zinc-blende structure, with lattice vacancies on the indium sublattice, it is possible to obtain solid solution between this compound and the $A^{II}B^{VI}$ tellurides which have the zinc-blende structure. Little investigation of the physical properties of the resulting alloy semiconductors has been reported, although some crystallographic work has been carried out. HAHN *et al.*[1] have investigated the variation of lattice parameter in the systems In_2Te_3–CdTe and In_2Te_3–ZnTe, although the parameter values given are rather approximate for use in determining the composition of alloys in these systems, and they have investigated a very limited range of the system In_2Te_3–HgTe. They report the occurrence of chalcopyrite-type ordering in each system at the composition In_2Te_3ATe, where A is Cd, Hg or Zn, with some degree of ordering of this type occurring over a range of composition around this stoichiometric value. BUSCH *et al.*[2] have investigated one or two of these chalcopyrite-type materials, shown to be semiconductors, and have measured the thermal energy gap at the stoichiometric composition by electrical conductivity methods.

In the work described here, the variation of lattice parameter as a function of composition has been accurately determined for the three systems In_2Te_3 with CdTe, HgTe and ZnTe, respectively, and hence the range of solid solution and range of ordering have been defined. For the In_2Te_3–CdTe and In_2Te_3–ZnTe systems, the variation of optical energy gap, E_g, as a function of composition has been determined by infrared absorption measurements.

2. PREPARATION OF ALLOYS AND X-RAY WORK

The four compounds concerned were each prepared by synthesis from the elements in vacuum in sealed quartz tubes, and then each of the alloys was prepared similarly from the appropriate compounds. The elements used were initially purified by distillation, starting from commercially pure materials. The alloys were annealed at a suitable temperature until equilibrium was attained, the temperature being always below that of the lower-melting-point compound concerned; X-ray photographs were used to indicate the attainment of equilibrium. (In all the X-ray work, Cu$K\alpha$ radiation and a 9-cm Unicam camera were used.) Details of the times and temperatures of annealing will be given separately for each alloy system in Section 4.

As indicated previously,[3] in order to reduce preferential loss of any element to a minimum, trial alloys were first investigated in order to determine the approximate time of annealing required. Further alloys could then be annealed for this length of time without being disturbed. After all measurements had been made, specimen alloys

were chemically analysed. It was found that in the case of the In_2Te_3–CdTe and In_2Te_3–ZnTe systems, the deviation from the weighed-out composition was $\gtrsim 2$ molecular per cent. In the case of the In_2Te_3–HgTe system, a similar accuracy was attained at the low-mercury end of the system, but for high-mercury alloys, deviations of 5–7 molecular per cent occurred, always corresponding to loss of mercury. These latter inaccuracies are indicated on the appropriate graph.

3. OPTICAL MEASUREMENTS

In the systems In_2Te_3–CdTe and In_2Te_3–ZnTe, measurements were made of the percentage transmission through various specimens as a function of wavelength. For this purpose, sections cut from ingots were ground to a parallel-sided plate and polished with diamond paste, giving specimens of thickness in the range 80–170μ. These were then used for normal transmission measurement with a converted Halle spectrometer, using a single beam and a calcium fluoride prism. The detector was a Schwartz thermocouple, the output from which was amplified by a Barr and Stroud thermocouple amplifier, the incident beam to the specimen being chopped at 5 c/s to give the necessary modulation.

To interpret these results obtained with polycrystalline specimens of unknown reflectivity, for each specimen a graph of log (I_0/I) vs. λ was plotted, where I_0 is the incident intensity and I the corresponding transmitted intensity. Assuming that the approximate equation $I = I_0B\exp(-kt)$ can be used for the transmitted intensity, and assuming also that over the range concerned B is reasonably independent of λ, this gives:

$$\log\left(\frac{I_0}{I}\right)_E - \log\left(\frac{I_0}{I}\right)_B = \frac{k_E - k_B}{2{\cdot}303}t \qquad (1)$$

where the subscript E indicates values at the wavelength λ_E, the absorption edge, and subscript B the background values where, in these cases, $\lambda = 2$–3μ. An arbitrary choice of definition of λ_E was made so that the LHS of equation (1) was equal to 1·5 when $t = 100\mu$. This gave a value of $k_E - k_B$ to be used to calculate log $(I_0/I)_E$ − log $(I_0/I)_B$ with specimens of other thicknesses and corresponded to a change in absorption coefficient of approximately 350 cm^{-1}. Using this value, λ_E and a corresponding value of energy gap, E_g, was determined for each specimen.

4. RESULTS

(a) In_2Te_3–CdTe *System*

The alloys of this system were annealed at 665°C and appeared to be in equilibrium after 12 days' annealing, although alloys in the miscibility gap mentioned below were further annealed for some 21 days to ensure that equilibrium was attained. The variation of lattice parameter, a_0, as a function of composition is shown in Fig. 1. It is seen that solid solution occurs over a large range of composition, but that a miscibility gap occurs in the range 50–72 molecular per cent In_2Te_3.*

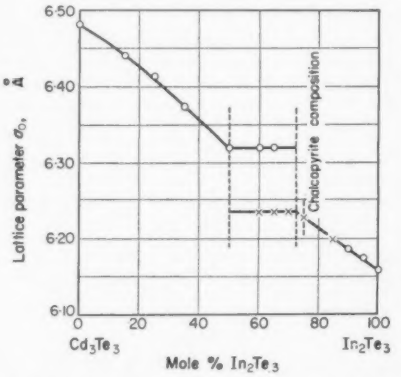

FIG. 1. Variation of lattice parameter a_0 as a function of composition in the system In_2Te_3–CdTe.
⊙ Disordered zinc-blende structure.
× Ordered chalcopyrite structure.

The alloys in the range 0–50 molecular per cent In_2Te_3 show the normal zinc-blende structure. Chalcopyrite-type ordering occurs from the limit of solid solution, viz. 72 molecular per cent In_2Te_3, to a point between 85 and 90 molecular per cent In_2Te_3. Although these alloys have a tetragonal structure, the c/a ratio was found to be 2 within the limits of experimental error, and so a pseudo-cubic a_0 parameter has been plotted for these alloys in Fig. 1. Accurate comparison with the results of HAHN *et al.*[1] is difficult owing to

* In calculating the molecular percentage in all systems composed of one $A^{II}B^{VI}$ compound and one $A_2^{III}B_3^{VI}$ compound, the molecules have been taken as $A_3^{II}B_3^{VI}$ amd $A_2^{III}B_3^{VI}$.

the very approximate form in which those results are presented. It would appear, however, that there is no serious disagreement between the values of lattice parameter and range of miscibility gap presented here and those given by HAHN.

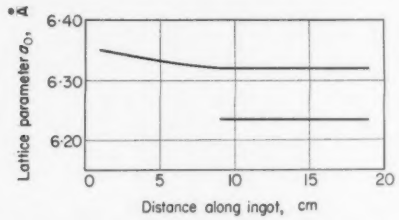

FIG. 2. Variation of lattice parameter a_0 as a function of distance along a directionally frozen ingot of mean composition 60 molecular per cent In_2Te_3, 40 molecular per cent Cd_3Te_3.

Although no attempt was made to determine the form of the solidus curve for the system, it was possible to determine whether the miscibility gap corresponded to a peritectic or a eutectic break in the solidus by means of a simple directional-freezing experiment. An ingot of mean composition 60 molecular per cent In_2Te_3 and some 20 cm in length was cooled in a temperature gradient so that the freezing surface slowly moved from one end of the ingot to the other. Sections were then taken at 1-cm intervals along the ingot and X-rayed. The variation of lattice parameter as a function of distance along the ingot was of the form shown in Fig. 2. This type of result, showing single-phase material at the end of the ingot which froze first and then two-phase material at the end which froze later, is typical of eutectic behaviour and indicates that the break in the In_2Te_3–CdTe system is a eutectic. The eutectic composition was estimated from these results to be of the order of 65 molecular per cent In_2Te_3.

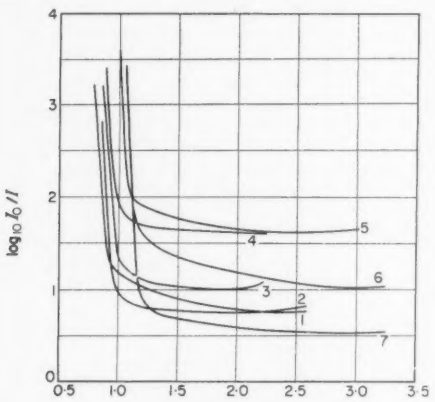

Specimen	Composition mol.-% In_2Te_3	mol.-% Cd_3Te_3	Thickness μ
1	0	100	132
2	15	85	153
3	25	75	170
4	50	50	100
5	75	25	125
6	85	15	139
7	100	0	88

FIG. 3. Variation of $\log_{10}(I_0/I)$ as a function of wavelength for transmission measurements on various alloys of the system In_2Te_3–CdTe.

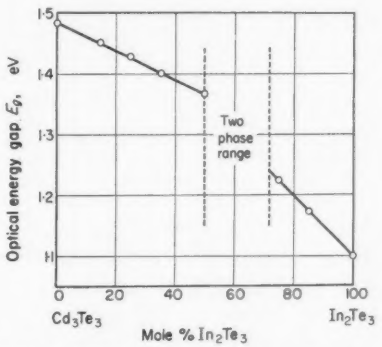

FIG. 4. Variation of optical energy gap, E_g, as a function of composition in the system In_2Te_3–CdTe.

Optical measurements were made, as indicated in Section 3, on alloys of this system which had been annealed to equilibrium. The curves of log (I_0/I) vs. λ for typical alloys are shown in Fig. 3. From these curves the effective values of E_g, as defined in Section 3, were determined, and the variation of E_g with composition is shown in Fig. 4.

Comparison with the results of BUSCH *et al.*[2] is possible for one composition, viz. $CdIn_2Te_4$, although it must be noted that the value of $E_g = 0{\cdot}9$ eV given by BUSCH for this material was obtained from electrical conductivity measurements. The corresponding value taken from the optical results shown in Fig. 4 is 1·23 eV.

(b) In_2Te_3–ZnTe *System*

These alloys were annealed at 665°C for 7 days, when all appeared to be single phase. The variation

of lattice parameter, a_0, as a function of composition is shown in Fig. 5. Once again, chalcopyrite-type ordering occurs over a range of composition from approximately 60 to 90 molecular per cent

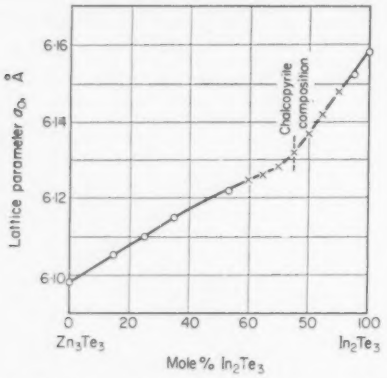

FIG. 5. Variation of lattice parameter a_0 as a function of composition in the system In_2Te_3–ZnTe.
○ Disordered zinc-blende structure.
× Ordered chalcopyrite structure.

In_2Te_3, but again the c/a ratio is 2 within the limits of experimental error, and so a pseudo-cubic parameter a_0 has been plotted in Fig. 5.

As indicated above, the approximate nature of the results of HAHN *et al.*[1] makes comparison difficult. There would appear to be no serious discrepancy in general for the lattice-parameter values, but at one composition (60 molecular per cent In_2Te_3–40 molecular per cent Zn_3Te_3) HAHN seems to indicate two-phase behaviour, whereas the present results indicate the occurrence of single-phase equilibrium throughout the whole range of composition.

Optical measurements were made for alloys of the system, and the variation of $\log(I_0/I)$ vs. λ for typical alloys is shown in Fig. 6. These have been used to determine E_g, and the variation of E_g as a function of composition is shown in Fig. 7. The value of $E_g = 1{\cdot}3$ eV for the composition $ZnIn_2Te_4$ from these optical measurements is to be compared with a value of 1·4 eV given by BUSCH *et al.*[2] from electrical conductivity work.

(c) In_2Te_3–HgTe *System*

Alloys of this system were annealed for approximately 14 days in the temperature range 620–650°C. Equilibrium was obtained in this time, but,

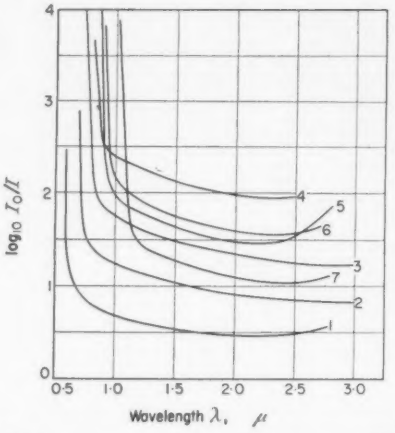

Specimen	Composition mol.-% In_2Te_3	mol.-% Zn_3Te_3	Thickness μ
1	0	100	99
2	15	85	100
3	25	75	108
4	35	65	134
5	50	50	126
6	65	35	137
7	85	15	70

FIG. 6. Variation of $\log_{10}(I_0/I)$ as a function of wavelength for transmission measurements on various alloys of the system In_2Te_3–ZnTe.

as previously indicated by HAHN, *et al.*[1], there was the problem of loss of mercury from alloys of high mercury content. Chemical analysis indicated that even with the precautions mentioned in Section 2, losses of mercury corresponding to 5–7 molecular per cent could occur for alloys containing <40

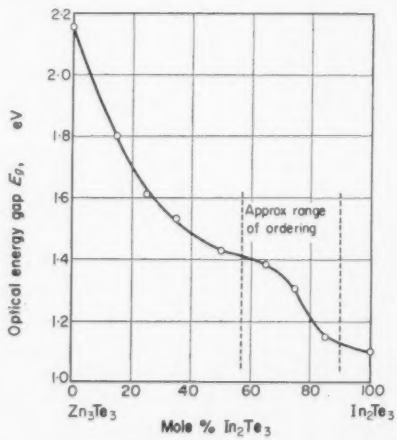

FIG. 7. Variation of optical energy gap E_g as a function of composition in the system In_2Te_3–ZnTe.

molecular per cent In_2Te_3. Fig. 8 shows the variation of cubic or pseudo-cubic lattice parameter, a_0 as a function of composition for the nominal composition of the alloys, with an indication of the possible spread of composition for the high-mercury alloys.

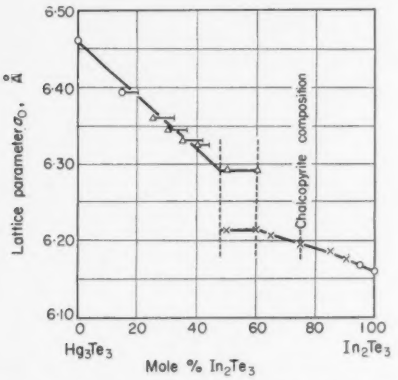

FIG. 8. Variation of lattice parameter a_0 as a function of composition in the system In_2Te_3–HgTe.

⊙ Disordered zinc-blende structure.
× Ordered chalcopyrite structure.
△ Ordered structure as yet undetermined.

Once again a miscibility gap occurs, the diagram being two-phase over a range from 60 to approximately 48 molecular per cent In_2Te_3. On the In_2Te_3 side of this gap, normal chalcopyrite-type ordering occurs over a range from 60 to approximately 90 molecular per cent In_2Te_3. Here again a pseudo-cubic parameter, a_0, is plotted, since $c/a = 2$. On the HgTe side of the miscibility gap, a new type of ordered structure is obtained. This structure, like the chalcopyrite, can be allocated a pseudo-cubic a_0, and this is plotted in Fig. 8. Preliminary work indicates that this ordered structure may be orthorhombic, but further work has to be carried out. The problem is similar to the problem of ordering in In_2Te_3 itself, discussed elsewhere.[4]

5. DISCUSSION

In the case of alloy semiconductors of the type considered here, it is of interest from both academic and technological viewpoints to know the variation of such semiconductor parameters as energy gap, etc., as a function of composition. The system germanium–silicon is so far the only one to be studied in any detail, and HERMAN and his co-workers[5,6] have shown, in the case of the optical energy gap, E_g, of these alloys, that although E_g varies continuously with composition, the graph of E_g vs. composition has two definite parts, the alloys in one part showing a germanium-type band structure, while those in the other part show a silicon-type band structure. Optical-energy-gap measurements have been made on other alloy systems, e.g. InAs–InP,[7] InAs–GaAs,[8] InSb–GaSb,[9] CdTe–HgTe,[10] CdTe–ZnTe,[11] but in no case are sufficient data available for an analysis similar to that for the germanium–silicon system to be carried out.

The systems described here differ in two respects from those mentioned above in that (*a*) ordering occurs over a certain range of composition and (*b*) in two cases a miscibility gap occurs. Both (*a*) and (*b*) can have a considerable effect on the form of variation of E_g (and other parameters) with composition. In investigating (*b*) it is important to bear in mind the difficulty of obtaining true equilibrium conditions in certain systems, owing to very low diffusion rates. In such cases, non-equilibrium material may be misinterpreted as being in two-phase equilibrium. Such effects are very important in alloys of $A^{III}B^{V}$ compounds,[12] but would appear to be less of a problem in the alloys discussed here.

In the In_2Te_3–CdTe system, there is a relatively wide miscibility gap giving two separate ranges in which solid solution occurs. In the range at the CdTe end of the system, where no ordering occurs and there is normal solid solution, the curve of a_0 vs. composition deviates little from linearity, while E_g varies linearly with composition over the whole range concerned (up to 50 molecular per cent In_2Te_3). At the In_2Te_3 end of the system, where chalcopyrite-type ordering occurs, again both a_0 and E_g show linear variations with composition. It would appear in this case that ordering has little effect on these parameters, although it should be noted that the range of ordering is rather limited, extending over only 2 molecular per cent (to 73 per cent In_2Te_3) from the stoichiometric ordered structure (75 per cent In_2Te_3) in one direction, while at 85 molecular per cent In_2Te_3 X-ray results indicate only a very limited degree of ordering.

In the In_2Te_3–ZnTe system, where solid solution occurs throughout the composition range, the

variation of a_0 with composition is, at the ends of the system, similar to that for the In_2Te_3–CdTe system. In this case, there is an extensive range in which ordering occurs, and the two practically linear parts of the graph are accommodated by a relatively abrupt change in slope at a composition close to that of the stoichiometric ordering composition (75 molecular per cent In_2Te_3). The existence of ordering gives a peculiar form to the E_g vs. composition curve. In the two disordered ranges, a smooth monotonic curve is obtained, which might easily be extrapolated to give a single disordered curve for the whole range of composition. Over the ordered range, however, this curve is considerably modified, giving a region in which the graph has a curvature opposite to that for the disordered ranges. Thus, in this system, the ordering has considerable effect upon the variation of both a_0 and E_g with composition.

The In_2Te_3–HgTe results are complicated by the occurrence of a miscibility gap and two types of ordering, each extending over a considerable range of composition, and also by the practical difficulties at the HgTe end of the system. At the In_2Te_3 end of the system, the variation of a_0 is of interest, as the occurrence of ordering in this case causes a considerable change in the slope of the a_0 vs. composition graph. It is hoped to carry out further work at least at this end of this system.

Acknowledgements—We are indebted to Dr. M. E. HAINE, of Siemens Edison Swan, Ltd., for a maintenance grant to one of us (B.R.) and to Dr. O. SIMPSON, of the Services Electronics Research Laboratory, Baldock, for the loan of the infrared spectrometer. We also wish to thank Mr. F. G. STICKLAND, of Siemens Edison Swan, Ltd., for the chemical analysis of the specimens.

REFERENCES

1. HAHN H., FRANK G., KLINGLER W., STÖRGER A. D. and STÖRGER G., *Z. anorg. Chem.* **279**, 241 (1955).
2. BUSCH G., MOOSER E. and PEARSON W. B., *Helv. Phys. Acta.* **29**, 192 (1956).
3. WOOLLEY J. C. and RAY B., *J. Phys. Chem. Solids* **13**, 151 (1960).
4. WOOLLEY J. C., PAMPLIN B. R. and HOLMES P. J., *J. Less Common Metals* **1**, 362 (1959).
5. BRAUNSTEIN R., MOORE A. R. and HERMAN F., *Phys. Rev.* **109**, 695 (1958).
6. HERMAN F., GLICKSMAN M. and PARMENTER R. H., *Progress in Semiconductors* Vol. 2. p. 1. Heywood and Co. London (1957).
7. FOLBERTH O. G., *Z. Naturf.* **10**A, 502 (1955).
8. ABRAHAMS M. S., BRAUNSTEIN R. and ROSI F. D., *J. Phys. Chem. Solids* **10**, 204 (1959).
9. WOOLLEY J. C., EVANS J. A. and GILLETT C. M., *Proc. Phys. Soc. Lond.* **74**, 244 (1959).
10. LAWSON W. D., NIELSEN S., PUTLEY E. H. and YOUNG A. S., *J. Phys. Chem. Solids* **9**, 325 (1959).
11. KOLOMIETS B. T. and MALKOVA A. A., *Zh. Tekhn. Fiz* **28**, 1662 (1958).
12. WOOLLEY J. C. and SMITH B. A., *Proc. Phys. Soc. Lond.* **72**, 214 (1958).

J. Phys. Chem. Solids Pergamon Press 1960. Vol. 15. pp. 33–38. Printed in Great Britain.

EXCITON-INDUCED PHOTOCONDUCTIVITY IN Cu_2O*

J. H. APFEL† and A. M. PORTIS

Department of Physics, University of California, Berkeley 4, California

(*Received* 9 *November* 1959)

Abstract—Structure in the photoconductivity spectrum of Cu_2O has been observed which corresponds to the "yellow" exciton series observed in optical absorption. From the fact that the photoconductivity in the exciton peaks is initially stimulated by illumination and then quenched, it is concluded that distinct electronic processes are associated with the exciton-induced photoconductivity. The most likely mechanism is excitation of localized carriers by excitons. The experimental evidence is insufficient to establish that the excitons are mobile. A comparison of d.c. and microwave conductivity measurements of Cu_2O establishes that the conductivity is limited by barriers.

VOL. 15 1960

1. INTRODUCTION

THE possibility of excited states of insulating crystals for which electron and positive hole are coupled together was first recognized by FRENKEL[1]. Such a combination has been termed an exciton. The detailed nature of the exciton states may be related to the structure of the valence and conduction bands of the crystal. The recent work of DRESSELHAUS[2] and ELLIOTT[3] shows how such a connection may be made in the effective mass approximation.

The exciton, being electrically neutral, cannot carry a current. However, the exciton may carry energy through the solid and might therefore play an important role in the process of photoproduction of charge carriers. Such energy transport has been demonstrated in organic molecular crystals by SIMPSON[4]. APKER and TAFT[5] have shown that illumination in the first fundamental absorption peak of the alkali halides results in the excitation of *F*-center electrons. VAN SCIVER and HOFSTADTER[6] have found evidence for exciton migration in the gamma-ray excitation of NaI.

Structure observed in the optical absorption of Cu_2O has been attributed to exciton formation.[7] The recent magneto-optical studies of GROSS[8] give strong support to this interpretation. However, there has been no direct evidence of the mobility of the exciton in Cu_2O. In search for evidence of exciton diffusion, we were led to an examination of the photoconductivity of Cu_2O. We report here the observation of structure in photoconductivity of Cu_2O which coincides with the "yellow" series observed in optical absorption.‡ Recently GROSS and PASTRNYAK[10] have confirmed the observation of structure in the "yellow" series. They have further shown that with natural unworked surfaces structure may be observed at the position of the "green" series, and also in the region of the first stage of photoconduction in the red.

The observation of structure in the photoconductivity does not in itself establish the presence of exciton diffusion. The increased absorption in the "yellow" and "green" series may result in photon absorption and possible reëmission closer to the surface. It is possible that, with the surface region more photosensitive than the bulk, this could produce an increased yield of photoexcited carriers at the absorption peaks. If we take the point of view that the increased photocurrent is insensitive to the initial absorption mechanism, it should not be possible to distinguish the

* Supported by the United States Atomic Energy Commission and the Office of Naval Research.

† Present Address: John Jay Hopkins Laboratory for Pure and Applied Science, General Atomic Division, General Dynamics Corporation, San Diego 12, California.

‡ A preliminary account of this work was given at the 1958 International Conference on Semiconductors, following the paper by Professor GROSS[9].

photoconductivity in the peaks from the background photoconductivity. Experimentally, we find that the transient behavior of the photoconductivity in the peaks is markedly different from the background conductivity. Although this observation does not prove that exciton diffusion is involved, it does establish that the process of photoproduction of charge carriers in the exciton peaks must involve electronic processes unlike those responsible for the background photoconductivity.

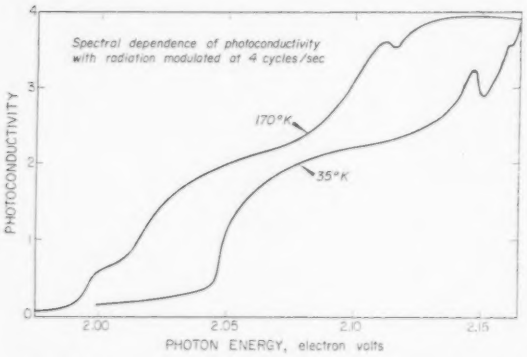

FIG. 1. Spectral dependence of photoconductivity with radiation modulated at 4 c/s. An enhanced photoconductivity in the vicinity of the "yellow" exciton series may be observed both at 35 and at 170°K.

2. PRINCIPAL OBSERVATIONS

Photoconductivity has been measured as a function of photon energy at a number of temperatures in the range from 30°K to room temperature. In Fig. 1 is shown the photoconductivity at 35 and 170°K. These curves were taken by chopping the incident light at 4 c/s and recording the 4 c/s component of the variation in sample conductivity. It will be seen that, imposed on the background photoconductivity, are peaks in the vicinity of the yellow region of the spectrum. The results of GROSS and PASTRNYAK[10] taken at 77°K with radiation chopped at 8 c/s are similar to these, except that they also reveal photoconductivity peaks in the green and a single peak in the red. In the more photosensitive samples it was found possible to measure the sample conductivity vs. photon energy with unchopped light. A curve taken at about 100°K is shown in Fig. 2. Again structure is observed in the vicinity of the green, but the lines appear to be inverted. An enlarged

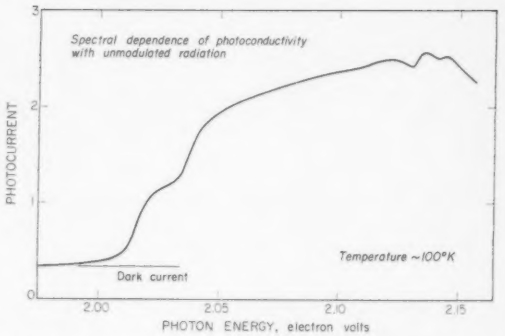

FIG. 2. Spectral dependence of the photoconductivity with unmodulated radiation. The photoconductivity in the vicinity of the "yellow" exciton series is observed to be partially quenched.

view of the photoconductivity structure with chopped light is shown in Fig. 3. The position of the peaks in photoconductivity coincides with the position of the exciton "yellow" series, as observed in absorption. In Fig. 4 is shown an enlarged view of the photoconductivity with unchopped light. It may clearly be seen that the conductivity is quenched in the vicinity of the exciton peaks. The position of the conductivity minimum was found to be a slight function of the rate at which photon energy was varied, indicating a relaxation time for the photoconductivity of the order of tens of seconds. No such effect was found for the a.c. photoconductivity observed with chopped light.

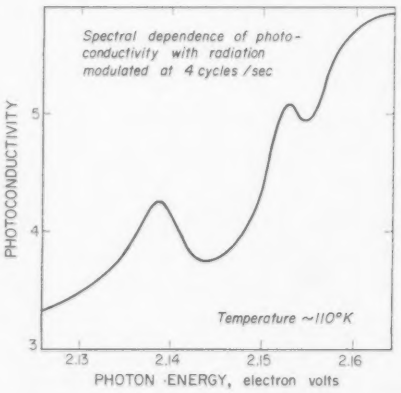

FIG. 3. An enlarged view of the spectral dependence of the photoconductivity in the vicinity of the "yellow" exciton series. Radiation is modulated at 4 c/s.

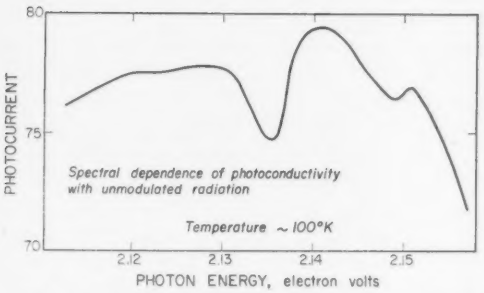

FIG. 4. An enlarged view of the spectral dependence of the photoconductivity in the vicinity of the "yellow" exciton series taken with unmodulated radiation.

VOL. 15 1960

A careful comparison has been made of the position of the most intense peak in the photoconductivity and the $n = 2$ line in the "yellow" exciton series as determined from optical absorption. This comparison is shown in Fig. 5. The

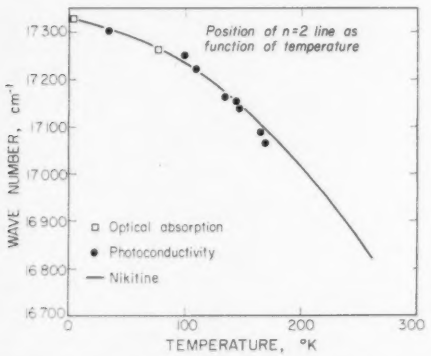

FIG. 5. A comparison between the position of the $n = 2$ line observed in photoconductivity and the same line observed in optical absorption.

solid curve is an empirical one given by NIKITINE *et al.*[11] and is in agreement with their exciton data. The open squares represent optical-absorption data obtained in this laboratory by APFEL and HADLEY[7]. To within the error associated with locating the maximum in photoconductivity, the conductivity and absorption data are in agreement.

3. EXPERIMENTAL TECHNIQUES

The photoconductivity of Cu_2O was studied by projecting monochromatic light onto a sample and measuring the spectral dependence of the change in electrical conductivity. Light in the vicinity of 6000 Å was obtained from a tungsten-ribbon filament source, using a Perkin–Elmer Model 98 monochromator with an NaCl prism.

For the low-temperature measurements the samples were mounted in an evacuated metal Dewar. This Dewar had a central tank filled with liquid helium or nitrogen and surrounded by an annular cylindrical tank filled with liquid nitrogen. An outside vacuum jacket at room temperature surrounded the whole assembly. The sample was attached to the bottom of the central tank and directly in line with an opening in the annular tank and a quartz window in the outer vacuum jacket. The Dewar was mounted adjacent to the monochromator, and the image of the monochromator exit slit was directed onto the sample by means of a pair of front-silvered mirrors.

The copper oxide samples were made available to us by Dr. WALTER BRATTAIN, of the Bell Telephone Laboratories. As received, the samples were squares approximately 2·5 cm on a side and 0·1 cm thick. Although the samples were polycrystalline, the crystallites appeared to be quite regular in size and shape, with a typical diameter of the order of 100 μ.

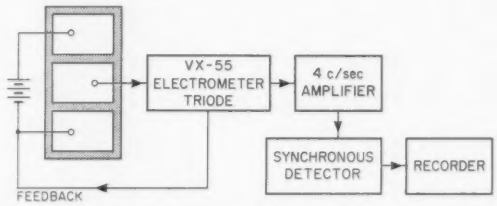

FIG. 6. Schematic diagram of sample and amplifying, detecting and recording units. The sample forms two arms of a bridge circuit. Negative feedback is employed to minimize capacitance effects.

The samples were prepared for the electrical studies by first grinding both surfaces smooth and then lightly etching in nitric acid solution. Three gold electrodes were vaporized onto one of the surfaces, as shown schematically in Fig. 6. The exposed regions between the electrodes were chosen to be of the same size as the projected image of the monochromator exit slit. The sensitive region of the sample was typically 0·5 cm long by 100 μ wide. The sample was finally cemented to a crystal sapphire substrate, mounted in the Dewar. Connections to the sample electrodes were made by phosphor-bronze pressure contacts. The temperature of the sample was measured with a copper/Constantan thermocouple attached to the sapphire substrate.

For the a.c. electrical measurements, all three electrodes were used, with the sample forming two arms of a bridge. With the bridge arrangement the effect of small temperature drifts could be minimized. Light from the monochromator was focussed across one pair of electrodes, causing an unbalance in the bridge. The unbalance signal was applied to the grid of a Victoreen VX-55 electrometer triode. The electrometer output was amplified, synchronously rectified and displayed on a chart recorder. The effective input capacitance of the

electrometer tube was reduced by applying negative feedback at the low-impedance point of the bridge. With this arrangement the electrometer tube operates with near unit gain. The effective input capacitance could have been reduced even more by inserting additional gain in the feedback loop.

4. FURTHER OBSERVATIONS

Our attention was further directed toward the difference between the photoconductivity structure with chopped light and with steady light. It was reasoned that in order to account for the experimental results there must be an initial rise in conductivity when the light is turned on, followed by a decay of the exciton associated conductivity to a negative value. That is, the over-all conductivity will decay to a value lower than what would be expected in the absence of excitons. It was found

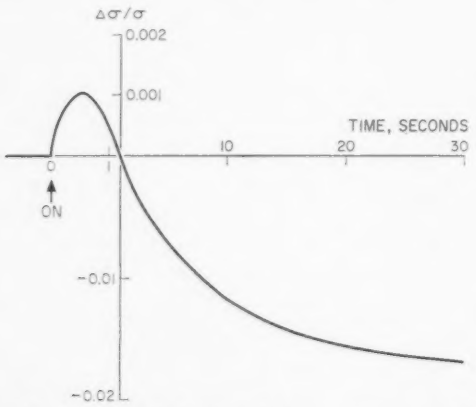

FIG. 7. Transient behavior of photocurrent when the monochromator is shifted onto the exciton line. An initial stimulation of photocurrent followed by a quenching action is observed. The rise is limited by circuit capacitance. Note that the second and fourth quadrants differ in scale.

preferable experimentally to shift the photon energy from a position just off the exciton line onto it. In this way the background conductivity remained largely unchanged. The conductivity was monitored by displaying the signal at the output of the electrometer on an oscilloscope. The wavelength of the light incident on the sample could be changed rapidly by rotating the Littrow mirror in the monochromater between the two pre-set positions. The conductivity was observed to show a rapid rise, followed by a decay to below the initial value, as expected. The rise time, which was a fraction of a second, was limited by the charging of the electrometer input capacitance. This characteristic is shown in Fig. 7. An enlarged view of the initial rise is shown in the second quadrant. These data confirm the interpretation of the earlier observations and present the relaxation effects in a much more direct way. Similar observations were made by shifting from the position of maximum exciton absorption to a point just off the exciton line. Under these conditions a rapid drop in conductivity was observed, followed by the slow rise to a value in excess of the initial one.

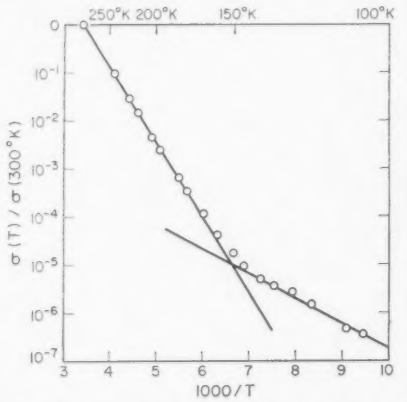

FIG. 8. Dark conductivity of Cu_2O vs. temperature. An activation energy of 0·09 eV is observed up to 150°K, followed by an activation energy of 0·3 eV at higher temperatures. The higher activation energy is associated with barriers.

GROSS and NOVIKOV[12] have reported an exciton-associated structure in CdS. They find two kinds of CdS crystals. In one type of crystal, the exciton absorption peaks correspond to maxima in the photoconductivity. In the other type, they correspond to minima in the conductivity. This is just the kind of effect that is observed here as between chopped light and steady light in the same sample.

It should be emphasized that very little is known about the mechanism of background photoconductivity in Cu_2O, let alone the exciton-induced part. The dark conductivity of the samples used was measured as a function of temperature (Fig. 8). Two activation energies are shown. Below 150°K

the conductivity rises with an activation energy of 0·09 eV; above 150°K the activation energy is 0·3 eV. The room temperature resistivity was about 5000 Ω-cm; at 100°K the resistivity had increased to 3×10^{10} Ω-cm. The sample resistivities were also measured at microwave frequencies. Further, the dark-carrier mobilities were determined by microwave Faraday rotation.[13]*

Measurements made at approximately 10 kMc/s are given in Table 1. It should be noted that while

Table 1. *Microwave measurements*

Temperature	ρ (Ω-cm)	μ (cm²/v-sec)
100	$1{\cdot}7 \times 10^5$	+110
300	700	+ 10

the room-temperature microwave conductivity is about ten times higher than the d.c. conductivity, the discrepancy at 100°K is more than five orders of magnitude. The microwave conductivity is consistent with a single activation energy of 0·09 eV. The microwave rotation data indicate that the samples are *p*-type, with mobilities as given in Table 1. It had been hoped that it would be possible to measure the sign of the photocarriers by this method. However, it was found that the samples were not sufficiently photosensitive for the microwave technique.

The comparison between the d.c. and microwave conductivities indicates that the d.c. conductivity is limited by barriers. Under these circumstances a change in barrier height with illumination would produce an appreciable change in conductivity. A mechanism of this kind has been discussed by SLATER[14]. Of course it is still necessary to excite free carriers in order to modify the barrier height; the initial mechanism of photoexcitation is an independent problem. Barrier modulation should not produce a change in microwave conductivity,[15] since the barrier susceptance will be large at these frequencies. As no photoconductivity was observed at microwave frequencies, we are unable to exclude barrier modulation as an important effect in Cu_2O.

* We are indebted to D. P. SNOWDEN for assistance with these measurements.

5. DISCUSSION

The photoconductivity spectrum, as reported here and as observed by GROSS and PASTRNYAK[10], shows the same features as the absorption spectrum. Both show an initial rise above dark conductivity in the red followed by a second rise in the yellow, and finally augmented by a third contribution in the green. BAUMEISTER[16] has recently made an absolute determination of the absorption spectrum and interpreted the absorption on the basis of the theory due to ELLIOTT[3]. BAUMEISTER concludes that the absorption in the red is connected with an indirect transition to the ground exciton state associated with a conduction-band minimum away from the center of the zone. The lines in the yellow are related to direct transitions to higher exciton states. Finally, the structure in the green may be associated with direct transitions across the gap. BAUMEISTER has found phonon contributions in the indirect absorption to support this interpretation.†

Of course, excitons themselves cannot carry current. To make a contribution to the photocurrent, the excitons must produce free carriers. Two likely mechanisms are: (1) the ejection of carriers from states in the gap and (2) the dissociation of excitons through collison with phonons. The relative temperature independence of the exciton-induced photoconductivity seems to rule out the second process. In addition, the quenching action observed at the exciton lines requires an increase in recombination rate for the background photocarriers. The possibility that the excitons excite localized charges seems most attractive. For this to occur, the excitons need not necessarily be mobile. The matter can hardly be decided when the centers from which carriers are excited are of unknown character and concentration. We hope that with the preparation of highly purified single crystals of Cu_2O and with the controlled introduction of recombination centers, it may be possible to establish whether excitons in this material are in fact mobile.

† *Note added in proof:* Dr. R. J. ELLIOTT and Prof. W. PAUL have independently suggested that the absorption edge observed in the red may be associated with an optical-phonon assisted transition to the 1*s* exciton band at the center of the zone. This mechanism would seem to offer a more natural explanation of BAUMEISTER's results.

Acknowledgements—We wish to thank D. P. SNOWDEN for his assistance with the microwave measurements. The generosity of Dr. WALTER BRATTAIN, of the Bell Telephone Laboratories, in making the Cu_2O samples available is acknowledged. A very helpful conversation with Dr. L. APKER on the subject of exciton migration is remembered with gratitude.

REFERENCES

1. FRENKEL J., *Phys. Rev.* **37**, 17 (1931).
2. DRESSELHAUS G., *Phys. Rev.* **106**, 76 (1957); *J. Phys. Chem. Solids* **1**, 14 (1956).
3. ELLIOTT R. J., *Phys. Rev.* **108**, 1384 (1957); ELLIOTT R. J. and LOUDON R., *J. Phys. Chem. Solids* **8**, 382 (1959).
4. SIMPSON O., *Proc. Roy. Soc.* A**238**, 402 (1956).
5. APKER L. and TAFT E. A., *Phys. Rev.* **79**, 964 (1950); **81**, 698 (1951); **82**, 814 (1951);
   See also PHILLIP H. R. and TAFT E. A., *Phys. Rev.* **106**, 671 (1957).
6. VAN SCIVER W. and HOFSTADTER R., *Phys. Rev.* **97**, 1181 (1957); VAN SCIVER J., *High-Energy Phys. Lab. Rep.* No. 38 (April 1955) unpublished.
7. GROSS E. F. and KARRYEV N. A., *Dokl. Akad. Nauk S.S.S.R.* **84**, 471 (1952); HAYASHI M. and KATSUKI K., *J. Phys. Soc. Japan* **7**, 599 (1952); NIKITINE S., PERNY G. and SIESKIND M., *C.R. Acad. Sci. Paris* **237**, 67 (1954); APFEL J. and HADLEY L. N., *Phys. Rev.* **100**, 1689 (1955).
8. GROSS E. F., *J. Phys. Chem. Solids* **8**, 172 (1959).
9. See *J. Phys. Chem. Solids* **8**, 193 (1959).
10. GROSS E. F. and PASTRNYAK I., *Sov. Phys.—Solid State* **1**, 143 (1959).
11. NIKITINE S., SIESKIND M. and PERNY G., *C.R. Acad. Sci. Paris* **238**, 1987 (1954).
12. GROSS E. F. and NOVIKOV B. V., *J. Tech. Phys.* (*U.S.S.R.*) **28**, 782 (1958).
13. PORTIS A. M., *J. Phys. Chem. Solids* **8**, 326 (1959).
14. SLATER J. C., *Phys. Rev.* **103**, 1631 (1956).
15. SNOWDEN D. P. and PORTIS A. M., *Phys. Rev.* (to be submitted).
16. BAUMEISTER P. M., Thesis, University of California Berkeley (1959).

J. Phys. Chem. Solids Pergamon Press 1960. Vol. 15. pp. 39–49. Printed in Great Britain.

A THEORETICAL STUDY OF POINT DEFECTS IN THE ROCKSALT STRUCTURE SUBSTITUTIONAL K^+ IN NaCl

J. R. HARDY*

H. H. Wills Physics Laboratory, University of Bristol

(*Received* 14 *September* 1959; *revised* 19 *November* 1959)

VOL. 15 1960

Abstract—A method based on lattice statics is given for studying the ionic displacements about a substitutional potassium ion in sodium chloride. These are evaluated for certain ions close to the defect and for certain specific directions at large distances from the defect. These last results are used to calculate the interaction energy between a widely separated pair of defects. The correspondence with the predictions of elastic-continuum theory is demonstrated, and a method for calculating the macroscopic volume changes produced by defects is presented.

1. INTRODUCTION

A POINT defect such as a vacancy or an impurity atom in a crystal lattice causes a certain distortion. This is largest close to the defect, and a long way from the defect the atomic displacements fall off inversely as the square of the distance.

Three approaches have been used for the investigation of this distortion. The first, due to ESHELBY[1], treats the defect as a singularity in an elastic continuum. The second considers the equilibrium of a few near neighbours of the defect in detail and assumes that the rest of the medium is adequately described by the continuum theory. This is the basis of the MOTT and LITTLETON[2] treatment of defects in ionic crystals, which considers the equilibrium of nearest neighbours in detail and regards the rest of the medium as a polarized continuum. Their treatment neglects long-range elastic distortion, but BRAUER[3] has taken this into account by using the solution for the long-range displacements in an isotropic continuum matched to the nearest-neighbour displacements. BASSANI and THOMSON[4] have used the same method, but they match the continuum solution to the average displacement of nearest and next-nearest neighbours when the defect has no net charge and there is no long-range polarization. The third method is that used by KANZAKI[5] and MATSUBARA[6] and is the one we also shall employ. This treats the problem as an exercise in lattice statics and is superior to the other methods in that it recognizes the discrete nature of a real lattice throughout the calculations.

The object of the present work is to treat the effect of substitutional impurity ions having the same charge as the ions that they replace on the sodium chloride type of lattice. The specific case that we shall consider is a potassium ion substituted into a sodium chloride lattice. This is a slightly more difficult problem than that treated by KANZAKI[5], who considered a vacancy in solid argon. The essential difference is that in KANZAKI's case the interatomic forces fall off rapidly with distance and only nearest-neighbour interactions need be considered, whereas in our case the ions carry a net charge and we must allow for the long-range electrostatic interaction between them. By excluding impurities of different valency from our treatment, we have avoided the complications arising from the long-range polarization which such defects produce.

Our aim is to consider first the effect of an isolated defect and then to go on to investigate the behaviour of two or more defects which are fairly close to one another. We are particularly interested in the variation of the energy of a pair of defects with relative orientation and separation. It

* Now at the Physics Research Laboratory, University of Reading.

is possible that we may be able to derive from this some conclusion as to the stability against segregation into two phases of a dilute solid solution.

We shall assume throughout the present work that sodium chloride is composed of point charges held apart by repulsive forces which act only between nearest neighbours. This is the Born–Mayer model in its most simple form. A fuller treatment of this problem, which allows for ionic polarizability and deformability, is being developed, but as this complicates the mathematical analysis without essentially altering the results of the simple theory, we shall not reproduce it here. Our object here is to present the more important results of the simple theory.

For defects in an isotropic elastic continuum, ESHELBY[1] has shown that the existence of a free surface gives rise to important effects which are not present when the medium is infinite. He presents an explicit solution to the problem of one defect at the centre of a sphere, and has extended the work in a further paper[7] to anisotropic continua. The simplest analogous lattice problem would be a defect at the centre of a finite cube, but this appears intractable.

To overcome this difficulty, we shall solve the problem for an infinite crystal containing a large regular superlattice of defects. The required solutions will be those with the periodicity of this superlattice. To study the behaviour of a finite but large superlattice, we allow the volume per supercell to vary and determine the variation that minimizes the energy. In this configuration there is no net hydrostatic pressure on the faces of the supercells. Our finite superlattice in this configuration and that with a completely free surface differ only in the presence of local surface tractions which average out to zero and which thus do not affect supercells below the surface. In this way, we may calculate the volume change of a finite real crystal containing a random array of widely separated defects if we assume it to be the same as that of a finite superlattice of the same volume and containing the same number of defects. If we have a non-zero hydrostatic pressure, p, we may discuss the behaviour of the crystal by adding a term pV to the energy of a volume, V, of crystal.

2. SHORT-RANGE DISTORTION

For the present we shall restrict ourselves to the distortion about one defect at constant volume. As already mentioned, we propose to consider an infinite sodium chloride lattice which contains a large superlattice of potassium ions. In order that we may use KELLERMANN's[8] numerical results in the subsequent work, it is convenient to make the superlattice face-centred. We now want to know the change in energy per supercell when there is a potassium ion present, relative to a supercell of perfect crystal. First, we define an energy

$$\psi(r) = v_{K^+}(r) - (r-r_0)v'_{Na^+}(r_0) - \tfrac{1}{2}(r-r_0)^2 v''_{Na^+}(r_0),$$

where $v_{K^+}(r)$ is the repulsive interaction energy between a potassium ion and a chlorine ion separated by a distance r, and r_0 is the equilibrium interionic separation in sodium chloride; $v'_{Na^+}(r_0)$ and $v''_{Na^+}(r_0)$ are the first and second derivatives of the sodium–chlorine repulsive interaction evaluated for the interionic separation r_0. Then, in order to obtain the total energy difference between a supercell containing a defect and a perfect undistorted supercell, we must add a term $\psi(r)$ for each potassium–chlorine bond to the energy of the distorted sodium chloride lattice, which is assumed to be quadratic in the ionic displacements.

In this way we treat the repulsive potassium–chlorine interaction exactly, but we neglect any third- or higher-order displacement terms in the Coulomb interaction. Hence the change in energy of the smallest possible supercell due to the array of defects is:

$$\Delta U = 6\psi(r_0+\xi_R) + \\ + \frac{1}{2}\sum_{\substack{l'l\alpha \\ k'k\beta}} \left[\frac{\partial^2 U}{\partial x_\alpha(_k^l)\partial x_\beta(_{k'}^{l'})}\right]_0 \xi_\alpha(_k^l)\xi_\beta(_{k'}^{l'}) \quad (1)$$

where l denotes a particular monatomic unit cell in the lattice of either sodium or chlorine ions and $k = 2$ for the former and 1 for the latter. $\Delta U =$ the energy per supercell and the suffix 0 on its second derivatives implies that these are evaluated for the undistorted lattice.

$$r(_k^l) = (x_\alpha(_k^l) \dots)_{\alpha=1,2,3}$$

is the position vector of the ion $(_k^l)$ in the undistorted lattice and

$$\xi(_k^l) = (\xi_\alpha(_k^l) \dots)_{\alpha=1,2,3}$$

is the displacement of $(_k^l)$ from the position $r(_k^l)$.

ξ_R is the radial displacement of the defect's nearest neighbours. If N is the number of monatomic cells in each supercell, then the summations over l are from $l = 0$ to $N-1$ and that over l' is unrestricted.

The subsequent analysis is very similar to that given by KANZAKI[5]. We minimize ΔU as a function of the ξ's and then Fourier decompose the ξ's:

$$\boldsymbol{\xi}(^{l}_{k}) = \frac{1}{N}\sum_{q} \boldsymbol{Q}^{k}_{(q)} \exp[i\boldsymbol{q}\cdot\boldsymbol{r}(^{l}_{k})]$$

and Fourier transform the equilibrium equation. This gives

$$\boldsymbol{Q} = \begin{bmatrix} k & k \\ \alpha & \beta \end{bmatrix}^{-1}_{q} \boldsymbol{G} \qquad (2)$$

where the 6×6 matrix

$$\begin{bmatrix} k & k' \\ \alpha & \beta \end{bmatrix}_{q}$$

is the coupling coefficient matrix given by KELLERMANN[8] and $\boldsymbol{G}$ is the 6-component column vector

$$2iF_R\begin{pmatrix} \sin q_\alpha r_0 \\ 0 \end{pmatrix} \equiv \begin{pmatrix} \boldsymbol{G}^1_{\alpha} \\ 0 \end{pmatrix},$$

F_R being defined as

$$-\frac{\partial\psi}{\partial\xi_R}(r_0+\xi_R).$$

We may write the matrix equation for $\boldsymbol{Q}$ as:

$$\begin{pmatrix} \begin{bmatrix} 1 & 1 \\ \alpha & \beta \end{bmatrix} - \begin{bmatrix} 1 & 2 \\ \alpha & \beta \end{bmatrix} & 0 \\ 0 & \begin{bmatrix} 1 & 1 \\ \alpha & \beta \end{bmatrix} + \begin{bmatrix} 1 & 2 \\ \alpha & \beta \end{bmatrix} \end{pmatrix}$$

$$\begin{pmatrix} \boldsymbol{Q}^1 - \boldsymbol{Q}^2 \\ \boldsymbol{Q}^1 + \boldsymbol{Q}^2 \end{pmatrix} = \begin{pmatrix} \boldsymbol{G}^1 \\ \boldsymbol{G}^1 \end{pmatrix} \qquad (3)$$

In deriving equation (3) from (2), we have used the facts that

$$\begin{bmatrix} 1 & 1 \\ \alpha & \beta \end{bmatrix} = \begin{bmatrix} 2 & 2 \\ \alpha & \beta \end{bmatrix}$$

and

$$\begin{bmatrix} 1 & 2 \\ \alpha & \beta \end{bmatrix} = \begin{bmatrix} 2 & 1 \\ \alpha & \beta \end{bmatrix},$$

which are consequences of the restriction to repulsive interactions between nearest neighbours only. Equation (3) has been solved numerically for a mesh of 1000 points which cover the Brillouin zone, and for which KELLERMANN has tabulated the coupling coefficients.

The $\xi(^{l}_{k})$ can then be calculated by direct summation of the Fourier series, weighting each point with $N/1000$. This gives

$$\begin{pmatrix} \xi_1(^{l}_{k}) \\ \xi_2(^{l}_{k}) \\ \xi_3(^{l}_{k}) \end{pmatrix} = \begin{pmatrix} \alpha_1(^{l}_{k}) \\ \alpha_2(^{l}_{k}) \\ \alpha_3(^{l}_{k}) \end{pmatrix} F_R \qquad (4)$$

To determine F_R, we need to know the form of the interionic repulsive potential and we assume it to be $Ae^{-r/\rho}$.

Thus

$$F_R = \left[\frac{A_{K^+}}{\rho_{K^+}}\exp[-(r_0+\xi_R)/\rho_{K^+}] + \frac{\xi_R A_{Na^+}}{(\rho_{Na^+})^2}\exp(-r_0/\rho_{Na^+}) - \frac{A_{Na^+}}{\rho_{Na^+}}\exp(-r_0/\rho_{Na^+})\right] \qquad (5)$$

where $A_{K^+} = 3{\cdot}63\times 10^{-9}$ erg, $A_{Na^+} = 1{\cdot}47\times 10^{-9}$ erg, $\rho_{K^+} = 0{\cdot}324\times 10^{-8}$ cm, $\rho_{Na^+} = 0{\cdot}328\times 10^{-8}$ cm, and $r_0 = 2{\cdot}814\times 10^{-8}$ cm, at room temperature. These constants are tabulated by BORN and HUANG[9] (p. 26). KELLERMANN determines the first derivative of the repulsive potential from the fact that the total lattice energy is minimal and the second derivative from the compressibility. This is all that is needed for the derivation of the coupling coefficients. A and ρ for a particular case are found by substitution in KELLERMANN's formulae of the exponential repulsive potential. Note, however, that all these results should be used with the experimental parameters appropriate to absolute zero, but in this work we shall follow KELLERMANN and use room-temperature data.

We now use equation (4) for the nearest neighbours of the defect $\xi_R = \alpha F_R$. This, with equation (5) determines ξ_R and thus F_R.

In this way we find $F_R = 7{\cdot}35\times 10^{-5}$ dyne. In Table 1 we show the values of α for various points close to the defect.

From these and the known value of F_R, we find

Table 1. *Displacements in units of* $F_R \times 10^{-5}$ *cm/dyne*

Ion	$(\frac{1}{2}, 0, 0)$	$(1, \frac{1}{2}, 0)$	$(\frac{1}{2}, \frac{1}{2}, 0)$	$(\frac{1}{2}, \frac{1}{2}, \frac{1}{2})$	$(1, 0, 0)$	$(3/2, 0, 0)$	$(1, 1, 0)$	$(1, 1, 1)$
ξ_1	2·040	0·285	0·469	−0·033	0·515	0·204	0·123	0·009
ξ_2	0	0·335	0·469	−0·033	0	0	0·123	0·009
ξ_3	0	0	0	−0·033	0	0	0	0·009

Table 2. *Displacements in* 10^{-10} *cm*

Ion	$(\frac{1}{2}, 0, 0)$	$(1, \frac{1}{2}, 0)$	$(\frac{1}{2}, \frac{1}{2}, 0)$	$(\frac{1}{2}, \frac{1}{2}, \frac{1}{2})$	$(1, 0, 0)$	$(3/2, 0, 0)$	$(1, 1, 0)$	$(1, 1, 1)$
ξ_1	15·0	2·09	3·45	−0·243	3·78	1·50	0·907	0·066
ξ_2	0	2·46	3·45	−0·243	0	0	0·907	0·066
ξ_3	0	0	0	−0·243	0	0	0	0·066
ξ	15·0	3·23	4·87	0·421	3·78	1·50	1·28	0·114

the actual displacements and their absolute magnitudes

$$[\xi = \sqrt{(\xi_1^2+\xi_2^2+\xi_3^2)}].$$

The value of ξ for $(\frac{1}{2}, 0, 0)$ is close to that obtained by BASSANI and THOMSON[4] ($12{\cdot}6\times10^{-10}$ cm) by more approximate methods. The small values for $(\frac{1}{2}, \frac{1}{2}, 0)$ and $(\frac{1}{2}, \frac{1}{2}, \frac{1}{2})$ are plausible, since any force they experience is of first order in $\xi(\frac{1}{2}, 0, 0)$, while the six ions $(\frac{1}{2}, 0, 0)$ receive a direct "push" from the oversize potassium ion.

3. LONG-RANGE DISTORTION

(a) *Lattice theory*

We shall now evaluate the displacements many interionic distances from the defect, and we shall find them to be functions of the macroscopic elastic constants. In Section 3(b) we shall solve the same problem by using continuum-elasticity theory, and it will then be possible to see how the two results correspond. It will appear that this distortion is essentially determined by the Fourier amplitudes $\boldsymbol{Q}$ for small wave numbers $\boldsymbol{q}$.

We may write equation (3) for these amplitudes as:

$$\begin{pmatrix} A_{\alpha\beta} & 0 \\ 0 & B_{\alpha\beta} \end{pmatrix} \begin{pmatrix} \boldsymbol{Q}_1-\boldsymbol{Q}_2 \\ \boldsymbol{Q}_1+\boldsymbol{Q}_2 \end{pmatrix} = 2iF_R r_0 \begin{pmatrix} \boldsymbol{q} \\ \boldsymbol{q} \end{pmatrix} \qquad (6)$$

where $A_{\alpha\beta}$ is a constant matrix, $B_{\alpha\beta} = 0(|\boldsymbol{q}|^2)$.

Thus $\boldsymbol{Q}^1-\boldsymbol{Q}^2 = 0(|\boldsymbol{q}|)$, while $\boldsymbol{Q}^1+\boldsymbol{Q}^2 = 0(1/|\boldsymbol{q}|)$ and hence we may say $\boldsymbol{Q}^1 = \boldsymbol{Q}^2 = \boldsymbol{Q}^0$ and the equation becomes:

$$(B_{\alpha\beta})\boldsymbol{Q}^0 = iF_R r_0 \boldsymbol{q} \qquad (7)$$

$$(B_{\alpha\beta}) = \begin{bmatrix} 1 & 1 \\ \alpha & \beta \end{bmatrix}_{\boldsymbol{q}} + \begin{bmatrix} 1 & 2 \\ \alpha & \beta \end{bmatrix}_{\boldsymbol{q}} = \sum_{L_1L_2L_3}{}' \exp(i\boldsymbol{q}\cdot\boldsymbol{R}) \left[\frac{\partial^2\Phi}{\partial x_\alpha \partial x_\beta}\{(L_1r_0+x_1)^2+(L_2r_0+x_2)^2+(L_3r_0+x_3)^2\}\right] \qquad (8)$$

where $R = (L_1r_0, L_2r_0, L_3r_0)$ denotes any lattice point the L's having any integral values. The term $L_1 = L_2 = L_3 = 0$ is excluded by the prime on the summation sign. $\Phi(r^2)$ denotes the interaction energy of a pair of ions a distance r apart and the suffix implies that the derivative is evaluated for $x_1 = x_2 = x_3 = 0$. Thus, if we write $L^2 = L_1^2+L_2^2+L_3^2$, we have

$$B_{\alpha\beta} = \sum_{L_1L_2L_3}{}' 2[L_\alpha r_0\Phi'(L^2r_0^2)\delta_{\alpha\beta}+2L_\alpha L_\beta r_0^2\Phi''(L^2r_0^2)] \exp(i\boldsymbol{q}\cdot\boldsymbol{R})$$

where $\Phi'(r^2)$ and $\Phi''(r^2)$ denote $[d\Phi/dr^2]_r$ and $[d^2\Phi/d(r^2)^2]_r$ respectively.

We expand the exponential as a power series in $|\boldsymbol{q}|$ as far as the second order. For a lattice in equilibrium, the Φ' term in $B_{\alpha\beta}$ is zero. This leaves the terms in Φ''. The zero and first-order terms of the power series vanish owing to the cubic symmetry of the lattice,

therefore

$$B_{\alpha\beta} = \sum_{L_1L_2L_3}{}' -2r_0^2(\boldsymbol{q}\cdot\boldsymbol{R})^2 L_\alpha L_\beta \Phi''(L^2r_0^2)$$

therefore

$$B_{\alpha\beta} = -q_\alpha q_\beta 4 \sum_{L_1L_2L_3}{}' L_\alpha L_\beta r_0^4 \Phi''(L^2r_0^2)$$

if $\alpha \neq \beta$ or

$$= -2r_0^4\Big[\sum_{L_1L_2L_3}{}' L_\alpha^2\Phi''(L^2r_0^2)\{L_\alpha^2q_\alpha^2+L_\gamma^2q_\gamma^2+L_\delta^2q_\delta^2\}\Big]$$

if $\alpha = \beta$, where α, γ and δ are all different.

Now

$$\sum_{L_1L_2L_3}{}' L_\alpha^4\Phi''(L^2r_0^2) = \frac{v_a}{4r_0^4}C_{11}$$

$$\sum_{L_1L_2L_3}{}' L_\alpha^2L_\beta^2\Phi''(L^2r_0^2) = \frac{v_a}{4r_0^4}C_{12}$$

where $v_a = 2r_0^3$ and C_{11} and C_{12} and $C_{12}(=C_{44})$ are the elastic constants of sodium chloride derived from the theoretical model that we have used (BORN and HUANG[9], pp. 133 and 142).

Thus:

$$B_{12} = -q_1q_2v_aC_{12}$$

$$B_{11} = \frac{v_a}{2}[q_1^2(C_{12}-C_{11})-|\boldsymbol{q}|^2C_{12}]$$

$$C_{11} = \frac{1}{v_a}\Big[\sum_{L_1L_2L_3}{}' \frac{e^2}{r_0}\frac{(L_1^4+L_2^4+L_3^4)}{L^5}(-)^{L_1+L_2+L_3} + \frac{3}{2}\frac{(A-B)}{r_0^5}e^2\Big]$$

$$C_{12} = \frac{1}{v_a}\Big[\sum_{L_1L_2L_3}{}' \frac{e^2}{r_0}\frac{(L_1^2L_2^2+L_2^2L_3^2+L_3^2L_1^2)}{L^5}(-)^{L_1+L_2+L_3}\Big]$$

where A and B are defined by KELLERMANN as

$$A = \frac{4r_0^3}{e^2}\left[\frac{d^2v(r)}{dr^2}\right]_{r=r_0} \qquad B = \frac{4r_0^2}{e^2}\left[\frac{dv(r)}{dr}\right]_{r=r_0}$$

$v(r)$ is the repulsive potential between nearest-neighbour ions.

The matrix equation (8) becomes:

$$\begin{pmatrix} C_{12}|\boldsymbol{q}|^2-q_1^2(C_{12}-C_{11}), & 2C_{12}q_1q_2, & 2C_{12}q_1q_3 \\ 2C_{12}q_2q_1, & C_{12}\boldsymbol{q}^2-q_2^2(C_{12}-C_{11}), & 2C_{12}q_2q_3 \\ 2C_{12}q_3q_1, & 2C_{12}q_3q_2, & C_{12}\boldsymbol{q}^2-q_3^2(C_{12}-C_{11}) \end{pmatrix}\begin{pmatrix} Q_1^0 \\ Q_2^0 \\ Q_3^0 \end{pmatrix} = -\frac{2iF_Rr_0}{v_a}\begin{pmatrix} q_1 \\ q_2 \\ q_3 \end{pmatrix}, \quad (9)$$

and the long-range distortion is given by:

$$\boldsymbol{\xi}(\boldsymbol{r}) = \int_{\substack{\text{Over first}\\ \text{Brillouin}\\ \text{zone}}}\int\int\int \frac{i\boldsymbol{Q}^0}{N}\sin\boldsymbol{q}\cdot\boldsymbol{r}\,dq_1dq_2dq_3\left[\frac{2Nr_0^3}{(2\pi)}\right]. \quad (10)$$

Equations (9) and (10) are now comparable with those which we shall deduce from elasticity theory in the following section.

(b) *Elasticity theory*

Following ESHELBY[7], we shall consider an anisotropic elastic continuum on which certain body forces, simulating the effect of the defect, are acting. A highly localized force acting radially outward at points close to the defect simulates the stress due to a foreign atom and may conveniently be represented by $-\mathscr{G}\ \mathrm{grad}\ \delta(r)$.

We shall find that the effects of all such highly localized distributions of body force F are the same provided that $\int \boldsymbol{r} \cdot \boldsymbol{F}\, dV$ over the specimen is the same.

The equations of elasticity appropriate to the problem are:

$$\frac{\partial}{\partial x_j} p_{ij} = \mathscr{G} \frac{\partial}{\partial x_i} \delta(\boldsymbol{r}) \tag{11}$$

where p_{ij} is the stress tensor. These are the equilibrium equations for an infinitesimal volume at any point.

Introducing the displacement $\xi = (\xi_1, \xi_2, \xi_3)$ at any point and using Hooke's law, equations (11) give:

$$\mathscr{G}\frac{\partial}{\partial x_1}\delta(r) = C_{11}\frac{\partial^2\xi_1}{\partial x_1^2} + C_{44}\left(\frac{\partial^2\xi_1}{\partial x_2^2} + \frac{\partial^2\xi_1}{\partial x_3^2}\right) + (C_{12}+C_{44})\left(\frac{\partial^2\xi_2}{\partial x_1\partial x_2} + \frac{\partial^2\xi_3}{\partial x_1\partial x_3}\right)$$

$$\mathscr{G}\frac{\partial}{\partial x_2}\delta(r) = C_{11}\frac{\partial^2\xi_2}{\partial x_2^2} + C_{44}\left(\frac{\partial^2\xi_2}{\partial x_1^2} + \frac{\partial^2\xi_2}{\partial x_3^2}\right) + (C_{12}+C_{44})\left(\frac{\partial^2\xi_1}{\partial x_1\partial x_2} + \frac{\partial^2\xi_3}{\partial x_2\partial x_3}\right)$$

$$\mathscr{G}\frac{\partial}{\partial x_3}\delta(r) = C_{11}\frac{\partial^2\xi_3}{\partial x_3^2} + C_{44}\left(\frac{\partial^2\xi_3}{\partial x_2^2} + \frac{\partial^2\xi_3}{\partial x_1^2}\right) + (C_{12}+C_{44})\left(\frac{\partial^2\xi_2}{\partial x_2\partial x_3} + \frac{\partial^2\xi_1}{\partial x_1\partial x_3}\right)$$

Where C_{11}, C_{12} $(= C_{44})$ are the elastic constants defined previously. To compare with the previous work, we require a periodic array of defects in which the inter-defect spacing is, for the present, fixed.

Thus ξ may be written as a Fourier series

$$\boldsymbol{\xi} = \sum_q \frac{\boldsymbol{Q}(q)}{N} \exp(i\boldsymbol{q}\cdot\boldsymbol{r})$$

where the wave vectors q are chosen to reproduce the superlattice periodicity.

Write the vector $\boldsymbol{Q} = (U, V, W)$ and since

$$\sum_{\text{supercells}} \delta(\boldsymbol{r}) = 1/2Nr_0^3 \sum_q \exp(i\boldsymbol{q}\cdot\boldsymbol{r}),$$

where $2Nr_0^3$ is the volume per defect, we have:

$$-\frac{i\mathscr{G}}{v_a}\begin{pmatrix} q_1 \\ q_2 \\ q_3 \end{pmatrix} = \begin{pmatrix} C_{12}|\boldsymbol{q}|^2+(C_{11}-C_{12})q_1^2, & 2C_{12}q_1q_2, & 2C_{12}q_1q_3 \\ 2C_{12}q_2q_1, & C_{12}|\boldsymbol{q}|^2+(C_{11}-C_{12})q_2^2, & 2C_{12}q_2q_3 \\ 2C_{12}q_3q_1, & 2C_{12}q_3q_2, & C_{12}|\boldsymbol{q}|^2+(C_{11}-C_{12})q_3^2 \end{pmatrix}\begin{pmatrix} U \\ V \\ W \end{pmatrix} \tag{12}$$

and

$$\boldsymbol{\xi} = \int \int_{-\infty}^{+\infty} \int \frac{\boldsymbol{Q}}{N} i \sin q\cdot r\, dq_1 dq_2 dq_3 \frac{2Nr_0^3}{(2\pi)^3} \tag{13}$$

If $\mathscr{G} = 2F_B r_0$, then equations (9) and (10) are almost equivalent to (12) and (13), apart from the difference in the two integrals over $\boldsymbol{q}$ space. That in equation (13) is not convergent, and to remedy this we introduce a convergence factor $e^{-\epsilon|\boldsymbol{q}|}$ which corresponds to a distribution of the body force over a finite region, such that $\int \boldsymbol{F}\cdot\boldsymbol{r}\, dv$ is unaltered. Then:

$$\xi_i = \frac{\mathscr{G}}{(2\pi)^3} \int \int_{-\infty}^{+\infty} \int \frac{q_i[Eq^4+Fq^2q_i^2+Hq_j^2q_k^2]\sin q\cdot r e^{-\epsilon|\boldsymbol{q}|}\, dq_1dq_2dq_3}{Dq^6+Bq^2(q_1^2q_2^2+q_2^2q_3^2+q_3^2q_1^2)+A(q_1q_2q_3)^2}$$

where

$$i \neq j \neq k \neq i, \quad E = (C_{11}-2C_{12})C_{12}, \quad F = 3C_{12}^2 - C_{11}C_{12}$$
$$H = 4C_{12}(2C_{12}-C_{11}), \quad A = (C_{11}-C_{12})(C_{11}-C_{12})^2 - 2C_{12}^2 + 16C_{12}^3$$
$$B = C12(C_{11}^2+2C_{11}C_{12}-3C_{12}^2), \quad D = C_{11}C_{12}^2.$$

We now transform to spherical polar co-ordinates $(q\theta\phi)$ (with the direction $\boldsymbol{r}$ as the axis $\theta = 0$. This gives us ξ_i in the form:

$$\xi_i = -\frac{\mathscr{G}}{(2\pi)^3}\left[\frac{\partial}{\partial x_i}\int_0^{2\pi}\int_0^{\pi}\int_0^{\infty} d\phi d\theta dq f_i(\theta\phi)\sin\theta e^{-\epsilon q}\cos(qr\cos\theta)\right]$$

(note that this does not imply any summation over i) or, writing $r\cos\theta = t$ and $f_i(\theta\phi) = F_i(t, \phi)$

$$\xi_i = -\frac{\mathscr{G}}{(2\pi)^3}\left[\frac{\partial}{\partial x_i}\int_0^{2\pi}\int_{-r}^{r}\int_0^{\infty} d\phi dt dq F_i(t\phi)e^{-\epsilon q}\cos qt\right] \tag{14}$$

As $\epsilon \to 0$ $\quad \int_0^{\infty}\cos qte^{-\epsilon q}\,dq \to \pi\delta(t)$

Thus

$$\xi_i = \frac{-\mathscr{G}}{8\pi^2}\left[\frac{\partial}{\partial x_i}\int_0^{2\pi}\frac{F_i(0\phi)}{r}d\phi\right] \tag{15}$$

Equation (10) of the lattice theory may be reduced to the same form as equation (15).

$$\xi_i = \frac{-2F_R r_0}{8\pi^2}\left[\frac{\partial}{\partial x_i}\int_0^{2\pi}\frac{F_i(0\phi)}{r}d\phi\right] \tag{16}$$

This is so because it may be shown that ξ is determined to order $1/r^2$ by the Fourier amplitudes $\boldsymbol{Q}$ from that part of $\boldsymbol{q}$ space close to the origin where the asymptotic form of $\boldsymbol{Q}$ is valid. We may, in fact, write

$$\xi_i = -\frac{2F_R r_0}{(2\pi)^3}\left[\frac{\partial}{\partial x_i}\int_0^{2\pi}\int_{-1}^{+1}\int_0^{Rr}\frac{f_i(\theta\phi)}{r}\cos(qr\cos\theta)\,d\phi d(\cos\theta)d(qr)\right]$$

where R is the radius of a small sphere about the origin in $\boldsymbol{q}$ space inside which the asymptotic form of $\boldsymbol{Q}$ is valid. However, Rr is still large enough for us to say that $\int_0^{Rr}\cos(qr\cos\theta)\,d(qr) \doteq \pi\delta(\cos\theta)$, and equation (16) follows from this. Thus, equations (15) and (16) are the same if $\mathscr{G} = 2F_R r_0$.

The $F_i(0\phi)$ are complicated functions of the direction cosines of the $(x_1x_2x_3)$ direction. The displacements at a distance $r = r_0\sqrt{(X_1^2+X_2^2+X_3^2)} =$ r_0X have been evaluated for the directions shown in Table 3 and are directed radially away from the defect.

Table 3. Displacement of an ion at distance Xr_0.

Direction	Displacement (cm. dyne^{-1})
⟨100⟩	$1{\cdot}78 \times 10^{-5} F_R X^{-2}$
⟨110⟩	$1{\cdot}24 \times 10^{-5} F_R X^{-2}$
⟨111⟩	$0{\cdot}747 \times 10^{-5} F_R X^{-2}$

The relative magnitudes are reasonable, as sodium chloride is not strongly anisotropic; hence one would expect the near equality of the three constants.

4. THE STATIC INTERACTION BETWEEN TWO DEFECTS AT CONSTANT VOLUME

We now want to discuss the situation when we have two defects interacting with one another. In particular, we want to know whether they attract

or repel each other. Thus we must define an "interaction" energy. We shall define it as the difference between the energy of each supercell in a superlattice of similarly placed pairs of defects and twice the same energy for a superlattice containing one defect in each supercell. If the separation between members of a supercell pair is small compared with the supercell dimensions, this gives us the interaction between an isolated pair of defects at constant volume.

(a) *Elasticity theory*

The extra energy stored in an elastic continuum containing two defects in each supercell is

$$\int_a p_{ij}^1 \frac{\partial \xi_i^2}{\partial x_j}\, dV + \int_b p_{ij}^2 \frac{\partial \xi_i^1}{\partial x_j}\, dV$$

per supercell. Repeated indices are summed over 1, 2, 3 and p_{ij} is the stress tensor. The affixes 1 and 2 denote the two defects. The first volume integral is carried out over the whole supercell except a small part containing defect (2), which is the domain of the second integral. This may be reduced to

$$\int (p_{ij}^1 \xi_i^2 - p_{ij}^2 \xi_i^1)\, dS_j$$

over any surface separating the two defects. Using Gauss's theorem, we may write this as:

$$-\mathscr{G} \int_{\text{supercell}} \delta(\boldsymbol{r}_2)\, \mathrm{div}\, \xi^1\, dV$$

$$= -\mathscr{G}(\mathrm{div}\, \xi^1)_{\boldsymbol{r}_2} \qquad (17)$$

where the second factor may be evaluated by using equation (15).

Table 4. Interaction energy of two K^+ ions Xr_0 apart

Direction	Interaction energy (10^{-5} erg (dynes)$^{-2}$)	Relative magnitudes (*a*) Present results (*b*) ESHELBY's results[7]	
		(*a*)	(*b*)
⟨100⟩	$+1{\cdot}648\ G^2 r_0^{-2} X^{-3}$	0·400	0·400
⟨110⟩	$+0{\cdot}404\ G^2 r_0^{-2} X^{-3}$	0·0981	−0·100
⟨111⟩	$-0{\cdot}605\ G^2 r_0^{-2} X^{-3}$	−0·147	−0·27

Again, we can evaluate the result only for specific orientations of the two defects, and in Table 4 the results for ΔE, the interaction energy, are given. They may be compared with those obtained by ESHELBY[7].

(b) *Lattice theory*

We want now to derive the lattice analogue of equation (17). To do this it is best to return to the basic principles which were used in the calculations for one defect in each supercell.

We label the two potassium ions in a supercell 1 and 2 as before, and in the subsequent work these labels denote the values of the physical quantities for the ion in question.

We again use the energy function $\psi(r)$ defined as the difference between the repulsive interaction of potassium and chlorine ions and that between sodium and chlorine ions at a separation r.

Then, if

$$\Psi_{1 \text{ or } 2} = \sum \psi(r)$$

over the six nearest-neighbour chlorine ions, we may write the energy change for a supercell containing two defects as:

$$\Delta U_2 = \frac{1}{2} \sum_{ij} \xi_i V_{ij} \xi_j + \Psi_1 + \Psi_2 \qquad (18)$$

where the ξ_i can be any component of the displacement of any ion. V_{ij} denotes

$$\left[\frac{\partial^2 U}{\partial \xi_i \partial \xi_j}\right]_0$$

evaluated for the perfect lattice. This equation is comparable with equation (1) for the single defect.

Thus, at equilibrium we have by minimizing ΔU_2:

$$\sum_j V_{ij} \xi_j + \frac{\partial \Psi_1}{\partial \xi_i} + \frac{\partial \Psi_2}{\partial \xi_i} = 0. \qquad (19)$$

Thus, the equilibrium energy is

$$\Delta U_2 = \Psi_1 + \Psi_2 - \frac{1}{2} \sum_i \left[\xi_i \frac{\partial \Psi_1}{\partial \xi_2} + \xi_i \frac{\partial \Psi_2}{\partial \xi_i} \right] \qquad (20)$$

If we have only one defect in a supercell then the equilibrium energy:

$$\left.\begin{aligned}\Delta U_1 &= \Psi - \frac{1}{2}\sum_i \frac{\partial \Psi}{\partial \xi_i}\xi_i \\ &= 6\psi(r_0+\xi_R)+3F_R\xi_R\end{aligned}\right] \quad (21)$$

where ξ_R is the nearest-neighbour displacement for an isolated defect and

$$F_R = -\frac{\partial \psi}{\partial \xi_R}(r_0+\xi_R).$$

We want

$$\Delta U_2 - 2\Delta U_1 = 2\left[\Psi_1 - \Psi - \frac{1}{2}\sum_i \left(\frac{\partial \Psi_1}{\partial \xi_i}\xi_i - F_R\xi_R\right)\right]$$

from equations (20) and (21). The argument of Ψ_1 is $(r_0+\xi_R+\xi_i^2)$ and that of Ψ is $(r_0+\xi_R)$. $\xi_i = \xi_R+\xi_i^2$, where ξ_i^2 is the radial displacement of one of the six nearest-neighbour chlorine ions *relative* to the first potassium ion, due to the presence of the second.

Thus

$$\Delta U_2 - 2\Delta U_1 = \sum_j \frac{\partial \Psi_1}{\partial \xi_j}\xi_j^2 - \sum_{ij}\frac{\partial^2 \Psi_1}{\partial \xi_i \partial \xi_j}\xi_i^1\xi_j^2 \quad (22)$$

where the derivatives are evaluated for the equilibrium configuration about an isolated defect and $\xi_i^1 = \xi_R$.

This gives, in the notation of equation (21):

$$\Delta U_2 - 2\Delta U_1 = -\sum_j \left(F_R - \xi_R \frac{\partial F_R}{\partial \xi_R}\right)\xi_j^2$$

$$= -\sum_j F_R(1+\gamma)\xi_j^2. \quad (23)$$

$$\gamma = -\frac{\xi_R}{F_R}\frac{\partial F_R}{\partial \xi_R} = -\alpha\frac{\partial F_R}{\partial \xi_R} \quad \text{as } \xi_R = \alpha F_R$$

Also, from the equation for ξ_j^2, we have:

$$\sum_j \xi_j^2 = 2\sum_{i=1,2,3}\frac{\partial \xi_i}{\partial X_i} + \alpha\sum_j \xi_j^2\frac{\partial F_R}{\partial \xi_R} \quad (24)$$

where the two defects are separated by $r_0(X_1, X_2, X_3)$ and

$$\sum_i \frac{\partial \xi_i}{\partial X_i}$$

is evaluated at defect (1) for the displacement due to defect (2). Hence, from equations (23) and (24),

$$\Delta U_2 - 2\Delta U_1 = -2r_0F_R(\operatorname{div}\boldsymbol{\xi}^2)_{r_1}$$
$$= -2r_0F_R(\operatorname{div}\boldsymbol{\xi}^1)_{r_2}$$

and, as $\mathscr{G} = 2F_Rr_0$ this is exactly the same as equation (17) for the continuum.

We now tabulate the actual energy for the same three directions as before and for the same separation (Table 5). It may be shown that the interaction energy is zero when integrated over all possible directions. To do this we must show

$$\int_{4\pi} (\operatorname{div}\boldsymbol{\xi}^1)_{r_2}\, d\omega = 0.$$

We expand $(\operatorname{div}\boldsymbol{\xi}^1)_{r_2}$ in spherical harmonics and we have:

$$\operatorname{div}\boldsymbol{\xi}^1 = a_0 + \sum_{lm} a_{lm}Y_l^m(\theta\phi)$$

where the a's are constants.

Table 5. Interaction energies

Direction	Interaction energy (eV)
⟨100⟩	$+0{\cdot}222\ X^{-3}$
⟨110⟩	$+0{\cdot}0545X^{-3}$
⟨111⟩	$-0{\cdot}0815X^{-3}$

The only non-zero term when integrated over all directions is

$$\int_{4\pi} a_0\, d\omega.$$

If $a_0 \neq 0$ this implies the existence of an isotropic solid for which $\operatorname{div}\boldsymbol{\xi}^1 \neq 0$, but this is impossible and hence our result is proved.

5. THE VOLUME CHANGE

We now suppose the dimensions of our supercells, containing one defect for the present, to

dilate by a factor δ such that the mean hydrostatic pressure across a cell interface is zero. This enables us to calculate the volume change per defect (ΔV_E or ΔV_L).

(a) *Elasticity theory*

The body force $F = -\mathscr{G}$ grad $\delta(\boldsymbol{r})$.

Thus

$$\int_{\text{supercell}} \boldsymbol{F}\cdot\boldsymbol{r}\,dV = -\int_{\text{supercell}} x_i \frac{\partial p_{ij}}{\partial x_j}\,dV$$

$$= \int_{\text{supercell}} p_{ii}\,dV \quad -\int_{\substack{\text{supercell}\\ \text{surface}}} x_i p_{ij} n_j\,dS$$

where we sum repeated indices over 1, 2, 3.

In the relaxed configuration the second term is zero, as $p_{ij}n_j = 0$. However, $p_{ii} = 3Ke$, where e is the local dilatation = div $\boldsymbol{\xi}$, and K is the bulk modulus.

Therefore

$$\Delta V_E = \int_{\text{supercell}} e\,dV = \frac{1}{3K}\int_{\text{supercell}} \boldsymbol{F}\cdot\boldsymbol{r}\,dV$$

therefore $\Delta V_E = \mathscr{G}/K$ when we substitute for $\boldsymbol{F}$ and use Gauss's theorem.

(b) *Lattice theory*

If we use equation (21), we may calculate the energy change of each supercell as a function of the linear dilatation.

Thus we have

$$\Delta U_1' = 6\psi[r_0(1+\delta)+\xi_R'] + 3F_R'\xi_R' + \frac{9}{2}K\delta^2(2Nr_0^3)$$

where primed quantities refer to the dilated lattice and the final term represents the energy stored in the dilated perfect lattice if K is the bulk modulus. We have, in addition, the result that $\xi_R' = \alpha' F_R'$, obtained by solving the equilibrium equations

$$\sum_j V_{ij}'\xi_j' + \frac{\partial \Psi''}{\partial \xi_i'} = 0,$$

which corresponds to the same equations, without the primes, solved for the undilated lattice to give $\xi_R = \alpha F_R$.

If we wish to establish the results corresponding to those of Hookeian elasticity theory, we must assume that $V_{ij}' = V_{ij}$, which is the equivalent of assuming that the elastic constants are unaltered by dilatation. If we do this, it follows that $\alpha = \alpha'$ and $\partial\alpha/\partial\delta = 0$. However, we shall retain terms in $\partial\alpha/\partial\delta$ as we wish to try and extend the formalism to include them.

Thus, if $\xi_R' = \xi_R(1+m\delta)$ to the first order in δ,

$$\xi_R m\delta = \frac{\partial\alpha}{\partial\delta}F_R\delta + \alpha\frac{\partial F_R}{\partial\delta}\delta \tag{25}$$

and

$$\Delta U_1' - \Delta U_1 = \Delta W = -6F_R(r_0\delta+\xi_R m\delta) + \\ +3F_R m\xi_R\delta + 3\xi_R\frac{\partial F_R}{\partial\delta}\delta + \frac{9}{2}K\delta^2 2Nr_0^3. \tag{26}$$

If we now substitute $[\xi_R m - F_R(\partial\alpha/\partial\delta)]\delta$ for $(\alpha\partial F_R/\partial\delta)\delta$ from equation (25) into equation (26), we have:

$$\Delta W = -6F_R r_0\delta - 3\frac{\xi_R F_R}{\alpha}\frac{\partial\alpha}{\partial\delta} + \frac{9}{2}K\delta^2(2Nr_0^3) \tag{27}$$

During this derivation we have neglected any terms in δ^2 whose coefficients are independent of N.

Thus, if we now minimize ΔW with respect to δ, we have:

$$\Delta V_L = 6Nr_0^3\delta = \frac{1}{K}\left[2F_R r_0 + \frac{\xi_R F_R}{\alpha}\frac{\partial\alpha}{\partial\delta}\right] \tag{28}$$

and, if $\partial\alpha/\partial\delta = 0$, $\Delta V_L = \mathscr{G}/K$ as $\mathscr{G} = 2F_R r_0$ and the result agrees with that of continuum theory.

Thus

$$\frac{\Delta V_L}{(2r_0)^3} = \frac{\Delta V_E}{(2r_0)^3} = 9{\cdot}93 \text{ per cent.}$$

An exact calculation of $\partial\alpha/\partial\delta$ would be very tedious, but we can make an estimate. If the coefficients $\left[\begin{smallmatrix}\xi & K'\\ \alpha & \beta\end{smallmatrix}\right]$, from which α is derived, were determined purely by the Coulomb interactions, $\partial\alpha/\partial\delta$ would equal 3α, and, if purely by the repulsive potential, $\partial\alpha/\partial\delta$ would equal 10α (approximately). The true value must lie between these extremes, and if we assume the latter is twice as important as the former, we obtain $\partial\alpha/\partial\delta \triangleq 8\alpha$. This weighting was estimated from KELLERMANN's tables of coupling coefficients. If we assume the two contributions to be of equal importance, we obtain $\partial\alpha/\partial\delta \triangleq 6{\cdot}5\alpha$. This is an underestimate, and we may thus assume that $\partial\alpha/\partial\delta \triangleq [8\mp 1{\cdot}5]\alpha$.

If we use this in equation (28),

$$\frac{\Delta V_L}{(2r_0)^3} = 12{\cdot}0 \pm 0{\cdot}4 \text{ per cent.}$$

Thus ΔV_L alters by 20 per cent and the final result is accurate to ∓ 4 per cent.

6. THE "VOLUME" INTERACTION

If we examine equation (27), we see that it would still be valid for a random array of defects of mean density $1/2Nr_0^3$ provided that the quantities ψ, F_R and ξ_R are not altered by the randomization. The energy ΔW would then be the mean change in energy per defect in such a random array. The assumption is equivalent to that made previously, namely, that the nearest-neighbour displacements about one defect do not depend on the details of our defect array. This is reasonable provided that the average interdefect spacing is large.

We now use equation (27) to calculate δ. This gives us the dilatation energy per defect:

$$\Delta W = -\frac{1}{2}\left[\frac{\partial \Delta U_1}{\partial \delta}\right]^2 \frac{1}{18KNr_0^3}.$$

If our specimen contains n defects per unit volume, then the dilatation energy for this volume:

$$\Delta W_n = -\frac{1}{2}\left[\frac{\partial \Delta U_1}{\partial \delta}\right]^2 \frac{n^2}{9K} \qquad (29)$$

If we introduce one extra defect into a unit volume, we change this energy by

$$\Delta W_{n+1} - \Delta W_n = -\frac{1}{2}\left[\frac{\partial \Delta U_1}{\partial \delta}\right]^2 \frac{(2n+1)}{9K}$$

$$= -3{\cdot}20 \times 10^{-23}(2n+1) \text{ eV}.$$

This energy may be regarded as the lattice equivalent of the interaction found by ESHELBY[7] for an isotropic solid containing many defects. This energy arose in a similar way from the presence of a free surface. The result implies that it is easier to introduce a defect if some are already present, as these dilate the lattice and thus reduce the misfit of the extra defect.

If we have a dilute solution, then the previous argument will apply: we should also note that, as the orientation dependent interaction averages out to zero, the only over-all interaction energy between the defects is the "volume" interaction.

7. COMMENTS

We have shown that the long-range distortion at constant volume in a sodium chloride crystal, due to a "wrong" ion which differs only in its nearest-neighbour interactions, may be simulated in elasticity theory by a force density $-\mathscr{G}\ \text{grad}\ \delta(\boldsymbol{r})$ applied to a continuum of the same elastic constants as sodium chloride, provided that $\mathscr{G}$ is suitably chosen. However, as the lattice is anharmonically strained close to the defect, we must derive $\mathscr{G}$ from the interionic force constants, and we cannot use the elasticity formula which relates $\mathscr{G}$ to the over-all volume change per defect. We have done this, but we have only partially included anharmonic effects. A more rigorous calculation would be very tedious and would not greatly modify our value for the volume change, as we have included the largest part of the anharmonic effect. We could include the effect of alterations in interactions between the defect and ions other than its nearest neighbours in the previous analysis. These are not significant for our particular case.

It is probable that the analysis could be generalized to treat lattices held together by non-central forces (e.g. diamond, germanium). The principal difficulty is that of determining the interaction energy of the various kinds of defect with the lattice. In strongly anisotropic crystals the actual numerical evaluation of the integrals occurring in the expressions for the displacements and interaction energies becomes difficult.

Acknowledgements—The writer wishes to thank Professor M. H. L. PRYCE, who suggested the problem, for continued helpful discussions and encouragement, and the Department of Scientific and Industrial Research for a Research Grant which made the work possible.

REFERENCES

1. ESHELBY J. D., *J. Appl. Phys.* **25,** 255 (1954).
2. MOTT N. F. and LITTLETON M. J., *Trans. Faraday Soc.* **34,** 485 (1938).
3. BRAUER P., *Z. Naturf.* **7**A, 372 (1952).
4. BASSANI F. and THOMSON R., *Phys. Rev.* **102,** 1264 (1956).
5. KANZAKI H., *J. Phys. Chem. Solids* **2,** 24, 107 (1957).
6. MATSUBARA T. J., *J. Phys. Soc. Japan* **7,** 270 (1952).
7. ESHELBY J. D., *Acta Met.* **3,** 487 (1955).
8. KELLERMANN E. W., *Phil. Trans.* **A238,** 513 (1940).
9. BORN M. and HUANG K., *Dynamical Theory of Crystal Lattices* Clarendon Press, Oxford (1954).

J. Phys. Chem. Solids Pergamon Press 1960. Vol. 15. pp. 50–53. Printed in Great Britain.

INFRARED ABSORPTION BY ONE-DIMENSIONAL IONIC LATTICES

H. B. ROSENSTOCK

U.S. Naval Research Laboratory, Washington, D.C.

(*Received* 21 *September* 1959; *revised* 2 *December* 1959)

Abstract—The absorption spectrum due to the atomic motion in a one-dimensional ionic lattice, considered to consist of point particles of equal mass and alternating charge with Coulomb interaction and nearest-neighbor repulsion, is found to consist of a line of shape

$$[-\ln(\omega_{max}-\omega)]^{1/2}/(\omega_{max}-\omega)^{3/2}.$$

VOL
15
196

I. INTRODUCTION

SEVERAL recent papers have attempted to calculate the structure of the far infrared absorption spectrum by ionic crystals which results from the ionic motion.[1–3] It has been shown that if the boundary conditions on the vibrating motion are taken into account correctly, the infinitely sharp absorption lines predicted by classical theory[4] are broadened and, in the case of crystals of more than one dimension, additional absorption peaks appear, as are indeed observed experimentally.

The models so far used in the above calculations have been guided more by mathematical simplicity than by resemblance to reality. Thus in all cases the atomic forces were taken to be short range for the lattice dynamical problem, but the charge on each atom was later used to provide the mechanism for the absorption. Since this electronic charge would provide a long range (Coulomb) force, it was realized that these two assumptions were not consistent but it seemed that the results obtained would nonetheless be qualitatively correct, and perhaps quantitatively reliable for crystals in which the short range forces are strong. The purpose of this paper is to present a calculation in which this inconsistent assumption is not made: we consider the one-dimensional monatomic ionic lattice consisting of N atoms with alternating charges of $\pm e$ and nearest neighbor repulsion and calculate the absorption of light at frequencies near the classical absorption line, taking correct account of both short range and Coulomb forces.

The results are as follows. As in the absence of Coulomb forces, the absorption spectrum of the one-dimensional lattice consists essentially of a single line. If we compare the finite lattice (correct boundary conditions) with the "cyclic" one, both including Coulomb forces, we find that the change in the frequency at which this line occurs is unobservably small, but the change induced in the form of the normal modes of vibration, though also small for any one mode, is such as to produce changes in the analytic shape of the absorption line, in the peak absorption that is attained and in the integrated absorption.

The physically most interesting features in the theoretical lattice absorption spectrum that arise from taking correct account of the boundary conditions are the subsidiary absorption lines. These should not be expected to appear in a one-dimensional problem as is treated in this paper, and they do not. Since the absorption spectrum due to the vibrations of a three-dimensional solid consists essentially of a number of distinct lines, with zero absorption between them, a complete calculation of it would involve two steps: (i) locating the position of the lines and (ii) calculating the shape and intensity of each. Only the first of these steps has been attempted so far;[3] in carrying it out, Coulomb forces were, of course, included, but not the effect on the Coulomb forces of the absence of atoms beyond the boundary of the real crystal. What the present paper teaches about the three-dimensional case is that the error incurred thereby

is essentially negligible, but that correct account would have to be taken of this effect if the second step in the program, viz. the calculation of the shape of each line, were to be taken.

The method we use is first-order perturbation theory; the unperturbed problem is taken to be the one-dimensional ionic lattice with cyclic boundary conditions[5] as far as Coulomb forces are concerned and free ends for the nearest neighbor force;[1] the perturbation is then the negative of the Coulomb force of the fictitious atoms which were included in the unperturbed (cyclic) calculations but are located outside the real crystal. The shape of the absorption line is found to be proportional to $[-\ln(\omega_c-\omega)]^{1/2}/(\omega_c-\omega)^{3/2}$ and the peak intensity (which would be reached if semiclassical radiation theory did not break down) to $N^3/\ln N$. These quantities are not too greatly different from $(\omega_c-\omega)^{-3/2}$ and N^2, respectively, which were obtained earlier[1] with neglect of Coulomb forces, but do differ appreciably from the delta function classically predicted with the use of cyclic boundary conditions.

II. PERTURBATION CALCULATION

After inserting exponential time dependence, the $j(1 \leqslant j \leqslant N)$ equations of motion can be written

$$2\alpha\lambda_j u_j(l) = F_j(l,\{u\}) \tag{1}$$

with

$$\lambda_j = m\omega_j^2/2\alpha$$

where ω_j is the frequency of the jth mode, m the mass of each particle and α the force constant for nearest neighbor interaction; the force F_j exerted on the lth particle is a linear function of the set $\{u\}$ of displacements $u_j(l)$ of all the l particles. Now introduce a perturbing force F_j^1

$$F_j = F_j^0 + F_j^1 \tag{2}$$

which will affect both the displacements

$$u_j = u_j^0 + u_j^1 \tag{3}$$

and frequencies

$$\lambda_j = \lambda_j^0 + \lambda_j^1 \tag{4}$$

where u_j^0 and λ_j^0 are known from the solution of the unperturbed problem and u_j^1 and λ_j^1 are small. Substitution into (1) then gives

$$2\alpha\lambda_j^0 u_j^1(l) - F_j^0(l,\{u^1\}) = F^1(l,\{u^0\}) - 2\alpha\lambda_j^1 u_j^0(l). \tag{5}$$

In our case the F are of the form

$$\left.\begin{aligned} F^0(l,\{u\}) &= \sum_{m=\{0\}} b_m^0 u(l+m) \\ F^1(l,\{u\}) &= \sum_{m=\{1\}} b_m^1 u(l+m), \end{aligned}\right\} \tag{6}$$

the sets $\{0\}$ and $\{1\}$ indicating summations over all particles (real and fictitious) and over the fictitious particles, respectively, as explained in the introduction. It is then convenient to write

$$u_j^0(l) = U_j\psi_j(l) \tag{7}$$

with U_j a constant independent of the space variable l and the ψ orthonormal,

$$\sum_{l=1}^{N} \psi_j(l)\psi_k(l) = 2N\delta_{jk}, \tag{8}$$

and to expand

$$u_j^1(l) = \sum_k c_{jk}\psi_k(l). \tag{9}$$

By the usual methods of first order perturbation theory one then finds

$$\lambda_j^1 = \frac{2}{2N\alpha}\sum_l \psi_j(l) \sum_{m=\{1\}} b_m^1\psi_j(l+m), \tag{10}$$

$$\frac{c_{jk}}{U_j} = \frac{1}{2N\alpha}\,\frac{\sum_l \psi_k(l) \sum_{m=\{1\}} b_m^1\psi_j(l+m)}{\lambda_j^0-\lambda_k^0}. \tag{11}$$

To evaluate (10) and (11) we need the unperturbed ψ and λ_j^0. The unperturbed eigenvalues for the cyclic lattice[5] are

$$\begin{aligned} \lambda_j^0 &= 1-\cos\phi_j - \sigma S(\phi_j/\pi), \\ S(p) &= \sum_{k=1}^{\infty} (-)^k k^{-3}(\cos k\pi p - 1), \\ \sigma &= 2e^2/\alpha a^3, \end{aligned} \tag{12}$$

a is the distance between nearest neighbors and e the atomic charge. The unperturbed eigenfunctions are generally $A\exp(il\phi_j)+B\exp(-il\phi_j)$, but it was shown in Section I that proper account is taken of the absence of nearest neighbor forces on particles l and N by simply closing A and B so as to make these functions

$$\psi_j(l) = \cos(l-\tfrac{1}{2})\phi_j, \qquad \phi_j = j\pi/N. \tag{13}$$

Note that these functions satisfy equation (8). The only perturbation is thus the negative of the Coulomb force exerted by the fictitious particles in the infinite cyclic lattice that are located outside the real crystal (i.e. particles numbered from $-\infty$ to -1 and from $N+1$ to $+\infty$). It can be put into suitable form in the usual way by expanding $1/r$ in terms of the $u_j(l)$,

$$-F_j^1(l,\{u\}) = \frac{2e^2}{a^3}\left[-\sum_{m=-\infty}^{-l} + \sum_{m=N+1-l}^{\infty}\right]\times$$
$$\times(-)^m m^{-3}[u(l+m)-u(l)]. \qquad (14)$$

Terms of order u^2/a^4, and ut/a^4, with t the static displacement of an atom from equilibrium on account of the asymetry of the coulomb force exerted on it by the finite lattice, have been neglected. Equation (14) is of the form (6), and equations (10), (11) can thus be evaluated with it.

In carrying out this evaluation, it is, first of all, convenient to consider the variable

$$\phi_j' = \pi-\phi_j = \pi(N-j)/N = \pi j'/N \qquad (15)$$

instead of ϕ_j, because the large absorption will occur for small ϕ_j'. One then encounters double sums of the form

$$\sum_{l=1}^{N}\sum_{m=l}^{\infty} f m^{-3}$$

where f is a trigonometric function of l, m, ϕ_k' and ϕ_j'. This may be replaced by

$$\sum_{l=1}^{\infty}\sum_{m=l}^{\infty} f m^{-3},$$

not only for $N\to\infty$, but also for fairly small N since the m^{-3} assures that only the terms corresponding to small l will contribute significantly. The sums may then be written

$$\sum_{m=1}^{\infty} m^{-3}\sum_{l=1}^{m} f$$

and the l-sum replaced by an integral with negligible error for our purposes, as can be shown by an application of the Euler–McLaurin formula. This then gives some trigonometric series of the form

$$\sum_{m=1}^{\infty}(\pm)^m m^{-2\text{ or }3}\begin{matrix}\sin\\ \cos\end{matrix}(m\phi')$$

which converge to known functions.[7]

The results are

$$\lambda_j^1 = \frac{\sigma\pi}{16N}\phi_j' \qquad (16)$$

and

$$\frac{c_{jk}}{U_j} = \frac{\sigma\pi}{4N}\frac{\phi_j'\phi_k'}{(\phi_j'+\phi_k')(\lambda_j^0-\lambda_k^0)} \qquad (17)$$

They are valid to first order in ϕ'; i.e. equations (16) and (17) should strictly be multiplied by a term $[1+0(\phi')]$. We note that the perturbation of the eigenvalue λ_j^1 is small and surely unobservable. c_{jk}/U_j is also small but may have more substantial effects on the optical properties, as is discussed in the next section.

III. DIPOLE MOMENTS

Defining M_j as the dipole moment of the lattice associated with mode j,

$$M_j = e\sum_l (-)^l u_j(l) \qquad (18)$$

we find with equations (3) (7) and (9)

$$M_j = eU_j[p_j^0+p_j^1] \qquad (19)$$

with

$$p_j^0 = \sum_l (-)^l\psi_j(l)$$
$$p_j^1 = \sum_k (c_{jk}/U_j)p_k^0. \qquad (20)$$

p_j^0 is given by equation (13) of Section II and may be expanded,

$$p_j^0 = \begin{cases} -2/\phi_j' & \text{if } j' \text{ is odd}\\ 0 & \text{if } j' \text{ is even.}\end{cases} \qquad (21)$$

p_j^1 becomes with equations (21) and (17)

$$p_j^1 = -\frac{\sigma\pi}{2N}\sum_{k'=\text{odd}}[(\phi_k'+\phi_j')(\lambda_{j'}^0-\lambda_{k'}^0)]^{-1}. \qquad (22)$$

To write λ as a function of ϕ' we use equation (12) expanded[5] for small ϕ' and get

$$p_j^1 = -\frac{\pi}{N}\phi_j'\sum_{k'=\text{odd}}[(\phi_k'+\phi_j')(\phi_k'^2\ln\phi_k'-\phi_j'^2\ln\phi_j')]^{-1}. \qquad (23)$$

The main contribution to this sum comes from near $k'=0$ because the large contribution from near $k'=j'$ cancels out (the term $k'=j'$ itself is

omitted from the sum). The sum can thus be replaced by an integral,

$$(-2\phi_j'^2 \ln \phi_j)^{-1} \int_{\phi_{s'}}^{} \frac{N\, d\mathrm{A}}{\pi \mathrm{A}}$$

and (23) becomes

$$p_{j'}^1 = -1/2\phi_j'. \tag{24}$$

Putting this and relation (21) into equation (19) yields then

$$M_j = \frac{eU_j}{2\phi_j} \begin{cases} 4+1 & j' \text{ odd} \\ 1 & j' \text{ even.} \end{cases} \tag{25}$$

It is interesting to note here that the effect of the perturbation on M is of the same order, ϕ^{-1}, as the unperturbed quantity and is only somewhat smaller numerically, in spite of the fact that the perturbation on u_j, as given by equation (17), was quite small.

The quantity of physical interest is $M_{j'}$ which we write as

$$(M_{j'})^2 = 13e^2U_j^2/4\phi_{j'}^2, \tag{26}$$

by squaring equation (25) and averaging contributions from even and odd j (because contributions from adjacent j's cannot be distinguished experimentally). In the absence of the perturbation, thirteen in equation (26) would be replaced by eight.

IV. THE ABSORPTION LINE

The absorption in frequency range $d\lambda$ is, in the notation of Section I, proportional to

$$\pi^2\, d\lambda = M^2 g(\lambda)\, d\lambda \tag{27}$$

where $g(\lambda)$ is the density of frequencies and M^2 of equation (26) has to be written as a function of λ rather than of the unobservable ϕ_j'. We have written here

$$\lambda = (2/\sigma)(\lambda_{j'}^0 - \lambda_0^0) \tag{28}$$

where

$$\lambda_0^0 = (2/\sigma)(1+\sigma\xi_3) \tag{29}$$

is the classical limiting frequency at which maximum absorption occurs.[5] The relation between ϕ' and λ is given by equation (12); for small λ it becomes[5]

$$\lambda = -\phi'^2 \ln \phi'. \tag{30}$$

GILLIS and WEISS[6] have solved this equation (for small ϕ'),

$$\phi' = (-2\lambda/\ln 2\lambda)^{1/2} \tag{31}$$

and have also given the frequency distribution

$$g(\lambda) = (-1/2\lambda \ln 2\lambda)^{1/2}. \tag{32}$$

Thus the shape of the absorption line, equation (27), becomes

$$\pi^2(\lambda)\, d\lambda \cong \frac{13}{4} e^2 \frac{(-\ln 2\lambda)^{1/2}}{(2\lambda)^{3/2}}. \tag{33}$$

Its peak value is taken on when $j' = 1$ or $\phi_j' = \pi/N$ or, by equation (30), when $\lambda \cong \ln N/N^2$; it is therefore, by equation (33), proportional to $N^3/\ln N$.

V. CONCLUSIONS

The lattice absorption spectrum of a one-dimensional ionic crystal has been calculated. The shape of the absorption line is found to be $[-\ln(\omega_c-\omega)]^{1/2}/(\omega_c-\omega)^{3/2}$, as compared to $(\omega_c-\omega)^{-3/2}$ with neglect of Coulomb forces. Also, the peak intensity is $N^3/\ln N$ instead of N^2. The position of the absorption line is found negligibly affected. This last fact indicates that the calculation of the positions of the absorption peaks in real crystals[3] needs no appreciable modification, even in three dimensions. The fact that the line shape is significantly affected in one dimension suggests the same in higher dimensions. Although the present method of treating the "absent" atoms beyond the boundaries of the real crystal as a perturbation on the cyclic lattice with Coulomb forces is, in principle, applicable to higher dimensions as well, its use presupposes knowledge, given by equation (30) in one dimension but not presently available for ionic crystals of dimensions higher than one, of the behavior of the dispersion relation near the critical points in reciprocal space.

Acknowledgements—I am grateful to Drs. R. F. WALLIS and C. C. KLICK for discussions.

REFERENCES

1. ROSENSTOCK H. B., *J. Chem. Phys.* **23,** 2415 (1955).
2. ROSENSTOCK H. B., *J. Chem. Phys.* **27,** 1194 (1957).
3. ROSENSTOCK H. B., *J. Phys. Chem. Solids* **4,** 201 (1958).
4. BORN M. and MAYER M. G., *Handbuch der Physik* Bd. 24, S.632. Springer, Berlin (1953).
5. ROSENSTOCK H. B., *Phys. Rev.* **111,** 755 (1958).
6. GILLIS J. and WEISS G., *Phys. Rev.* **115,** 1520 (1959).
7. DWIGHT H. B., *Tables of Integrals* p. 83. MacMillan, New York (1947).

VOL. 15 1960

J. Phys. Chem. Solids Pergamon Press 1960. Vol. 15. pp. 54–65. Printed in Great Britain.

HIGH FIELD MAGNETIZATION STUDY OF FERRIMAGNETIC ARRANGEMENTS IN CHROMITE SPINELS

I. S. JACOBS

General Electric Research Laboratory, Schenectady, New York

(*Received* 9 *October* 1959; *revised* 14 *November* 1959)

Abstract—The observation of a differential susceptibility at high magnetic fields and low temperatures in spinel-type compounds has been shown to be useful for detecting non-collinear ferrimagnetic arrangements. Such an increase in net magnetization with field is not expected for the Néel model of tetrahedral *A*-site moments antiparallel to octahedral *B*-site moments. It is, however, expected for the triangular arrangements proposed by YAFET and KITTEL in which the moments on one kind of site subdivide into two groups making angles with each other. The latter arrangements have frequently been suggested for chromium-containing spinels, usually on the basis of the observed anomalously low spontaneous magnetizations. Measurements of magnetization curves at 4·2°K in pulsed fields up to 140 kOe reveal high field susceptibilities in $MnFe_{2-t}Cr_tO_4$, $t > 0$; $CuCr_2O_4$; $FeCr_2O_4$; and $NiFe_{2-t}Cr_tO_4$, $t > 1$. These are interpreted as triangular ferrimagnetic arrangements and choices are made between alternative triangular models. In some cases the sign of the dominant anisotropy is suggested. Néel antiparallel ferrimagnetic arrays are confirmed for $MnFe_2O_4$ and for $NiFe_{2-t}Cr_tO_4$, $t < 1$. The present evidence for these conclusions is of a new and occasionally more direct type.

INTRODUCTION

FERRIMAGNETIC compounds with spinel-type crystal structure which contain chromium frequently have anomalously low spontaneous magnetizations when viewed from the simple NÉEL[1] model with tetrahedral *A*-site moments antiparallel to octahedral *B*-site moments. The deviations are usually more pronounced as the composition approaches MCr_2O_4, where M is a divalent metal ion. The effects are seen in studies on the substitution of chromium for iron in ferrite spinels MFe_2O_4, whose magnetic properties are well understood from the Néel theory. The main features of the ferrimagnetism of chromites emerged from the work of MCGUIRE and co-workers,[2] GORTER[3] and LOTGERING[4]. A number of additional studies have elaborated on the magnetic behavior of mixed spinels containing chromium.[5–11]

One simplification in the study of chromite spinels is the strong affinity of Cr^{3+} ions for the *B*-sites, revealed first by X-ray studies,[12,13] and confirmed by neutron diffraction.[14–16] Using this feature, LOTGERING[4] made a detailed application of the YAFET–KITTEL[17] theory to several "normal" chromites $M[Cr_2]O_4$, where the square brackets indicate the occupation of octahedral *B*-sites. The latter authors noted that when *A*–*A* or *B*–*B* antiparallel interactions are comparable to the *A*–*B* interaction, the moments on either *A* or *B* site will divide into two parts, making an angle with each other but with the resultant moment antiparallel to the moment on the other kind of site. Such a configuration is called a triangular arrangement and is qualitatively capable of accounting for anomalous spontaneous magnetizations. LOTGERING's analysis showed that the properties of $MnCr_2O_4$ and $FeCr_2O_4$ were consistent with a triangular ferrimagnetic arrangement. The Yafet–Kittel model had been invoked qualitatively by many other workers studying the magnetic properties of chromium spinels, while another detailed analysis was performed by EDWARDS[7] on the series $MnCr_{2-t}Al_tO_4$. EDWARDS also found considerable evidence for triangular ferrimagnetic arrangements.

From a neutron diffraction study of $CuCr_2O_4$, PRINCE[14] found strong support for the Yafet–Kittel model in the appearance of magnetic reflections

VOL. 15 1960

forbidden by the nuclear structure and requiring the division of the Cr^{3+} ion moments into two non-parallel groups. However, similar investigations by PICKART and NATHANS of several manganese[15] and nickel[16] ferrite–chromites yielded no evidence for ordered triangular arrangements, although anomalous magnetic properties had been reported previously.[3,6,11] They note that neutron diffraction would be insensitive to such arrangements if they exist with only short range rather than long range order. An alternative suggestion of "spin-quenched" moments on Cr^{3+} ions has also been offered[18] to account for the low spontaneous magnetizations.

Recently, both EDWARDS[7b] and the author[19] independently pointed out that a consequence of a triangular moment arrangement is that at fields higher than those required for ferrimagnetic domain alignment and at low temperature, there should be a linear increase in the net magnetization with field. This differential susceptibility at high fields measures the exchange between the groups of moments which have split to make angles. Qualitatively similar behavior should occur in any non-collinear arrangement, but should be absent in the simple antiparallel ferrimagnetic scheme. Applied to a series of manganite spinels,[19] this high field technique proved useful in detecting the Yafet–Kittel arrangements. A neutron diffraction study on Mn_3O_4 by KASPER[20] confirmed and elaborated upon this conclusion.

Néel has proposed a non-collinear arrangement in which the magnetization of the group of ions on one site is not saturated. As noted by EDWARDS, this arrangement would exhibit a high field susceptibility at low temperatures. This model has often been criticized, particularly at absolute zero. It predicts a non-zero slope for the temperature dependence of spontaneous moment at low temperature. This is not observed in magnetization measurements on the simple chromite spinels.[4,7] It is also not observed in neutron diffraction measurements on a mixed ferrite–chromite.[15] Additional evidence for rejection is found in the positive neutron diffraction results cited for some ordered non-collinear arrays. Consequently the alternative provided by this Néel model with unsaturated site moments will not be considered further herein.

The present work applies the high field technique to a number of chromium-containing spinels.[21] Evidence is presented which supports previous views of the ferrimagnetic arrangements in some compounds, both of the Néel type and the Yafet–Kittel type. For certain compounds, the evidence enables a resolution of ambiguities regarding the spin arrangement. It proves to be particularly useful in detecting non-collinear arrangements which are unresolved by neutron diffraction, such as in disordered mixed ferrite–chromites.

EXPERIMENTAL

The compounds studied are all in powder form. Measurements on single crystals would be preferable in most cases in that the troublesome aspects of crystal anisotropy could be directly assessed and the ferrimagnetic structure analysed more quantitatively. These aspects are discussed below. In most cases the powder sample material was identical with that used in previous studies of the magnetic or structural properties.

The principal measurement made on each compound was the magnetization curve at temperatures of 77°K, 20·4°K and/or 4·2°K. Pulsed fields up to 140 kOe were used, with the measurement technique described earlier.[22] The samples were demagnetized before each pulse measurement, either thermally, by raising them above their Curie temperature, or magnetically, by decreasing to zero an a.c. field (60 c/s) whose maximum amplitude was 6 kOe. The latter technique permitted an observation of the hysteresis loop to ± 6 kOe with the same detectors used in the pulse measurement. The demagnetized state, as well as the remanent states, were measured by a sample motion method using a Grassot type fluxmeter.

The manganese ferrite–chromite series, $MnFe_{2-t}Cr_tO_4$ is studied on the set of compositions $t = 0, 0{\cdot}5, 1{\cdot}0, 1{\cdot}5, 2{\cdot}0$. The ferrite ($t = 0$) was obtained from V. C. WILSON of this Laboratory and is part of the sample used in a neutron diffraction study.[23] The others were obtained from the U.S. Naval Ordnance Laboratory through S. J. PICKART, T. R. MCGUIRE and P. L. EDWARDS. These latter samples are identical with those used in previous work.[7,15] All of the compounds in this group retain the cubic spinel crystal structure, even at low temperature.[15,23,24]

Copper chromite, $CuCr_2O_4$, is included in this work, with a sample prepared at the Bell Telephone Laboratories, obtained through E. PRINCE. It is part of the lot used in his neutron diffraction investigation.[14] This compound has a tetragonally distorted spinel structure[2,25] at room temperature with a c/a ratio of 0·91 (referred to the spinel-like unit cell). The temperature of a possible transformation to a cubic spinel is not known.

Iron chromite, $FeCr_2O_4$, is also studied in a sample prepared at this Laboratory by A. U. SEYBOLT. Very finely divided FeO and Cr_2O_3 powders were ball milled together in alcohol and subsequently fired at 1300°C for

15 hr in a nitrogen atmosphere. Chemical analysis for the cations indicated a composition $Fe_{1.01}Cr_{2.00}O_4$, while X-ray diffraction showed a single phase, of cubic structure, having a lattice parameter $a_0 = 8{\cdot}376 \pm 0{\cdot}002$ Å in agreement with previous work.[26] Below room temperature the structure distorts tetragonally,[24,27] starting at about $-90°C$.

Lastly, the nickel ferrite–chromite series, $NiFe_{2-t}Cr_tO_4$, is studied in the same way. Samples with $t = 0{\cdot}5$, $1{\cdot}0$, $1{\cdot}5$, $1{\cdot}85$ and $2{\cdot}0$ were obtained from T. R. McGuire, and are identical with material used in previous studies.[6,8,16] The crystal structure is cubic in the composition range $0 \leqslant t \leqslant 1$, while it is tetragonal in the range $1 < t \leqslant 2$,[8,11,28] below room temperature. An exception is the compound $t = 2$ which distorts at 30°C. At still lower temperature part of the latter range shows further distortion to orthorhombic symmetry,[8,11] rather like the behavior in the iron ferrite–chromite series.[27]

In the above listing much attention is paid to distortions from the cubic spinel structure. The origin of these Jahn–Teller type distortions has recently been the subject of much theoretical effort.[29–31] Broadly speaking there is good agreement between prediction and observation on this point. The occurrence of such distortions has two important consequences for the understanding of the present measurements. The first arises from the possibility of a large magnetocrystalline anisotropy associated with distorted structures. In high field magnetization measurements on *powders*, where one looks for a differential susceptibility at high field as the clue to a non-collinear ferrimagnetic array, it is necessary to distinguish this from an approach to saturation against a large magnetocrystalline anisotropy, K. In the present case the safest situation for analysis exists when one may prove or assume that the maximum anisotropy field ($H_A = 2K/M_0$, M_0 being the spontaneous magnetization) does not exceed about half the maximum measuring field, or $H_A \lesssim 70$ kOe. For most pure chromites, MCr_2O_4, the value of M_0 is about 100 or less, which leads to a requirement that K be less than 4×10^6ergs/cm^3. While this is easily satisfied by most cubic materials, it is unsafe to assume its validity for lower symmetry structures. Thus caution is necessary in interpreting magnetization curves of such compounds.

For a dominating uniaxial magnetocrystalline anisotropy energy of the form $E_K = K \sin^2\phi$, there are two cases of interest, corresponding to either positive or negative values of K. For negative K, a particular direction is quite hard magnetically, and the plane normal thereto is easy. (There may, of course, be anisotropy within this easy plane, but this is assumed to be much smaller than that out of the plane.) As noted earlier,[19b] in the presence of an anisotropy field exceeding the maximum measuring field, the spontaneous magnetization estimated from powder data by linear extrapolation back to zero field will be about $\pi/4$ times the true value. The observed high field susceptibility in this case may be higher than that characterizing the exchange in a non-collinear ferrimagnetic, but this observed susceptibility will decrease with increasing anisotropy field to a value which is also $\pi/4$ times the true value. The ratio of remanence to spontaneous magnetization may lie between $\pi/4$ and $\frac{1}{2}$, depending on the effective number of easy directions in the magnetically easy plane (between all directions equally preferred and uniaxial anisotropy, respectively). An important case is that of 2 perpendicular easy axes in the plane, for which the ratio is $\sqrt{2}/2$).[32] For positive K, one direction is magnetically easy, and the plane normal thereto is hard. In favorable examples of this case it may be possible to detect the presence of a very large anisotropy field from the field dependence of the isothermal remanence, or its value compared to the thermoremanence, or simply from the shape of the magnetization curve.[33] The ratio of saturated remanence to spontaneous magnetization is $\frac{1}{2}$, which allows a specific estimate of the latter quantity. The observed high field susceptibility may again be higher or lower than that characterizing the non-collinear exchange, depending on the ratio of the anisotropy field to the maximum measuring field. In the limit of very high anisotropy field the observed high field susceptibility will be about half the "true" value. These arguments assume approximately equivalent anisotropies for the ionic moments on different sites. If these anisotropies differed considerably, a more detailed analysis would be required, and modified conclusions would be expected.

For the two cases of uniaxial anisotropy it appears possible to estimate roughly the spontaneous magnetization from remanence measurements in addition to the estimate made from an extrapolation to $H = 0$. Decisions about the magnitude of the high field exchange susceptibility are less precise, except in favorable cases. Each of these considerations is left uncertain by the absence of prior

VOL. 15 1960

information which could suggest a choice between $K < 0$ or $K > 0$ for most of the materials studied. The magnetization data on each compound must be examined individually.

The second general consequence of such distortions arises from the usefulness of magnetic parameters derived from measurements at higher temperatures.[4,7,19] Thus the ferrimagnetic Curie temperature T_f, the asymptotic Curie temperature found from the paramagnetism at high temperatures T_a, and the slope of the reciprocal susceptibility vs. temperature curve are important. The distortions in these chromite spinels usually occur at a temperature above the ferrimagnetic Curie temperature. If the temperature of the structure distortion is known to be sufficiently high that the parameters are derived from data with the same low temperature structure, the possible correlations are valid. Otherwise, they may be suspect since the strength of the magnetic interactions can depend on the crystal symmetry, as well as on the interionic distances.

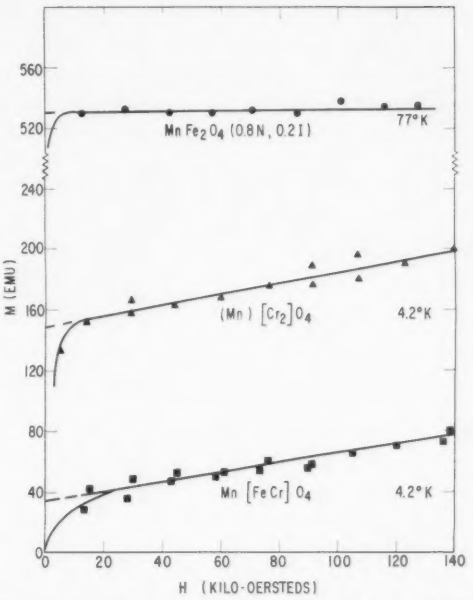

FIG. 1. Magnetization per unit volume M vs. field H for 3 powder samples in the system $MnFe_{2-t}Cr_tO_4$. The designation (N, I) refers to normal and inverse distribution of cations. The square brackets indicate octahedral B-site occupation.

RESULTS AND DISCUSSION

The System $MnFe_{2-t}Cr_tO_4$:

Magnetization curves at high fields are shown in Fig. 1 for three of the compounds in this series, $t = 0$, 1 and 2. A summary of data taken at several temperatures for all five compounds is presented in Table 1, where the data on the differential

Table 1. *Summary of data for the system* $MnFe_{2-t}Cr_tO_4$

t	T (°K)	M_0 (e.m.u./cm³)	m_0 (μ_B/molecule)	Vol. susc. ($10^4\kappa$, c.g.s.)
0	77	530	4·4	$<0·5$
	4·2	—	4·6*	—
0·5	4·2	230 ± 5	$1·90 \pm 0·05$	$0·5 \pm 0·5$
	20, 77	230 ± 5	$1·90 \pm 0·05$	$1·5 \pm 0·5$
1·0	4·2	37 ± 5	$0·30 \pm 0·05$	$2·8 \pm 0·5$
	20	32 ± 5	$0·26 \pm 0·05$	$3·1 \pm 0·5$
	77	31 ± 5	$0·26 \pm 0·05$	$2·3 \pm 0·5$
1·5	4·2	91 ± 5	$0·74 \pm 0·05$	$3·5 \pm 0·5$
	20	93 ± 5	$0·76 \pm 0·05$	$3·3 \pm 0·5$
2·0	4·2	150 ± 5	$1·21 \pm 0·05$	$3·6 \pm 0·5$
	20	155 ± 5	$1·25 \pm 0·05$	$4·5 \pm 0·5$

* Reported by HASTINGS and CORLISS on this material, Ref. (23); author's unpublished measurements to 5 kOe give $4·5 \pm 0·1$.

susceptibility (volume) at high fields is of principal interest. Since there are no Jahn–Teller type distortions in these compounds, the presence of such susceptibilities for $t > 0$ is probably to be associated with the ferrimagnetic arrangement and *not* with an approach to saturation against magnetocrystalline anisotropy.

This system has previously been studied by magnetic measurements[3,4,7] and by neutron diffraction.[23,15] The former studies indicated low net magnetization for $t > 0$ and suggested the possibility of triangular arrangements, while the latter work for $t = 0{\cdot}5$, $1{\cdot}0$ and $1{\cdot}5$ was unable to detect these. For $t = 0$, $MnFe_2O_4$, most magnetic measurements have indicated a moment/molecule, m_0, of about $4{\cdot}6\ \mu_B$, which is a little lower than the predicted value of $5{\cdot}0\ \mu_B$ per molecule. The present observation of no high field susceptibility is consistent with the Néel antiparallel ferrimagnetic arrangement, while it sheds no light on the various suggestions for the lower moment, such as stoichiometric deviations,[34] or that the moment of the Mn^{2+} ion on tetrahedral A-sites is reduced to $4{\cdot}6\ \mu_B$ from $5\ \mu_B$.[35]

The ionic distribution revealed by neutron diffraction indicates about 80 per cent of the A-sites occupied by Mn^{2+} at $t = 0$[23] with an increase upon addition of Cr^{3+}. The Mn^{2+} occupation of A-sites is nearly 100 per cent at $t = 1{\cdot}5$.[15] At $t = 2$, the distribution is undoubtedly that of a "normal" spinel, $Mn[Cr_2]O_4$.

The effective magnetic moment per ion may be determined from a plot of reciprocal susceptibility vs. temperature in the *paramagnetic* state. For $MnCr_2O_4$, the measurements of McGuire and coworkers[2] insure that the spin-only values are appropriate for the Mn^{2+} and Cr^{3+} ions.

$MnCr_2O_4$ thus is ideally suited to analysis by Lotgering's formulation of the Yafet–Kittel theory. Both Lotgering[4] and Edwards[7] correlated the magnetic observations on this compound with the theory, and each concluded that there is good evidence for a triangular ferrimagnetic arrangement. The spontaneous moment/molecule, m_0, of about $1{\cdot}2\ \mu_B$, observed at low temperature, may be obtained with two possible triangular arrangements assuming spin-only moments/ion; in one the B-site moments split into two groups so that the net B-site moment is $3{\cdot}8\ \mu_B$ directed oppositely to the net A-site moment of $5\ \mu_B$, while in the second the A-site moments split slightly to yield a net A-site moment of $4{\cdot}8\ \mu_B$ opposed by a net (unsplit) B-site moment of $6\ \mu_B$. Lotgering rules out the array with angles on the A-sites on the ground that strong interactions between A-site moments are unlikely. Edwards considers both cases but, with Lotgering, favors that with angles on the B-sites based on the magnetic behavior upon substitution of Al^{3+}, and on the correlation of theory and experiment for the effective g-value found by magnetic resonance.

As shown previously[19,7] the reciprocal of the high field susceptibility at low temperature measures the exchange interaction between moments on the site with angles. In Lotgering's notation this is $n\beta$ or $n\alpha$ for angles on B-sites or A-sites, respectively. (n is the Weiss constant for antiferromagnetic A–B interaction, and β or α are the ratios of B–B or A–A interactions to A–B interaction.) Lotgering estimates $n\beta = 50$ (molar units), and Edwards calculates $n\beta = 60 \pm 5$ or $n\alpha = 65 \pm 5$, with the uncertainty arising from two different versions of the theory. These estimates are obtained from theory, using m_0 and the higher temperature parameters T_a and T_f. The values of this exchange parameter ($n\beta$ or $n\alpha$) obtained directly from the observed high field susceptibilities (Table 1) are 62 ± 6 at $4{\cdot}2$°K and 49 ± 6 at 20°K, which are in good agreement with either of the predictions. Thus the high field measurement does not distinguish between the two possible triangular arrays but does provide considerable support for the existence of a triangular array in $MnCr_2O_4$.

It is interesting to note that a choice may be made from high field data if the two possible arrays considered use, as an alternate assumption, a moment per Mn^{2+} ion of $4{\cdot}6\ \mu_B$,[35] along with the spin-only moment for Cr^{3+}. Both arrays have angles on the B-sites; one with a large angle between B-site moments and a net B-site moment of $3{\cdot}4\ \mu_B$, and the second with a small angle and a net B-site moment of $5{\cdot}8\ \mu_B$. This latter version is the *only* one which has angles on the site having the larger net moment, and thus would show ferrimagnetic saturation, at $1{\cdot}4\ \mu_B$/molecule ($M = 175$ e.m.u.) in sufficiently large fields. Inasmuch as the data in Fig. 1 easily exceed this value, this particular arrangement is rejected, leaving that one with a large angle between B-site moments.

In the absence of a neutron diffraction solution to the magnetic structure, there is no direct evidence for a choice between the allowable arrangements. To the indirect evidence and arguments

VOL. 15 1960

cited above in favor of a version with *B*-site angles, may be added the neutron diffraction observation on mixed ferrite-chromites[15] ($t = 0{\cdot}5$, $1{\cdot}0$ and $1{\cdot}5$) that the net *B*-site moment is much lower than predicted by the Néel antiparallel model. It would be surprising if this trend were reversed at $t = 2$. The theoretical arguments put forth by WICKHAM and GOODENOUGH[36] also infer strong antiferromagnetic interactions between Cr^{3+} ion moments.

A somewhat different magnetic structure for $MnCr_2O_4$, with some *B*-site moments *parallel* to *A*-site moments, the remainder being antiparallel thereto, is suggested by WICKHAM and GOODENOUGH[36], similar to models used by GORTER[3] and MCGUIRE[11]. The physical basis behind this structure has not been elucidated. Calculations on a simplified linear chain model indicate that such a structure would have a field dependence and magnitude which does not fit the present results.

The arguments and correlation with theory cited above in support of a triangular ferrimagnetic arrangement in $MnCr_2O_4$ do not require long range order of the *B*-site moments. Although the *B*-sites are occupied solely by Cr^{3+} ions, the difficulties in obtaining long range magnetic order on these sites in a *cubic* spinel have been pointed out by ANDERSON[37] and by KAPLAN[38]. For example, the angle between the individual *B*-site moments and the *A*-site moment may be constant while the orientations of the transverse component of these *B*-site moments may be nearly randomly distributed on the plane normal to the *A*-site moment. With this randomness, or with short range order in these orientations, neutron diffraction investigation of the Bragg peaks would fail to provide positive evidence for a *triangular* arrangement, but would indicate the magnitude of the net moment on each type of site. In this connection, several non-collinear antiferromagnetic structures have been proposed i.e. multispin axis structure[39] and screw type structure.[40]

Considering the mixed manganese ferrite–chromites, $t = 0{\cdot}5$, $1{\cdot}0$ and $1{\cdot}5$, it is apparent that detailed analysis is more difficult. The focus of attention is on the *B*-sites because neutron diffraction studies by PICKART and NATHANS[15] and magnetization studies by GORTER[3] have shown that the net *B*-site moment of these compounds is lower than expected from the Néel antiparallel model. These and other investigations have shown that the ionic occupation of the *B*-sites is almost completely Fe^{3+} and Cr^{3+} i.e. $[Cr_tFe_{2-t}]$. PICKART and NATHANS also show that there is no long range order on the *B*-sites, in agreement with the prediction of ANDERSON[37] that short range ionic order is likely but long range order is not. A theoretical analysis would thus require a minimum of six Weiss interaction coefficients, while three are adequate for a minimal treatment of a "normal" spinel $X[Y_2]O_4$. Further, the approximately linear variation of lattice parameter and ferrimagnetic Curie temperature[3] indicate that the compounds are rather homogeneous.

The results presented in Table 1 indicate a monotonic increase in the value of the high field susceptibility as the chromium content increases. The data are not sufficiently precise to attach significance to the apparent non-linearity of this increase. From a simple point of view the behavior is consistent with a gradual change from an antiparallel Néel ferrimagnetic at $t = 0$ to a triangular Yafet–Kittel ferrimagnetic at $t = 2$, the average *A*–*B* interaction gradually weakening while the average *B*–*B* interaction increases. However, an alternate model has been proposed and needs to be examined.

It was pointed out by GORTER that the decrease of spontaneous moment upon substitution of Cr^{3+} ions for Fe^{3+} in $MnFe_2O_4$ may be approximately fitted in the range $0 \leqslant t < 0{\cdot}5$ by the assumption that the moment of the Cr^{3+} ion on the *B*-site is aligned *parallel* to the moment on the *A*-site. As noted above, this assumption has been extended to cover $MnCr_2O_4$ and also intermediate members of the series,[36] provided that an upper limit is kept to the number of such reversely oriented ionic moments. The objection to this model based on an expected non-linear field dependence is particularly applicable in this range.

With a decision in favor of angled moments, the spontaneous moment values must be accounted for with such a structure. The deviation from the Néel model for small additions of chromium depends on the first power of the chromium content.[3] This suggests that each Cr^{3+} ion moment initially perturbs its Fe^{3+} environment, by the introduction of *B*-site angles, enough to bring about a net reduction of the total moment nearly equal to that caused by reversing the Cr^{3+} ion moment. (The same Cr^{3+}–Fe^{3+} interaction would

be required in the reversed moment model, also.) This is probably aided by the fact that the *A–B* interaction in $MnFe_2O_4$ is weaker than for most other ferrites, judged by their Curie temperatures,[41] and that the introduction of Cr^{3+} will tend to weaken this further. The likelihood of significant antiferromagnetic *B–B* interactions between Cr^{3+} and Fe^{3+} is also suggested by WICKHAM and GOODENOUGH[36].

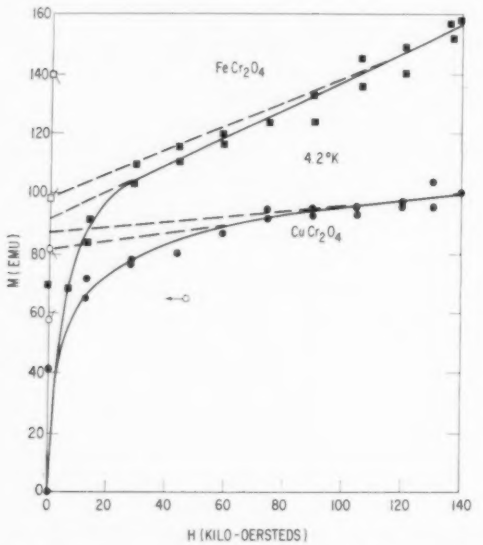

FIG. 2. Magnetization per unit volume M vs. field H for $CuCr_2O_4$ and $FeCr_2O_4$ powders at 4·2°K. Along the $H = 0$ axis are shown the remanence, M_R, for each compound (solid symbol) and the points indicating $\sqrt{(2)}M_R$ and $2M_R$ (open symbol with upward flag and downward flag, respectively). For $CuCr_2O_4$, the open circle with horizontal arrow indicates the previously reported saturation magnetization.

The same remarks as above regarding the difficulty of observing angled moments with neutron diffraction are applicable to these mixed ferrite–chromites, with the added emphasis deriving from the ionic disorder.

In summary, the system $MnFe_{2-t}Cr_tO_4$ presents good evidence for triangular ferrimagnetic arrangements for $t > 0$. These Yafet–Kittel type arrangements appear to be present even in the absence of long range ionic or magnetic moment order. The evidence from various studies points to angles between moments on the *B*-sites with a change of the larger net moment from *B*-site at $t = 0$ to *A*-site at $t = 2$, as suggested by GORTER.

$CuCr_2O_4$:

The high field magnetization curve at 4·2°K, the remanent magnetization as measured by a flux-meter and the previously reported "saturation" magnetization[14] for this compound are shown in Fig. 2. Also indicated are points corresponding to $\sqrt{(2)}M_R$ and $2M_R$. It is clear that magnetization values appreciably higher than the "saturation" can be attained. As noted above, $CuCr_2O_4$ has a special position in that the neutron diffraction study by PRINCE revealed a division of the Cr^{3+} ion moments into two non-parallel groups with long range order. This constituted strong support for the Yafet–Kittel model. The present measurements complement the previous work.

From an examination of the magnetization curve above 70 kOe, it is difficult to say with certainty that a high field susceptibility is present, although one is suggested and may be roughly estimated at $1{\cdot}0 \pm 0{\cdot}5 \times 10^{-4}$ c.g.s. (volume). By extrapolation back to zero field, the spontaneous moment may be estimated as $M_0 = 87 \pm 5$ e.m.u./cm³ ($m_0 = 0{\cdot}66 \pm 0{\cdot}04\ \mu_B$/molecule). A complication is the pronounced tetragonality of the Jahn–Teller type, but this may be turned to advantage by making use of the remanence. Its value at 4·2°K shown in Fig. 2 is 41 e.m.u. while that at 77°K is 39 e.m.u. Both are saturated isothermal remanances (to 140 kOe) and both are accompanied by d.c. coercivities of about 1600 Oe. With this stability it may be safe to assume that no demagnetization by reversely oriented domains has occurred. For the extreme case of positive uniaxial anisotropy a lower limit to the spontaneous magnetization is two times the remanence or 82 e.m.u. at 4·2°K ($m_0 = 0{\cdot}62\ \mu_B$). The closeness of this value to the other estimate suggests that this is a "favorable" case. It also indicates that a strong negative uniaxial anisotropy is unlikely. If this estimate of M_0 is correct, then the presence of a high field susceptibility is insured, and its value is fixed at $1{\cdot}3 \times 10^{-4}$ c.g.s. A low value of this magnitude for the susceptibility is expected from the rather high ferrimagnetic Curie temperature of 135°K.[2] Thus the present measurements support the picture of triangular ferrimagnetic arrangements in $CuCr_2O_4$.

As PRINCE has pointed out, there are two

possible triangular ways of arranging the ionic moments to yield the observed spontaneous moment per molecule. Each has angles on the *B*-sites, but they differ as to which site, *A* or *B*, has the greater net moment. The neutron diffraction study was unable to resolve these. If one adopts the assumption of LOTGERING[4] that the interaction of an *A*-site ion with other *A*-site ions is weaker than its interaction with the *B*-site ions, then it is possible to suggest which of the two arrangements is correct. This is done with an α–β interaction diagram, following LOTGERING[4,7], by invoking the higher temperature data as described for the manganite spinels.[19] The model with greater net *B*-site moment is suggested for $CuCr_2O_4$.

$FeCr_2O_4$:

The only previous magnetic study of this compound is by LOTGERING[4] who concluded that there is good evidence for a triangular ferrimagnetic arrangement. The present measurements provide additional support for this view.

The high field magnetization curve at 4·2°K, the remanent magnetization and two "estimates" of the spontaneous moment; namely, $\sqrt{(2)}$ and 2 times the remanence, are shown in Fig. 2. An almost identical curve occurs at 20·4°K with the same remanence, 70 e.m.u. At both temperatures coercivity (at 60 c/s) is about 3 kOe. LOTGERING's data at 20·4°K to fields of 25 kOe superpose on the present curves.

The appearance of a high field susceptibility in $FeCr_2O_4$ is striking, and it appears to be constant from 30 kOe to the maximum field, 140 kOe. In view of the tetragonal distortion of the lattice, an analysis similar to that used for $CuCr_2O_4$ will be attempted. The spontaneous moment may be initially estimated as $M_0 \approx 90$ e.m.u./cm^3, by extrapolation back to zero field. Considering the remanence as saturated (and assuming no demagnetization), the spontaneous moment may be estimated as $2M_R = 140$ e.m.u. for the case of positive uniaxial anisotropy or as $\sqrt{(2)}M_R = 99$ e.m.u. for the case of negative uniaxial anisotropy (with two perpendicular easy axes in the "easy plane"). The closeness of the latter estimate to the initial one, determined by extrapolation, and the failure of the magnetization curve to change slope near $2M_R$, both suggest that the estimate $M_0 = \sqrt{(2)}M_R$ is a good one. This corresponds to a spontaneous moment/molecule of $m_0 = 0{\cdot}8\mu_B$, in agreement with LOTGERING's estimate, but with more certainty. This choice implies that the sign of the dominant uniaxial anisotropy is negative. It also serves to fix the value of the high field susceptibility at $3{\cdot}9 \pm 0{\cdot}5 \times 10^{-4}$ c.g.s. (volume) and to associate it with the ferrimagnetic arrangement.

As in the previous compound, there are two possible triangular arrangements of the ionic moments which yield the observed spontaneous moment. Each has angles on the *B*-sites, but they differ as to which site has the greater net moment.

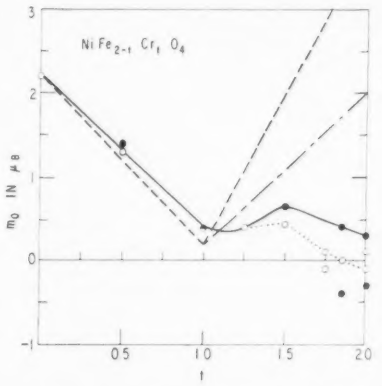

FIG. 3. Spontaneous moment, m_0, in Bohr magnetons, μ_B, per molecule vs. t for the system $NiFe_{2-t}Cr_tO_4$. Open circles are data of MCGUIRE and GREENWALD[11], while closed circles are data of this study. The dashed lines indicate predictions of the Néel antiparallel ferrimagnetic array. The regular short dashed line assumes $g_{Ni} = 2{\cdot}2$, while the alternating short-long dashed line assumes $g_{Ni}(\text{oct.}) = 2{\cdot}2$ and $g_{Ni}(\text{tet.}) = 4$.

LOTGERING discussed these, noting that the high temperature susceptibility (in the cubic phase) indicated that spin-only values were appropriate for the moment/ion. He chose the arrangement with the dominant moment on the *A*-site (4 μ_B on *A*-site vs. 3·2 μ_B on *B*-site). The present data support that choice.

The System $NiFe_{2-t}Cr_tO_4$:

A number of studies, cited earlier, have shown that the properties of this system are simple over the range of $0 \leqslant t \leqslant 1$ and complex over the remaining range. It is convenient to divide the discussion of the present results into the two parts thus suggested.

Considering the composition range $0 \leqslant t \leqslant 1$, where the crystal structure remains cubic even at low temperatures,[8,11] the spontaneous moment conforms to the Néel antiparallel ferrimagnetic arrangement. Starting at $t = 0$, the neutron diffraction results of HASTINGS and CORLISS[42] confirm that the magnetic structure is that of an "inverse" spinel, $Fe[NiFe]O_4$. Substitution of Cr^{3+} for Fe^{3+} takes place with Cr^{3+} ions entering the octahedral *B*-sites, the likely formula being $Fe[NiFe_{1-t}Cr_t]O_4$. Magnetic moment measurements of MCGUIRE and GREENWALD[6,11] and of

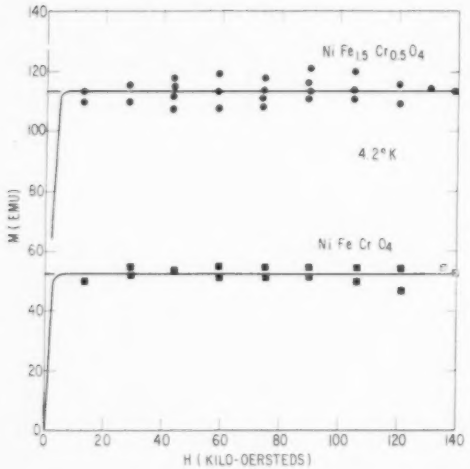

FIG. 4. Magnetization per unit volume M vs. field H for $NiFe_{1.5}Cr_{0.5}O_4$ and $NiFeCrO_4$ powders at 4·2°K.

MIYAHARA and TSUSHIMA[9] reveal a linear decrease to very small m_0 values as t approaches 1. This behavior is shown in Fig. 3, and there is good agreement with the prediction of the above ionic distribution.

The results of high field magnetization experiments on the compounds $t = 0{\cdot}5$ and $t = 1{\cdot}0$ are shown in Fig. 4. Within the experimental error, there is no increase in moment at high field. This is in accord with the view that their magnetic structure has the antiparallel ferrimagnetic arrangement, notwithstanding the low spontaneous moment.

The results suggest that strong antiferromagnetic *B–B* interactions do not occur between Ni^{2+} ions and Fe^{3+} or Cr^{3+} ions, compared to the *A–B* interactions. That the latter interactions remain strong in this composition range is indicated by the relatively slow decrease of the ferrimagnetic Curie temperature.[11] For compositions $t > 1$, the decrease of Curie temperature with Cr^{3+} content is more rapid. It is of interest that the proposals of WICKHAM and GOODENOUGH[36] indicate that the Ni^{2+} ion on *B*-sites should not strongly interact with other *B*-site ions. There is also, however, the possibility of antiferromagnetic *B–B* interactions between the Fe^{3+} and Cr^{3+} ions. These were considered in the system $MnFe_{2-t}Cr_tO_4$ and found to be quite important. For the nickel ferrite–chromite system, it must be concluded that this interaction is rather weaker *compared to the A–B interaction*. Support for this is derived from the fact that the ferrimagnetic Curie temperatures in the nickel series are about 50 per cent greater than those in the manganese series for this range $(0 \leqslant t \leqslant 1)$.

In the composition range $1 < t \leqslant 2$, there is the complication of distorted crystal structures and also the question of the magnetic moment on the Ni^{2+} ion in tetrahedral co-ordination. This arises because further substitution of Cr^{3+} for Fe^{3+} brings about a gradual displacement of Ni^{2+} from octahedral *B*-sites to tetrahedral *A*-sites. The likely formula for this range is $(Fe^{3+}_{2-t}Ni^{2+}_{t-1})[Ni^{2+}_{2-t}Cr^{3+}_t]O_4$. In the preceding it was assumed that g_{Ni}(oct.) is 2·2, in agreement with magnetization and resonance data for octahedrally co-ordinated Ni^{2+}. While it is sometimes taken that g_{Ni}(tet.) has this same value, SMART[43] has discussed the possibility of much larger values, perhaps as high as four which would mean a moment of 4 μ_B per Ni^{2+} ion. Also, the high temperature susceptibility data for $NiCr_2O_4$[2] in the cubic phase may be interpreted to yield g_{Ni}(tet.) = 3·5. To account for the two extremes, separate lines ($g = 2{\cdot}2$, $g = 4$) are shown on Fig. 3 in this composition range for the predicted values of m_0 according to the Néel antiparallel ferrimagnetic arrangement. The observations reported elsewhere[4,6,11] and herein reveal large deviations from these predictions.

The high field magnetization curves at 4·2°K for $t = 1{\cdot}5$ and $t = 1{\cdot}85$ are shown in Fig. 5. Also shown are the remanence values, M_R, and the points $\sqrt{(2)}M_R$ and $2M_R$ to be used as with $CuCr_2O_4$ and $FeCr_2O_4$.

For the compound $NiFe_{0.5}Cr_{1.5}O_4$ ($t = 1{\cdot}5$),

curves taken at 4·2°K and 20·4°K nearly superpose, have identical remanences, and almost identical coercivities of $3{\cdot}8 \pm 0{\cdot}1$ kOe (at 60 c/s). An extrapolation to $H = 0$ is in reasonable accord with $M_0 = \sqrt{(2)}M_R = 85$ e.m.u., or $m_0 = 0{\cdot}65\,\mu_B$.

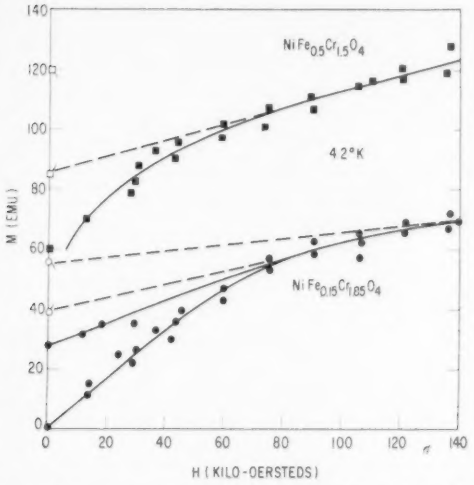

FIG. 5. Magnetization per unit volume M vs. field H for $NiFe_{0.5}Cr_{1.5}O_4$ and $NiFe_{0.15}Cr_{1.85}O_4$ powders at 4·2°K. Remanences and points derived therefrom are shown as indicated for Fig. 2.

In a previous investigation of this same compound, McGUIRE and GREENWALD[11] reported zero spontaneous moment. This composition appeared to mark a compensation point in the m_0 vs. t curve. The discrepancy is understood by noting that this compound showed a remanance coercivity (reverse field required to reduce the previously saturated remanence to zero) equal to 13 kOe at 77°K and 16 kOe at 20·4°. (These were pulsed fields damped to be four times slower than usual.[22]) Fields of 50 kOe were required to saturate the remanence. The presence of a few percent NiO impurity was established by X-ray examination. This antiferromagnetic interacting in exchange contact[44] with the ferrimagnetic could account for this anisotropy.

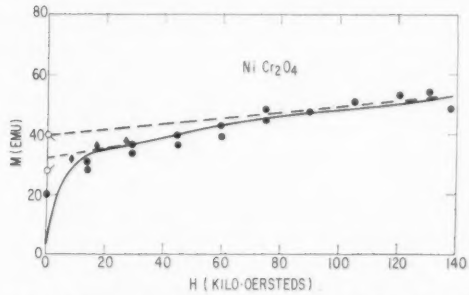

FIG. 6. Magnetization per unit volume M vs. field H at 4·2°K for $NiCr_2O_4$ powder. Remanence and points derived therefrom are shown as indicated for Fig. 2. Data of LOTGERING[4] at 20·4°K shown by diamond symbol.

This agrees with earlier estimates from higher temperature data.[6,11] With this choice, the high field susceptibility value is 3×10^{-4} c.g.s. (volume), and appears to be associated with the ferrimagnetic arrangement. The possibility of a gradual change in the slope of the magnetization curve near $M = 2M_R$ is not clearly resolved by the data. If such occurs, the correct estimate of M_0 would be higher than assigned here and the question of a high field susceptibility, as well as its value, would be left open.

For the compound $NiFe_{0.15}Cr_{1.85}O_4 (t = 1{\cdot}85)$, a curve is observed at 20·4°K identical to that shown for 4·2°K. The problems in deciding upon the correct M_0 are very evident in this case. The continual curvature at high fields makes either "estimate" possible, but the safest course seems to be a choice of $M_0 = 2M_R = 56$ e.m.u., or $m_0 = 0{\cdot}4\,\mu_B$. A high field susceptibility still remains, with an approximate value of 1×10^{-4} c.g.s., markedly lower than suggested for $t = 1{\cdot}5$.

The high field magnetization curve of $NiCr_2O_4$ at 4·2°K is shown in Fig. 6. Also shown are the remanence, the two points $\sqrt{(2)}M_R$ and $2M_R$, and several data points from LOTGERING's[4] curve at 20·4°K. The coercivity at 60 c/s for this powder at 4·2°K is 3·6 kOe. It is difficult to determine the spontaneous moment with certainty. The best estimate would appear to be $M_0 = 2M_R = 40$ e.m.u., or $m_0 = 0{\cdot}3\,\mu_B$. There is also a high field susceptibility whose value is 1×10^{-4} c.g.s. This low spontaneous moment, considered from the Yafet–Kittel point of view, requires angles on the B-sites. The dominant net site moment could be either A or B. (This problem is discussed below for the composition range, $1 < t \leqslant 2$.) The application of an α–β diagram does not help in this choice for $NiCr_2O_4$, partly because of the low value of m_0.

The variation of spontaneous moment m_0 with Cr^{3+} content is shown in Fig. 3 with earlier data[11] (open circles) and present data (closed

circles). Points plotted below the $m_0 = 0$ line indicate that the net A-site moment dominates the net B-site moment. A guide point at $t = 1{\cdot}5$, plotted above the line (for dominant B-site moment), is based on the neutron diffraction results of PICKART and NATHANS[15b,16]. Proceeding to higher t from this point, the simplest curve is that drawn without a compensation point. On this basis the choice for B-site moment dominant extends over the whole range.

The presence of high field susceptibility in each of the compounds with $t > 1$ suggests non-collinear Yafet–Kittel type ferrimagnetic arrangements. The preferred experimental curve may be compared with either of the curves predicted by the Néel antiparallel model and the difference associated with angles between the B-site moments. This difference increases monotonically at a rate which is between the first and second power of t. This is reasonable as arising from the strong antiferromagnetic B–B interactions between Cr^{3+} ions. As t increases above 1, the appropriate configurations become more common, while the A–B interaction decreases in strength. The occurrence and growth of angles between B-site moments is a natural consequence. It is interesting to speculate that one factor preventing angles at $t < 1$ may be that short range order prevents the favorable Cr–Cr configurations. The role played by the structure distortions in the range $t > 1$ is not clear in this crude treatment.

No evidence for triangular arrangements was found in the neutron diffraction study of the $t = 1{\cdot}5$ compound.[15b,16] In view of the arguments offered in the discussion of the manganese ferrite–chromite system, this result is not surprising. A more favorable situation might be expected for tetragonal $NiCr_2O_4$, but a structure solution has not been found.

Alternate models have been suggested for these compounds, as for others, based on moment reversal in the B-sites. As argued for the preceding compounds, there are objections to such a magnetic structure.

In summary, the system $NiFe_{2-t}Cr_tO_4$ is found to conform to the Néel antiparallel ferrimagnetic array in the range $0 \leqslant t \leqslant 1$, and to show considerable evidence for Yafet–Kittel triangular type arrays when $t > 1$. The angles in the latter composition range are among the B-site moments, and it is suggested that the net B-site moment remains dominant over the whole series.

CONCLUSION

High field magnetization studies at low temperatures on chromium-containing spinels provide information about their ferrimagnetic arrangement. The presence of a differential susceptibility at high fields is presented as evidence for the existence of Yafet–Kittel type triangular ferrimagnetic arrays in $MnFe_{2-t}Cr_tO_4$, $t > 0$; $CuCr_2O_4$; $FeCr_2O_4$; and $NiFe_{2-t}Cr_tO_4$, $t > 1$. Choices are made between alternative triangular models, and, in some cases, the sign of the dominant anisotropy is suggested. Néel antiparallel ferrimagnetic arrays are confirmed for $MnFe_2O_4$ and for $NiFe_{2-t}Cr_tO_4$, $t \leqslant 1$. Certain of these conclusions have been suggested previously, but the evidence presented herein is of a new and occasionally more direct type. A secondary conclusion is that particular care is required in the interpretation of magnetic data on powders of compounds with low crystal symmetry.

Acknowledgements—The author is indebted to various people, cited above, who generously co-operated in making samples available. Considerable stimulus to this work was provided in discussions with T. R. MCGUIRE, P. L. EDWARDS, S. J. PICKART and E. PRINCE. Helpful discussions were contributed by the author's colleagues, C. P. BEAN, J. S. KASPER and D. S. RODBELL. The author wishes to acknowledge his continuing debt to P. E. LAWRENCE for assistance with the measurements and for maintenance and improvement of the experimental apparatus.

REFERENCES

1. NÉEL L., *Ann. Phys., Paris* **3,** 137 (1948).
2. MCGUIRE T. R., HOWARD L. N. and SMART J. S., *Ceramic Age* **60,** No. 1, 22 (1952); SCHINDLER A. I., MCGUIRE T. R., HOWARD L. N. and SMART J. S., *Phys. Rev.* **86,** 599 (1952).
3. GORTER E. W., *Philips Res. Rep.* **9,** 295, 321, 403 (1954).
4. LOTGERING F. K., *Philips Res. Rep.* **11,** 190 (1956).
5. MIYAHARA S. and OHNISHI H., *J. Phys. Soc. Japan* **11,** 1296 (1956).
6. MCGUIRE T. R. and GREENWALD S. W., *Bull. Amer. Phys. Soc.* (ser. 2) **2,** 22 (1957).
7. EDWARDS P. L., (a) *Bull. Amer. Phys. Soc.* (ser. 2) **3,** 43 (1958); (b) *Phys. Rev.* **116,** 294 (1959).
8. MCGUIRE T. R. and GREENWALD S. W., *Bull. Amer. Phys. Soc.* (ser. 2) **3,** 43 (1958).

9. MIYAHARA S. and TSUSHIMA T., *J. Phys. Soc. Japan* **13,** 758 (1958).
10. DERBYSHIRE W. D. and YEARIAN H. J., *Phys. Rev.* **112,** 1603 (1958).
11. MCGUIRE T. R. and GREENWALD S. W., *Proc. Int. Solid State Conf., Brussels, June* 1958. *Solid State Physics in Electronics and Telecommunications* Vol. 13. (edited by DÉSIRANT M. and MICHIELS J. L.) Academic Press, New York (1960).
12. VERWEY E. J. W. and HEILMANN E. L., *J. Chem. Phys.* **15,** 174 (1947).
13. ROMEIJN F. C., *Philips Res. Rep.* **8,** 321 (1953).
14. PRINCE E., *Acta Cryst., Camb.* **10,** 554 (1957).
15. PICKART S. J., (a) *Bull. Amer. Phys. Soc.* (ser. 2) **3,** 42 (1958); (b) *Nav. Ordn. Rep.* No. 6101, Nav. Ordn. Lab., White Oak, Maryland; (c) PICKART S. J. and NATHANS R., *Phys. Rev.* **116,** 317 (1959).
16. PICKART S. J. and NATHANS R., *Bull. Amer. Phys. Soc.* (ser. 2) **3,** 231 (1958).
17. YAFET Y. and KITTEL C., *Phys. Rev.* **87,** 290 (1952).
18. BALTZER P. K. and WOJTOWICZ P. J., *J. Appl. Phys.* **30,** p. 27s (1959).
19. JACOBS I. S., (a) *J. Appl. Phys.* **30,** p. 301s (1959); (b) *J. Phys. Chem. Solids* **11,** 1 (1959).
20. KASPER J. S., *Bull. Amer. Phys. Soc.* (ser. 2) **4,** 178 (1959).
21. A partial report on this work has appeared: JACOBS I. S., *Bull. Amer. Phys. Soc.* (ser. 2) **4,** 178 (1959).
22. JACOBS I. S. and LAWRENCE P. E., *Rev. Sci. Instrum.* **29,** 713 (1958).
23. HASTINGS J. M. and CORLISS L. M., *Phys. Rev.* **104,** 328 (1956).
24. FRANCOMBE M. H., *XVI Congrès Int. Chim., Paris,* 1957, p. 129.
25. BERTAUT E. F. and DÉLORME C., *C.R. Acad. Sci., Paris* **239,** 504 (1954).
26. YEARIAN H. J., KORTWRIGHT J. M. and LANGENHEIM R. H., *J. Chem. Phys.* **22,** 1196 (1954).
27. FRANCOMBE M. H. and ROOKSBY H. P., *Nature, Lond.* **178,** 586 (1956); FRANCOMBE M. H., *J. Phys. Chem. Solids* **3,** 37 (1957).
28. For $t = 2$, $NiCr_2O_4$, $c/a = 1{\cdot}025$; see Refs. (4) and (24) and DÉLORME C., *C.R. Acad. Sci., Paris* **241,** 1588 (1955).
29. GOODENOUGH J. B. and LOEB A. L., *Phys. Rev.* **98,** 391 (1955).
30. DUNITZ J. D. and ORGEL L. E., *J. Phys. Chem. Solids* **3,** 20, 318 (1957).
31. MCCLURE D. S., *J. Phys. Chem. Solids* **3,** 311 (1957).
32. WOHLFARTH E. P. and TONGE D. P., *Phil. Mag.* **23,** 1333 (1957).
33. STONER E. C. and WOHLFARTH E. P., *Phil. Trans. Roy. Soc.* A**240,** 599 (1947).
34. HARRISON F. W., OSMOND W. P. and TEALE R. W., *Phys. Rev.* **106,** 865 (1957).
35. WICKHAM D. G., *Mass. Inst. Tech., Lincoln Lab. Group Rep.* 53–7, Lexington, Mass., unpublished.
36. WICKHAM D. G. and GOODENOUGH J. B., *Mass. Inst. Tech., Lincoln Lab. Group Rep.* 53–7, Lexington, Mass.; *Phys. Rev.* **115,** 1156 (1959).
37. ANDERSON P. W., *Phys. Rev.* **102,** 1008 (1956).
38. KAPLAN T. A., *Mass. Inst. Tech., Lincoln Lab. Group Rep.* 53–16, Lexington, Mass.; *Phys. Rev.* **116,** 888 (1959).
39. LOEB A. L. and GOODENOUGH J. B., reported at *Conference on Magnetism and Magnetic Materials, Boston, Mass. Oct.* 16–18, 1956 (unpublished); ROTH W. L., *Phys. Rev.* **111,** 772 (1958).
40. YOSHIMORI A., *J. Phys. Soc. Japan* **14,** 807 (1959).
41. American Institute of Physics Handbook pp. 5–211. McGraw-Hill, New York (1957).
42. HASTINGS J. M. and CORLISS L. M., *Rev. Mod. Phys.* **25,** 114 (1953).
43. SMART J. S., *Phys. Rev.* **94,** 847 (1954).
44. MEIKLEJOHN W. H. and BEAN C. P., *Phys. Rev.* **102,** 1413 (1956); **105,** 904 (1957).

VOL. 15 1960

J. Phys. Chem. Solids Pergamon Press 1960. Vol. 15. pp. 66–71. Printed in Great Britain.

THE TEMPERATURE DEPENDENCE OF THE CONDUCTIVITY OF DRY CELLULOSE*

E. J. MURPHY

The Rockefeller Institute, New York, N.Y.

(*Received* 18 *September* 1959)

Abstract—An experimental investigation of the conductivity of dry cellulose is described. It leads to the following expression for the conductivity:

$$\sigma = 4{\cdot}50 \times 10^{2} \exp(-30{\cdot}7 \times 10^{3})/RT + 3{\cdot}55 \times 10^{-10} \exp(-10{\cdot}6 \times 10^{3})/RT$$

where σ is the conductivity in $(\Omega\ \text{cm})^{-1}$, R the gas constant, and T the absolute temperature. This has the form usual in the theory of ionic conduction in crystals. From the coefficient of the first term, the lattice constant for conduction can be calculated: the value obtained is 5·4 Å. The observed energy in the Boltzmann factor for the first term can be regarded as splitting into the sum of two terms: a dissociation energy of 40·2 kcal/mole and an activation energy for mobility of 10·6 kcal/mole; this gives $(40{\cdot}2/2)+10{\cdot}6 = 30{\cdot}7$, the observed value. The second term, which is due to impurity conduction of some kind, has an activation energy for mobility of 10·6 kcal/mole. This agrees approximately with the activation energy for conduction in ice; consequently the second term is regarded as due to conduction in adsorbed water. The first term is regarded as representing volume conduction in which dissociation requires 40·2 kcal/mole, but mobility is governed by the breaking of two hydrogen bonds. The ratio $3{\cdot}55 \times 10^{-10}/4{\cdot}50 \times 10^{2}$ $(= 0{\cdot}79 \times 10^{-12})$ is proportional to the concentration of "impurities". It is unusually small. A possible significance of this is discussed.

1. INTRODUCTION

UNDER ordinary conditions of temperature and relative humidity all but a practically infinitesimal fraction of the conductivity of cellulose is due to the water which is adsorbed on its internal surfaces. This will be evident from the data to be given here. However, the conductivity of any dielectric increases with rising temperature, and dry cellulose is no exception. In fact the data will show that cellulose behaves remarkably like an inorganic crystal with regard to the dependence of its conductivity on temperature. In spite of the great difference in chemical and physical structure between rock-salt, for example, on the one hand and cellulose on the other there is not a great deal of difference between their conductivity–temperature curves.

Cellulose has a rather complicated structure as compared with that of an ionic crystal. X-ray diffraction indicates that it has a substantial degree of crystallinity. It is able to adsorb a large amount of water vapor on its internal surfaces, and it comes rapidly into equilibrium with the relative humidity of the air. These considerations indicate that cellulose may be regarded as a crystal structure permeated by a system of internal surfaces containing adsorption sites. In fact the conduction behavior of cellulose containing water can be explained by a model in which the conduction takes place in the adsorbed water and the cellulose itself acts essentially as a container which imposes on the adsorbed water a concentration distribution which reflects the distribution of adsorption sites.[1] In such a structure as this it is possible that the presence of a system of internal surfaces would appear strongly in the conduction behavior even when the material is dry. However, the evidence of the present investigation is that the main features of behavior refer to the crystal structure, though secondary effects may be derived from the presence of a structure of internal surfaces.

* A portion of this work was aided by a National Science Foundation grant.

VOL. 15 1960

2. EXPERIMENTAL PROCEDURE

The measurements were made upon natural cellulose in the form of condenser paper. This substance has a standardized composition and is described as 99·9 per cent cellulose. The specimens were sealed in a pyrex glass tube through which electrical connections were made to the metal electrodes by tungsten-to-glass seals. The outer surface of the glass surrounding the electrical leads was coated with a cerecin wax in order to prevent surface leakage. The tube containing the specimen was immersed in an oil bath maintained at constant temperature. The conductivity measurements were made by the current–voltage method, using a galvanometer of high sensitivity.

Owing to the great sensitivity of the conductivity of cellulose to its water content, the usefulness of attempting to study the conduction behavior of *dry* cellulose depends upon the experimental feasibility of taking the cellulose to a low enough water content. The procedure adopted was as follows: The tube containing the specimen was sealed onto a vacuum system and pumped out. The temperature was raised to 120°C and the system closed off from the pump. The pressure which developed in several hours was measured by a McLeod gauge. In this way it was found that the final stage of the drying process is very slow. By applying a trap at −79°C it was found that not all of the pressure which developed was due to water vapor. It became evident that it was going to be difficult to distinguish between the evolution of water vapor coming from the adsorbed state and water vapor coming from thermal decomposition. An auxilliary investigation of this aspect of the problem was made with the following results.

The gas evolved by cellulose at 120°C includes carbon dioxide and monoxide as well as water vapor. At the beginning of drying water vapor is the dominant constituent of the mixture but in the later stages the three constituents are coming off in comparable proportions. Finally a stable ratio between the constituents is reached which can be regarded as approximately stoichiometrical. At this stage the process responsible for the water vapor evolved is slow thermal decomposition, not drying. We define the end-point in the drying operation as the state existing when approximate stoichiometric proportions first appear in the evolved gas mixture. An auxilliary investigation showed that the small amount of thermal decomposition which takes place during the drying operation does not noticeably affect the conductivity.

It was found desirable in the course of the study of drying to make an investigation of the thermal decomposition of natural cellulose at low temperatures *in vacuo* (i.e. at temperatures between 80°C and 200°C). Some of the results of this investigation are used in the discussion of the conduction behavior.

The conductivity of a dielectric of this type can be affected by polarization currents and by electrolytic effects, leading to large errors. This aspect of the problem has been investigated in great detail in other parts of the writer's work[2] and will not be discussed here; the conductivity values given here are believed to refer to the conductivity due to free ions, without substantial error due to polarization currents or electrolytic effects.

3. EXPERIMENTAL RELATIONS

The results are given in two curves: the first is a direct plot of the logarithm of conductivity as a function of temperature (Fig. 1); the second gives the logarithm of conductivity as a function of the reciprocal of the absolute temperature (Fig. 2). The

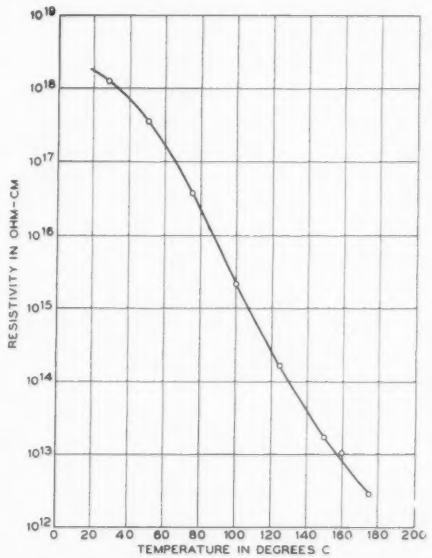

FIG. 1. The conductivity of dry cellulose as a function of temperature.

first curve is given merely in order to emphasize the point that the data are discriminative with respect to the theoretical relation expressed in equation (2). Fig. 2 shows that the conductivity of cellulose is given by:

$$\sigma = 4{\cdot}50\times10^{2}\exp(-30{\cdot}7\times10^{3})/RT+ \\ +3{\cdot}55\times10^{-10}\exp(-10{\cdot}6\times10^{3})/RT \quad (1)$$

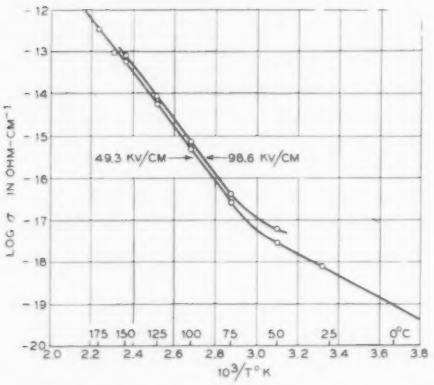

FIG. 2. The conductivity of dry cellulose as a function of the reciprocal of the absolute temperature, for two voltage gradients.

where σ is the conductivity in $(\Omega\ \text{cm})^{-1}$, R the gas constant and T the temperature in °K. This is the conductivity at a voltage gradient of 49·3 kV/cm. It is somewhat larger at 98·6 kV/cm, as Fig. 2 shows. In another place it is shown that the conductivity is an increasing function of the voltage gradient involving the hyperbolic sine in a manner to be expected from the theory of ionic conduction.

Equation (1) has the general form of the theoretical expression for the conductivity due to mobile ions, namely:

$$\sigma = \sigma_{01}\exp(-W_1/RT)+\sigma_{02}\exp(-W_2/RT)+\ \ldots \quad (2)$$

where σ_{01} refers to self-conduction and σ_{02} to "impurity" conduction, i.e. to conduction attributable to small concentrations of substances other than the main constituent. Comparison of equations (1) and (2) gives:

W_1 = 30·7 kcal/mole = 1·33 eV/molecule; $\sigma_{01} = 450\ (\Omega\ \text{cm})^{-1}$.

W_2 = 10·6 kcal/mole = 0·46 eV/molecule; $\sigma_{02} = 3{\cdot}55\times10^{-10}\ (\Omega\ \text{cm})^{-1}$.

A theoretical expression for the conductivity, in more detail, is:

$$\sigma_1 = (9\times10^{11}h)^{-1}N_1e^2\,d^2P_1\times \\ \times\exp-(\tfrac{1}{2}W_{d1}+W_{a1})/NkT \\ \sigma_2 = (9\times10^{11}h)^{-1}N_2e^2\,d^2P_2\times \\ \times\exp-(\tfrac{1}{2}W_{d2}+W_{a2})/NkT \quad (3)$$

where $\sigma_1+\sigma_2=\sigma$. The subscripts 1 and 2 refer respectively to the first term, which is due to intrinsic conductivity, and to the second term, which is due to impurity conduction or to a secondary structure. W_{d1} and W_{d2} are the energies required for dissociation into ions, W_{a1} and W_{a2} the activation energies for mobility. It is usual to consider that $W_{d2}=0$, because the second term is often due to impurities which are dissociated completely. h is Planck's constant; N is Avogadro's number; k is the Boltzmann constant; e is the electronic charge. N_1 is the number of unit cells per cm³, N_2 is the number of unit cells (or impurity ions) per cm³ contributing to the second term. d is the lattice constant for conduction; in the simplest case it is one of the lattice constants of the crystal, i.e. the length of the unit cell in the direction of the applied field. P_1 and P_2 are products of partition functions involving vibration frequencies and the ratio of the number of states of equal energy available in the activated condition as compared with the normal state. Under simple enough conditions the natural logarithms of P_1 and P_2 may be considered to be configurational entropies of activation and calculated from the conductivity data. But for the present we are content to see whether the model works reasonably well on the simplifying assumption that $P_1=P_2=1$. There is some justification for this simplification in the writer's experience with other materials where reasonable agreement between theory and experiment is obtained on the basis of this assumption. Moreover, calculations of the value of $P_1(=P_2)$ on the basis of estimates of the values of the factors involved suggest that unity is not an unreasonable value. Thus it seems desirable to take $P_1=P_2=1$ as a norm and to note deviations from it, rather than to complicate the model. It is also true that e in the above expressions should be replaced by Ze, where

VOL. 15 1960

Z is a positive or negative small integer, but this modification can be introduced if there is evidence that the ions are in some cases multivalent.

Several expressions have been derived for ionic conductivity by different authors.[3] They have a great deal in common; the differences may in fact be regarded in some cases as refinements of the model which are beyond the precision attainable in the determination of σ_0 in most experiments. The form given in equation (3) is equivalent to the other theoretical expressions for ionic conductivity, except that some of the factors in σ_0 are suppressed by assuming that $P_1 = 1$. We have chosen to compare theory with experiment by calculating d, the lattice constant, on the basis of assumptions regarding the values of the other constants. We could have made the comparison by calculating e, or preferably P_1, using the X-ray diffraction value for d. This can be done when it is considered that the experimental values of σ_0 and the theoretical expression for P_1 warrant the calculation of P_1.

4. LATTICE CONSTANT FOR CONDUCTION

Substituting the values of the constants in the expression for σ_0, we have:

$$\sigma_{01} = N_1 e^2 d^2/9\times 10^{11} h = 0{\cdot}154\times 10^2\, d_A^2 \quad (4)$$

where d_A is the lattice constant expressed in angstrom units. From the experimental value of σ_{01} given in equation (1) we obtain:

$$0{\cdot}154\times 10^2\, d_A^2 = 4{\cdot}50\times 10^2; \text{ or } d_A = 5{\cdot}4\ \text{Å} \quad (5)$$

The unit cell in cellulose is 10·3 Å in its longest dimension. So the agreement between the lattice constant calculated from conduction data and the length of the cellulose molecule is good, in fact better than either the accuracy of the experimental data or the refinement of the theoretical model is likely to warrant. However, it is evident that there is at least approximate agreement.

5. ACTIVATION ENERGIES

The energies in the Boltzmann factors of equation (1) are $W_1 = 30{\cdot}7$ kcal/mole, $W_2 = 10{\cdot}6$ kcal/mole. The latter value is approximately equal to the activation energy for conduction in ice. It seems justifiable to regard it as due to conduction in very strongly absorbed water.

For W_1 we have the expression $W_1 = \frac{1}{2}W_d + W_a$. If we assume that the activation energy W_a is equal to the Boltzmann factor in the second term, as is often apparently the case (because the impurities are already ionized), we obtain: $W_d = 2(W_1 - W_a) = 2(30{\cdot}7 - 10{\cdot}6) = 40{\cdot}2$ kcal/mole. On the basis of the assumptions involved in this calculation the energy required for the dissociation of some part of the cellulose unit cell into mobile ions is 40·2 kcal/mole. In experiments upon the thermal decomposition of cellulose, to be described elsewhere, the activation energy for thermal decomposition turned out to be 39·5 kcal/mole. This approximate numerical agreement is considered only to be significant in indicating that a dissociation energy of 40·2 kcal/mole is not unreasonably large for cellulose.

We shall call the above explanation of the observed energy in the Boltzmann factors Model I. It assumes that a rather large energy is required for the dissociation of some part of the cellobiose chain into mobile ions, but that the activation energy for mobility is about the same as that in ice. We can go to the opposite extreme by assuming that the dissociation energy is small and the activation energy for mobility large, that is, in the limit that $W_1 = W_a$. We shall call this Model II. This would correspond to the simultaneous breaking of five or six hydrogen bonds in order to account for an activation energy of 30·7 kcal/mole. The actual situation may lie between the extremes represented by these two models; however, Model I is preferred, because of the very general finding that the energy in the Boltzmann factor in the "impurity" (or second) term is the activation energy for mobility. We shall therefore drop Model II from further consideration here.

6. THE SECOND TERM IN THE CONDUCTIVITY EXPRESSION

The ratio σ_{02}/σ_{01} gives the concentration of impurities or their equivalent, subject to simplifying assumptions such as those discussed earlier. Taking the values of σ_{01} and σ_{02} from equation (1) we have:

$$\sigma_{02}/\sigma_{01} = N_2/N_1$$
$$= 3{\cdot}55\times 10^{-10}/4{\cdot}5\times 10^2 = 0{\cdot}79\times 10^{-12} \quad (6)$$

This implies that the number of unit cells contributing to the second term in the conductivity

(equation 1) is only about 10^{-12} of the total number of cells in a cubic centimetre of cellulose. Taking $N_1 = 3{\cdot}94 \times 10^{21}$, we obtain $N_2 = 3{\cdot}1 \times 10^{9}$ for the number of unit cells containing impurities. By comparison with the behavior of other dielectrics containing small amounts of impurities the factor 10^{-12} appears to be entirely too small for a material such as cellulose, and particularly the natural cellulose of condenser paper. Yet, as Fig. 2 shows, the data are quite definite on this point. The behavior would be given a simple explanation if it turned out that we were measuring a conduction current at the higher temperatures, but shifted to a polarization current below about 50°C without recognizing the change in the character of the current. The current does change in this way, but the change was expected and the potential error which it would cause was avoided; the low temperature measurements of conductivity are the conductivity values taken after the polarization currents had dropped to a negligible level.

We are left then with the need to explain the smallness of the factor 10^{-12} in equation (6), and the following is proposed.

In the general case it can not be assumed that impurities will necessarily affect the conductivity in a given interval of temperature. Suitable impurities contribute to the conductivity because they are ionized and mobile (or in semiconductors because they act as donors or as acceptors of electrons); other impurities, however, may not affect the conductivity in a given range of temperatures either because they are not ionized, or because they are insufficiently mobile. Since impurities are certainly present in the cellulose used in this investigation, we must consider that the latter condition applies in some form. An explicit proposal is made below.

It has been shown that the conductivity of cellulose is very sensitive to its water content; and there must be some water present as an impurity. The propositions of the last paragraph imply that water should contribute rather substantially to the second term in the conductivity. The following is proposed as a way of making this consistent with the observed small value (10^{-12}) of the ratio of impurity conduction to self-conduction. The study of the dependence of conductivity on water content has shown that the water in cellulose must be distributed in a way equivalent to having a system of alternating constrictions and expansions in the conducting water path. This structure can also be described in terms of a probability function for adsorption and brought into relation with the distribution of adsorption sites, as has been shown elsewhere[1]. We shall call the factor by which the contribution of water to the conductivity is reduced in this way the distribution factor or geometric factor (f). The discussion of the conduction behavior of cellulose containing adsorbed water shows that the factor f could readily have a value such as 10^{-10} or 10^{-12} for nearly dry cellulose. On the basis of this hypothesis the factor f should be inserted in the second term of equation (3). The factor f can be identified with the ratio $(\alpha/\alpha_0)^9$, which appears in the conductivity–water content relationship.[1]

7. INFLUENCE OF VOLTAGE GRADIENT

As the curves of Fig. 2 show, there is a voltage dependence of the conductivity of cellulose. This is discussed in some detail in another place, where it is shown that the voltage dependence gives a value for the lattice constant for conduction.

8. INFLUENCE OF WATER GENERATED BY THERMAL DECOMPOSITION

An auxilliary investigation was made of the temperature dependence of the rate of thermal decomposition of the cellulose used in this investigation. The experimental expression obtained is:

$$k = 10^{11} \exp(-39{\cdot}5 \times 10^{3}/RT) \qquad (7)$$

where k is the rate of generation of water vapor (and other gases) expressed in moles of water vapor per mole of cellulose per second. Equation (7) has the standard form for reaction rates. It indicates that the activation energy for thermal decomposition of cellulose is 39·5 kcal/mole.

We have already considered how water present as an impurity could contribute to the *second* term in the conductivity. Here we are concerned with the question as to whether water generated by thermal decomposition could be responsible for the main term in the conductivity; this question arises because the conductivity of cellulose is sensitive to water content and because water is generated by thermal decomposition at all temperatures.

From equation (7) it may be seen that the probability of a given molecule of cellulose decomposing in unit time is proportional to $\exp(-39{\cdot}5 \times$

$\times 10^3/RT$). If N_1 is the number of molecules per cubic centimeter, the number of water molecules generated is $N_1 k$. If we assume that the rate of diffusion increases much less rapidly with temperature than the rate of thermal decomposition—since the activation energy for diffusion is equal to that for mobility and the latter has the value 10·6 kcal/mole according to our estimate—we may conclude that the conductivity, at high temperatures, is given by

$$\sigma = N_1 \exp(-39{\cdot}5 \times 10^3/RT) \times \times e^2 d^2 (9 \times 10^{11} h)^{-1} \exp(-W_a/RT) \quad (8)$$

In this expression the only aspect of present interest is the fact that the total energy in the Boltzmann factor is $(39{\cdot}5 \times 10^3 + W_a)$; if W_a has the value $10{\cdot}6 \times 10^3$, the total energy in the Boltzmann factor would be 50·1 kcal/mole. This is much larger than the observed value, which is 30·7 kcal/mole. On account of this large quantitative discrepancy, it is concluded that the observed conductivity of cellulose at high temperatures is not due to water generated by thermal decomposition.

A direct experimental test of this possibility was also made during the experiments by closing off the system from the pump until water vapor had accumulated to a small but appreciable pressure. No change of conductivity occurred when this was done. This test was made at 160°C. This confirms the evidence given by the above comparison of activation energies. It implies that the conduction is of normal type, as in an ordinary crystal, so far as our evidence goes.

The results given here suggest that the energy for the dissociation of cellulose into ions is not very different from the *activation* energy which controls the rate of thermal decomposition of the material.

9. TOTAL CONDUCTIVITY OF CELLULOSE CONTAINING ADSORBED WATER

The conductivity of cellulose containing adsorbed water is in general the sum of terms due to the conduction of the cellulose alone (σ_c) and terms due to the conduction in the cellulose–water adsorption complex (σ_w). Equation (1) of this paper and equation (6) of Ref. (1) give, respectively, σ_c and σ_w. The two functions, $\sigma_c(T)$ and $\sigma_w(\alpha/\alpha_0)$, make contact at one point, namely the conductivity of dry cellulose at 25°C, and agree reasonably well there, giving approximately $\sigma_{25°C} = 8 \times 10^{-19}$ $(\Omega\ \mathrm{cm})^{-1}$ as the conductivity of dry cellulose at that temperature. The expressions involved in σ_c and σ_w are free of arbitrary constants, except for the value of the constant W_d for cellulose. Thus it is possible to cover by means of theoretically based expressions the conductivity of cellulose in the extreme condition where the conduction is practically all intrinsic conduction in the cellulose and also at the other extreme where it is essentially conduction in the cellulose–water complex, the contribution of the cellulose itself being negligibly small.

However, there are pairs of values of temperature and water content such that the contributions of σ_c and σ_w to the total conductivity (σ_t) are comparable. For these it is possible that the water content should be treated as an impurity contributing to σ_c, in proportion to its concentration. In short, there may be a third term in σ_t, due to the interaction of the water with the self-conduction of the cellulose, which makes itself evident when σ_c and σ_w are both sufficiently small. There is some experimental evidence for this, which may be given in another connection.

REFERENCES

1. MURPHY E. J., *J. Phys. Chem. Solids*, in press.
2. MURPHY E. J. and MORGAN S. O., *Bell Syst. Tech. J.* **28,** 502 (1939).
3. See, for example, MOTT and GURNEY, *Electronic Processes in Ionic Crystals*. Clarendon Press, Oxford (1940).

J. Phys. Chem. Solids Pergamon Press 1960. Vol. 15. pp. 72–81. Printed in Great Britain.

SUR LA RESISTIVITE ELECTRIQUE DES ALLIAGES METALLIQUES EN FONCTION DE L'ORDRE

M. T. BEAL

Faculté des Sciences, Laboratoire de Physique des Solides, Orsay (S. & O.), France

(*Received* 16 *October* 1959)

Résumé—Nous avons étudié, de façon théorique, en fonction de la température, les phénomènes d'ordre dans les alliages et la variation de résistivité qui en découle. Nous avons utilisé une méthode de champ moléculaire avec interactions entre atomes premiers voisins seulement. Un calcul de proche en proche donne les paramètres d'ordre des couches de voisins à distances croissantes d'atomes donnés. La résistivité est ensuite calculée en ne tenant compte que des premiers voisins et avec un modèle d'électrons libres dans l'approximation de Born. Notre étude est générale au-dessus de la température critique T_c ; au-dessous, nous nous sommes limités au cas simple du laiton β. Nous concluons essentiellement à la faible influence de l'ordre à courte distance sauf au voisinage immédiat de T_c. L'ordre à courte distance donne au terme de résistivité dû au désordre une pente finie juste au-dessous de T_c, et une pente non nulle juste au-dessus de T_c. Ces conclusions sont en accord raisonnable avec les observations faites sur Cu_3Au, $Cu–Zn_\alpha$, $Cu–Zn_\beta$ et Au_3Cu.

Abstract—We have studied theoretically how the ordering of alloys and its influence on resistivity vary with temperature. A molecular-field approximation has been used, with interactions between nearest neighbours only. A recurrence formula gives the ordering parameters of shells of neighbours at increasing distances from given atoms. The resistivity is then computed, taking into account nearest neighbours only, and with a model of free electrons scattered in the Born approximation. This study is quite general above the critical temperature T_c; only the simple case of β-brass has been studied below T_c. The short-range order is found to have very little effect, except in the immediate neighbourhood of T_c. It contributes to the resistivity a term with a finite slope just below T_c, and with a non-vanishing slope just above T_c. These conclusions are in fairly reasonable agreement with observations made on Cu_3Au, $Cu–Zn_\alpha$, $Cu–Zn_\beta$ and Au_3Cu.

1. INTRODUCTION

On se propose, ici, d'étudier, de façon théorique, les phénomènes, d'ordre dans un alliage métallique de composition donnée, en fonction de la température, et leur répercussion sur sa résistivité.

On fera abstraction de la partie de la résistivité dûe aux phonons. On sait que la résistivité thermique est à peu près proportionnelle à la température absolue ; sa soustraction peut se faire expérimentalement de façon précise en mesurant la résistivité résiduelle à basse température après trempe rapide depuis la température T. Le terme dû aux lacunes n'est sensible qu'aux très hautes températures ; sa variation exponentielle avec la température T permet de le soustraire aisément des valeurs mesurées.

Dans l'état parfaitement ordonné, à 0°K, et si l'alliage a une composition stoechiométrique, chaque type d'atome est réparti sur un sous-réseau périodique ; l'alliage doit avoir une résistivité résiduelle nulle. Quand la température T croît, l'alliage se désordonne progressivement ; ce désordre introduit une certaine résistivité $\Delta\rho$. Aux très hautes températures, où le désordre est pratiquement parfait, $\Delta\rho$ doit être constante, indépendante de T.

Pour étudier les variations de $\Delta\rho$ avec T, il faut tenir compte de la température critique d'ordre T_c. On sait que, quand T croît jusqu'à T_c, les sous-réseaux échangent un nombre croissant d'atomes; au-dessus de T_c, le désordre est tel qu'on ne peut plus définir les sous-réseaux sans ambiguïté l'ordre à grande distance disparaît; il subsiste seulement un ordre local qui diminue quand la température s'élève.

On étudiera d'abord le degré d'ordre et sa

VOL. 15 1960

contribution à la résistivité de l'alliage au-dessus de la température critique, puis à des températures comprises entre 0° et T_c.

Au-dessous de T_c, les calculs seront faits dans un cas particulier, celui du laiton β, c'est-à-dire l'alliage Cu–Zn à structure cubique centrée dans l'état désordonné et cubique simple dans l'état ordonné; les résultats obtenus se généraliseraient assez facilement à d'autres structures cristallines. Les formules obtenues au-dessus de T_c seront tout à fait générales et indépendantes des caractéristiques de l'alliage considéré : structure cristalline et nature attractive ou répulsive des interactions. Les conclusions générales de cette étude seront très voisines de celles de DE GENNES et FRIEDEL[1] pour le désordre magnétique. La méthode d'étude utilisée ici est, en fait, très semblable à la leur, mais un peu plus simple au-dessous de T_c par suite de la simplicité des interactions. Le calcul de l'ordre se fait par une méthode de champ moléculaire en se limitant aux interactions entre premiers voisins ; l'approximation de Born est utilisée pour le calcul de la résistivité.

2. ÉTUDE DU PARAMÈTRE D'ORDRE AU-DESSUS DE LA TEMPÉRATURE CRITIQUE

Comme nous l'avons indiqué dans l'introduction, cette étude sera relative à un alliage AB quelconque, de concentration c en atomes A et $(1-c)$ en atomes B.

(a) *Choix du paramètre d'ordre*

Pour $T \gg T_c$, le désordre est total et on a des probabilités c et $(1-c)$ de trouver un atome A ou B respectivement comme proche voisin d'un atome quelconque.

Lorsque la température diminue, on voit apparaître un ordre local $\sigma(\boldsymbol{r})$ défini de la façon suivante : si $p(\boldsymbol{r})$ est la probabilité de trouver un A à une distance $\boldsymbol{r}$ d'un A choisi arbitrairement comme atome central

$$\sigma(\boldsymbol{r}) = \frac{p(\boldsymbol{r}) - p_{\text{moyen}}}{p_{\text{moyen}} - p_{\text{max.}}}.$$

p_{moyen} est la valeur prise par $p(\boldsymbol{r})$ à une distance de l'atome central très grande par rapport à la distance entre plus proches voisins ; à cette distance, l'ordre local n'existe plus et on retrouve le cas des hautes températures ; d'où $p_{\text{moyen}} = c$. D'autre part, $p_{\text{max.}} = 1$; ce qui donne

$$\sigma(\boldsymbol{r}) = \frac{p(\boldsymbol{r}) - c}{c - 1} \tag{1}$$

Comme $p(\boldsymbol{r})$ et c prennent que des valeurs comprises entre 0 et 1, on a évidemment

$$0 \leqslant |\sigma(\boldsymbol{r})| \leqslant 1$$

(b) *Calcul du paramètre d'ordre*

Soit T la température à laquelle on fait le calcul.

Supposons l'origine des coordonnées fixée arbitrairement sur un atome A : soit A_0 cet atome.

On calculera $p(\boldsymbol{r})$ en évaluant l'énergie E nécessaire pour échanger un A situé à une distance $\boldsymbol{r}$ de A_0 et un B situé à une distance infinie de ce même A_0.

Si $p(\boldsymbol{r})$ est la probabilité de trouver un A à la distance $\boldsymbol{r}$ de A_0, $1-p(\boldsymbol{r})$ sera celle d'y trouver un B ; $p(\boldsymbol{r})$ prend la valeur c à une distance infinie de A_0 et $1-p(\boldsymbol{r})$, la valeur $1-c$. La loi d'action de masse donne :

$$\frac{p(\boldsymbol{r}) \,.\, (1-c)}{[1-p(\boldsymbol{r})] \,.\, c} = \exp\left[-\frac{E}{kT}\right] \tag{2}$$

k est la constante de Boltzmann, T la température considérée ; enfin E est l'énergie pour l'échange des positions :

$$E = E(A_r) + E(B_\infty) - E(B_r) - E(A_\infty) \tag{3}$$

Les interactions entre premiers voisins sont seules considérées. Soient V_{AA}, V_{AB} et V_{BB} les énergies d'interaction des couples AA, AB et BB respectivement. Dans l'approximation du *champ moléculaire*, on peut écrire :

$$\left.\begin{aligned} E(A_r) &= \sum_{r'} V_{AA} p(\boldsymbol{r}') + \sum_{r'} V_{AB}[1-p(\boldsymbol{r}')] \\ E(B_r) &= \sum_{r'} V_{AB} p(\boldsymbol{r}') + \sum_{r'} V_{BB}[1-p(\boldsymbol{r}')] \\ E(A_\infty) &= z[cV_{AA} + (1-c)V_{AB}] \\ E(B_\infty) &= z[cV_{AB} + (1-c)V_{BB}] \end{aligned}\right\} \tag{4}$$

$\sum_{r'}$ désigne ici une sommation sur tous les proches voisins de l'atome situé à la distance $\boldsymbol{r}$ de l'atome central A_0 ; z est le nombre de ces proches voisins.

En posant $W = V_{AA}+V_{BB}-2\,V_{AB}$, (1) s'écrit en tenant compte des équations (2), (3) et (4) :

$$\sigma(\boldsymbol{r}) = -c\frac{\exp\left[-\dfrac{W(c-1)}{kT}\cdot\sum_{\boldsymbol{r}'}\sigma(\boldsymbol{r}')\right]-1}{c\,.\exp\left[-\dfrac{W(c-1)}{kT}\cdot\sum_{\boldsymbol{r}'}\sigma(\boldsymbol{r}')\right]-c+1} \tag{5}$$

(c) *Forme approchée du paramètre d'ordre pour les hautes températures*

Le calcul explicite de $\sigma(\boldsymbol{r})$ nécessiterait des approximations successives qui ne donneraient un résultat ni exact, ni concluant. Nous nous bornerons donc à considérer, aux très hautes températures, le premier terme du développement de (5) en puissance de $1/T$:

$$\sigma(\boldsymbol{r}) \simeq -\frac{c(1-c)W}{kT}\sum_{\boldsymbol{r}'}\sigma(\boldsymbol{r}') \tag{6}$$

A titre d'indication d'ordre de grandeur, nous extrapolerons cette formule à $T = T_c$.

3. CONTRIBUTION DE L'ORDRE LOCAL A LA RÉSISTIVITÉ DE L'ALLIAGE AU-DESSUS DE LA TEMPÉRATURE CRITIQUE

(a) *Approximations utilisées*

Nous nous plaçons dans les conditions suivantes :

—les électrons de valence sont considérés comme des *électrons libres.*

—les sections efficaces différentielles de diffusion sont calculées dans l'*approximation de Born*, avec des puits de potentiel carrés pour chaque atome diffusant.

Si V_A est le potentiel dû à un atome A et V_B celui dû à un atome B, nous pouvons prendre comme origine des potentiels le potentiel moyen :[2] $cV_A+(1-c)\,V_B$.

Alors le potentiel relatif d'un atome A est :

$$V_A - [cV_A + (1-c)V_B] = (1-c)(V_A-V_B);$$

celui d'un atome B est de même : $-c(V_A-V_B)$. Le potentiel diffusant probable $V(\boldsymbol{r})$, en un site à une distance $\boldsymbol{r}$ d'un atome central, sera :

$$\begin{aligned} V(\boldsymbol{r}) &= (1-c)(V_A-V_B)p(\boldsymbol{r})+ \\ &\quad +(-c)(V_A-V_B)[1-p(\boldsymbol{r})] \\ &= (V_A-V_B)(c-1)\sigma(\boldsymbol{r}) \end{aligned} \tag{7}$$

(b) *Rappel de l'expression de la résistivité*

On sait[3] que la résistivité $\Delta\rho$ est proportionnelle à l'inverse du temps de relaxation τ. Si nous appelons $\Delta\rho_0$ la résistivité, indépendante de la température, correspondant au désordre total et τ_0 le temps de relaxation correspondant :

$$\frac{\Delta\rho}{\Delta\rho_0} = \frac{\tau_0}{\tau} \tag{8}$$

Nous avons :

$$\frac{1}{\tau_0} = \alpha s_0 \tag{9}$$

où s_0 est la section efficace incohérente par atome et α une constante. De même :

$$\frac{1}{\tau} = \alpha\,.\,2\pi\int_0^{\pi}\sin\theta\,d\theta(1-\cos\theta)\frac{ds}{d\Omega} \tag{10}$$

où θ est l'angle de diffusion entre les vecteurs d'onde $\boldsymbol{k}$ et $\boldsymbol{k}_F$ de l'électron de conduction après et avant diffusion (Fig. 1).

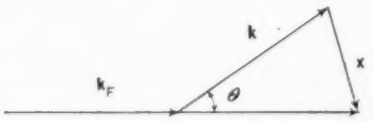

FIG. 1. Angle θ et vecteur $\mathbf{x}$ de diffusion.

Dans l'approximation de Born, la section efficace différentielle par atome $ds/d\Omega$ est donnée, en fonction de la section efficace incohérente par :

$$\frac{\dfrac{ds}{d\Omega}}{\dfrac{s_0}{4\pi}} = \frac{|\sum_{\boldsymbol{r}}\exp -i\boldsymbol{k}\,.\,\boldsymbol{r}\,.\,V(\boldsymbol{r})\,.\exp i\boldsymbol{k}_F\,.\,\boldsymbol{r}|^2}{cN[(1-c)(V_A-V_B)]^2+(1-c)N[(-c)(V_A-V_B)]^2},$$

où N est le nombre total d'atomes, cN le nombre d'atomes A et $(1-c)\,N$ le nombre d'atomes B.

Soit $\boldsymbol{x} = \boldsymbol{k}_F - \boldsymbol{k}$ le vecteur de diffusion (Fig. 1). $|\boldsymbol{k}| = |\boldsymbol{k}_F|$ est la valeur au niveau de Fermi, et par conséquent $|\boldsymbol{x}| = 2\ k_F \sin\theta/2$. Alors :

$$\frac{ds}{d\Omega} = \frac{s_0}{4\pi}\frac{1}{c(1-c)(V_A-V_B)^2}\times \times\frac{1}{N}\Big|\sum_{\boldsymbol{r}} V(\boldsymbol{r})\exp i\boldsymbol{x}\,.\,\boldsymbol{r}\Big|^2 \qquad (11)$$

(c) *Calcul explicite de la section efficace différentielle par atome*

En tenant compte de (7), (11) s'écrit :

$$\frac{ds}{d\Omega} = \frac{s_0}{4\pi}\frac{1-c}{c}\frac{1}{N}\Big|\sum_{\boldsymbol{r}}\sigma(\boldsymbol{r})\exp i\boldsymbol{x}\,.\,\boldsymbol{r}\Big|^2 \qquad (12)$$

En utilisant pour $\sigma(R)$ la formule approchée (6), il vient :

$$\sum_{\boldsymbol{R}}\sigma(R)\exp i\boldsymbol{x}\,.\,\boldsymbol{R} = \sigma(0) - \frac{c(1-c)W}{kT}\sum_{\boldsymbol{R}\neq 0}\Big(\sum_{\boldsymbol{R}'}\sigma(R')\Big)\exp i\boldsymbol{x}\,.\,\boldsymbol{R} \qquad (16)$$

$\boldsymbol{R}'$ désigne les proches voisins de l'atome situé en $\boldsymbol{R}$.

En posant $\boldsymbol{R}-\boldsymbol{R}' = \boldsymbol{d}$ et en écrivant :

$$\sum_{\boldsymbol{R}\neq 0} = \sum_{\boldsymbol{R}} - \sum_{\boldsymbol{R}=0}$$

on peut écrire :

$$\sum_{\boldsymbol{R}}\sigma(R)\,.\,\exp i\boldsymbol{x}\,.\,\boldsymbol{R} = \sigma(0) - \frac{c(1-c)W}{kT}\Big[\Big(\sum_{\boldsymbol{R}}\sigma(R)\,.\,\exp i\boldsymbol{x}\,.\,\boldsymbol{R}\Big)\Big(\sum_{\boldsymbol{d}}\exp i\boldsymbol{x}\,.\,\boldsymbol{d}\Big) - \sum_{-\boldsymbol{d}}\sigma(-\boldsymbol{d})\Big] \qquad (17)$$

Soit, en développant :

$$\frac{ds}{d\Omega} = \frac{s_0}{4\pi}\frac{1-c}{c}\frac{1}{N}\Big[\sum_{A}\sigma_A(0)\,.\sum_{R_A}\sigma(R_A)\exp i\boldsymbol{x}\,.\,\boldsymbol{R}_A + \sum_{B}\sigma_B(0)\,.\sum_{R_B}\sigma(R_B)\exp i\boldsymbol{x}\,.\,\boldsymbol{R}_B\Big] \qquad (13)$$

$\sum_{R_A}, \sum_{R_B}$

désignent des sommations faites sur les sites $\boldsymbol{R}$ autour d'un atome A ou B pris comme origine :

$\sum_{A}, \sum_{B}$

désignent des sommations sur tous les atomes A ou B ; $\sigma_A(0)$ et $\sigma_B(0)$ sont les valeurs prises par $\sigma(0)$ si l'origine est occupée par un atome A ou un atome B ; on remarque que :

$$\sigma_A(0) = -1 \text{ et } \sigma_B(0) = \frac{c}{1-c} \qquad (14)$$

L'égalité (13) fait intervenir des expressions de la forme $\sum_{\boldsymbol{R}}\sigma(R)\exp i\boldsymbol{x}\boldsymbol{R}$ que nous allons calculer à part :

$$\sum_{\boldsymbol{R}}\sigma(R)\exp i\boldsymbol{x}\,.\,\boldsymbol{R} = \sigma(0) + \sum_{\boldsymbol{R}\neq 0}\sigma(R)\exp i\boldsymbol{x}\,.\,\boldsymbol{R} \qquad (15)$$

L'équation (6) montre que les fonctions $\sigma(\boldsymbol{r})$, sauf $\sigma(o)$, sont au moins du 1er ordre en $1/T$; par suite, *si nous nous limitons dans* (17) *aux termes en* $1/T$,

$$\sum_{\boldsymbol{R}}\sigma(\boldsymbol{R})\exp i\boldsymbol{x}\,.\,\boldsymbol{R}$$

se réduit à son premier terme $\sigma(0)$ (cf. (15)) et

$$\sum_{-\boldsymbol{d}}\sigma(-\boldsymbol{d})$$

est négligeable devant $\sigma(0)$.

On obtient donc finalement la relation suivante :

$$\sum_{\boldsymbol{R}}\sigma(R)\exp i\boldsymbol{x}\,.\,\boldsymbol{R} = \sigma(0)\Big[1 - \frac{c(1-c)W}{kT}\sum_{\boldsymbol{d}}\exp i\boldsymbol{x}\,.\,\boldsymbol{d} + 0\Big(\frac{1}{T^2}\Big)\Big] \qquad (18)$$

Cette méthode rejoint celle employée par DE GENNES et FRIEDEL[1] dans un calcul analogue mais qui n'était pas valable à l'origine ; notre

équation est valable à toutes distances à l'ordre de $1/T$. Dans ces conditions, l'expression (13) devient, avec (14) et (18) :

$$\frac{ds}{d\Omega} = \frac{s_0}{4\pi}\left[1 - \frac{c(1-c)W}{kT}\sum_d \exp i\boldsymbol{x}\,.\,\boldsymbol{d}\right] \quad (19)$$

(d) *Calcul de la résistivité*

Nous pouvons alors donner une forme approchée pour la résistivité (8). Avec (9), (10) et (19), il vient :

$$\frac{\Delta\rho}{\Delta\rho_0} = \frac{1}{2}\int_0^\pi \sin\theta(1-\cos\theta)\,d\theta \times \times\left[1 - \frac{c(1-c)W}{kT}\sum_d \exp i\boldsymbol{x}\,.\,\boldsymbol{d}\right] \quad (20)$$

Nous remplaçons alors $\sum_d \exp i\boldsymbol{x}.\boldsymbol{d}$ par sa moyenne sur toutes les orientations possibles du vecteur $\boldsymbol{x}$, ce qui revient à prendre la *moyenne de* $\Delta\rho$ *sur les angles* :

$$\sum_d \exp i\boldsymbol{x}\,.\,\boldsymbol{d} = z\frac{\sin xD}{xD} \quad (21)$$

où D est la distance entre proches voisins et z le nombre de ces voisins. En posant : $y^2 = 2(1-\cos\theta)$, (20) conduit à la formule :

$$\frac{\overline{\Delta\rho}}{\overline{\Delta\rho_0}} = \frac{1}{4}\int_0^2 y^3\,dy\left[1 - \frac{c(1-c)W_z}{kT}\frac{\sin(k_FD)y}{(k_FD)y}\right] \quad (22)$$

$$\frac{\overline{\Delta\rho}}{\overline{\Delta\rho_0}} = 1 + c(1-c)z\frac{W}{kT}A(k_FD) \quad (23)$$

$$A(k_FD) = \frac{1}{(k_FD)^2}\times \times\left[\cos 2k_FD - \frac{\sin 2k_FD}{k_FD} + \frac{1-\cos 2k_FD}{2(k_FD)^2}\right].$$

4. APPLICATIONS NUMÉRIQUES

(a) *Résultats généraux*

Des calculs classiques dans l'approximation de BRAGG–WILLIAMS[4] montrent que l'on peut relier directement W à une température critique d'ordre T_c, au-dessous de laquelle apparaît l'ordre à longue distance :

$$W = \lambda\frac{kT_c}{zc(1-c)}, \quad (24)$$

$\lambda = 1$ lorsque l'on peut considérer l'alliage AB comme décomposable en deux sous-réseaux, l'un de A, l'autre de B, identiques, avec z premiers voisins d'un atome donné, de même nature entre eux ; et, s'ils ne le sont pas, λ est différent de 1 et dépend de la structure des sous-réseaux et de la nature de l'environnement de chaque atome.

L'équation (23) se réduit à :

$$\frac{\overline{\Delta\rho}}{\overline{\Delta\rho_0}} = 1 + \frac{T_c}{T}\lambda A(k_FD). \quad (25)$$

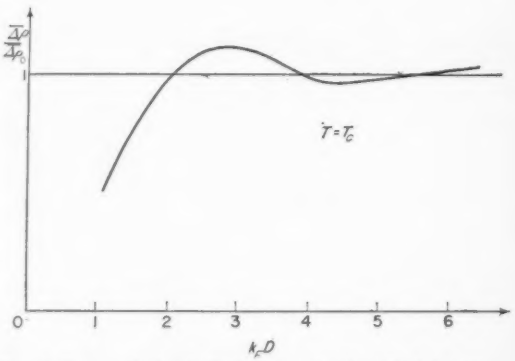

FIG. 2. Extrapolation à T_c de la courbe de résistivité d'un alliage AB quelconque en fonction de k_FD, k_F étant le vecteur d'onde au niveau de Fermi et D la distance entre atomes voisins ; la résistivité dûe aux phonons est omise dans toutes les figures.

Nous en concluons à une dépendance hyperbolique de la résistivité en fonction de la température. D'autre part, cette formule, extrapolée à T_c, donne un ordré de grandeur de l'écart maximum de la résistivité $\overline{\Delta\rho}$ à sa valeur de désordre total $\overline{\Delta\rho_0}$, donné par le signe de la fonction $A(k_FD)$ en fonction de l'énergie k_F.

Nous avons tracé, sur la Figure 2, pour $\lambda = 1$, la courbe donnant $\overline{\Delta\rho}/\overline{\Delta\rho_0}$ extrapolée à T_c, en fonction de k_FD, et, sur la Figure 3, différentes courbes illustrant la formule (25) pour différentes valeurs de k_FD.

Nous remarquons sur la Figure 2 que, à T_c, les valeurs maxima des écarts de $\overline{\Delta\rho}$ à $\overline{\Delta\rho_0}$ sont faibles et diminuent quand k_FD augmente: les maxima positifs sont, au plus, égaux au premier, soit environ 12 pour cent. Les écarts négatifs ne sont importants que pour $k_FD \ll 2$, condition sans doute

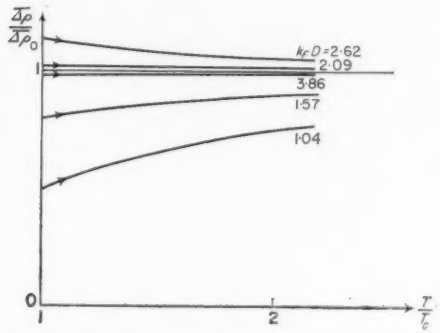

FIG. 3. Courbes de résistivité en fonction de la température, au-dessus de T_c et pour différentes valeurs du paramètre k_FD.

rarement observée dans un métal. Signalons aussi que la formule (25), n'étant qu'un développement limité, ne peut donner un résultat pour k_FD voisin de 0, et nous avons donc arrêté la courbe de la Figure 2 pour k_FD voisin de 1.

(b) *Résultats particuliers à T_c et comparaison avec l'expérience*

Dans le cas d'une structure cubique simple, MURAKAMI[5] avait déjà montré que l'ordre à courte distance amène un léger écart de la résistivité à sa valeur correspondant au désordre total.

Pour Cu_3Au où $k_FD \simeq 3{,}46$ et $\lambda = 2{,}84$, DAMASK[6] a observé expérimentalement (avec $T_c = 393°C$) :

$$\frac{\rho_{460°C} - \rho_{T_c}}{\rho_{T_c}} \times 100 = -0{,}74,$$

en prenant soin de retrancher la résistivité dûe aux phonons; dans nos calculs, la même formule donne $-1{,}66$; un calcul théorique de GIBSON[7] basé sur des paramètres d'ordre local expérimentaux est en accord avec les résultats de DAMASK.

Pour Au_3Cu, qui a la même valeur de k_FD, WRIGHT et GODDARD[8] trouvent également une diminution de résistivité juste au-dessus de T_c. Pour ce même alliage, d'après les expériences de KOREVAAR.[9]

$$\frac{\rho_{450°C} - \rho_{T_c}}{\rho_{T_c}} = -0{,}08$$

et nos calculs donnent, pour ce même rapport $-0{,}06$.

Les calculs antérieurs et les nôtres concordent quant au sens de variation de la résistivité; cette variation est très lente sur la courbe de DAMASK, elle l'est un peu moins dans notre étude mais elle reste néanmoins faible et une étude plus poussée à T_c donnerait peut-être un résultat plus proche de celui de DAMASK.

Pour $CuZn_\alpha$ où $k_FD \simeq 3{,}78$, le calcul de GIBSON[7] donne :

$$\frac{\rho_{190°C}}{\rho_{\text{désordre total}}} = 1{,}004.$$

On n'observe pas de température critique, mais nous pouvons connaître W[10] et nos formules donnent alors 1,026; ces deux résultats indiquent, comme pour Cu_3Au, une faible diminution dans la résistivité quand T augmente jusqu'à la valeur de désordre total alors que les expériences de DAMASK[11] semblent indiquer une très faible augmentation de résistivité; mais les écarts à la valeur de désordre total, bien que de signes contraires, sont extrêmement faibles, et nous ne pouvons affirmer, pour l'instant, qu'une étude plus détaillée du voisinage du point critique ne nous rapprocherait pas plus des résultats expérimentaux.

Enfin pour $CuZn_\beta$ que nous considérerons plus spécialement à $T < T_c$ et où $k_FD \simeq 3{,}86$, l'extrapolation de (25) à T_c donne :

$$\frac{\overline{\Delta\rho}}{\overline{\Delta\rho_0}} - 1 \simeq -\frac{1}{100}.$$

5. ÉTUDE DU PARAMÈTRE D'ORDRE AU-DESSOUS DE T_c

Une étude générale analogue au cas $T > T_c$ serait ici plus délicate car il faut tenir compte explicitement de la structure au voisinage de 0°K. Nous étudierons seulement le cas simple de l'alliage Cu–Zn_β. A l'état complètement ordonné (0°K), ce réseau cristallin est décomposable en deux sous-réseaux cubiques simples de cuivre et de

zinc respectivement, où chaque atome d'un sous-réseau est entouré de 8 premiers voisins de l'autre sous-réseau.

L'ordre à grande distance est défini par :

$$S = \frac{C_n - C_e}{C_n + C_e}. \tag{26}$$

où C_n et C_e sont les concentrations en atomes n et e respectivement. n désigne les atomes qui occupent les mêmes sites qu'au 0°K (ordre parfait), et e ceux qui occupent des positions différentes de celles du 0°K. On a évidemment $0 \leqslant |S| \leqslant 1$; dans ces conditions, si N est le nombre total d'atomes, le nombre d'atomes n est $(1+S)N/2$; celui des atomes e est $(1-S)N/2$.

L'ordre à courte distance peut se définir par des probabilités de présence d'atomes n ou e autour d'un site central, de façon analogue au cas des hautes températures mais en considérant à part chacun des sous-réseaux.

Soit $p_{ij}(\mathbf{r})$ la probabilité de trouver, à la distance $\mathbf{r}$ d'un atome central i, un atome j de même nature (cuivre ou zinc), i, j pouvant être n ou e ; alors $1-p_{ij}(\mathbf{r})$ est la probabilité de trouver à $\mathbf{r}$ de l'atome central i un atome j de nature différente; on a $0 \leqslant p_{ij} \leqslant 1$. A très grande distance de l'atome central considéré, seul est sensible l'ordre à grande distance, d'où :

$$\left.\begin{aligned} p_{ij}(\infty) &= \frac{1+S}{2} \qquad \text{si } j = n \\ p_{ij}(\infty) &= \frac{1-S}{2} \qquad \text{si } j = e \end{aligned}\right\} \tag{26}$$

et $\begin{cases} p_{ii}(0) = 1 \\ p_{ij}(0), \text{ si } j \neq i \text{ n'existe évidemment pas.} \end{cases}$ (27)

Le calcul explicite des $p_{ij}(\mathbf{r})$ s'effectue par la même méthode qu'au § 2(b).

Calculons par exemple p_{nn} : soit un atome Cu_n "central". On évalue l'énergie nécessaire pour échanger un Cu_n à la distance $\mathbf{r}$ du premier et un Zn_n à une distance infinie, ce qui donne :

$$\frac{p_{nn}(\mathbf{r}) \cdot \dfrac{1+S}{2}}{[1-p_{nn}(\mathbf{r})] \cdot \dfrac{1-S}{2}} =$$

$$= \exp - \frac{1}{kT}[E(\mathrm{Cu}_r)_n - E(\mathrm{Zn}_r)_e + E(\mathrm{Zn}_\infty)_n - E(\mathrm{Cu}_\infty)_e] \tag{28}$$

avec :

$$\left.\begin{aligned} E(\mathrm{Cu}_r)_n &= \sum_{r'} V_{\mathrm{CuCu}} p_{ne}(\mathbf{r}') + \sum_{r'} V_{\mathrm{CuZn}}[1 - p_{ne}(\mathbf{r}')] \\ E(\mathrm{Zn}_r)_e &= \sum_{r'} V_{\mathrm{CuZn}} p_{ne}(\mathbf{r}') + \sum_{r'} V_{\mathrm{ZnZn}}[1 - p_{ne}(\mathbf{r}')] \\ E(\mathrm{Zn}_\infty)_n &= V_{\mathrm{CuZn}} 8 \frac{1+S}{2} + V_{\mathrm{ZnZn}} 8 \frac{1-S}{2} \\ E(\mathrm{Cu}_\infty)_e &= V_{\mathrm{CuCu}} 8 \frac{1+S}{2} + V_{\mathrm{CuZn}} 8 \frac{1-S}{2} \end{aligned}\right\} \tag{29}$$

où V_{CuCu}, V_{CuZn}, V_{ZnZn} sont les énergies d'interaction définies comme précédemment. En tenant compte de la valeur à l'infini de (28), et à l'aide de (26) et (27) on retrouve l'équation classique de l'ordre à longue distance :

$$\frac{1+S}{1-S} = \exp 2S \frac{T_c}{T} \tag{30}$$

Et, tout calculs faits, on trouve pour $p_{nn}(\mathbf{r})$ l'expression suivante :

$$\frac{p_{nn}(\mathbf{r})}{1-p_{nn}(\mathbf{r})} = \exp - \frac{T_c}{2T}[\sum_{r'} p_{ne}(\mathbf{r}') - 4]$$

$\sum_{r'}$ est la sommation sur les 8 premiers voisins de l'atome situé en $\mathbf{r}$. De façon plus générale et par des calculs analogues, il vient :

$$\frac{p_{ij}(\mathbf{r})}{1-p_{ij}(\mathbf{r})} = \exp - \frac{T_c}{2T}[\sum_{r'} p_{ik}(\mathbf{r}') - 4] \tag{31}$$

$i, j, k = n$ ou e, mais $j \neq k$.

Nous faisons alors le changement de variables suivant :

$$\left.\begin{aligned} p_{ij}(\mathbf{r}) &= p_{ij}(\infty) + P_{ij}(\mathbf{r}) \qquad \text{si } j \equiv n \\ p_{ij}(\mathbf{r}) &= p_{ij}(\infty) - P_{ij}(\mathbf{r}) \qquad \text{si } j \equiv e \end{aligned}\right\} \tag{32}$$

de façon à mettre en évidence les écarts des p_{ij} par rapport à l'ordre à grande distance. La distinction de signe permet de considérer des P_{ij} positifs quel que soit j. Alors :

$$P_{ij}(\boldsymbol{r}) = \frac{1-S^2}{2} \frac{1}{S+1+\dfrac{2}{\exp\dfrac{T_c}{2T}\sum\limits_{\boldsymbol{r}'} P_{ik}(\boldsymbol{r}')-1}} \tag{33}$$

De façon générale, $V(\boldsymbol{r})$ aura pour expression, pour un atome central i ($i = n$ ou e) :

$$V(\boldsymbol{r}) = [V_{\mathrm{Cu}}-V_{\mathrm{Zn}}][P_{in}(\boldsymbol{r})-P_{ie}(\boldsymbol{r})] \tag{36}$$

Dans le calcul de la résistivité (cf. § 3), $V(\boldsymbol{r})$ intervient par l'expression :

$$|\sum_{\boldsymbol{r}} V(\boldsymbol{r}) \exp i\boldsymbol{x} \,.\, \boldsymbol{r}|^2$$

que nous allons développer.

$$\frac{|\sum\limits_{\boldsymbol{r}} V(\boldsymbol{r}) \exp i\boldsymbol{x} \,.\, \boldsymbol{r}|^2}{[V_{\mathrm{Cu}}-V_{\mathrm{Zn}}]^2} = \sum_{i=n} \{[P_{in}(0)-P_{ie}(0)] \,.\, \sum_{\boldsymbol{R}_n} ([P_{in}(R_n)-P_{ie}(R_n)] \exp i\boldsymbol{x} \,.\, \boldsymbol{R}_n)\}$$
$$+ \sum_{i=e} \{[P_{in}(0)-P_{ie}(0)] \,.\, \sum_{\boldsymbol{R}_e} ([P_{in}(R_e)-P_{ie}(R_e)] \,.\, \exp i\boldsymbol{x} \,.\, \boldsymbol{R}_e)\} \tag{37}$$

Les P_{ij} ne prennent que des valeurs bien inférieures à l'unité, d'après leur définition même. On peut donc considérer, en première approximation, dans la formule (33) ;

$$\exp\frac{T_c}{2T}\sum_{\boldsymbol{r}} P_{ik}(\boldsymbol{r}') \neq 1+\frac{T_c}{2T}\sum_{\boldsymbol{r}} P_{ik}(\boldsymbol{r}') \tag{34}$$

Ce qui conduit à une expression approchée pour P_{ij} :

$$P_{ij}(\boldsymbol{r}) \simeq (1-S^2)\frac{T_c}{8T}\sum_{\boldsymbol{r}} P_{ik}(\boldsymbol{r}') \tag{35}$$

6. CONTRIBUTION DES PARAMÈTRES D'ORDRE A LA RÉSISTIVITÉ POUR $T<T_c$

(a) *Calcul de la résistivité pour* $\mathrm{Cu}\text{–}\mathrm{Zn}_\beta$

On utilise, pour cette étude, les mêmes méthodes de calcul et les mêmes approximations qu'au § 3.

Soient V_{Cu} et V_{Zn} les potentiels respectifs d'un atome de cuivre et d'un atome de zinc. Pour un atome Cu_n central, par exemple, le potentiel diffusant probable $V(\boldsymbol{r})$ à la distance $\boldsymbol{r}$, sera:

$$V_{\mathrm{Cu}}\left[P_{nn}(\boldsymbol{r})-\frac{1+S}{2}+P_{ne}(\boldsymbol{r})-\frac{1-S}{2}\right]+$$
$$+V_{\mathrm{Zn}}\left[1-P_{nn}(\boldsymbol{r})-\frac{1-S}{2}+1-P_{ne}(\boldsymbol{r})-\frac{1+S}{2}\right]$$
$$=[V_{\mathrm{Cu}}-V_{\mathrm{Zn}}][P_{nn}(\boldsymbol{r})-P_{ne}(\boldsymbol{r})]$$

$$\sum_{\boldsymbol{R}_n}, \sum_{\boldsymbol{R}_e}$$

désignent des sommations faites sur les sites $\boldsymbol{R}$ autour d'un atome n ou e pris comme origine ;

$$\sum_{i=n}, \sum_{i=e}$$

désignent des sommations sur tous les atomes n ou e.

Un calcul analogue à celui du § 3(c). donne successivement (pour $\boldsymbol{d}$ voisin de 0) :

$$\left.\begin{aligned}
&\sum_{\boldsymbol{R}_n}[P_{nn}(\boldsymbol{R}_n)-P_{ne}(\boldsymbol{R}_n)]\exp i\boldsymbol{x} \,.\, \boldsymbol{R}_n = \\
&\quad = \frac{1-S}{2}\left[1-(1-S^2)\frac{T_c}{8T}\sum_{\boldsymbol{d}}\exp i\boldsymbol{x} \,.\, \boldsymbol{d}\right] \\
&\sum_{\boldsymbol{R}_e}[P_{en}(\boldsymbol{R}_e)-P_{ee}(\boldsymbol{R}_e)]\exp i\boldsymbol{x} \,.\, \boldsymbol{R}_e = \\
&\quad = -\frac{1+S}{2}\left[1-(1-S^2)\frac{T_c}{8T}\sum_{\boldsymbol{d}}\exp i\boldsymbol{x} \,.\, \boldsymbol{d}\right]
\end{aligned}\right\} \tag{38}$$

En remarquant qu'il faut multiplier par 2 le second membre de (37) puisqu'il y a deux sous-réseaux identiques,

$$|\sum_{\boldsymbol{r}} V(\boldsymbol{r})\exp|x \,.\, r|^2 = \frac{N[V_{\mathrm{Cu}}-V_{\mathrm{Zn}}]^2}{4}\times$$
$$\times(1-S^2)\left[1-(1-S^2)\frac{T_c}{8T}\sum_{\boldsymbol{d}}\exp i\boldsymbol{x} \,.\, \boldsymbol{d}\right] \tag{39}$$

Avec les notations du § 3(d), nous trouvons pour expression de la résistivité moyenne :

$$\frac{\overline{\Delta\rho}}{\overline{\Delta\rho_0}} = \frac{1}{4}\int_0^2 y^3\,dy(1-S^2)\left[1-(1-S^2)\frac{T_c}{T}\frac{\sin(k_FD)y}{(k_FD)y}\right] \tag{40}$$

Et d'après le calcul de § 4(a) pour k_FD :

$$\frac{\overline{\Delta\rho}}{\overline{\Delta\rho_0}} = \frac{1}{4}\int_0^2 y^3\,dy(1-S^2)\left[1-(1-S^2)\frac{T_c}{T}\frac{\sin 3{,}86y}{3{,}86y}\right]$$

D'où :

$$\frac{\overline{\Delta\rho}}{\overline{\Delta\rho_0}} \simeq (1-S^2)\left[1-\frac{1-S^2}{100}\frac{T_c}{T}\right] \tag{41}$$

avec :

$$\frac{1+S}{1-S} = \exp 2S\frac{T_c}{T}.$$

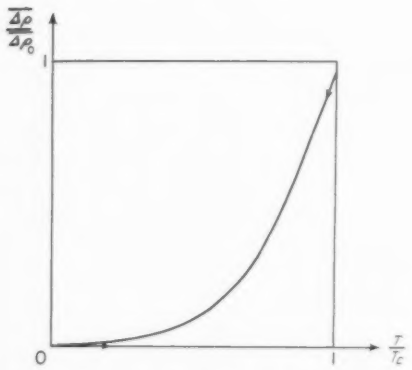

FIG. 4. Courbe donnant la résistivité de l'alliage Cu–Zn_β en fonction de la température, au-dessous de T_c.

Remarques :

(i) Pour $T\to T_c$, $S\to 0$ et on retrouve la formule (23) établie pour $T>T_c$. Les formules (23) et (41) donnent donc des *résistivités continues à la température* T_c.

(ii) Pour $T\to 0$, $(1-S^2)/100\ T_c/T$ est négligeable devant 1 : $\overline{\Delta\rho}/\overline{\Delta\rho_0}$ varie comme $1-S^2$ et tend vers 0 avec T. Ce dernier résultat au voisinage du 0°K est conforme à des travaux antérieurs;[12–15] il est général pour n'importe quelle structure : *à très basse température, l'ordre à grande distance intervient seul.*

Nous avons tracé sur la Figure 4 la courbe donnant la résistivité de l'alliage Cu–Zn_β à $T<T_c$ et k_FD correspondant au niveau de Fermi et, sur la Figure 5, la famille des courbes donnant pour le même alliage, la résistivité que l'on calculerait en fonction de la température à $T<T_c$ et $T>T_c$ pour différentes valeurs de kD.

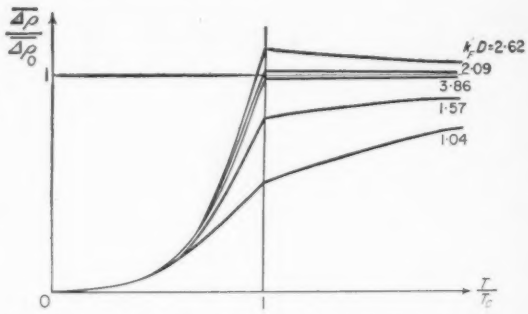

FIG. 5. Courbes donnant la résistivité de l'alliage Cu–Zn_β au-dessous et au-dessus de T_c, pour plusieurs valeurs du paramètre k_FD.

(b) *Comparaison avec l'expérience*

Des courbes classiques[16, 17] de résistivité de Cu–Zn_β à $T<T_c$ semblent indiquer une variation analogue à la nôtre, en $1-S^2$ à très basses températures si on prend la précaution de leur retrancher la résistivité dûe aux phonons. On observe, d'autre part, juste au-dessous de T_c, une pente $d\Delta\rho/\Delta\rho\ dT_c = 3$. Notre calcul donne une pente de 2,95, donc en très bon accord.

7. CONCLUSIONS

Cette étude, bien qu'approximative, donne des renseignements intéressants et semble en assez bon accord avec l'expérience. Les formules simples que nous obtenons mettent en évidence une influence réelle bien que faible de l'ordre à courte distance, qui donne à la courbe de résistivité une pente faible mais non nulle juste au-dessus de T_c et une pente finie juste au-dessous ; nous concluons aussi à une décroissance rapide de la résistivité avec T, au-dessous de T_c, suivant à peu près la loi en $1-S^2$ prédite par l'ordre à grande distance. Il resterait à calculer avec plus de précision la valeur de la résistivité à T_c et à faire une étude générale des paramètres d'ordre au-dessous de T_c, applicable à une structure quelconque. Ceci impliquerait de considérer à part les alliages ayant une transition

d'ordre à longue distance de première espèce comme $AuCu_3$ et, d'autre part, parmi ceux dont la transition est de seconde espéce, le cas plus spécial de CuAu, par exemple, où les atomes s'ordonnent par plans successifs, d'où un choix de paramètre d'ordre non isotrope.

Remerciement—Je tiens à exprimer ici mes plus vifs remerciements à Monsieur le Professeur J. FRIEDEL qui m'a proposé cette étude et m'a constamment guidée tout au long de mon travail.

VOL. 15 1960

BIBLIOGRAPHIE

1. DE GENNES P. G. et FRIEDEL J., *J. Phys. Chem. Solids* **4,** 71 (1958).
2. NORDHEIM L. W., *Ann. Phys., Lpz.* **9,** 641 (1931).
3. MOTT N. F. and JONES H., *The Theory of the Properties of Metals and Alloys* Chap. VII, § 12, Oxford University Press (1936).
4. FOWLER R. H. and GUGGENHEIM E. A., *Statistical Thermodynamics* Chap. XIII, Cambridge University Press (1939).
5. MURAKAMI T., *J. Phys. Soc. Japan* **8,** 458 (1953).
6. DAMASK A., *J. Phys. Chem. Solids* **1,** 23 (1956).
7. GIBSON J. B., *J. Phys. Chem. Solids* **1,** 27 (1956).
8. WRIGHT P. and GODDARD K. F., *Proc. Phys. Soc.* **71,** 507 (1958).
9. KOREVAAR B. M., Thèse d'ingénieur docteur, Delft (1960).
10. LUMSDEN J., *Thermodynamics of Alloys* p. 259. *Institute of Metals*, London (1952).
11. DAMASK A., *J. Appl. Phys.* **27,** 610 (1956); *J. Phys. Chem. Solids* **4,** 177 (1958).
12. MUTO T., *Sci. Pap. Inst. Phys. Chem. Res. Tokyo* **30,** 99 (1936).
13. SEEMANN H. J., *Z. Phys.* **62,** 824 (1930).
14. DIENES G. J., *J. Appl. Phys.* **22,** 1020 (1951).
15. JONES F. W. and SYKES C., *Proc. Roy. Soc.* A**166,** 376 (1938).
16. JOHANSONN C. H. et LINDE J. O., *Ann. Phys., Lpz.* **5,** 762 (1930); **25,** 1 (1936).
17. BORELIUS G., *Proc. Phys. Soc.* **49,** 77 (1937).

J. Phys. Chem. Solids Pergamon Press 1960. Vol. 15. pp. 82–85. Printed in Great Britain.

THE ANALYSIS OF SPECTRAL YIELD AND ACCELERATING FIELD CHARACTERISTICS OF THE PHOTOELECTRIC EMISSION FROM SEMICONDUCTORS

D. HANEMAN* and E. W. J. MITCHELL

Physics Research Laboratories, The University, Reading

(*Received* 6 *November* 1959; *revised* 3 *December* 1959)

Abstract—The relation between yield and accelerating field characteristics of the photoelectric emission from semiconductors is discussed. A comparison of the photoelectric thresholds deduced from these two characteristics is made for germanium, gallium arsenide and indium antimonide.

1. INTRODUCTION

In photoelectric emission experiments on semiconductors it is necessary to distinguish between the work function (ϕ) and the photoelectric threshold energy (ϕ'). The work function is the energy of an electron at the Fermi level, taking as zero the energy of an electron just outside the semiconductor. The threshold is the energy, referred to the same zero, of an electron at the top of the valence band in the surface region from which photoelectrons are emitted.

For a non-degenerate semiconductor there are no photoelectrons originating from the Fermi level, so that it is not possible to determine ϕ by analysis of the electron emission alone. Carroll[1] has deduced a parameter (4·78 eV)—which he called the work function—from measurements by Apker *et al.*[2] of the emission from tellurium. The value agreed well with the values of ϕ (4·76–4·83 eV) found by Apker *et al.* from contact potential measurements. We show below that the parameter deduced by Carroll was ϕ' and suggest that the agreement with ϕ for the one case tested was probably fortuitous.

The main point of the paper, however, arises from the method used by Carroll. The particular results which he analysed were of the increase of photoelectric emission with applied collector voltage. It is shown that an exactly complementary analysis may be made of yield curves. Both field and yield curves have been measured for the same surfaces, for which ϕ has also been determined from contact potential measurements in the same tubes.

2. THEORY

The correspondence between the two effects arises because the principal role of the accelerating field is to decrease the work function barrier by some amount $\Delta\phi$ (Schottky effect). This will have the same effect on the yield as increasing the photon energy by $\Delta\phi$ if

$$\left(\frac{\partial Y}{\partial(h\nu)}\right)_{\phi} = -\left(\frac{\partial Y}{\partial\phi}\right)_{h\nu} \tag{1}$$

where Y is the yield in electrons per incident quantum. Condition (1) will be satisfied if the yield function has the general form:

$$Y = f^{n}(h\nu - \phi') \tag{2}$$

A detailed theory of the form of the yield function for semiconductors does not exist but Apker *et al.*[2] have derived power laws for specific idealized models. These power laws are of the form

$$Y \propto q(\nu) \,.\, (h\nu - \phi')^{m+2} \tag{3}$$

and represent a good approximation to the observed shapes of yield curves over certain ranges of

* Now at Brown University, Providence, Rhode Island, U.S.A.

VOL. 15 1960

photon energy. In equation (3) $q(\nu)$ is a frequency dependent excitation probability and m is a constant for a given material.

Provided that $q(\nu)$ is a slowly varying function of frequency, equation (3) satisfies the condition (1). In the absence of a detailed calculation of Y as a function of $h\nu$ and of gross experimental deviations from $Y\alpha(h\nu-\phi')^{m+2}$, we shall use this relation to illustrate the effects of equation (1).* From equation (3) we have:

$$M = Y\left(\frac{\partial Y}{\partial(h\nu)}\right)^{-1}_{\phi'} = \frac{h\nu-\phi'}{m+2} \qquad (4)$$

Under these conditions a plot of M as a function of $h\nu$ should be linear, having a slope $(m+2)^{-1}$ and intercept ϕ'.

The amount of lowering of the work function barrier in an applied field F is given by the Schottky relation:

$$\Delta\phi = -e^{3/2}F^{1/2}\left(\frac{K-1}{K+1}\right)^{1/2}$$

where e is the electronic charge and K the dielectric constant of the semiconductor. If $F = \alpha V$ where V is the applied voltage we can define a quantity R and derive the result that:

$$R = Y\left(\frac{\partial Y}{\partial V^{1/2}}\right)^{-1}_{h\nu}$$

$$= \left(\frac{K+1}{K-1}\right)^{1/2} e^{-3/2}\alpha^{-1/2}\left(\frac{h\nu-\phi'}{m+2}\right) \qquad (5)$$

(This is similar to the expression given by CARROLL.) Thus ϕ' is the intercept on the photon energy axis of the plots, which should be linear, of R as a function of $(h\nu)$. It would also be possible to determine m if K and α were known.

If the assumptions and analysis are correct then experiments should show:

(i) M increasing linearly with $h\nu$, enabling ϕ' and m to be determined.

(ii) R increasing linearly with $h\nu$, enabling ϕ' and m to be determined—which values should agree with those found from (i).

(iii) The values of ϕ' should be greater than ϕ determined from contact potential measurements on the same surfaces.

* The physical significance of the value of the quantity ϕ' as determined from equation (3) is open to discussion.

Apart from experimental errors the above conclusions may not be found to be exact because the relation

$$Y \propto (h\nu-\phi')^{m+2} \qquad (6)$$

is itself an approximation. Thus in a typical example equally good fits to an experimental yield curve over a range of about 1 eV from the threshold may be obtained with $m = 1{\cdot}5$, $\phi' = 4{\cdot}68$ eV as with $m = 2{\cdot}0$ and $\phi' = 4{\cdot}63$ eV. These departures become more significant at the higher photon energies.

Nevertheless ϕ' and m—as found from equations (6) or (3)—are commonly used to represent photoelectric data on semiconductors. The point of our analysis has been to indicate two simple and complementary ways of determining the ϕ' and m of equation (3).

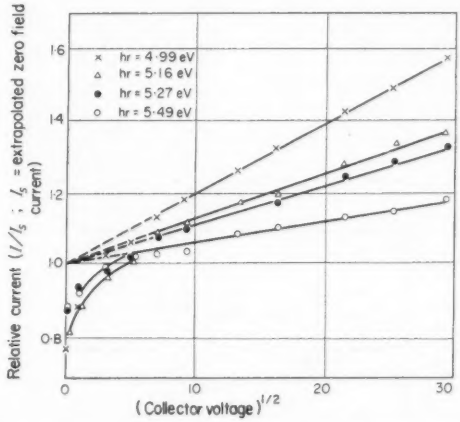

FIG. 1. Schottky plots of the emission from indium antimonide for different photon energies.

3. EXPERIMENTAL RESULTS AND DISCUSSION

Measurements have been made in sealed off tubes of the emission characteristics of InSb, GaAs and Ge surfaces. The details of the tube construction and the method of measurement have already been given by HANEMAN[3].

Typical plots of Y against $V^{1/2}$ are shown in Fig. 1. The curves shown are for an InSb surface—created by fracturing a single crystal in the experimental tube. The departures from the $Y \propto V^{1/2}$ relation at low applied voltages is probably due to patch effects. It is found that the values of V at

Table 1

Surface	ϕ'(field) $\pm 0{\cdot}1$ eV	ϕ'(yield) $\pm 0{\cdot}1$ eV	ϕ(cpd) $\pm 0{\cdot}03$ eV	m(yield)
Ge etched	4·45	4·5	4·40	0·5
InSb ground	4·2	4·15	4·15	2·0
GaAs ground	4·45	4·5	4·20	2·0
InSb ground broken	4·6	4·6	4·49	2·0

which the square root relation begins to be valid are different for different surfaces.

The values of R as a function of $h\nu$ are shown in the lower part of Fig. 2 and it will be seen that the three lowest points lie on a straight line intersecting the abscissa at 4·6 eV. There is an uncertainty of $\pm 0{\cdot}1$ in determining the position of the intercept. The variation of R with $h\nu$ for other surfaces is also shown in the lower part of Fig. 2 and the values of the intercepts are given in Table 1.

Some results of the variation of M with $h\nu$ are presented in the upper part of Fig. 2. Reasonable straight lines are obtained but, as with the R vs. $h\nu$ plots, the intercept cannot be determined to better than about $\pm 0{\cdot}1$ eV. Values of the intercepts are given in Table 1, together with the values of work functions (ϕ) for the same surfaces. The method of determining the work functions has already been described by HANEMAN[3]. It will be seen from Table 1 that the two sets of values of ϕ' agree, within the limits given above, and that $\phi' \geqslant \phi$, which we should expect to be true for semiconductors.

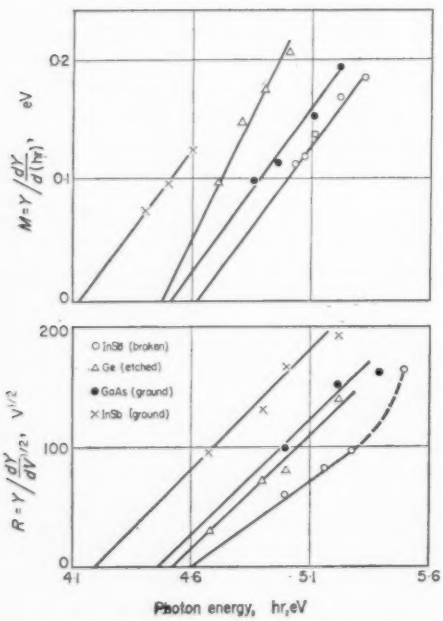

FIG. 2. The variation of the quantities M and R with photon energy for different surfaces.

Finally, we consider the values of the slopes in Fig. 2. For the lower curves the slopes should be given by

$$\frac{dR}{d(h\nu)} = \left(\frac{K+1}{K-1}\right)^{1/2} e^{-3/2}\alpha^{-1/2}(m+2)^{-1}$$

as may be seen from equation (5). When K is large—e.g. 12(Si), 16(Ge) and 16(InSb)—the slope is given, to a good approximation, by $e^{-3/2}\alpha^{-1/2}(m+2)^{-1}$, so that m can be found if α is known. A value of α could be found by the following method. For $(h\nu - \phi') > 0{\cdot}3$ eV the yield from a metal satisfying the Fowler relation approximates to equation (1) with $q(\nu) \neq f^n(\nu)$ and $m = 0$. Consequently, in this region the slope of R vs. $h\nu$ for such a metal would be $\frac{1}{2}e^{-3/2}\alpha^{-1/2}$. However, α determined in this way was found to be sensitive to the exact shape of the metal emitter, and reproducible results could not be obtained using metal caps which fitted closely to the semiconductor. The theory was tested when a film of carbon was accidentally deposited on to the broken InSb surface. The emission from this film could also be represented as above so that, with some error because of the uncertainty in $[(K+1)/(K-1)]^{1/2}$, we could determine α for the exact shape of the underlying semiconducting emitter which had been previously measured. The values found were

$\alpha = 2{\cdot}8\ \text{cm}^{-1}$ and $m = 2{\cdot}7$. A more exact value could be determined by deliberately evaporating metal films on to the semiconductor, but this was not appreciated when our measurements were made.

The quantity m is given more directly by the yield analysis and values of $m \approx 2$ were found as indicated in Table 1.

4. CONCLUSIONS

The field and yield characteristics of the photoelectric emission from semiconductors are shown to be similarly related. These characteristics do not give accurate values of the photoelectric threshold (ϕ') occurring in equation (3), but within the limits of error ($\pm 0{\cdot}1$ eV) the same values are obtained.

In cases where the best accuracy is not required, or where the more complicated energy distribution measurements are not available, the methods described give useful estimates of ϕ' and m. Further, ϕ' may be determined from the accelerating field characteristics without having to measure absolute light intensities.

Acknowledgements—We should like to thank Professor DITCHBURN for his interest, Mr. W. DIXON for his glass-blowing and the Admiralty for financial support.

REFERENCES

1. CARROLL P. E., *Phys. Rev.* **104,** 660 (1956).
2. APKER L., TAFT E. and DICKEY J., *Phys. Rev.* **74,** 1462 (1948).
3. HANEMAN D., *J. Phys. Chem. Solids* **11,** 205 (1959).

VOL. 15 1960

J. Phys. Chem. Solids Pergamon Press 1960. Vol. 15. pp. 86–96. Printed in Great Britain.

THE EXCITON SPECTRUM OF ZINC OXIDE

D. G. THOMAS

Bell Telephone Laboratories, Inc., Murray Hill, New Jersey

(*Received* 27 *October* 1959)

Abstract—The absorption and reflection spectra of ZnO crystals have been observed in the near ultraviolet at temperatures between 300° and 4·2°K. At 77°K three well-marked reflection peaks occur: two for light polarized with $E \perp c$ (c is the hexagonal axis) and one for $E \| c$. The reflectance data have been analysed by means of the Kramers–Kronig relation. The three peaks arise from $n = 1$ exciton transitions involving holes from each one of the three valence bands. At 4·2°K the $n = 2$ exciton states become apparent in reflection, allowing estimates to be made of the exciton binding energy and reduced mass. In absorption the lowest energy exciton may be seen in the "wrong" mode of polarization indicating mixing of certain exciton states. Longitudinal excitons and various forbidden transitions are also observed together with a considerable number of "impurity" exciton transitions. At 4·2°K sharp fluorescent lines occur which are associated with the impurity effects. Zeeman effects have been seen in a field of 32,000 G.

INTRODUCTION

ZINC oxide can be grown as single crystals which are completely transparent in the visible region of the spectrum but show strong absorption in the near ultraviolet. This absorption marks the onset of intrinsic band-to-band transitions and is associated with photoconduction.[1] SCHAROWSKY[2] observed that as single crystals of ZnO were progressively treated in zinc vapor at a high temperature, the absorption at room temperature extended to longer wavelengths eventually giving the crystals a yellow color. The crystals used were comparatively thick and no marked structure was seen. As will be shown below it is likely that the extended absorption arose from lattice distortion produced by the high temperature treatment. MOLLWO[3] measured the transmission of films of polycrystalline ZnO a few thousand angstroms thick at room temperature. Absorption coefficients in excess of 10^5 cm^{-1} were found in the ultraviolet and some rather diffuse structure was seen. Since ZnO is hexagonal, the use of single crystals and polarized light is necessary to derive the maximum information, and it seems likely that low temperatures and thin single crystals are also essential. These conditions have been met in the work to be described here.

The behavior of electrons and donors in n-type ZnO have been extensively investigated and is interpreted in terms of the band theory of semiconductors as distinct from the tight binding or Heitler–London model. The binding energy of several donors is about 0·05 eV.[4] p-Type ZnO has not so far been described presumably because of the difficulty of introducing an excess of low lying acceptors into the crystals. However, the photoconduction experiments mentioned above do indicate that holes having reasonable mobilities can exist in ZnO. It seem likely therefore, that excitons should occur in ZnO with binding energies comparable to the donor binding energy. The maximum of the valence band is presumably p-like, while the conduction band is s-like. Consequently the exciton transitions would fall into ELLIOTT's[5] "allowed" classification and if the band extrema occurred at the same value of crystal momentum in the Brillouin zone they would occur as strong absorption lines. Such strong lines cannot easily be seen in transmission as extremely thin single crystals are required. However, if the lines have sufficient strength and small width, they may be observed in reflection; analysis of the reflection data by means of the Kramers–Kronig relation then yields the optical constants in the wavelength region examined. This method has been used to determine the absorption in BaO[6] where the

results were found to be in agreement with the absorption measured directly on thin films.

In this paper reflection from ZnO at low temperatures is described which reveals the existence of three separate series of excitons explicable in terms of the three p-like valence bands. Because of their strong absorption these transitions cannot be distinguished in transmission experiments with crystals of thickness 1 μ or greater. However, transmission in thicker crystals does reveal considerable structure. This structure will be discussed and shown to arise from a variety of causes.

VOL. 15 1960

EXPERIMENTAL PROCEDURE

The ZnO crystals used were grown in these Laboratories from the vapor phase at about 1200°C. They usually occurred in the form of hexagonal needles several mm long and about 2×10^{-2} cm thick. Sometimes flakes grew only a few microns thick with the hexagonal c-axis lying in the plane of the flake; these were convenient for measurements of high absorption coefficients. A polarizing microscope indicated the principal crystal directions. Thin crystals were also obtained by polishing the hexagonal needles. This was done by waxing the crystals to a piece of glass and carefully polishing them to a thickness of about 15 μ. They were then removed from the glass and etched in concentrated phosphoric acid until the thickness was reduced to about 7 μ. The thickness of these crystals could sometimes be determined from interference effects. The more usual method was to focus a microscope alternately on the top and bottom surfaces of the crystal and determine the distance between the two positions. The refractive index of ZnO in the visible region of the spectrum is about 2·0.[7]

The crystals were mounted by sticking them at the ends over a slot cut in a molybdenum plate. Very thin crystals were usually stuck only at one end. This method of mounting minimized external strain on the crystal. (One crystal was inadvertently partially covered with glue; this part of the crystal showed broadened and displaced absorption lines presumably because of the strain produced by the glue. Removal of the glue restored normal behavior.)

The initial measurements of transmission and reflection were made using light from the exit slit of a Perkin–Elmer double pass monochromator equipped with an NaCl prism. A resolution of about 1 Å was attained in the region near 3650 Å. The crystal was mounted in the vacuum space of a metal Dewar with quartz windows, and a photomultiplier was used as a detector. Next to the slot over which the crystal was mounted there was an identical blank slot which could be moved into the crystal position by sliding the Dewar between two stops. The optics were so arranged that by rotating a mirror the transmitted or reflected beam could be examined. The reflectivity was determined for an angle of incidence less than 10°. The blank slot enabled absolute values of the transmission and reflection to be determined. The reflection from the window of the Dewar was blanked out at a focal point. For most of the work a tungsten lamp was used although for shorter wavelengths a hydrogen lamp was employed.

Higher resolution was attained using a Bausch and Lomb grating spectrograph, with a grating having 55,000 lines/in. The instrument had dispersion of 2 Å/mm in the first order. A resolution of 0·1 Å was readily obtained. The detector used was a photographic plate. Since lengthy exposures were possible the sensitivity was high and inhomogeneities in the behavior of a single crystal could be examined. Plate calibrations were made so that quantitative interpretation was possible of the microphotometer traces taken from the plates.

Since there is doubt about the precise temperature of a crystal mounted in a vacuum space of a Dewar, for all the precise work quoted here the crystals were immersed in the refrigerant. This was done in the tip of a Pyrex Dewar with an outer diameter of $\frac{5}{8}$ in. The tip could be placed between the pole pieces of a magnet in a field of 32,000 G.

The polarizer was a Glan–Thomson prism which had to be used slightly off axis. Care was taken that any lenses or mirrors between the crystals and polarizer did not interfere with the polarization.

For the experiments in which the crystals were in the Dewar vacuum space it was found that the reflectivity did not change appreciably in the course of a run so that condensation on the surface of the crystal did not seem to be a serious problem.

RESULTS

Reflection

The determination of the absolute reflectivity of one surface of a transparent crystal is hindered by

the reflection from the back surface which, if the two surfaces are not quite parallel, will make an unknown contribution. Furthermore surface irregularities reduce the observed reflectivity particularly for etched crystals. These difficulties could be overcome if polished crystals were used, however, it will be shown that polishing alters both the reflection and absorption data. Consequently the reflectivities have been normalized to the value required by the known refractive index in the wavelength region near the onset of strong absorption, where the crystal absorption removes the contribution from the back surface but does not affect the reflectivity. The refractive index is obtained by extrapolating the data of MOLLWO[7] to slightly

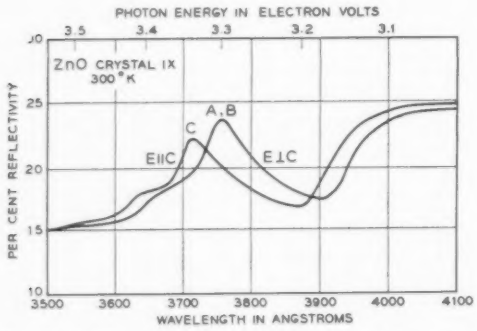

FIG. 1. Reflection from an as-grown ZnO crystal at 300°K. The light is polarized either parallel or perpendicular to the hexagonal c-axis.

shorter wavelengths, and by shifting it by the appropriate amount for temperatures below 300°K; (the shift was taken to be the same as the shift displayed by the reflection peaks). For most crystals the normalization changed the observed reflectivity by less than 10 per cent.

Figure 1 shows the reflectivity spectrum of an as-grown crystal at 300°K in the wavelength region of interest for the two modes of polarization of the light. At a photon energy of about 3·1 eV the observed reflectivity begins to fall as absorption commences and the contribution to the reflectivity from the back surface drops out. The dichroism of the crystal is evident. (In subsequent figures reflection from only one surface is shown.) Two reflection peaks are seen: one for $E \perp c$, labeled A, B, occurs at about 3·30 eV; and one for $E \| c$, labeled C, lies near 3·34 eV. ($E \perp c$ means here light

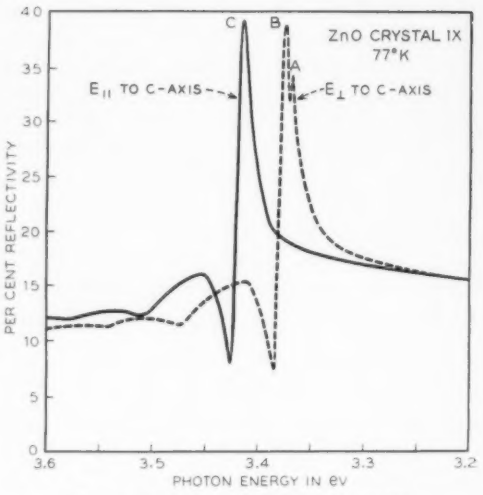

FIG. 2. Reflection from ZnO at 77°K.

polarized with its electric vector perpendicular to the hexagonal c-axis of the crystal.)

At 77°K the structure becomes more pronounced. Fig. 2 shows the reflectivity at this temperature obtained with the Perkin–Elmer monochromator. The peak A, B is now split into two components A and B. Peak C is, however, not split. Fig. 3 shows the reflectivity over a wider range of photon energies for $E \perp c$ at 77°K. For energies below 3·1 eV MOLLWO's data was used, extrapolating it to zero frequency (neglecting, of course, the *reststrahl* effects). Above 3·6 eV unpolarized light was used. The falling reflectivity in this range may partly arise from the increase of the

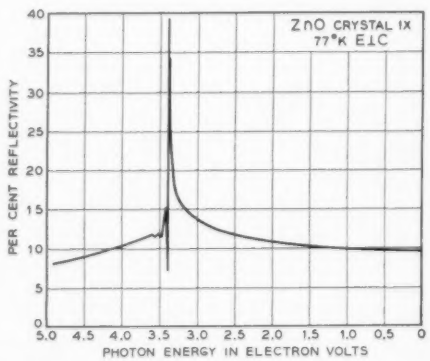

FIG. 3. Reflection from ZnO at 77°K for E c over a wide range of photon energies.

light scattered from surface imperfections as the wavelength is decreased. The data shown in this figure above and below the central peaks were used in the Kramers–Kronig analyses to be described. The data at higher photon energies were, however, smoothly joined onto the highest energy points of a particular curve. At 4·2°K no further structure was seen between 3·6 and 4·9 eV. At 77°K the reflection peaks occur at the following photon energies;

A 3·3708 eV

B 3·378 eV

C 3·418 eV

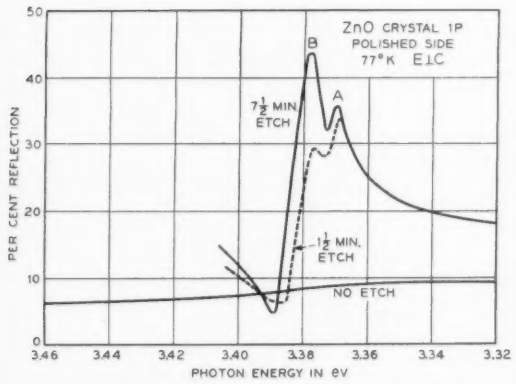

FIG. 4. Reflection from a polished ZnO crystal before and after etching with phosphoric acid. The etch rate is about 1 μ/min.

The reflection peaks are sensitive to the condition of the surface. Fig. 4 shows the reflection at 77°K for $E \perp c$ for a crystal with a polished surface and for the same crystal after etching in concentrated phosphoric acid at room temperature. The absolute reflectivity values in this figure are only approximate. The polished surface reflectivity shows no structure presumably because the surface layers have been damaged. When several microns of the surface are etched away the characteristic structure shown by as-grown crystals reappears, in which peak *A* is lower than peak *B*.

At 4·2°K additional structure is seen in the reflectivity. Fig. 5 shows the reflectivity for $E \perp c$ and Fig. 6 for $E \| c$. The additional peaks A', B' and C' are marked. Weaker subsidiary lines may be distinguished near A' and B' in Fig. 5. There are also weak peaks at 3·50 and 3·54 eV for $E \perp c$ and $E \| c$ respectively. A splitting, approximately equal in energy difference to the energy difference between peaks *A* and *B*, may just be discerned for the peak at 3·50 eV. However, the peak at 3·54 eV is not

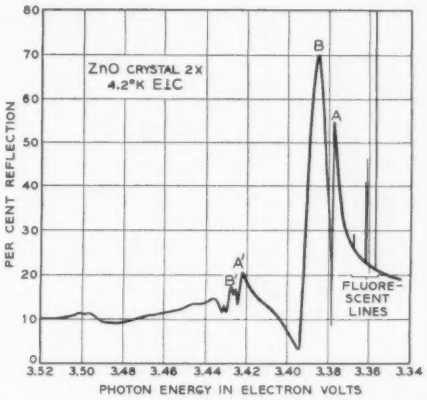

FIG. 5. Reflection from ZnO at 4·2°K for $E \perp c$. Note the strong fluorescent lines.

split. Fig. 5 shows a series of four fluorescent lines which are excited by the tungsten lamp and which may be seen against the background of specularly reflected light. If the light is directed in a non-specular direction these lines become even more

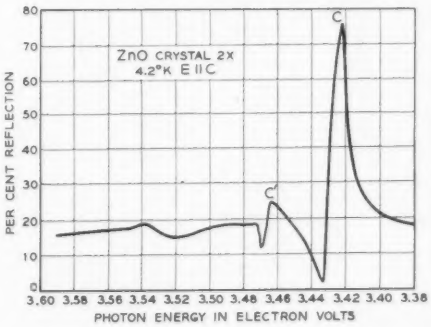

FIG. 6. Reflection from ZnO at 4·2°K for $E \| c$. No fluorescence is seen.

prominent. The width of the lines is two wave numbers or less. Very similar lines occur in all crystals which have been examined. They are always polarized with $E \perp c$.

Table 1. (4·2°K)

Oscillator	Position (±0·0005 eV)	Difference (eV)	Oscillator strength	Full width at half height (eV)
A	3·3768	0·0457	13×10^{-4}	0·0015
A'	3·4225		$3{\cdot}5\times10^{-4}$	0·003
B	3·383	0·0445	45×10^{-4}	0·0022
B'	3·4275		$2{\cdot}2\times10^{-4}$	0·0025
C	3·4215	0·0435	60×10^{-4}	0·0017
C'	3·465		15×10^{-4}	0·009

The positions of the reflection peaks at 4·2°K are:

A 3·377 eV A' 3·422 eV

B 3·3845 eV B' 3·4275 eV

C 3·4225 eV C' 3·465 eV

Analysis of the reflection data

The Kramers–Kronig relation was used in the manner previously described[6,8] to give the values of the optical constants near the reflection peaks.

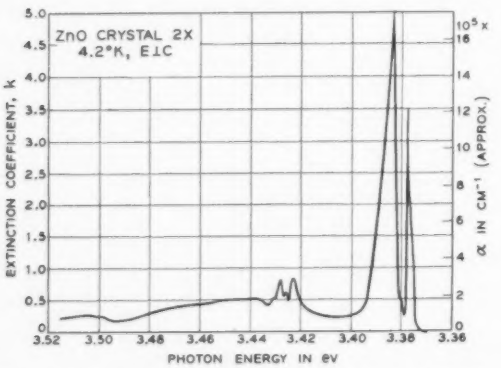

FIG. 7. The extinction coefficient for ZnO at 4·2°K for $E\ c$ as derived from the Kramers–Kronig analysis of the data in Fig. 5.

Approximately 130 points were used for each mode of polarization of the light. In Fig. 7 is plotted the extinction coefficient for $E\perp c$ at 4·2°K, and in Fig. 8 the imaginary part of the dielectric constant for $E\|c$ at 4·2°K as derived from this analysis. It is interesting that the crystals display strong absorption between the peaks A, B or C, and A', B' or C'. From the plots of the imaginary part of the

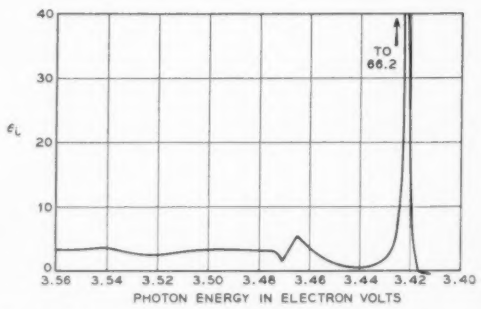

FIG. 8. The imaginary part of the dielectric constant of ZnO at 4·2°K as derived from the Kramers–Kronig analysis of the data in Fig. 6.

dielectric constant the positions, strengths and widths of the various oscillators may be determined and are given in Table 1.

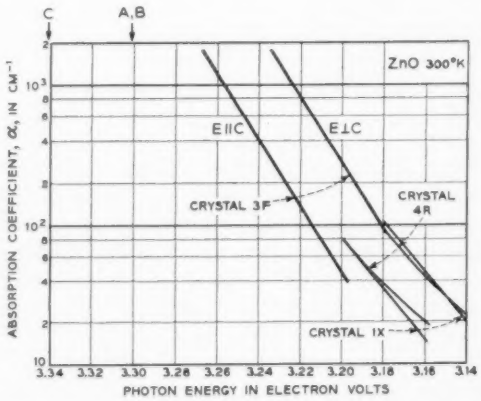

FIG. 9. Absorption of various ZnO crystals at 300°K. The positions of the reflectance peaks at 300°K are marked.

In the determination of the strengths of the weaker lines there is the likelihood of considerable error since a sizable base subtraction has to be made.

Absorption results

Figure 9 illustrates some absorption data taken at 300°K. The position of the reflection peaks at room temperature are indicated in this figure. No structure is seen in the absorption although there is appreciable dichroism. The absorption appears to increase exponentially with photon energy as was found for CdS and other substances.[9] The absorption varies somewhat from one crystal to another as illustrated in Fig. 9.

Figure 10 shows the behavior of various crystals at 77°K. An absorption line marked A_m was seen in all crystals in which observations could be made in this range. As has been described elsewhere[10] a line A_L corresponding to a longitudinal exciton derived from exciton A, may also be seen at 77°K provided the angle between the direction of propagation of the light and the c-axis is less than about 88°. A weak line was seen in crystal $H2$ for $E\|c$ near 3·36 eV and is probably similar to certain lines seen at 4·2°K. Crystal $4R$, which shows considerable absorption at low photon energies, was a crystal obtained from commercial sources and doped with lithium. Consequently its purity is low. Fig. 11 illustrates that the polishing of the surface of a crystal can do sufficient damage to alter the absorption spectra. The line A_m is almost obscured in the polished crystal but is restored after etching. This indicates that the absorption edge can be spread out in a strained or damaged crystal.

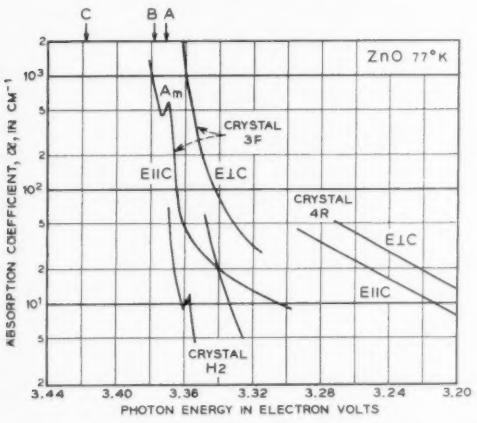

FIG. 10. Absorption of various ZnO crystals at 77°K. The positions of the reflectance peaks at 77°K are marked.

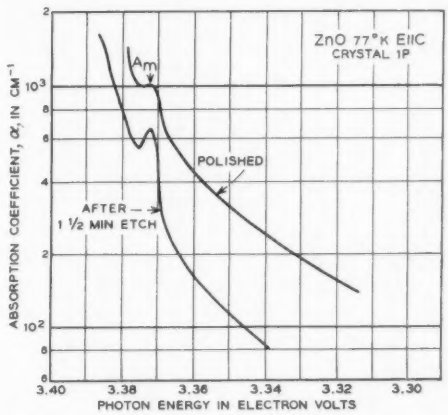

FIG. 11. Absorption of a polished ZnO crystal before and after etching with phosphoric acid for $E\|c$ at 77°K.

Figure 12 shows that at 4·2°K many absorption lines are revealed, some of them having a width of only 1 cm^{-1}. Again crystal $4R$ shows absorption at low energies presumably because of an imperfect lattice. For $E\|c$ a number of lines are seen in pure crystals which are believed to be intrinsic lines. These are labeled A_m, A_L, B_F and B_L and their positions are given in Table 2.

The strength of line B_F is not accurately known but is at least 10 times weaker than A_m. The origins of these four lines are discussed later.

Table 2

Line	Position (eV)	Strength
A_m	3·3758 ± 0·0002	ca. 10^{-6}
A_L	3·3779 ± 0·0002	
B_F	3·3819 ± 0·0002	
B_L	3·3931 ± 0·0002	

At energies less than that of A_m the line absorption is believed to arise from excitons associated with impurities. For $E\perp c$ a set of rather strong lines is seen at energies above about 3·355 eV. These lines show slight variations from one crystal to another in strength and position. Between 3·35 and 3·32 eV

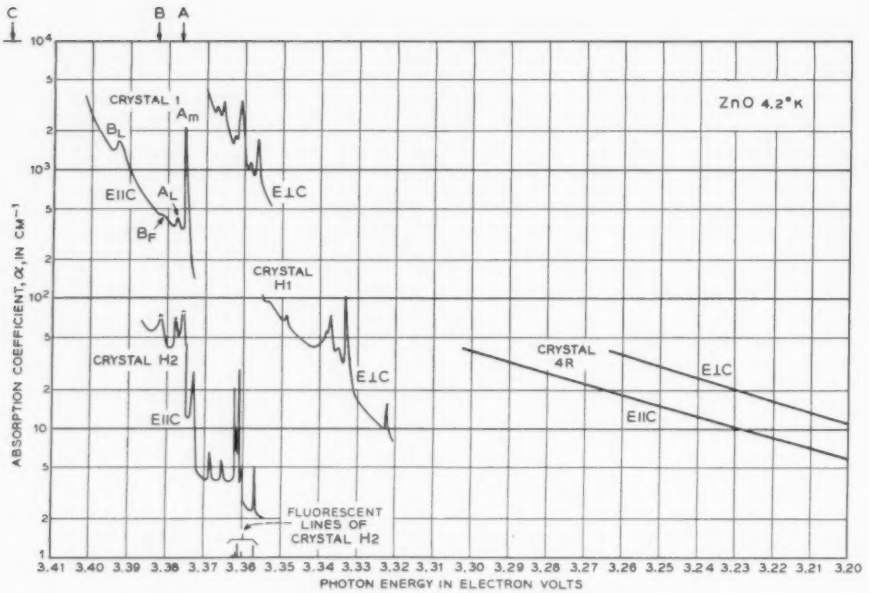

FIG. 12. Absorption of various ZnO crystals at 4·2°K. The positions of the resonant energies associated with the reflectance peaks at 4·2°K are indicated.

other weaker lines were seen in crystal $H1$, while in crystal $H2$ only two very weak lines were seen in this region, although these fell at energy levels very close to the stronger lines seen in $H1$. For $E\|c$ a set of very weak lines was seen in crystal $H2$ in the same region as the set of strong lines seen for $E\perp c$. In this region with $E\|c$, crystal $H1$ shows some lines but they are still weaker than those of $H2$.

Some very thin crystals were found and mounted over a hole 0·004 in. in diameter. The thickness of these crystals was obtained from interference effects observed in transmission at wavelengths slightly greater than that of peak A. In this region of "anomalous dispersion" the refractive index which changed rapidly was known from the Kramers–Kronig analysis. One such crystal was found to be 5000 Å thick. At 77° and 4·2°K it revealed a weak pass-band at photon energies between peaks A, B and A', B'. It was estimated that α in this region had a value of about 4×10^4 cm^{-1} which was in good agreement with the value deduced from the Kramers–Kronig analysis.

Fluorescence

Strong sharp fluorescent lines excited by the continuum of a tungsten lamp have been found in a number of ZnO crystals at 4·2°K. They fall in the region between A_m and 3·35 eV. They are completely polarized with $E\perp c$ and are believed to coincide with the strong absorption lines seen in this region for $E\perp c$. Some of these lines are shown in Fig. 5 for crystal $2X$. The emission lines from crystal $H2$ correspond in energy with the five lowest energy absorption lines seen in this crystal for $E\|c$.

The effect of a magnetic field

With the magnetic field and polarization vector parallel to the c-axis, and the direction of propagation of the light normal to the c-axis it was found that line A_m split into two lines symmetrically placed about the original position of A_m and separated by 0·0007 eV in a field of 32,000 G. The line A_L was not affected by the field. Some of the impurity lines were affected by the field but so far no study of this has been made.

DISCUSSION

A formal discussion of the theory of the work reported here is given in the accompanying paper

by HOPFIELD[11]. Consequently only a qualitative outline of the theory follows.

Reflection

The most striking result is the observation at low temperatures of three sharp reflectance peaks, A, B and C, of which A and B occur for light with $E\perp c$, and C for light with $E\|c$. Analysis shows these peaks to correspond to quite narrow absorption lines, and the only reasonable explanation of these lines is that they arise from direct exciton transitions, most probably at the origin of the Brillouin zone ($\mathbf{k} = 0$). These transitions may be plausibly discussed in terms of angular momentum as follows, although a proper treatment of the transitions is given by ELLIOTT[5]. The extremum of the valence band in ZnO has p-like symmetry, while the conduction band is s-like. Consequently in transferring an electron from the valence to the conduction band at $\mathbf{k} = 0$ the angular momentum changes by one unit and the transition is allowed. The same is true of the exciton transition provided there is no further momentum change. As a result, excitons are formed with high probability which have s-like spatial characters and so no gross orbital angular momentum. Further selection rules arise from the condition that $\Delta S = 0$. The oscillator strengths of these transitions are between 10^{-3} and 10^{-2}, considerably less than the analogous atomic transitions because of the large size of the exciton.

BIRMAN[12] and others have pointed out that at $\mathbf{k} = 0$ the three p-like valence bands are degenerate in a cubic crystal in which spin is neglected. This degeneracy is completely lifted in a hexagonal crystal in which, as well as the non-isotropic crystal field, there is also a spin–orbit interaction. The three excitons observed in ZnO are made up from an electron and a hole from each one of the valence bands. Two of the bands may be called $P_{x,y}$ and the third P_z, where x and y correspond to the directions perpendicular to the hexagonal c-axis, and z to the c-direction. (We neglect, for the moment, mixing between the $P_{x,y}$ and P_z bands.) The $P_{x,y}$ bands interact with light polarized $\perp$ to c, and P_z to light polarized $\|$ to c. It is clear from the observed polarization properties that in ZnO reflection peaks A and B correspond to excitons involving holes from the $P_{x,y}$ bands which are split from each other by spin–orbit effects. Peak C corresponds to excitons derived from the P_z band, which is split from the $P_{x,y}$ bands by the crystal field. The splitting which arises from the crystal field is large compared to the spin–orbit interaction. The spin–orbit effect "mixes" two of the three excitons and HOPFIELD[11] has given formulae for this mixing, the extent of which is controlled by the relative magnitudes of the spin–orbit and crystal field splittings. If the line which occurs only for $E\perp c$ is taken as the energy origin (line B in ZnO), then the energies of the two other exciton lines are given by

$$E = \frac{\delta+\Delta}{2} \pm \sqrt{\left[\left(\frac{\delta+\Delta}{2}\right)^2 - \frac{2}{3}\delta\Delta\right]}$$

where δ is the spin–orbit parameter, i.e. the energy separation between the hole bands produced by the spin–orbit interaction in the absence of a crystal field and Δ the analogous crystal field parameter. The composition of the $\mathbf{k} = 0$ wave functions for the two mixed valence bands may be expressed as follows:

$$(P_x - iP_y) + \left(2 - 3\frac{E}{\delta}\right)P_z$$

or

$$(P_x + iP_y) - \left(2 - 3\frac{E}{\delta}\right)P_z.$$

In ZnO the energies of the mixed excitons are

$$E_A = -0{\cdot}0062 \text{ eV}$$

$$E_C = +0{\cdot}0385 \text{ eV}$$

which lead to the following values of δ and Δ:

$$\delta = -0{\cdot}0087 \text{ eV}$$

$$\Delta = +0{\cdot}0410 \text{ eV}.$$

The mixing ratio for line A is then predicted to be,

$$\left(2 - 3\times\frac{0{\cdot}0062}{0{\cdot}0087}\right)^2 = 1{\cdot}95\times10^{-2}.$$

In ZnO the crystal field splitting dominates and the mixing is weak. It is for this reason that peaks A and B are seen in reflection only for $E\perp c$, and C only for $E\|c$. This situation contrasts with that for CdS.[8] Here, because of the greater nuclear charge of sulphur the spin–orbit effect is comparable to the crystal field effect and there is virtually complete mixing of the two hole bands. The bands

which mix in CdS correspond to exciton peaks B and C and so these peaks occur roughly equally in both modes of polarization. Peak A occurs only for $E \perp c$ in CdS. Mixing is, however, apparent in ZnO in absorption. It was pointed out above that an absorption line occurs for $E \| c$ at the energy corresponding to exciton peak A. This line occurs in all crystals examined and shows that band C is weakly mixed with band A. (Presumably for $E \perp c$ there is an analogous weak absorption line at the position of peak C which is masked by other effects.) It is interesting to note that the bands which mix are different for CdS than for ZnO. The strength of line A_m is about 10^{-6}. Half the sum of the strengths of reflection peaks A and B from Table 1 is $5{\cdot}8 \times 10^{-3}$. The observed mixing ratio is, therefore,

$$\frac{10^{-6}}{5{\cdot}8 \times 10^{-3}} = 1{\cdot}7 \times 10^{-4}.$$

This value is considerably less than the expected value of 2×10^{-2}. Possible reasons for this discrepancy are discussed in HOPFIELD's paper.

Table 1 shows that the combined strength of peaks A and B (58×10^{-4}) approximately equals that of peak C (60×10^{-4}). This is the expected result if the optical matrix elements for the two modes of polarization are the same. The fact that there are two x, y bands does not double the strength of peaks A or B, since in a particular experiment the light is polarized along the "x" or "y" directions (which are of course equivalent), but not along both simultaneously. The strengths of A and B are not equal presumably because A and B are sufficiently close to mix, and there is a redistribution of strength in order to minimize the energy. This mixing might also shift the positions of peaks A and B so that their separation would not correspond to the valence band splitting; (see below the discussion on exciton ionization energies). However, the observation that the $n = 2$ exciton states (see next paragraph) are separated by the same amount as the $n = 1$ states indicates that this effect is probably not large.

The peaks A', B' and C' seen in reflection correspond to excited exciton states, presumably the $n = 2$ quantum states. ELLIOTT's theory[5] indicates that these states should have $\frac{1}{2}^3 = \frac{1}{8}$ the strength of the $n = 1$ transitions. Table 1 shows that this is not the case, the strength of C' being a factor of 2 above the theoretical value. However, the situation for the $n = 2$ states is complicated by two factors:

(a) There may be mixing of the $2S$ and $2P$ states (which may not have identical energies), and although this should not alter the total strength, it may account for the multiple structure seen in A' and B'.

(b) Peak C' falls in the ionization continuum of excitons A and B. Consequently C' may autoionize very rapidly and so suffer from lifetime broadening. This effect probably accounts for the great width of peak C in CdS.[8]

It is clear that the lack of quantitative agreement with ELLIOTT's theory indicates that the simple exciton model is not quantitatively applicable to ZnO. This is not surprising since many complications such as effective mass anisotropy have been ignored.

It will be assumed that the peak values of the imaginary part of the dielectric constant in the vicinity of A', B' and C' mark the $n = 2$ energies. These energies are given in Table 1. The energy differences between the $n = 1$ and $n = 2$ states are practically the same for all three excitons, having a value of $0{\cdot}0445 \pm 0{\cdot}001$ eV. If it is assumed that the excitons have a hydrogen-like set of energy levels:

$$E_n = E_{\text{Gap}} - \frac{E_I}{n^2}$$

where n is the main quantum number; then the exciton ionization energy is

$$E_I = \frac{4}{3} \times 0{\cdot}045 = 0{\cdot}059 \text{ eV}.$$

It is interesting to notice that no discontinuity in the reflection can be detected at or near the energy at which the ionization continuum is expected, as is shown in Figs. 7 and 8. Although the total strength of the band-to-band optical transitions is much higher than the exciton transitions, because the band-to-band transitions are spread over a wide range of energy the corresponding absorption coefficient is comparatively small and the reflectance is not sharply affected by the onset of the continuum. E_I can be expressed in terms of the

dielectric constant ϵ and the reduced exciton mass μM_0

$$E_I = \frac{e^4 \mu M_0}{2\hbar^2 \epsilon^2} = 13{\cdot}6 \frac{\mu}{\epsilon^2} \text{ eV}$$

where M_0 is the free electron mass. We use the low frequency dielectric constant 8·5[4] (which is assumed to be isotropic), since the exciton ionization energy is less than the longitudinal optical phonon energy, 0·073 eV.[13] The reduced exciton mass is thus found to be:

$$\mu = 0{\cdot}31 M_0.$$

VOL. 15 1960

Since all the excitons have the same ionization energy it is likely that the electron mass is considerably less than the hole mass, and so dominates the reduced mass expression.

The exciton Bohr radius is given by

$$a = \frac{\hbar^2 \epsilon}{\mu M_0 e^2} n^2 = 5{\cdot}3 \times 10^{-9} \frac{\epsilon}{\mu} n^2.$$

In the present case for the $n = 1$ orbit,

$$a = 14 \text{ Å}.$$

Because the excitons in ZnO are not very large there is probably a central cell correction so that the values of E_I and μ just quoted will be too large. The assumption has been made, doubtless incorrectly, that the bands are spherical. It should also be pointed out that the electron mass appropriate for these calculations is the mass at $\mathbf{k} = 0$, which may well not be the mass derived from measurements of the properties of conduction electrons in ZnO, since these electrons may be at a different minimum in the conduction band. (Collins and Kleinman[13] from infrared reflectance measurements have found an electron effective mass of 0·06 M_0. See also Hutson[15].)

The Kramers–Kronig analysis shows that the absorption remains quite high between the $n = 1$ and $n = 2$ lines, and this result is confirmed by the direct transmission measurements on very thin crystals. Hopfield[14] has attributed this absorption to indirect processes involving scattering by phonons or impurity centers.

It may be noted that whereas the lowest energy exciton occurs for $E \perp c$, Mollwo's[7] measurements show that in the visible spectral region the refractive index is greater for $E \| c$ than for $E \perp c$. As a consequence of this the reflectivity curves cross near the exciton region.

Finally, weak peaks are seen in the reflection curves at 4·2°K near 3·5 eV for $E \perp c$ and near 3·54 eV for $E \| c$ as shown in Figs. 5 and 6. For $E \perp c$ the peak is split by approximately the same amount as the separation between peaks A and B. For both modes of polarization the weak peaks lie about 0·115 eV above the corresponding $n = 1$ exciton states. The origin of these weak peaks is not known although it may be speculated that they arise from excitons connected with a second conduction band.

Absorption

Figure 12 shows the absorption spectrum at 4·2°K for various crystals. The reflection results just described show that nearly all the structure that can be seen lies at lower energies than exciton A.

There are, however, at least four "intrinsic" lines occurring for $E \| c$ which are labeled A_m, A_L, B_F and B_L. Line A_m shows that exciton A is weakly mixed with exciton C as discussed above. Comparison of the absorption and reflection data indicate that the position of the reflection oscillator lies roughly 0·0008 eV above that of line A_m. This splitting may arise from several sources, one of which is the possibility of mixing of lines A and B. However, uncertainties associated with reflection and its analysis make such a conclusion tentative. Line B_F is much weaker than A_m. It falls approximately 0·001 eV below the derived position of oscillator B. Since excitons A and C are mixed, group theory shows that B should only occur for $E \perp c$. However, this is only true for vertical transitions. Since a photon has finite momentum the transition will not be precisely vertical so that the selection rules break down and the transition occurs very weakly. Such transitions may be called forbidden. If this is the origin of B_F the line should be identical in position with the reflection oscillator, but again the observed difference may be accounted for by uncertainties in the analysis of the reflection data. The lines A_L and B_L are longitudinal excitons derived from excitons A and B, respectively, and have been described elsewhere.[10]

For $E \perp c$ a set of fairly strong lines can be seen between the position of peak A and 3·355 eV.

These lines vary from one crystal to another in strength and position, although it must be added that the variations are not large. These lines are thought to arise from exciton transitions taking place in the vicinity of a crystal imperfection producing immobile "impurity" excitons. The influence of the imperfections apparently is to lower the energy of formation of the excitons by amounts up to 40 per cent of the exciton ionization energy. In thicker crystals with $E\|c$ Fig. 12 shows that a set of lines can be seen in the same energy region. These lines are much weaker than those for $E\perp c$ and it seems likely that they are forbidden transitions corresponding to the $E\perp c$ transitions. They seem to be more numerous than the $E\perp c$ lines presumably because transitions are also occurring which are forbidden for $E\perp c$. The states in this energy region appear to be responsible for the emission lines seen polarized with $E\perp c$. Emission lines have been observed in thin crystals at the same energies as absorption lines, and the coincidence of emission lines in crystal $H2$ with absorption lines for $E\|c$ supports the suggestion that the latter correspond to much stronger lines for $E\perp c$. These impurity states favor the radiative decay of excitons since they provide coupling to the lattice.[8]

For $E\perp c$ lines have also been seen between 3·32 and 3·35 eV which are weaker than the lines at higher energies. These presumably are also impurity excitons although their small strength suggests that they may have a different origin from those seen at higher energies.

The Zeeman effect

Arguing from grounds of plausibility, since the excitons in ZnO have *s*-like spatial character, no Zeeman effects will arise from exciton orbital angular momentum and so it is not possible from these measurements to gain direct information concerning the difference of the effective masses of the hole and electron. (The *p*-like hole does, of course, have an orbital moment which is, however, "fine grained".) The splitting of the line A_m when $H\|c$ arises from the mixing of the Γ_1 and Γ_2 states of exciton A.[11] Γ_1 corresponds to the line A_m seen in zero field, while the Γ_2 transition is forbidden in zero field. The symmetry of the effect indicates that the mixing is complete, hence:

$$\left(\frac{\mu H}{\Delta E}\right)^2 > 1$$

where μ is the sum of the magnetic moments of the hole and electron, H is the magnetic field (32,000 G) and ΔE is the energy difference between the Γ_1 and Γ_2 states. From the splitting of 0·0007 eV, μ is calculated to be 4 Bohr magnetons, and it is apparent that ΔE is much less than 0·0007 eV. Since μ is the sum of the magnetic moments of the hole and the electron it is not at present possible to derive individual magnetic moments. The longitudinal line A_L is not split by the magnetic field since it is removed from all other levels with which it might mix by the longitudinal–transverse energy difference of 0·0016 eV. This is sufficiently large compared to μH to prevent the occurrence of any observable effects.

Acknowledgements—Thanks are due to E. A. SADOWSKI for much competent experimental assistance. The author also wishes to acknowledge many very informative discussions with J. J. HOPFIELD.

REFERENCES

1. COLLINS R. J. and THOMAS D. G., *Phys. Rev.* **112,** 388, (1958);
   HEILAND G., *J. Phys. Chem. Solids* **6,** 155 (1958).
2. SCHAROWSKY E., *Z. Phys.* **135,** 318 (1953).
3. MOLLWO E., *Reichsber. Phys.* **1,** 1 (1944).
4. HUTSON A. R., *Phys. Rev.* **108,** 222 (1957).
5. ELLIOTT R. J., *Phys. Rev.* **108,** 1384 (1957).
6. JAHODA F. C., *Phys. Rev.* **107,** 1261 (1957).
7. MOLLWO E., *Z. angew. Phys.* **6,** 257 (1954).
8. THOMAS D. G. and HOPFIELD J. J., *Phys. Rev.* **116,** 573 (1959).
9. DUTTON D., *Phys. Rev.* **112,** 785 (1958).
10. HOPFIELD J. J. and THOMAS D. G., *J. Phys. Chem. Solids,* **12,** 276 (1960).
11. HOPFIELD J. J., following article.
12. BIRMAN J. L., *Phys. Rev. Letters* **2,** 157 (1959).
13. COLLINS R. J. and KLEINMAN D. A., *J. Phys. Chem. Solids,* **11,** 190 (1959).
14. HOPFIELD J. J., unpublished.
15. HUTSON A. R., *J. Phys. Chem. Solids* **8,** 467 (1959).

J. Phys. Chem. Solids Pergamon Press 1960. Vol. 15. pp. 97–107. Printed in Great Britain.

FINE STRUCTURE IN THE OPTICAL ABSORPTION EDGE OF ANISOTROPIC CRYSTALS

J. J. HOPFIELD

Bell Telephone Laboratories, Murray Hill, New Jersey

(*Received* 27 *October* 1959)

VOL. 15 1960

Abstract—The group theory of weakly bound direct excitons is developed without explicit use of effective mass theory. For the usual case in which the direct band gap occurs at a point of high symmetry, direct exciton wave functions can be expanded in one-electron wave functions which have the symmetry of this point. The expansion is the k-space analogue to the expansion of a tightly bound exciton envelope wave function in real space. A quasi-cubic model of the valence band structure for hexagonal ZnO, CdS and ZnS is developed. The model, in conjunction with the group theory of weakly bound excitons, explains on a semi-quantitative basis most of the observed exciton fine structure in ZnO and CdS. A theorem which aids in constructing higher order "Kubic Harmonics" (for any point group) is given in an appendix.

I. INTRODUCTION

It has long been recognized that optical experiments near the fundamental absorption edge can be a useful tool for studying energy band parameters in semiconductors and insulating crystals. Little use has been made of this tool in anisotropic crystals; indeed, very few detailed measurements of the optical properties near the fundamental absorption edge of anisotropic crystals have been made until recently.

Dresselhaus[1] has pointed out that the shape of the fundamental absorption edge in polarized light can yield information about band symmetries in anisotropic crystals. From an experimental point of view, it has proved difficult to obtain information from the shape of the absorption edges in CdS and ZnO, two anisotropic crystals on which detailed optical measurements have recently been made. In these crystals the shape of the "fundamental absorption edge" is a function of surface treatment.[2] Furthermore, the shape of the absorption edge does not always agree with existing theory.[3] In CdS and ZnO, however, line structure which can be associated with direct (vertical) transitions is present in the absorption (or reflection) edge spectrum.[4,5] The primary purpose of this paper is to lay the groundwork for analysis of the information available from the exciton spectrum in anisotropic crystals, with particular emphasis on the wurtzite structure. The anisotropic semiconductors of greatest current interest are the II–VI compounds having this structure. We seek to understand as much of the exciton level structure as possible from a symmetry point of view without actually computing exciton binding energies (far too little data is yet available to make detailed mass estimates).

A brief review of direct exciton wave functions is given in Section II. In Section III, the group theory of exciton fine structure is developed. The formal theory of fine structure can be applied to all direct excitons, but has real usefulness only for relatively weakly bound excitons.

The theory of Section III is applied to the wurtzite structure in Section V to determine the exciton fine-structure. It is shown that the observed exciton fine-structure and Zeeman effects are in agreement with the assumed valence and conduction band structure. A quasi-cubic model of the wurtzite energy bands is developed in Section IV to aid in correlating observed exciton oscillator strengths with the observed exciton energies, and by this means to deduce band-structure information from the observed exciton energies.

II. SELECTION RULES AND EXCITON WAVE FUNCTIONS

Direct excitons (i.e. those excitons having a wave vector near $\boldsymbol{k} = 0$) can be grouped into two principal classes, according to the behavior of their optical matrix elements. If the matrix element of the operator

$$\boldsymbol{p}_{\boldsymbol{k}} = \sum_{\substack{n \\ \text{electrons}}} \exp(i\boldsymbol{k} \cdot \boldsymbol{r}_n)\boldsymbol{p}_n$$

between the crystal ground state and the exciton state $\boldsymbol{k}$ is finite for $\boldsymbol{k} \to 0$, the excitons will be called "allowed". If the matrix element of $\boldsymbol{p}_{\boldsymbol{k}}$ goes to zero for $\boldsymbol{k} \to 0$, the excitons will be called "forbidden". The allowed exciton transitions are the solid-state analogue of atomic dipole transitions; the forbidden exciton transitions are the analogue of atomic quadrupole and higher order transitions. For wavelengths in the optical region, forbidden transitions should have oscillator strengths about 10^{-4}–10^{-5} times the oscillator strengths of allowed transitions. Forbidden transitions have been observed, but only after the fact. After the exciton level structure is known from the energies and strengths of allowed transitions, it has sometimes been possible to ascribe other weak lines in the spectrum to forbidden transitions. Because these forbidden transitions always occur in conjunction with the much more easily observed allowed excitons and can usually be separated from allowed excitons on the basis of oscillator strength, we will neglect the forbidden transitions and work in the limit $\boldsymbol{k} \to 0$.

In order to discuss the details of exciton binding, it is necessary to make an assumption about the most important factors in exciton binding. For one extreme, the tight-binding case, the electron and hole kinetic energy is negligible, and the potential energy of electron–hole interaction is the dominant term in the Hamiltonian. In this case, the Wannier functions are logical basis functions, for they allow maximum localization of the electron and hole, and thus permit fullest utilization of the potential energy for binding. DEXTER, OVERHAUSER and KNOX and INCHAUSPE[6] have recently investigated the theory of such models for the alkali halides. It is perhaps simplest to discuss the extension of the transfer model used by OVERHAUSER. OVERHAUSER's treatment is oversimplified in that he forced the electron and hole to be on nearest-neighbor atoms. His treatment could be extended to include the possibility of larger electron–hole separations but would rapidly become unwieldy. The reason for the difficulty is that one would be attempting to characterize a state having a large radius in real space (large compared to a lattice constant) by the symmetries of the n^{th} neighbor lattice points in real space. On the other hand, this large radius in real space implies a small radius in $\boldsymbol{k}$-space. This small radius indicates that in some sense it should be easier to characterize the exciton by the symmetries of the bands from which it is made, rather than the symmetries of the n^{th} neighbor Wannier functions.

In the other extreme (weak binding) the exciton binding can be considered to be dominated by the electron and hole "kinetic energies". The logical basis functions are the Bloch functions, which minimize this kinetic energy. In this case, states extending a finite distance in $\boldsymbol{k}$-space must be used to represent a bound state. If the extent of the wave functions in $\boldsymbol{k}$-space is not too large, the binding can be treated in the effective mass approximation.[7] It seems desirable, however, to treat the group theory of the problem without explicit use of the effective mass formalism in order to more easily investigate selection rules, polarization effects and energy splittings in the presence of complex band structures. (The effective mass approximation often has excess degeneracies not required by group theory.)

In Section III we construct a theory of exciton fine structure for weakly bound excitons. The theory is the analogue of the tight binding theory, with Bloch functions rather than Wannier functions as basis functions.

III. GROUP THEORY OF EXCITON FINE STRUCTURE FOR WEAKLY BOUND EXCITONS

The wave function for an exciton can most easily be written in terms of an exciton creation operator ψ_{exciton}. Let $\boldsymbol{\psi}^*_{c\boldsymbol{k}}$ be the operator which creates an electron in the Bloch state $|c\boldsymbol{k}>$ (previously unoccupied) and $\boldsymbol{\psi}_{v\boldsymbol{k}}$ be the operator which annihilates an electron in the Bloch state $|v\boldsymbol{k}>$ (previously occupied). The operator

$$\psi_{\text{exciton}} = \sum_{\boldsymbol{k},\, v,c} f_{cv}(\boldsymbol{k})\boldsymbol{\psi}^*_{c\boldsymbol{k}}\boldsymbol{\psi}_{v\boldsymbol{k}} \qquad (1)$$

acting on the crystal ground state ψ_G creates an

VOL. 15 1960

exciton having wave vector zero. The $f_{cv}(\boldsymbol{k})$ are expansion coefficients. It is implicitly assumed that the effects of "vacuum polarization" (the virtual excitation of electron–hole pairs by the exciton) can be adequately included as a modification of the electron–hole interaction. In the usual case, only one conduction band and one valence band contribute appreciably to the sum in relation (1).

Equation (1) can be conveniently interpreted as an exciton wave function. If the operators ψ^*_{ck} and ψ_{vk} are replaced by the Bloch wave functions $\psi_{ck}(\boldsymbol{r}_e)$ and $\psi^*_{vk}(\boldsymbol{r}_h)$ respectively, equation (1) defines an exciton wave function $\psi_{\text{exciton}}(\boldsymbol{r}_e, \boldsymbol{r}_h)$ in ordinary (nonoperator) form. This form of the exciton wave function is useful because it explicitly displays the two particle nature of the wave function. With this definition of the exciton wave function, matrix elements of the total momentum operator $\boldsymbol{P}$ (the matrix elements for optical transitions) between the crystal ground state and a one exciton state are given by

$$\langle \psi_G | \boldsymbol{P} | \psi_{\text{exciton}} \rangle = \\ = \sum_{c,v,\boldsymbol{k}} f_{cv}(\boldsymbol{k}) \int \psi^*_{vk}(\boldsymbol{r}) \frac{\hbar}{i} \nabla \psi_{ck}(\boldsymbol{r})\, d^3\boldsymbol{r}.$$

It would be desirable to be able to characterize weak binding excitons by the symmetry of the electron and hole bands from which the exciton is made and the symmetry of the electron–hole orbit. There are two primary difficulties in attempting this. First, only the total symmetry of the exciton state, not the symmetries of the electron or hole components alone, is a good quantum number. (The analogous difficulty arises in the states of many electron atoms where, for example, the total angular momentum is a good quantum number but the angular momentum of a particular electron is only an approximate quantum number.) Secondly, the important terms in the sum over $\boldsymbol{k}$ in equation (1) come from a region in $\boldsymbol{k}$-space and the wave function symmetry at a general point in $\boldsymbol{k}$-space is extremely low.

The first difficulty is inevitable, and will be shown to lead to configuration mixing. The second difficulty can be overcome by choosing expansion functions which have the symmetries of a point in $\boldsymbol{k}$-space of high symmetry. The direct band gap in most substances lies at a point in $\boldsymbol{k}$-space of high symmetry, where both conduction and valence bands exhibit extrema. (That the presence of spin-orbit coupling can move the extrema a small distance away from the point of high symmetry is unimportant.) In those few crystals in which direct excitons are observed and the band structure is known,* the symmetry point of interest is the $\boldsymbol{k} = 0$ symmetry point Γ. We shall therefore assume that the electron and hole valleys are near $\boldsymbol{k} = 0$. (The treatment we are about to perform could also be done at other symmetry points, but with algebraic complications resulting in the case of several equivalent valleys due to the necessity of performing a multicenter expansion of the wave functions.) Indirect excitons are not considered.

Let the irreducible representations of the group of the wave vector zero be denoted by $\{\Gamma_i\}$. The ground state of the entire crystal (if, as in ZnO and CdS, there is no spin degeneracy), is the identity representation denoted by Γ_1. The state of the entire crystal with one $\boldsymbol{k} = 0$ exciton present will belong to one of the irreducible representations $\{\Gamma_i\}$. The wave functions of single electrons or holes in the crystal belong to representations of the *double* group; the exciton states representing an electron–hole pair belong to irreducible representations of the *single* group.

Unfortunately even this simplest of group theoretic statements is not exactly true. For those excitons for which the dipole matrix element between the crystal ground state and the exciton state vanishes, the above paragraph is correct. For those excitons for which this dipole matrix element is nonzero, long range coulomb effects produce energy differences between longitudinal and transverse excitons.[8,9] This energy difference can be calculated from classical dielectric theory if the exciton oscillator strength and the dielectric constant due to all other causes at frequencies near the exciton frequency are known.[9] This long range effect can break up "group theoretic degeneracies" even along principal axes of a crystal. For an exciton wave vector $\boldsymbol{k}$ (infinitesimal) along principal directions there is no mixing of different irreducible representations by this long range coulomb interaction. The relation of the optical effects of excitons and group theory in uniaxial crystals can thus be established in the following order. First, investigate the group theory of the exciton band

* Germanium is perhaps the best example.

structure neglecting the long range coulomb effects. Secondly, insert the coulomb effects and calculate the energy shifts by perturbation theory, noting that the exciton symmetry remains unaltered. Finally, the optical properties for light traveling in a general direction in the crystal can be computed from the optical properties along principal directions. Group theory enters only the first step, where the effects of the long range coulomb interactions are neglected.

We attack the main part of the problem by expanding the Bloch functions in the wave function (1) in terms of the wave functions of effective mass theory.[10] If

$$\Psi_{nk} = u_{nk} \exp(i\boldsymbol{k} \cdot \boldsymbol{r}),$$

then

$$\Psi_{vk} = \sum_n g_{nk} u_{nk} \exp(i\boldsymbol{k} \cdot \boldsymbol{r}). \tag{2}$$

In an expansion around $\boldsymbol{k} = 0$, $g_{vk} = 1 + 0(k)$, and g_{nk} for $v \neq n$ is $0(k)$. If equation (2) and its equivalent for the valence band are inserted in equation (1), a simple expansion of relation (1) in terms of wave functions at $\boldsymbol{k} = 0$ results. An individual term referring to two specific bands in the exciton wave function would then have the form

$$h_{nn',\boldsymbol{k}} \exp(i\boldsymbol{k} \cdot \boldsymbol{r}_e) \exp(-i\boldsymbol{k} \cdot \boldsymbol{r}_h) u_{on,i}(r_e) u^*_{on',i'}(r_h) \tag{3}$$

The functions $\{u_{on}\}$ for fixed n (there may be several such functions i if band n is degenerate at $\boldsymbol{k} = 0$) transform among themselves under the symmetry operations of the crystal. If the exciton state is to belong to irreducible representation Γ_t, each term like expression (3) when summed over $\boldsymbol{k}$ occurring in the expansion must also belong to Γ_t.

So far no use has been made of the restriction to weakly bound excitons formed from bands at $\boldsymbol{k} = 0$. We shall now proceed to expand around $\boldsymbol{k} = 0$. The symmetry operations applied to terms such as (3) generate for a given $\boldsymbol{k}$, $N_k D_n D_{n'}$ wave functions which transform among themselves, where D_n and $D_{n'}$ are the degeneracies at $\boldsymbol{k} = 0$ of bands n and n', and N_k is the number of wave vectors in the "star of $\boldsymbol{k}$".

"Crystal Harmonics" analogous to "Kubic Harmonics"[11] can, of course, be defined for any lattice. Different "Crystal Harmonics" can be characterized physically as having different structures of angular and radial nodes. The weak binding exciton can also be regarded as having angular and radial nodes in its envelope wave function. It seems desirable then to sum certain terms of the form of expression (3) to obtain terms characterized by an angular dependence. The terms of (3) should then be re-expressed as

$$\sum_{\boldsymbol{k},m} L_{m,l,j''}(\boldsymbol{k}) \exp(i\boldsymbol{k} \cdot \boldsymbol{r}_e) \times \times \exp(-i\boldsymbol{k} \cdot \boldsymbol{r}_h) u_{onj}(r_e) u^*_{on'j'}(r_h) \tag{4}$$

where $L_{m,l,j''}(\boldsymbol{k})$ is a "Crystal Harmonic" belonging to irreducible representation m, and j and j' are degeneracy indices. The index l is the order of the harmonic. (There is a problem concerning counting the number of states which is treated in the appendix. The transformation between the functions (3) and (4) is not unitary. The terms in (4) contain the terms (3) in a redundant fashion.) $L_{m,l,j''}(\boldsymbol{k})$ belongs to an irreducible representation Γ_m of the single group. The subscript j'' is needed in the event that Γ_m is more than one dimensional. Let Γ_n and $\Gamma_{n'}$ be the irreducible representations corresponding to bands n and n' at $\boldsymbol{k} = 0$. It is now easy to show that the set of $D_m D_n D_{n'}$ wave functions described by expression (4) belong to the irreducible representations described by the product representation $\Gamma_m \times \Gamma_n \times \Gamma_{n'}$.

This relation is the dual of the tight binding case. For the tight binding case, Γ_n and $\Gamma_{n'}$ for the bands at $\boldsymbol{k} = 0$ will be replaced by the irreducible representation of the Wannier functions in bands n and n' (which also belong to Γ_n and $\Gamma_{n'}$), and Γ_m will be replaced by an irreducible representation of the nearest neighbor symmetry.

There are essentially two different kinds of mixing which can go on to destroy m as a good quantum number. First, even within the effective mass theory, it is necessary to include mixing with other bands in order to obtain the effective mass.[10] This perturbation gives rise to a mixing in of other bands in an amount which is of the order of the effective mass "kinetic energy" of the electron and hole divided by a typical interband energy (e.g. the direct band gap). This mixing is small, and of primary importance in selection rules only when the $\boldsymbol{k} = \boldsymbol{0} \rightarrow \boldsymbol{k} = \boldsymbol{0}$ optical matrix element is small or zero for the bands from which the exciton

VOL. 15 1960

is chiefly made.* The second kind of mixing which destroys m as a quantum number is due to degenerate energy bands. This kind of behavior also occurs in acceptor-state wave functions in germanium, where the "orbital" part of the acceptor wave function contains both S and D terms even in the effective mass approximation.[12]

We are not going to make use of the full formalism for ZnO. Too little is known about the band parameters to enable one to make energy level calculations. It will be shown, however, that rather simple symmetry arguments based on the general ideas of this section will be sufficient to make rather detailed predictions about degeneracies and splittings in the ZnO exciton level structure.

IV. A QUASI-CUBIC MODEL OF THE $k = 0$ BAND STRUCTURE FOR THE WURTZITE LATTICE

Consider a cubic crystal having P-like valence bands and an S-like conduction band at $\boldsymbol{k} = 0$. Denote the orbitals for the six degenerate valence bands by $(P_x, P_y, P_z) \times (\alpha, \beta)$ where α and β are the spin-wave functions for spin parallel to z and spin antiparallel to z. The zero of energy for the system is taken as the valence band at $\boldsymbol{k} = 0$. The band gap will be denoted by E_g.

If a small amount of spin–orbit coupling is now turned on (such that the spin–orbit energy δ is small compared to E_g), the only matrix elements of importance will be those which mix the P-bands. The S-states will still be doubly degenerate ($S\alpha$ and $S\beta$); the P-states will now have a Hamiltonian matrix which can be written

$$H = \begin{array}{c|cccccc|c} & \frac{\delta}{3} & i\frac{\delta}{3} & -\frac{\delta}{3} & 0 & 0 & 0 & P_x\alpha \\ & -i\frac{\delta}{3} & \frac{\delta}{3} & -i\frac{\delta}{3} & 0 & 0 & 0 & P_y\alpha \\ & -\frac{\delta}{3} & i\frac{\delta}{3} & \frac{\delta}{3}+\Delta & 0 & 0 & 0 & P_z\beta \\ & 0 & 0 & 0 & \frac{\delta}{3} & -i\frac{\delta}{3} & \frac{\delta}{3} & P_x\beta \\ & 0 & 0 & 0 & i\frac{\delta}{3} & \frac{\delta}{3} & i\frac{\delta}{3} & P_y\beta \\ & 0 & 0 & 0 & \frac{\delta}{3} & -i\frac{\delta}{3} & \frac{\delta}{3}+\Delta & P_z\alpha \end{array} \qquad (5)$$

For the present, Δ should be set equal to zero. This form can be obtained by transforming from the $P_{3/2}$, $P_{1/2}$ representation where $H_{\text{spin-orbit}}$ is diagonal and the eigenvalues are respectively 0 and δ. If a small strain is applied to the crystal (the strain energy $\Delta \ll E_g$) in the z-direction, all states are unaffected in lowest order. In second order, however,

* ELLIOTT[3] has classified the direct excitons as "allowed" if this matrix element exists and "forbidden" if the matrix element vanishes. We have defined the terms somewhat differently, reserving the term "forbidden" for those excitons (not considered by ELLIOTT) which do not interact with light of infinite wavelength. In ZnO, the weak spin–orbit coupling results in excitons which are so weakly "allowed" (in the Elliott notation) that they are considerably weaker than "forbidden" lines would be in the same material. There are in addition exciton-states for which ELLIOTT's equations (3.6) (optical matrix element for "allowed" processes) and (3.14) (optical matrix element for "forbidden" excitons) contribute comparable amounts to the oscillator strength of a single exciton. Such an exciton cannot really be considered either "allowed" or "forbidden" in ELLIOTT's notation. For these reasons we have abandoned his use of these terms. The qualitative distinction made by ELLIOTT (caused from the present point of view by band mixing) is nevertheless of use in estimating the strengths of many exciton lines.

[*continued in next column*

the state P_z suffers an energy shift different from that undergone by the equivalent states P_x and P_y. Let this difference in energy shifts be denoted by Δ. If Δ is much less than E_g, we may neglect the wave function admixtures between the P-bands and other bands (percentage admixtures of order $(\Delta/E_g)^2$ and simply add the term Δ to the energies of the P_z states. The total Hamiltonian matrix then becomes that of equation (5). The basis functions are still, to lowest order, the P-basis functions. It is important to note that there will be errors only of order Δ/E_g and δ/E_g in the optical matrix elements between the P-band and the S-like conduction band, and that the crystal Hamiltonian has the symmetry of a uniaxial crystal. The eigenstates of equation (5) are:

States	Energy E
$[2]^{-1/2}\begin{vmatrix}(P_x+iP_y)\alpha\\(P_x-iP_y)\beta\end{vmatrix}$	$E_1 = 0$
$\left[2+\left(2-\frac{3E}{\delta}\right)^2\right]^{-1/2}\begin{vmatrix}(P_x-iP_y)\alpha+\left(2-\frac{3E}{\delta}\right)P_z\beta\\(P_x+iP_y)\beta-\left(2-\frac{3E}{\delta}\right)P_z\alpha\end{vmatrix}$	$E_2 = \frac{\delta+\Delta}{2}+\sqrt{\left[\left(\frac{\delta+\Delta}{2}\right)^2-\frac{2}{3}\delta\Delta\right]}$
Same form of states as on line above.	$E_3 = \frac{\delta+\Delta}{2}-\sqrt{\left[\left(\frac{\delta+\Delta}{2}\right)^2-\frac{2}{3}\delta\Delta\right]}$

(6)

If the crystal has been squashed far enough along the z-axis, it is possible that the optical matrix elements between P_x and S will not be quite the same as the optical matrix elements between P_z and S.

Let the optical matrix element (for light polarized in the x-direction) between the conduction band and the P_x state be H. The matrix element (for light polarized parallel to the z-direction) between the conduction band P_z state will be written $(1+\epsilon)H$. (From previous arguments, ϵ is small.) This then provides a model of a slightly uniaxial crystal.

This model may represent a reasonable approximation to the actual band-structure in hexagonal (or cubic) ZnO, CdS and ZnS. (In cubic crystals, Δ is of course zero.) In cubic crystals, it can be shown that the error in the model is only of order (δ/E_g). In the wurtzite structure, each atom retains in a general way the tetrahedral nearest neighbor environment present in the cubic crystal. If, as it seems reasonable to assume, the holes are concentrated chiefly on the sulfur atoms, the fact that the third neighbors are in a hexagonal configuration should not influence appreciably the spin–orbit interaction; i.e., the spin–orbit interaction should remain roughly isotropic. The error in the quasi-cubic model spin–orbit interaction is then probably of order (Δ/E_g). (There are also errors of order (δ/E_g) which occur in cubic crystals.)

The effect of the deviation of the c/a ratio from ideal (the distortion of the nearest neighbor tetrahedra) is taken into effect in a general way by the parameters Δ and ϵ. The error which is most difficult to estimate arises from the fact that this zincblende structure has only one molecule per unit cell, while the wurtzite structure has two. Because the molecules in this wurtzite structure are crystallographically equivalent (but not translationally equivalent), it is possible to calculate wave functions for only one molecule to obtain band wave functions, if appropriate nonperiodic boundary conditions are used. The error made in the energies by distorting the boundary shape and boundary conditions on this cell to those appropriate to the zincblende is the chief error in the

VOL. 15 1960

model. Clearly if the tight binding approximation were a reasonable starting point for energy band calculations in ZnO, CdS or ZnS, the quasi-cubic model should also be a reasonable approximation.

It may be hoped that all errors do not add, and that the model represents a valid approximation to ZnO, CdS and ZnS. In the last analysis, the model stands or falls on the basis of its agreement with experiment.

In CdS, where the energy bands are separated by reasonable distances compared to the exciton binding energies (and thus optical matrix elements could be determined unambiguously), excellent agreement was found between the predictions of the model and experimental fact.[5] In brief review of Ref. (5), ϵ (poorly determined experimentally) was found to be about 1/7, a bit larger than expected but small compared to 1. The matrix element H was, of course, determined from experiment. The *three* parameters ϵ, H and (δ/Δ) give correctly—by using the optical matrix elements determined from the band wave functions (6)—all *five* optical matrix elements within experimental error. The determination of (δ/Δ) (which does not depend on the value of ϵ) could be made within about 10 per cent. The ratio E_2/E_3 can be computed directly from (δ/Δ) and was found to agree within experimental error with the measured value. One prediction that would be of interest to check is the valence band splitting in cubic CdS. This valence band splitting should be δ rather than E_2 or E_3.

The work of THOMAS[2] has shown that the quasi-cubic model succeeds only qualitatively in predicting the properties of ZnO. The parameter ϵ is zero within experimental accuracy. The chief failing is that the model predicts the existence of weak lines in the "wrong" mode of polarization having strengths about 1/50 of the strong lines, whereas the observed ratio is about 1/5000. There exists some difficulty in experimentally identifying the optical matrix elements referring to a given *band* (rather than to a given *exciton*) since the two highest valence bands are only split by about 1/10 of the exciton binding energy, and exciton and configuration mixing is inevitable. The interpretation given to the experimental results may therefore be in error. Alternatively, the model may simply not be accurate enough in powers of (δ/E_g) and Δ/E_g to expect to be able to calculate such small matrix elements with any degree of precision.

Perhaps the most important single piece of evidence relating to the inadequacy of the model is the fact that δ has the wrong sign (opposite to the usual free ion sign) in ZnO. This sign is a direct consequence of the experimental interpretation which paces the Γ_9 valence band *below* the Γ_7 valence band from which it is split only by spin–orbit coupling. There are many possible reasons for the "observation" of an inverted multiplet in the bands of ZnO. If the valence band actually represents an inverted multiplet (which in the atomic case, can arise only from configuration interactions between different spatial one-electron wave functions) it is likely that the model (which allows for no configuration interactions between wave functions of different one-electron bands) is not adequate.

The model could be made to agree with experiment by the *ad hoc* introduction of a nonisotropic spin–orbit interaction (and one additional parameter to characterize this additional interaction). This elaboration has not been added, for the model in its present crude form seems to fulfill its purpose of providing a semiquantitative basis for correlating the observed properties of the valence band.

V. APPLICATION TO ZnO

The point group of ZnO is C_{6v}^4. The symmetry operations, irreducible representations, and character table have recently been discussed by BIRMAN[13] and CASELLA[14]. A copy of BIRMAN's character table is included for reference in Table 1. There are believed to be three P-like valence bands at $\boldsymbol{k} = 0$, two belonging to Γ_7 and one belonging to Γ_9.[15] The existence of the three valence bands and the general character of the wave functions can be understood on the basis of the quasi-cubic model. The conduction band at $\boldsymbol{k} = 0$ is believed to be S-like, and also belongs to Γ_7.

For light traveling in a principal direction in the crystal, excitons belonging to Γ_5 are observable for light polarized perpendicular to the c-axis, and excitons belonging to Γ_1 are observable in light polarized parallel to the c-axis. All other exciton transitions are forbidden.

Experimental evidence[2] supports the assumption that the electron is lighter than the hole and

Table 1. *Character table for the double groups of the wave vector* **0** *in the wurtzite structure* (*after* BIRMAN).

	E	$\overline{E}$	$2C_2$	$2C_3$	$2\overline{C}_3$	$2C_6$	$2\overline{C}_6$	$6\sigma_d$	$6\sigma_v$
Γ_1	1	1	1	1	1	1	1	1	1
Γ_2	1	1	1	1	1	1	1	−1	−1
Γ_3	1	1	−1	1	1	−1	−1	1	−1
Γ_4	1	1	−1	1	1	−1	−1	−1	1
Γ_5	2	2	−2	−1	−1	1	1	0	0
Γ_6	2	2	2	−1	−1	−1	−1	0	0
Γ_7	2	−2	0	1	−1	$\sqrt{(3)}$	$-\sqrt{(3)}$	0	0
Γ_8	2	−2	0	1	−1	$\sqrt{(3)}$	$\sqrt{(3)}$	0	0
Γ_9	2	−2	0	−2	2	0	0	0	0

dominates the reduced mass. The off diagonal components of the effective mass tensor in this case arise only from spin–orbit interaction and can be regarded as small. The most likely estimate for the ground-state wave function would be that it is roughly hydrogenic, so that the spatial part of the wave function belongs to Γ_1 and is analogous to a 1 S-state in hydrogen. In the lowest approximation, applying the rules of Section III, there are three sets of four ground state excitons derived from the bands as shown in Table 2. Corresponding to these twelve states should be five optically observable lines, three observable for $E \perp c$ and two for $E \| c$. To lowest order, the strengths of these lines are proportional to the $\boldsymbol{k} = 0$ matrix elements for band-to-band transitions, and have been estimated by THOMAS[2] on the basis of the band model of Section IV. The lines listed as weak have oscillator strengths which vanish if the spin-orbit interaction is zero.

Table 2. *The ground-state excitons in* ZnO. *The rows represent the different valence bands*

Valence band	States analogous to the hydrogenic S-state	Oscillator strength
Γ_7	Γ_1 (weak)	f_1
	Γ_2	0
	Γ_5 (strong)	f_2
Γ_9	Γ_5 (strong)	f_3
	Γ_6	0
Γ_7	Γ_1 (strong)	f_4
	Γ_2	0
	Γ_5 (weak)	f_5

In the absence of electron–hole spin interactions (which arise chiefly from the exclusion principle) and long range coulomb effects, all the exciton states would be four-fold (accidentally) degenerate, corresponding to the four orientations of electron and hole spin. We have found by a rather general argument three sets of four states, each set of which is expected to have approximately the same energy. This must continue to be true (neglecting the above two interactions) in spite of the various configuration interactions which can occur.

For hydrogenic excitons, the spin–spin interaction is expected to be very small because of the relatively large exciton radius. Experimentally, the Γ_1 exciton belonging to the highest lying valence band has little oscillator strength, and should be little affected by the long-range Coulomb effects. The same statement should be true for the Γ_5 exciton belonging to the lowest valence band.

The two lowest energy Γ_5 excitons are separated in energy rather little compared to their experimental energy of binding, and have large oscillator strengths. The long-range coulomb interactions are then expected to mix and shift these two excitons.

The optical matrix elements are much more sensitive to band mixing, and therefore more difficult to estimate. On the basis of the model of Section IV, and neglecting configuration mixing, it is expected that $f_2 \approx f_3 \approx \frac{1}{2}f_4$. The mixing of excitons 2 and 3 can easily upset $f_2 \approx f_3$, but $f_2 + f_3 = f_4$ is still expected to be valid (and is true within experimental error). The difficulty in estimating f_1 was briefly considered in Section IV.

VOL. 15 1960

Table 3. *The low lying optically observable excited states of excitons in* ZnO. *The column heading gives the analogous hydrogenic state; the rows represent the different valence bands*

Valence band	$2P_{\pm1}$	$2S$	$2P_0$
Γ_7	$2\Gamma_5$(accidentally degenerate)(?) Γ_1(weak)	Γ_5(strong) Γ_1(weak)	Γ_5(?) Γ_1(weak)
Γ_9	Γ_5(?) Γ_1(weak)	Γ_5(strong)	Γ_5(?)
Γ_7	$2\Gamma_5$(accidentally degenerate) (weak) Γ_1(?)	Γ_5(weak) Γ_1(strong)	Γ_5(weak) Γ_1(?)

It is experimentally observed[2] that the lowest energy (weak) Γ_1 (nondegenerate from the point of view of group theory) line exhibits what appears to be a *linear* Zeeman effect for a magnetic field applied along the hexagonal axis. Such a magnetic field has symmetry Γ_2, and mixes Γ_1 only with Γ_2 (or other Γ_1 states) to all orders. The linear Zeeman effect is expected from the previous theoretical argument, for we have shown that the energy difference between the lowest Γ_1 and Γ_2 states arises only from the very weak spin–spin forces between electrons and holes.

The excited states observed in reflection are much more complicated. On the basis of a hydrogenic model the possible low lying excited states should be $2P_{\pm1}$, $2S$ and $2P_0$. The (approximate) spatial symmetries for the envelope functions will be respectively Γ_5, Γ_1 and Γ_1. The optically observable excitons which should arise from these configurations are given in Table 3. The lines classified as weak involve either the spin–orbit interaction (which is very small) or band mixing (as in Section III) or both to produce their oscillator strength, and will be unobservable in reflection. The lines for which the intensity is given by a question mark are weak for the same reasons, but can be easily mixed with the corresponding $2S$ (strong) states by deviations from the effective mass approximation and the nondiagonal part of the tensor mass. This mixing will certainly take place if the $2P_{\pm1}$ and $2S$ (or $2P_0$ and $2S$) states lie close together.

The observation of one strong line and one or two weak lines for each band is then easily understood on the basis of Section III. Since the effective mass approximation should be a fair approximation for these excited states, the experimental observations by THOMAS[2] of multiplet $n = 2$ levels indicates the presence of a small reduced mass anisotropy (the dielectric constant is very nearly isotropic) in ZnO at $\boldsymbol{k} = 0$. This anisotropy must be small, for the accidental $2S$–$2P$ degeneracy of the hydrogen atom is very nearly present in the excitons in ZnO.

VI. CONCLUSION

The group theory of weakly bound excitons was

developed in terms of the symmetries of electron and hole bands. Direct excitons belong to irreducible representations of the single group of the point Γ (whether or not the optical band gap occurs at Γ). The symmetries of weakly bound excitons can be found in two steps. On the basis of the effective mass approximation, the orbital symmetry which should correspond to a given energy level can be estimated. This orbital symmetry is not an exact quantum number. The exact exciton symmetries of excitons having approximately the effective mass energy can then be found by taking products of electron and hole symmetries with the orbital symmetry estimated in the effective mass approximation.

If sufficient further experiments can be performed on ZnO, it should be possible to completely determine the $\boldsymbol{k} = 0$ bands parameters from the optical absorption spectrum. The present work was performed because of the observed complexity of the exciton spectrum. Allowed excitons, forbidden excitons, longitudinal excitons and excited states of excitons have all been observed in ZnO. Both group theory and a band model seemed necessary to interpret the observed data. The combination of a simple band model with a knowledge of the symmetry properties and accidental degeneracies of weakly bound exciton states has produced a qualitative (and in some respects quantitative) understanding of the exciton level structure in ZnO and CdS. This understanding is necessary in order to make use of the exciton states as a tool for the energy band structure in ZnO and CdS.

Acknowledgements—The author would like to thank Dr. D. G. THOMAS for his constant stimulation, and for his willingness to try any experiment which might demonstrate (or disprove) a theoretical point. He would also like to thank the many others whom he has consulted on points of group theory and band structure.

APPENDIX

Let $Y_{lm}(\theta, \phi)$ be a spherical harmonic, and S a proper rotation of three-dimensional space. Then the function

$$f_{lm} = \sum_S Y_{lm}(S^{-1}\theta, \phi) \exp(i\boldsymbol{k}S\boldsymbol{r})$$

transforms under rotations like Y_{lm}. The sum is performed over all proper rotations S. The function f_{lm} is orthogonal to $f_{l'm'}$ for either $m \neq m'$ or $l \neq l'$.

Let $L_{m,l,i}(\boldsymbol{k})$ be a crystal harmonic, and S be a symmetry operation of the point group. The analogous theorem would be that the functions

$$f_{m,l,i} = \sum_S L_{m,l,i}(S^{-1}\boldsymbol{k})\psi_{\boldsymbol{k}}(S\boldsymbol{r}) \qquad \text{(A1)}$$

were also orthogonal as in the case of the continuous group. (If they were orthogonal, the transformation from the terms in equation (3) to those in equation (4) would be unitary.) This, however, can clearly not be true, since there are but a finite number of operations S and thus a finite number of equivalent functions $\psi_{\boldsymbol{k}}$, whereas there are an infinite number of functions $f_{m,l,i}$. For a general $\boldsymbol{k}$ there are exactly N possible independent functions $f_{m,l,i}$, where N is the order of the group. The symmetry of the possible functions $f_{m,l,i}$ can be deduced by noting that the set $\{\psi_{\boldsymbol{k}}(S\boldsymbol{r})\}$ is a basis for the regular representation. Thus if Γ_i is an M_i dimensional representation of the point group exactly M_i sets (of M_i functions each) of functions of equation (A.1) will belong to M_i. This is the basis of the counting difficulty in equation (4). Writing the sum over *all* crystal harmonics is redundant.

The following theorem can then be proved. Let Γ_i be an M_i dimensional representation of a point group. Let Γ_1 be the identity representation. For $i \neq 1$, there are exactly M_i sets (of M_i functions) of crystal harmonics which are independent. All other crystal harmonics belonging to Γ_i can be written as linear combinations of these M_i sets times crystal harmonic belonging to Γ_1.

As an example, the crystal harmonics for the wurtzite structure are given below. The simplest co-ordinate system to use is cylindrical co-ordinates r, z, ϕ. The normalization factors have been omitted.

$$\Gamma_1 f(r, z) \times [1,\ e^{6i\phi}+e^{-6i\phi},\ e^{12i\phi}+e^{-12i\phi},\ \ldots]$$

$$\Gamma_2 \quad \times [e^{6i\phi}-e^{-6i\phi},\ e^{12i\phi}-e^{-12i\phi},\ \ldots]$$

$$\Gamma_3 \quad \times [e^{3i\phi}+e^{-3i\phi},\ e^{9i\phi}+e^{-9i\phi},\ \ldots]$$

$$\Gamma_4 \quad \times [e^{3i\phi}-e^{-3i\phi},\ e^{9i\phi}-e^{-9i\phi},\ \ldots]$$

$$\Gamma_5 \quad \times \begin{bmatrix} e^{i\phi},\ e^{-5i\phi},\ e^{7i\phi},\ e^{-11i\phi},\ e^{13i\phi},\ \ldots \\ e^{-i\phi},\ e^{5i\phi},\ e^{-7i\phi},\ e^{11i\phi},\ e^{-13i\phi},\ \ldots \end{bmatrix}$$

$$\Gamma_6 \quad \times \begin{bmatrix} e^{2i\phi},\ e^{-4i\phi},\ e^{8i\phi},\ e^{-10i\phi},\ e^{14i\phi},\ \ldots \\ e^{-2i\phi},\ e^{4i\phi},\ e^{-8i\phi},\ e^{10i\phi},\ e^{-14i\phi},\ \ldots \end{bmatrix}$$

For illustration of the theorem, we see that $e^{5i\phi}$ and $e^{-5i\phi}$ cannot be made up of linear combinations of harmonics belonging to Γ_1 and $e^{i\phi}$ and $e^{-i\phi}$. On the other hand

$$e^{7i\phi} = e^{i\phi}[e^{6i\phi}+e^{-6i\phi}] - e^{-5i\phi}$$

The theorem can be used as an aid in constructing higher order crystal harmonics. Similarly, VON DER LAGE and BETHE's Kubic Harmonics[11] $(\gamma_6)_1$ and $(\gamma_6)_2$ can be written as linear combinations of $[(\gamma_4)_1$ and $(\gamma_2)_1]$ and $[(\gamma_4)_2$ and $(\gamma_2)_2]$, respectively.

Perhaps the simplest way to understand the redundancy of expression (4) is in analogy with the full rotation

group. For the full rotation group, a general function can be expanded

$$f(\mathbf{r}) = \sum_{l,m} g_{lm}(|\mathbf{r}|) Y_{lm}(\theta, \phi)$$

where $g_{lm}(|\mathbf{r}|)$ is a rotationally invariant function. The sum goes over all l and all m. For a finite group, one may write

$$f(\mathbf{r}) = \sum_{m\, l,i} g_{m,l,i}(\mathbf{r}) L_{m,l\,i}(\mathbf{r})$$

where $g_{m,l,i}(\mathbf{r})$ is a function which is invariant under the symmetry operations of the finite group, and $L_{m,l,i}(\mathbf{r})$ are crystal harmonics. If the group has order N, it is necessary to keep only N terms in the sum. If these N terms are properly chosen, all other possible terms will be redundant.

VOL. 15 1960

REFERENCES

1. DRESSELHAUS G., *Phys. Rev.* **105,** 135 (1957).
2. THOMAS D. G., preceding article.
3. ELLIOTT R. J., *Phys. Rev.* **108,** 1384 (1957); DEXTER D. L., *Nuovo Cim.* (*Suppl.*) **7,** 245 (1958).
4. DUTTON D., *Phys. Rev.* **112,** 785 (1958).
5. THOMAS D. G. and HOPFIELD J. J., *Phys. Rev.* **116,** 573 (1959).
6. DEXTER D. L., *Phys. Rev.* **83,** 435 (1951); **108,** 707 (1957); OVERHAUSER A. W., *Phys. Rev.* **101,** 1702 (1956); KNOX R. S. and INCHAUSPE N., to be published.
7. See, for example, DRESSELHAUS G., *J. Phys. Chem. Solids* **1,** 14 (1956).
8. HELLER W. R. and MARCUS A., *Phys. Rev.* **84,** 809 (1951).
9. HOPFIELD J. J. and THOMAS D. G., *J. Phys. Chem. Solids,* **12,** 276 (1960).
10. See, for example, LUTTINGER J. M. and KOHN W., *Phys. Rev.* **97,** 869 (1955).
11. VON DER LAGE F. C. and BETHE H. A., *Phys. Rev.* **71,** 612 (1947).
12. See, for example, KOHN W., *Solid State Physics* (Edited by SEITZ F. and TURNBULL D.) Vol. V, p. 300. Academic Press, New York (1957).
13. BIRMAN J. L., *Phys. Rev.* **114,** 1490 (1959).
14. CASELLA R. C., *Phys. Rev.* **114,** 1514 (1959).
15. BIRMAN J. R., *Phys. Rev. Letters* **2,** 157 (1959).

J. Phys. Chem. Solids Pergamon Press 1960. Vol. 15. pp. 108–111. Printed in Great Britain.

THE DIFFUSION OF OXYGEN IN SILICON AND GERMANIUM

C. HAAS

Philips Research Laboratories, N.V. Philips' Gloeilampenfabrieken, Eindhoven, Netherlands

(*Received* 29 *October* 1959)

Abstract—Using a simple model for the structure of oxygen in silicon and germanium crystals and making the assumption that internal friction and diffusion are both due to the same relaxation phenomenon, the diffusion coefficient of oxygen was calculated from experimental data on internal friction. The results are: $D = D_0 \exp -(U/kT)$; O in Si: $D_0 = 0{\cdot}21$ cm²/sec, $U = 2{\cdot}55$ eV; O in Ge: $D_0 = 0{\cdot}17$ cm²/sec, $U = 2{\cdot}02$ eV. The calculated values of D are in reasonable agreement with available experimental data.

1. INTRODUCTION

DURING recent years the study of the intricate properties of oxygen in silicon has attracted much attention; a recent paper[1] shows that oxygen in germanium exhibits similar complicated phenomena. In silicon and in germanium crystals which contain oxygen, it is possible to convert the dissolved oxygen atoms partly into oxygen complexes, which act as donors, by an appropriate heat treatment. The kinetics of the formation of these donors has been the subject of a paper by KAISER *et al.*[2] The transport of oxygen atoms by diffusion plays an important role in the processes occurring during heat treatment; little, however, is known about the diffusion of oxygen. Following the line of thought originally due to SNOEK[3], we shall try to calculate the diffusion coefficient of oxygen in silicon and germanium crystals from data on internal friction.

We shall assume that oxygen dissolved in a silicon crystal forms chemical bonds with two silicon atoms which originally were linked by a covalent bond. This structure was proposed by KAISER[4], and is in agreement with the infrared absorption spectrum.[5] Because the properties of oxygen in germanium are similar to those of oxygen in silicon, we assume that this model, as well as the following discussion, applies also to oxygen in germanium.

2. DIFFUSION

Diffusion of oxygen can take place by oxygen atoms jumping from one position to another. The process that requires the lowest activation energy is probably the jump from one Si–Si line to a neighbouring Si–Si line in such a way that only one Si–O bond is broken (Fig. 1a). The nonlinear Si–O–Si bridge will, because of the symmetry of the crystal, have six equivalent positions (Fig. 1b).

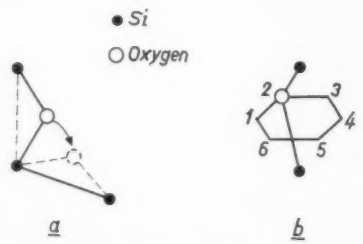

FIG. 1. (a) Jumping of oxygen atom to a neighbouring position:

——— chemical bonds before jump,
— — — chemical bonds after jump.

(b) Six equivalent positions of a Si–O–Si bridge; transitions 1 → 2 etc. are much faster than jumps in (a).

Because transitions between these six positions (rotation around the Si–Si line) do not involve the breaking of a chemical bond, they will probably require a small activation energy, and will be much faster than the jump from one Si–Si line to another.

The probability that an oxygen atom jumps in

dt sec to a definite neighbouring site is dt/τ, where τ is a relaxation time depending on temperature as follows: $\tau = \tau_0 \exp(U/kT)$. We assume the jumps to be completely uncorrelated; rapid rotation around the Si–Si line will help to realize this condition.

The diffusion coefficient of oxygen can now be expressed in terms of τ by: $D = \Delta^2/\tau$, where Δ is the distance over which the diffusing atoms jump. Owing to the rapid rotation around the Si–Si line, we may use the average oxygen position at the middle of the Si–Si line to calculate Δ. We find $\Delta = a(2/3)^{1/2}$, if a is the Si–Si distance in a silicon crystal. The expression for the diffusion coefficient of oxygen in silicon becomes:

$$D = 2a^2/3\tau = D_0 \exp(-U/kT) \text{ with } D_0 = 2a^2/3\tau_0 \qquad (1)$$

3. INTERNAL FRICTION

The process of jumping introduced to describe diffusion will lead to absorption of acoustical waves in the crystal.* In a crystal subjected to a stress along the $\langle 111 \rangle$ directions, the various positions of the oxygen atoms are no longer equivalent. Therefore transfers between these positions will give rise to a damping of mechanical vibrations. From the symmetry of the crystal, it is clear that this damping will occur for vibrations that set up a stress parallel to a $\langle 111 \rangle$ direction; it will be absent for vibrations with a stress parallel to $\langle 100 \rangle$, because in that case all oxygen positions remain equivalent.

If the number of oxygen atoms in a position of type i ($i = 1, 2, 3, 4$; see Fig. 2) is n_i, the change of n_i with time in an unstressed crystal is given by:

$$dn_i/dt = 1/\tau[-6n_i + 2 \sum_{j \neq i} n_j] \qquad (2)$$

The deformation of the crystal parallel to Z (Fig. 2) due to an oxygen atom in a position of type 2, 3 or 4 is one-third of the corresponding deformation due to an oxygen atom in a position of type 1. Therefore the quantity that determines the internal friction for a vibration with a stress parallel to $\langle 111 \rangle$ will be $y = n_1 - \frac{1}{3}(n_2 + n_3 + n_4)$. From equation (2) we find for the change of y with time:

$$dy/dt = -8y/\tau = -y/\tau^* \qquad (3)$$

* For the theory of internal friction due to impurities see POLDER[6].

We see that the relaxation time for internal friction τ^* is related to the relaxation time for diffusion τ by:

$$\tau^* = \tau/8 = (\tau_0/8) \exp(U/kT) \qquad (4$$

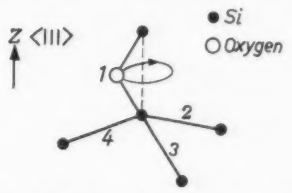

FIG. 2. Under the effect of a compression parallel to Z, the oxygen atom will prefer the positions 2, 3 or 4 to position 1.

The internal friction has a maximum value for $\omega\tau^* = 1$, where ω is the angular frequency of the acoustical wave. SOUTHGATE[7–9] has measured the damping of acoustical waves with a frequency of 100 kc/s as a function of temperature in silicon and germanium crystals. He found in both crystals a relaxation maximum which is probably due to the presence of oxygen. The peak occured at a rather high temperature (770°C for germanium, 1030°C for silicon), where the concentration of oxygen complexes is small. Therefore this peak must be due to isolated oxygen atoms.

The peak was found if the longitudinal mechanical vibration was parallel to a $\langle 111 \rangle$ direction; it was absent for a vibration parallel to $\langle 100 \rangle$. This anisotropy is just what we would expect on basis of the model discussed above.

From the position and the shape of the measured curve, it is possible to determine the relaxation time τ^* and its activation energy. From SOUTHGATE's data we find $\tau_0 = 1{\cdot}8 \times 10^{-15}$ sec and $U = 2{\cdot}55$ eV for oxygen in silicon.

For oxygen in germanium, the experimental data are not accurate enough to permit a reliable calculation of U. Because $1/\tau_0$ is related to the vibration frequency of the oxygen atoms, we use as an approximate value of τ_0 for oxygen in germanium,

$$\tau_0(\text{Ge}) = \tau_0(\text{Si}) \times (1110/856)$$

(the vibration frequencies of oxygen in germanium and silicon are respectively 856 and 1100 cm^{-1}[1,4]). From the position of the relaxation peak, as determined by SOUTHGATE, we find $\tau_0 = 2{\cdot}3 \times 10^{-15}$ sec and $U = 2{\cdot}02$ eV for oxygen in germanium.

From these values of U and τ_0, the diffusion coefficient of oxygen and its activation energy U are readily found: oxygen in silicon $D_0 = 0{\cdot}21$ cm^2/sec, $U = 2{\cdot}55$ eV; oxygen in germanium $D_0 = 0{\cdot}17$ cm^2/sec, $U = 2{\cdot}02$ eV.

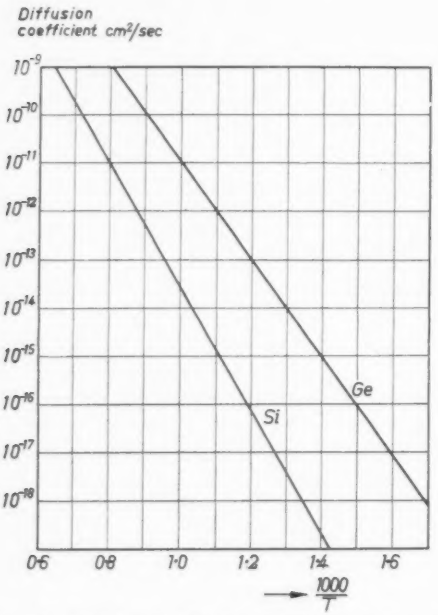

FIG. 3. Calculated diffusion coefficients of oxygen in germanium and in silicon crystals.

4. COMPARISON WITH EXPERIMENT

Experimental data on the diffusion of oxygen in silicon and germanium are very scarce. LOGAN and PETERS[10] made use of the formation of oxygen donors by heat treatment to determine the diffusion coefficient of oxygen in silicon at 1300°C. Oxygen was diffused into p-type silicon at 1300°C, and subsequently the crystal was heated a long time at 450°C to convert the oxygen atoms partly into the donor form. By measuring the thickness and conductivity of the n-layer formed, and by assuming the donor concentration to be proportional to the oxygen concentration, they found a value of $1{\cdot}8\times10^{-10}$ cm^2/sec for the diffusion coefficient of oxygen in silicon at 1300°C.

This result should be corrected, because recent measurements[2] indicate that the donor concentration after heat treatment at 450°C is proportional to the third power of the oxygen concentration. Application of this correction to the results of LOGAN and PETERS leads to a diffusion coefficient of oxygen in silicon of $1{\cdot}0\times10^{-9}$ cm^2/sec at 1300°C.

During experiments on the adsorption of gases on germanium crystal powder (particle diameter $\sim 60\mu$) in our laboratory,[11] it was found that the surface was free from oxygen after heating for ~ 1 hr at 800°C in high vacuum. The surface of germanium powder with an oxygen concentration of 10^{17} cm^{-3} in the bulk was not, however, oxygen free until heated in high vacuum at 800°C for ~ 30 hr. This difference must be due to diffusion of oxygen from the bulk to the surface. From these data we obtain a value of $\sim 10^{-11}$ cm^2/sec for the diffusion coefficient of oxygen in germanium at 800°C.

KAISER[2] used kinetic data on the formation of oxygen donors to estimate the diffusion coefficient of oxygen in silicon; he found $D = 3\times10^{-18}$ cm^2/sec at 450°C.

Finally, we compare these experimentally determined values with the values we calculate from the internal-friction data (see Table 1). The agreement is reasonable, especially if we take into account the inaccuracy of the experimental results, and in one case the long extrapolation of SOUTHGATE's data, obtained at 1000°C, to a temperature of 450°C. This agreement supports our hypothesis that diffusion of oxygen and internal friction are due to a common relaxation phenomenon.

Table 1. *Diffusion coefficient* (D) *as determined by experiment and as calculated from internal-friction data*

	Temp. (°C)	D(cm^2/sec) Expl.	D(cm^2/sec) Calc.
O in Si	1300	$1{\cdot}0\times10^{-9}$	$1{\cdot}4\times10^{-9}$
O in Si	450	3×10^{-18}	$3{\cdot}6\times10^{-19}$
O in Ge	800	$\sim 10^{-11}$	$5{\cdot}6\times10^{-11}$

Note added in proof: LOGAN and PETERS* have recently published more extensive measurements of the diffusion coefficient of oxygen in silicon. They represent their results with $D_0 = 135$ cm^2/sec and $U = 3{\cdot}5\pm1{\cdot}0$ eV.

* LOGAN R. A. and PETERS A. J., *J. Appl. Phys.* **30,** 1630 (1959).

The experimental data are almost equally well described with $D_0 = 0{\cdot}21$ cm^2/sec and $U = 2{\cdot}55$ eV.

The latter values of U and D_0, obtained from internal friction data, probably have a smaller uncertainty than the values obtained by LOGAN and PETERS.

Acknowledgements—I wish to express my thanks to Mr. P. D. SOUTHGATE and Dr. M. J. SPARNAAIJ for permission to use unpublished results of their work.

REFERENCES

1. BLOEM J., HAAS C. and PENNING P., *J. Phys. Chem. Solids* (to be published).
2. KAISER W., FRISCH H. L. and REISS H., *Phys. Rev.* **112,** 1546 (1958).
3. SNOEK J. L., *Physica* **8,** 711 (1941).
4. KAISER W., *Phys. Rev.* **105,** 1751 (1957).
5. HROSTOWSKI H. J. and KAISER R. H., *Bull. Amer. Phys. Soc.* **4,** 27 (1959).
6. POLDER D., *Philips Res. Rep.* **1,** 5 (1945).
7. SOUTHGATE P. D., *Proc. Phys. Soc. Lond.* B**70,** 800 (1957).
8. SOUTHGATE P. D., *Phys. Rev.* **110,** 855 (1958).
9. SOUTHGATE P. D., *Mullard Res. Lab. Rep.* (unpublished).
10. LOGAN R. A. and PETERS A. J., *J. Appl. Phys.* **28,** 819 (1957).
11. SPARNAAIJ M. J., Private communication.

VOL. 15 1960

J. Phys. Chem. Solids Pergamon Press 1960. Vol. 15. pp. 112–118. Printed in Great Britain.

THE EFFECT OF PRESSURE ON THE ABSORPTION SPECTRA OF ALKALI HALIDE PHOSPHORS*

R. A. EPPLER and H. G. DRICKAMER

Department of Chemistry and Chemical Engineering, University of Illinois, Urbana, Illinois

(*Received* 18 *November* 1959; *revised* 10 *December* 1959).

Abstract—The effect of pressure (over 150,000 atm) has been measured on the spectra of twenty-six alkali halide phosphors, including nine doped with Tl^+, two doped with In^+, twelve doped with Pb^{++}, two doped with Cu^{++} and one doped with Bi^{+++}. ν_{max} for the Tl^+ doped phosphors depends very strongly on the crystal structure and very little, if any, on the halide ion involved, which is consistent with the Seitz model. The In^+ doped phosphors behave like the Tl^+ analogs. For the Pb^{++} phosphors, the shift of ν_{max} depends very strongly on the halide ion, and only incidentally on the lattice structure. This is consistent with the complex model.

INTRODUCTION

THIS work is concerned with the effect of pressure on the *A* absorption band due to the presence of low concentrations of impurities such as thallium and lead in alkali halide crystals. Since irradiation in this band is directly responsible for the occurrence of luminescence in these crystals, this is a study of the effect of pressure on the luminescent center.

Two models have been advanced to explain the nature of the luminescent center in alkali halide phosphors:

One of these, commonly called the Seitz model,[1] pictures the luminescence process as being confined to the internal transition of the valence electron(s) of the impurity ion from the $^1S_0$ to the $^3P_1$ states, perturbed by the crystalline field of the lattice. One would expect such a model to be strongly dependent upon the structure of the bulk crystals, but relatively independent of the nature of the nearest neighbor halide ions.

The other model, called the complex ion model,[2–5] pictures the luminescence process as being an electron transition within a tightly bound impurity–halide ion complex. Here one would expect the system to be a strong function of the nature of the bound halide ions, but relatively independent of the structure of the bulk crystal.

The phosphors studied and the techniques used to synthesize them are shown in Table 1. The melting procedure is a simplified Kyropoulos method.[6] The grinding technique is similar to that used by dentists for mixing dental filling compounds. Press fusing consists of compressing the sample to around 15,000 atm on the anvil of a cylindrical tube type press.

The high pressure optical system used is that of Fitch *et al.*[7] At 1 atm, the absorption spectra of impurity ions in alkali halides have been measured by several investigators over the past 25 years. However, the literature in the field is by no means complete, so that for some of the materials studied, it was necessary to measure the 1-atm spectra. In Table 2 are listed the 1-atm peak frequency of the *A* band for all of the impurity activated alkali halides used in this investigation. Where no reference is given in column four, the 1-atm spectra were first measured here.

The effect of pressure on the spectra of the *A* band in twenty-six different alkali halide phosphors is shown in Figs. 1–9. Typical sets of experimental points are shown in Figs. 4 and 5. The maximum pressure attained on each phosphor is shown in column five of Table 2. The results, except for KBr:Bi (Fig. 5) are discussed below.

* This work was supported in part by AEC Contract AT(11-1)-67, Ch.E. Project 5.

Table 1. *Phosphor crystals*

Phosphor	Starting materials		Source		Preparative procedure(s)
	Host crystal	Impurity	Host	Impurity	
Low impurity KI:Tl for concentration study	Single crystal KI:Tl (0·1–0·2%)		Harshaw Chemical Co.		Melting (impurity dilution) and press fusing
0·8KI/0·2KBr:Tl	Single crystal KI:Tl and KBr:Tl		Harshaw Chemical Co.		Melting, press fusing
0·6KI/0·4KBr:Tl	Single crystal KI:Tl and KBr:Tl		Harshaw Chemical Co.		Melting, press fusing
0·4KI/0·6KBr:Tl	Single crystal KI:Tl and KBr:Tl		Harshaw Chemical Co.		Melting, press fusing
0·2KI/0·8KBr:Tl	Single crystal KI:Tl and KBr:Tl		Harshaw Chemical Co.		Melting, press fusing
NaCl:Tl	Single crystal NaCl	Chemically pure TlCl	Harshaw Chem. Co.	Fairmount Chem. Co.	Grinding press fusing
NaBr:Tl	Chemically pure NaBr	Chemically pure TlCl	Schaar Co.	Fairmount Chem. Co.	Melting, press fusing
CsBr:Tl	Single crystal CsBr:Tl		Harshaw Chemical Co.		None
RbBr:Tl	Chemically pure RbBr	Chemically pure TlCl	A.D. Mackay, Inc.	Fairmount Chem. Co.	Melting, press fusing
RbI:Tl	Chemically pure RbI	Chemically pure TlCl	A. D. Mackay, Inc.	Fairmount Chem. Co.	Melting, press fusing
NaCl:Pb	Single crystal NaCl	Chemically pure $PbCl_2$	Harshaw Chem. Co.	Allied Chem. and Dye	Melting, press fusing
NaBr:Pb	Chemically pure NaBr	Chemically pure $PbCl_2$	Schaar Co.	Allied Chem. and Dye	Melting, press fusing
NaI:Pb	Single crystal NaI	Chemically pure $PbCl_2$	Harshaw Chem. Co.	Allied Chem. and Dye	Grind together, press fusing
	Single crystal KCl:Pb		Dr. A. B. Scott, Oregon State College		None
KCl:Pb	Single crystal KCl	Chemically pure $PbCl_2$	Harshaw Chem. Co.	Allied Chem. and Dye	Melting, press fusing
KBr:Pb	Single crystal KBr	Chemically pure $PbCl_2$	Harshaw Chem. Co.	Allied Chem. and Dye	Melting, press fusing
KI:Pb	Single crystal KI	Chemically pure $PbCl_2$	Harshaw Chem. Co.	Allied Chem. and Dye	Melting, press fusing
RbCl:Pb	Chemically pure RbCl	Chemically pure $PbCl_2$	A. D. Mackay, Inc.	Allied Chem. and Dye	Grind together, press fusing
RbBr:Pb	Chemically pure RbBr	Chemically pure $PbCl_2$	A. D. Mackay, Inc.	Allied Chem. and Dye	Melting, press fusing
RbI:Pb	Chemically pure RbI	Chemically pure $PbCl_2$	A. D. Mackay, Inc.	Allied Chem. and Dye	Melting, press fusing Grind together, press fusing

VOL. 15 1960

Table 1. *Phosphor crystals*—(continued)

Phosphor	Starting materials		Source		Preparative procedure(s)
	Host Crystal	Impurity	Host	Impurity	
CsI:Pb	Single crystal CsI	Chemically pure $PbCl_2$	Harshaw Chem. Co.	Allied Chem. and Dye	Melting, press fusing
CsCl:Pb	Chemically pure CsCl	Chemically pure $PbCl_2$	Fisher Scientific Co.	Allied Chem. and Dye	Melting, press fusing
NH_4Br:Pb	Chemically pure NH_4Br	Chemically pure $PbCl_2$	Allied Chem. and Dye	Allied Chem. and Dye	Melting, press fusing
KCl:In	Single crystal KCl:In		Dr. F. E. Williams, General Electric Co.		None
KBr:In	Single crystal KBr	Chemically pure In	Harshaw Chem. Co.	A. D. Mackay, Inc.	Melting, press fusing
KBr:Bi	Single crystal KBr	Chemically pure $BiCl_3$	Harshaw Chem. Co.	Allied Chem. and Dye	Melting, press fusing
KCl:Cu	Single crystal KCl	Chemically pure $CuCl_2$	Harshaw Chem. Co.	Mallinkrodt Chem. Co.	Melting, press fusing
KBr:Cu	Single crystal KBr	Chemically pure $CuCl_2$	Harshaw Chem. Co.	Mallinkrodt Chem. Co.	Melting, press fusing

DISCUSSION

The effect of pressure on the Tl^+ *ion in alkali halide lattices*

The effect of pressure on the spectra of the *A* band in ten alkali halides activated with thallium has been measured to as high as 158,000 atm. In five cases (NaI:Tl, KCl:Tl, KBr:Tl, KI:Tl and CsI:Tl) the data have been reported previously.[13] The data on the other five phosphors (NaCl:Tl, NaBr:Tl, RbBr:Tl, RbI:Tl and CsBr:Tl) are shown in Fig. 1. For those phosphors which crystallize in the sodium chloride structure (face-centred cubic), the shift with increasing pressure is to lower energy. On the other hand, for those which crystallize in the cesium chloride structure (simple cubic), up to 15,000 atm a shift to higher energy is observed. At higher pressures the shift is to lower energy. A plot of the initial frequency shift vs. pressure for these crystals (see Fig. 2) reveals two important facts. In the first place, the shift is strongly dependent upon the crystal structure, or in other words, the impurity center is dependent upon the bulk crystalline field. On the other hand, no significant

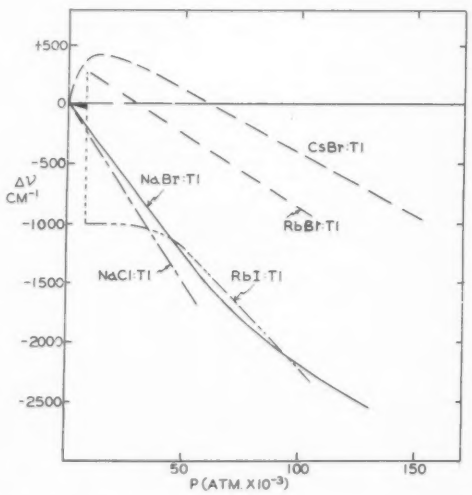

FIG. 1. "*A*" peak frequency vs. pressure—five alkali halides activated by Tl^+.

dependence upon the nearest neighbor halides is observed. For example, similar shifts are observed for KI:Tl, KBr:Tl and KCl:Tl. Thus the halide

Table 2. Spectral location of the "A" band adsorption due to impurities in alkali halide crystals

Crystal	Impurity	Peak (Å)	Ref. No.	Max. pressure (atm.)
NaCl	Thallium	2540	8	50000
NaBr	Thallium	2670	8	127000
NaI	Thallium	2930	8	50000
KCl	Thallium	2475	8	50000
KBr	Thallium	2610	8	130000
KI	Thallium	2870	8	129500
RbBr	Thallium	2590	8	94000
RbI	Thallium	2860	8	110000
CsBr	Thallium	2630	8	158000
CsI	Thallium	2990	8	118000
0·8KI/0·2KBr	Thallium	2858	—	124000
0·6KI/0·4KBr	Thallium	2836	—	50000
0·4KI/0·6KBr	Thallium	2810	—	50000
0·2KI/0·8KBr	Thallium	2708	—	50000
KCl	Indium	2815	9	120500
KBr	Indium	2930	10	131000
KBr	Bismuth	3712	—	114000
NaCl	Lead	2740	11	131000
NaBr	Lead	3040	11	111500
NaI	Lead	3578	—	50000
KCl	Lead	2730	11	140000
KBr	Lead	3020	11	170000
KI	Lead	3542	—	130500
RbCl	Lead	2720	11	50000
RbBr	Lead	3004	—	120000
RbI	Lead	3541	—	5000
CsCl	Lead	2849	—	89000
CsI	Lead	3705	—	50000
NH_4Br	Lead	3077	—	143000
NH_4I	Lead	3580	—	1
KCl	Copper (ic)	2650	12	50000
KBr	Copper (ic)	2650	12	117000

ions next to the impurity produce at most a perturbation on the system, but not a first-order effect. This is consistent with the Seitz model, but inconsistent with the complex ion model.

At phase transitions, such as occur in the potassium halides at around 20,000 atm, a discontinuous shift in the *A*-band frequency is observed. These shifts are to lower energies for the alkali iodides and to higher energies for the alkali bromides or chlorides. This is possibly related to the much stronger spin–orbital interaction

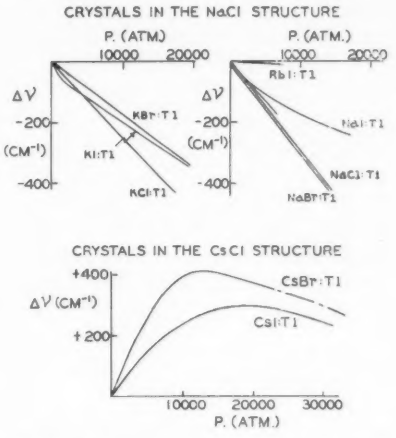

FIG. 2. Initial frequency shift vs. pressure—ten alkali halides activated by Tl^+.

of the iodide ion, compared to the chloride or bromide.

A study was made to determine if varying the impurity concentration affected the pressure shift of the impurity spectra. Thallium activated potassium iodide, in concentrations from 2×10^{-1} per cent to 4×10^{-3} per cent was used for the study. No dependence on concentration was observed.

Measurements have been made of the spectra of several mixed crystals of potassium bromide and potassium iodide, activated by thallium, and of the effect of pressure on this spectra. The spectral

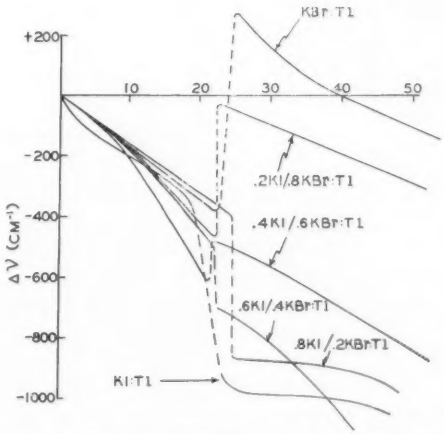

FIG. 3. The effect of pressure on *A*-band spectra in mixed crystals of KI:Tl and KBr:Tl.

position of the *A* band at 1 atm. in these mixed crystals is tabulated in Table 2. It can be seen that in the mixed crystals, the iodide ion is a much stronger perturbing force than the bromide ion, since the mixed crystal spectra are displaced towards KI:Tl. This is to be expected, since the iodide ion is both larger and more polarizable than the bromide ion.

The effect of pressure on these mixed crystals is shown in Fig. 3. A gradual change in the magnitude of the transition discontinuity occurs, proceeding from KI:Tl to KBr:Tl in a regular manner.

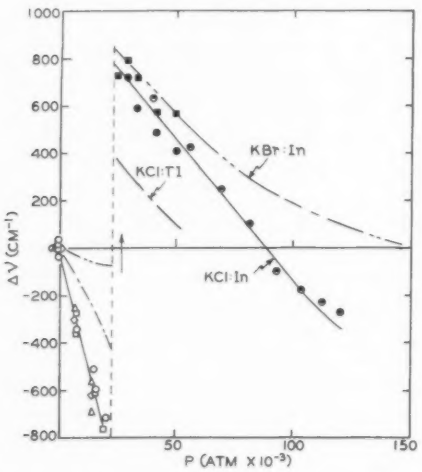

FIG. 4. "*A*" peak frequency vs. pressure—KCl:In; KBr:In (KCl:Tl shown for comparison); data points are for KCl:In.

The effect of pressure on the In^+ *ion in alkali halide lattices*

Studies have also been made of the effect of pressure on the spectra of the *A* band in potassium chloride and potassium bromide activated by indium (see Fig. 4). The shifts are similar to those for thallium, but greater in magnitude. This difference can possibly be attributed to the difference in ground state force constant of the two impurity ions.

The effect of pressure on the lead ion in alkali halide lattices

The effect of pressure on the spectra of the *A* band in twelve alkali halides activated with lead

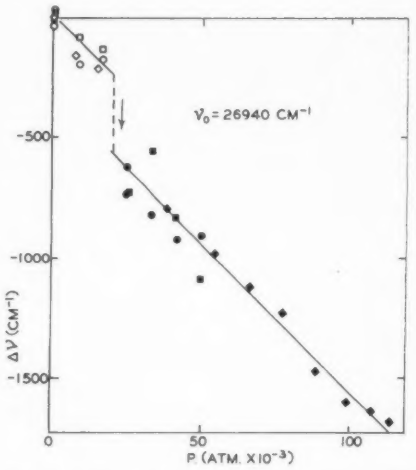

FIG. 5. "*A*" peak frequency vs. pressure—KBr:Bi.

has been measured to as high as 170,000 atm. The systems studied and the pressure range for each are given in Table 2. The data are shown in Figs. 6–8. In general, the frequency of the band initially shifts to higher energy, except at phase transitions. Then, at very high pressures the shift reverses and moves to lower energy. It is believed that the tendency to shift to higher energy may be connected

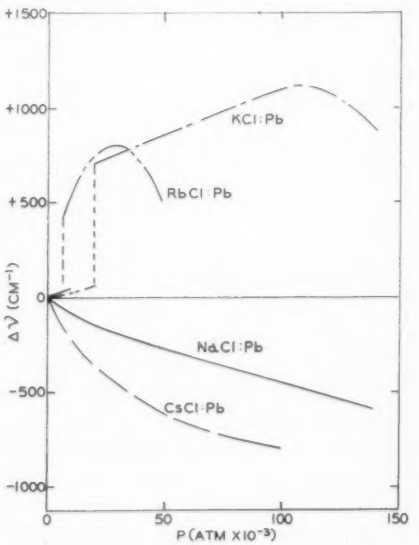

FIG. 6. "*A*" peak frequency vs. pressure—four alkali chlorides activated by Pb^{++}.

VOL. 15 1960

with the presence of a bound vacancy, adjoining the divalent impurity (it has been shown that such vacancies are usually completely bound to the impurity atoms[14]).

It can be seen that the initial frequency shift versus pressure for these crystals follows quite a different pattern from the thallium data discussed above. In the first place, the shift is strongly dependent upon the nature of the nearest neighbor

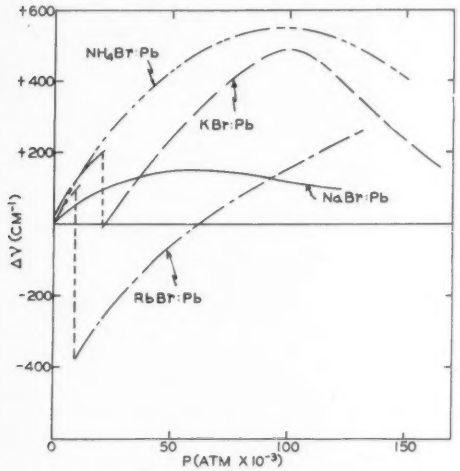

FIG. 7. "*A*" peak frequency vs. pressure—four alkali bromides activated by Pb^{++}.

halide ions; a dependence, moreover, which is consistent throughout the four cation systems studied. On the other hand, there is no significant difference between those crystals in the cesium chloride structure (the cesium halides) and those in the sodium chloride structure (the others). This is consistent with the complex ion model, but inconsistent with the Seitz model. This is also in agreement with the findings of FREDERICKS and SCOTT[15] that the mobile lead-containing center in transference measurements on these crystals is negatively charged, and must therefore be a complex containing halide ions.

It should be noted here that a shift to lower energy occurs for all alkali halide phosphors, regardless of impurity or of crystal structure, given sufficiently high pressure. At these very high pressures, the system is compressed to the point where the repulsive energy is probably the dominant contribution to the crystal energy in the ground

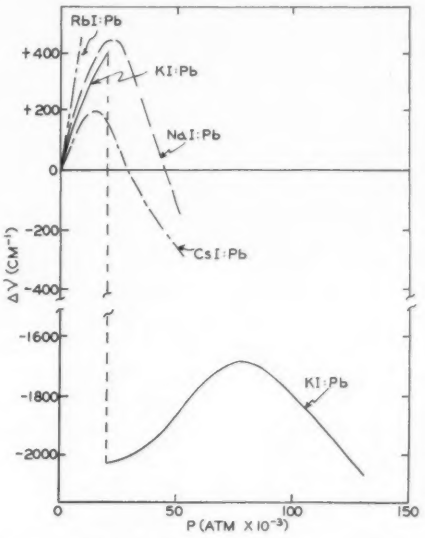

FIG. 8. "*A*" peak frequency vs. pressure—four alkali iodides activated by Pb^{++}.

state. This repulsive energy is very sensitive to changes in the lattice constant. The excited state probably has a flatter curve of energy vs. lattice constant than the ground state. Thus the energy

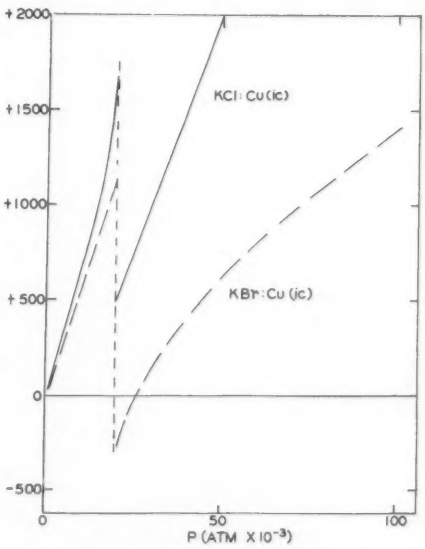

FIG. 9. "2500 Å" peak frequency vs. pressure KC1:Cu(ic) and KBr:Cu(ic).

of the ground state would increase with pressure more rapidly than the excited state energy, causing a lowering of the transition energy.

The effect of pressure on the copper ion in alkali halide lattices

Experiments with both cuprous and cupric ion impurity in alkali halides confirm the findings of BOESMAN and DEKEYSER[16] to the effect that the absorption band at approximately 2500 Å is caused by copper in the cupric state. This band has been studied as a function of pressure to 117,000 atm in potassium bromide and to 50,000 atm in potassium chloride (see Fig. 9). Very similar shifts occur in the two cases; strongly to higher energy except at phase transitions. This leads to the conclusion that the band results from an almost completely internal transition, probably between *d* electron levels split by the crystal field.

Acknowledgements—The authors wish to thank F. E. WILLIAMS, of General Electric Research Laboratories, and A. B. SCOTT of Oregon State College for supplying us with single crystal phosphors.

R. A. EPPLER would like to acknowledge support from a Shell Oil Company Fellowship and a Dow Chemical Company Fellowship.

REFERENCES

1. SEITZ F., *J. Chem. Phys.* **6,** 150 (1938).
2. FROMHERZ H. and MENSCHICK W., *Z. Phys. Chem.* B**3,** 1 (1929).
3. FROMHERZ H., *Z. Phys.* **68,** 233 (1931).
4. KATO M., *Sci. Pap. Inst. Phys. and Chem. Res., Tokyo* **41,** 113 (1943); **42,** 35 and 95 (1944).
5. PRINGSHEIM P., *Rev. Mod. Phys.* **14,** 132 (1942).
6. KYROPOULOS S., *Z. anorg. Chem.* **154,** 308 (1926).
7. FITCH R. A., SLYKHOUSE T. E. and DRICKAMER H. G., *J. Opt. Soc. Amer.* **47,** 1015 (1957).
8. FORRO M., *Z. Phys.* **58,** 613 (1930).
9. WILLIAMS F. E., SEGALL B. and JOHNSON P. D., *Phys. Rev.* **108,** 46 (1957).
10. LUSHCHIK N. E. and LUSHCHIK C. B., *Trud. Inst. Fiz. i Astron. Akad. Nauk Est. S.S.R.* **6,** 149 (1957).
11. HILSCH R., *Z. Phys.* **44,** 860 (1927).
12. SMAKULA A., *Z. Phys.* **45,** 1 (1927).
13. EPPLER R. A. and DRICKAMER H. G., *J. Phys. Chem. Solids* **6,** 180 (1958).
14. LIDIARD A. B., *Handbuch der Physik* Bd. **20,** S.246. Springer, Berlin (1957).
15. FREDERICKS W. J. and SCOTT A. B., *J. Chem. Phys.* **28,** 249 (1958).
16. BOESMAN E. and DEKEYSER W., *Physica, s'Grav.* **24,** 52 (1958).

J. Phys. Chem. Solids Pergamon Press 1960. Vol. 15. pp. 119–126. Printed in Great Britain.

SURFACE HETEROGENEITY IN IRRADIATED SOLIDS*

D. A. YOUNG†

Brookhaven National Laboratory, Upton, New York

(*Received* 1 *October* 1959; *revised* 18 *November* 1959)

Abstract—Experiments on the physical adsorption of krypton on unirradiated and neutron irradiated alumina have been performed and analysed in terms of localized adsorption without marked lateral interaction on surfaces of varying heterogeneity. This interpretation is supported by the shape of the isotherm on unirradiated material and the dependence on coverage of the differential molar entropy of the adsorbed phase. The nature of the surface heterogeneities introduced by irradiation is discussed speculatively.

VOL. 15 1960

It has been observed in studies of the etching of solids that one of the effects of neutron irradiation[1] or heavy-ion bombardment[2] is to increase the number of surface heterogeneities at which etch-pits may be formed. Because the technique employed is destructive of the imperfections produced it has not so far proved to be of great diagnostic value. Furthermore, non-destructive examination with the electron microscope has not as yet given information on the nature of the individual heterogeneities because they are too small to be replicated, although grosser effects in heavily irradiated solids may readily be observed. The field-ion microscope, though it has proved a powerful tool in the hands of Müller[3] for the examination of metals after bombardment with gaseous ions, has not as yet yielded useful results on the surface damage originating from displacements produced within the solid by penetrating radiation.[4] For reasons of this kind it appears necessary at the present stage to use rather more indirect methods. Slow electron diffraction may prove to be useful if single crystalline solids can be irradiated without simultaneous surface contamination. The simplest method, however, and one moreover which is suited to a preliminary analysis of any solid, appears to be the physical adsorption of an inert gas at a low temperature with subsequent analysis in terms of the shape of the adsorption isotherm and the differential molar entropy of the adsorbed phase. This approach is completely non-diagnostic, but in favorable cases should permit separation of the surface heterogeneities into groups in terms of the heat of adsorption.

For this purpose a system was chosen for which the adsorption would be expected to be localized, in the sense that the partition function of the adsorbed phase contains vibrational terms only, but for which the surface mobility is adequate for the adsorbed phase to adopt its equilibrium configuration within reasonable experimental times. These conditions can be met in the system argon–rutile for which thermodynamic data has been obtained by Drain and Morrison[5], but unfortunately it is found that the radioactivity of commercially available titanium dioxide is inconveniently high after the necessary neutron dose (10^{19} neutrons cm^{-2}), in addition to which there is doubt as to whether stoichiometry is retained in highly irradiated material. For these reasons it was decided to investigate aluminum oxide using krypton instead of argon because relatively small surface areas were expected.

EXPERIMENTAL

(a) *Preparation*

The aluminum oxide used was prepared by heating γ-alumina obtained from the Linde

* Work performed under the auspices of the U.S. Atomic Energy Commission.

† Guest Scientist on leave of absence from Atomic Energy Research Establishment, Harwell, England.

Company to 1040°C. in air for 170 hr.* About 3 g of the powder so obtained was loaded into a silica irradiation capsule equipped with a break seal. The powder and capsule were then outgassed at a pressure less than 5×10^{-6} mm for 24 hr at 700°C. The furnace was then switched off and the sample allowed to cool to room temperature through another 24 hr period. At this stage the capsule was sealed at a pressure of ca. 10^{-6} mm, care being taken to allow gas released from the silica during sealing to be pumped away. Three such specimens were prepared.

The krypton and helium gases were reagent grade products from the Airco Company and were used without further purification. Only freshly delivered liquid nitrogen was used and liquid oxygen was prepared as required.

(b) *Irradiation*

One of the specimens described in (a) was irradiated in the core of the Brookhaven reactor at about 40°C in a flux of 6×10^{12} thermal neutrons cm^{-2} sec^{-1} to a total dose of $7{\cdot}5 \times 10^{18}$ thermal neutrons cm^{-2} or approximately 2×10^{18} fast neutrons cm^{-2}.

(c) *Apparatus*

The gas adsorption apparatus employed was of conventional design except that a multirange McLeod gauge was used throughout, and that the adsorption cell was equipped with a magnet operated steel ball to break the capsule seals. Dead volumes, amounting to ca. 500 cm^3 were measured with helium under the temperature conditions of the experiment and the adsorption isotherms determined with krypton at 78 and 90°K.

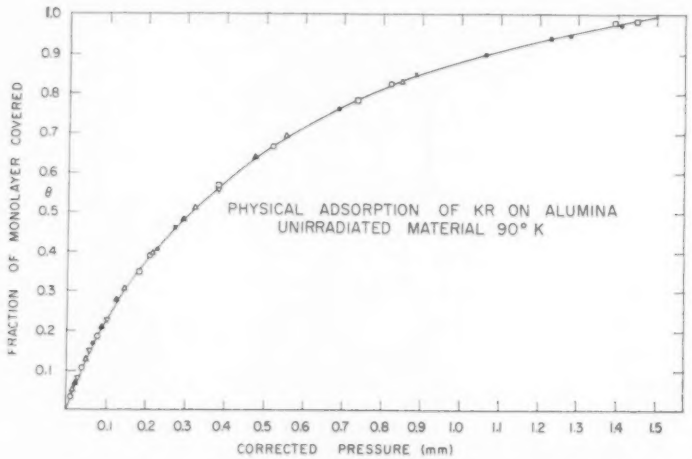

FIG. 1. Corrected isotherm for the physical adsorption of krypton on unirradiated alumina at 90°K. The open triangles, apex upwards, denote run U_1, the remaining symbols denote runs U_2.

RESULTS

One six-point isotherm was taken at 90°K for one unirradiated sample (U_1) and six for the other (U_2). Six isotherms were then taken for sample U_2 at 78°K. The isotherms obtained at 90°K on samples U_1 and U_2 agreed within 2 per cent. Twelve six-point isotherms were taken for the irradiated sample (I), six at 78°K and six at 90°K. At relative pressures in excess of 0·14 the isotherms at 90°K for samples U_1, U_2 and I were indistinguishable and yielded a B.E.T. monolayer capacity of $2{\cdot}5 \pm 0{\cdot}03 \times 10^{19}$ atoms of kryton adsorbed/g. Not much faith is placed in the absolute value of this monolayer capacity because the B.E.T. equation was not obeyed outside the range of relative pressure 0·1–0·25 and the C-value was only thirty-seven. The point of interest is that whatever the monolayer capacity, it is the same

* The material so prepared is believed to be the α-modification of the oxide.

for both irradiated and unirradiated material. The isotherms U_2 and I differ below $\theta = 1$ in that for a given coverage isotherm I is found at lower pressures. The difference between U_2 and I at 90°K is superficially very slight though there is a marked difference at 78°K.

Corrections applied

Care was taken to maintain the level of the adsorption cell coolant to within 1 mm, but small corrections still had to be applied for changes in atmospheric pressure and temperature. These were applied first. The results so obtained were then corrected for Knudsen flow using the equations and data quoted by BENNETT and TOMPKINS[6]. This correction was significant on the pressure axis below 50 μ but no significant effect on θ was found. The smallest value of the Knudsen flow correction R applied to any result was 0·714 and the lowest value of θ measured was 2 per cent.

A typical isotherm so corrected is illustrated in Fig. 1.

DISCUSSION

Before any discussion of radiation damage phenomena can proceed it is essential to determine from the data as much as possible about the nature of the adsorption process itself in any particular case. The alumina–krypton system was chosen because it was suspected that the adsorption would be localized and that adsorbate–adsorbate interactions would be small at low coverage, though no convincing argument for this view could be sustained without experimental data. The procedure adopted was therefore as follows.

The differential isosteric heats of adsorption (q_{ST}) were calculated for samples U_2 and I from the Clausius–Clapeyron equation at values of θ ranging from 0·01 to 1·0 using the smoothed curves drawn through the experimental isotherm points. The variations with θ of these heats are of the general form shown in Fig. 2, though the actual values of these heats are slightly larger (see later). It was noted that for the unirradiated sample U_2 the variation of the differential isosteric heat between $0{\cdot}1 < \theta < 0{\cdot}6$ is only 250 cal mole^{-1} and that therefore the isotherms for this material are suitable for the analysis of adsorption type employed by GARDEN and KINGTON[7]. These

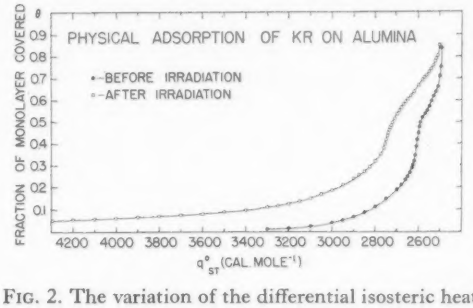

FIG. 2. The variation of the differential isosteric heat of adsorption at 0°K with surface coverage, illustrating the effect of neutron irradiation.

authors point out that in the limiting cases of localized adsorption without interactions, localized adsorption with interactions, mobile adsorption of finite atoms without interactions and mobile adsorption of finite atoms with interactions, the following four equations can be obtained by statistical mechanical methods.[8]

Localized adsorption without interactions:

$$p = K_L\left(\frac{\theta}{1-\theta}\right) \tag{1}$$

Localized adsorption with interactions:

$$p = K_{LI}\left(\frac{\theta}{1-\theta}\right)\left[\frac{2(1-\theta)}{\{1-4\theta(1-\theta)[1-\exp(-2w/ZkT)]\}^{1/2}+1-2\theta}\right]^{z} \tag{2}$$

where w is the attractive interaction energy between a pair of adsorbed atoms at equilibrium separation and Z is the number of nearest neighbors in the adsorbed phase.

Mobile adsorption of finite atoms without interactions; one or two degrees of translational freedom:

$$p = K_M\left(\frac{\theta}{1-\theta}\right)\exp\left(\frac{\theta}{1-\theta}\right) \tag{3}$$

Mobile adsorption with interactions; two

degrees of translational freedom; two dimensional van der Waals' gas:

$$p = K_{MI}\left(\frac{\theta}{1-\theta}\right)\exp\left(\frac{\theta}{1-\theta}-\alpha\theta\right) \qquad (4)$$

where α contains the van der Waals' coefficients.

The isotherm constants K_L, K_{LI}, K_M and K_{MI} were then calculated using a suitable experimental isotherm and plotted against θ to determine the range of validity, if any, of each isotherm equation. The results obtained using the isotherm illustrated in Fig. 1 are shown in Fig. 3. In these calculations, the value of α in equation (4) was chosen to be unity and for equation (2) the number of nearest neighbors in the adsorbed phase (Z) was chosen to be four. The attractive interaction w was calculated from the Lennard–Jones 6:12 potential to be approximately 160 cal mole^{-1}.

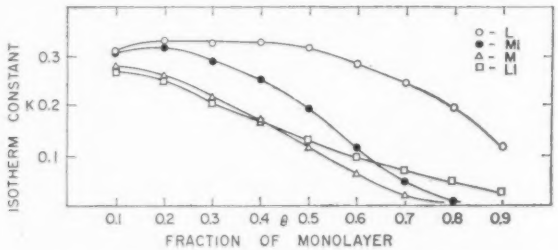

FIG. 3. Analysis of the isotherm in Fig. 1, according to equations (1)–(4).

It is immediately clear that neither equation (3) nor equation (4) is satisfactory and it was further determined that no constant value of w which represents an *attractive* interaction can increase the range in θ over which K_{LI} is sensibly constant. This equation (2) may, however, be made to fit if w is given values for *repulsive* interaction of 7 cal mole^{-1} at $\theta = 0{\cdot}5$ rising to 78 cal mole^{-1} at $\theta = 0{\cdot}9$. Owing to the onset of second layer formation at high θ-values these numbers have only qualitative significance. It is not surprising, however, that a small net repulsive interaction should appear at $\theta > 0{\cdot}5$ in this case, because the electrostatic field of the Al^{3+} ions would be expected to polarize the adsorbed krypton. This slight repulsion is thus ascribed to the dipole–dipole interactions amongst the adsorbate atoms rather than to the van der Waals' repulsive forces, because it is known that the isosteric heat of adsorption rises sharply by 60 cal mole^{-1} between $\theta = 0{\cdot}9$ and $\theta = 1{\cdot}0$ at the onset of second layer formation. These repulsive terms are maximum values because they include some of the effects of surface heterogeneity. They will therefore be neglected in what follows and we shall proceed on the assumption suggested by the good fit of equation (1) over the region $\theta = 0{\cdot}1$ to $\theta = 0{\cdot}6$ that adsorption occurs in a localized manner without interactions. The fact that the differential isosteric heat rises rather than falls below $\theta = 0{\cdot}1$ suggests that the hopping frequency is sufficiently high for the equilibrium configuration to be attained.

While the adequate fit of the Langmuir expression, equation (1), for a homogenous surface is indicative of the mechanism of localized adsorption without interactions, it has frequently been pointed out in the past that a mere test of the shape of an adsorption isotherm is not in itself conclusive and that it is essential to compare experimental thermodynamic quantities with the calculated values they assume on the basis of the adsorption model under test.[9,10] The differential isosteric molar heat capacity of the adsorbed phase is perhaps the best quantity, but this is not accessible, so recourse is had to the differential isosteric molar entropy. This quantity is obtained from the differential isosteric heat by substitution in equation (5).

$$\bar{S}_s = S_g^0 + R\ln\frac{P_0}{P} - \frac{q_{ST}}{T} - \frac{27}{32}R\frac{T_c^3}{T^3}\cdot\frac{P}{P_c} \qquad (5)$$

where $\bar{S}_s$ is the differential isosteric molar entropy of the adsorbed phase and $S_g^0 + R\ln P_0/P$ is the molar

VOL. 15 1960

entropy of the gas at pressure p and temperature T. T_c and P_c are the critical temperature and pressure for krypton.

The last term in equation (5) proves to be negligible in the pressure range of interest, so the differential isosteric molar entropy plotted in Fig. 4 is not corrected for gas imperfection.

The entropy of the adsorbed phase may also be calculated from the experimental results on the basis of models of localized or mobile adsorption by methods due principally to KEMBALL[11] and HILL[12]. Expressions for the configurational and non-configurational contributions to the molar entropy of the adsorbed phase for the case of localized adsorption on a random distribution of sites are given by HILL[12] and by DRAIN and MORRISON[13], and will not be repeated here. It is sufficient at this stage to note that the two functions of importance are the distribution function of adsorption potential over the surface $f(\epsilon)\,d\epsilon$, and the partition function of an adsorbed atom $j(\epsilon,T)$, where ϵ is the adsorption potential.

One method of approach is to guess the distribution function $f(\epsilon)\,d\epsilon$ and proceed therefrom by trial and error, but this is tedious and, as HONIG[14] has shown, is not a clear test for the actual form of the distribution function. The effects of surface heterogeneity dominate the equation via the dependence of $j(\epsilon,T)$ on ϵ rather than via the distribution function itself. It was therefore considered adequate to obtain $f(\epsilon)\,d\epsilon$ by differentiating θ with respect to the differential isosteric heat of adsorption (q_{ST}^0) after correction to 0°K. In the absence of calorimetric data, this correction can only be made approximately as follows:

$$\frac{dq_{ST}}{dT} = C_P(\mathrm{G}) - \bar{C}_\theta \qquad (6)$$

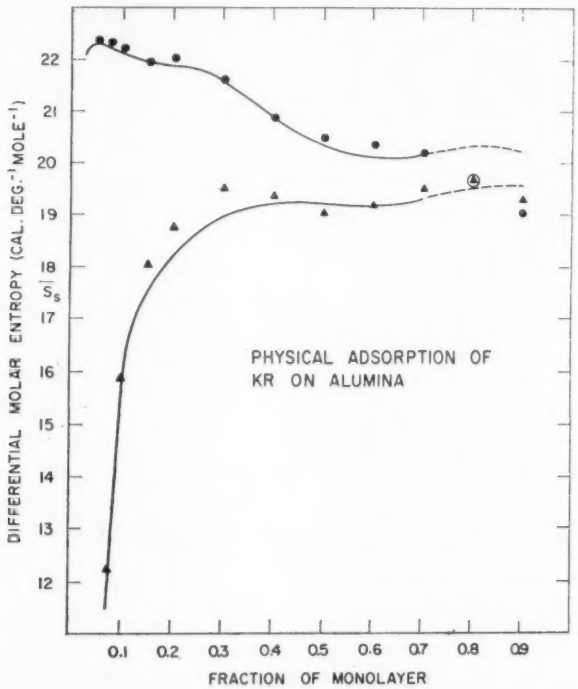

FIG. 4. Experimental and calculated differential molar entropies plotted against coverage. The solid circles and triangles are the experimental values for unirradiated and irradiated material respectively. The lines are the theoretical values minus 2 cal deg^{-1} mole^{-1}.

where $C_P(G)$ is the molar heat capacity of the gas at constant pressure and $\bar{C}_\theta$ is the differential molar heat capacity of the adsorbed phase at constant amount adsorbed. This latter quantity ($\bar{C}_\theta$) must be estimated on the basis of a model. In the first instance we regard the adsorbed phase as an assembly of independent monochromatic isotropic oscillators. This is a crude model, but will serve to indicate the order of magnitude of the correction. On this model, the differential isosteric heat of adsorption at 0°K is given by

$$q_{ST}^0 = q_{ST} - \frac{5}{2}RT + 3\,RT\frac{h\nu/kT}{\exp(h\nu/kT)-1} \quad (7)$$

where

$$\nu = (V_0/4M_S^2)^{1/2} \text{ as given by Hill} \quad (7a)$$

where $V_0 = q_{ST}$ in ergs $\cong$ 2500 cal mole^{-1}

$M = 83{\cdot}7$

S = separation of potential troughs in cm $\cong 5\times10^{-8}$

whence $\nu = 3{\cdot}52\times10^{11}$ sec^{-1}

This frequency is low, hence to a close approximation the molar heat capacity of the adsorbed phase is 3 RT. The differential isosteric heat at 0°K obtained from equation (7) is illustrated in Fig. 2. Surface heterogeneity exerts only a minor influence (~3 per cent) on this correction owing to the relatively low vibrational frequencies involved, thus at this stage surface heterogeneity is neglected.

The differentiation of the $\theta - q_{ST}^0$ curve in this particular case is more difficult than the differentiations carried out by DRAIN and MORRISON[15] in their classical work on rutile, because for the krypton–alumina system $d\theta/dq_{ST}^0$ actually becomes negative as $\theta = 0{\cdot}9$ is approached and it is not clear at which point the distribution function should be terminated for normalization. Each distribution function contains two sharp peaks. For the unirradiated material these occur at 2610 and 2495 cal mole^{-1} and for the irradiated material at 2745 and 2500 cal mole^{-1}. The second sharp peak undoubtedly arises partly from homogeneity of the nearly covered surface and partly from the effects of multilayer adsorption. Only this latter effect should be eliminated by termination. Fortunately a simple qualitative test is available. It is found that the isotherms are moderately well reproduced up to $\theta = 0{\cdot}8$ by the expression

$$\theta = \int_0^\infty \frac{f(\epsilon)\,d\epsilon}{1+(j(\epsilon,T))^{-1}\exp[-(\mu+\epsilon)/RT]} \quad (8)$$

if the heights of the two low-energy peaks are made the same and the distribution cut off sharply at this point before normalization.

For the calculation of the partition function $j(\epsilon,T)$ of the adsorbed phase, the condition that the oscillators shall be monochromatic is relaxed. In this case, retaining the condition that the oscillators shall be isotropic, i.e. $\nu_x = \nu_y = \nu_z$, the partition function is given by

$$(j(\epsilon,T))^{-1} = (1-\exp[-h\nu/kT])^3 \quad (9)$$

Here, ν, calculated from expression (7a), is set equal to $A\epsilon_M^{1/2}\epsilon^{1/2}$ for $\epsilon = \epsilon_M = 2500$ cal mole^{-1} where ϵ_M is the expected value of q_{ST}^0 for a smooth surface, whence we obtain[16]

$$\frac{h\nu}{kT} = 3{\cdot}74\,\epsilon^{1/2}\times10^{-3}$$

with ϵ in cal mole^{-1}.

The molar entropies were computed by the methods outlined above, and the sum

$$S_s\,(\text{theor}) = S_C + S_{NC}$$

for both samples U_2 and I differentiated with respect to θ and substituted in the well-known expression for the differential molar entropy

$$\bar{S}_s = \left(\frac{\partial}{\partial\theta}S_s\right)_\theta \theta + S_s \quad (10)$$

and the quantities $\bar{S}_s(U_2)$ and $\bar{S}_s(I)$ compared with the experimental results. It was noted that the calculated differential entropies were both 2 cal deg^{-1} mole^{-1} too high throughout the range $0{\cdot}05 < \theta < 0{\cdot}7$, so the quantity $\bar{S}_s - 2$ was plotted for comparison with the experimental results, as illustrated in Fig. 4. The fit is adequate between $0{\cdot}05 < \theta < 0{\cdot}7$. There are several reasons for the general discrepancy of 2 cal deg^{-1} mole^{-1} including the crudity of the approximation for the differential molar heat capacity of the adsorbed phase and the neglect of anharmonicity, but it is believed that the fundamental reason for the discrepancy

VOL. 15 1960

is the assumption of isotropic oscillators. The assumption will affect the term $T(\partial/\partial T)\ln j + \ln j$ in the expression for S_{NC}. The value of S_{NC} is almost independent of surface coverage (θ) thus the assumption of isotropic oscillators will affect the value of $\bar{S}_s$ by nearly the same amount over the full range of θ.

The agreement between the calculated and observed entropies is sufficiently good, when taken with the analysis of the adsorption isotherm, to justify the assumption of localized adsorption in an equilibrium configuration. In support of this view, preliminary calculations using a partition function containing one vibrational and two translational terms were performed. They indicated that no satisfactory agreement could be obtained, doubtless due to the weaker dependence of j on ϵ.

It is also of interest to note that most of the dependence of $\bar{S}_s$ on θ is contained in the configurational term. For example, $S_{NC}(U)$ rises monotonically from 14·98 to 15·83 cal deg^{-1} mole^{-1} over the range $0{\cdot}05 < \theta < 0{\cdot}7$ whereas $S_C(U)$ falls from 8·62 to 7·11 cal deg^{-1} mole^{-1}, while in the case of the irradiated material $S_{NC}(I)$ rises from 14·41 to 15·42 cal deg^{-1} mole^{-1} with $S_C(I)$ rising from 0·31 to 4·53 cal deg^{-1} mole^{-1}. DRAIN and MORRISON[15] and HILL[16] found a similar relative importance of S_C and S_{NC}.

The changes in surface heterogeneity on irradiation can be displayed in a different way. In Fig. 5 is plotted the square root of the differential with respect to q_{ST}^0 of $(\theta_I - \theta_U)q_{ST}^0$ written as

$$\left(\frac{\partial}{\partial q_{ST}^0}(\theta_I - \theta_U)\right)_{q_{ST}^0}^{1/2}$$

The square root is employed simply to expand the scale at low values of the ordinate. The linear plot integrates approximately to zero indicating that the over-all number of sites remains sensibly constant, in agreement with the B.E.T. results. From the plot it appears that a large number of low-energy sites (2625 cal mole^{-1}) representing the relatively uniform surface of the unirradiated material is replaced essentially by three families of sites. Most of the sites are enhanced in energy by 125 cal mole^{-1}, a smaller number by 320 cal mole^{-1} and the remainder by varying amounts up to 1500 cal mole^{-1}. One may speculate on the nature of these new sites within the framework of the views expressed by MORRISON *et al.*[15] and DE BOER[17] on the relative importance of polarization and dispersion forces with increasing coverage, who point out that at high coverage the polarization contribution is small. The existence of the three families of sites can be understood if it is supposed that radiation damage can modify the sites of the

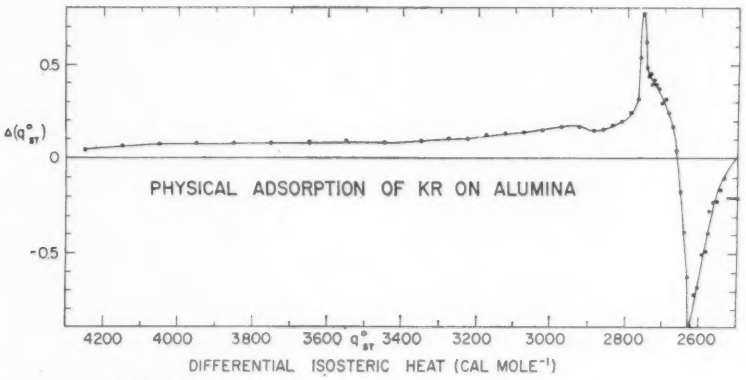

FIG. 5. The function

$$\left(\frac{\partial}{\partial q_{ST}^0}(\theta_I - \theta_U)\right)_{q_{ST}^0}^{1/2}$$

plotted against the differential isosteric heat at 0°K(q_{ST}^0).

homogeneous surface either by

(a) increasing the dispersion forces or
(b) increasing the polarization forces or
(c) increasing the polarization and dispersion forces simultaneously.

In this event we tentatively propose the following model: The high energy tail is to be ascribed to adsorption on defect sites, surface vacancies and discontinuities in steps, at which an electron or a hole has been trapped. This is effect (c). The peak at 2950 cal mole^{-1} arises from adsorption at surface vacancies or discontinuities in ledges which have not trapped an electron or a hole. This is effect (a). The main peak at 2750 cal mole represents adsorption on a topochemically smooth surface perturbed only by electrons or holes trapped in surface states. This is effect (b).

In conclusion it is suggested that this technique should prove useful for the preliminary analysis of surface heterogeneities in irradiated solids.

Acknowledgements—I would like to thank G. J. DIENES for his encouragement and G. H. VINEYARD, J. W. SUTHERLAND and J. P. HOIGNE for discussions.

REFERENCES

1. GILMAN J. S. and JOHNSTON W. G., *J. Appl. Phys.* **29,** 877 (1958).
2. YOUNG D. A., *Nature, Lond.* **182,** 375 (1958).
3. MULLER E. W., *J. Appl. Phys.* **28,** 1 (1957).
4. WORTMAN R., private communication (May 1959).
5. DRAIN L. E. and MORRISON J. A., *Trans. Faraday Soc.* **48,** 840 (1952); MORRISON J. A., LOS J. M. and DRAIN L. E., *Trans. Faraday Soc.* **47,** 1023 (1951).
6. BENNETT M. J. and TOMPKINS F. C., *Trans. Faraday Soc.* **53,** 185 (1957).
7. GARDEN L. A. and KINGTON G. L., *Proc. Roy. Soc.* A**234,** 24, 35 (1956).
8. FOWLER R. and GUGGENHEIM E. A., *Statistical Thermodynamics.* Cambridge University Press (1949).
9. EVERETT D. H., *Trans. Faraday Soc.* **46,** 453, 942, 957 (1950).
10. TOMPKINS F. C., *Trans. Faraday Soc.* **46,** 569, 580 (1950).
11. KEMBALL C., *Advanc. Catalys.* **2,** 233 (1950).
12. HILL T. L., *J. Chem. Phys.* **17,** 762 (1949).
13. DRAIN L. E. and MORRISON J. A., *Trans. Faraday Soc.* **48,** 316 (1952).
14. HONIG J. M., *Ann. N.Y. Acad. Sci.* **58,** 741 (1954).
15. DRAIN L. E. and MORRISON J. A., *Trans. Faraday Soc.* **48,** 316 (1952); **49,** 654 (1953).
16. HILL T. L., *J. Chem. Phys.* **16,** 181 (1948).
17. DE BOER J. H., *Advanc. Catalys.* **8,** 17 (1956).

J. Phys. Chem. Solids Pergamon Press 1960. Vol. 15. pp. 127–133. Printed in Great Britain.

DIFFUSION OF ZINC IN GALLIUM ARSENIDE

F. A. CUNNELL and C. H. GOOCH

Services Electronics Research Laboratory, Baldock, Herts.

(*Received* 21 *October* 1959)

Abstract—The diffusion of zinc into gallium arsenide from the vapour phase has been investigated for a range of diffusion temperatures and zinc pressures. Experiments to investigate the influence of arsenic pressure on the diffusion have also been performed.

The results obtained depart radically from those expected for a constant diffusion coefficient and possible reasons for this are discussed.

VOL. 15 1960

INTRODUCTION

INTEREST in gallium arsenide for device purposes is growing. One of the operations essential to the fabrication of many semiconductor devices is the preparation of *p–n* junctions by diffusion. The diffusion of an impurity in silicon and germanium can normally be accomplished under conditions which yield a good approximation to a simple complementary error function distribution. This paper is intended to show that such is not the case in GaAs. Possible reasons for the difference are discussed and a selection of zinc diffusion curves is presented for specified diffusion conditions.

The p–n junction method for determination of diffusion constants

The first attempts to measure diffusion coefficients of zinc in gallium arsenide employed a technique used successfully for impurities in germanium. This consists of diffusing the impurity under identical circumstances into two specimens of different known electron concentrations. The *p–n* junction depths are measured accurately and assuming a constant surface concentration, C_0, and a concentration independent diffusion coefficient D, C_0 and D can be deduced simply. Although the measurement of junction depths in GaAs could be made to about 1 per cent accuracy, the values of C_0 were invariably several orders of magnitude higher than was reasonable. It was shown subsequently by the radio-tracer technique to be described, that the assumptions made in deducing C_0 and D were invalid, and by the nature of the diffusion process fictitiously high C_0 values would be expected from the *p–n* junction method.

EXPERIMENTAL TECHNIQUES

The diffusion profile of zinc in GaAs was studied by diffusing the neutron activated metal from the vapour phase. The radioactive isotope was Zn^{65} which is a γ-emitter (1·11 MeV) with a half life of 245 days. Diffusion was carried out in evacuated quartz tubes. Although the residual air pressure inside the tube was in the region 10^{-5}–10^{-6} mm Hg prior to sealing off, it deteriorated after sealing and was probably not better than 10^{-2}–10^{-3} mm Hg during the experiment. This could not be improved readily since the presence of the radioactive zinc made outgassing of the entire quartz tube during evacuation rather difficult.

A furnace system was designed to provide a monotonic variation of temperature over the length of the diffusion tube. The GaAs specimen was situated at one end of the tube which was maintained at a constant temperature, T_2, while the zinc source was located at the other extremity and at a lower constant temperature, T_1 (Fig. 1). Temperature control was within ± 1°C. Zinc temperatures in the range 600°C–800°C, which would correspond to saturated zinc pressures of 10–250 mm Hg, were used in most of the experiments. Preliminary investigation had shown that surface alloying occurred under conditions of high zinc pressure (e.g. $>$ 650 mm Hg at 1000°C). To produce a saturated zinc vapour pressure of 250 mm Hg roughly 0·5 mg of zinc metal were

required in a standard diffusion tube of 2 cm³ volume. In general, samples of zinc weighing 1–2 mg were used.

The sides and edges of the diffused specimens were removed by grinding to a depth in excess of

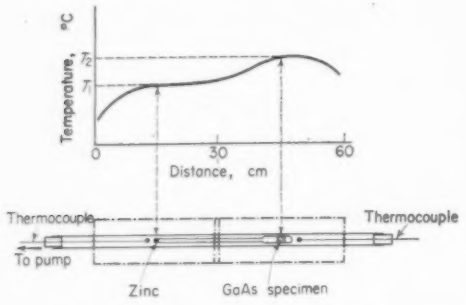

FIG. 1. Furnace system for diffusion.

the anticipated penetration depth. The two opposite active faces remaining were both examined in every case. This not only acted as a check on uniformity of diffusion but improved the over-all accuracy. Successive layers were removed from a face by grinding on 000 Hubert polishing paper lubricated with oil. The grinding machine which accomplished this operation was such that the grindings could be confined to a small reproducible

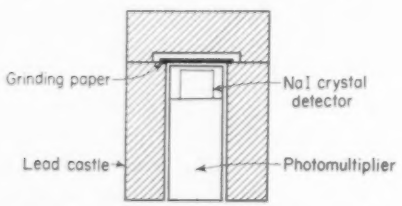

FIG. 2. System for counting activity in gallium arsenide removed by grinding.

circular area of paper.* Furthermore, plane parallel layers a few microns in thickness could be removed with ease. The activity on the paper was measured using a scintillation counter as shown in Fig. 2. The location of the paper relative to the NaI crystal detector was reproducible. The concentration of zinc at any depth was calculated from the count rate per milligram of material removed and the count rate of a standard solution of active zinc chloride absorbed on a filter paper of the same area as the grinding area.

The method of removing and counting a small interval of material from one face leads to an averaged value of the zinc concentration over that interval. However, it can be shown that an accurate representation of the distribution can be obtained provided the intervals are reasonably small. Layers about 10 μ thick were normally removed over a total examined depth of about 150 μ in most cases. The limit of detection was set by the specific activity of the zinc (roughly 10–100 mc/g) and the background count rate. This limit corresponded to about 10^{17} zinc atoms/cm³ for the specimens of normal size (i.e. roughly 0·3–0·5 cm² section). Zinc in the form of small particles of metal and also in the form of an evaporated metal film on the inside of a quartz tube was used. In the form of a film the metal tended to be somewhat oxidized. No difference in diffusion could be discerned, however, when the radioactive source used was slightly oxidized or when it was rendered free from oxide by sublimation.

Specimens of GaAs were selected from single crystal material grown in a horizontal boat or in a floating zone equipment. The normal dimensions were $1 \times 0{\cdot}4 \times 0{\cdot}3$ cm. After cutting to the approximate dimensions with a diamond wheel, the samples were ground plane parallel on 600 grade emery paper followed by a final polish on Hubert's 000 polishing paper. Approximately 10 μ was removed by etching for 2 min in a warm etch of the following composition:†

H_2SO_4	3 vols.
H_2O_2 (100 vols.)	1 vol.
H_2O	1 vol.

This etch left a very good polished finish. An alternative etch which has been used consisted of HCl and HNO_3 in the ratio 3:1. A preliminary experiment was performed to determine the influence of surface preparation on diffusion in GaAs. Table 1 below summarizes the various combinations of grinding and etching treatments used. Material

* The authors are indebted to Mr. R. WICKHAM and Mr. W. LESTER of this laboratory for design of this precision machine.

† The authors are indebted to Mr. N. RAIN of this laboratory for developing this etch.

Table 1

Face examined	Material	Final grinding paper	Etch
1	Floating zone	000	H_2SO_4, H_2O_2, H_2O
2	Floating zone	600	H_2SO_4, H_2O_2, H_2O
1	Horizontally grown	000	H_2SO_4, H_2O_2, H_2O
2	Horizontally grown	000	HCl, HNO_3

grown from horizontal boats and also floating zoned single crystals were checked for similar behaviour.

The four diffusion profiles obtained after the same diffusion programme on both specimens were identical. It was concluded that variations in diffusion behaviour brought about by slight changes in surface preparation were negligible.

VOL. 15 1960

EXPERIMENTAL RESULTS

Diffusion of zinc into GaAs at 900°C, 1000°C

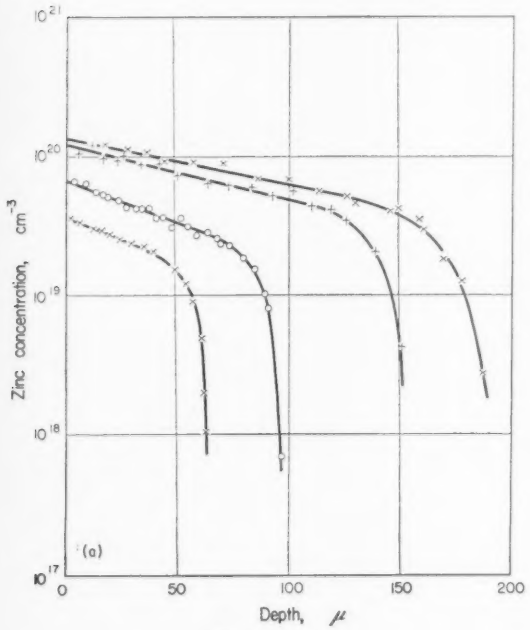

FIG. 3(a)

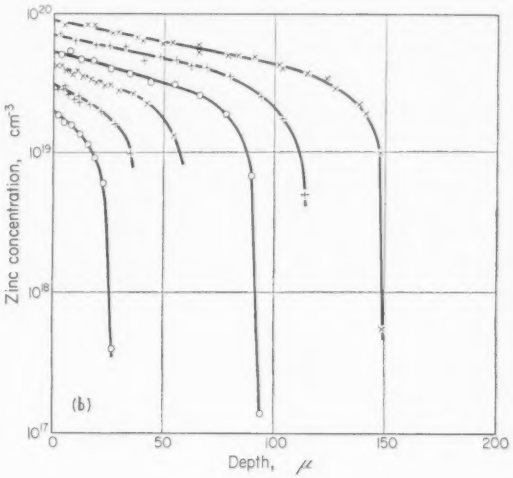

FIG. 3(b)

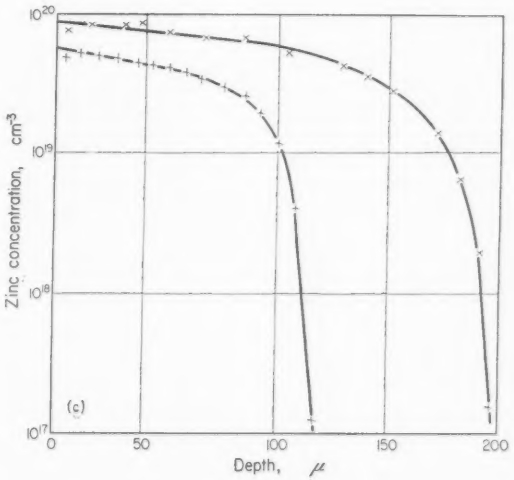

FIG. 3(c)

FIG. 3. Zinc concentration vs. distance from surface.
(a) Diffusion temperature 900°C.
(b) Diffusion temperature 1000°C.
(c) Diffusion temperature 1100°C.
Diffusion time is 10^4 sec in all three cases.

and 1100°C was investigated. Figs. 3(a) (b) and (c) illustrate the results obtained. (The results obtained at 1100°C are not considered to be as reliable as those at lower temperatures. Alloying was a severe problem.) In each figure the parameter varied from curve to curve was the zinc temperature. Fig. 4 shows the way in which the surface

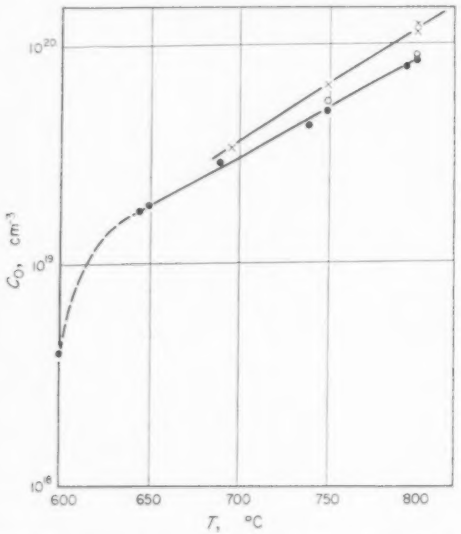

FIG. 4. Surface concentration vs. zinc reservoir temperature.

× Diffusion temperature 900°C.
● Diffusion temperature 1000°C.
○ Diffusion temperature 1100°C.

concentration, C_0, is related to the zinc reservoir temperature. It cannot be assumed that the zinc pressure is the vapour pressure of pure zinc at the temperature of the reservoir since there will be an association of zinc and arsenic evaporated from the specimen which will reduce the zinc pressure. The rapid fall of C_0 as the temperature is reduced below 650°C may be attributable to this effect.

C_0 was determined in every case by extrapolating the diffusion profile back to the surface of the crystal. On occasions an excessively high counting rate was found for the first layer removed from the specimen face. This could be due to condensation of zinc vapour on the specimen surface when the diffusion tube was removed from the furnace.

It can be seen from Fig. 3 that for high values of C_0 the diffusion curves are characterized by a very sharp change in gradient at a concentration of about 3 to 4×10^{19} atoms cm^{-3}. A possible explanation of this effect has been advanced which is based on the difference in diffusion coefficient of ionized and unionized zinc atoms.[1,2] If it can be assumed that above a concentration C' all zinc centres are unionized and below C' all ionized, then the diffusion profile can be represented by two separate curves intersecting at C' each describable in terms of complementary error functions.[2] This approximation corresponds to the case of a

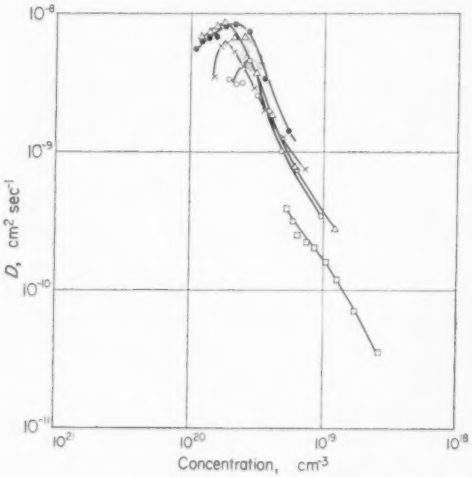

FIG. 5. Diffusion coefficient vs. concentration of zinc. Diffusion temperature 1000°C.

	Zinc temp. (°C)	Diffusion time (sec)
×	1000	10^4
△	800	3×10^4
●	800	10^4
○	750	10^4
□	650	$1{\cdot}8 \times 10^5$

step-like Fermi function. The curve for which $C < C'$ is of the form $C = C_f \operatorname{erfc} [x/2\sqrt{(D_i t)}]$ where C_f is the fictitious high surface concentration obtained from the p–n junction measurements described in a previous section. D_i is the smaller diffusion coefficient associated with the ionized zinc atoms. If the simplification of a step-like Fermi function is not made then the diffusion coefficient of zinc atoms must be considered as decreasing continuously with decreasing concentration. At very high concentrations and at very low concentrations the function $D = D(C)$ would

VOL. 15 1960

approach the limiting values D_u (unionized) and D_i respectively. In support of the general explanation of the sharp change in gradient of the diffusion curves it should be noted that when the surface concentration is reduced towards the concentration associated with the onset of the "knee", the plateau corresponding to the fast diffusion near the surface almost disappears.

Some of the experimental diffusion curves have been analysed by a standard method used to determine the variation of D with C. This method is suitable for any case in which D is a function of C only.[3] Fig. 5 shows the results of the analysis of several curves. The monotonic variation of D with C expected on the basis of the proposed model is not found in general. Instead, the diffusion coefficient apparently rises from the surface up to a maximum value before falling rapidly at a concentration roughly corresponding to the position of the knee. The exception to the general behaviour is found in the case of the lowest value of C_0 where diffusion was allowed to continue for a much longer period (54 hr). It follows from the analysis of the diffusion curves that in addition to the complication arising from the existence of two states of the zinc atom there is a further mechanism to be considered in explaining the experimental zinc distribution.

The effect of diffusing zinc in the presence of a background arsenic pressure was examined. Sufficient arsenic was added to the diffusion tube to provide a pressure of about 1 atm neglecting association of arsenic and zinc. The result of two experiments at 1000°C for zinc temperatures of 1000°C and 800°C are shown in Fig. 6 in the form of C vs. x curves. These curves are to be compared with the family of curves of Fig. 3(b). The effect in both cases is to cause the diffusion to be slower in a region adjacent to the surface. In curve A the plateau associated with the fast diffusion of unionized zinc is still present followed by the characteristic "knee" at the same value of concentration as before. In curve B the smaller value of C_0 together with the slow diffusion at the surface have suppressed the plateau. It is not clear why the value of C_0 in A is higher than the C_0 corresponding to no additional arsenic.

The dependence on time of the distance x measured from the surface to a particular zinc concentration C has been determined by the

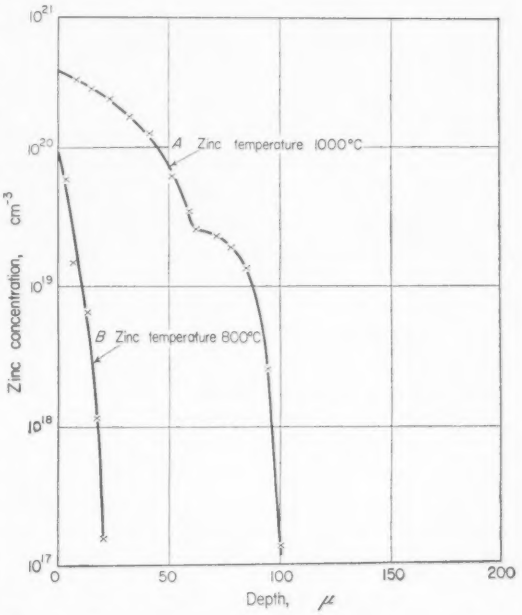

FIG. 6. Zinc concentration vs. distance from surface after diffusion in presence of excess arsenic.

Diffusion temperature 1000°C.
Diffusion time 10^4 sec.

radio-tracer technique and also by measuring p–n junction depths in the specimens of identical material diffused for different times. Fig. 7 shows the result of the latter method. It is clear from this that a law $\lambda \propto \sqrt{t}$ is obeyed. Curves obtained from the radio-tracer method for different times of diffusion fit

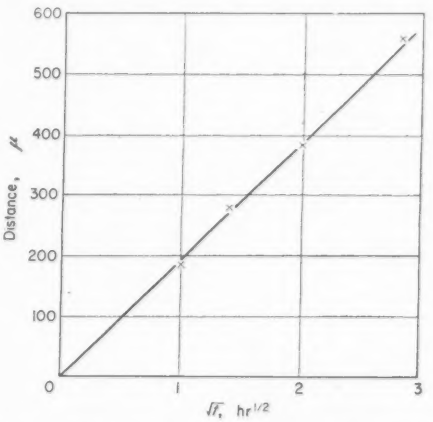

FIG. 7. Depth of p–n junction vs. (diffusion time)$^{1/2}$.

the family of curves shown in Fig. 3 when adjusted to a standard time by applying a $\sqrt{t}$ law.

DISCUSSION OF RESULTS

It has been shown experimentally that there are at least two factors which complicate the diffusion of zinc in gallium arsenide. They are the changing ratio of ionized and unionized atoms as the concentration of zinc varies and the dependence of diffusion rate on the pressure of arsenic vapour surrounding the crystal. The first of these complications could apply to almost any semiconductor and any impurity provided the surface concentration is sufficiently high. The requirement is simply that at the temperature of diffusion the Fermi level should pass through the impurity level at some concentration less than the surface concentration. This is discussed at length in the subsequent paper.[2] The second complication is relevant in principle to any compound semiconductor.

It can be deduced from the phase rule that the composition of a specimen of gallium arsenide which is in equilibrium with arsenic vapour at a given temperature is uniquely determined by the pressure of the arsenic and the temperature. A departure from the stoichiometric composition is achieved by a modification of the concentrations of atomic defects of several possible types. In general one type of defect will predominate. The possibility considered here is that arsenic and gallium vacancies are predominant among the defects and their concentrations unequal in a non-stoichiometric solid. Applying the law of mass action to the following equilibrium equations,

$$(1-\delta)\ \mathrm{GaAs} + \delta\mathrm{Ga\ (vapour)} \rightleftharpoons \mathrm{GaAs} + \delta V_{\mathrm{As}}$$
$$4(1-\delta)\ \mathrm{GaAs} + \delta\mathrm{As_4(vapour)} \rightleftharpoons 4\mathrm{GaAs} + 4\delta V_{\mathrm{Ga}}$$
$$\mathrm{As_4\ (vapour)} + 4\mathrm{Ga\ (vapour)} \rightleftharpoons 4\mathrm{GaAs}$$

we obtain the relationships

$$\frac{P_{\mathrm{Ga}}}{[V_{\mathrm{As}}]} = K_1 \text{ (a constant)} \qquad (1)$$

$$\frac{P_{\mathrm{As_4}}}{[V_{\mathrm{Ga}}]^4} = K_2 \qquad (2)$$

$$P_{\mathrm{As_4}} P_{\mathrm{Ga}}^4 = K_3 \qquad (3)$$

where V_{As} and V_{Ga} represent concentrations of arsenic and gallium vacancies, and P_{Ga}, $P_{\mathrm{As_4}}$ represent the partial pressures of the vapours.

Hence

$$[V_{\mathrm{Ga}}]^4\,[V_{\mathrm{As}}]^4 = \frac{K_3}{K_2 K_1^4}$$

or

$$[V_{\mathrm{Ga}}]\ [V_{\mathrm{As}}] = \text{a constant} \qquad (4)$$

This gives a simple relationship between the two types of neutral vacancies. If, as is most likely, the vacancies may accept or donate electrons, then equations must also be written down to relate charged vacancies, ionized foreign impurities, electrons and holes. The complete analysis is involved and necessitates assuming the electrical behaviour of arsenic and gallium vacancies (i.e. acceptor or donor centre?) before performing the analysis. However, given information on the predominant lattice defects together with their behaviour it should be possible to derive a relationship between arsenic pressure and the concentrations of charged and neutral vacancies. Assuming that zinc atoms diffuse by successive jumps into vacant gallium sites, the observed diffusion rate in a crystal could then be related to arsenic pressure. It is not proposed to attempt a detailed calculation of the form of the diffusion curves on the above model. Instead it is intended to make certain observations concerning the diffusion of zinc in gallium arsenide which illustrate some of the factors which must be considered.

A stoichiometric specimen of gallium arsenide heated in an evacuated capsule will lose arsenic to its surroundings until an equilibrium is attained such that the pressure of arsenic in the tube is equal to the dissociation pressure of arsenic over the crystal. The material will no longer be stoichiometric, the concentration of vacancies having been modified by out-diffusion or in-diffusion from the surface or by diffusion from internal sources, e.g. dislocations. The time required to establish equilibrium may be appreciably longer than the corresponding time for an elementary semiconductor since the unit jump of a vacancy in a compound involves a transition to a next nearest neighbour site. The diffusion of a substitutional impurity in the material of modified composition would be quite different from diffusion in the

original material. The degree of non-stoichiometry will be a function of the temperature, the volume of the capsule and the volume of the specimen. The rate of approach to equilibrium would be a function of the surface area to volume ratio of the specimen. In the presence of a source of zinc a new equilibrium would be attained. Arsenic would tend to combine with the zinc source and the degree of association would be a function of the temperature of the zinc. Consequently the new equilibrium would be reached at a different arsenic pressure and would depend on the quantity of zinc present in the capsule. The experiments which have been performed in this work have been aimed at providing sufficient empirical information to predict the diffusion behaviour of zinc under certain conditions. Consequently the volume of the diffusion tubes has been roughly the same in each case and kept to a minimum (2 cm^3). Similarly the quantity of zinc and dimensions of the specimen were fairly standard. However, comparison experiments have been made varying the volume of the tube by a factor three without detecting any difference in the diffusion curve obtained. Similar small variations in surface area to volume ratio of the specimen and the weight of zinc used have also proved non-critical.

Acknowledgements—The authors wish to thank Miss B. J. HART for assistance in the experiments, Mr. J. W. ALLEN and Mr. P. GURNELL for reading the manuscript and the Admiralty for permission to publish the work.

VOL. 15 1960

REFERENCES

1. ALLEN J. W. and CUNNELL F. A., *Nature, Lond.* **182,** 1158 (1958).
2. ALLEN J. W., following paper.
3. CRANK J., *Mathematics of Diffusion.* Oxford University Press (1956).

J. Phys. Chem. Solids Pergamon Press 1960. Vol. 15. pp. 134–139. Printed in Great Britain.

THE DIFFUSION OF IONIZED IMPURITIES IN SEMICONDUCTORS

J. W. ALLEN

Services Electronics Research Laboratory, Baldock, Herts.

(*Received* 21 *October* 1959)

Abstract—The diffusion coefficient of an impurity in a semiconductor depends on the state of ionization of the impurity, i.e. on whether the Fermi level lies above or below the impurity energy level. A simple model, namely the one-dimensional diffusion of a shallow acceptor, is used to illustrate this and the results are applied to the diffusion of zinc in gallium arsenide.

VOL
15
196

INTRODUCTION

THE electrically active impurities of chief importance in semiconductors are those which have two or more different states of ionization. An example of this is a simple acceptor which can exist in two states, that in which it has accepted an electron and that in which it has not. Let us suppose that such an acceptor is the predominant impurity in the semiconductor and that its energy level lies near the valence band. If the concentration of impurities is sufficiently high and the band gap is large enough then the Fermi level will lie within the valence band and only a small fraction of impurity atoms will accept electrons. As the concentration decreases the Fermi level will rise and the proportion of impurities which have accepted electrons will rise and become close to unity.

Now if the diffusion coefficient of the impurities is different in the two ionization states the effective diffusion coefficient will be concentration dependent. In this paper some of the consequences of this will be described. The model which is here treated in detail is the one just mentioned, but of course the ideas and the method of treatment are not limited to the case of simple acceptors. The extension to donors or to impurities with more complex ionization schemes will be obvious.

In the next section we show how the position of the Fermi level varies as the concentration changes, and in the subsequent section we write down the diffusion equation and find an approximate solution. In later sections the validity of the solution will be discussed, and some of its implications will be pointed out. For numerical calculations we will take as an example the diffusion of zinc into gallium arsenide, and we will compare the predictions of the theory with CUNNELL's experimental results for this system as described in the preceding paper.

POSITION OF THE FERMI LEVEL

Consider an acceptor impurity with a concentration of N_I atoms/unit volume and with an energy level at E_I, assumed to be in the lower half of the energy gap. Let the concentration of impurities which have accepted an electron be N_e and of those which have not be N_p. Then

$$N_I = N_e + N_p \tag{1}$$

Let the density of holes in the valence band be p. If the density of shallow acceptors is much greater than the intrinsic number of holes and electrons then the effect of the electrons in determining the position of the Fermi level is negligible and one can write for the condition of charge neutrality

$$N_e = p \tag{2}$$

If N_v is the effective density of states in the valence band, E_v is the energy level of the top of this band and E_F is the Fermi energy, then it is known that:

$$p = \frac{2}{\sqrt{\pi}} \cdot N_v \cdot F\left(\frac{E_v - E_F}{kT}\right) \tag{3}$$

$$N_e = \frac{N_I}{1+\exp\left(\frac{E_I-E_v}{kT}\right)\exp\left(\frac{E_v-E_F}{kT}\right)} \quad (4)$$

where $F(x)$ is the Fermi–Dirac integral of MACDOUGALL and STONER. Equations (2–4) determine p, N_e and E_F, but since they are implicit equations they need to be solved numerically or graphically.

We have done this using values for the parameters which might be applicable to the case of zinc in gallium arsenide. Assuming an effective mass for holes of $0{\cdot}4m$ the effective density of states at 1000°C is found to be $5{\cdot}55\times10^{19}$ cm^{-3} and if the effective mass of electrons is $0{\cdot}04\,m$, the intrinsic number of electrons and holes at this temperature is only $2{\cdot}7\times10^{16}$ cm^{-3}. The values of N_e, N_p and E_F have been found at 1000°C for impurity concentrations ranging from 10^{22} cm^{-3} to 10^{18} cm^{-3}, and for two values of the impurity ionization energy, namely zero (which is a useful approximation for $E_I-E_v \ll kT$, 0·11 eV at 1000°C) and 0·10 eV. The results for the case of E_I-E_v zero are given in Table 1. In Fig. 1 the ratios of N_e and N_p to N_I are plotted for both values of E_I-E_v and it will be seen that the curves are qualitatively similar.

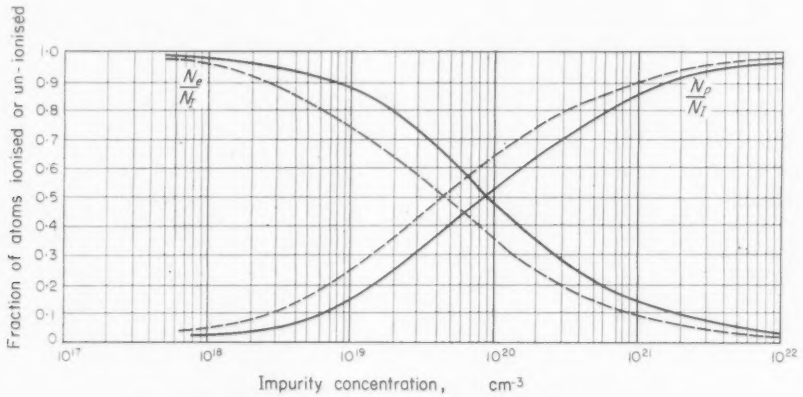

FIG. 1. Variation of impurity ionization with impurity content.

THE DIFFUSION EQUATIONS

It is to be expected that an impurity atom will have different diffusion coefficients in different states of ionization. In our model let D_p be the diffusion coefficient when the impurity has not accepted an electron and D_e when it has. The rate of increase with time of the total impurity concentration is contributed to by the diffusion currents of atoms in both states of ionization. FICK's law, in one dimension, therefore becomes

$$\frac{\partial}{\partial x}\left(D_e\frac{\partial N_e}{\partial x}+D_p\frac{\partial N_p}{\partial x}\right)=\frac{\partial N_I}{\partial t} \quad (5)$$

where it has been assumed that electronic processes are much faster than atomic ones. Since N_e and N_p are known as functions of N_I from the considerations of the previous section, the problem of diffusion in our model is solved in principle. However, the solution for the impurity concentration as a function of distance must be found by numerical methods and this procedure does not readily show how the qualitative features of the solution depend on the physical parameters. We therefore use an approximation which allows us to express the solution in terms of well-known functions.

The approximation is that above a certain concentration N_0 of impurities none of them have accepted an electron, whereas below N_0 all have accepted an electron. This is equivalent to approximating the curves of Fig. 1 by step functions. Although this may not appear to be very good *a priori*, the solutions obtained justify this form of approximation, as will be shown in the discussion.

We consider diffusion into the semi-infinite slab $x>0$ when the concentration of impurity at the surface $x=0$ is maintained at the constant

value N_s. Equation (5) then becomes

$$D_p \frac{\partial^2 N}{\partial x^2} = \frac{\partial N}{\partial t} \qquad N > N_0$$
$$D_e \frac{\partial^2 N}{\partial x^2} = \frac{\partial N}{\partial t} \qquad N < N_0 \tag{6}$$

The boundary conditions to be satisfied are

$$N = 0 \text{ for } x > 0, \quad t = 0$$
$$N = N_s \text{ for } x = 0, \quad t > 0 \tag{7}$$

There is in addition the condition that the diffusion current be continuous at the boundary $N = N_0$:

$$D_p \left(\frac{\partial N_p}{\partial x}\right)_{N=N_0} = D_e \left(\frac{\partial N_e}{\partial x}\right)_{N=N_0} \tag{8}$$

Equation (8) immediately shows that if the diffusion coefficient changes discontinuously at this boundary then a plot of impurity concentration against distance into the solid must have a discontinuous change of slope at $N = N_0$.

Diffusion equations of this type have been discussed by WAGNER in connection with diffusion into solids in which a change of phase occurs (cf. JOST[2]). A solution is obtained by assuming that the depth at which the boundary $N = N_0$ occurs varies as $(D_p t)^{1/2}$, i.e. that if $x = \xi$ when $N = N_0$ then

$$\xi = \gamma . 2\sqrt{(D_p t)} \tag{9}$$

where γ is a constant to be determined from the boundary condition. The solution of the problem is then given by

$$N = N_s - (N_s - N_0) \frac{\operatorname{erf}\left[\dfrac{x}{2\sqrt{(D_p t)}}\right]}{\operatorname{erf} \gamma} \qquad 0 < x < \xi \tag{10}$$

$$N = N_0 \frac{\operatorname{erfc}\left[\dfrac{x}{2\sqrt{(D_e t)}}\right]}{\operatorname{erf} \gamma\alpha} \qquad x > \xi \tag{11}$$

where $\alpha \equiv (D_p/D_e)^{1/2}$ and γ is to be found from the implicit equation

$$\alpha \left(\frac{N_s - N_0}{N_0}\right) = \frac{\operatorname{erf} \gamma}{\operatorname{erfc} \gamma\alpha} \exp\left[-\gamma^2(\alpha^2 - 1)\right] \tag{12}$$

In the case that $\alpha \gtrsim 4$, equation (11) reduces to a form more suitable for calculation:

$$N \simeq N_0 \frac{\xi}{x} \exp\left(-\frac{x^2 - \xi^2}{4D_e t}\right) \tag{13}$$

DISCUSSION OF THE THEORY

If $N_s \gg N_0$ and α is greater than unity but not too great (say $\alpha = 2$ or $D_p = 4D_e$) then equation (10) becomes in good approximation

$$N = N_s \operatorname{erfc}\left[\frac{x}{2\sqrt{(D_p t)}}\right] \qquad 0 < x < \xi \tag{14}$$

i.e. the change of diffusion coefficient has very little effect on the form of the diffusion curve near the surface, since equation (14) is that usually obtained for diffusion into a semi-infinite solid from a constant surface concentration of impurities. Equation (11) is of the same form, but the "effective surface concentration" N_s^*, i.e. that obtained by extrapolating back to $x = 0$, is given by

$$N_s^* = \frac{N_0}{\operatorname{erfc} \gamma\alpha} \tag{15}$$

and does not necessarily bear any close relation to the true surface concentration N_s. This suggests that even if the points in an experimental determination of impurity concentration against distance lie exactly on a complementary error function curve there is no justification in extrapolating such a curve back to zero to find the surface concentration if the value obtained corresponds to degeneracy in the semiconductor. The effective concentration N_s^* can be greater or less than the true surface concentration depending on whether D_p is greater or less than D_e.

These features of the solution are illustrated in Fig. 2 where we have taken $N_s = 5 \times 10^{20}$ cm^{-3}, $N_0 = 5 \times 10^{19}$ cm^{-3}, $\alpha = 2$, and $\sqrt{(D_p t)} = 10^{-2}$ cm, which for $t \sim 3$ hr corresponds to $D_p \sim 10^{-8}$ cm^2/sec. In this case γ is found to be 1·20.

The validity of the approximation of a discontinuous change of diffusion coefficient will now be examined for the case in which the values of the physical parameters are those used in the examples above. It can be seen from Table 1 that while the

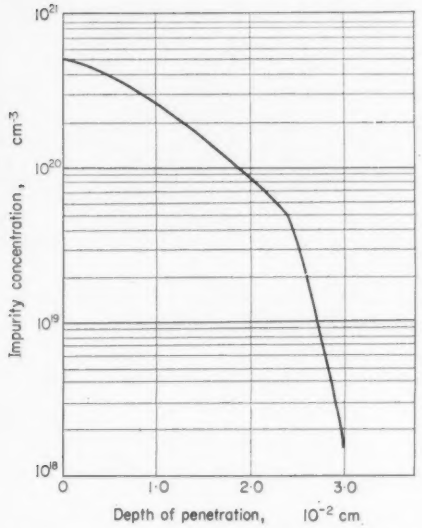

FIG. 2. Impurity concentration as a function of depth of penetration. Parameters assumed: $\alpha = 2$, $\sqrt{(D_p t)} = 10^{-2}$ cm.

ξ the Fermi level is well above the impurity levels and N_p becomes very small, while N_e is almost exactly equal to N_I. So even though D_p has been assumed greater than D_e as long as it is not too much greater the condition

$$D_p \frac{\partial^2 N_p}{\partial x^2} \ll D_e \frac{\partial^2 N_e}{\partial x^2}$$

can be satisfied by going sufficiently far into the crystal. There is, however, a region just beyond the boundary $x = \xi$ where the two terms on the left-hand side of equation (5) are of the same order of magnitude and here the solution given by equation (11) will not be good. Although this region may correspond to a change of N_I by an order of magnitude the change in x is quite small and the most striking feature of the diffusion curve, the sudden change in gradient, will be preserved. One might therefore summarize by saying that if $N_s \gg N_0$, and $\alpha > 1$ but not too great, the solution presented in equations (10) and (11) will be a good approximation except for a small region just beyond the boundary $N = N_0$. For other conditions the approximation will fail in different regions, but the methods of argument used above can be used to determine these regions in each case.

Table 1

N_I (cm^{-3})	$\frac{E_v - E_F}{kT}$	$E_v - E_F$ (eV)	N_e (cm^{-3})	N_p (cm^{-3})
10^{22}	3·50	0·38	3·0 10^{20}	9·71 10^{21}
10^{21}	1·77	0·19	1·42 10^{20}	8·54 10^{20}
10^{20}	0·10	0·01	4·75 10^{19}	5·24 10^{19}
10^{19}	−1·84	−0·20	8·8 10^{18}	1·37 10^{18}
10^{18}	−4·02	−0·44	9·8 10^{17}	1·76 10^{16}

Fermi level is in the valence band N_e changes considerably less rapidly than N_p. If $\alpha > 1$ then $D_p > D_e$, and the condition

$$D_p \frac{\partial^2 N_p}{\partial x^2} \gg D_e \frac{\partial^2 N_e}{\partial x^2}$$

is readily satisfied. Since it has been seen that the solution of the diffusion equation in this region for these values of the parameters is almost unchanged by the change in diffusion coefficient further in the crystal, it follows that for $N_s \gg N_0$ and α greater than unity but not too great, equation (10) is a good approximation for values of x almost up to ξ. Conversely, for values of x much greater than

COMPARISON WITH EXPERIMENT

CUNNELL has shown[1] that there are a number of complicating factors involved in the diffusion of zinc into gallium arsenide, but it seems clear that the process described above is occurring in this system. In particular, the existence of a sharp change of slope in the concentration–depth curve seems to be well confirmed, and the concentration at which this occurs is of the right order of

magnitude. As the surface concentration of zinc decreases the diffusion profile changes in the expected manner, the change of slope disappearing when the surface concentration is less than the critical concentration. Some of the experimental curves can be quite well fitted by equations (10) and (11). However, a detailed comparison of theory and these experiments will not be attempted here for two reasons: firstly that the surface concentration cannot be made much greater than the critical concentration, so our theoretical approximations are not very good, and secondly that other factors are present of which we have not taken account, such as the dependence of the diffusion on the arsenic pressure.

The first evidence of the existence of a steep front in the diffusion of zinc in GaAs was obtained when a p–n junction made by diffusing zinc into n-type GaAs was viewed in cross-section in the near infra-red. Transitions between filled zinc levels and the conduction band produce absorption in this wavelength region. The absorption is therefore a measure of N_e. It can be seen from Fig. 3 that there is a fairly well-defined edge where this quantity changes considerably. Inspection of Table 1 shows that a sharp change in N_e requires an even sharper change in N_I, so the existence of a step is qualitatively substantiated.

A method frequently used to determine diffusion coefficients in semiconductors is to diffuse an acceptor impurity under identical conditions of temperature and time into two n-type specimens of differing donor concentrations. Assuming that the diffusion coefficient is constant under the given conditions, i.e. that it is independent of concentration or time, then it is possible to calculate both this coefficient and the surface concentration from the p–n junction depths and the initial donor concentrations, assumed known. However, in the zinc–GaAs system the existence of the steep diffusion front means that to a first approximation the position of the p–n junction is independent of the donor concentration, as long as this is less than the critical value N_0. If more accurate measurements of junction depth are made then an apparent diffusion coefficient and surface concentration can be obtained. The former is the "slow" coefficient D_e, and has reasonable values, but the latter is quite unrelated to the true surface concentration, as shown by equation (15), and can attain values up to 10^{30} cm^{-3} or so, clearly an absurd value for a concentration. If on the other hand a single specimen is heated at a constant temperature then equation (9) shows that the junction depth, approximately equal to ξ, varies as the square root of the time, and CUNNELL has confirmed this experimentally. Studies of p–n junction depths therefore gave rise to considerable confusion in the early stages, for they gave a reasonable diffusion coefficient, a variation of depth with time of the expected form, but a wildly unreasonable surface concentration, and sense was only restored to the scene by the realization of the existence of a region of fast diffusion followed by a steep diffusion front.

CONCLUSION

The conditions for the existence of an anomalous diffusion of the type considered here are that the diffusing impurity should be present in such high concentrations that it dominates the electrical behaviour at the temperature of diffusion, and the impurity should be able to exist in at least two states of ionization. These conditions are not often satisfied, especially as an impurity at high concentrations tends to have its levels merged into the nearest band, i.e. if the condition of high concentration is satisfied then the condition of the existence of two ionization states is no longer satisfied. However, there are many systems in which the conditions should be fulfilled within suitable temperature ranges. Similar phenomena should occur when an impurity gives rise to a number of electron levels well within the energy gap, as for instance gold in germanium. Such an impurity should show a change of diffusion coefficient whenever the Fermi level passes through such an electron level. Since the position of the Fermi level may be strongly influenced by the presence of other impurities and by the temperature, the actual diffusion process may be quite complicated. Emphasis here has been placed on systems with fast diffusion at high concentration, slow diffusion at low concentration, and with high carrier concentrations compared with the intrinsic number. This has been for the sake of clarity and because the treatment has immediate application to an experimental situation. To enumerate all the possibilities with different parameters would be tedious; however, the principles laid down here should be applicable in most cases with little modification.

VOL.
15
1960

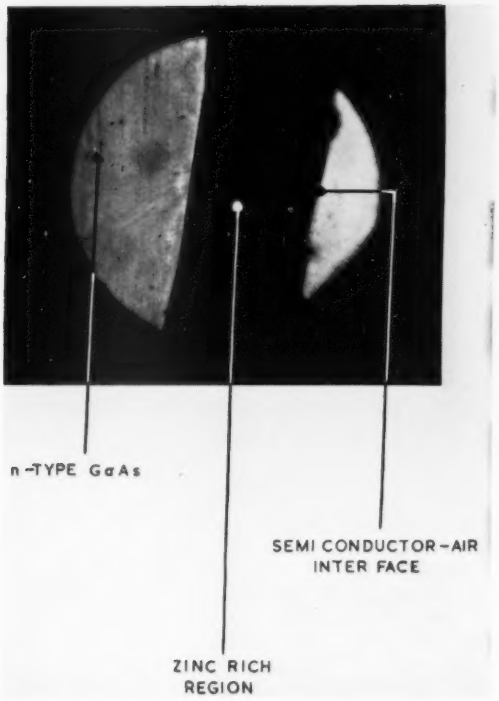

FIG. 3. Gallium arsenide p–n junction viewed in the near infra-red.

[*facing p.* 138

Acknowledgements—The theory described here was developed to account for the experimental data of Dr. CUNNELL, and I am grateful to him for extensive discussions of these data. Acknowledgement is also made to the Admiralty for permission to publish this paper.

VOL.
15
1960

REFERENCES

1. CUNNELL F. A., preceding paper.
2. JOST W., *Diffusion in Solids, Liquids, Gases*. Academic Press, New York (1952).

J. Phys. Chem. Solids Pergamon Press 1960. Vol. 15. pp. 140–145. Printed in Great Britain.

THEORY OF THE RESISTANCE MINIMUM IN DILUTE PARAMAGNETIC ALLOYS

A. D. BRAILSFORD and A. W. OVERHAUSER

Scientific Laboratory, Ford Motor Company, Dearborn, Michigan

(*Received* 11 *December* 1959)

Abstract—The observed anomalous temperature dependence of the resistivity of dilute paramagnetic alloys is attributed to *s–d* exchange scattering of conduction electrons by nearest neighbor pairs of ferromagnetically coupled solute ions. Occurrence of a resistance minimum can be explained quantitatively only if the effective range of the *s–d* exchange potential is not too short; and only if the periodic structure of energy bands is taken into account. The size of the minimum is proportional to the square of the solute concentration in the limit of extreme dilution (less than 1 per cent). Deviations from this law at higher concentrations are explained satisfactorily.

1. INTRODUCTION

A MINIMUM in the resistance as a function of temperature has been observed in several dilute paramagnetic alloys of a transition metal in a noble metal.[1] At temperatures below that of the minimum the resistance increases monotonically with decreasing temperature. In addition, the anomalous change in resistivity with atomic per cent of solute has been found to vary with solute concentration near extreme dilution. Although not conclusively established, it appears very probable that these effects are associated with paramagnetic ions in random solid solution.[2]*

The first attempt to explain the anomalous temperature dependence of the resistivity was due to KORRINGA and GERRITSEN[3]. They introduced the concept of localized impurity states, centered at each paramagnetic ion, with an energy very close to the Fermi energy of the conduction electrons. This model yielded some results in qualitative agreement with experiment. However, no independent evidence for the existence of such impurity states has been found. Later, SCHMITT[4] pointed out that a temperature dependent resistivity would occur if the spin degeneracy of the states of the paramagnetic ion were removed. This effect was explored in detail by YOSIDA[5] in a calculation of the resistivity of the antiferromagnetic Cu–Mn alloys, where the spin degeneracies of the manganese ions are split by a molecular field. He found that below the Néel temperature the resistivity decreased with decreasing temperature, whereas above it the resistance was independent of temperature. Consequently the resistance minimum can not be ascribed to residual effects of some cooperative magnetic transition at lower temperature.

In this paper a new model for the resistance minimum is presented in detail. (The method has been outlined briefly in a previous note.[6]) The mechanism invoked is similar to that of SCHMITT, who postulated the presence of scattering centers with closely spaced energy states. Such states do indeed arise when pairs of nearest neighbor paramagnetic ions interact. The magnetic states of the pair are split into a sequence of degenerate levels, the energy separation of which depends on an effective exchange integral W. We show that the average elastic *s–d* exchange scattering cross section of each state of a level is

* *Note added in proof:* It has now been established that the minimum which has been observed with various group B solutes (e.g. Ga, Ge, Sn) in Cu is not a direct consequence of the solute itself but arises only insofar as the solute is able to reduce any iron oxide present as an impurity and thus bring iron into solid solution (GOLD A. V., MACDONALD D. K. C., PEARSON W. B. and TEMPLETON I. M., *Phil. Mag.*, to be published). We are indebted to these authors for details of this work in advance of publication.

VOL. 15 1960

proportional to the square of the total spin of that level. Thus, for ferromagnetic coupling, ($W > 0$), the lower the energy of a level, the greater is its elastic cross section. This implies an increasing contribution to the resistivity as the temperature decreases, and so explains the resistance minimum. Of course, account must be taken of the opposing tendency of the resistivity contribution arising from inelastic processes, which become frozen out at low temperatures. It is found, however, that elastic processes always dominate at high temperatures ($kT > W$) and therefore, when the phonon resistivity is included, a resistance minimum usually results.

One immediate consequence of the model outlined above is that the anomalous resistance change for a given temperature increment below the minimum should be proportional to the square of the concentration of the paramagnetic solute. This relation is expected to hold only for extreme dilution. At higher concentrations the resistivity will be affected both by larger clusters of neighboring ions, and by randomly distributed single solute ions interacting by means of the pseudo-exchange mechanism.[7] The latter effect will ordinarily be the more important. As a result of these interactions the spin degeneracy of a paramagnetic level is removed. Consequently scattering processes for which an electron spin is reversed become inelastic and are frozen out at low temperatures. The resulting resistivity decrease with decreasing temperature competes with the net increase arising from coupled nearest neighbor pairs, so that the minimum in the total resistivity varies less rapidly with concentration than the quadratic dependence, characteristic of extreme dilution. We believe this effect to be the qualitative explanation of the concentration dependence of the minimum in dilute Cu–Co alloys, for example.

In Section 2, the resistivity arising from scattering by coupled nearest neighbor solute pairs is calculated. A resistance minimum is obtained only if the range of the effective s–d exchange potential is not too short. Furthermore, in Section 3 it is found necessary to take into account the periodicity of energy bands in $\boldsymbol{k}$ space in order to obtain quantitative agreement between theory and experiment. In Section 4, the contribution of isolated paramagnetic ions to the anomalous low temperature resistivity is estimated and found adequate to explain the concentration dependence of the resistance minimum.

2. RESISTIVITY CONTRIBUTION FROM SCATTERING BY PAIRS

In an electric field E_z the conduction electron gas reaches a steady state when the rate of change of the electron momentum P_z produced by the field is balanced by the rate of change produced by collisions:

$$dP_z/dt - neE_z = 0, \tag{1}$$

where n is the electron concentration, and dP_z/dt is the rate of change of momentum (per unit volume) produced by collisions, which can be calculated by transition probability theory if the distribution function $f(\boldsymbol{k})$ is known. For resistivity calculations it is well known that the distribution function can be taken to be

$$f(\boldsymbol{k}) = f_0(E_k) + aE_z \cos\theta \, df_0/dE_k, \tag{2}$$

where $f_0(E_k)$ is the equilibrium distribution, depending only on the electron energy E_k. The angle between $\boldsymbol{k}$ and the z axis is θ; and a can be taken to be a constant since only its value at the Fermi surface, k_0, enters when one calculates the current density,

$$j = neaE_z/\hbar k_0. \tag{3}$$

The electrical resistivity is evaluated immediately from equations (1) and (3) after equation (2) is employed for calculating dP_z/dt. The problem of this section is to perform the latter calculation for a pair of nearest neighbor solute spins, $\boldsymbol{S}_1$ and $\boldsymbol{S}_2$.

The Hamiltonian for an electron with spin $\boldsymbol{S}$ interacting with a pair of nearest neighbor solute ions at 0 and $\boldsymbol{R}$ will be taken to be the sum of the following two expressions:

$$H_0 = (p^2/2m) + U(\boldsymbol{r}) - W\boldsymbol{S}_1 \cdot \boldsymbol{S}_2, \tag{4}$$

$$H_1 = V(\boldsymbol{r}) + V(\boldsymbol{r}-\boldsymbol{R}) - 2J(\boldsymbol{r})\, \boldsymbol{s}\cdot\boldsymbol{S}_1 - \\ -2J(\boldsymbol{r}-\boldsymbol{R})\boldsymbol{s}\cdot\boldsymbol{S}_2. \tag{5}$$

$V(\boldsymbol{r})$ and $J(\boldsymbol{r})$ are the spin-independent and spin-dependent potentials of the solute–electron interaction, $U(\boldsymbol{r})$ is the periodic potential of the lattice, and W is the effective exchange interaction between solute spins. The energy levels of H_0 are:

$$E_I(\boldsymbol{k}) = E_k + W_I, \tag{6}$$

where,

$$W_I = \tfrac{1}{2}W[2S(S+1)-I(I+1)]. \tag{7}$$

Each solute pair energy level, W_I, is $(2I+1)$-fold degenerate; and I assumes integral values between 0 and $2S$.

In evaluating the various transitions caused by the perturbation (5), it is necessary in principle to specify the spin of the initial and final conduction electron states and to distinguish the distribution functions for spin-up and spin-down. However, since the spins of the paramagnetic pairs are randomly oriented, $f^+(k) = f^-(k)$, and the distinction may be neglected. The rate of change of momentum of the electron gas caused by elastic scattering $(I \to I)$ is:

$$\frac{dP}{dt} = \frac{4\pi}{N^2}\sum_{k,k'} q_z|1+\exp(-i\boldsymbol{q}\cdot\boldsymbol{R})|^2\delta(E_k-E_{k'})f(\boldsymbol{k})\times$$

$$\times[1-f(\boldsymbol{k}')]\sum_{I=0}^{2S} p_I \sum_{M=-I}^{I}\{|V_{\boldsymbol{k}\boldsymbol{k}'}+$$

$$+\tfrac{1}{2}MJ_{\boldsymbol{k}\boldsymbol{k}'}|^2+\tfrac{1}{4}(I-M)(I+M+1)|J_{\boldsymbol{k}\boldsymbol{k}'}|^2\}, \tag{8}$$

where $\boldsymbol{q} = \boldsymbol{k}'-\boldsymbol{k}$, N is the number of atoms per unit volume, $V_{\boldsymbol{k}\boldsymbol{k}'}$ and $J_{\boldsymbol{k}\boldsymbol{k}'}$ are the matrix elements of V and J between Bloch states normalized in an atomic volume, $\delta(E)$ is a delta function, and p_I is the probability that a given pair state of level W_I is occupied.

$$p_I = \exp(-W_I/kT)/\sum_{I=0}^{2S}(2I'+1)\exp(-W_{I'}/kT) \tag{9}$$

The first term in the brackets of equation (8) arises from scattering processes for which the conduction electron spin is not flipped, whereas the second term is associated with processes for which the spin is flipped. The corresponding expression for inelastic scattering $(I \to I\pm 1)$ is,

$$\frac{dP}{dt} = \frac{\pi}{N^2}\sum_{\boldsymbol{k},\boldsymbol{k}'} q_z|1-\exp(-i\boldsymbol{q}\cdot\boldsymbol{R})|^2 f(\boldsymbol{k})[1-f(\boldsymbol{k}')]\times$$

$$\times|J_{\boldsymbol{k}\boldsymbol{k}'}|^2\sum_{I=0}^{2S} p_I \sum_{M=-I}^{I}\Big\{\delta[E_I(\boldsymbol{k})-E_{I+1}(\boldsymbol{k}')]\times$$

$$\times\frac{(2I+3)(I+M+1)[(2S+1)^2-(I+1)^2]}{4(I+1)^2-1}+$$

$$+\delta[E_I(\boldsymbol{k})-E_{I-1}(\boldsymbol{k}')]\times$$

$$\times\frac{(2I-1)(I-M)[(2S+1)^2-I^2]}{4I^2-1}\Big\}. \tag{10}$$

One should notice the factors $|1\pm\exp(-i\boldsymbol{q}\cdot\boldsymbol{R})|^2$ in equations (8) and (10) because they account for the interference between the waves scattered by the two solute ions of a pair. If $\mathbf{q}\cdot\boldsymbol{R}$ is not too large, the interference is constructive for elastic scattering and destructive for inelastic scattering. In the last analysis it is just this behavior that allows the elastic scattering to predominate over the inelastic, and so produce a resistance minimum.

In order to evaluate expressions of the foregoing type it is customary to make the following approximations:

$$V_{\boldsymbol{k}\boldsymbol{k}'} \sim V(q);\quad J_{\boldsymbol{k}\boldsymbol{k}'} \sim J(q). \tag{11}$$

This step is almost always made for the sake of expediency, and cannot be considered more than a crude approximation. Equations (8) and (10) must be multiplied by N_p, the number of solute pairs per unit volume; and the interference factors must be averaged over all orientations of $\boldsymbol{R}$. After inserting expression (2) for the distribution function, the sums over $\boldsymbol{k}$, $\boldsymbol{k}'$ and M can be carried out, and the elastic and inelastic contributions to the electrical resistivity derived from equations (1) and (3). They are:

$$\rho_{\text{elastic}} = \alpha(A+\beta_+B_+), \tag{12}$$

$$\rho_{\text{inelastic}} = \alpha\beta_-B_- \tag{13}$$

where,

$$\alpha = m^2N_pk_0/\pi ne^2\hbar^3N^2, \tag{14}$$

$$A = \int_0^{\pi}|V(q)|^2[1+(\sin qR)/qR](1-\cos\theta)\sin\theta\,d\theta, \tag{15}$$

$$\beta_+ = \sum_{I=0}^{2S} p_I(2I+1)I(I+1)/4, \tag{16}$$

$$\beta_- = \sum_{I=1}^{2S} p_Ip_{I-1}I[(2S+1)^2-I^2]/(p_I+p_{I-1}), \tag{17}$$

$$B_\pm = \int_0^{\pi}|J(q)|^2[1\pm(\sin qR)/qR](1-\cos\theta)\sin\theta\,d\theta. \tag{18}$$

With regard to the integrations in definitions (15) and (18), it should be noted that q is a function of the scattering angle. The character of this functional dependence will be discussed in considerable detail below, and it will be concluded that the conventional choice is in fact not the correct one.

VOL. 15 1960

The temperature dependence of the resistivity is contained in the coefficients $\beta_{\pm}$. From equations (9), (16) and (17) their asymptotic forms at high and low temperatures can be easily derived. For high T:

$$\beta_+ \cong \tfrac{1}{2}S(S+1)[1 \pm WS(S+1)/3kT]; \tag{19}$$

and for low T with $W > 0$:

$$\beta_+ \cong \tfrac{1}{2}S(2S+1) - S[(4S-1)/(4S+1)] \times \times \exp(-2WS/kT), \tag{20}$$

$$\beta_- \cong 2S \exp(-2WS/kT); \tag{21}$$

whereas for low T with $W < 0$:

$$\beta_+ \cong 3/2 \exp(W/kT), \tag{22}$$

$$\beta \cong 4S(S+1) \exp(W/kT). \tag{23}$$

The net resistivity contribution arising from exchange scattering by pairs is, for high T,

$$\rho \cong \tfrac{1}{2}\alpha S(S+1) \times \times [B_+ + B_- + WS(S+1)(B_+ - B_-)/3kT]. \tag{24}$$

Consequently, if $W(B_+ - B_-) > 0$, the resistance will increase with decreasing temperature, and should yield a resistance minimum when added to the phonon resistance contribution.

Except for paramagnetic systems which become antiferromagnetic at low temperatures (e.g. Cu–Mn alloys), the anomalous resistance increase below the minimum appears to be monotonic all the way to $T = 0$.[1] The foregoing analysis implies then that $W > 0$; that is, the spins of a pair are ferromagnetically coupled. For if $W < 0$, the temperature dependence of definitions (22) and (23) would yield a decreasing resistance with decreasing temperature near $T = 0$. For $W > 0$, the temperature dependence of expressions (20) and (21) yields an increasing resistance with decreasing temperature near $T = 0$ only if

$$B_+/B_- > 2(4S+1)/(4S-1). \tag{25}$$

Furthermore, we have verified by numerical evaluation of equations (16) and (17) for intermediate temperatures that the resistance increase is monotonic everywhere below the minimum as long as the criterion (25) is satisfied. It is clear from definition (24) that a minimum is possible as long as $B_+/B_- > 1$, but a resistance maximum (below the minimum) would occur if expression (25) were not also satisfied.

3. QUANTITATIVE DISCUSSION OF THE MODEL

There remains the task of estimating the values of the parameters, W and $B_{\pm}$, which occur in the model described above, and deciding whether the quantitative magnitudes necessary for agreement with experiment can be justified on an *a priori* basis. Very little can be said theoretically regarding the value of W. Experimentally $W \sim 20°\text{K}$. Mechanisms which contribute to W are direct overlap of the localized paramagnetic orbitals and pseudo-exchange interactions (via *s–d* exchange interactions), as treated by Yosida[7]. The latter calculation considers an idealized problem, and one cannot expect it to be quantitatively reliable for a real situation, for which one cannot neglect *s–s* exchange interactions and the finite size of the paramagnetic orbitals, for example.

The magnitudes of B_+ and B_- determine the size of the anomalous resistance increase below the minimum, which is:

$$\Delta\rho = \tfrac{1}{2}\alpha S[SB_+ - (S+1)B_-]. \tag{26}$$

For a $\frac{1}{2}\%$ Cu–Co alloy, $\Delta\rho \sim 0{\cdot}01\mu\,\Omega\,\text{cm}$. Equation (26) yields this magnitude provided the average *s–d* exchange matrix element, $\bar{J}$, defined by

$$\bar{J}^2 = \frac{1}{2}\int_0^{\pi} |J(q)|^2(1-\cos\theta)\sin\theta\, d\theta = \tfrac{1}{4}(B_+ + B_-) \tag{27}$$

has a value, $\sim 0{\cdot}3$ eV. This figure equals the magnitude of the *s–d* exchange interaction constant of a transition element ion. Consequently it appears at first sight that the model is satisfactory. However, a real difficulty arises when one tries to satisfy equation (25) and at the same time maintain the value of definition (27). This problem can be appreciated by considering the integrals (18) which define $B_{\pm}$.

In order that B_+/B_- be large enough to satisfy expression (25), it is necessary that the factor $(\sin qR)/qR$ be positive and not too small ($> \sim \frac{1}{3}$) for *most* of the integration. In the free electron approximation it is appropriate to take,

$$q = 2k_0 \sin(\theta/2). \tag{28}$$

Then, $\sin qR$ becomes negative for scattering angles greater than 54°. Consequently $J(q)$ must fall off quickly with increasing q so as to allow the predominance of small angle scattering. (It is true that $\sin qR$ becomes positive again for angles greater than 130°, but $\sin qR/qR$ remains very small for large angle scattering.) Although one can easily satisfy equation (25) by choosing $J(q)$ so as to allow only small angle scattering, the total effective cross section in expression (27) is seriously reduced (by two orders of magnitude) if $J(0)$ is left unchanged.

The foregoing difficulty can be alleviated by the following considerations which are pertinent to all calculations of scattering by lattice imperfections. In real life one is always interested in the scattering between two Bloch states $\psi_{\boldsymbol{k}}$ and $\psi_{\boldsymbol{k}'}$ caused by a perturbation, say $J(\boldsymbol{r})$. The wave functions have the usual form,

$$\psi_{\boldsymbol{k}} = \exp(i\boldsymbol{k}\cdot\boldsymbol{r})u_{\boldsymbol{k}}(\boldsymbol{r}). \tag{29}$$

In calculating matrix elements of $J(\boldsymbol{r})$ it is customary to neglect the variation of $u_{\boldsymbol{k}}(\boldsymbol{r})$ with $\boldsymbol{k}$, if not to neglect $u_{\boldsymbol{k}}(\boldsymbol{r})$ altogether. In principle one can expand $u_{\boldsymbol{k}'}(\boldsymbol{r})$ in a power series in $\boldsymbol{q}=\boldsymbol{k}'-\boldsymbol{k}$ and neglect, perhaps, the linear term in $\boldsymbol{q}$. Such an approximation may be adequate as long as $\boldsymbol{q}$ is small. Now, it is well known that Bloch states are periodic in $\boldsymbol{k}$ space, and that all states $\psi_{\boldsymbol{K}}$ are *identical* to $\psi_{\boldsymbol{k}}$, for the set of $\boldsymbol{K}$ which satisfy

$$\boldsymbol{K}=\boldsymbol{k}+2\pi\boldsymbol{G}, \tag{30}$$

$\boldsymbol{G}$ being the reciprocal lattice vectors. Therefore, in performing a scattering calculation in which the above mentioned approximations are made, one should examine all equivalent final state wave vectors $\boldsymbol{K}'$ and pick that $\boldsymbol{K}'$ for a given scattering event which makes

$$\boldsymbol{K}'-\boldsymbol{k}=\boldsymbol{q}+2\pi\boldsymbol{G} \tag{31}$$

have the smallest magnitude. We shall define this smallest vector, $\boldsymbol{K}'-\boldsymbol{k}=\boldsymbol{q}_0$. It is interesting to know that for a monovalent metal such as Cu, q_0 is smaller than q for about $\frac{2}{3}$ of the scattering events.

We should like to emphasize that if one were calculating matrix elements with exact Bloch functions, it would not matter which $\boldsymbol{K}'$ is chosen to represent the final state. However, if one is going to use the Fourier transform $J(\boldsymbol{q})$ of $J(\boldsymbol{r})$ as the matrix element of the scattering event $\boldsymbol{q}$, one should always use $J(\boldsymbol{q}_0)$ instead of $J(\boldsymbol{q})$. (It may be noted that q_0 is a continuous function of q, so that the scattering probability remains a continuous function of angle.) The importance of this procedure with regard to quantitative answers may be easily understood. In a monovalent metal many areas of the Fermi surface are close to the Brillouin zone boundary. States corresponding to velocity reversal (180° scattering) are only a small wave vector distance away in the direction of the zone face, whereas they are $2k_0$ away by the usual description. A scattering potential whose range is not too short will have a Fourier transform that falls off rapidly with increasing q. Consequently it is essential that q_0 be used in order to obtain proper account of large angle scattering events, especially since they are the important ones in a resistivity calculation.

The authors are aware that the foregoing remarks call into question the quantitative significance of most previous calculations of scattering arising from lattice imperfections in metals. They make no pretense that the suggested improvements will adequately approach the results of a "correct" calculation. But they submit that the proposed treatment incorporates contributions from large angle scattering that have frequently been overlooked.

Returning now to the problem of the resistance minimum, one should replace q by q_0 in the integrals (15) and (18). The indicated summations were carried out with a digital computor by considering all scattering events between (100), (110), (111) and (123) type wave vectors. The function,

$$J(q_0)=J(0)/(1+\lambda^2 q_0^2), \tag{32}$$

was used for matrix elements of the *s–d* exchange interaction. It was found possible to satisfy expression (25) with $\lambda\sim$ lattice constant; and the magnitude of definition (27) could be retained if $J(0)\sim 1$ eV. Such values of λ and $J(0)$ are not unreasonable. It must be remembered that the scattering center is a paramagnetic orbital *together* with a conduction electron spin density readjustment. The *s–d* exchange interaction attracts conduction electrons of spin parallel to that of the *d* orbitals into their locality, and the (attractive) *s–s* exchange interaction amplifies this effect by an appreciable factor. The effective ("renormalized")

VOL. 15 1960

s–d exchange interaction includes not only the "bare" *s–d* exchange interaction, but also an *s–s* contribution from scattering by the conduction electron spin density readjustment. Since the *s–s* exchange interaction of a free electron gas is ~ 5 eV /electron, a value for $J(0)$ of ~ 1 eV does not seem inordinately large.

We conclude that the present theory of the resistance minimum in dilute paramagnetic alloys can yield quantitative agreement with experiment without too much strain on the imagination.

4. EFFECTS OF SCATTERING BY SINGLE IONS

Multiple clusters of paramagnetic solute ions should modify the quadratic dependence of the resistance minimum at high solute concentrations. However, one would not expect such effects to be important for $c \sim 1$ per cent, where indeed the c^2 dependence appears to break down in the case of Cu–Co alloys.[8] This failure can be attributed to long range spin dependent interactions between isolated solute ions, which split the magnetic egeneracy of solute levels and reduce thereby the inelastic contribution of spin disorder scattering when the temperature is smaller than the characteristic splitting. We shall estimate this splitting by assuming the pseudo-exchange interaction between any two solute spins $\boldsymbol{S}_1$ and $\boldsymbol{S}_2$ to be

$$H = W_0 \exp(-r_{12}/\lambda)\boldsymbol{S}_1 \cdot \boldsymbol{S}_2. \tag{33}$$

(The oscillatory distance dependence ascribed to this interaction by YOSIDA[7] arises by imposing an abrupt cut off in certain integrations instead of allowing $J(q)$ to be a smoothly diminishing function with increasing q. If a smooth $J(q)$ is employed, we find the interaction to have approximately the form given in equation (33).) For a random distribution of solute spins the root mean square splitting of adjacent magnetic states is,

$$\bar{W}^2 = W^2 cS(S+1)\sum_n{}' \exp[2(R-r_n)/\lambda], \tag{34}$$

where the prime on the summation sign indicates that the nearest neighbors are excluded from the sum over all neighbors (at distance r_n) of a given ion. W is the nearest neighbor interaction constant, as defined by equation (4), and R the nearest neighbor distance. The parameter λ is essentially the same as that employed in equation (32). The summation is easily evaluated numerically and has a value ~ 4. Consequently,

$$\bar{W} \sim 2W[cS(S+1)]^{1/2}. \tag{35}$$

For a 1% alloy with S = 5/2, $\bar{W} \sim 0{\cdot}6W$, which should be compared with the splitting $5W$ between the $I = 2S$ and $I = 2S-1$ levels of a nearest neighbor pair.

The spin disorder scattering arising from "isolated" ions is given by,

$$\rho = \gamma \bar{J}^2 S[S+1-B_S(\bar{W}/kT)\tanh(\bar{W}/2kT)], \tag{36}$$

where $\gamma = \alpha cN/N_p$ and $B_S(x)$ is the standard Brillouin function. (The second term in expression (36) differs from that which would obtain were $\bar{W}$ caused by an applied magnetic field, because it is assumed here that the effective fields associated with $\bar{W}$ are randomly oriented.) Since $B_S(x)$ and $\tanh(x)$ are both increasing functions of x, this resistivity contribution decreases with decreasing temperature. Fortunately this decrease does not cancel the increase derived previously for nearest neighbor pairs. The high temperature expansion of equation (36) is

$$\rho \cong \gamma \bar{J}^2 S(S+1)[1-1/6(\bar{W}/kT)^2], \tag{37}$$

which varies quadratically with $\bar{W}/kT$. The corresponding result, equation (24), for the contribution from nearest neighbor pairs varies linearly with W/kT, so that a resistance minimum phenomenon will remain. However, the increase in $\bar{W}$ with c causes the low temperature effects of expression (36) to move to higher temperature so as to diminish the total size of the minimum. Quantitative estimates of definition (36) indicate that departure of the minimum from its c^2 dependence in the 1% range can be explained.

REFERENCES

1. GERRITSEN A. N., *Physica, s'Grav.* **25,** 489 (1959).
2. PEARSON W., RIMEK D. and TEMPLETON I., *Phil. Mag.* **4,** 612 (1959).
3. KORRINGA J. and GERRITSEN A. N., *Physica, s'Grav.* **19,** 457 (1953).
4. SCHMITT R. W., *Phys. Rev.* **103,** 83 (1956).
5. YOSIDA K., *Phys. Rev.* **107,** 396 (1957).
6. BRAILSFORD A. D. and OVERHAUSER A. W., *Phys. Rev. Letters* **3,** 331 (1959).
7. YOSIDA K., *Phys. Rev.* **106,** 893 (1957).
8. JACOBS I. S. and SCHMITT R. W., *Phys. Rev.* **113,** 459 (1959).

J. Phys. Chem. Solids Pergamon Press 1960. Vol. 15. pp. 146–151. Printed in Great Britain.

GROUP THEORY OF SCATTERING PROCESSES IN CRYSTALS

R. J. ELLIOTT and R. LOUDON

Clarendon Laboratory, Oxford

(*Received* 12 *November* 1959)

Abstract—A general method is given for determining selection rules for scattering of various types in crystals by using the properties of space groups. The method is particularly useful for those lattices which contain screw axes or glide planes and diamond is considered in detail. Examples of particular kinds of selection rule which are of interest in silicon and germanium are examined.

1. INTRODUCTION

THERE are many problems in the theory of solids, where the discussion is helped by the consideration of the symmetry properties introduced by the periodicity of the lattice. The group theory associated with this periodic symmetry has been developed by several authors[1–5]. Every disturbance in the lattice, e.g. electrons in the one-particle band approximation, vibrations, spin waves, is propagated from cell to cell like a wave of a certain wave vector $\mathbf{k}$ which lies within the first Brillouin zone.

In considering the properties of states of a particular $\mathbf{k}$ it has been shown[2] to be useful to consider that subgroup G^k of operations of the crystal lattice space group, which leaves $\mathbf{k}$ invariant or changes it by a reciprocal lattice vector. At points of high symmetry in the Brillouin zone, G^k contains some of the operations other than translations (rotations, glide or screw displacements) and from its irreducible representations useful information can be obtained about the eigenfunctions. Since band extrema frequently occur at such points, important physical properties often depend on these states, and the group theory proves useful.

2. CHARACTER TABLES

The subgroup G^k will always contain all the pure translations of the space group $(\epsilon|t)$. SEITZ'S[1] notation is employed, where the first symbol defines the rotation (here the unit element) and the second the translation vector. In irreducible representations of G^k appropriate to a wave-function having momentum eigenvalue $\hbar\mathbf{k}$ the character of $(\epsilon|t)$ is equal to $\exp(i\mathbf{k}.\mathbf{t})$ multiplied by the dimension of the irreducible representation. For many of the pure translations in the group of the crystal lattice $\exp(i\mathbf{k}.\mathbf{t})$ is unity when $\mathbf{k}$ is the wave-vector of a symmetry point in the Brillouin zone. The translations which have this property form an invariant subgroup T^k, say, of G^k. Hence all the irreducible representations of G^k for which the character associated with every translation in T^k is equal to the dimension of the irreducible representations may be obtained by considering the factor group G^k/T^k. The characters of the irreducible representations of G^k/T^k can be calculated in the usual way, using the relation between class multiplication and character multiplication[3]. The character table thus obtained will be square, i.e. the number of irreducible representations is equal to the number of classes of conjugate operations in G^k/T^k. However, except for the group of $\mathbf{k} = 0$, for which case alone G^k/T^k contains no pure translations, not all the irreducible representations satisfy the requirement that the character of $(\epsilon|t')$ is $\exp(i\mathbf{k}.\mathbf{t}')$ times the dimension of the representation, where $(\epsilon|t')$ is in G^k/T^k. That this must be so can be seen as follows. The product of two irreducible representations of G^k/T^k must be expressible as a linear sum of such representations and the corresponding characters must satisfy the same equation as the representations for every

VOL. 15 1960

class of the group. In general there must be irreducible representations in which the character of $(\epsilon|t')$ is $\exp(i\mathbf{k}'\cdot\mathbf{t}')$ times the dimension of the representation, where $\mathbf{k}' = n\mathbf{k}$ and n is any integer. We shall refer to an irreducible representation of G^k/T^k of this kind as corresponding to, or being associated with, the wave-vector $\mathbf{k}'$. For symmetry points $\mathbf{k}$ in the Brillouin zone there is some small integer n for which $n\mathbf{k}$ differs from $\mathbf{k}$ by a reciprocal lattice vector so that in this case the number of irreducible representations is limited, corresponding to the fact that the number of classes of G^k/T^k is finite for points of symmetry. Previously published tables have given only the characters of the irreducible representations of G^k/T^k associated with wave-vector $\mathbf{k}$. We shall see that in dealing with scattering processes it is frequently convenient to know the characters of the other irreducible representations of G^k/T^k.

For wave-vectors corresponding to general points in the zone including those on symmetry lines, it is clear that there must be an infinite number of irreducible representations since there is an infinite number of non-equivalent $\mathbf{k}$-vectors. This is consistent with the fact that G^k/T^k is a direct product of a group containing an infinite number of pure translations, and a subgroup of G^k containing the rotation elements. The representations fall into sets corresponding to particular $\mathbf{k}'$ which only differ in that $\exp(i\mathbf{k}'\cdot\mathbf{t})$ appears in the character of $(\alpha|t)$.

For the cubic bravais lattices every G^k/T^k is a direct product of a group of pure translations with a point group and the construction of the character table from that of the point group is trivial. The diamond lattice considered by HERRING[3] is however more complicated. The factor group for the symmetry point Γ ($\mathbf{k} = 0$) contains no pure translations and all the irreducible representations correspond to zero wave-vector. For a point having L symmetry, such as $\mathbf{k}_L = (\frac{1}{2}, \frac{1}{2}, \frac{1}{2})2\pi/a$, doubling the $\mathbf{k}$-vector gives a point equivalent to $\mathbf{k} = 0$ and trebling it gives an L point equivalent to the original one. The factor group for L therefore has irreducible representations corresponding to two different wave-vectors. The structure of the character table is particularly simple in this case, for G^{k_L}/T^{k_L} is a direct product of a group of pure translations with a point group, and the characters can be easily constructed from the L point group table in Ref. (2). The only pure translation is $(\epsilon|t_{xy})$ and the character of an operation $(\alpha|t_{xy})$ is the same as that of $(\alpha|0)$ for irreducible representations corresponding to $\mathbf{k} = 0$, and is the negative of this quantity for irreducible representations corresponding to $\mathbf{k}_L = (\frac{1}{2}, \frac{1}{2}, \frac{1}{2})2\pi/a$. There are twelve classes and twelve irreducible representations.

Now consider a point having X symmetry in the diamond structure Brillouin zone, e.g., $\mathbf{k}_X = (0, 0, 1)2\pi/a$. The point $2\mathbf{k}_X$ is equivalent to $\mathbf{k} = 0$ and $3\mathbf{k}_X$ is equivalent to $\mathbf{k}_X$ so that there are again irreducible representations corresponding to two different wave-vectors. However, the group

Table 1. *Complete character table of group G^X/T^X in the diamond lattice*

32	14 classes	${}^1X_1$	${}^1X_2$	${}^1X_3$	${}^1X_4$	${}^2X_1^+$	${}^2X_2^+$	${}^2X_3^+$	${}^2X_4^+$	${}^2X_5^+$	${}^2X_1^-$	${}^2X_2^-$	${}^2X_3^-$	${}^2X_4^-$	${}^2X_5^-$
1	$(\epsilon\|0)$	2	2	2	2	1	1	1	1	2	1	1	1	1	2
1	$(\epsilon\|t_{zx})$	−2	−2	−2	−2	1	1	1	1	2	1	1	1	1	2
4	$(\delta_{2x}, \delta_{2y}\|0, t_{zx})$	0	0	0	0	1	−1	1	−1	0	1	−1	1	−1	0
1	$(\delta_{2z}\|0)$	2	2	−2	−2	1	1	1	1	−2	1	1	1	1	−2
1	$(\delta_{2z}\|t_{zx})$	−2	−2	2	2	1	1	1	1	−2	1	1	1	1	−2
4	$(\delta_{4z}, \delta_{4z}^{-1}\|\tau, \tau+t_{zx})$	0	0	0	0	1	1	−1	−1	0	1	1	−1	−1	0
2	$(\delta_{2xy}\|\tau)(\delta_{2\bar{x}y}\|\tau+t_{zx})$	0	0	2	−2	1	−1	−1	1	0	1	−1	−1	1	0
2	$(\delta_{2xy}\|\tau+t_{zx})(\delta_{2\bar{x}y}\|\tau)$	0	0	−2	2	1	−1	−1	1	0	1	−1	−1	1	0
2	$(i\|\tau, \tau+t_{zx})$	0	0	0	0	1	1	1	1	2	−1	−1	−1	−1	−2
4	$(\rho_x, \rho_y\|\tau, \tau+t_{zx})$	0	0	0	0	1	−1	1	−1	0	−1	1	−1	1	0
2	$(\rho_z\|\tau, \tau+t_{zx})$	0	0	0	0	1	1	1	1	−2	−1	−1	−1	−1	2
4	$(\sigma_{4z}, \sigma_{4z}^{-1}\|0, t_{zx})$	0	0	0	0	1	1	−1	−1	0	−1	−1	1	1	0
2	$(\rho_{xy}, \rho_{\bar{x}y}\|0)$	2	−2	0	0	1	−1	−1	1	0	−1	1	1	−1	0
2	$(\rho_{xy}, \rho_{\bar{x}y}\|t_{zx})$	−2	2	0	0	1	−1	−1	1	0	−1	1	1	−1	0

G^{k_X}/T^{k_X} is not a direct product of a group of pure translations with a point group and the characters must be determined from first principles. Table 1 gives the characters for this group, drawn from tables in Refs. (2) and (3). The preceding superscript attached to the symbol denoting a given representation is the multiple of $\mathbf{k}_X$ to which the representation corresponds. A group having a character table with a somewhat more complicated structure is that of a symmetry point W, say $\mathbf{k}_W = (0, -1, \frac{1}{2})2\pi/a$. The point $2\mathbf{k}_W$ has X symmetry, $3\mathbf{k}_W$ is again a W point but not equivalent to the original one, $4\mathbf{k}_W$ is a point of Γ symmetry and $5\mathbf{k}_W$ is a W point equivalent to the one we started with. The factor group G^{k_W}/T^{k_W} therefore has irreducible representations corresponding to four different wave-vectors, and the characters are set out in Table 2. It is worth remarking that in the block of a character table corresponding to $\mathbf{k} = 0$ the characters are just those of the point group formed from the rotational parts of the transformations of G^k/T^k, a factor unity being associated with the translational parts of the transformations. Thus the characters in the part of the W table corresponding to $4\mathbf{k}_W$ are those of the point group D_{2d}.

3. SELECTION RULES IN A SCATTERING PROCESS

In a scattering process several particles or energy quanta are involved and these may have different $\mathbf{k}$-vectors. Group theory can only give useful information about the scattering matrix elements if all the $\mathbf{k}$-vectors involved correspond to symmetry points or symmetry lines in the Brillouin zone, so we restrict our considerations to these cases. In some types of process all the $\mathbf{k}$-vectors appearing in the initial and final states of the system are the same, or nearly the same, and the group theory of the problem can be worked out in the standard way. However, in general the n wave-functions required for calculating scattering matrix elements have different $\mathbf{k}$-vectors, which we denote by $\mathbf{k}_1, \mathbf{k}_2, \ldots \mathbf{k}_n$, and the transformations which leave the Hamiltonian of the problem invariant are those common to all the space groups $G^{k_1}, G^{k_2}, \ldots G^{k_n}$. Let the group formed from these transformations, i.e. the intersection of $G^{k_1}, G^{k_2} \ldots G^{k_n}$, be G^{k_s} and let the intersection of the associated invariant subgroups of pure translations $T^{k_1}, T^{k_2}, \ldots T^{k_n}$ be T^{k_s}. To treat the scattering process it is clear that we should work in terms of the irreducible representations of the factor group

Table 2. Complete character table of group G^W/T^W in the diamond lattice

32	14 classes	${}^1W_1$	${}^1W_2$	${}^2W_1$	${}^2W_2$	${}^2W_3$	${}^2W_4$	${}^2W_5$	${}^3W_1$	${}^3W_2$	${}^4W_1$	${}^4W_2$	${}^4W_3$	${}^4W_4$	${}^4W_5$
1	$(\epsilon\|0)$	2	2	1	1	1	1	2	2	2	1	1	1	1	2
1	$(\epsilon\|t_{xy})$	−2	−2	1	1	1	1	2	−2	−2	1	1	1	1	2
1	$(\epsilon\|t_{yz})$	$-2i$	$-2i$	−1	−1	−1	−1	−2	$2i$	$2i$	1	1	1	1	2
1	$(\epsilon\|t_{zx})$	$2i$	$2i$	−1	−1	−1	−1	−2	$-2i$	$-2i$	1	1	1	1	2
2	$(\delta_{2z}\|0)\ (\delta_{2z}\|t_{xy})$	0	0	−1	−1	−1	−1	2	0	0	1	1	1	1	−2
2	$(\delta_{2z}\|t_{yz})\ (\delta_{2z}\|t_{zx})$	0	0	1	1	1	1	−2	0	0	1	1	1	1	−2
4	$(\delta_{2xy}\|\tau, \tau+t_{xy})$ $(\delta_{2\bar{x}y}\|\tau+t_{yz}, \tau+t_{zx})$	0	0	−1	−1	1	1	0	0	0	1	−1	1	−1	0
4	$(\delta_{2\bar{x}y}\|\tau, \tau+t_{xy})$ $(\delta_{2xy}\|\tau+t_{yz}, \tau+t_{zx})$	0	0	1	1	−1	−1	0	0	0	1	−1	1	−1	0
2	$(\sigma_{4z}\|0)\ (\sigma_{4z}^{-1}\|t_{yz})$	$(1-i)$	$-(1-i)$	$-i$	i	$-i$	i	0	$(1+i)$	$-(1+i)$	1	1	−1	−1	0
2	$(\sigma_{4z}\|t_{xy})\ (\sigma_{4z}^{-1}\|t_{zx})$	$-(1-i)$	$(1-i)$	$-i$	i	$-i$	i	0	$-(1+i)$	$(1+i)$	1	1	−1	−1	0
2	$(\sigma_{4z}\|t_{yz})\ (\sigma_{4z}^{-1}\|t_{xy})$	$-(1+i)$	$(1+i)$	i	$-i$	i	$-i$	0	$-(1-i)$	$(1-i)$	1	1	−1	−1	0
2	$(\sigma_{4z}\|t_{zx})\ (\sigma_{4z}^{-1}\|0)$	$(1+i)$	$-(1+i)$	i	$-i$	i	$-i$	0	$(1-i)$	$-(1-i)$	1	1	−1	−1	0
4	$(\rho_x\|\tau, \tau+t_{xy})\ (\rho_y\|\tau+t_{yz}, \tau+t_{zx})$	0	0	i	$-i$	$-i$	i	0	0	0	1	−1	−1	1	0
4	$(\rho_y\|\tau, \tau+t_{xy})\ (\rho_x\|\tau+t_{yz}, \tau+t_{zx})$	0	0	$-i$	i	i	$-i$	0	0	0	1	−1	−1	1	0

G^{k_s}/T^{k_s}. Note that this group is not necessarily the factor group associated with one of the symmetry points of the Brillouin zone. The irreducible representations of the factor groups G^{k_1}/T^{k_1}, ... G^{k_n}/T^{k_n} corresponding to the n wave-functions under consideration must then be reduced into irreducible representations of the factor group G^{k_s}/T^{k_s}. We therefore require the irreducible representations of G^{k_s}/T^{k_s} corresponding to the wave-vectors $\mathbf{k}_1, \mathbf{k}_2, \ldots . \mathbf{k}_n$, and also to their sum (for a momentum conserving process $\mathbf{k}_1+\mathbf{k}_2+ \ldots +\mathbf{k}_n = 0$). With the symmetry properties of all the wave-functions expressed in terms of the irreducible representations of a single group, the group theory of the scattering process may be worked out by the usual methods. For example, if the process is to be allowed the direct product of the irreducible representations associated with all the wave-functions and interactions involved in the scattering matrix element must contain the scalar representation, i.e. that representation of G^{k_s}/T^{k_s} whose characters are all unity.

4. EXAMPLES

(a) *Optical absorption section rules at* X

We are here concerned with the matrix element of the electron–photon interaction between two electron wave functions corresponding to X. Since the wave vector of the photon is virtually zero the interaction transforms like a vector. This can be decomposed into representations of G^X/T^X with $\mathbf{k} = 0$, in fact ${}^2X_2^-$ and ${}^2X_5^-$ in Table 1. The π transitions for the polarization along z require that ${}^1X_A \times {}^1X_B \times {}^2X_2^-$ contains ${}^2X_1^+$, the scalar representasentation. ${}^1X_1 \to {}^1X_1$, ${}^1X_2 \to {}^1X_2$ and ${}^1X_3 \to {}^1X_4$ are allowed. For σ polarization ${}^1X_1$, ${}^1X_2 \to {}^1X_3$, ${}^1X_4$.

(b) *Scattering from* Γ *to* X

The probability of scattering an electron or hole between the positions of the extrema in the valence and conduction bands is important in the discussion of indirect optical absorption.[6] In silicon the conduction band minima are close to X and the valence band maximum is at Γ, so that it is instructive to consider electron scattering in the lowest conduction band from Γ_{15} to ${}^1X_1$. The product of $\Gamma_{15} = {}^2X_2^- + {}^2X_5^-$ with ${}^1X_1$ and the phonon representations must contain ${}^2X_1^+$ if scattering is allowed. The longitudinal acoustic (LA) and optic (LO) phonons transform like ${}^1X_1$, transverse acoustic (TA) like ${}^1X_3$ and the transverse optic (TO) like ${}^1X_4$; and scattering is allowed for all. At Δ, where the conduction band minima are actually located in silicon, a similar analysis shows that the TA(Δ_5), TO(Δ_5) and LA(Δ_1) phonons can scatter but not the LO(Δ_2') phonons. This latter can, however, occur in the hole scattering in, for example, the highest valence band[7] from Γ_{25}' to Δ_5. Thus there is no group theory selection rule to account for the absence of a contribution from the longitudinal phonons to the indirect absorption and emission in silicon.[8]

(c) *Scattering from* L *to* L

In germanium the electron valleys are at the points L so that the selection rules for scattering from one valley to another are determined largely by scattering from L to L by phonons of type X. The effect of this inter-valley scattering on transport properties has been considered by HERRING[9] and others. The character table for the intersection group when L is $\pi/a(1, 1, 1)$, L′ is $\pi/a(1, 1, -1)$ and X is $2\pi/a(0, 0, 1)$ is given in Table 3. For the three

Table 3. Character table of intersection of groups of $L=\pi/a(1,1,1)$, $L'=\pi/a(-1-1\,1)$ *and* $X=2\pi/a(0,0,1)$

16	16 classes	${}^\Gamma A_1$	${}^\Gamma A_2$	${}^\Gamma A_3$	${}^\Gamma A_4$	${}^L A_i$	${}^{L'} A_i$	${}^X A_i$
1	$(\epsilon\|0)$	1	1	1	1	$\chi({}^\Gamma A_i)$	$\chi({}^\Gamma A_i)$	$\chi({}^\Gamma A_i)$
1	$(\delta_{2\bar{x}y}\|\tau)$	1	−1	−1	1			
1	$(i\|\tau)$	1	1	−1	−1			
1	$(\rho_{\bar{x}y}\|0)$	1	−1	1	−1			
4	$(\alpha\|a)\times(\epsilon\|t_{\bar{z}})$	$\chi(\alpha\|a)$				$\chi({}^\Gamma A_i)$	$-\chi({}^\Gamma A_i)$	$-\chi({}^\Gamma A_i)$
4	$(\alpha\|a)\times(\epsilon\|t_{zx})$	$\chi(\alpha\|a)$				$-\chi({}^\Gamma A_i)$	$\chi({}^\Gamma A_i)$	$-\chi({}^\Gamma A_i)$
4	$(\alpha\|a)\times(\epsilon\|t_{xy})$	$\chi(\alpha\|a)$				$-\chi({}^\Gamma A_i)$	$-\chi({}^\Gamma A_i)$	$\chi({}^\Gamma A_i)$

phonon types the decomposition is $\mathrm{X}_1 = {}^{\mathrm{X}}A_1 + {}^{\mathrm{X}}A_3$, $\mathrm{X}_3 = {}^{\mathrm{X}}A_2 + {}^{\mathrm{X}}A_3$, $\mathrm{X}_4 = {}^{\mathrm{X}}A_1 + {}^{\mathrm{X}}A_4$, while for the two band extrema one $\mathrm{L}_1^+ = {}^{\mathrm{L}}A_1$ and the other $\mathrm{L}_1'^+ = {}^{\mathrm{L}'}A_1$. On forming the products it is seen that scattering by X_1 (longitudinal) and X_4(TO) phonons is allowed but not by X_3 (TA) phonons.

(d) *Scattering from* Δ *to* Δ

In silicon the inter-valley scattering is by Σ phonons between two valleys at Δ chosen along the x and y axes. The intersection group contains only $(\epsilon|0)$ and $(\rho_z|\tau)$ and the pure translations. There are therefore only two kinds of representation which are even or odd with regard to the reflection,

(e) *Excitons at* X

The group theoretical discussion of exciton states in the effective mass approximation has been given recently by LOUDON and MCLEAN[10]. The exciton wave functions are products of electron and hole Bloch functions in conduction and valence bands, together with a function describing the relative motion of the pair of particles. This function of $\mathbf{r}_e - \mathbf{r}_h$ is unaffected by lattice translations but is invariant under the rotations etc. which appear in the group of X. Thus it is correctly described by an irreducible representation of the group of X corresponding to $\mathbf{k} = 0$. An exciton built from a hole in the valence band at Γ and an

Table 4. *Character table of intersection of the three groups of* X

32	14 classes	$^{x}\mathrm{X}_1$	$^{x}\mathrm{X}_2$	$^{y}\mathrm{X}_1$	$^{y}\mathrm{X}_2$	$^{z}\mathrm{X}_1$	$^{z}\mathrm{X}_2$	$^{0}\mathrm{X}_1^+$	$^{0}\mathrm{X}_2^+$	$^{0}\mathrm{X}^+$	$^{0}\mathrm{X}^+$	$^{0}\mathrm{X}_1^-$	$^{0}\mathrm{X}^-$	$^{0}\mathrm{X}^-$	$^{0}\mathrm{X}_-$
1	$(\epsilon\|0)$	2	2	2	2	2	2	1	1	1	1	1	1	1	1
1	$(\epsilon\|t_{yz})$	2	2	−2	−2	−2	−2	1	1	1	1	1	1	1	1
1	$(\epsilon\|t_{zx})$	−2	−2	2	2	−2	−2	1	1	1	1	1	1	1	1
1	$(\epsilon\|t_{xy})$	−2	−2	−2	−2	2	2	1	1	1	1	1	1	1	1
2	$(\delta_{2x}\|0, t_{yz})$	2	−2	0	0	0	0	1	1	−1	−1	1	1	−1	−1
2	$(\delta_{2x}\|t_{zx}, t_{xy})$	−2	2	0	0	0	0	1	1	−1	−1	1	1	−1	−1
2	$(\delta_{2y}\|0, t_{zx})$	0	0	2	−2	0	0	1	−1	1	−1	1	−1	1	−1
2	$(\delta_{2y}\|t_{xy}, t_{yz})$	0	0	−2	2	0	0	1	−1	1	−1	1	−1	1	−1
2	$(\delta_{2z}\|0, t_{xy})$	0	0	0	0	2	−2	1	−1	−1	1	1	−1	−1	1
2	$(\delta_{2z}\|t_{xz}, t_{yz})$	0	0	0	0	−2	2	1	−1	−1	1	1	−1	−1	1
4	$(i\|\tau, \tau+t_{yz}, \tau+t_{zx}, \tau+t_{xy})$	0	0	0	0	0	0	1	1	1	1	−1	−1	−1	−1
4	$(\rho_x\|\tau, \tau+t_{yz}, \tau+t_{zx}, \tau+t_{xy})$	0	0	0	0	0	0	1	1	−1	−1	−1	−1	1	1
4	$(\rho_y\|\tau, \tau+t_{yz}, \tau+t_{zx}, \tau+t_{xy})$	0	0	0	0	0	0	1	−1	1	−1	−1	1	−1	1
4	$(\rho_z\|\tau, \tau+t_{yz}, \tau+t_{zx}, \tau+t_{xy})$	0	0	0	0	0	0	1	−1	−1	1	−1	1	1	−1

and these pairs of representations exist with all values of $\mathbf{k}$. The valleys in silicon have wavefunctions belonging to Δ_1 and the vibrations are Σ_1 (LA); Σ_3 and Σ_4 (TA); Σ_3 (LO); and Σ_1 and Σ_2 (TO). Only Σ_1 and Σ_4 phonons can scatter. Since the minima are close to X the scattering between X points $2\pi/a(1, 0, 0)$ and $2\pi/a(0, 1, 0)$ by an X phonon at $2\pi/a$ (0, 0, 1) has been considered. The intersection group G/T is now larger and the characters are given in Table 4. Again the representations are of different $\mathbf{k}$ types, corresponding to the three X points and to $\mathbf{k} = 0$. On constructing products it is readily seen that all phonons give scattering between any pair of representations of the two points—and there is no destructive selection rule.

electron at X will have representations built from the product of representations $\Gamma_i \times {}^{1}\mathrm{X}_j \times {}^{2}\mathrm{X}_l$. Γ_i can be decomposed into ${}^{2}\mathrm{X}_m$ representations and the whole written as a sum of ${}^{1}\mathrm{X}_n$ representations describing the whole exciton state. In silicon, if the conduction band minimum were at the edge where states are like ${}^{1}\mathrm{X}_1$ and the valence maximum is like $\Gamma_{25}' = {}^{2}\mathrm{X}_2^+ + {}^{2}\mathrm{X}_5^+$, the exciton states with relative motion like ${}^{2}\mathrm{X}_1^+$, which are likely to be lowest, have possible symmetries ${}^{1}\mathrm{X}_2$, ${}^{1}\mathrm{X}_3$ and ${}^{1}\mathrm{X}_4$.

REFERENCES

1. SEITZ F., *Ann. Math.* **37,** 17 (1936).
2. BOUCKAERT L. P., SMOLUCHOWSKI R. and WIGNER E., *Phys. Rev.* **50,** 58 (1936).
3. HERRING C., *J. Franklin Inst.* **233,** 525 (1942).

4. ELLIOTT R. J., *Phys. Rev.* **96,** 280 (1954).
5. KOSTER G. F., *Solid State Physics* **5,** 173 (1957).
6. MACFARLANE G. G., MCLEAN T. P., QUARRINGTON J. E. and ROBERTS V., *Phys. Rev.* **108,** 1377 (1957); ELLIOTT R. J., *Phys. Rev.* **108,** 1384 (1957).
7. PHILLIPS J. C., *Phys. Rev.* **112,** 685 (1958).
8. MACFARLANE G. G., MCLEAN T. P., QUARRINGTON J. E. and ROBERTS V., *J. Phys. Chem. Solids* **8,** 388 (1959); HAYNES J. R., LAX M. and FLOOD W. F., *J. Phys. Chem. Solids* **8,** 392 (1959); BROCKHOUSE B. N., *J. Phys. Chem. Solids* **8,** 400 (1959).
9. HERRING C., *Bell. Syst. Tech. J.* **34,** 237 (1955); HERRING C. and VOGT E., *Phys. Rev.* **101,** 944 (1956).
10. LOUDON R. and MCLEAN T. P., *J. Phys. Chem. Solids*, **13,** 1 (1960).

VOL.
15
1960

J. Phys. Chem. Solids Pergamon Press 1960. Vol. 15. pp. 152–156. Printed in Great Britain.

THE PREPARATION AND CRYSTALLOGRAPHY OF FeNiN AND THE SERIES $Fe_{4-x}Ni_xN$*

R. J. ARNOTT and A. WOLD†

(*Received* 2 *October* 1959; *revised* 19 *November* 1959)

Abstract—The system $Fe_{4-x}Ni_xN$, $0 \leqslant x \leqslant 4$, has been investigated. In the range $0 \leqslant x \leqslant 3{\cdot}33$, the compounds have the γ' (Fe_4N) structure; when $3{\cdot}33 \leqslant x \leqslant 4$, a two phase region $Ni_3M + M_4N$ exists. Calculation of X-ray line intensities from diffraction patterns of the series $Fe_{4-x}Ni_xN$ indicate that the first nickel atom replaces the iron on the corners of the unit cell and that additional nickel replaces iron in a random manner.

At ratios of Fe:Ni close to 1:1 a new phase is formed having the approximate composition FeNiN. This phase can be assigned a primitive tetragonal cell having $a = 2{\cdot}830$ Å and $c = 3{\cdot}713$ Å. The iron and nickel atoms are ordered with iron atoms located at the corners of the unit cell and nickel atoms at the body centers. The nitrogen atoms apparently lie at the c-face centers.

INTRODUCTION

A CONSIDERABLE body of information exists on the preparation and crystallographic properties of iron nitrides. HÄGG[1], EISENHUT and KAUPP[2], BRILL[3] and JACK[4] have prepared $\gamma'(Fe_4N)$ and the range of composition was found to be 5·7–6·1 per cent N at 450°C. JACK[4] has reported that the unit cell is cubic with $a = 3{\cdot}787$ *kX*. The γ'-phase reported by BRILL[3] is a face-centered cubic close-packed array of iron atoms with nitrogen atoms occupying one-fourth of the number of octahedral interstices in a completely ordered structure as shown in Fig. 1(a) where the nitrogen atoms are located at the body centers. There appears to be no equivalent Ni_4N compound, although Ni_3N has been prepared by JUZA and SACHSZE[5].

GUILLAUD and CREVEAUX[6] have reported a saturation moment of 2·22 Bohr magnetons per metal atom for Fe_4N. Recently, WIENER and BERGER[7] have proposed a magnetic structure for Fe_4N and several related compounds. Iron atoms possessing ferromagnetically aligned moments of $3\mu_B$ and $2\mu_B$ occupy the corners and face-centered positions respectively of the cubic unit cell. The difference in moments is apparently based on the ability of nitrogen at the body center to act as a donor of three electrons to the 3*d* shells of three iron atoms located at the face centers. FRAZER[8] has confirmed the proposed structure of Fe_4N by neutron diffraction measurements.

Much less information is available concerning mixed transition metal nitrides. WIENER and BERGER[7] have prepared and studied the crystallographic and magnetic properties of Fe_3NiN and Fe_3PtN. Such systems are of interest because they provide information concerning the rela ionship between ferro-magnetism and metal–nonmetal bonding. The present paper deals with the preparation and properties of the system $Fe_{4-x}Ni_xN$ and an ordered tetragonal phase FeNiN.

EXPERIMENTAL

$Fe_{4-x}Ni_xN$

γ' Fe_4N was prepared by the reduction of Fe_2O_3 with purified hydrogen at 750°C followed by nitriding the finely divided iron powder at 500°C in a stream of NH_3/H_2 in a ratio of 3:2 for 12 hr. The product was analysed by standard procedures and was found to have the composition Fe_4N. The saturation moment measured at liquid helium temperature with various field strengths and extrapolated to infinite field was $2{\cdot}20 \pm 0{\cdot}05$ Bohr magnetons per metal atom.

* The work reported in this paper was performed by Lincoln Laboratory, a center for research operated by Massachusetts Institute of Technology with the joint support of the U.S. Army, Navy and Air Force.

† Staff Members, Lincoln Laboratory, Massachusetts Institute of Technology.

Table 1. Conditions of preparation and cell edges of the series $Fe_{4-x}Ni_xN$

Composition	Condition of prep.	Unit cell
Fe_4N	500°C 6 hr $NH_3/H_2 = 3/2$	$a = 3{\cdot}797 \pm 0{\cdot}001$ Å
$Fe_{3{\cdot}55}Ni_{0{\cdot}45}N_{1{\cdot}07}$	500°C 6 hr $NH_3/H_2 = 3/2$	3·789
$Fe_{2{\cdot}97}Ni_{1{\cdot}03}N_{1{\cdot}11}$	550°C 6 hr NH_3	3·784
$Fe_{2{\cdot}69}Ni_{1{\cdot}31}N_{1{\cdot}16}$	500°C 6 hr NH_3	3·782
$Fe_{1{\cdot}96}Ni_{2{\cdot}04}N_{1{\cdot}19}$	500°C 6 hr NH_3	3·773
$Fe_{1{\cdot}68}Ni_{2{\cdot}32}N_{1{\cdot}19}$	375°C 6 hr NH_3	3·768
$Fe_{1{\cdot}05}Ni_{2{\cdot}95}N_{1{\cdot}20}$	350°C 6 hr NH_3	$3{\cdot}755 \pm 0{\cdot}002$
$Ni_3N_{1{\cdot}16}$	350°C 12 hr NH_3	$a = 2{\cdot}669 \pm 0{\cdot}001$ $c = 4{\cdot}308 \pm 0{\cdot}001$

VOL. 15 1960

No equivalent compound Ni_4N could be obtained but Ni_3N was prepared by reducing NiO at 700°C with hydrogen and nitriding the finely divided nickel powder at 350°C for 16 hr.

Members of the system $Fe_{4-x}Ni_xN$ were prepared by coprecipitation of the oxalates[9] followed by their ignition to oxides in air at 650°C. The finely divided oxides were transferred to a silica boat, reduced with hydrogen at 700°C, and then nitrided with ammonia at various temperatures depending upon the iron:nickel ratio. Lower nitriding temperatures were required for the samples of higher nickel content. Single phases having the γ' structure were obtained in the composition range $0 \leqslant x \leqslant 3{\cdot}33$. A two-phase region of M_4N and Ni_3N was found in the composition range $3{\cdot}33 \leqslant x \leqslant 4$. Table 1 summarizes the preparative conditions and the crystallographic data for the system.

All of the intermediate members of the system were found to contain nitrogen in excess of that required by the formula M_4N. Several samples of the compositions $Fe_{3{\cdot}55}Ni_{0{\cdot}45}N_{1{\cdot}07}$ and $Fe_{1{\cdot}05}Ni_{2{\cdot}95}N_{1{\cdot}20}$ were heated in a stream of ammonia at elevated temperatures until traces of alloy formed. Analysis of these compounds showed that they still contained excess nitrogen. These samples were renitrided to the pure γ' phase under the conditions of the original preparations and their nitrogen content did not deviate by more than 0·2 wt.% from that formerly measured.

FeNiN

At ratios of Fe:Ni close to 1:1, from $Fe_{0{\cdot}97}Ni_{1{\cdot}03}$ to $Fe_{1{\cdot}02}Ni_{0{\cdot}98}$, the γ' phase Fe_2Ni_2N can be further nitrided (350°C with a rapid stream of ammonia) to produce a new phase having the approximate composition FeNiN. The nitriding process requires approximately 70 hr under these conditions. The crystallographic data are summarized in Table 2.

Table 2. Comparison of observed and calculated X-ray intensities for tetragonal FeNiN

No.	*hk*1	$d_{meas.}$	I_0	I_c	
				ordered	random
1	001	3·701	0·8	0·7	2·7
2	100	2·824	5·2	5·3	2·1
3	101	2·249	100·0	100·7	101·6
4	110	1·999	53·2	53·2	53·7
5	002	1·855	18·9	19·9	20·1
6	111	—	—	0·1	0·6
7	102	1·551	1·3	1·2	0·4
8	200	1·415	15·6	15·6	15·7
9	112	1·361	29·1	28·4	28·6
10	201	—	—	<0·1	0·2
11	210	1·266	0·4	0·7	0·2
12	003	—	—	<0·1	0·1
13	211	1·198	29·7	29·8	30·1
14	103	1·134	17·5	15·2	15·4
15	202	1·125	22·8	22·4	22·6
16	113	—	—	<0·1	0·2
17	220	1·001	19·9	19·6	19·8

The X-ray patterns were obtained with a Norelco diffractometer using FeKα radiation. In calculating line intensities, dispersion corrections for iron and nickel atomic scattering factors were made using data given by JAMES[10]. A correction for temperature effect was made using the

temperature factor for iron.* The observed line intensities were obtained by scanning across each line a number of times (as many as 8 times for weak lines), and accumulating the total count. The background was measured on both sides of each peak and subtracted from the total count to give the measured intensity.

RESULTS AND DISCUSSION

Pure Fe_4N was prepared and the crystallographic and magnetic data of JACK and GUILLAUD are confirmed. The system $Fe_{4-x}Ni_xN$ was studied and was seen that very little iron enters the Ni_3N phase whereas single phase compositions containing up to 80 per cent nickel were prepared which possess the γ' Fe_4N cubic structures.

WIENER and BERGER proposed an ordered structure for Fe_3NiN in which the nickel atoms replace the iron atoms on the corners of the unit cell. This has been confirmed by calculation of the X-ray line intensities. Such calculations for members of the series higher in nickel indicate that the additional nickel atoms replace iron in a random manner. The first two superlattice lines (100) and (110), are the most readily measured and the relative intensities are sensitive to ordering of the metal atoms. Their structure factors are:

$$F_{100} = f_A - f_B - f_B + f_B - f_N = f_A - f_B - f_N$$
$$F_{110} = f_A + f_B - f_B - f_B + f_N = f_A - f_B + f_N$$

where A is the metal atom at the corners of the unit cell, B the metal atoms on the face centers,

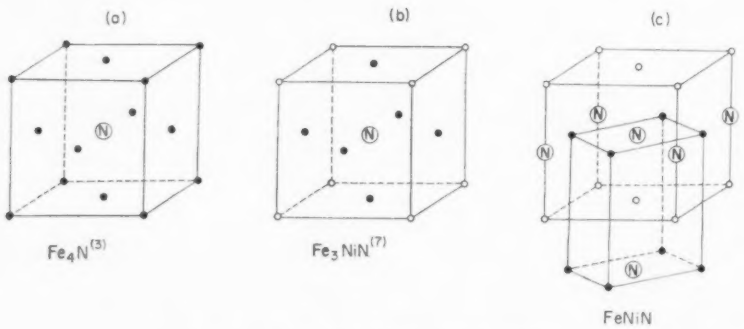

FIG. 1. Structures of iron nickel nitrides.

It can be seen from Table 1 that the nitrogen content for members of the series $Fe_{4-x}Ni_xN$ was in excess of that required by the composition M_4N. The ratio of the nitrogen to total metal atoms increases from 1:4 to 1·19:4 at the composition $Fe_{1.96}Ni_{2.04}Ni_{1.19}$. The excess nitrogen then levels off to a constant value until the two-phase region M_4N and Ni_3N is reached. It appears that an excess of nitrogen is needed to stabilize the M_4N structure when nickel is substituted for iron. This may be due to the smaller size of the nickel atom.

and N the nitrogen at the body center. When no ordering of the metal atoms is involved, as in Fe_4N, f_A would be equal to f_B and the ratio of the intensities of these two lines (I_{100}/I_{110}) should be about 1·5. If no ordering were involved, this value should apply to the whole series. When the A position is occupied by nickel and the B positions by iron, as in Fe_3NiN, the calculated ratio drops to 0·15; and as further nickel is substituted randomly for iron in the B positions, the ratio increases and would again reach 1·5 at Ni_4N if such a composition could be prepared. A plot of this ratio I_{100}/I_{110} calculated on the above ordering scheme for the whole series is given in Fig. 3. The measured ratios are given and are close to those calculated.

It was observed that at ratios of Fe:Ni close to 1:1, increasing the nitrogen content produced a

* The temperature correction for iron was made using data from *Internationale Tabellen zur Bestimmung von Kristallstrukturen*, Bd. 2; Borntträger, Berlin (1935). Since the calculated intensities after this correction agreed well with the observed data, no other temperature factors were considered.

VOL. 15 1960

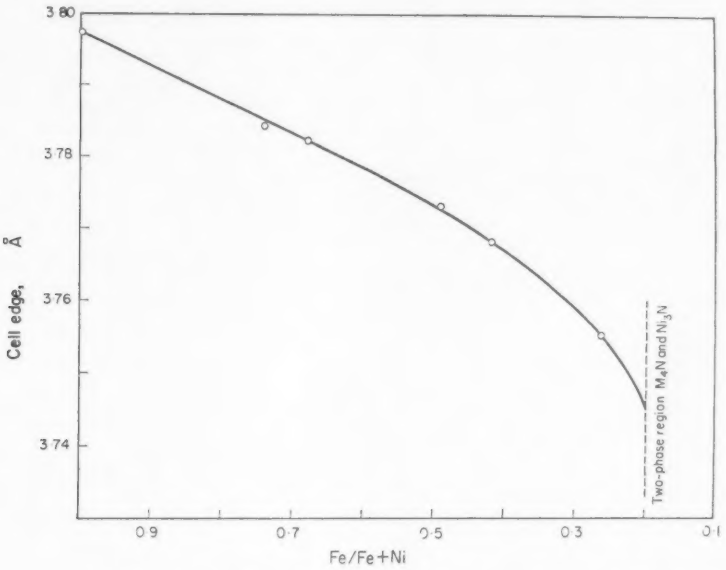

FIG. 2. Cell edge versus composition for the series $Fe_{4-x}Ni_xN$.

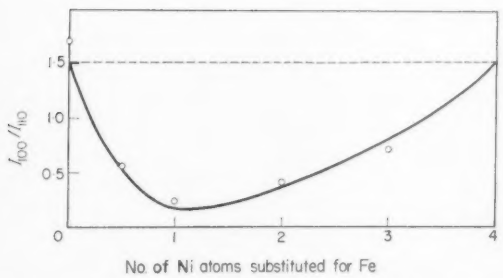

FIG. 3. Comparison of X-ray intensity ratios (I_{100}/I_{110}) obtained for members of the series $Fe_{4-x}Ni_xN$ with ratios calculated for both ordered and unordered metal atoms.

— — — No ordering of metal atoms
——— Ordering of first Ni atom only
○ Measured ratios

new phase having a composition close to FeNiN. This ratio of iron to nickel is critical in that even relatively slight deviations result in two phases, the new phase and M_4N. FeNiN is tetragonal and can be derived from the face centered cubic Fe_4N cell (Fig. 1) by an expansion in the *a* direction and a contraction in the *c* direction. A simpler primitive tetragonal cell having $a = 2{\cdot}830$ Å and $c = 3{\cdot}713$ Å can be selected (Fig. 1). Examination of the strong lines of the X-ray pattern indicated that the metal atoms are located on a body centered tetragonal lattice. From theoretical considerations,[11] it was proposed that the iron and nickel atoms are ordered with iron atoms located at the corners of the unit cell and nickel atoms at the body centres. The nitrogen atoms were located on the centres of the *c* faces. Calculated intensities for all possible reflections based on this structure are reported in Table 2. Intensity calculations based on a model without ordering of the metal atoms are also included for comparison. Agreement of the ordered model with the observed intensities indicates strongly that this is the preferred structure. The space group of this structure is $P4/mmm$ (D^1_{4h}).

Acknowledgements—The authors would like to thank Dr. J. B. GOODENOUGH for his helpful advice and Mr. R. W. SMALL who performed the several chemical analyses.

REFERENCES

1. HÄGG G., *Z. Phys. Chem.* **B8,** 455 (1930).
2. EISENHUT O. and KAUPP E., *Z. Elektrochem.* **36,** 392 (1930).
3. BRILL R., *Z. Kristallogr.* **68,** 379 (1928).

4. JACK K. H., *Proc. Roy. Soc.* A**195,** 34 (1948).
5. JUZA R. and SACHSZE W., *Z. anorg Chem.* **251,** 201 (1943).
6. GUILLAUD C. and CREVEAUX H., *Cr. Acad. Sci. Pen's* **222,** 1170 (1946).
7. WIENER G. W. and BREGER J. A., *J. Metals, N.Y.* **7,** 360 (1955).
8. FRAZER B. C., *Phys. Rev.* **112,** 751 (1958).
9. WICKHAM D. G., *Tech. Rep.* **89** *Lab. Insul. Res. MIT* (1954).
10. JAMES R. W., *The Optical Principles of the Diffraction of X-rays*, Appendix III, Bell, London (1958).
11. GOODENOUGH J. B., WOLD A. and ARNOTT R., to be published.

VOL
15
196

J. Phys. Chem. Solids Pergamon Press 1960. Vol. 15. pp. 157–166. Printed in Great Britain.

SURFACE PHENOMENA DURING THE INTERACTION BETWEEN MgO(s) AND VARIOUS GASES AT ELEVATED TEMPERATURES

D. M. SPEROS and L. J. SCHUPP

Lamp Research Laboratory, Lamp Development Department, General Electric Company, Nela Park, East Cleveland 12, Ohio

VOL. 15 1960

(*Received* 4 *November* 1959; *revised* 15 *December* 1959)

Abstract—The interaction between MgO(s) and various gases at elevated temperatures causes the appearance of pronounced etch patterns on the surface of the crystal. These patterns are of two distinct types with respect to their orientation relative to the crystallographic axes. In some atmospheres the etch lines are parallel to the edges of the naturally cleaved cubic MgO(s) while in other atmospheres the etch lines form a 45° angle with the edges of the crystal. In all the cases etch patterns consist of multi-atomic layer surface discontinuities that render them clearly visible to the unaided eye.

Experimental and theoretical evidence is offered supporting the following postulates:

(1) The pronounced surface discontinuities (i.e. multi-layer steps, kinks, pyramids, etc.) caused by etching are fundamentally due to the dependence of protective chemisorption on surface structure.

(2) The orientation of the etch patterns is dependent on whether the etching agent attacks one surface ion (Mg^{++} or $O^{=}$) preferentially over the other.

INTRODUCTION

In the course of another investigation, a number of single crystals of MgO, approximately $3 \times 3 \times 10$ mm, were heated in various gases either by passing 60 c/s alternating current along their longest axis or in the uniform temperature zone of a furnace. The etch patterns on the surfaces of the crystal as shown in Figs. 1 and 2, consist of series of steps forming rectangular figures. In some gases such as CO_2 the steps were parallel to the edges of the naturally cleaved cubic MgO (Fig. 1). In other atmospheres, as for example H_2(g), the steps formed a 45° angle with the edges of the crystal (Fig. 2). In inert gases, no definite etch patterns appeared.

The steps of the etch patterns as shown in Figs. 1 and 2 are ascending from the hotter regions near the central areas of the crystal toward the cooler crystal edges.

Although etching is a phenomenon observed and used by man since antiquity, its production is still largely an art and its fundamental explanation still a matter of conjecture. This is especially true for etching caused by a solid–gas reaction at elevated temperatures. Therefore, the purpose of this work was to investigate:

(1) The reasons for the sharp surface discontinuities that render the patterns visible.

(2) The factors that determine the orientation and shape of the etch patterns.

ON THE FORMATION OF SURFACE DISCONTINUITIES ASSOCIATED WITH ETCHING

Many hypotheses have been submitted to account for the appearance of etch patterns along the crystallographic planes of single crystals; as for instance, surface migration effects,[1, 2] crystal imperfections[3, 4] and other thermodynamic and kinetic factors.[5, 6] Other hypotheses involve surface tension and adsorption on different crystallographic planes,[7] the "tie up" of crystal steps because of impurities[4] and surface

contamination.[8] FRANK *et al.*[9], in order to explain etch figures in diamonds, suggested that, in the presence of oxygen, lattice steps become stabilized as –C–O–C–O– zig-zag chains such as are present in the polyoxymethylene polymers of aldehydes.

To add to the above, it is conceivable that species leaving the crystal from regions of higher temperatures condense on the surface at regions of lower temperature due to convection currents or a thermal Langmuir sheath. Also free radical or ionic species formed by reactions between the atmosphere and the crystal surface at a given temperature could come in contact with the surface at regions of a different temperature where the reaction may be reversed. The sequence in Fig. 3 more fully described in the next section indicates that this mechanism is within the realm of possibility. However, none of the above can account for the etch patterns encountered in this work.

Kinetic considerations

The end result of etching is the formation of edges, steps, corners or kinks on the surface of the crystal. Therefore etching occurs when the following conditions prevail:

$$k_c < k'_e < k'_f \tag{1}$$

where k'_c, k'_e, and k'_f are the specific rate constants for the detrition of atoms that form the corners, edges or flat surface of a single crystal, respectively.*

The energy of activation ΔE for processes involving surface species is often approximated by considering the net number of bonds broken in the particular process.[10] More rigorous treatments[11–13] show this to be a serviceable approximation. Therefore, whether a thermal or a chemical process is involved

$$\Delta E_c < \Delta E_e < \Delta E_f$$

and hence, in general,

$$k_c > k_e > k_f \tag{2}$$

since a corner atom is held in the solid by three formal bonds, an edge atom by four, and a flat surface atom by five.

According to inequalities (2), the tendency of sublimation and chemical reaction is to smoothen rather than roughen the surface. This is in direct contradiction to inequalities (1), which are the prerequisite for the formation of etch patterns.

Protective chemisorption as a cause of etching

The course of a reaction between a solid X(s) and a gas H(g) may be visualized as follows:

Reaction step:

$$X(s) + H(g) \rightarrow XH' \rightarrow XH''(s) \tag{3}$$

where XH′ is the activated complex for the initial interaction that results in the chemisorbed "product" XH″(s).

Desorption step:

$$XH''(s) \rightarrow XH''' \rightarrow XH(g) \tag{4}$$

where XH‴ represents the final stage of XH″(s) before separation from the underlying crystal surface to produce the desorbed molecule XH(g). Processes (3) and (4) can be quite independent. For example the chemisorption of oxygen by tungsten or graphite occurs at temperatures several hundred degrees lower than those at which tungsten or carbon oxides are evolved.[14]

The specific rate of desorption k_d will be given by

$$k_d = \frac{kT}{h} \frac{f^{\neq}[XH'''] }{f[XH''(s)]} \exp\left[-\left(\frac{\Delta E_d}{RT}\right)\right] \tag{5}$$

$\Delta E_d = E_{XH'''} - E_{XH''(s)}$. Whether the adsorption sites are atoms on crystal corners or edges or flat surfaces the bond between them and XH‴ is, by definition, at the last stage of its existence while its vibrational frequency is approaching zero. On the other hand, XH″(s) is held in more intimate contact with the solid by the unsaturated surface bonds. This surface unsaturation involves, in general, one formal bond per atom on a flat surface, two per atom at a crystal edge and three per atom on a crystal corner. Thus, while $E_{XH'''}$ is not very dependent on surface topography, the energy level for $E_{XH''}$ is lower at corners than at edges than at flat surfaces of the crystal. As a result,

$$\Delta E_{d,c} > \Delta E_{d,e} > \Delta E_{d,f}$$

and since the ratio of partition functions involves

* The term "atoms" hereafter may refer to ions, molecules, etc., as appropriate for the particular case under consideration.

VOL.
15
1960

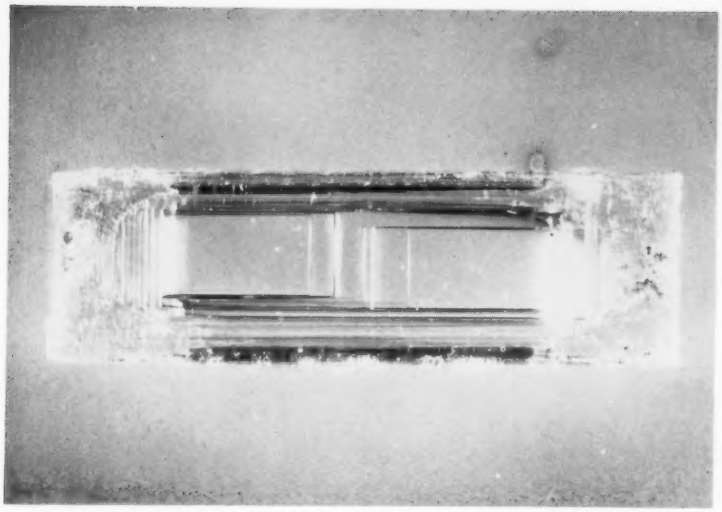

FIG. 1. Etch patterns on the 100 face of MgO crystal heated in CO_2. Crystal dimensions in this and all subsequent photographs: $3 \times 3 \times 10$ mm.

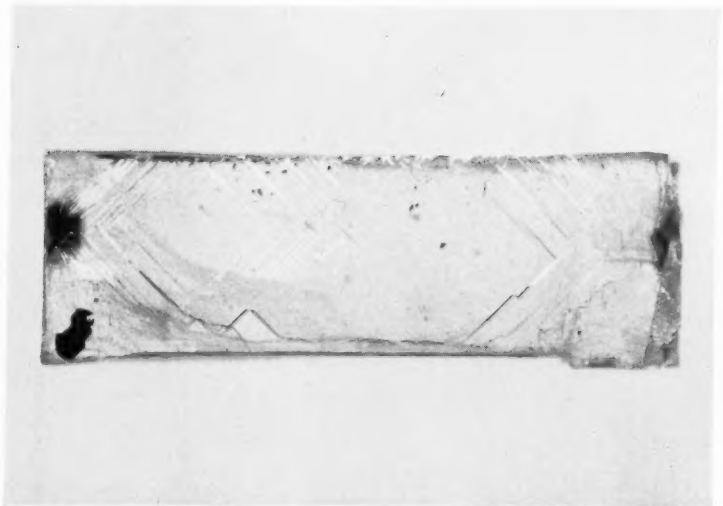

FIG. 2. Etch patterns on the 100 face of MgO crystal heated in H_2.

[*facing p.* 158

FIG. 3(a)

FIG. 3(b)

FIG. 3(c)

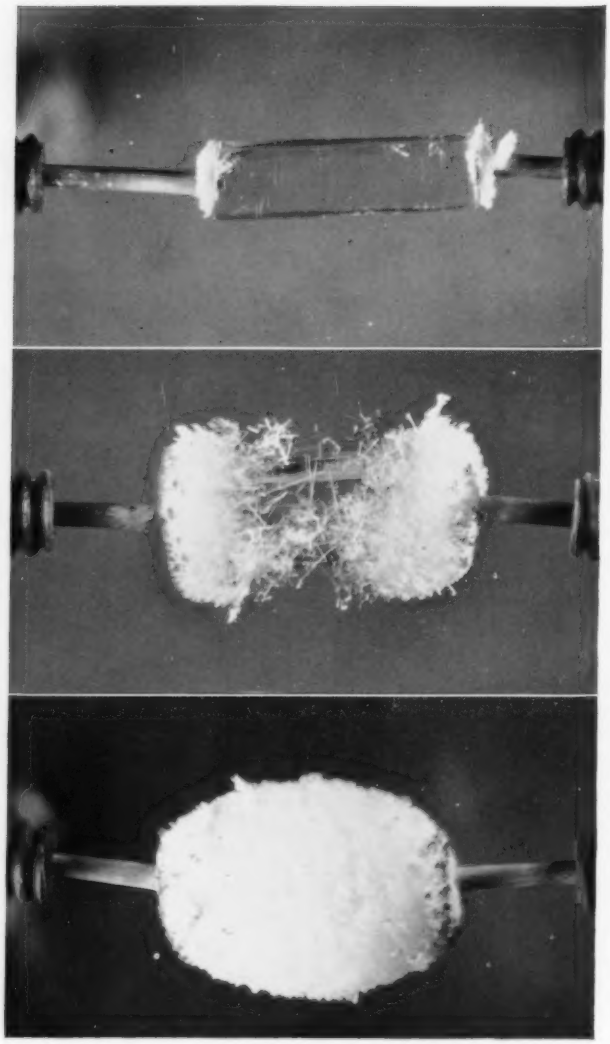

FIG. 3. "Cocoon" formation around MgO crystal heated in H_2–CO_2 mixtures.

(a) Whiskers of MgO begin to appear on the electrodes.
(b) Whisker growth begins to envelop the crystal.
(c) Cocoon formation completed.

VOL.
15
1960

FIG. 7(a)

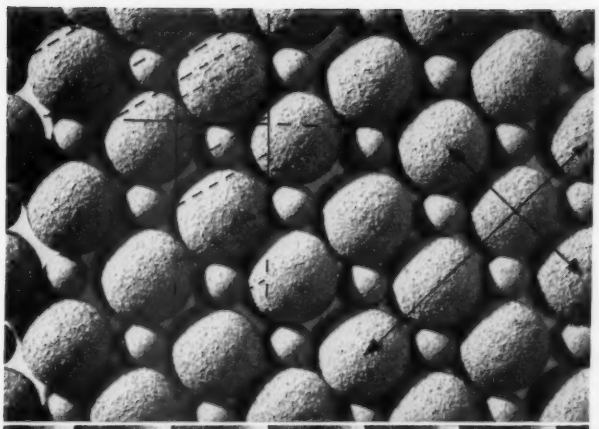

FIG. 7(b)

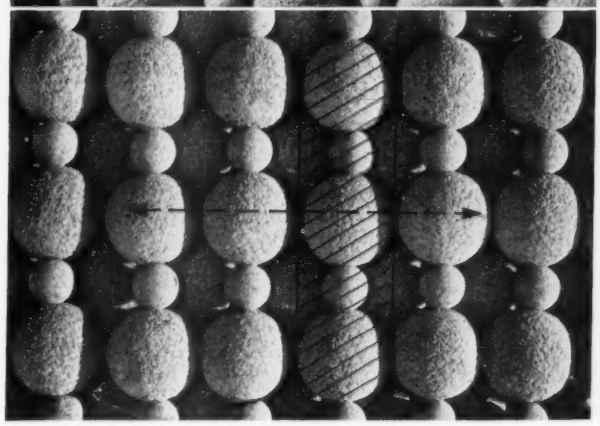

FIG. 7(a). Cork ball model of the 100 face of MgO.

FIG. 7(b). Cork ball model of the "ideal" 110 face of MgO.

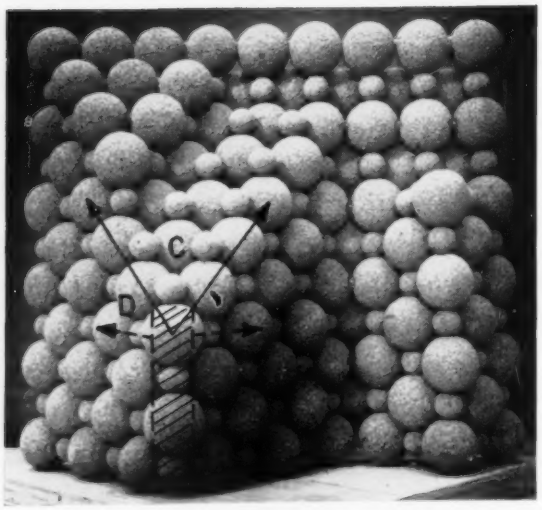

FIG. 7(c). Cork ball model of 100 and 111 surfaces on a 110 face.

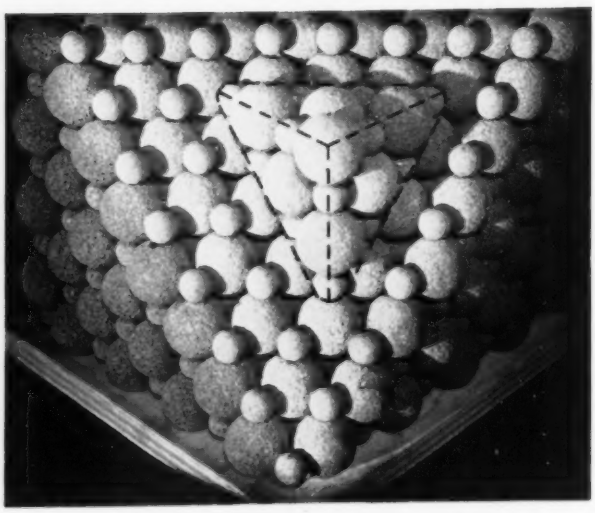

FIG. 7(d). Cork ball model of 100 surfaces on the 111 face.

VOL
15
196

VOL. 15 1960

mainly vibrational contributions

$$k_{d,c} < k_{d,e} < k_{d,f} \tag{1a}$$

in the same order as inequalties (1).*

As a result of inequalities (1a), the proportion of corner atoms covered by chemisorbed species will be higher than the proportion of edge or flat surface atoms. Since covered atoms are protected from further interaction with the atmosphere, it is concluded that the rate of detrition of corner atoms is less than that of edge atoms, which in turn is less than that of atoms in flat surfaces as shown by inequalities (1). Therefore, if process (4) is the rate determining step, conditions for etch patterns prevail. If, however, process (3) determines the rate, inequalities (2) come into effect and, as discussed, there can be no etch patterns.

Experimental tests of the protective chemisorption postulate

The two sets of experiments listed below were designed for the purpose of testing the above deductions.

Set 1. If protective chemisorption is a primary cause of etching, then the patterns should disappear if, while the temperature is held constant at some elevated value, the reaction atmosphere is changed into one that does not interact with the crystal. Then inequalities (2) will come into effect, due to sublimation, resulting in a flat surface. The patterns should reappear if the atmosphere is changed to the original.

The reactive atmospheres used were mixtures of argon with either hydrogen or carbon dioxide. After etching at over 2000°C the atmosphere was replaced by one of pure argon. In other experiments, after etching, the gases were pumped out and a pressure of 10^{-4} mm Hg was attained. In either case, the etch patterns slowly disappeared. Upon introduction of the reactive gas, the patterns reappeared immediately. It was ascertained that both the disappearance and the reappearance of the etch patterns was accompanied by a decrease in weight.

Set 2. The specific rate for the desorption process, equation (4) will be given by equation (5) which may be approximated by:

$$k_d = \frac{kT}{h} \exp\left[-\left(\frac{\Delta E_d}{RT}\right)\right] \tag{6}$$

since the partition functions for the chemisorbed species and its complex will essentially cancel each other.

On the other hand, the specific rate for the reaction step, equation (3), will be given in approximate form by

$$k_r = \frac{kT}{h} \frac{1}{f_g} \exp\left[-\left(\frac{\Delta E_r}{RT}\right)\right] \tag{7}$$

which involves the translational partition function f_g of the reagent gas H. Therefore, at a sufficiently high temperature, the reaction process will always determine the rate. However, the two rate vs. temperature curves may cross at a temperature T_E such that

$$RT_E \ln f_g = \Delta E_d - \Delta E_r. \tag{8}$$

The condition for such a crossing to occur is that $\Delta E_d > \Delta E_r + RT \ln f_g$ otherwise the reaction step will determine the rate at all temperatures.

Since etch patterns appear on MgO(s), the $k = f(T)$ curves must cross. Therefore if the crystal were heated above the temperature T_E in equation (8) at which $k_d = k_r$, *without changing the atmosphere that caused etching below* T_E, the etch patterns should disappear.†

The above is illustrated in Fig. 4. It is seen that at each T the lowest curve represents the sites of greatest stability. Up to temperatures T_E, desorption is the rate determining process, inequalities (1) or (1a) are in effect and etch patterns are to be expected. Above temperatures T_E, inequalities (2) take over as the process becomes reaction-controlled and a flat surface should result although the reaction between MgO and the atmosphere will be proceeding at a high rate. Furthermore, as temperature $T_{E,1}$ is surpassed, the rate of detrition of edge atoms should become larger than that of atoms in flat surfaces. Hence, small etch patterns should begin to expand and grow together forming larger patterns as shown schematically in Fig. 5(a). Since up to $T_{E,2}$ the rate of detrition of corner atoms is less than that of edge atoms, the former will leave

* This deduction is also indicated in previous work.[15, 16]

† Provided, of course, that $T_E < T_{\text{melting}}$.

only when the edges to which they belong merge to eliminate corner atoms. Above $T_{E,2}$, however, the rate of detrition of corner atoms will be the highest. However, as each corner atom leaves, it uncovers two other corner atoms just as vulnerable and the growth of etch patterns should follow the

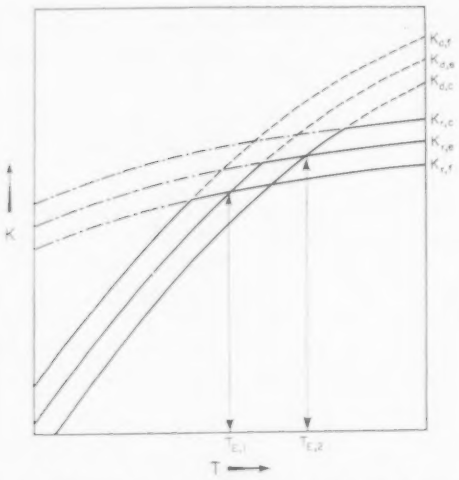

FIG. 4. Schematic diagram of the dependence of reaction and desorption rates on the temperature for corner, edge and flat surface sites.

pattern shown on Fig. 5(b). After sufficient time at temperatures higher than $T_{E,2}$ the exposed surfaces should appear optically flat.*

To check experimentally the above deductions a number of crystals were electrically heated in various etching atmospheres at progressively higher temperatures. As the temperature was increased above the point at which etching became visible the etch patterns fused into larger patterns the edges of which retreated toward the cooler crystal boundaries leaving an optically flat surface in the middle.

Therefore the theoretical prediction that at a sufficiently elevated temperature no etch figures should exist on the surface was proven correct experimentally.

The first step for the experimental check of the deductions for the range between $T_{E,1}$ and $T_{E,2}$ consisted in obtaining an idea of the surface temperature distribution on crystals heated electrically. Fig. 6 shows the results of a representative set of measurements obtained by means of a micropyrometer. It is to be noted that the values of the isotherms do not involve emissivity corrections and that they represent average values for the entire crystal thickness rather than surface temperatures.

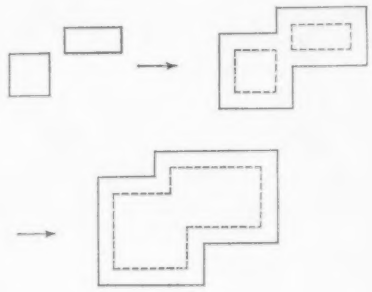

FIG. 5(a)

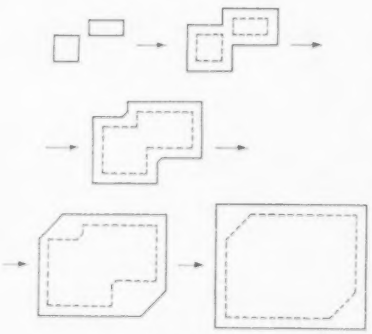

FIG. 5(b)

FIG. 5. Schematic diagram for the growth of etch patterns on the 100 faces.

(a) At temperatures higher than $T_{E,1}$ but less than $T_{E,2}$ (see Fig. 4 and text).
(b) At temperatures higher than $T_{E,2}$.

Since the crystal was being heated in a flow of gas, as during the etching experiments, the surface temperatures must be somewhat less. Likewise the temperature gradients along the surface must be more severe than those measured through the entire thickness of the crystal. Therefore the temperature values given to each isotherm are too high and the temperature difference between them too small; but the morphology of the temperature distribution (i.e. the shape and place, with respect to the crystal, of the isotherms) is correct.

* i.e. approach crystallographic planes.

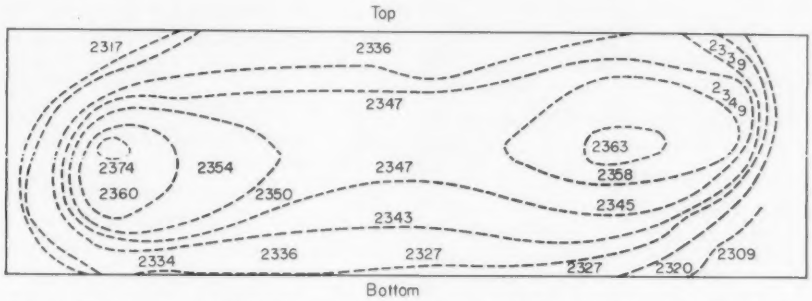

FIG. 6. Temperature distribution on the 100 face of MgO crystals heated electrically. Compare with Figs. 1 and 2.

VOL. 15 1960

If, therefore, the high temperature regions of the crystal were held at temperatures higher than $T_{E,2}$ and the coolest regions below $T_{E,1}$ by adjusting the current and gas flow,* the contour of the etch patterns should fit closely the contour of the isotherms of Fig. 6.

As it is seen in Figs. 1 and 2, this fit is striking. Between the unetched "hot" center and the distinctly etched "cool" edges of the crystal, a zone corresponding to the transition range $T_{E,1}-T_{E,2}$ existed: close examination revealed patterns corresponding to Fig. 5(a) toward the $T_{E,1}$ direction and patterns corresponding to Fig. 5(b) toward the $T_{E,2}$ (hotter region) direction.

As a result of the evidence presented in this section, it is postulted that the fundamental cause of etch figures on MgO is the dependence of protective chemisorption on surface structure.

ON THE ORIENTATION OF ETCH PATTERNS WITH RESPECT TO CRYSTALLOGRAPHIC AXES

An investigation of the dependence of the pattern orientation on the gas atmosphere revealed that gases expected to cause the detrition of MgO(s) predominantly by means of dissociation, produced etch patterns with steps parallel to 110 planes of the crystal. For example, the patterns of Fig. 2, hereafter referred to as "diamond" patterns, were produced by heating the crystal in a mixture of hydrogen and argon. On the other hand, heating the crystals in gases such as CO_2, CO, NH_3 and N_2 suspected of reacting essentially with MgO molecules caused the appearance of etch patterns the steps of which were parallel to the 100 cleavage planes (Fig. 1). These hereafter will be referred to as "square" patterns.

A postulate for the general tendency of the patterns to orient themselves as observed is illustrated with the aid of Fig. 7(a). The separation of a single MgO molecule from the surface can only occur as indicated by the shading on the figure, parallel to the cleavage (100) planes, further "sublimation" then proceeding from the step thus formed; while the reaction of hydrogen with the surface depends on the oxygen ions which are located parallel to the 110 planes, as indicated by the full lines drawn on Fig. 7(a).

The prerequisites for this postulate are as follows:

(1) The processes of thermal dissociation and sublimation should be of approximately equal importance at the temperature range of interest.

(2) Either process can be made to predominate by selection of the proper atmosphere.

As it will be seen, in the case of MgO(s) neither of these propositions has been previously established.

A consideration of the more obvious thermal equilibria involving MgO

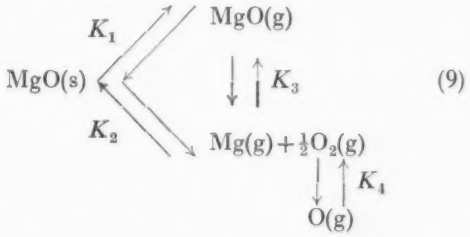

(9)

* or by suddenly increasing the electric current through the crystal.

yields:

$$\frac{\eta_{Mg(g)}}{\eta_{MgO(g)}} = 1{\cdot}26\frac{K_3}{K_2^{1/2}} \qquad (10)$$

where η is the number of moles of the species indicated by the subscript in each case, ideal gaseous behavior having been assumed.

The insertion of the appropriate thermodynamic quantities found in the literature[17, 18] in equation (10) leads to the plot of Fig. 8. Dissociation and

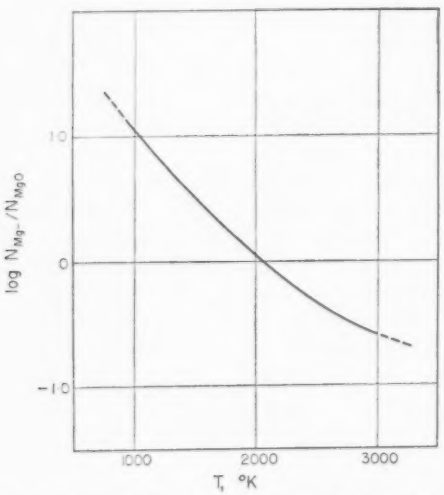

FIG. 8. The dependence of thermal dissociation and sublimation processes on temperature for MgO.

sublimation are equally important, ($\eta_{Mg(g)}/\eta_{MgO(g)}$ equal to unity) at about 2000°K. This is based on a value of 130 ± 4 kcal/mole for the standard heat of sublimation of MgO(s) reported in the newest compilation of thermochemical data.[17] However, results of preliminary experiments in this laboratory and of an inspection of the heats of sublimation, crystal structures and ionic radii of the other alkaline earth oxides indicate that the value of 130 kcal/mole is a possible minimum rather than an average value. As a result, 2000°K is the minimum temperature at which $\eta_{Mg(g)}/\eta_{MgO(g)} = 1$. Regardless of uncertainty in the data used the following conclusions may be drawn:

(a) Both processes take place in MgO(s), dissociation being the more important low temperature cause of detrition while sublimation is the high temperature cause.

(b) The temperature at which the two processes are equally important lies somewhere above 2000°K.

Fortunately, the temperature range at which the etching phenomena become readily apparent is quite wide, approximately 1400°K to well over 2000°K. In this temperature range, both detrition processes vary by approximately a factor of two in importance as seen in Fig. 8. Therefore the first prerequisite is fulfilled.

The rate of weight loss by MgO(s) is several orders of magnitude higher when heated in hydrogen than when heated in argon under the same conditions. The tendency of hydrogen, especially in the atomic state,* to attack the electronegative surface $O^=$ is much greater than its tendency to attack surface Mg^{++}. This should result in "diamond" patterns and these are indeed observed.

A reagent, such as OH, capable of attacking both surface Mg^{++} and $O^=$ should cause in accordance to the above, "square" etch patterns as illustrated in Fig. 7(a). This type of pattern is indeed predominantly obtained if the crystals are heated in argon containing water vapor or even in hydrogen saturated with water vapor. Likewise, heating in CO or CO_2 causes an increased rate of weight loss by MgO(s) and results in "square" patterns.

The etch patterns may be changed from "square" to "diamond" and vice versa simply by changing the atmosphere in which the crystals are being heated. For instance, "diamond" patterns are obtained in an atmosphere containing hydrogen and carbon dioxide if the hydrogen content is higher than approximately 90 per cent by volume. If the atmosphere than is enriched with CO_2 the "diamond" etch figures slowly change into "square" figures. If the atmosphere is subsequently enriched with H_2 the "square" patterns revert to "diamond" patterns once again.

The above indicate that the second prerequisite is fulfilled in principle. Unfortunately it is not possible to predict thermodynamically which gases will enhance reaction with both ions and which with only one. Essentially, this is due to the fact that the end result of the interaction between MgO(s) and either H_2(g) or CO_2(g) is MgO(s).

As shown in the sequence of Fig. 3, this occurs

* At 1900°K $P_{H(g)} = P^{1/2}_{H_2(g)}$.

in an interesting manner: At first crystal whiskers start forming on the electrodes whose temperature is substantially lower than that of the crystal. The whiskers grow until eventually whiskers originating from opposite electrodes join to form a cocoon-like structure containing the crystal. The whiskers were examined and found to be highly purified MgO(s). The possibility that several intermediate stages may be involved is corroborated by the fact that the species MgOH has been detected.[19]

In order to examine the consistency of the orientation postulate the following experiments were performed.

VOL. 15 1960

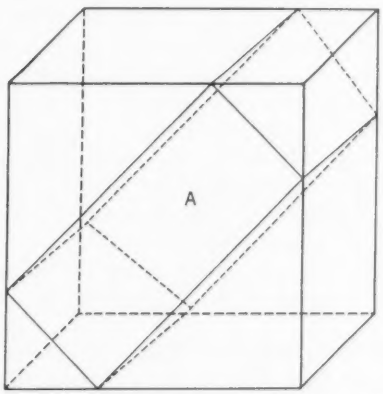

FIG. 9. Mode of sawing of MgO crystal (large parallelopiped) along the face diagonal (see text).

A number of single crystals were sawed along the face diagonal as shown in Fig. 9, heated in the atmospheres of interest and the *A* (or 100) surfaces examined. As expected, the atmospheres enhancing MgO "sublimation" created diamond (100) patterns while those that enhanced "dissociation" caused square patterns to appear; thus each etch pattern was rotated 45° from its normal position because the crystal was sawed at an angle of 45° from the normal 100 cleavage plane of the crystal.

Hence, the characteristic orientations of the etch patterns are shown to be independent of the direction of the gas or heating current flow.

Because of the mode of heating, appreciable temperature gradients existed along the crystal faces. Therefore a number of crystals were heated in a tungsten furnace within a bell jar, under more uniform temperature conditions than those in Figs. 1 and 2. There was no gas flow through the bell jar. The etch patterns observed under these conditions show the same characteristics as crystals electrically heated except that the distribution of etch patterns on the face of the crystal is more uniform. Hence, the orientation is unaffected by the mode of heating.

Crystals heated at pressures other than atmospheric (a few mm Hg to approximately 3 atm) showed no change in the expected orientation of the patterns.

Crystals containing impurities only to the extent of a few parts per million presented the same orientation of patterns under the same etching conditions as crystals deliberately doped with as much as 0·5 per cent of calcium, aluminum, iron, cobalt, manganese, etc., oxides.

This study was extended to MgO surfaces sawed to expose the 110 and 111 crystal faces. The ideal 110 surface would appear as in Fig. 7(b). In this case one would have expected patterns in which one dimension shaded for the separation of MgO molecules, dotted line for dissociation would be more prominent than the other. As shown in Figs. 10 and 11, this expectation was fulfilled; but the prominent directions of etching in these two cases were parallel instead of perpendicular to each other. The reason for this is illustrated in Fig. 7(c): an actual 110 surface will contain the edges or ridges of the 100 face (*D*), the normal cleaving planes of the simple cubic crystal. Hence, as in the case of the 100 face, dissociation proceeds along the full lines drawn on the figure, resulting in the prisms seen in Fig. 10. On the other hand, the separation of MgO molecules proceeds as shown in Fig. 11 by the shaded area eroding down on either side of the prism, thereby producing the prisms shown in Fig. 11. It will be noted that the separation of MgO molecules along the direction denoted by the shading in Fig. 11 will involve the breakage of six bonds while their separation along the direction denoted by the arrows will involve the breakage of seven bonds.

In Fig. 10 (or 7c) it is interesting to note that the planes *C* are 111 surfaces, one of the least stable crystallographic planes. Therefore their existence indicates that the overwhelming factor is not the relative resistance to detrition of the various crystallographic planes but the tendency of the chemical reaction to proceed along the direction explained above. This is further modified by

the consideration of chemisorption effects. The surfaces *C* (111 planes) consist of only one type of ion, Mg^{++} or $O^{=}$, while the planes *D*(100 surfaces) consist of both types. During the MgO–H_2 reaction, the formation of OH, for instance, is very likely. On the 100 plane, the most stable configuration of the chemisorbed species will probably be as follows:

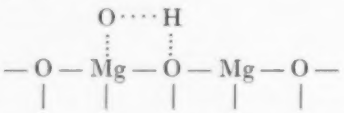

while it is very likely that the most stable configuration on the 111 plane will involve only one bond between sorbent and adsorbate:

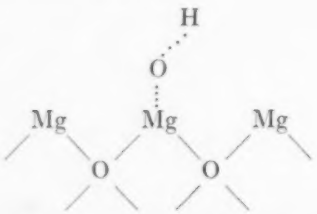

On the other hand, the surface unsaturation on the 111 plane involves three formal bonds per adsorbing site (see Fig. 7(d)) while the 100 plane involves only one.

A model of the 111 face, Fig. 7(d), shows that the 100 planes now form tetrahedra slightly inclined to one side and that both processes (i.e. dissociation and MgO molecule separation) should result in the same tetrahedral etching producing three-faced pyramid-like structures. This is seen to be the case in Fig. 12 (MgO molecule separation) and Fig. 13 (dissociation).

In conclusion, the influence of factors other than the nature of the atmosphere and the crystal structure of MgO are of no consequence in the orientation of these patterns.

As a result of the evidence presented in this section, it is postulated that the orientation of the etch patterns is dependent on whether the etching agent prefers to attack one surface ion (Mg^{++} or $O^{=}$) or both. This has an analogue in reactions involving polyfunctional organic molecules or polymers where it has long been known that the reagent may selectively attack one or more specific atoms or functional groups or sites without touching the others.

MODIFYING EFFECTS

For the purpose of this paper it has not been necessary to examine certain effects of quantitative importance.

Surface features were grouped in the three general categories of corner, edge or flat surface sites. Since there are many types of sites in each category[20] a more complete treatment would involve, for instance, a spectrum of curves in Fig. 4 instead of the three curves examined here. This factor is of importance because the same chemical species could be chemisorbed strongly at one type of corner or edge site but weakly at another.

The migration of chemisorbed species will follow paths dependent on the spatial distribution of surface atoms and will proceed in the general direction of corners and edges since these represent potential minima into which the migrating species may be trapped. This will tend to alter the relative magnitudes of $k_{d,c}$ $k_{d,e}$ and $k_{d,f}$ but it will not change the direction of inequalties (1a).

The possibility of transport of species through the gas phase has already been considered (Fig. 3).

Interaction of chemisorbed species will tend to change the shape of the $k_d = f(T)$ relation.

APPLICATION TO OTHER PHENOMENA

This theory of etching may be used in the study of substances and conditions other than those of primary interest in this work.

Solution etching

Unless a product of the interaction between the solvent and the solid is capable of chemisorption by the solid, no etch patterns will appear on single crystallographic planes of single crystals, since the effect of the solvent will be to smooth the surface irregularities in accordance with inequalities (2). If these irregularities are small, then, before the action of the solvent rendered them visible, they would be smoothened out. Therefore, a second constituent in the solution, capable of being so strongly adsorbed by the solid that it is taken out of solution, is necessary.*

* The thermodynamic condition for this is that the chemical potential for chemisorption must be equal to or higher than the chemical potential for solution of the constituent in the solvent. The kinetic conditions are identical to those for the higher temperature etching covered here.

VOL.
15
1960

FIG. 10. Etch patterns on the 110 face of MgO in H_2. Compare with Fig. 7(c). The prisms protrude from the surface.

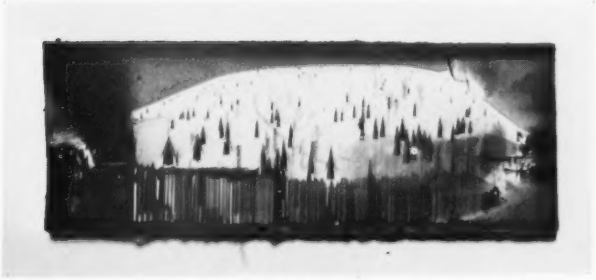

FIG. 11. Etch patterns on the 110 face of MgO in CO_2. Compare with Fig. 7(c). The prisms protrude from the surface.

FIG. 12. Etch patterns on the 111 face of MgO in CO_2. Compare with Fig. 7(d). The pyramids protrude from the surface.

[*facing p.* 164

FIG. 13. Etch patterns on the 111 face of MgO in H_2. Compare with Fig. 7(d). The pyramids protrude from the surface.

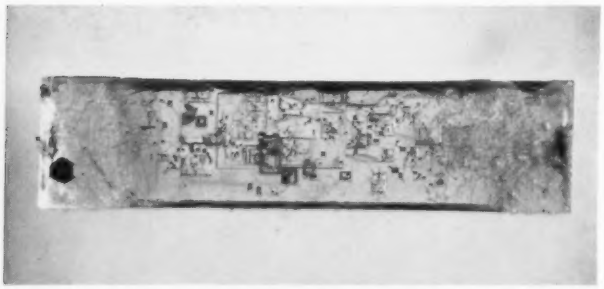

FIG. 14. Etch patterns caused by CO_2 on the 100 face of MgO that was sprinkled with Fe_2O_3 powder. The characteristic "square" patterns are present but the enhanced attack at the Fe_2O_3–MgO interfaces has caused the "pits" shown. In some cases these are 1 mm deep.

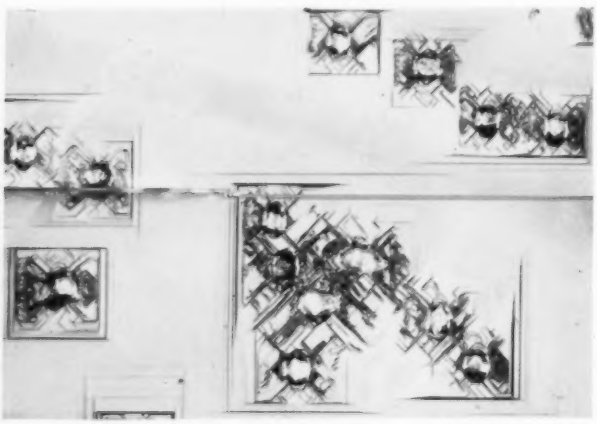

FIG. 15. Etch figures caused by CO or CO_2 on the 100 face of MgO sprinkled with Al_2O_3 powder. The characteristic (large) "square" patterns are present.

In addition etch patterns on the Al_2O_3 particles and the spinel product are discernible within the "square" etch figures.

The Al_2O_3 particles are 0·1–0·5 mm in diameter.

VOL. 15 1960

The preferential adsorption of the second constituent by the corners and edges of the irregularity will reduce their rate of dissolution below that of flat surfaces. Hence, as in the case of high temperature etching, corners and edges will disappear only after the flat surfaces that they border have gone leaving therefore the next layer of atoms exposed in the same corner–edge configuration as the one that was just dissolved. These new corners and edges, in turn, then acquire the adsorbent and the irregularity becomes enlarged every time the "cycle" is repeated without smoothening out. Thus etching will originate at surface irregularities such as fracture ridges or the ends of dislocations.* However, as was shown, their presence is not a prerequisite for etching.

Crystal growth

Some aspects of crystal growth by condensation from the gas phase were encountered in this work. At higher temperature, long crystal whiskers of MgO could be grown as shown in Fig. 3. However, at lower temperatures the MgO deposits consisted of amorphous powder. In addition to other possible factors, chemisorption may contribute to these phenomena as indicated by this theory. At lower temperatures, the surface unsaturation is reduced because of species, more strongly chemisorbed on corners and edges than on flat surfaces. Therefore, the condensation of new species from the gas phase may not be expected to result in sharply defined crystallites. However, at some higher temperature, the rate of desorption is high enough to clean the surface of foreign matter. Then the higher unsaturation of corners and edges will lead to the preferential deposition on and migration to these sites and the single crystal or whisker may be expected to grow.

Solid–solid reactions

The applicability of this theory to the study of solid–solid reactions was also examined. For example, a number of MgO crystals were sprinkled with powdered Fe_2O_3. Upon heating in CO(g) or CO_2(g), for instance, the familiar "square" etch patterns appeared. However, the attack of the gas on the sites of the contact between MgO and Fe_2O_3 was far more severe. These effects are shown in Fig. 14. At first the attack is manifested by expanding polygonal etch figures which eventually develop into "square" figures while the depth of the attack is increased resulting in deep, ever narrowing but well defined "pits". Finally these come to points and disappear as the iron oxide is consumed. Since iron and magnesium oxides are both soluble into each other and reactive toward the gas atmospheres used, this "catalytic" activity may involve little more than the formation of a liquid interface. This, of course, would be a flat surface, hence incapable of the mode of stabilization described in this work.

To check this, oxides of chromium, cobalt and aluminum were sprinkled on the crystal instead of Fe_2O_3. The melting points of these or of any combination between them and MgO (eutectics, compounds, etc.) are of course higher than in the Fe_xO_y–MgO system. As expected the *depth* attack was much less and nil in the case of Al_2O_3. In this last case, it is interesting to note:

(i) the etch figures on Al_2O_3, MgO and the magnesium aluminate interface were such as to clearly delineate the reactants and their product, suggesting that the progress of a solid–solid interaction can be followed by this means (Fig. 15);

(ii) the extent of the reaction between MgO and Al_2O_3 in a CO(g) atmosphere, for instance, is much larger than in an inert atmosphere or vacuum;

(iii) the extent of the surface reaction in the horizontal direction is larger than in the vertical direction as seen in Fig. 15.

Acknowledgements—Indebtedness is expressed to Drs. J. S. SABY and R. L. HANSLER for continued interest; to many members of this laboratory for discussions and critical reading of the manuscript but especially to Dr. D. W. MAGEE for discussions and suggestions especially concerning the transfer mechanisms; to Drs. J. J. GILMANN, J. C. FISHER and G. W. SEARS of the Research Laboratory for reading and commenting upon an early version of the manuscript; to M. CSICSERY for general assistance and to G. W. ARMSTRONG for preparing crystal specimens.

* Also in the high temperature phenomena of this work, etching is first detected along the ridges and other irregularities of the surface. As explained, these should be the first sites to be attacked and then hold chemisorbed species.

REFERENCES

1. ASHWORTH F., *Advanc. Electronics* **3,** 1 (1957).
2. MÜLLER E. W., *Phys. Rev.* **102,** 618 (1956).
3. FRANK F. C. and PUTTICK K. E., *Phil. Mag.* **3,** 1262 (1958).

4. GILMAN J. J., JOHNSTON W. and SEARS G., *J. Appl. Phys.* **29,** 747 (1958).
5. HIRTH J. P. and POUND G. M., *J. Chem. Phys.* **26,** 1216 (1957).
6. MOORE A. J. W., *Acta Met.* **6,** 293 (1958).
7. CHALMERS B., KING R. and SHUTTLEWORTH R., *Proc. Roy. Soc.* A**193,** 465 (1948).
8. BATTERMAN B. W., *J. Appl. Phys.* **28,** 1236 (1957).
9. FRANK F. C., PUTTICK K. E. and WILKS E. M., *Phil. Mag.* **3,** 1268 (1958).
10. HIRTH J. P. and POUND G. M., *J. Chem. Phys.* **26,** 1216 (1957).
11. HARKINS W. D., *The Physical Chemistry of Surface Films* p. 291. Reinhold, New York (1952).
12. LENNARD-JONES J. E. and TAYLOR P. A., *Proc. Roy. Soc.* A**109,** 476 (1925).
13. LENNARD-JONES J. E. and DEVONSHIRE A. F., *Proc. Roy. Soc.* A**156,** 6 (1936).
14. For example EHRLICH G. and HUDDA F. G., *J. Chem. Phys.* **30,** 493 (1959).
15. GLASSTONE S., LAIDLER K. J. and EYRING H., *The Theory of Rate Processes* p. 392. McGraw-Hill, New York (1941).
16. GOMER R., WORTMAN R. and LUNDY R., *J. Chem. Phys.* **26,** 1147 (1957).
17. KUBACHEWSKI O. and EVANS E. Ll., *Metallurgical Thermochemistry* Wiley, New York (1958).
18. ROSSINI F. D. *et al.*, *Nat. Bur. Stand. Cir.* No. 500 (1952).
19. PESIC D. and GAYDON A. G., *Proc. Phys. Soc.* **73,** 244 (1959).
20. STRANSKI I., *Z. Phys. Chem.* **136,** 259 (1928).

VOL
15
196

J. Phys. Chem. Solids Pergamon Press 1960. Vol. 15 pp. 167–182. Printed in Great Britain.

ETUDE PARAMAGNETIQUE DES FERRITES D'YTTRIUM ET DE TERRES RARES DE FORMULE $5Fe_2O_3 . 3M_2O_3$

ROLAND ALÉONARD

Laboratoire d'Électrostatique et de Physique du Métal, Grenoble, France

(*Received* 17 *December* 1959)

VOL. 15 1960

Sommaire—On a effectué l'étude paramagnétique des ferrites à structure grenat, de formule $5Fe_2O_3 . 3M_2O_3$, pour M = Y, Gd, Tb, Dy, Ho, Er, Tm, Yb et Lu, entre leur point de Curie et 1500°K. La théorie du ferrimagnétisme de NÉEL permet d'interpréter les résultats expérimentaux.

Selon que l'ion M est ou n'est pas magnétique, les courbes des inverses des susceptibilités en fonction de la température sont du troisième ou du second degré. De ces courbes, on a déduit les coefficients de champ moléculaire qui caractérisent les interactions des ions magnétiques entre eux et le coefficient de variation thermique du champ moléculaire.

Abstract—The paramagnetic susceptibilities of the ferrites of formula $5Fe_2O_3 . 3M_2O_3$ with garnet structure have been measured between the Curie point and 1500°K, for M = Y, Gd, Tb, Dy, Ho, Er, Tm, Yb and Lu. The experimental results can be interpreted on the basis of NÉEL's theory of ferrimagnetism.

The curve of the reciprocal susceptibility as a function of temperature is of the third or second degree, for magnetic and non-magnetic M ions, respectively. From these curves, the molecular field coefficients, which are a measure of the interactions between the magnetic ions, can be determined, as well as their temperature coefficient.

1. INTRODUCTION

LES ferrites à structure grenat, de formule générale $5Fe_2O_3 . 3M_2O_3$, où M est l'ion yttrium ou un ion de terres rares, sont maintenant bien connus. BERTAUT et FORRAT[1], qui les ont découverts, en ont fait l'étude cristallographique. PAUTHENET[2] a étudié en détail leurs propriétés magnétiques au-dessous de leur point de Curie. L'objet de ce travail est l'étude de leurs propriétés paramagnétiques au-dessus du point de Curie.

Nous avons mesuré à l'aide d'une balance de translation, les susceptibilités paramagnétiques du ferrite grenat d'yttrium et de tous les ferrites de terres rares qui ont pu être préparés (M = Sm, Eu, Gd, Tb, Dy, Ho, Er, Tm, Yb et Lu), dans un intervalle de température s'étendant du point de Curie jusqu'à 1500°K environ. La théorie du ferrimagnétisme de NÉEL[3] nous a permis d'interpréter nos résultats expérimentaux.

2. MÉTHODE GÉNÉRALE D'EXPÉRIMENTATION

Nos mesures de susceptibilités en fonction de la température ont été effectuées sur une balance de translation du type FOËX et FORRER[4], mise au point par FALLOT et MARONI[5,6].

L'attraction, dans un champ non uniforme, de l'échantillon à mesurer, est équilibrée par l'attraction, dans le champ d'un aimant permanent, d'une bobine de compensation parcourue par un courant ajustable.

La bobine de compensation et l'échantillon sont placés aux deux extrémités d'un fléau suspendu par cinq fils, ne lui accordant qu'un degré de liberté suivant la direction du gradient de champ.

Le champ non uniforme est créé par un électro-aimant dont les pôles ont une forme appropriée. La valeur moyenne du champ auquel est soumis chaque échantillon est de l'ordre de 5200 oersteds.

Le courant de compensation passe dans une résistance aux bornes de laquelle est branché un potentiomètre : on ramène ainsi les mesures de force à des mesures de différence de potentiel.

L'appareil est étalonné avec une substance de susceptibilité connue. Nous avons utilisé, comme

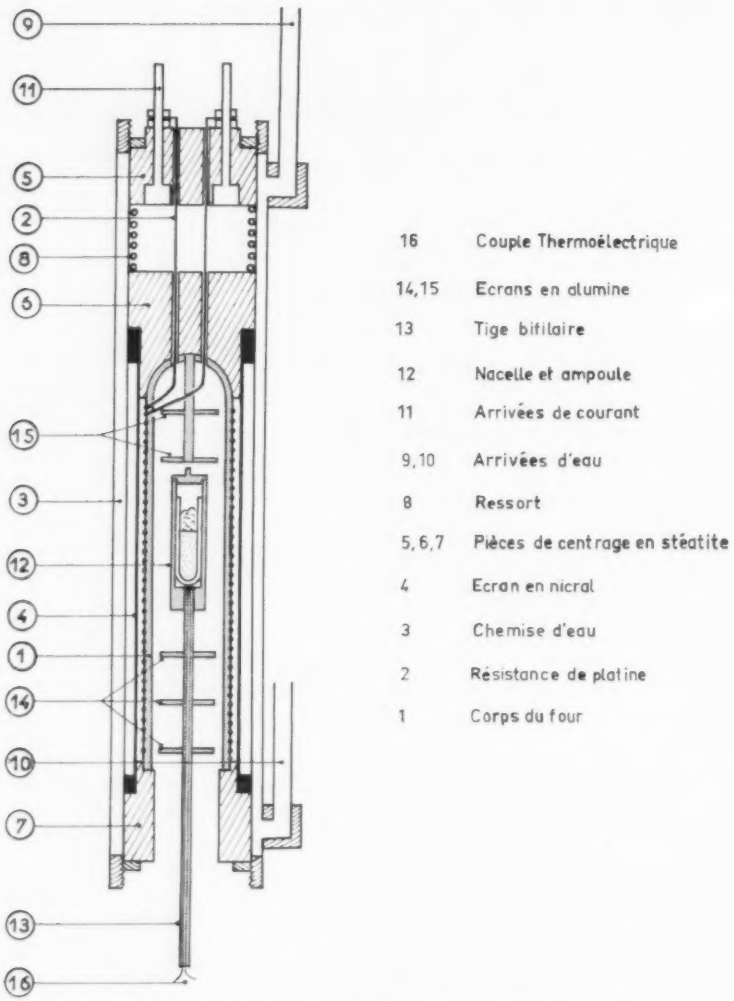

FIG. 1. Schéma du four et du porte-échantillon.

substance étalon, du pyrophosphate de manganèse qui nous a été fourni par FALLOT[5]. Ce corps suit rigoureusement la loi de Curie–Weiss. Sa susceptibilité a été étudiée par FOËX:

$$\chi \text{ à } T°\text{K} = \frac{28\,689}{T+4} \cdot 10^{-6} \text{ u.e.m. C.G.S.} \quad (1)$$

La susceptibilité de la substance mesurée est donnée par :

$$\chi = \frac{Af_1}{m_1} \quad (2)$$

où A est la constante d'étalonnage, f_1 la force d'attraction de l'échantillon exprimée en microvolts et m_1 la masse de l'échantillon.

L'ampoule de quartz contenant l'échantillon à mesurer est placée dans une nacelle en alumine, solidaire de la balance. Un four (Fig. 1), dont on peut régler la température, vient coiffer l'ensemble. Les mesures de température se font à l'aide d'un couple platine / platine rhodié dont la soudure, placée à la partie inférieure de la nacelle, est en contact avec l'ampoule de quartz contenant l'échantillon.

Des écrans en alumine, les uns solidaires du four, les autres fixés sur la balance, permettent de diminuer le gradient de température et de réduire les courants de convection.

La nacelle, la tige qui la supporte, le couple thermoélectrique et l'ampoule de quartz ont une susceptibilité importante qui s'ajoute à celle de l'échantillon et il y a lieu d'effectuer des corrections.

Pour contrôler le couple thermoélectrique, nous avons utilisé la méthode de discontinuité du diamagnétisme de l'or à son point de fusion, préconisée par WEIL[7].

Cette méthode a l'avantage de donner un étalonnage qui correspond aux conditions de mesures. Le cas échéant, nous avons corrigé les températures données par les tables à l'aide d'une loi linéaire.

VOL. 15 1960

3. LOI DE PARAMAGNÉTISME DES FERRITES GRENATS

Les ferrites à structure grenat ont pour formule générale $5Fe_2O_3 \cdot 3M_2O_3$, M étant l'ion yttrium ou un ion de terres rares.

Dans ces substances, les ions oxygène plus gros que les autres, forment un empilement dans les interstices duquel sont placés les ions métalliques. Ceux-ci ont à leur disposition trois sortes de sites, caractérisés par le nombre d'atomes d'oxygène qui les entourent : les sites tétraédriques 16*a* entourés de 4 atomes d'oxygène et les sites octaédriques 24*d* entourés de 6 atomes d'oxygène, sont occupés par les ions fer, les sites cubiques 24*c* entourés de 8 atomes d'oxygène, sont occupés par les ions M. Les ensembles d'ions qui occupent les sites 16*a*, 24*d* et 24*c*, constituent les sous-réseaux *a*, *d* et *c*.

Les proportions des ions qui occupent les trois sous-réseaux sont : $\frac{2}{8}$ pour *a*, $\frac{3}{8}$ pour *d*, $\frac{3}{8}$ pour *c*.

Pour expliquer les propriétés magnétiques de ces ferrites, NÉEL[8] a émis l'hypothèse que les ions du sous-réseau *d* étaient orientés antiparallèlement, d'une part avec les ions du sous-réseau *a*, d'autre part avec les ions du sous-réseau *c*.

(a) *Loi de paramagnétisme d'une substance à trois sous-réseaux*

La loi de paramagnétisme d'une telle substance se déduit de la théorie de NÉEL[3].

Dans l'approximation du champ moléculaire local, on suppose que les actions des ions voisins sur un ion donné, sont équivalentes à l'action d'un champ moléculaire :

$$\boldsymbol{h}_i = \sum_{j=1}^{j=3} \boldsymbol{h}_{ij}$$

$\boldsymbol{h}_{ij}$ caractérisant les actions des ions voisins j, sur un ion i donné

$$\boldsymbol{h}_{ij} = n_{ij} \cdot \boldsymbol{J}_j$$

$\boldsymbol{J}_j$ étant l'aimantation des ions j dans la substance et n_{ij} un coefficient de champ moléculaire. Pour satisfaire au modèle magnétique de NÉEL[8], on impose les conditions suivantes :

$$n_{ij} = n_{ji},\ n_{ij} < 0$$

Avec ces conventions, on peut écrire :

$$\boldsymbol{h}_a = n_{aa}\boldsymbol{J}_a + n_{ad}\boldsymbol{J}_d + n_{ac}\boldsymbol{J}_c \qquad (3)$$

$$\boldsymbol{h}_d = n_{ad}\boldsymbol{J}_a + n_{dd}\boldsymbol{J}_d + n_{cd}\boldsymbol{J}_c \qquad (4)$$

$$\boldsymbol{h}_c = n_{ac}\boldsymbol{J}_a + n_{cd}\boldsymbol{J}_d + n_{cc}\boldsymbol{J}_c \qquad (5)$$

L'aimantation de la substance sera donnée par :

$$\boldsymbol{J} = \sum \boldsymbol{J}_j = \boldsymbol{J}_a + \boldsymbol{J}_d + \boldsymbol{J}_c \qquad (6)$$

Dans la région paramagnétique, la loi de Curie est applicable :

$$\boldsymbol{J}_a = \frac{C_a}{T}(\boldsymbol{H} + \boldsymbol{h}_a) \qquad (7)$$

$$\boldsymbol{J}_d = \frac{C_d}{T}(\boldsymbol{H} + \boldsymbol{h}_d) \qquad (8)$$

$$\boldsymbol{J}_c = \frac{C_c}{T}(\boldsymbol{H} + \boldsymbol{h}_c) \qquad (9)$$

C_a, C_d et C_c sont les constantes de Curie relatives aux ions des sous-réseaux *a*, *d* et *c*, T est la température absolue et H le champ appliqué.

$\chi = J/H$ étant la susceptibilité de la substance, des relations (3), (4), (5), (6), (7), (8) et (9) on tire :

$$\frac{1}{\chi} = \frac{T^3 + aT^2 + bT + c}{a'T^2 + b'T + c'} \qquad (10)$$

$a' = C_a + C_d + C_c$ est égal à la constante de Curie de la substance; a, b, c, b', c' sont des fonctions des coefficients de champ moléculaire n_{ij}. Il y a cinq fonctions pour déterminer six coefficients : il existe donc une relation entre ces coefficients.

L'expression (10) peut se mettre sous la forme :

$$\frac{1}{\chi} = \frac{T}{C} + \frac{1}{\chi_0} - \frac{\sigma T + m}{T^2 - \theta T + l} \tag{11}$$

en posant :

$$C = a' \tag{12}$$

$$\frac{1}{\chi_0} = \frac{aa' - b'}{a'^2} \tag{13}$$

$$\sigma = -\frac{b}{a'} + \frac{c'}{a'^2} + b'\frac{(aa' - b')}{a'^3} \tag{14}$$

$$\theta = -\frac{b'}{a'} \tag{15}$$

$$m = c'\frac{(aa' - b')}{a'^3} - \frac{c}{a'} \tag{16}$$

$$l = \frac{c'}{a'} \tag{17}$$

Si l'on tient compte de la loi de variation linéaire du coefficient de champ moléculaire avec la température, formulée par NÉEL[9] et si l'on suppose que cette loi de variation thermique est la même pour tous les coefficients de champ moléculaire :

$$n_{ij} = n_{(ij)0}(1 + \gamma T) \tag{18}$$

$n_{(ij)0}$ étant le coefficient de champ moléculaire à 0°K et T la température absolue. L'expérience montre que le coefficient de variation thermique γ est de l'ordre de 10^{-4} et que l'on peut négliger les termes en γ de degré supérieur à un. L'équation (10) prend alors la forme :

$$\frac{1}{\chi} = \frac{T^3(1 + a\gamma) + T^2(a + 2b\gamma) + T(b + 3c\gamma) + c}{T^2(a' + b'\gamma) + T(b' + 2c'\gamma) + c'}, \tag{19}$$

a, b, c, a', b', c' étant les fonctions déjà définies.

L'équation (19) peut encore s'écrire:

$$\frac{1}{\chi} = \frac{T}{C'} + \frac{1}{\chi'_0} - \frac{\sigma' T + m'}{T'^2 - \theta' T + l'} \tag{20}$$

C', $1/\chi'_0$, σ', m', θ' et l' étant des fonctions de a, b, c, a', b' c' et γ.

(b) *Loi de paramagnétisme d'une substance à deux sous-réseaux*

Les ions Y^{+++} et Lu^{+++} ont des moments magnétiques nuls : les grenats d'yttrium et de lutétium sont donc des substances à deux sous-réseaux magnétiques. Les expressions du paragraphe précédent sont toujours valables, mais se simplifient :

$$\frac{1}{\chi} = \frac{T^2 + aT + b}{a'T + b'} \qquad (c = c' = 0) \tag{21}$$

$$\frac{1}{\chi} = \frac{T}{C} + \frac{1}{\chi_0} - \frac{\sigma}{T - \theta} \qquad (l = m = 0) \tag{22}$$

$$\frac{1}{\chi} = \frac{T^2(1 + a\gamma) + T(a + 2b\gamma) + b}{T(a' + b'\gamma) + b'} \tag{23}$$

$$\frac{1}{\chi} = \frac{T}{C'} + \frac{1}{\chi'_0} - \frac{\sigma'}{T - \theta'} \tag{24}$$

En identifiant (23) et (24) et en utilisant les équations (12), (13), (14) et (15), on tire :

$$\frac{1}{C} = \frac{1}{C'} - \gamma\frac{1}{\chi'_0} \tag{25}$$

$$\theta = \frac{\theta'}{1 + \gamma\theta'} \tag{26}$$

$$\frac{1}{\chi_0} = \frac{1}{\chi'_0} + 2\gamma\sigma' \tag{27}$$

$$\sigma = \sigma'(1 - 3\gamma\theta') \tag{28}$$

C est la constante de Curie de la substance ($C = a'(12)$); C', $1/\chi'_0$, θ' et σ' sont des paramètres qui se déduisent de la courbe expérimentale $(1/\chi, T)$ représentée par l'équation (24) : les formules (25), (26), (27) et (28) permettent de calculer γ, θ, $1/\chi_0$ et σ, d'où l'on déduit les trois coefficients de champ moléculaire n_{aa}, n_{dd} et n_{ad}.

Par la suite, nos résultats se rapporteront à une molécule-gramme de substance : $5Fe_2O_3 \,.\, 3M_2O_3$.

4. NATURE DES ÉCHANTILLONS MESURÉS

(a) *Préparation*

Les ferrites à structure grenat, $5Fe_2O_3 \,.\, 3M_2O_3$, que nous avons mesurés, provenaient des mêmes échantillons que ceux étudiés par PAUTHENET[2] pour M = Y, Sm, Eu, Gd, Dy et Er. Les ferrites correspondant à M = Tb, Ho, Tm, Yb et Lu provenaient d'échantillons différents de ceux étudiés par PAUTHENET, mais avaient été préparés avec les mêmes oxydes, dans les mêmes conditions.

Les préparations ont été faites par Mme

VOL. 15 1960

PAUTHENET, à partir d'une méthode de décomposition des nitrates, mise au point par BERTAUT et FORRAT.

Les ferrites à structure grenat ne se forment pas avec M = La, Ce, Pr, Nd, et n'ont pu être préparés avec Pm, qui est radioactif.

m étant la masse moléculaire de la substance mesurée :

$$m = m_1 + m_2 \begin{cases} m_1 = \text{masse de } Fe_2O_3\alpha \text{ en excès} \\ m_2 = \text{masse du grenat pur.} \end{cases}$$

Placée dans un champ H, la substance prend un

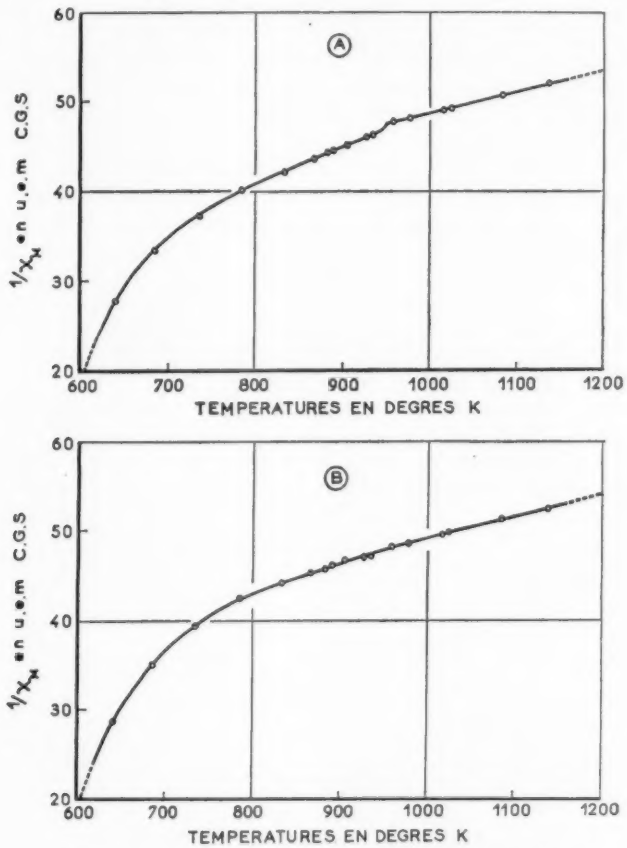

FIG. 2. Courbes ($1/\chi$, T) relatives au grenat d'yttrium : (A) non corrigée de $Fe_2O_3\alpha$; (B) corrigée.

(b) *Correction de* $Fe_2O_3\alpha$ *en excès*

Sur nos courbes expérimentales ($1/\chi$, T) au voisinage de 950°K, existait une discontinuité que nous avons attribuée au point de Curie (948°K) d'un excès de $Fe_2O_3\alpha$ non combiné. Les propriétés magnétiques de cette substance ont été étudiées en détail par PAUTHENET[2,10]. En utilisant ses résultats, nous avons pu évaluer les quantités de $Fe_2O_3\alpha$ en excès et effectuer les corrections.

moment magnétique :

$$M = \chi \,.\, m \,.\, H = (\sigma_1 + \chi_1 \,.\, H)m_1 + \chi_2 \,.\, m_2 \,.\, H \quad (29)$$

χ est la susceptibilité spécifique de l'échantillon mesuré; σ_1 est l'aimantation spontanée spécifique du ferromagnétisme de $Fe_2O_3\alpha$; χ_1 est la susceptibilité spécifique d'antiferromagnétisme de $Fe_2O_3\alpha$ indépendante de la température de 300 à 948°K, et égale à $20 \,.\, 10^{-6}$ u.e.m. C.G.S. par gramme; χ_2 est

Tableau 1

Ferrite	Y	Sm	Eu	Gd	Tb	Dy	Ho	Er	Tm	Yb	Lu
Teneur en $Fe_2O_3\alpha$ (pour cent)	1,5	4,3	2,7	0,6	2,7	1,4	2,0	0,9	1,5	4,3	2,2

la susceptibilité spécifique du ferrite de grenat pur.

Au-dessus de 948°K, σ_1 devient nul et χ_1 varie avec la température, mais les variations sont suffisamment faibles pour que nous puissions les négliger ici.

$\chi_2 . m$, susceptibilité moléculaire du ferrite de grenat pur, est donnée par l'expression suivante, déduite de la relation (29) :

$$\chi_2 . m = \left| \chi . m - \left(\chi_1 + \frac{\sigma_1}{H} \right) m_1 \right| \frac{m}{m_2} \qquad (30)$$

La discontinuité à 950°K, sur les courbes expérimentales $(1/\chi, T)$ des ferrites grenats, correspond à la disparition de l'aimantation spontanée du ferromagnétisme de $Fe_2O_3\alpha$. Pour une température voisine de 950°K, on mesure la différence de susceptibilité $\Delta\chi . m$ correspondant à cette discontinuité, et l'on a :

$$\Delta\chi . m = \frac{m_1 . \sigma_1}{H} \qquad (31)$$

On en déduit m_1, puis $m_2 = m - m_1$.

A l'aide de l'expression (30) et de la courbe (σ_1, T) déterminée par PAUTHENET, on calcule les susceptibilités moléculaires corrigées, correspondant à un ferrite de grenat pur. La Figure 2 donne un exemple de courbes $(1/\chi, T)$ non corrigée (A) et corrigée (B), relatives au ferrite grenat d'yttrium.

Le Tableau 1 indique pour chacun des ferrites grenats que nous avons étudiés, la teneur en $Fe_2O_3\alpha$ non combiné.

Le raisonnement précédent n'est pas tout à fait exact, nous aurions dû écrire :

$$m = m_1 + m_2 + m_3 \begin{cases} m_1 = \text{masse de } Fe_2O_3\alpha \text{ en excès} \\ m_2 = \text{masse du grenat pur} \\ m_3 = \text{masse de } M_2O_3 \text{ en excès} \end{cases}$$

Alors qu'il est facile de déduire m_1 de la discontinuité à 950°K sur la courbe $(1/\chi, T)$, nous ne possédons aucune donnée pour calculer m_3.

L'excès de $Fe_2O_3\alpha$ peut aussi bien être dû à une erreur de pesée (les quantités de ferrite préparées étaient de l'ordre de 200 mg) qu'à un équilibre de phase; dans ce cas, à la masse de $Fe_2O_3\alpha$ non combiné, doit correspondre une certaine proportion de M_2O_3 non combiné. Rien ne permet de trancher entre ces deux hypothèses qui peuvent être vraies simultanément. Remarquons que les proportions de $Fe_2O_3\alpha$ non combiné semblent arbitraires dans les différents ferrites grenats (Tableau 1).

(c) *Correction du diamagnétisme sous-jacent des ions* Fe^{+++}, M^{+++} *et* O^{--}

Pour éviter toute confusion, nous représenterons les susceptibilités diamagnétiques par K et les susceptibilités paramagnétiques par χ.

Nous avons utilisé la méthode d'additivité : le diamagnétisme d'une molécule-gramme de ferrite étant égal à la somme des diamagnétismes des ions-grammes qu'elle contient :

$$K_M = 10\, K_{at}Fe^{+++} + 6\, K_{at}M^{+++} + 24\, K_{at}O^{--} \qquad (32)$$

Nous avons calculé le diamagnétisme de chacun des ions par la formule de SLATER[11] :

$$K_{at} = -0{,}79 . 10^{-6} \sum_z \frac{n^{*2}(n^* + \frac{1}{2})(n^* + 1)}{(Z - s)^2} \qquad (33)$$

z est le nombre total d'électrons dans l'ion considéré, Z est le nombre atomique de l'ion, s est la constante d'écran relative à chaque électron contenu dans l'ion, et déterminée au moyen de la règle indiquée par SLATER.

Entre le nombre quantique principal n et n^*, existe la correspondance :

Tableau 2

n^*	1	2	3	3,7	4	4,2
n	1	2	3	4	5	6

On trouve ainsi :

$$K_{at}Fe^{+++} = -15{,}5 \cdot 10^{-6} \text{ u.e.m. C.G.S.}$$

$$K_{at}O^{--} = -12{,}9 \cdot 10^{-6} \text{ u.e.m. C.G.S.}$$

Les K_{at} des ions M^{+++} sont données dans le Tableau 3 avec les K_M des ferrites grenats correspondant.

Il est difficile d'évaluer la précision que l'on a sur ces résultats : la formule de SLATER est approximative et se rapporte à des ions supposés isolés, alors qu'ici ils se trouvent dans un réseau cristallin.

Dans le Tableau 3, nous indiquons, pour chaque ferrite, la valeur du diamagnétisme sous-jacent des ions par rapport à la moyenne des susceptibilités paramagnétiques. Ces valeurs sont comprises entre 0,6 et 3,2 pour cent : une erreur assez importante dans la détermination du diamagnétisme sous-jacent des ions, entraîne une erreur négligeable sur la susceptibilité paramagnétique corrigée.

Tableau 3

M^{+++}	Y	Sm	Eu	Gd	Tb	Dy	Ho	Er	Tm	Yb	Lu
Z	39	62	63	64	65	66	67	68	69	70	71
$K_{at} \cdot 10^6$ de M^{+++}	−17,8	−27,3	−27,0	−26,6	−26,2	−25,8	−25,3	−24,9	−24,5	−24,0	−23,6
$K_M \cdot 10^6$ de $5Fe_2O_3 \cdot 3M_2O_3$	−571	−628	−626	−623	−621	−618	−616	−613	−611	−608	−605
Valeur relative de K_M par rapport à χ_M en pour cent	2,7	2,3	1,7	1,0	0,7	0,6	0,6	0,7	1,0	1,8	3,2

5. LES FERRITES GRENATS D'YTTRIUM ET DE LUTÉTIUM

Les ions Y et Lu ont un moment magnétique nul : les ferrites grenats d'yttrium et de lutétium sont des substances à deux sous-réseaux magnétiques. La loi de paramagnétisme de telles substances a été développée à la Section 3(b) :

$$\frac{1}{\chi} = \frac{T}{C'} + \frac{1}{\chi'_0} - \frac{\sigma'}{T-\theta'} \qquad (24)$$

(a) *Equation de l'hyperbole* (24)

La courbe expérimentale $(1/\chi, T)$ est une hyperbole, dont nous allons établir l'équation. Pour cela, nous allons déterminer à partir de cette courbe, les paramètres C', $1/\chi'_0$, θ' et σ' de l'équation (24).

Nous avons utilisé la méthode de NÉEL[3] développée par MARONI[12].

Sur la courbe expérimentale, on choisit un point fixe $(1/\chi_a, T_a)$ soumis aux deux conditions simultanées suivantes : T_a doit être aussi élevé que possible, et l'on doit avoir le maximum de précision sur $1/\chi_a$. On détermine les pentes des cordes passant par ce point fixe et les points courants $(1/\chi, T)$.

$$p = \frac{1/\chi_a - 1/\chi}{T_a - T} = \frac{\sigma'}{(T_a-\theta')(T-\theta')} + \frac{1}{C'} \qquad (34)$$

On calcule ensuite :

$$q = \frac{1}{p-1/C'} = \frac{T_a-\theta'}{\sigma'}(T-\theta') \qquad (35)$$

q, fonction de T, est représentée par une droite qui coupe l'axe des abscisses en $T = \theta'$ et dont la pente est $(T_a-\theta') \rightarrow (T_a-\theta')/\sigma'$): la droite (q, T) permet d'obtenir θ' et σ'.

Cette méthode suppose que l'on connaisse C' avec précision; dans le cas contraire, C'_0 étant la valeur exacte, on a :

$$C' = C'_0+dC' \text{ et } q = q_0+dq$$

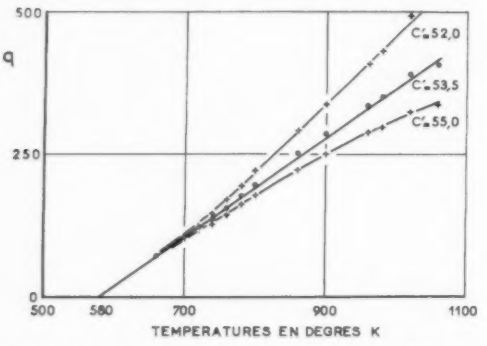

FIG. 3. Variation avec T de la quantité q définie par l'équation (35), pour le grenat d'yttrium.

avec :

$$dq = -dC' \cdot \frac{q_0^2}{C'^2_0}$$

d'où :

$$q = q_0\left(1-q_0\frac{dC'}{C'^2_0}\right) \qquad (36)$$

(q, T) est alors une courbe dont la concavité est dirigée vers l'axe des q ou l'axe des T, suivant que dC' est négatif ou positif, c'est-à-dire suivant que C' est inférieure ou supérieure à la valeur exacte C'_0.

(i) *Détermination de C', θ' et σ'.* La droite d'équation :

$$f(T) = \frac{T}{C'} + \frac{1}{\chi'_0}$$

est une asymptote à l'hyperbole (24). Sa pente est $1/C'$; en traçant une parallèle à la branche infinie de la courbe, on a un ordre de grandeur de cette pente. On en déduit une valeur moyenne de C' et on trace les courbes (q, T) correspondant à C' et à des valeurs voisines. On obtient un faisceau dont la Figure 3, relative au grenat d'yttrium, donne un exemple. En procédant par approximations successives, on obtient une droite correspondant à la valeur exacte de C'. De cette droite on déduit les valeurs de θ' et σ', comme nous l'avons exposé plus haut. Pour la clarté de la figure nous n'avons tracé que trois courbes, choisies parmi les plus caractéristiques.

Ces trois paramètres peuvent être également

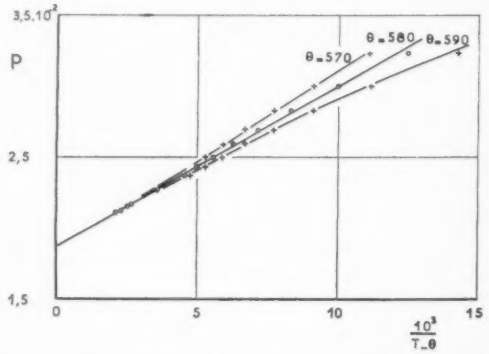

FIG. 4. Variation avec $1/(T-\theta')$ de la quantité p définie par l'équation (34), pour le grenat d'yttrium.

déterminés en considérant la fonction $[p, 1/(T-\theta')]$ (34). Cette fonction est représentée par une droite d'ordonnée à l'origine $1/C'$ et de pente $\sigma'/(T_a-\theta')$.

Cette méthode nécessite la connaissance de θ'. Si θ' n'est pas connu avec précision, le problème est le même qu'à propos de C' : on prend des valeurs voisines d'une valeur moyenne, et l'on obtient un faisceau de courbes dont les concavités sont tournées vers l'axe des p ou l'axe des abscisses, suivant que les valeurs fixées pour θ' sont trop petites ou trop grandes. A la valeur exacte correspond une droite. La Figure 4 représente le faisceau des courbes $[p, 1/(T-\theta')]$, relatif au grenat d'yttrium.

La seconde méthode fait surtout intervenir les points à haute température; comme ce sont ceux pour lesquels nous avons le moins de précision, nous avons utilisé cette méthode seulement comme vérification des résultats de la première.

Nous évaluons entre un et deux pour cent, la

précision avec laquelle ces méthodes graphiques nous ont permis de déterminer C', θ' et σ', dans le cas des grenats d'yttrium et de lutétium.

(ii) *Détermination de* $1/\chi'_0$. Connaissant C', θ' et σ' à l'aide de l'équation (24) et des valeurs $(1/\chi, T)$ de la courbe expérimentale, il est facile de calculer $1/\chi'_0$. Nous avons pris un certain nombre de points régulièrement espacés, et nous avons fait la moyenne. La précision était de l'ordre de quelques millièmes.

Le Tableau 4 donne, pour les ferrites d'yttrium et de lutétium, les valeurs des paramètres déduits des courbes expérimentales.

Tableau 4

	C'	$1/\chi'_0$	θ'	σ'
$5Fe_2O_3 \cdot 3Y_2O_3$	53,5	31,6	1050	580
$5Fe_2O_3 \cdot 3Lu_2O_3$	55,0	33,1	1030	550

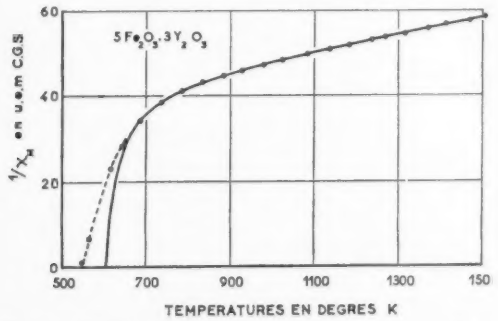

FIG. 5. Paramagnétisme du grenat d'yttrium. Points expérimentaux et courbe théorique en trait plein.

Sur la Figure 5, relative au grenat d'yttrium, nous avons représenté, en trait plein, la courbe correspondant à l'équation:

$$\frac{1}{\chi_M} = \frac{T}{53{,}5} + 31{,}6 - \frac{1050}{T-580}$$

Sur la Figure 6, relative au grenat de lutétium, nous avons représenté, en trait plein, la courbe correspondant à l'équation :

$$\frac{1}{\chi_M} = \frac{T}{55{,}0} + 33{,}1 - \frac{1030}{T-550}$$

La loi de paramagnétisme exprimée par l'équation (24) n'est applicable, comme l'a montré NÉEL[3], qu'à partir de 50 à 80 degrés au-dessus du point de Curie. Compte tenu de cet écart, attribué aux fluctuations du champ moléculaire, on voit que les points expérimentaux représentés sur les deux figures par des cercles, se disposent bien par rapport aux courbes théoriques.

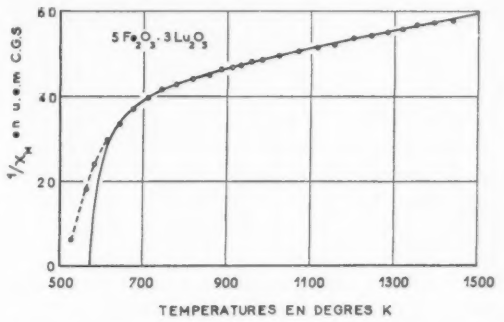

FIG. 6. Paramagnétisme du grenat de lutétium. Points expérimentaux et courbe théorique en trait plein.

(b) *Calcul du coefficient de variation thermique* γ

Nous avons vu (Section 3(b)) que le paramètre C' était lié à la constante de Curie C, par la relation :

$$\frac{1}{C} = \frac{1}{C'} - \gamma \frac{1}{\chi'_0} \qquad (25)$$

C' et $1/\chi'_0$ ont été déterminés plus haut. Les ions Y et Lu ayant un moment magnétique nul, la constante de Curie des ferrites grenat d'yttrium et de lutétium est égale à la somme des constantes de Curie des ions ferriques : pour la molécule-gramme, dans les deux ferrites on a:

$$C = 43{,}8$$

La relation (25) permet de calculer γ :

$5Fe_2O_3 \cdot 3Y_2O_3$: $\gamma = -1{,}31 \cdot 10^{-4}$

$5Fe_2O_3 \cdot 3Lu_2O_3$: $\gamma = -1{,}40 \cdot 10^{-4}$

(c) *Calcul des coefficients de champ moléculaire*

Connaissant θ', $1/\chi'_0$, σ' et γ, à l'aide des relations (26), (27) et (28) (Section 3(b)), on calcule θ, $1/\chi_0$ et σ : ces trois paramètres sont des fonctions des coefficients de champ moléculaire n_{aa}, n_{dd} et n_{ad}, comme nous l'avons vu (Section 3(a)).

Dans le cas des ferrites grenats d'yttrium et de lutétium, où les deux sous-réseaux a et d sont occupés par des ions magnétiques identiques (les ions ferriques), il est intéressant, pour déterminer les coefficients de champ moléculaire, d'utiliser les notations et les méthodes de calcul de NÉEL[3].

On pose :

$$n_{aa} = n\alpha$$

$$n_{dd} = n\beta$$

$$n_{ad} = -n \qquad \text{avec } n > 0.$$

n_{aa} et n_{dd} étant négatifs (Section 3(a)) et n positif, α et β doivent être négatifs.

On désigne par λ et μ le nombre d'ions ferriques qui occupent les sous-réseaux a et d. D'après notre convention de la Section 3(b), nos résultats expérimentaux se rapportent à une molécule-gramme et l'on a : $\lambda = 4$ et $\mu = 6$.

Enfin, C'' étant la constante de Curie rapportée à un ion-gramme (pour l'ion ferrique, $C'' = 4{,}38$), les relations (13) (14) et (15) (Section 3(a)) prennent la forme :

$$\frac{1}{\chi_0} = \frac{n}{(\lambda+\mu)^2}(2\lambda\mu - \lambda^2\alpha - \mu^2\beta) \tag{37}$$

$$\sigma = \frac{\lambda\mu C''}{(\lambda+\mu)} n^2 \left| \frac{\lambda(1+\alpha)-\mu(1+\beta)}{(\lambda+\mu)} \right|^2 \tag{38}$$

$$\theta = \frac{\lambda\mu C'' n(2+\alpha+\beta)}{(\lambda+\mu)} \tag{39}$$

En posant :

$$\tau = \frac{\eta(\sigma\lambda\mu C)^{1/2}}{\theta} \tag{40}$$

avec $\eta = \pm 1$

$$\rho = \lambda\mu \left| \frac{1}{\chi_0} \cdot \frac{C}{\theta} + 1 \right| \tag{41}$$

On vérifie que :

$$\alpha = \frac{-\rho+\mu|(\lambda+\mu)+2\tau|}{\rho+\tau(\lambda-\mu)} \tag{42}$$

$$\beta = \frac{-\rho+\lambda|(\lambda+\mu)-2\tau|}{\rho+\tau(\lambda-\mu)} \tag{43}$$

τ a deux valeurs, correspondant à $\eta = \pm 1$: on a donc deux solutions pour α et β. Ces deux quantités devant être négatives, on élimine la solution qui donne α positif.

En portant les valeurs de α et β ainsi calculées dans l'une des relations (37), (38) ou (39), on peut déterminer n, puis $n_{aa} = n\alpha$, $n_{dd} = n\beta$ et $n_{ad} = -n$.

Le Tableau 5 donne les valeurs des paramètres et coefficients, calculés selon ces méthodes, pour les ferrites d'yttrium et de lutétium.

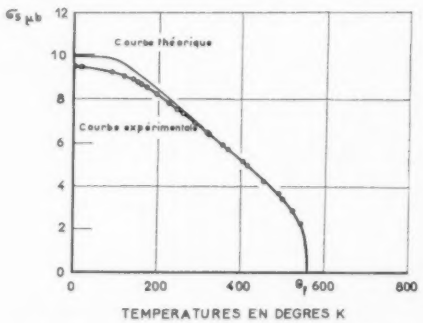

FIG. 7. Courbes théorique et expérimentale d'aimantation spontanée en fonction de la température, relatives au grenat d'yttrium, d'après PAUTHENET.

PAUTHENET[2] a calculé la courbe théorique de l'aimantation spontanée σ_s en fonction de la température T, pour le ferrite grenat d'yttrium, en utilisant les coefficients de champ moléculaire et le coefficient γ déterminés suivant la méthode ci-dessus. Il a comparé cette courbe théorique à la courbe expérimentale (σ_s, T) résultant de ses

Tableau 5

	θ	$1/\chi_0$	σ	τ	ρ	α	β	n_{ad}	n_{aa}	n_{dd}
$5Fe_2O_3 \cdot 3Y_2O_3$	628	31,3	1289	±1,854	76,90	−0,486	−0,274	−48,2	−23,4	−13,2
$5Fe_2O_3 \cdot 3Lu_2O_3$	596	32,8	1268	±1,937	81,84	−0,526	−0,307	−48,6	−25,6	−14,9

mesures (Figure 7) : on voit que l'accord est satisfaisant.

Dans la Section 6(a), nous émettrons l'hypothèse que les coefficients de champ moléculaire caractérisant les interactions fer–fer, et les coefficients γ sont les mêmes dans tous les ferrites à structure grenat. Les résultats ci-dessus, relatifs aux grenats d'yttrium et de lutétium, justifient d'autant mieux cette hypothèse que dans le Tableau de Mendéléeff, tous les éléments de terres rares sont compris entre l'yttrium et le lutétium.

VOL. 15 1960

6. LES FERRITES GRENATS DE GADOLINIUM, TERBIUM, DYSPROSIUM, HOLMIUM, ERBIUM, THULIUM ET YTTERBIUM

Les ions Gd, Tb, Dy, Ho, Er, Tm et Yb sont magnétiques : les ferrites grenats correspondant à ces ions sont des substances à trois sous-réseaux magnétiques. La loi de paramagnétisme de telles substances a été développée à la Section 3(a) :

$$\frac{1}{\chi} = \frac{T}{C'} + \frac{1}{\chi'_0} - \frac{\sigma' T + m'}{T^2 - \theta' T + l'} \qquad (20)$$

C', $1/\chi'_0$, m', θ' et l' sont des fonctions des six coefficients de champ moléculaire n_{ij}, du coefficient de variation thermique γ et des constantes de Curie relatives aux ions fer et aux ions M contenus dans le ferrite.

On pourrait calculer les coefficients n_{ij} et γ à partir de la courbe expérimentale $(1/\chi, T)$, comme nous l'avons fait pour les grenats d'yttrium et de lutétium, mais, par suite du manque de précision, ces résultats n'auraient pas de signification.

(a) *Hypothèses préliminaires*

Nous adoptons les hypothèses suivantes :

(1°) L'étude cristallographique de BERTAUT et FORRAT[1] a montré que les distances entre les ions fer étaient sensiblement les mêmes dans tous les ferrites grenats : nous pouvons donc supposer que les coefficients n_{aa}, n_{dd} et n_{ad}, caractérisant les interactions entre les ions fer, sont les mêmes pour tous les grenats.

(2°) γ, coefficient de variation thermique, est proportionnel au coefficient de dilatation : il doit être le même pour tous les grenats.

Les résultats que nous avons obtenus pour les ferrites grenats d'yttrium et de lutétium, justifient ces deux hypothèses (Section 5 (a) et (b)). Nous prendrons pour valeurs constantes de n_{aa}, n_{dd}, n_{ad} et γ, les moyennes des valeurs obtenues pour ces deux ferrites.

(3°) PAUTHENET[2] a montré que les coefficients n_{cc} caractérisant les interactions des ions terres rares entre eux étaient très faibles. Nous verrons (Section 6(d)), comment nos résultats expérimentaux peuvent servir à confirmer cette hyphohèse. Nous supposerons donc, en première approximation, que l'on a $n_{cc} = 0$.

Tableau 6

	n_{aa}	n_{dd}	n_{ad}	γ
$5Fe_2O_3 \cdot 3Y_2O_3$	−23,4	−13,2	−48,2	$-1{,}31 \cdot 10^{-4}$
$5Fe_2O_3 \cdot 3Lu_2O_3$	−25,6	−14,9	−48,6	$-1{,}40 \cdot 10^{-4}$
Moyenne adoptée pour $5Fe_2O_3 \cdot 3M_2O_3$	−24,5	−14,0	−48,4	$-1{,}35 \cdot 10^{-4}$

(b) *Calcul de n_{cd} et de n_{ac}*

Nous nous sommes fixé n_{aa}, n_{dd}, n_{ad}, n_{cc} et γ. La constante de Curie de Fe^{+++} rapportée à un ion-gramme est 4,38 ; les constantes de Curie de M^{+++} rapportées à un ion-gramme ont été calculées par PAUTHENET[2].

L'expression (20) ne dépend plus alors que de n_{cd} et n_{ac}. On trace les courbes (n_{cd}, n_{ac}) pour différentes températures, en utilisant les valeurs expérimentales. Ces courbes doivent se couper en un point dont les coordonnées sont les valeurs de n_{cd} et n_{ac} pour le ferrite considéré.

Nos hypothèses ne sont pas rigoureusement exactes et nos produits contiennent probablement des impuretés ; aussi, les courbes (n_{cd}, n_{ac}) ne convergent-elles pas en un point, mais en une

Tableau 7

M	Gd	Tb	Dy	Ho	Er	Tm	Yb
C_c	7,9	11,795	14,17	14,08	11,50	7,155	2,578

région du plan. Il s'agit alors de choisir dans cette région, un point tel que les valeurs n_{cd} et n_{ac} correspondantes, donnent une courbe théorique $(1/\chi, T)$ qui s'ajuste le mieux possible avec la courbe expérimentale.

La Figure 8 représente le faisceau des courbes (n_{cd}, n_{ac}) relatif au ferrite grenat de gadolinium. Le point M correspond à la valeur choisie pour n_{cd} et n_{ac}. Sur la Figure 9, nous représentons, en trait plein, la courbe théorique $(1/\chi, T)$ obtenue avec ces valeurs :

$$n_{cd} = -1{,}7 \qquad n_{ac} = -0{,}6$$

On voit, compte tenu des fluctuations du champ moléculaire (Section 5(a)), que les points expérimentaux représentés par des cercles, se disposent bien par rapport à la courbe théorique.

(c) *Discussion sur ces résultats*

Les coefficients n_{aa}, n_{dd} et n_{ad} sont très importants par rapport à n_{cc}, n_{cd} et n_{ac}. Cela se traduit par le fait qu'en se fixant les trois premiers, et en supposant les trois autres nuls, on obtient une courbe théorique $(1/\chi, T)$ qui diffère relativement peu de la courbe expérimentale. L'écart entre les deux courbes étant une fonction de n_{cc}, n_{cd} et n_{ac}, toute imprécision sur la courbe expérimentale entraîne une grosse imprécision relative sur les valeurs calculées de ces trois coefficients.

Indiquons que les causes d'imprécision sur la

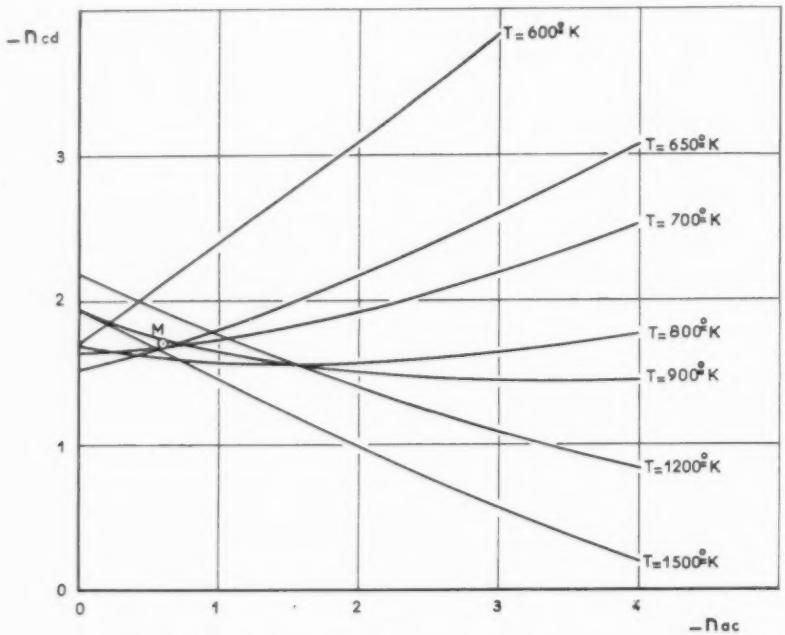

FIG. 8. Courbes (n_{cd}, n_{ac}) à différentes températures, pour le grenat de gadolinium.

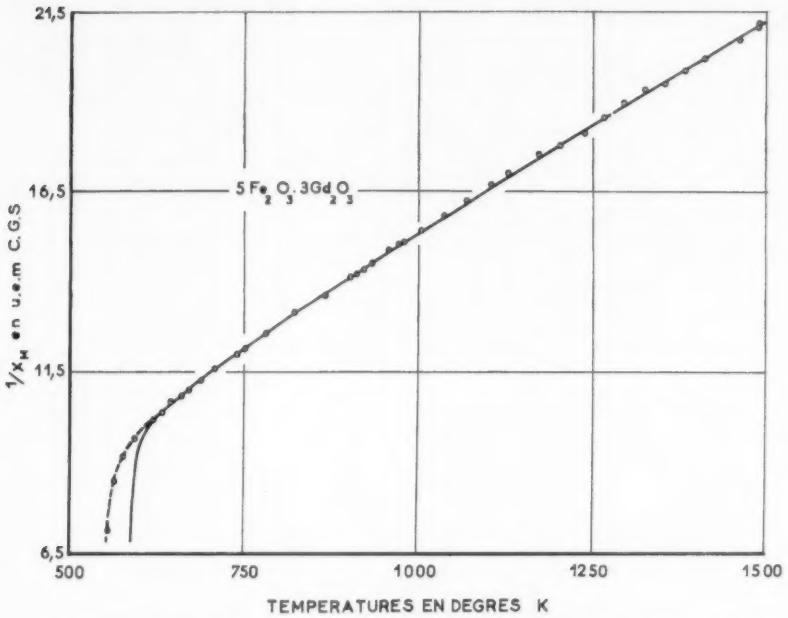

FIG. 9. Paramagnétisme du grenat de gadolinium. Points expérimentaux et courbe théorique en trait plein.

courbe expérimentale sont :

(1°) Précision relative de nos mesures;

(2°) Impuretés contenues dans le ferrite, notamment M_2O_3 non combiné.

(d) *Discussion sur la valeur de* n_{cc}

Au début de ce chapitre, nous avons souligné que PAUTHENET[2] avait trouvé pour n_{cc} des valeurs très faibles. A l'aide de nos résultats, nous allons montrer que ce coefficient doit être petit pour tous les grenats. Si l'on fait croître la valeur absolue de n_{cc}, on constate que la région de convergence du faisceau des courbes (n_{cd}, n_{ac}) de la Figure 8, s'élargit et que la courbe théorique $(1/\chi, T)$ correspondant au meilleur choix de M, s'ajuste de plus en plus mal avec la courbe expérimentale.

Ce moyen de déterminer une limite supérieure de la valeur absolue de n_{cc} n'a rien de précis, mais peut donner une idée de la grandeur de ce coefficient.

Dans le cas du ferrite grenat de gadolinium, pour les valeurs de n_{cc} comprises entre $-0,4$, et $-0,8$, l'ajustement des courbes théorique et expérimentale devient de moins en moins bon; on peut apprécier que n_{cc} ne saurait être inférieur à $-0,5$. Pour le ferrite grenat de dysprosium, cette limite semble être du même ordre.

(e) *Résultats relatifs aux ferrites grenats de* Gd, Tb, Dy, Ho, Er, Tm *et* Yb

A l'aide de la méthode exposée plus haut, nous avons calculé les valeurs de n_{cd} et n_{ac} relatives à

Tableau 8

	Gd	Tb	Dy	Ho	Er	Tm	Yb
n_{cd}	$-1,7$	$-2,3$	$-1,8$	$-1,2$	$-0,5$	0,0	$-4,4$
n_{ac}	$-0,6$	$-2,2$	$-1,6$	$-2,0$	$-0,3$	0,0	$-0,5$

ces sept ferrites. Nos résultats figurent dans le Tableau 8.

Les courbes théoriques ($1/\chi$, T) correspondant à ces valeurs et à :

$$\gamma = -1{,}35.\ 10^{-4},\ n_{aa} = -24{,}5,$$

$$n_{dd} = -14{,}0,\ n_{cc} = 0,\ n_{ad} = -48{,}4$$

sont représentées en trait plein : sur la Figure 9 pour le gadolinium, sur la Figure 10 pour le terbium et le dysprosium, sur la Figure 11 pour l'holmium et l'erbium et sur la Figure 12, pour le thulium et l'ytterbium. Les points expérimentaux sont représentés par des cercles.

Moyennant certaines hypothèses, on peut donc déterminer les six coefficients de champ moléculaire qui caractérisent les interactions des ions magnétiques entre eux, dans des substances à trois sous-réseaux. Ces valeurs ne constituent cependant qu'un ordre de grandeur; les courbes théoriques ($1/\chi$, T) que l'on en déduit, s'ajustent bien avec les courbes expérimentales.

Pour les grenats d'yttrium, de lutétium et de gadolinium, les résultats de ce travail diffèrent quelque peu de ceux publiés antérieurement[13,14]. *Ces différences sont dues au fait que dans nos dernières mesures on a d'une part, tenu compte du diamagnétisme sous-jacent des ions, d'autre part, utilisé un échantillon de grenat de lutétium ayant une plus grande pureté.*

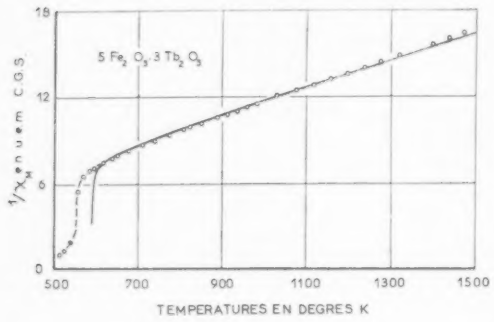

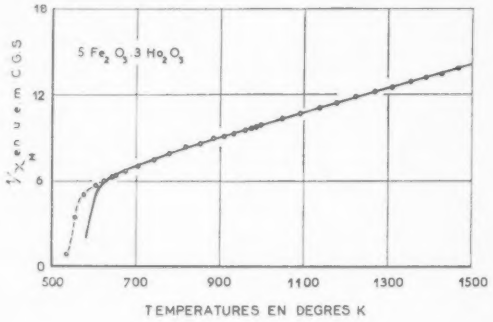

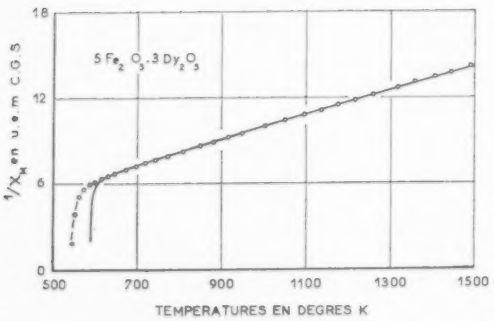

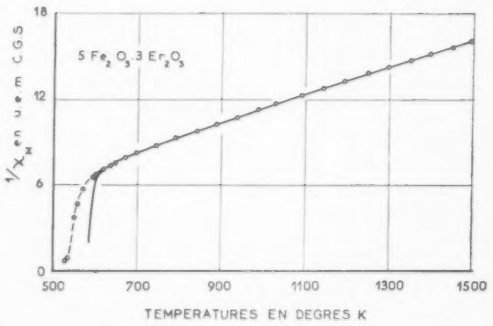

FIG. 10. Paramagnétisme des grenats de terbium et de dysprosium. Points expérimentaux et courbes théoriques en traits pleins.

FIG. 11. Paramagnétisme des grenats d'holmium et d'erbium. Points expérimentaux et courbes théoriques en traits pleins.

7. LES FERRITES GRENATS DE SAMARIUM ET D'EUROPIUM

D'après VAN VLECK[15], le moment effectif des ons Sm et Eu doit varier avec la température: la loi de Curie n'est plus applicable et l'on ne peut utiliser la méthode d'interprétation que nous avons développée pour les autres ferrites grenats. (Section 3.)

La Figure 13 représente les courbes expérimentales ($1/\chi$, T) relatives aux ferrites grenats de

VOL. 15 1960

samarium et d'europium; la correction de diamagnétisme sous-jacent des ions n'a pas été faite. Nous remarquerons que ces courbes ont l'allure générale de celles obtenues pour les autres ferrites grenats.

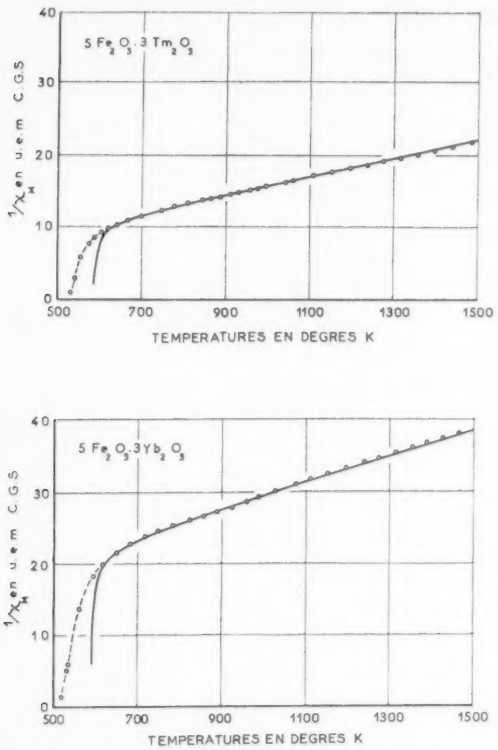

FIG. 12. Paramagnétisme des grenats de thulium et d'ytterbium. Points expérimentaux et courbes théoriques en traits pleins.

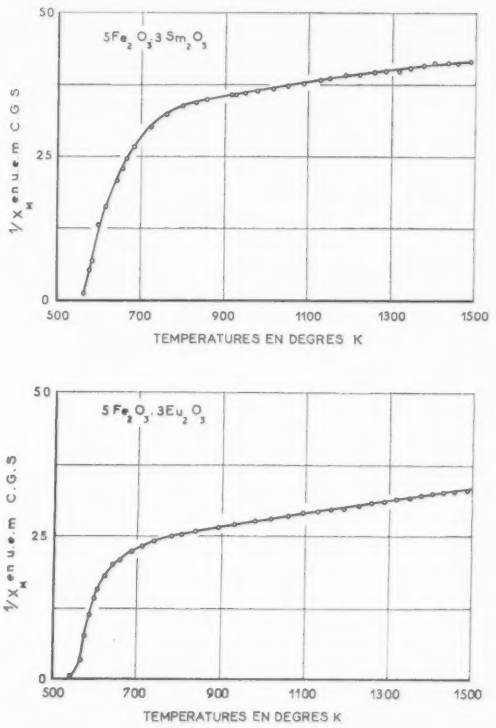

FIG. 13. Paramagnétisme des grenats de samarium et d'europium. Courbes expérimentales.

8. CONCLUSION

La théorie du ferrimagnétisme de NÉEL pour les substances à deux sous-réseaux magnétiques, et son extension aux substances à trois sous-réseaux, nous a permis d'interpréter nos résultats expérimentaux de mesure des susceptibilités paramagnétiques des grenats d'yttrium et de terres rares, au-dessus de leur point de Curie.

Les courbes expérimentales des grenats d'yttrium et de lutétium, qui sont des substances à deux sous-réseaux, nous ont permis de calculer les trois coefficients de champ moléculaire caractérisant les interactions fer–fer. Ces coefficients ont des valeurs très voisines dans les deux ferrites. L'étude cristallographique ayant montré que les distances entre les ions fer étaient sensiblement les mêmes dans tous les grenats, nos résultats nous permettent d'émettre l'hypothèse que ces trois coefficients sont constants pour tous les ferrites grenats.

Pour les grenats de gadolinium, terbium, dysprosium, holmium, erbium, thulium et ytterbium qui sont des substances à trois sous-réseaux, nous avons montré que le coefficient de champ moléculaire caractérisant les interactions terres rares entre elles, devait être très petit, ce qui confirme les résultats de PAUTHENET. En négligeant ce terme, nous avons pu calculer les deux coefficients de champ moléculaire caractérisant les interactions fer–terres-rares, et avoir ainsi, pour chacun de ces

ferrites, un ordre de grandeur des six coefficients de champ moléculaire.

Remerciements—J'exprime ma profonde et très respectueuse reconnaissance à M. le Professeur NÉEL, qui m'a accueilli dans son Laboratoire et m'a confié l'étude qui fait l'objet du présent mémoire. Je remercie M. BARBIER pour la bienveillante sollicitude avec laquelle il a dirigé mes travaux et n'a cessé de me prodiguer ses conseils et ses encouragements. Je remercie également M. PAUTHENET de l'intérêt qu'il a manifesté pour mon travail et de l'obligeance avec laquelle il m'a fait profiter de son expérience sur les ferrites. Je tiens à exprimer à M. BRISSONNEAU, qui m'a initié aux diciplines de la recherche et m'a orienté dans cette voie, ma plus vive gratitude. Je remercie M. BERTAUT, directeur du Laboratoire des rayons X et ses collaborateurs, Mme PAUTHENET et M. FORRAT à qui je dois la préparation et l'étude cristallographique des ferrites que j'ai mesurés. Enfin, je remercie tous mes camarades du Laboratoire d'Electrostatique et de Physique du Métal de Grenoble, pour leur aide et leur dévouement à mon égard.

BIBLIOGRAPHIE

1. BERTAUT F. et FORRAT F., *C.R. Acad. Sci., Paris* **242,** 382 (1956).
2. PAUTHENET R., Thèse, Grenoble (1957).
3. NÉEL L., *Ann. Phys., Paris* **3,** 137 (1948).
4. FOËX G. et FORRER R., *J. Phys. Radium* **7,** 180 (1926).
5. FALLOT M., *J. Phys. Radium* **5,** 153 (1944).
6. FALLOT M. et MARONI P., *J. Phys. Radium.* **12,** 256 (1951).
7. WEIL L., Thèse, Strasbourg (1941).
8. NÉEL L., *C.R. Acad. Sci., Paris* **239,** 8 (1954).
9. NÉEL L., *J. Phys. Radium* **12,** 258 (1951).
10. NÉEL L. et PAUTHENET R., *C.R. Acad. Sci., Paris* **234,** 2172 (1952).
11. SLATER J. C., *Phys. Rev.* **36,** 57 (1930).
12. MARONI P., Communication personnelle.
13. ALÉONARD R. et BARBIER J. C., *C.R. Acad. Sci. Paris* **245,** 831 (1957).
14. ALÉONARD R. et BARBIER J. C., *J. Phys. Radium* **20,** 378 (1959).
15. VAN VLECK J. H., *The Theory of Electric and Magnetic Susceptibilities*. Oxford University Press (1932).

LETTER TO THE EDITOR

Electrical properties of Ag_2Te

(*Received* 18 *September* 1959; *revised* 16 *November* 1959)

POLYCRYSTALLINE specimens of β-Ag_2Te have been made in these laboratories; Hall measurements indicate that they behave like normal semiconductors with an energy gap of $\sim$0·025 eV.

A range of compositions from 3 atomic per cent excess silver to 3 atomic per cent excess tellurium above the stoichiometric Ag_2Te has been made. (Excess silver gives rise to *n*-type, and excess tellurium to *p*-type, material.) The α (cubic) form exists above 150°C and the β (orthorhombic) form below. The ingots were produced by vertical lowering, directional freezing or zone refining, from Tadanac (99·999 per cent) silver and Asarco (99·999 per cent) tellurium. Carbon or quartz crucibles were used; carbon was found to be the more satisfactory, since there is a strong tendency for silver to attack and stick to quartz. No problems of dissociation were encountered; the dissociation vapor pressure of tellurium at the melting point of Ag_2Te was checked by the method of FOLBERTH[1] and found to be $<10^{-6}$ mm Hg.

The Hall coefficient and resistivity of the specimens were measured between 55°C and room temperature (see Figs. 1 and 2). The forbidden band gap of 0·025 eV was determined from a plot of $\log 1/RT^{3/2}$ vs. $1/T$ for the *n*-type sample W-5C and from a plot of np/T^3 vs. $1/T$ for the *p*-type samples. These curves deviated from a straight line at both high and low temperatures, as was observed by HARMAN *et al.*[2] in HgTe. The *p*-type samples W-6C and W-8 overshot the intrinsic line, a phenomenon observed in InSb by WELKER and WEISS[3].

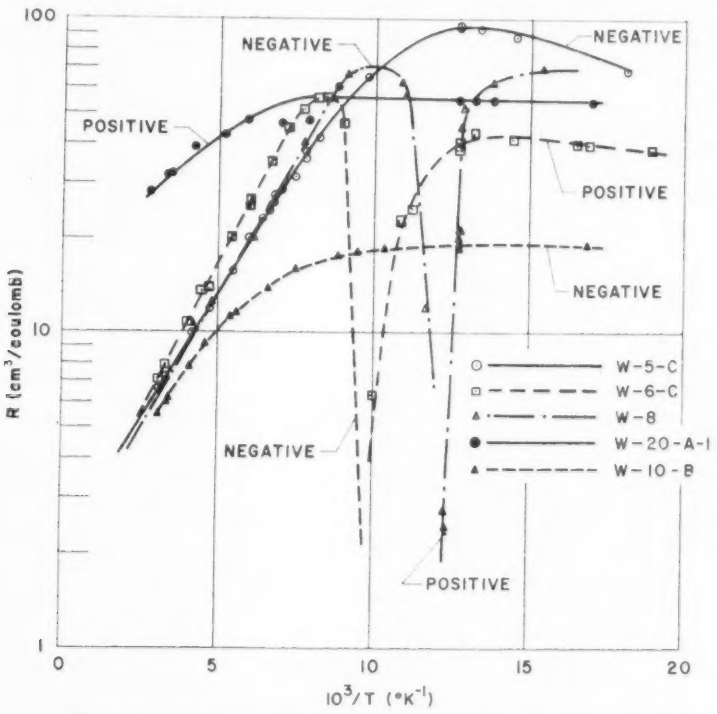

FIG. 1. The Hall coefficient (cm^3/C) of β-Ag_2Te as a function of reciprocal temperature ($10^3/T$ °K^{-1}).

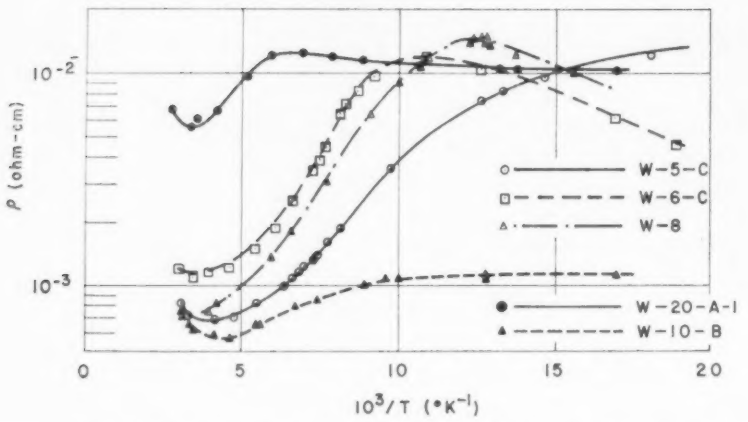

FIG. 2. The resistivity (Ω-cm) of β-Ag_2Te as a function of reciprocal temperature ($10^3/T$ °K^{-1}).

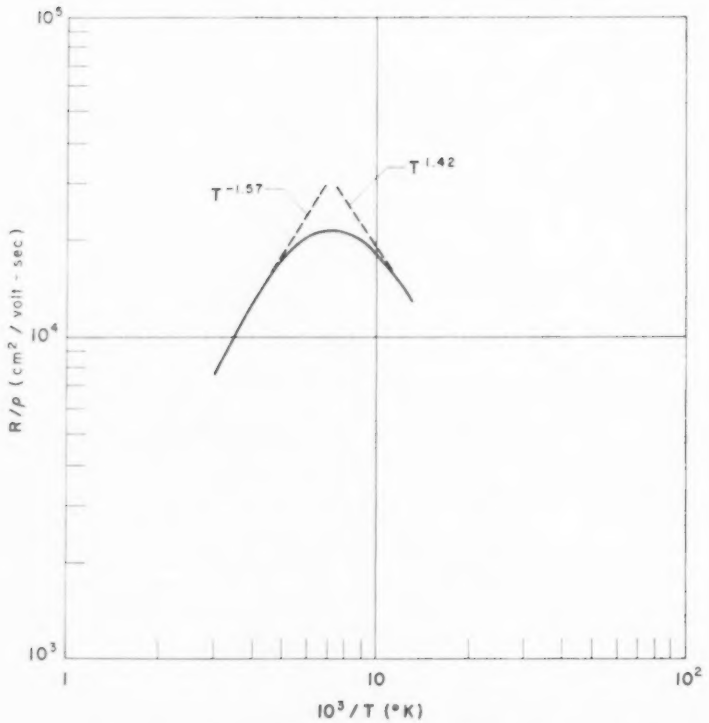

FIG. 3. R/ρ (cm²/V-sec) of specimen W-5C as a function of reciprocal temperature ($10^3/T$ °K^{-1}), obtained from Figs. 1 and 2.

From the ratio of heights of the maximum to the extrinsic value of the Hall curves on p-type material, mobility ratios have been calculated. The results are shown in Table 1. Values of room-temperature mobility were calculated from the expression $\mu_e = -8/3\pi\, R\sigma/(b-1)$ and are also given in Table 1. A mobility ratio of six was assumed for the n-type sample. The R/ρ vs. $1/T$ curve for the n-type sample (Fig. 3) follows the usual pattern of increasing in value as the temperature falls, reaching a maximum at 130°K and then decreasing. The temperature-dependence of this curve in the high-temperature region is approximately $T^{-3/2}$, indicating that we are in the lattice scattering range. In this scattering range, the mobility is proportional to the 5/2 power of the effective mass. From this relationship, effective mass values have been determined at room temperature.[4] These values have been obtained by ignoring any change in energy gap with temperature.

Table 1. *The electrical properties of* β-Ag_2Te*

	W-8	W-6C	W-5C
Gap width (eV)	0·025	0·025	0·025
Mobility ratio	5·8	7·0	—
Effective masses:			
m_n/m	0·1	0·1	0·1
m_p/m	0·2	0·2	0·2
np(cm^{-6}) (300°K)	$8{\cdot}8\times10^{35}$	$7{\cdot}9\times10^{35}$	$6{\cdot}3\times10^{35}$
Mobility of electrons 300°K(cm^2/V-sec)	10,500	6860	8370
Mobility of holes 300°K(cm^2/V-sec)	1810	980	1400

* The effects of degeneracy which will be present due to the small gap have been neglected in this analysis owing to a lack of data on the variation of energy gap with temperature.

An increase in resistivity with increasing temperature appears at the upper end of the temperature range. In addition, the Hall and resistivity curves are closely, but not exactly, reproducible on repeated runs, although the activation energies are always the same. These anomalies have not as yet been explained, but they could be due to atomic rearrangements.[5]

The possibility was considered that these measurements might reflect surface, rather than bulk, properties; however, agreement between measurements on lapped and etched specimens indicated that this was not the case.

A disturbing note was that APPEL[6] had obtained a wide spread of Hall-constant values near room temperature which are inconsistent with a small energy gap. However, one specimen (W-20-Al) that was measured in these laboratories also exhibited properties at variance with those of W-8, W-6C, W-10B and W-5C. X-ray measurements on this specimen indicated the presence of two phases: Te (40–50 per cent) and $Ag_{(2-x)}Te$ (50–60 per cent), where $0{\cdot}4 \leqslant x \leqslant 1$.[7] X-ray measurements on W-8, W-6C, W-10B and W-5C indicated β-Ag_2Te.

Acknowledgements—We would like to acknowledge the assistance given during the course of this work by Dr. M. H. FRANCOMBE, Mr. J. FLOOD and Mr. V. HARRAP.

Research Division
Philco Corporation
Philadelphia, Pa.

G. E. GOTTLIEB
W. M. KANE
J. F. WALSH
C. WOOD

References

1. FOLBERTH O. G., *J. Phys. Chem. Solids* **7**, 295 (1958).
2. HARMAN T. C., LOGAN M. J. and GOERING H. L., *J. Phys. Chem. Solids* **7**, 228 (1958).
3. WELKER H. and WEISS H., *Solid State Physics* (edited by SEITZ F. and TURNBULL D.) Vol. 3, Academic Press, New York (1957).
4. BRECKENRIDGE R. G., BLUNT R. F., HOSLER W. R., FREDERIKSE H. P. R., BECKER J. H. and OSHINSKY W., *Phys. Rev.* **96**, 571 (1954).
5. MIYATANI S., *J. Phys. Soc. Japan* **14**, 996 (1959).
6. APPEL J., *Z. Naturf.* **10**A, 530 (1955).
7. THOMPSON R., PEACOCK M. A., ROWLAND J. F. and BERRY L. G., *Amer. Min.* **36**, 458 (1951).

BOOK REVIEW

W. F. DeJong (with the collaboration of J. Bouman): **General Crystallography: A Brief Compendium.** W. H. Freeman and Co., San Francisco, 1959. ix + 281 pp., $6.00.

This compendium, divided into four parts, is essentially a translation of the 1951 Dutch edition with some sections enlarged and others rewritten. Part I, *Geometric Crystallography* is a fairly traditional treatment of symmetry, crystal classes and calculations discussed by means of the stereographic projection. Less than one page is devoted to the gnomonic projection. The direct and indirect (reciprocal) lattices are considered briefly. In Part II, *Structural Crystallography*, mention of Bravais lattices and space groups is followed by discussions of the various film methods for studying crystals by X-ray diffraction. Intensities, Fourier analyses and Patterson diagrams are also considered.

Part III, *Chemical Crystallography* is largely devoted to descriptions of individual crystal structures and only a brief treatment is given to a discussion of the general principles of crystal chemistry. Part IV, *Physical Crystallography*, covers a variety of topics: second and higher order tensors, deformation of crystals, optical crystallography, conductivity, electrical properties, elasticity, structural imperfections, hardness, gliding, ionic conduction, etc.

This book packs into a small number of pages a wealth of crystallographic information and does most effectively as the author states in the Preface ". . . serve undergraduate students as a summary of the modern view of crystallography." It will not only serve students but instructors as well, who, by use of the many well chosen references, can build around it a thorough-going, comprehensive course.

C. S. Hurlbut, Jr.

VOL.
15
1960

ERRATUM

J. A. HOFMANN, A. PASKIN, K. J. TAUER and R. J. WEISS, Analysis of ferromagnetic and antiferromagnetic second order transitions, *J. Phys. Chem. Solids* **1**, 45 (1956).

We wish to thank Dr. L. D. JENNINGS for pointing out that the value used in our paper for the coefficient in the Bloch spin wave $T^{3/2}$ law for the low temperature saturation magnetization of a ferromagnet was incorrect for the case of a hexagonal close packed lattice. In the Bloch equation

$$M(T) = M(0)\ (1 - CT^{3/2})$$

where $C = (0{\cdot}0587/\lambda s)\ (k/2Js)^{3/2}$, we previously used $\lambda = 2$ for hexagonal close packed gadolinium, whereas the correct value is $\lambda = 4$. Using the Bloch equation the experimental low temperature magnetization then leads to a value of $J = 0{\cdot}00014$ eV for gadolinium instead of the value of $J = 0{\cdot}00023$ eV given in Table 3. Thus, as in the case of Ni and Fe, there is actually poor agreement in Gd between the value of J calculated from low temperature magnetization and the value of $J = 0{\cdot}00021$ eV calculated from magnetic energy W. It should be noted, however, that our previous error in the value used for λ does not invalidate the spin wave low temperature specific heat for Gd plotted as a dotted line in Fig. 7, since λ and J appear in the spin wave specific heat expression given in equation (14) as the product $\lambda J^{3/2}$ which is exactly the way they enter in the expression given for the constant C above.

PAPERS TO BE PUBLISHED IN FUTURE ISSUES

P. A. FLINN, G. M. MCMANUS and J. A. RAYNE: Elastic constants of ordered and disordered Cu_3Au fron 4·2 to 300°K.

R. J. ELLIOTT and R. LOUDON: Theory of the absorption edge in semiconductors in a high magnetic field.

A. G. CHYNOWETH and W. L. FELDMANN: Ferroelectric domain delineation in triglycine sulphate and domain arrays produced by thermal shocks.

R. I. BEECROFT and C. A. SWENSON: On the existence of a critical point for the phase transition in cerium.

J. FORTEN and E. R. JOHNSON: The radiation induced decomposition of potassium nitrate.

E. M. CONWELL and A. L. BROWN: Scattering of hot carriers in germanium.

W. ALBERS, C. HAAS and F. VAN DER MAESEN: The preparation and the electrical and optical properties of SnS crystals.

J. HORNSTRA: Dislocations, stacking faults and twins in the spinel structure.

H. H. SCHMIDT and G. JURA: The grain boundary energy and configuration of inert gas crystals.

H. H. SCHMIDT and G. JURA: Surface energy and configuration of inert gas crystals.

J. J. LANDER: Reactions of lithium as a donor and an acceptor in ZnO.

J. C. SLONCZEWSKI: Origin of magnetoelastic effects in cobalt–iron ferrite.

R. J. SLADEK: Magnetoresistance of high-purity InSb in the quantum limit.

A. SEEGER and H. BROSS: Elektronentheoretische Untersuchungen über Fehlstellen in Metalle—VIII.

J. P. SUCHET: Rayons atomiques, electronegativités et energies d'activation dans les composés sem conducteurs mineraux.

F. E. PRETZEL, G. N. RUPERT, C. L. MADER, E. K. STORMS, G. V. GRITTON and C. C. RUSHING: Properties of lithium hydride—I. Single crystals.

J. Phys. Chem. Solids Pergamon Press 1960. Vol. 15. pp. 189–195. Printed in Great Britain.

ELASTIC CONSTANTS OF ORDERED AND DISORDERED Cu_3Au FROM 4·2 TO 300°K

P. A. FLINN, G. M. McMANUS and J. A. RAYNE

Westinghouse Research Laboratories, Pittsburgh, Pennsylvania

(*Received* 30 *September* 1959; *revised* 14 *December* 1959)

VOL. 15 1960

Abstract—The elastic constants of ordered and disordered Cu_3Au have been measured from 4·2 to 300°K. The room temperature data are in good agreement with previous work. At liquid helium temperatures the ordered material, with $S = 0{\cdot}95$, gives

$$\begin{aligned} c_{11} &= 1{\cdot}893 \pm 0{\cdot}015 \times 10^{12} \text{dyn cm}^{-2} \\ c_{12} &= 1{\cdot}319 \pm 0{\cdot}015 \times 10^{12} \text{dyn cm}^{-2} \\ c_{44} &= 0{\cdot}736 \pm 0{\cdot}002 \times 10^{12} \text{dyn cm}^{-2} \end{aligned} \quad (1)$$

The corresponding value of Debye temperature is

$$\theta_{\text{ordered}} = 283{\cdot}8 \pm 3{\cdot}5°\text{K},$$

which compares very well with the calorimetric figure of 285 ± 2°K. For the disordered alloy, the elastic data give a Debye temperature of

$$\theta_{\text{disordered}} = 281{\cdot}6 \pm 3{\cdot}5°\text{K},$$

which is within experimental error of the calorimetric value of 278 ± 2°K. The elastic constants for the disordered alloy indicate that the Fermi surface is less distorted than that in pure copper.

1. INTRODUCTION

THE only extensive measurements relating to the elastic properties of ordered and disordered Cu_3Au are those of SIEGEL[1]. These experiments, which cover the range 300–720°K, were made on a series of crystals of unknown degree of order using the composite oscillator technique. In view of the improved accuracy now available using the ultrasonic pulse method, it appeared desirable to check the room temperature values of the elastic constants of Cu_3Au on a crystal of known degree of order. Furthermore, owing to recent experimental and theoretical work on the lattice dynamics of metals and alloys, it was considered of interest to extend elastic constant measurements to liquid helium temperatures. The latter data enable a comparison to be made between the Debye temperatures of disordered and ordered Cu_3Au, as determined from elastic constants, and those obtained from low temperature heat capacity measurements[2] as well as low temperature resistance studies.[3,4]

2. EXPERIMENTAL

(a) *Specimen preparation*

A single crystal of Cu_3Au was prepared from a melt of the appropriate composition using the Bridgman method, with a cooling rate of approximately 2°C/hr. The resulting ingot was etched electrolytically in a solution of silver cyanide and potassium cyanide and oriented with X-rays by the usual Laue back reflection technique. A specimen was then carefully machined from the crystal, so as to produce a cylinder approximately $\frac{5}{8}$ in. in diameter and $\frac{5}{8}$ in. long, with the axis of the cylinder along the [110] crystallographic direction. The ends of the cylinder were carefully lapped to parallelism within 0·0001 in., after which they were lightly etched in the same solution as used previously. A thin slice of material, also cut so as to expose a (110) face, was taken from the ingot adjacent to the ultrasonic specimen for the purpose of determining the degree of order by X-rays. Chemical analysis gave the composition of both specimens as being 50·66 per cent gold by weight,

which figure is within the experimental error of the ideal composition, viz. 50·85 per cent by weight.

In all subsequent work the specimens were heat treated simultaneously so as to insure their having identical properties. They were first disordered by water quenching from 775°C. X-ray measurements revealed no presence of any superlattice lines. To order the specimens, a procedure different from that employed by JONES and SYKES[5] was used. They were first annealed just below the critical temperature, at 370°C for 70 hr, so as to produce large anti-phase domains. After quenching the samples were reheated to 230°C for 170 hr. From the experiments of FEDER *et al.*[6], it was known that this heat treatment would produce essentially the maximum possible degree of order.

(b) *Determination of the degree of order*

To determine the long range order parameter S, X-ray intensity measurements were made with a counter spectrometer. Molybdenum K-radiation, monochromated by reflection from a bent LiF crystal, was used with a thallium activated, sodium iodide scintillation counter as a detector. The beam divergence was adjusted to $\frac{1}{2}°$, approximately equal to the mosaic spread of the specimen. The specimen was mounted with the [001] direction vertical, and intensity measurements made on all ($hh0$) reflections ranging from (330) to (770). Measurements were also made on reflections of the type ($hh1$) by rotating the crystal about the [001] direction. For these unsymmetrical reflections, there is a correction to the intensity[7] which can be eliminated by taking the mean of measurements made with the crystal rotated to either side of the axis.

To make the intensity measurements, the counter slit was adjusted to a width corresponding to an angular displacement in Bragg angle of 1°. The intensity was then recorded as the crystal was rotated through 4° about the Bragg position. In this way the effects of mosaic spread and beam divergence were eliminated. Owing to the presence of the $K\alpha_1$–$K\alpha_2$ doublet, it was not possible to encompass the entire reflection in a single counter setting. Accordingly, the intensity was recorded with the counter displaced from the Bragg position by $\pm 1°$, $\pm 2°$. The total intensity of the line was taken as the sum of the separate contributions, corrected for background.

The expressions for the integrated intensity of the fundamental and superlattice peaks for Cu_3Au are*

$$I_f = K[3f_{Cu}\exp(-M_{Cu})+f_{Au}\exp(-M_{Au})]^2\,\text{P.L.} \quad (2)$$

$$I_s = KS^2[f_{Au}\exp(-M_{Au})-f_{Cu}\exp(-M_{Cu})]^2\,\text{P.L.}$$

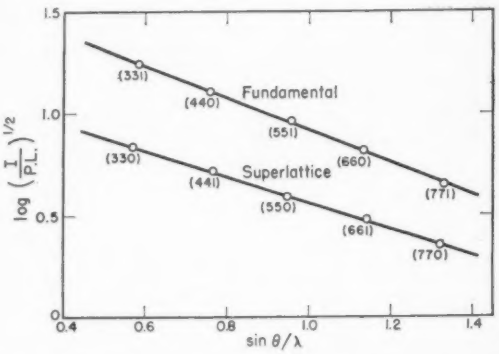

FIG. 1. $\log(I/\text{P.L.})^{1/2}$ versus $\sin\theta/\lambda$ for fundamental and superlattice reflections of Cu_3Au.

where P.L. has been written for $(1+\cos^2 2\theta_0 \times \cos^2 2\theta)/\sin 2\theta$, θ_0 being the take-off angle of the monochromator. These intensities are shown in Fig. 1. Using this graph and tables of f_{Au}[8] and f_{Cu}[9] corrected for Hönl dispersion,[10] it was then possible to determine $K^{1/2}e^{-M}$ vs. $\sin\theta/\lambda$ for a given value of S in a fashion described by CHIPMAN[11]. This result is shown in Fig. 2. Clearly, the value of S must be very close to $S = 0{\cdot}95$. The root mean square amplitudes of vibration of the copper and gold atoms, determined from the slopes of the lines in Fig. 2, are $\langle U^2_{Cu}\rangle^{1/2} = 0{\cdot}088$ Å and $\langle U^2_{Au}\rangle^{1/2} = 0{\cdot}068$ Å, which values are very close to CHIPMAN's values of 0·093 Å and 0·069 Å, respectively. Using our values of $\langle U^2\rangle$, we can find S for each fundamental reflection using the data of Fig. 1. and equation (2). A simple average of these results gives $S = 0{\cdot}94 \pm 0{\cdot}02$. It can be shown that if M_{Au} and M_{Cu} are taken as only approximately determined, then the error terms in the M's can be

* The actual f's are complex, but the absolute values were used and treated as real for convenience. The maximum error involved is of the order of 3 per cent.

developed in a power series, and a least squares analysis applied to the data. A quadratic fit to the data does not significantly change the average value given above.

For the lattice parameter in the disordered and ordered condition we find, respectively, $a = 3{\cdot}7490 \pm 0{\cdot}0003$ Å, and $3{\cdot}7426 \pm 0{\cdot}0003$ Å at 25°C.

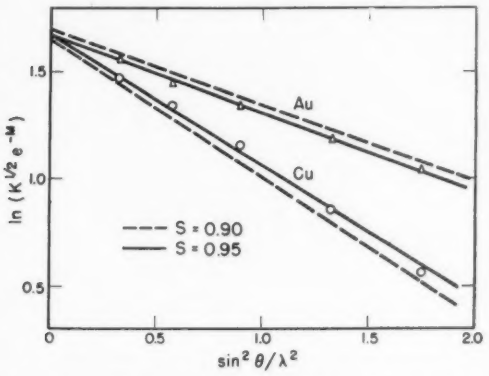

FIG. 2. $\ln(K^{1/2}e^{-M})$ versus $(\sin\theta/\lambda)^2$ for $S = 0{\cdot}90$ and $S = 0{\cdot}95$.

According to FEDER *et al.*[6], the lattice parameter for $S = 0{\cdot}95$ should be $a = 3{\cdot}7471$ Å at 25°C, which figure differs from our measurement by an amount well outside the estimated combined error. About half of this discrepancy can be accounted for by differences in the chemical composition of the two samples (0·43 per cent by weight of gold); for the remainder it is perhaps enough to remark that the value given by FEDER is based on the measurements of WARREN and KEATING[12], which work was done on polycrystalline samples, without taking account of the differences in temperature factor for the gold and copper atoms. It has been shown by CHIPMAN[11] that the neglect of this difference causes a significant overestimate of S. For this reason, we are inclined to discount the difference between the S predicted from the equilibrium order curve and that found here. It is perhaps more appropriate to compare the *difference* in lattice parameters for the ordered and disordered alloys, since this difference will be quite insensitive to the chemical composition. Our measurements yield a difference of 0·0064 Å, while BETTERIDGE[13], from measurements an alloy containing 49·59 per cent by weight gold, finds a difference of 0·0066 Å.

(c) *Elastic constant measurements*

The elastic constants of the crystal were measured in the disordered and ordered states using an Arenberg* pulsed oscillator and wide band amplifier in conjunction with a Tektronix oscillograph. Details of the measuring techniques have been described in previous papers[14, 15] and need no further elaboration, except as regards the bonding used between the crystal and transducer. Thus, at temperatures below 120°K, it was found that both glycerin and EPA[14] tended to crack. A satisfactory bond was obtained using Dow Corning silicone fluid of 200 cS viscosity. This was applied at room temperature and the assembly rapidly cooled in liquid nitrogen, after which the apparatus was placed in the regular Dewar and cooled in helium temperatures. Using this technique, no difficulty was experienced in obtaining good echoes in the range 4·2–77°K.

To obtain the temperature variation of the elastic constants it is necessary to know the corresponding variation of the lattice parameter of Cu_3Au in the disordered and ordered states. The lattice parameter in the disordered state was measured at 4·2°K, 77°K and 298°K in a cryostat to be described in a later paper. Table 1 gives the results

Table 1. *Values of the lattice parameter of disordered* Cu_3Au

Temperature (°K)	Lattice parameter (Å)
298	$3{\cdot}7490 \pm 0{\cdot}0003$
77	3·7376
4·2	3·7367

of these measurements. Values of the lattice parameter at intermediate temperatures were obtained graphically, assuming that the parameter varied linearly above 77°K and that the curve had zero slope near absolute zero. Since the lattice parameter for the ordered state at 25°C differs by only 0·0064 Å from that in the disordered state, little error is incurred by assuming a similar variation with temperature of the ordered lattice parameter.

* Arenberg Ultrasonic Laboratory, Boston, Mass.

Table 2. Adiabatic elastic constants for Cu_3Au *in ordered and disordered states at* 4·2°K *and* 300°K*

State	Temperature (°K)	c_{11} (10^{12}dyn cm^{-2})	c_{12} (10^{12}dyn cm^{-2})	c_{44} (10^{12}dyn cm^{-2})
Disordered	4·2	1·870 ± 0·015	1·324 ± 0·015	0·745 ± 0·002
	300	1·849	1·353	0·687
Ordered	4·2	1·893	1·319	0·736
	300	1·871	1·349	0·678
		(1·91 ± 0·17)	(1·39 ± 0·17)	(0·662 ± 0·005)

* The values in parentheses are those derived from SIEGEL's data. See Ref. (1).

3. RESULTS

Values for the adiabatic elastic constants of ordered and disordered Cu_3Au at 4·2°K and 300°K are summarized in Table 2. The uncertainties quoted in this table are the probable errors arising from the velocity determinations. No definite figure can be adduced for an estimate of the error caused by crystal imperfections and transit time

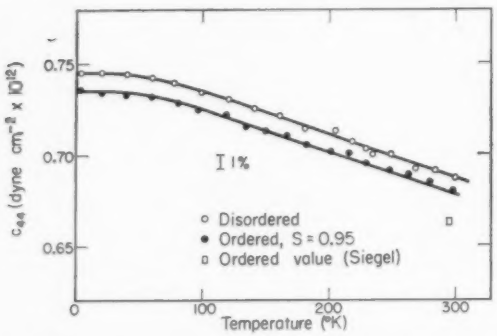

FIG. 3. Temperature variation of c_{44} for Cu_3Au in ordered and disordered condition.

effects. These, however, will affect neither the *relative* change of the elastic constants on ordering nor their variation with temperature. These latter are shown in Figs. 3–5, together with the data of SIEGEL[1] at 300°K for ordered Cu_3Au.

4. DISCUSSION

(a) *Changes in elastic constants on alloying*

Reference to Figs. 3–5 and Table 2 shows that there is fairly good agreement between our results and those of Siegel for the elastic constants of ordered Cu_3Au at 300°K. No significance attaches

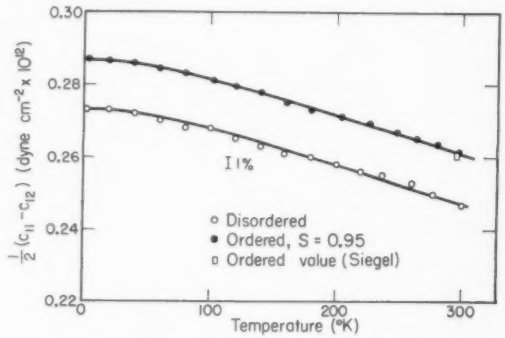

FIG. 4. Temperature variation of $\frac{1}{2}(c_{11}-c_{12})$ for Cu_3Au in ordered and disordered condition.

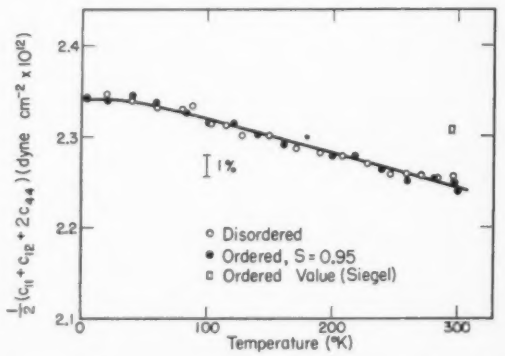

FIG. 5. Temperature variation of $\frac{1}{2}(c_{11}+c_{12}+2c_{44})$ for Cu_3Au in ordered and disordered condition.

to the discrepancy between the values of $\frac{1}{2}(c_{11}+c_{12}+2c_{44})$, since there is a large uncertainty in the figure derived from the compliance data, due to the fact that $s_{11}+2s_{12} \sim 0$. The difference

between the values of c_{44} seems to be slightly outside the estimated combined error; no definite explanation can be advanced for this discrepancy.

From Figs. 3–5, it can be seen that the curves for the temperature variation of the elastic constants of ordered and disordered Cu_3Au are very nearly parallel to each other. Of particular interest is the fact that at temperatures well below the critical temperature, the shear constant c_{44} for the disordered alloy is *greater* than that for the ordered alloy while the reverse holds for the shear constant $\frac{1}{2}(c_{11}-c_{12})$. This behavior is to be contrasted with that near the critical temperature where both c_{44} and $\frac{1}{2}(c_{11}-c_{12})$ increase on ordering. Clearly the reason for this difference must arise from the fact that, at higher temperatures, the order parameter S is changing significantly with temperature and hence there is a resulting contribution to the elastic constants.

It is of interest to analyze the low temperature elastic constants of the ordered and disordered alloy in the manner described in a previous paper.[14] Thus, we write for the difference between the shear constants $C = c_{44}$ and $C' = \frac{1}{2}(c_{11}-c_{12})$ of the pure metal and the alloy

$$\Delta C = (\Delta C)_{\text{lattice}} + (\Delta C)_{\text{alloying}} \qquad (3)$$

with a similar expression for $\Delta C'$.

For disordered Cu_3Au, the changes in C and C' due to lattice expansion can be computed using the values 3·6158 Å and 3·7490 Å for the lattice parameters of copper and the alloy at 25°C and assuming $r/\rho = 17$ in the expression for the ion-core interaction energy. Since copper and gold are monovalent, there can be no change in the effective non-localized electron density. Furthermore, since overlap presumably takes place in the $\langle 111 \rangle$ directions, there is no contribution[14] to the shear constant C' and we may write

$$(\Delta C)_{\text{alloying}} = \alpha x C_I + (\Delta C)_{\text{overlap}}$$
$$(\Delta C')_{\text{alloying}} = \alpha x C_I' \qquad (4)$$

where αx is constant, x being the molar concentration of solute. From the known change in C', the second of these equations may be used to determine the constant α. In this way we find $\alpha = +2{\cdot}75$, which figure does not appear unreasonable, since the gold atom is larger than that of the copper and one would hence expect a larger ion-core interaction energy. Substituting into the first equation, one then finds

$$(\Delta C)_{\text{overlap}} = -0{\cdot}16 \times 10^{12} \text{dyn cm}^{-2}.$$

This value implies that the overlap *decreases* on alloying, or at least that the Fermi surface becomes more spherical. This conclusion is in accord with the theory of COHEN and HEINE[16], insofar as their work predicts that the addition of gold to copper should cause a decrease in the gap across the {111} zone faces, i.e. the sphericity of the Fermi surface should increase. Under these conditions, the density-of-states for the alloy would be closer to the free electron value, in agreement with experiment.[2]

(b) *Change in elastic constants on ordering*

In the ordered state the zone structure for the alloy is different from that in the disordered condition. It is known[2] that the basic Brillouin zone for the f.c.c. lattice is subdivided into subzones corresponding to the basic cubic cell, and that the Fermi surface must overlap into the third such subzone. Since the second subzone is similar to that for a b.c.c. lattice, it follows from the work of JONES[17], that the resulting overlap gives contributions to both C and C'.

Using the lattice parameters for ordered and disordered Cu_3Au, viz. 3·7426 and 3·7490 Å at 25°C, to compute $\Delta a/a$, one can again find changes in C and C' due to contraction of the lattice on ordering, the experimentally determined changes in C and C', one then finds

$$\alpha x C_I + (\Delta C)_{\text{overlap}} = -0{\cdot}030 \times 10^{12}$$
$$\alpha x C_I' + (\Delta C')_{\text{overlap}} = +0{\cdot}008 \times 10^{12}. \qquad (5)$$

The magnitude of αx for the transition from the disordered to the ordered phase may be estimated roughly by noting that, insofar as the copper atoms are concerned, the number of nearest neighbor gold atoms changes from three in the disordered state to four in the ordered state. Hence from the α value in the disordered state, we find $\alpha x = +0{\cdot}7/3 = 0{\cdot}24$, whence from equation (5)

$$(\Delta C)_{\text{overlap}} = -0{\cdot}186 \times 10^{12} \text{ dyn cm}^{-2}$$
$$(\Delta C)_{\text{overlap}} = -0{\cdot}048 \times 10^{12} \text{ dyn cm}^{-2}. \qquad (6)$$

Although these values do not appear to be

unreasonable, it is difficult to infer very much information about the overlap from them, since the overlap contribution in the disordered state is not known. Since $\Delta C'$ is fairly large and negative, however, it seems likely that there must be a considerable contribution from the third subzone, i.e. the second subzone contains a fairly large number of holes.

(c) *Debye temperature of ordered and disordered* Cu_3Au

Using the values of the low temperature elastic constants of disordered and ordered Cu_3Au and the lattice expansion data of Table 1, the corresponding values of Debye temperature may readily be computed from the formula[18]

$$\theta^3 = \frac{9N}{4\pi V}\left(\frac{h}{k}\right)^3\left(\frac{c_{44}}{\rho}\right)^{3/2}\frac{9}{18+\sqrt{3}}f(s,t), \qquad (7)$$

where $f(s,t)$ is a tabulated function of the variables $s=(c_{11}-c_{44})/(c_{12}+c_{44})$ and $t=(c_{12}-c_{44})/(c_{44})$. The results of these calculations are shown in Table 3, together with the data obtained from low temperature heat capacity and electrical resistance studies.

Table 3. Comparison of Debye temperature of Cu_3Au *as determined by various methods*

Experiment	Debye temperature	
	Disordered	Ordered
Calorimetric*	278 ± 2	285 ± 2
Elastic constant†	281·6 ± 3·5	283·8 ± 3·5
Resistance‡	175§	197§

* See Ref. (2).
† Present work.
‡ See Ref. (3).
§ Errors not known.

It will be seen that there is very good agreement between the θ values obtained from the elastic data and those obtained calorimetrically, the differences in both cases being within the estimated experimental errors. Apparently it seems to be a good approximation, even in the disordered condition, to treat the alloy as an anisotropic cubic metal having the same density and elastic constants, without any allowance for such fine details of structure as short range order. The effects of the latter would, of course, be quite small and it is quite possible that the present experimental errors are too large to detect them.

The Debye temperatures, obtained from low temperature resistance measurements, differ markedly from those obtained by other methods. Furthermore, the change in θ on ordering obtained by BOWEN appears to be much too large. In this connection, it is of interest that PASSAGLIA and LOVE find a maximum difference of only 5°K, which value is more in accord with the figure obtained in the present work. Since their experiments also show a strongly temperature dependent value of Debye temperature, it seems that there is little significance to be attached to the magnitude of θ determined from resistance studies.

5. CONCLUSION

Elastic constant measurements have been made between 4·2–300°K on Cu_3Au in the disordered and ordered state. From the elastic constants in the disordered condition, it is concluded that the addition of gold to copper increases the sphericity of the Fermi surface. The values of Debye temperature, as computed from the elastic data at 4·2°K, are in good agreement with those obtained calorimetrically. It is concluded that little significance can be attached to θ values obtained from resistance measurements on Cu_3Au.

Acknowledgement—Thanks are due to Mr. J. ROTHENBERG for his great assistance in making the intensity measurements used in determining the long range order parameter.

REFERENCES

1. SIEGEL S., *Phys. Rev.* **57,** 537 (1940).
2. RAYNE J., *Phys. Rev.* **108,** 649 (1957).
3. BOWEN D. B., *Acta Met.* **2,** 573 (1954).
4. PASSAGLIA E. and LOVE W. F., *Phys. Rev.* **98,** 1006 (1955).
5. JONES F. W. and SYKES E., *Proc. Roy. Soc.* A**166,** 376 (1938).
6. FEDER R., MOONEY M. and NOWICK A. S., *Acta Met.* **6,** 266 (1958).
7. See JAMES R. W., *The Optical Principles of the Diffraction of X-Rays* p. 279. Bell, London (1954).
8. VEENENDAAL A. L., MACGILLAURY C. H., STAM B., POTTERS M. L. and RÖMGENS M. J. H., *Acta Cryst., Camb.* **12,** 242 (1959).
9. f_{Cu} computed independently on IBM 704 from Hartree–Fock calculation for Cu^+. See HARTREE

D. R. and HARTREE W., *Proc. Roy. Soc.* **A157,** 490 (1936).
10. DAUBEN C. H. and TEMPLETON D. H., *Acta Cryst., Camb.* **8,** 841 (1954).
11. CHIPMAN D. R., *J. Appl. Phys.* **27,** 739 (1956).
12. KEATING D. T. and WARREN B. E., *J. Appl. Phys.* **22,** 286 (1951).
13. BETTERIDGE W., *J. Inst. Met.* **75,** 559 (1949).
14. RAYNE J., *Phys. Rev.* **112,** 1125 (1958).
15. RAYNE J., *Phys. Rev.* **115,** 63 (1959).
16. COHEN M. and HEINE V., *Advanc. Phys.* **7,** 395 (1958).
17. JONES H., *Phil. Mag.* **43,** 105 (1952).
18. DELAUNAY J., *Solid State Phys.* **2,** 285 (1956).

VOL.
15
1960

J. Phys. Chem. Solids Pergamon Press 1960. Vol. 15. pp. 196–207. Printed in Great Britain.

THEORY OF THE ABSORPTION EDGE IN SEMICONDUCTORS IN A HIGH MAGNETIC FIELD

R. J. ELLIOTT and R. LOUDON*

Clarendon Laboratory, Parks Road, Oxford

(*Received* 3 *November* 1959)

Abstract—A theory based on the effective mass approximation is given for hole–electron pairs in a semiconductor in a magnetic field. The intensity of the absorption edge is determined by the wave function of relative motion of the pair, so that essentially it becomes necessary to solve the Schrödinger equation for a hydrogen atom in a magnetic field. This is done in an approximation valid in high fields which assumes that the Coulomb term affects only the motion along the field, and uses a potential form which allows the solutions to be written in terms of confluent hypergeometric functions. The results show that the main intensity in each magnetic sub-band transition is thrown into the lowest exciton line and that the absorption in the continuum is reduced to an insignificant shoulder. The peaks observed in the so-called magneto-optic effect will all be exciton peaks.

1. INTRODUCTION

RECENT measurements of the absorption edge in semiconductors have led to a greatly increased understanding of the band structure of these substances, and in particular of the properties of the important energy states which lie on either side of the forbidden gap. The transition at the absorption edge is one in which an electron is promoted into the conduction band across this gap leaving behind a hole. This hole–electron pair has an important Coulomb interaction which can give rise to bound pair states, known as excitons, and to an associated fine structure in the absorption. A magnetic field is found to have a spectacular effect on this absorption, splitting the exciton lines in a kind of Zeeman effect and causing new peaks to appear in the region of continuous absorption.[1,2]

A theory of the form and intensity of the edge with excitonic effects has been given by DRESSELHAUS[3] and ELLIOTT[4]. The effect of peaking the continuous absorption has also been treated by a number of authors[5,6] neglecting the effect of the Coulomb interaction. It is apparent from this work that the Coulomb interaction has a marked effect on the form of the continuous absorption and it therefore seemed important to try and treat the effect of the Coulomb attraction and the magnetic field simultaneously. This is done here in an approximation valid in very large magnetic fields such that the zero-point energy shift of the continuum limit is large compared to the Coulomb binding energy of the hole–electron pair. These two quantities are equal in a hydrogen atom for a field $H = 2{\cdot}4 \times 10^9$ G. In Cu_2O the field is $6{\cdot}5 \times 10^6$ G so that the conditions cannot be practically attained but in germanium and InSb they are 8,900 G and 1,900 G, respectively, and experiments have been performed to which this approximation is applicable.

2. BASIC FORMULAE

A review of the general theory has been given by the authors in an earlier paper.[7] Because the photons involved have essentially zero wave vector, transitions take place only to pair states which have zero total momentum. If the relative hole–electron motion is defined by a quantum number n, the absorption is related to the matrix element of the momentum $\langle n,0|\boldsymbol{p}+(e/c)\boldsymbol{A}|0\rangle$ where the ket describes the ground state. In fact for discrete lines the f-value is

$$f_n = \frac{2}{mh\nu} |\langle n,0|\boldsymbol{\xi}\cdot\boldsymbol{p}+(e/c)\boldsymbol{A}|0\rangle|^2 \qquad (1)$$

* University of California, Berkeley, California.

VOL. 15 1960

where ν is the photon frequency, and $\boldsymbol{\xi}$ the polarization vector. If the absorption is continuous, the absorption coefficient K is

$$K = \frac{2\pi e^2}{Vm^2\nu c\eta} |\langle n,0|\boldsymbol{\xi}\cdot\boldsymbol{p}+(e/c)\boldsymbol{A}|0\rangle|^2 S_n(E) \quad (2)$$

$S_n(E)$ is the density of excited states per unit energy range and per unit volume, η is the refractive index and V the volume of the crystal.

The matrix element can be written using the effective mass approximation in terms of the matrix element $p_{cv}(\boldsymbol{k})$ of p between the electron states of wave vector $\boldsymbol{k}$ in the conduction and valence bands.

$$V^{-1/2}\langle n,0|\boldsymbol{\xi}\cdot\boldsymbol{p}+(e/c)\boldsymbol{A}|0\rangle = \left[\boldsymbol{\xi}\cdot\boldsymbol{p}_{cv}(0)+ \frac{ie\hbar H(\boldsymbol{\xi}\times\boldsymbol{p}_{cv}(0))}{mcE_G}\right] U_n(0)+ +[\boldsymbol{M}_{cv}\cdot\boldsymbol{\Pi}U_n(\boldsymbol{r})]_{\boldsymbol{r}=0} \quad (3)$$

κ is the dielectric constant, E_n is the energy of the pair state relative to the gap energy E_G.

Apart therefore from the band properties which give p_{cv}, the problem reduces to a calculation of $U(\boldsymbol{r})$ near the origin, i.e. the probability that an electron and hole are on the same atom.

3. METHOD OF APPROXIMATION

The approximation used is valid for large H which is conveniently defined as $\beta \gg 1$ where 2β is the ratio of the energy of cyclotron precession to the Coulomb binding energy $R = \mu e^4/2\hbar^2\kappa^2$ i.e.

$$\beta = \frac{\kappa^2\hbar^3 H}{\mu^2 e^3 c} \quad (6)$$

In the absence of a Coulomb term the relative motion is free along the direction of H and circular in the plane perpendicular to it. The wave functions U are

$$\psi_{NM}(\rho,\phi)\frac{1}{\sqrt{L_z}}\exp(ikz)$$
$$= \left[\frac{(N-M)!}{2\pi\lambda^2 L_z(N!)^3}\right]^{1/2}(-i)^N \exp(iM\phi)\sigma^{M/2}\exp(-\tfrac{1}{2}\sigma)L_N^M(\sigma)\exp(ikz) \qquad (M\geqslant 0)$$
$$= \left[\frac{N!}{2\pi\lambda^2 L_z(N-M)!^3}\right]^{1/2}(-i)^N \exp(iM\phi)\sigma^{-M/2}\exp(-\tfrac{1}{2}\sigma)L_{N-M}^{-M}(\sigma)\exp(ikz) \quad (M\leqslant 0) \quad (7)$$

where

$$\boldsymbol{M}_{cv} = \frac{1}{\hbar}[\nabla_k(\boldsymbol{\xi}\cdot\boldsymbol{p}_{cv}(\boldsymbol{k}))]_{\boldsymbol{k}=0} \quad (4)$$

and $\boldsymbol{\Pi} = -i\hbar\nabla+(e/2c)\boldsymbol{H}\times\boldsymbol{r}$.

U_n is the wave function of over-all relative motion of the electron and hole, and is given by the effective mass equation

$$\left[-\frac{\hbar^2}{2\mu}\nabla^2-\frac{ie\hbar}{2c}\left(\frac{1}{m_e}-\frac{1}{m_h}\right)\boldsymbol{H}\cdot\boldsymbol{r}\times\nabla+ +\frac{e^2}{8\mu c^2}(\boldsymbol{H}\times\boldsymbol{r})^2-\frac{e^2}{\kappa r}\right] U_n(\boldsymbol{r}) = E_n U_n(\boldsymbol{r}) \quad (5)$$

where m_e, m_h are the effective electron and hole masses and μ is the reduced mass $m_e m_h/(m_e+m_h)$.

where $N = 0, 1, 2 \ldots$ and M takes all integral values less than or equal to N. Also $\sigma = \rho^2/2\lambda^2$ and $\lambda = \sqrt{(\hbar c/eH)}$ is the dimension of the cyclotron orbit: cylindrical coordinates (ρ, ϕ, z) are used with z along the direction of H. L_z is the length of the crystal in that direction. The notation follows that of LIPPMANN and JOHNSON[8] rather than DINGLE[9]. The eigenvalues are

$$E^{NMk} = \frac{e\hbar H}{c}\left(\frac{1}{\mu}(N+\tfrac{1}{2})-\frac{1}{m_h}M\right)+\frac{\hbar^2 k^2}{2\mu} \quad (8)$$

The first term is the usual cyclotron energy, the second arises from the angular momentum about the direction of H, and the third is free kinetic energy along that axis.

In the presence of the Coulomb term, equation (5) is not soluble because it can no longer be

separated in these or other co-ordinates. Following SCHIFF and SNYDER[10] we force an artificial separation by assuming that the ρ and ϕ dependence continues to be given by equation (7) but that the z dependence is altered.

The equation for the z-motion is now

$$\left[-\frac{\hbar^2}{2\mu}\frac{d^2}{dz^2}+V_{NM}(z)\right]\zeta_{NM}^{\iota}(z)=E_z^{MN\iota}\zeta_{NM}^{\iota}(z) \quad (9)$$

where $V_{NM}(z)$ is the effective potential obtained by averaging the Coulomb term over the radial functions

$$V_{NM}(z) = -\int\int\psi_{NM}^{*}(\rho,\phi)\frac{e^2}{\kappa\sqrt{(\rho^2+z^2)}}\psi_{NM}(\rho,\phi)\rho d\rho d\phi \quad (10)$$

The eigenvalue may be written

$$E^{NM\iota}=\frac{e\hbar H}{c}\left(\frac{1}{\mu}(N+\tfrac{1}{2})-\frac{1}{m_h}M\right)+E_z^{NM\iota} \quad (11)$$

Because the Coulomb potential is localized there will be some discrete energy levels with negative $E_z^{NM\iota}$ corresponding to bound states. The energies of the continuum states with positive $E_z^{NM\iota}$ are unchanged by the perturbation and can still be written $\hbar^2k^2/2\mu$ although the eigenfunction is no longer a sine wave. The density of such states is still given by the free particle value

$$S(E)=\frac{L_z\mu}{\pi\hbar^2k} \quad (12)$$

The actual form of $V_{NM}(z)$ has been calculated for the three cases which give the lowest groups of energy levels.

$$V_{00}(z) = -\frac{e^2\sqrt{2}}{\kappa\lambda}\exp(z^2/2\lambda^2)\mathrm{Erfc}\left(\frac{|z|}{\lambda\sqrt{2}}\right) \quad (13)$$

$$V_{11}(z)=V_{0-1}(z)=-\frac{e^2}{\kappa}\left[\frac{|z|}{2\lambda^2}+\frac{1}{\lambda\sqrt{2}}\times\right.$$

$$\left.\times\exp(z^2/2\lambda^2)\left(1-\frac{z^2}{\lambda^2}\right)\mathrm{Erfc}\left(\frac{|z|}{\lambda\sqrt{2}}\right)\right] \quad (14)$$

These potentials are plotted in Fig. 1.

It is, of course, not possible to solve equation (9) with forms of V like equations (13) and (14). V may, however, be closely approximated by expressions of the form

$$V(z)=-\frac{e^2}{\kappa(a+|z|)}+\frac{Aae^2}{\kappa(a+|z|)^2} \quad (15)$$

when the solutions of equation (9) are Whittaker functions. a and A are parameters chosen for each N,M to approximate V_{NM}.

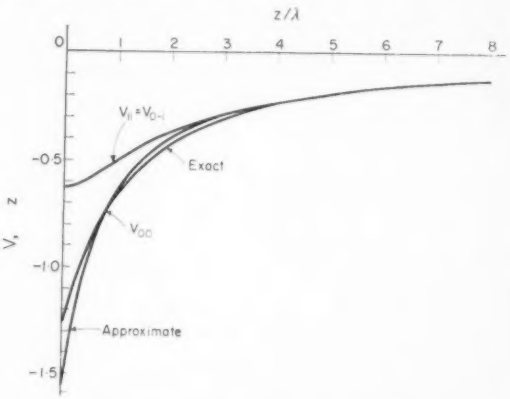

FIG. 1. Effective potentials for motion along the magnetic field. In the case of V_{00} both the exact potential and the approximation to it are shown. The potentials are measured in units of $e^2/\kappa\lambda$.

4. BOUND STATE SOLUTIONS OF THE EQUATION

It is convenient to characterize the negative energy bound solutions by introducing a parameter α defined by

$$E_z=-\frac{\hbar^2k_0^2}{2\mu\alpha^2}$$

where

$$a_0=1/k_0=\hbar^2\kappa/\mu e^2 \quad (16)$$

is the effective Bohr radius. Further changing the variable to

$$x=2k_0(a+|z|)/\alpha \quad (17)$$

and defining

$$m=(\tfrac{1}{4}+2Aak_0)^{1/2} \quad (18)$$

the wave equation reduces to

$$\frac{d^2\zeta}{dx^2}-\left[\tfrac{1}{4}-\frac{\alpha}{x}+\frac{m^2-\frac{1}{4}}{x^2}\right]\zeta=0 \quad (19)$$

which has the form of Whittaker's equation.

Bound state solutions must have $\zeta \to 0$ as $x \to \infty$ and such solutions are,[11]

$$\zeta = N_0 W_{\alpha,m}(x) \to N_0 x^{\alpha} \exp(-\tfrac{1}{2}x) \qquad (20)$$

asymptotically. N_0 is the normalization constant.

The other independent solution of equation (19) $V_{\alpha,m}(x)$ diverges like $x^{-\alpha}e^{x/2}$. The point $x = 0$ is excluded from the range by the definition (17) so that expression (19) has no singularities except for $x = \infty$. The potential is invariant under the reflection $z \to -z$ and the wave functions must be either even or odd in z. Since the wave functions and their slope must be continuous at $z = 0$, the matching conditions at that point lead to an eigenvalue relation which is only satisfied by certain values of α. For an odd state α must be such that

$$W_{\alpha,m}(2k_0 a/\alpha) = 0 \qquad (21)$$

while for an even state

$$\left[\frac{d}{dz} W_{\alpha,m}(2k_0\overline{a+z}/\alpha)\right]_{z=0} = 0 \qquad (22)$$

For a given value of the magnetic field a and m are determined, and the solutions of equations (21) and (22) for α are interspersed, giving alternately odd and even states with rising energy. The quantum number i may be defined as the number of nodes in the function and gives the correct order of the levels.

To assess the general behaviour of the energy levels at large β where the approximation holds, it is convenient to consider the limit of infinite field. The potential $V_{NM}(z)$ then becomes $-e^2/\kappa|z|$ for all N,M, and the problem is that of a one-dimension hydrogen atom which has been considered by LOUDON[12]. The energies of z motion relative to each continuum edge are then

$$E_z^{NM_i} = -R/\nu^2 \quad \nu = 0, 1, 2 \ldots \qquad (23)$$

where $i = 2\nu$ for even states and $i = 2\nu - 1$ for odd states. All the levels are doubly degenerate (one even and one odd) at the hydrogen atom energies, except for the lowest state which is single and has infinite binding energy. A one-to-one correspondence exists between the hydrogen atom levels in zero field and the infinite field values, and the energy levels will connect these pairs as H varies from 0 to ∞. KLEINER[13] has pointed out that this correspondence may be seen by examining the nodes of the functions. In the hydrogen atom state with quantum numbers n, l, M, there are $n-l-1$ nodal spheres and $l-|M|$ nodal cones with a z-axis. In infinite field there are for states in expression (7) $N-\frac{1}{2}(M+|M|)$ nodal cylinders and for ζ^i given by equation (9) there are i nodal planes perpendicular to the z-axis. The effect of the field has been to extend the z-axis till the spheres became cylinders and the cones became planes. Thus the correspondence is

$$i \to l-|M|$$
$$N-\tfrac{1}{2}(M+|M|) \to n-l-1 \qquad (24)$$

and of course M is a good quantum number throughout. The lowest group of levels in infinite field is the $(N = 0, i, M = 0)$ and comes from the $(n = i+1,\ l = i,\ M = 0)$ hydrogen levels. The binding energy decreases from the hydrogenic energy for quantum number ν to that having quantum number $2\nu+1$ (for $i = 2\nu$) or 2ν (for $i = 2\nu-1$) as H decreases to zero.

For the levels with small quantum numbers, however, the two levels which come from ν at infinite H do not decrease across the $\nu+1$th levels as H decreases until β is so small (< 2) that this theory has no validity. This may be seen from Figs. 2 and 3. In this region there are two bound levels between each pair of hydrogenic energies.

At high ν values where the levels crowd together it is convenient to define a density of bound states. Because of the correspondence this is

$$S(E) = \alpha^3/2R \qquad (25)$$

the same for even and odd states.

For complete knowledge of the solution, expression (20), the normalization integral must be evaluated, which is not over the whole range of x but has the region $-2k_0 a/\alpha < x < 2k_0 a/\alpha$ excluded. For small values of i this represents a significant effect (particularly for $i = 0$) and the results have been computed by numerical integration (see Section 7). For the states close to the continuum, however, it is a good approximation to take the integral over the whole range of x. Even this integral, however, has not been done for general values of α and m. For α integral and m half integral, $W_{\alpha,m}(x)$ becomes the solution of the hydrogen atom problem containing a Laguerre

polynomial, and

$$\frac{\alpha}{2k_0}\int_{-\infty}^{\infty}|W_{\alpha,m}(x)|^2\,dx = N_0^{-2}$$
$$=\frac{2\alpha^2}{k_0}\Gamma(\tfrac{1}{2}+\alpha+m)\Gamma(\tfrac{1}{2}+\alpha-m) \qquad (26)$$

The important properties of W like its asymptotic form and the positions of its zeros vary smoothly and continuously through these values of α and m. It should therefore be a good approximation to use equation (26) for intermediate values close to the continuum limit.

5. FREE STATE SOLUTIONS OF THE EQUATION

For the free states, with positive E_z, a parameter similar to equation (16) may be defined by

$$E_z = \hbar^2k^2/2\mu = \hbar^2k_c^2/2\mu\alpha^2 \qquad (27)$$

Introducing

$$x = 2ik_0(a+|z|)/\alpha \qquad (28)$$

the wave equation reduces to

$$\frac{d^2\zeta}{dx^2}-\left(\frac{1}{4}+\frac{i\alpha}{x}+\frac{m^2-\frac{1}{4}}{x^2}\right)\zeta = 0 \qquad (29)$$

with m still given by equation (18). This time there are two acceptable solutions with the following asymptotic forms

$$W_{-i\alpha,m}(x) \to \exp(-\tfrac{1}{2}x)\,x^{-i\alpha}$$
$$V_{-i\alpha,m}(x) \to \exp(\tfrac{1}{2}x+\pi\alpha)\,x^{i\alpha} \qquad (30)$$

Even and odd states may be built from these, and since the functions are oscillatory with constant amplitude at large x they may be normalized, using their asymptotic forms, to a length L_z. The resulting solutions are

$$\zeta_g^{\mathbf{k}}(z) = \frac{\exp[-(\frac{1}{2}\pi\alpha)][V(2ik_0(a+|z|)/\alpha)W'(2ik_0a/\alpha)-W(2ik_0(a+|z|)/\alpha)V'(2ik_0a/\alpha)]}{L_z^{1/2}[|W'(2ik_0a/\alpha)|^2+|V'(2ik_0a/\alpha)|^2]^{1/2}} \qquad (31)$$

$$\zeta_u^{\mathbf{k}}(z) = \frac{\tau_z\exp[-(\frac{1}{2}\pi\alpha)][V(2ik_0(a+|z|)/\alpha)W(2ik_0a/\alpha)-W(2ik_0(a+|z|)/\alpha)V(2ik_0a/\alpha)]}{L^{1/2}[|W(2ik_0a/\alpha)|^2+|V(2ik_0a/\alpha)|^2]^{1/2}} \qquad (32)$$

where $\tau_z = +1$, $z>0$ and $\tau_z = -1$, $z<0$. The prime denotes differentiation with respect to z.

For energies much higher than the continuum limit, i.e. $\alpha \ll 1$ these reduce to the free particle wave-functions. The density of even and odd states in the continuum is the same

$$S(E) = L_z\kappa\alpha/2\pi e^2. \qquad (33)$$

6. ABSORPTION COEFFICIENTS

The form of the expressions in Section 2 indicate that the properties of the functions (20), (31) and (32) are required at the origin. There are three distinct cases depending on whether the absorption between bands is allowed ($\mathbf{p}_{cv}(0) \neq 0$) or forbidden ($\mathbf{p}_{cv}(0) = 0$) and in the latter case depending further on the polarization of the light relative to $\boldsymbol{H}$.

(a) *Allowed*

Here only the first term in equation (3) is required and hence $U(0)$. Only the even functions will give a contribution to the absorption. For the discrete states, using expressions (1), (7) and (20)

$$f_i = \frac{VN_0^2\beta}{h\nu m\pi a_0^2}|W_{\alpha,m}(2k_0a/\alpha)|^2|\boldsymbol{\xi}\cdot\mathbf{p}_{cv}(0)|^2 \quad i \text{ even} \qquad (34)$$

Close to the limit the discrete states form a pseudo-continuum where, using expressions (2), (7), (20), (25) and (26)

$$K = \frac{\beta\kappa\alpha|W_{\alpha,m}(2k_0a/\alpha)|^2|\boldsymbol{\xi}\cdot\mathbf{p}_{cv}(0)|^2}{2\nu m^2ca_0^2\eta\Gamma(\frac{1}{2}+\alpha+m)\Gamma(\frac{1}{2}+\alpha-m)} \qquad (35)$$

In the true continuum using equations (2), (7), (31) and (33)

$$K = \frac{2\beta\kappa e^{\pi\alpha}|\boldsymbol{\xi}\cdot\mathbf{p}_{cv}(0)|^2}{\pi\nu m^2ca_0^4\eta\alpha[|W'_{-i\alpha,m}(2ik_0a/\alpha)|^2+|V'_{-i\alpha,m}(2ik_0a/\alpha)|^2]} \qquad (36)$$

where the Wronskian

$$W_{\alpha,m}(x)\frac{d}{dx}V_{\alpha,m}(x)-V_{\alpha,m}(x)\frac{d}{dx}W_{\alpha,m}(x)=\exp(i\pi\alpha) \qquad (37)$$

has been used to simplify the numerator of equation (31).

It is of particular experimental interest to know the behaviour of the absorption as it crosses the continuum limit, i.e. to compare equations (35) and (36) as $\alpha \to \infty$. This comparison is aided by using the Wronskian expression (37) to transform equation (35). Because of definition (22), equation (35) becomes

$$K = C/\alpha\Gamma(\tfrac{1}{2}+\alpha+m)\Gamma(\tfrac{1}{2}+\alpha-m)\times \\ \times|V'_{\alpha,m}(2k_0a/\alpha)|^2 \qquad (38)$$

where C is a constant. Equation (36) is

$$K = C/\pi\alpha\exp(-\pi\alpha)[|W'_{-i\alpha,m}(2ik_0a/\alpha)|^2+ \\ +|V'_{-i\alpha,m}(2ik_0a/\alpha)|^2] \qquad (39)$$

The functions W and V can be written in terms of the usual confluent hypergeometric functions by

$$M_{\alpha,m}(x) = \exp(-x/2)x^{m+1/2}\times \\ \times{}_1F_1(\tfrac{1}{2}-\alpha+m,\ 2m+1;\ x) \qquad (40)$$

and

$$W_{\alpha,m}(x) = \frac{\Gamma(-2m)}{\Gamma(\tfrac{1}{2}-\alpha-m)}M_{\alpha,m}(x)+ \\ +\frac{\Gamma(2m)}{\Gamma(\tfrac{1}{2}-\alpha+m)}M_{\alpha,-m}(x).$$

$$V_{\alpha,m}(x) = -i\left\{\frac{\exp(-i\pi m)\Gamma(-2m)}{\Gamma(\tfrac{1}{2}+\alpha-m)}M_{\alpha,m}(x)+ \right. \\ \left. +\frac{\exp(i\pi m)\Gamma(2m)}{\Gamma(\tfrac{1}{2}+\alpha+m)}M_{\alpha,-m}(x)\right\} \qquad (41)$$

For large values of α, M and Γ may be expanded in inverse powers of α^2

$$M_{\alpha,m}(2k_0a/\alpha) = (2k_0a)^{1/2}\alpha^{-1/2-m}\Gamma(2m+1)\times \\ \times\{J_{2m}(\sqrt{8k_0a})+(k_0a/\alpha)^2[\tfrac{1}{3}(2k_0a)^{-1/2}J_{2m+1}(\sqrt{8k_0a}) \\ +\tfrac{1}{6}(2m-1)(2k_0a)^{-1}J_{2m+2}(\sqrt{8k_0a})]+0(\alpha^{-4})\} \qquad (42)$$

where J_m are Bessel functions and

$$\Gamma(\tfrac{1}{2}+\alpha+m) = \alpha^{\alpha+m}\exp[-\alpha-\tfrac{1}{2}\alpha(\tfrac{1}{12}-m^2)]\times \\ \times\sqrt{2\pi}\left\{1-\frac{m(4m^2-1)}{24\alpha^2}+0(\alpha^{-4})\right\} \qquad (43)$$

by Stirling's expansion.

Equations (38) and (39) are very similar in form and in fact in the limit they are equal and are continuous in slope

$$K = A(1\pm B/\alpha^2)+0(1/\alpha^4), \qquad (44)$$

the $\pm$ applying above and below the edge. This remains true for the other two cases to be treated below and appears to be characteristic of a theory which includes Coulomb attraction effects (cf. Ref. 4). A different conclusion about the shape of the edge given by the authors in a previous paper[7] was a result of algebraic errors. The actual forms of A and B are very complicated and will not be given. Numerical results are given later in Table 1.

(b) *Forbidden* $\boldsymbol{\xi}\|\boldsymbol{H}$

This type of absorption comes from the final term in equation (3) and depends on

$$[\Pi_z\zeta(z)]_{z=0}$$

i.e. on

$$-i\hbar(d\zeta/dz)_{z=0}.$$

It therefore comes from odd states. As before, there is a series of lines below a continuum for each value of N and M.

$$f_i = \frac{VN_0^2\beta\hbar}{2\pi^2mva_0^2}|W'_{\alpha,m}(2k_0a/\alpha)|^2|M^z_{cv}|^2 \quad i \text{ odd}. \qquad (45)$$

Below the limit the overlapping lines give a pseudo-continuum where

$$K = \frac{\beta\kappa\hbar^2\alpha|W'_{\alpha,m}(2k_0a/\alpha)|^2|M^z_{cv}|^2}{2m^2vc\eta a_0^2\Gamma(\tfrac{1}{2}+\alpha+m)\Gamma(\tfrac{1}{2}+\alpha-m)} \qquad (46)$$

and in the true continuum

$$K = \frac{2\beta\kappa\hbar^2e^{\pi\alpha}|M^z_{cv}|^2}{\pi m^2vc\eta a_0^4\alpha[|W_{-i\alpha,m}(2ik_0a/\alpha)|^2+|V_{-i\alpha,m}(2ik_0a/\alpha)|^2]} \qquad (47)$$

Equations (46) and (47) are again continuous at the edge.

(c) *Forbidden* $\boldsymbol{\xi}\perp\boldsymbol{H}$

This absorption arises from transitions to $M=-1$ states for left circularly polarized radiation and to $M=+1$ for right polarized. The form of the absorption is the same in both cases, since from equations (7) and (10)

$$V_{N,1}=V_{N-1,-1} \tag{48}$$

except that the latter takes place at an energy lower by an amount

$$\frac{e\hbar H}{c}\left(\frac{1}{m_h}-\frac{1}{m_e}\right).$$

We therefore consider only one and choose the right-handed polarization. In the last term in equation (3) Π_- operates only on the $\psi_{N,M}$ in expression (7)

$$[\Pi_- U(r)]_{r=0}=\sqrt{(2N)}\hbar\psi_{N-1,0}(0)\zeta^{\mathrm{f}}_{N,1}(0)/\lambda \tag{49}$$

and this may be substituted in equations (1) and (2). Only even states in z will contribute. The discrete lines have

$$f_i=\frac{VN_0^2\beta^2N\hbar}{\pi^2mva_0^4}|W_{\alpha,m}(2k_0a/\alpha)|^2|\boldsymbol{M}^+_{cv}|^2 \qquad i \text{ even} \tag{50}$$

The pseudo continuum has

$$K=\frac{\beta^2\kappa\hbar^2\alpha N|W_{\alpha,m}(2k_0a/\alpha)|^2|\boldsymbol{M}^+_{cv}|^2}{m^2vc\eta a_0^4\Gamma(\frac{1}{2}+\alpha+m)\Gamma(\frac{1}{2}+\alpha-m)} \tag{51}$$

and the true continuum

$$K=\frac{4\beta^2\kappa N\hbar^2e^{\pi\alpha}|\boldsymbol{M}^+_{cv}|^2}{\pi m^2vc\eta a_0^6\alpha[|W_{-i\alpha,m}(2ik_0a/\alpha)|^2+|V_{-i\alpha,m}(2ik_0a/\alpha)|^2]} \tag{52}$$

parameters A and a were chosen so that the exact and approximate potential curves have the same slope at the origin and enclose equal areas with the axis of z. (The alternative arrangement of making the curves equal at the origin was estimated to make little difference.) The resulting potentials for $N=M=0$ are compared in Fig. 1.

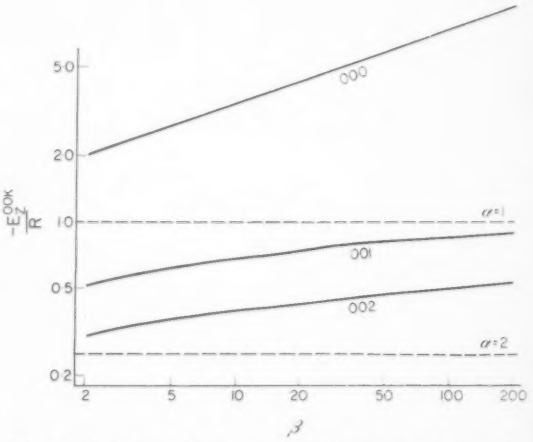

FIG. 2. Variation with magnetic field of the energies of the three lowest states of the set $N=M=0$. Energy is measured in terms of the effective Rydberg unit R.

For any field therefore a and m are determined and the eigenvalue problem, equations (21) or (22), can be solved numerically. Unfortunately there are only a few tables of Whittaker functions for attractive Coulomb fields[14] in the region of small $x=2k_0a/\alpha$ required, and these are of use largely for the $i=0$ states. For the remaining states a series expansion of W was used—fortunately it converges rapidly for when $\beta>2$, $2k_0a/\alpha<\frac{1}{2}$.

7. NUMERICAL RESULTS

Numerical calculations have been carried out for the three lowest groups of levels, i.e. $N=M=0$, $N=M=1$ and $N=0$, $M=-1$. Because of equation (48) the last two give the same relative energies and intensities and only the first two need be calculated in detail. The first step is to fit approximate potentials of the form of expression (15) to (13) and (14). The arbitrary

Variations of the bound state energies are shown in Figs. 2 and 3 where the designation is (N, M, i). The $i=0$ levels tend logarithmically to infinity as $\beta\to\infty$ while the $i=1,2$ levels tend to the $\alpha=1$ line. The (0,0,0) and the (0,0,2) are observed in the allowed case; (0,0,1) in the forbidden $\boldsymbol{\xi}\|\boldsymbol{H}$; and (1,1,0) or (0,−1,0) and (1,1,2) or (0,−1,2) in

the forbidden $\xi \perp H$. The (1,1,1) level cannot be observed and so was not calculated.

The f-values of the $N = 0$ levels are related to the quantities plotted in Fig. 4 by using equations (1) and (3). For allowed states (0,0,0) and (0,0,2) the dimensionless quantity $a_0^3|U_{00}^k(0)|^2$ is plotted. In the absence of a field its value is π^{-1} in the lowest exciton state and it is clear that the magnetic field increases the intensity of the lines. Most of the effect is the linear dependence from $|\psi_{00}(0)|^2 = 1/2\pi\lambda^2$ but there is a further increase from the variation of W and its normalization factor. For the lowest forbidden state (0,0,1) the dimensionless quantity $a_0^5|(\partial U(\boldsymbol{r})/\partial z)_{r=0}|^2$ is plotted. This has the value $1/32\pi$ for the lowest state when $H = 0$, and again it is clear that as H increases, the increase in the absorption is somewhat more rapid than the linear dependence determined by the ρ,ϕ motion. For the forbidden case and $\xi \perp H$ the variation of the f value of the (1,1,0) and (1,1,2) lines is similar to that for (0,0,0) and (0,0,2) except for an extra factor of β which comes from the Π operation on ψ, making the overall variation more rapid than in the other two cases.

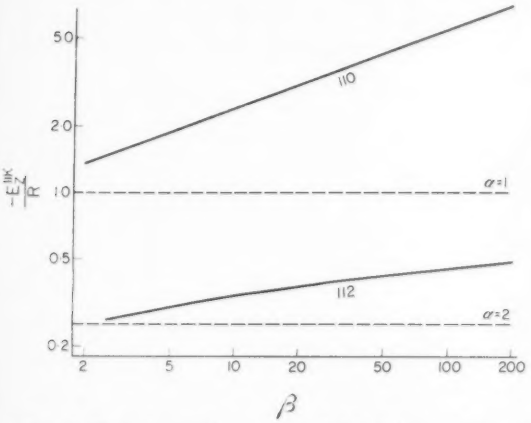

FIG. 3. Variation with magnetic field of the energies of the two lowest observable states of the $N = M = 1$ group.

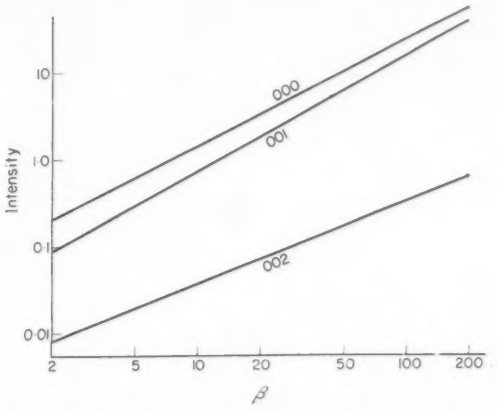

FIG. 4. Variation with magnetic field of the intensities of the absorption lines due to the three lowest states of the $N = M = 0$ set. The unit of intensity for the (0,0,1) line is not the same as that for the other two lines (see text).

The absorption coefficients close to the edge have been calculated using the asymptotic forms developed in the last section. Values of dimensionless quantities A' and B are given in Table 1. A'

Table 1

$\frac{\hbar^2 a_0}{\mu} S(E)\|U_{00}^k(0)\|^2$			$\frac{a_0^3}{\mu} S(E)\|\Pi_z U_{00}^k(r)\|_{r=0}^2$			$\frac{a_0^3}{\mu} S(E)\|\Pi_- U_{11}^k(r)\|_{r=0}^2$		
Allowed			Forbidden $\xi \parallel H$			Forbidden $\xi \perp H$		
β	A'	B	β	A'	B	β	A'	B
1·4	0·041	−0·12	1·4	0·12	0·15	3·1	0·52	−0·102
3·7	0·085	−0·061	3·7	0·39	0·10	8·0	2·8	−0·051
7·1	0·14	−0·034	7·1	0·85	0·072	15	8·7	−0·025

The absorption coefficients are proportional to the dimensionless quantities shown at the head of the table. The values of these quantities close to the edge for the given β are presented in the form $A'(1+B/\alpha^2)$.

differs by a constant multiple from A as defined in equation (44). The sign of B/A applies in the true continuum above the edge. The β are chosen in order that m shall be such that the Bessel functions in expression (42) are tabulated.

8. DISCUSSION

(a) *Allowed*

In the absence of a Coulomb field the absorption[5] is proportional to $HE^{-1/2}$ where the energy is measured from each sub-band edge. Well above the edge, as $\alpha \to 0$, equation (36) becomes equal to this expression given in Ref. (5). It is clear from the above that the effect of the Coulomb field is to smooth out the peak to give a continuous curve at this point rising towards lower energies. For the lowest $N = 0$ set calculated above, the value of the absorption at the edge rises with H but the dependence is less than linear. On the other hand the exciton lines, and particularly the lowest one, increase in intensity more rapidly than H and move to lower energies relative to the edge. Thus the effect of the Coulomb field is to remove absorption intensity from the peak at the edge and to concentrate this more and more in the lowest exciton line as H increases. In the limit of infinite H, the lowest line has infinite intensity and infinite binding energy.

A sketch of the absorption is given in Fig. 5 for $\beta \sim 2$, assuming a line width of about a Rydberg R for the exciton lines and is compared to the results with $H = 0$ and neglecting Coulomb effects.

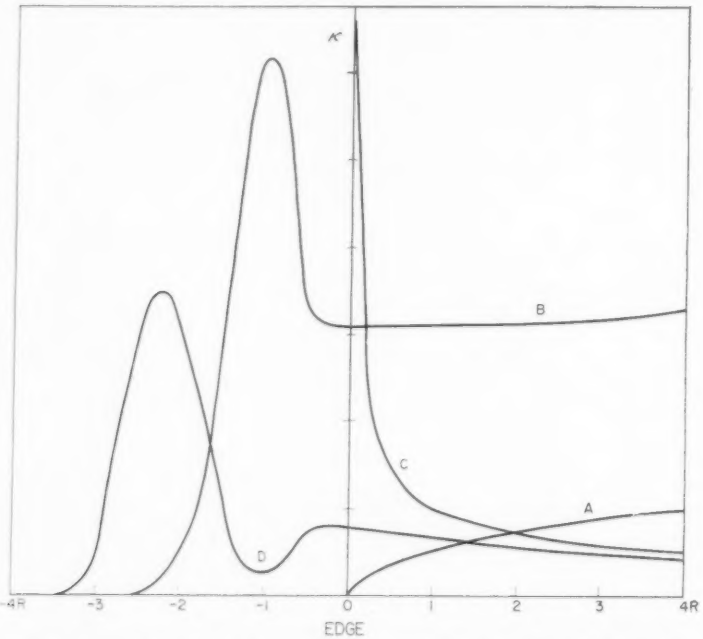

FIG. 5. Comparison of the shapes of the absorption edge predicted for various cases. (a) Free hole–electron pairs. (b) Exciton effects with $H = 0$ (after Ref. 4). (c) Magnetic field included $\beta = 2$, but Coulomb effects neglected (after Ref. 5). (d) This theory, $\beta = 2$. A line width of about R was assumed for the exciton lines.

All but the first line have become merged with the edge and form an insignificant shoulder which peaks below the true edge. There is no distinguishing feature at the edge itself. The dominance of the lowest exciton line is increased at large fields, and experimental measurements will usually be of this line, particularly if the widths are large. It is possible that the shoulder will be observable for the lowest $N = 0$ band and possibly other lines as well if the widths are narrow. A qualitative discussion of the behaviour of higher sub-bands is given in the next section.

(b) *Forbidden* $\boldsymbol{\xi} \| \boldsymbol{H}$

For this case the absorption in the absence of a Coulomb effect is proportional to $HE^{1/2}$. Again the Coulomb field causes a smooth variation across the edge, and causes absorption to appear at lower energies. The relative amount below the edge increases with H. The increase in the lowest line (0,0,1) in Fig. 3, is more rapid than linear, and the actual value of K at the edge behaves similarly. The intensity of the line is relatively much smaller than in case (a) of this section—in fact over the region $2 < \beta < 10$ investigated, if the width of the exciton lines were R, the peak intensity and that at the edge would be similar. Moreover the binding energy of the lowest exciton is smaller, increasing with H from $\frac{1}{4}R$ to R (cf. Fig. 2), and it will be difficult to resolve lines in this case unless the width is small. The overall intensity of the forbidden spectra, which are proportional to $\boldsymbol{M}_{cv}$ rather than $\boldsymbol{p}_{cv}$, is expected to be smaller than that of the allowed spectra by a factor of order (atomic radius/exciton radius)^2.

VOL. 15 1960

(c) *Forbidden* $\boldsymbol{\xi} \perp \boldsymbol{H}$

In the absence of Coulomb effects the absorption is proportional to $H^2E^{-1/2}$ and has peaks like case (a) of this section. The overall effect of the Coulomb field is similar to that in case (a) and again the maximum in the absorption is expected to come from the lowest exciton line. As H increases, relatively more of the absorption is concentrated into this line and the continuum only forms an insignificant shoulder. In fact the whole behaviour is similar to case (a) except that there is throughout an extra factor of order (exciton radius/magnetic orbit radius)^2 which gives another factor of H. There is a further factor of order (atomic radius/exciton radius)^2 because of the forbidden nature of the transitions.

9. BEHAVIOUR OF HIGHER BANDS

No detailed calculations of the exciton binding energies etc. have been made for bands other than those, discussed above, which produce the line series at the lowest energy. However, some qualitative discussion is possible. For $M = 0$ states, for example, giving allowed absorption, there will be a spectrum similar to that for the $N = 0$ band for all N, spaced from the former by $e\hbar H/\mu c$.

The average radius of the cyclotron orbit given by equation (7) is proportional to N. If we considered a simpler approximation than equation (15) with $A = 0$, a would therefore be roughly proportional to N and the energies in the problem would depend only on a. Thus the binding energy could be obtained for a given field from Fig. 2 by using the value for $\beta_N = \beta/N$. The binding energy of the lowest $(N,0,0)$ level in each series is seen to decrease with N.

The width of the lines coming from higher N series will also be broader than the $N = 0$ series, for they have the same energy as continuum states of other N series, and there is a probability that a transition will take place. This will be proportional to the square of the matrix element of the Coulomb potential between the states and the density of states in the continuum $S_1(E)$.

$$P = \frac{2\pi}{\hbar} S_1(E) |\mathscr{M}|^2 \tag{53}$$

where

$$\mathscr{M} = -\int U^{i*}_{NM}(\boldsymbol{r}) \frac{e^2}{\kappa r} U^{k}_{N'M}(\boldsymbol{r})\, d\boldsymbol{r} \tag{54}$$

This has been estimated in detail for the (1,0,0) bound state interacting with the $(0,0,k)$ continuum and gives a width

$$\Delta E \sim (-8RE_z^{1,0,0}/\beta)^{1/2} \tag{55}$$

For larger N values the line width will be roughly $\Delta E \sim R(N/\beta)^{1/2}$.

10. COMPARISON WITH EXPERIMENT

The main conclusion of the above discussion is that the Coulomb interaction completely changes the form of the absorption edge in a strong magnetic field. In the allowed case the peaks in the absorption occur not at the Landau energies but at the lowest exciton levels associated with each sub-band. For the lowest band $N = 0$, other lines and a shoulder might be distinguishable, but they will be small. For higher N values it is likely that the broadening will smooth out other features unless β is very large. In interpreting data it is important to realize that the peaks are shifted from the edge. Similar considerations apply to the forbidden case with perpendicular polarization. For

parallel polarization, where the absorption forms a series of steps, the steps will begin at the exciton energies and not at the edges and may show a line structure.

Exciton absorption in a magnetic field has so far been observed in only two semiconductors. In Cu_2O[1] β was always $\ll 1$ so that this theory does not apply. In germanium, however, LAX *et al.*[2] had sufficiently large fields and made three separate measurements with β between 2 and 4. Unfortunately the complicated valence band makes the theory more difficult and the energies are not given by equation (8) for low N.[5, 6, 15] In addition the experimental arrangements have been criticized[16] on the grounds that the specimen was in a state of non-uniform strain due to its mounting. This strain produces a splitting of the exciton line into two in zero field.[16, 17]

LAX *et al.* interpret the lowest two lines in a field as the lowest $N = 0$ exciton and a peak at the $N = 0$ continuum edge. This is at variance with the above theory and we would attribute the second peak to the strain splitting. The edge should give a shoulder which may be hidden under the second line. Furthermore, the energy difference between the lines does not vary greatly with field at large H as predicted in Fig. 2. The comparison must therefore await the results on unstrained crystals. However the intensity of the lowest line is in rough agreement with the increase with H predicted in Fig. 4 for the (0,0,0) line. The peaks at higher energies appear to increase in width with distance from the edge as predicted in Section 9.*

11. ACCURACY OF THE METHOD

In the perturbation theory method outlined in Section 3 there were two main approximations. The first arose from separating out the (ρ,ϕ) dependence. This error depends on the size of the matrix elements of $-e^2/\kappa r$ linking the eigenfunctions. In Section 9 the broadening of higher energy states was estimated. The perturbation will also cause changes of energy. An estimate of the shift of the (0,0,0) level by perturbation from the (1,0,0) gives

$$\Delta E \sim -\frac{2}{\beta}(E_z^{0,0,0}\, E_z^{1,0,0})^{1/2}$$

The perturbation by other levels is considerably less because of the form of their wave functions. Even in a small field there will be some bound states close to the edge which, because they are concentrated at distances well removed from the origin, will have small matrix elements of $-e^2/\kappa r$.

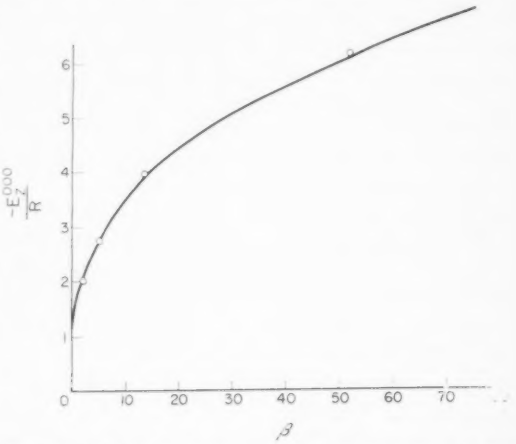

FIG. 6. The binding energy of the ground state of the system. The isolated points represent the results of the present calculation while the continuous line is the curve obtained by KEYES[18].

The energies of these states is given well by the approximation of Section 3 for $\beta < 1$, and SCHIFF and SNYDER[10] used it for this purpose. However, the approximation to the wave functions is still poor and our method of calculating absorption coefficients does not hold for $\beta \sim 1$ even close to the edge or in the continuum.

The second main approximation is the replacement of the effective potential (10) by equation (15). KEYES[18] has calculated the energy of the (0,0,0) level numerically using the potential (13). His results are compared in Fig. 6 and differ from ours by less than 2 per cent. WALLIS and BOWLDEN[19] and YAFET *et al.*[20] have made variational calculations of the energies of the ground state and several low-lying discrete states which may be compared with the results in Figs. 2 and 3 and show reasonable agreement.

* *Note added in proof:* The conclusions of this section regarding the interpretation of the peaks observed in the magneto-optic absorption in germanium have received experimental support in the recent work of D. F. EDWARDS and V. J. LAZAZZERA (to be published).

REFERENCES

1. Burstein E., Picus G. S., Wallis R. F. and Blatt F., *J. Phys. Chem. Solids* **8,** 305 (1959);
   Lax B., Roth L. M. and Zwerdling S., *J. Phys. Chem. Solids* **8,** 311 (1959);
   Gross E. F., *J. Phys. Chem. Solids* **8,** 172 (1959).
   (See these review papers for a complete list of references.)
2. Zwerdling S., Lax B., Roth L. M. and Button K. J., *Phys. Rev.* **114,** 80 (1959).
3. Dresselhaus G., *Phys. Rev.* **106,** 76 (1957).
4. Elliott R. J., *Phys. Rev.* **108,** 1384 (1957).
5. Elliott R. J., McLean T. P. and Macfarlane G. G., *Proc. Phys. Soc. Lond.* **72,** 553 (1958).
6. Burstein E., Picus G. S., Wallis R. F. and Blatt F., *Phys. Rev.* **113,** 15 (1959);
   Roth L. M., Lax B. and Zwerdling S., *Phys. Rev.* **114,** 90 (1959).
7. Elliott R. J. and Loudon R., *J. Phys. Chem. Solids* **8,** 382 (1959).
8. Johnson M. H. and Lippmann B. A., *Phys. Rev.* **76,** 828 (1949).
9. Dingle R. B., *Proc. Roy. Soc.* **211,** 500 (1952).
10. Schiff L. I. and Snyder H., *Phys. Rev.* **55,** 59 (1939).
11. Whittaker E. T. and Watson G. N., *Modern Analysis.* University Press, Cambridge (1927);
    Erdélyi A., Magnus W., Oberhettinger F. and Tricomi F. G., *Higher Transcendental Functions* Vol. 1. McGraw-Hill, New York (1953).
12. Loudon R., *Amer. J. Phys.* **27,** 649 (1959).
13. Kleiner W. H., *Lincoln Lab. Progr. Rep.*, Feb. 1958.
14. Charney J. G., *J. Met.* **4,** 135 (1947).
15. Luttinger J. M., *Phys. Rev.* **102,** 1030 (1956).
16. MacFarlane G. G., McLean T. P., Quarrington J. E. and Roberts V., *Phys. Rev. Letters* **2,** 252 (1959).
17. Kleiner W. H. and Roth L. M., *Phys. Rev. Letters* **2,** 334 (1959).
18. Keyes R. W., *Westinghouse Res. Rep.* (1958) unpublished.
19. Wallis R. F. and Bowlden H. J. *J. Phys. Chem. Solids* **7,** 78 (1958).
20. Yafet Y., Keyes R. W. and Adams E. N., *J. Phys. Chem. Solids* **1,** 137 (1956).

VOL. 15 1960

J. Phys. Chem. Solids Pergamon Press 1960. Vol. 15. pp. 208–217. Printed in Great Britain.

SCATTERING OF HOT CARRIERS IN GERMANIUM

E. M. CONWELL and A. L. BROWN

General Telephone and Electronics Laboratories Inc., Bayside, New York

(*Received* 30 *November* 1959)

Abstract—The variation of lattice mobility of hot carriers with their average energy or "temperature" has been investigated. An expression is derived for the relaxation time due to single phonon acoustical mode scattering which remains valid to very high carrier temperatures at lattice temperatures of 20°K and above. In the limit where carriers interact mainly with lattice oscillators having only zero point energy it is found that the relaxation time is proportional to the inverse square of the speed rather than to the inverse first power as for thermal carriers. Lattice mobility is plotted as a function of average carrier energy for various values of the ratio of coupling constants for optical and acoustical modes, and various effective masses, for lattice temperatures of 300°, 78° and 20°K. The effect of dropping the assumption of equipartition of energy among the acoustical lattice oscillators is to increase the scattering effect of the acoustical modes, the more so the lower the lattice temperature, the higher the carrier temperature, and the higher the mass of the carriers. Impurity scattering has not been included in the quantitative calculations, but it is shown that the increase in hot-carrier mobility which can be caused by this scattering process will generally be less than has been expected.

1. INTRODUCTION

A THEORY for lattice mobility of hot carriers in germanium was described in an earlier publication,[1] and used there for the calculation of mobility, μ, as a function of electric field intensity, E. The agreement of the calculated μ vs. E with 300°K experimental data was good for n-germanium, although not so good for p-germanium. It is worthwhile to study further the predictions of this theory for the variation of μ with "carrier temperature" in order to obtain an idea of how the relative importance of the different scattering processes varies as the carriers are heated. Such results can also be used to deduce, at least approximately, carrier temperatures from the experimentally observed mobility variations. In what follows we shall present the calculated mobility as a function of carrier temperature for lattice temperatures of 300, 78 and 20·4°K. Impurity scattering has not been included in the quantitative calculations, but we shall discuss its effects in a later section.

2. SCATTERING BY LATTICE VIBRATIONS

The major premise of the present theory of hot carrier mobility is that the predominant scattering is by single phonons of acoustical and optical lattice modes and of course impurities when they are pres nt in sufficient quantity. Application of the theory is simplified by assuming spherical constant energy surfaces and parabolic bands for the carriers.* With these simplifications we can write for the probability per unit time of interaction with an acoustical phonon causing a carrier with momentum P_1 and energy ϵ_1 to make a transition into the energy range $d\epsilon_2$ at ϵ_2:[2]

$$W_{12}\,d\epsilon_2 = \frac{V}{2\pi\hbar^4} m_f |U|^2 \frac{P_\gamma}{P_1}(-dP_\gamma) \qquad (1)$$

where V is the volume of the crystal, m_f the effective mass of the carrier after scattering, P_γ the momentum of the phonon involved in the transition and $|U|^2$ is given by:[1]

$$|U|^2 = \frac{E_{1ac}^2}{2Vc_l} cP_\gamma\left(n + \frac{1}{2} + \frac{\delta n}{2}\right) \qquad (2)$$

* For treatments of mobility which take into account the detailed band structure of germanium but are carried through only for low field see HERRING C. and VOGT E., *Phys. Rev.* **101,** 944 (1956) and EHRENREICH H. and OVERHAUSER A. W., *Phys. Rev.* **104,** 331 (1956).

VOL. 15 1960

where E_{1ac} is the deformation potential or coupling constant for acoustical mode scattering, c_l an average elastic constant, c the sound velocity in the crystal, n the number of phonons in the lattice oscillator with which the carrier interacts, and δn the change in this number due to the interaction with the carrier. The quantity $cP_\gamma(n+\frac{1}{2}+\delta n/2)$ is the average energy of the lattice oscillator involved in the transition. The number n is given by $n = [\exp(cP_\gamma/kT)-1]^{-1}$. When equipartition is valid, the average energy of the oscillator can be approximated by kT, and $|U|^2$ is independent of phonon size and thus of the angle θ through which the carrier is scattered. This leads to $\langle\cos\theta\rangle = 0$, with the consequence that the relaxation time, τ, is identical with the mean free time between collisions.[3] This is no longer the case, however, when equipartition is not valid, and the factor $(1-\cos\theta)$ must be included in the integration to obtain τ.[3] When this is done, the relaxation time for acoustical mode scattering can be written:

case by SHOCKLEY[2]. By use of the conservation conditions the quantity $(1-\cos\theta)$ can also be expressed as a function of P_1, P_0 and P_γ.

Integration of equation (3) would be greatly simplified if terms involving P_0 could be neglected. At 20°K and above, $(P_0/P_1) < 1$ except for the slowest carriers. These are not of particular interest because they are so few in number that their contribution to μ would be small in any case. Also, that contribution would be knocked out by impurity scattering. Consider the values of P_0/P_1 for carriers with the thermal velocity, $v_T = \sqrt{(2kT/m)}$. At 300°K, for intraband scattering of carriers with mass $0{\cdot}3\ m_0$, $(P_0/P_1) = c/v_T \simeq 0{\cdot}03$. At 20·4°K for this case $(P_0/P_1) = 0{\cdot}12$. For carriers with mass m_0 the values would be larger, (P_0/P_1) at 20·4° being 0·22. For light holes with mass $0{\cdot}04\ m_0$ making a transition into a heavy hole band with mass $0{\cdot}3\ m_0$, the values are even larger, (P_0/P_1) being 0·32 at 20·4°. Still, the values of (P_0/P_1) are small enough for carriers with $v = v_T$ that it is useful to make expansions of equations (5a) and (5b) in the form:

$$\frac{1}{\tau_{ac}} = \frac{1}{l_{ac}}\frac{1}{4m_fP_1}\left[\int_{P_{\gamma\,min}}^{P_{\gamma\,max}}(n+1)\frac{cP_\gamma}{kT}(1-\cos\theta)P_\gamma\,dP_\gamma + \int_{P_{\gamma\,min}}^{P_{\gamma\,max}} n\frac{cP_\gamma}{kT}(1-\cos\theta)P_\gamma\,dP_\gamma\right] \quad (3)$$

where:

$$l_{ac} = \frac{\pi\hbar^4 c_l}{m_f^2 E_{1ac}^2 kT} \quad (4)$$

The first term in the angular bracket of equation (3) corresponds to phonon emission, the second to absorption. The limits of integration are determined by applying to the transitions the conditions of conservation of energy and crystal momentum. With the notation m_i for mass in the initial state, and P_0 for m_fc, the limits of integration are given by

$$P_{\gamma\,min} = \sqrt{\left(\frac{m_f}{m_i}P_1^2 \mp 2P_0P_1 + P_0^2\right)} - P_1 \pm P_0 \quad (5a)$$

$$P_{\gamma\,max} = \sqrt{\left(\frac{m_f}{m_i}P_1^2 \pm 2P_0P_1 + P_0^2\right)} + P_1 \pm P_0 \quad (5b)$$

where the upper set of signs is for absorption, the lower for emission. For scattering within the same band $m_f/m_i = 1$, and these reduce simply to $P_{\gamma min} = 0$, $P_{\gamma max} = 2(P_1 \pm P_0)$, as obtained for this

$$P_\gamma = P_1\sum_{\alpha=0}^{\infty} A_\alpha(P_0/P_f)^\alpha,$$

where the A_α's are constant coefficients. An expansion in powers of (P_0/P_1) can also be made for $(1-\cos\theta)$. For carriers with $v = v_T$, (cP_γ/kT) is still small enough so that n can be expanded in terms of it and only a few terms kept in the series. It is then possible to evaluate $1/\tau_{ac}$ for $v = v_T$ explicitly as a series in (P_0/P_1), and it is found that the terms linear in (P_0/P_1) drop out, and the terms in $(P_0/P_1)^2$, etc., give a correction which can be neglected for present purposes. For carriers with $v > v_T$, (P_0/P_1) is of course still smaller and can certainly be neglected. Thus it is a reasonable approximation to neglect all terms in the integral (3) involving (P_0/P_1) down to 20·4°, although this would not be the case at lower temperatures.

When terms in (P_0/P_1) are neglected, the emission and absorption terms of expression (3) can be

combined, and for the intraband scattering case $(1-\cos\theta)$ is given by $P_\gamma^2/2P_1^2$. Using the substitution $x=\epsilon/kT$, we then obtain for the relaxation time for acoustical mode scattering:

$$\frac{1}{\tau_{ac}}=\frac{\sqrt{(2kT/m_f)}}{l_{ac}}\left(\frac{kT}{m_fc^2}\right)^2 x^{-3/2}\times \times \int_{u=0}^{\sqrt{(2m_fc^2/kT)}\sqrt{(x)}} u^4\coth u\,du \qquad (6)$$

which is essentially the expression of Ref. (1). This is now valid for arbitrary degree of excitation of acoustical lattice oscillators. An expression similar in form can be obtained for the interband scattering case. It gives the same result as equation (6) in the limit where $\sqrt{(2m_fc^2x/kT)}$ is small, thus giving equal relaxation times for light and heavy holes of the same energy at low fields, but is different from expression (6) in the limit of $\sqrt{(2m_fc^2x/kT)}$ large. The expression (6), however, will provide an adequate approximation for the interband scattering case of interest here—the light holes scattered into the heavy hole band. This is the case because for p-germanium at the larger values of x optical mode scattering dominates the acoustical mode scattering. Also, at such energies the light hole mass will have increased.[4]

It is of interest to write down explicitly the limiting forms of expression (6) for small x, or $\sqrt{(2m_fc^2x/kT)}\ll 1$, and for large x, or $\sqrt{(2m_fc^2x/kT)}\gg 1$. The case of the parameter $\ll 1$ corresponds, of course, to equipartition of energy among the lattice oscillators. In this limit there is the familiar result:

$$\frac{1}{\tau_{ac}}\to\frac{\sqrt{(2kT/m_f)}}{l_{ac}}\sqrt{(x)}=\frac{v_1}{l_{ac}}\quad\text{Equipartition} \qquad (7a)$$

In the other limit, where $\sqrt{(2m_fc^2x/kT)}\gg 1$, the lattice oscillators have only the zero point energy, $cP_\gamma/2$. In this limit the integral is well approximated by setting coth $u=1$. Then:

$$\frac{1}{\tau_{ac}}\to\frac{8}{5}\frac{c}{l_{ac}}x=\frac{4}{5}\left(\frac{m_fc^2}{kT}\right)\frac{v_1^2}{cl_{ac}}\quad\text{Zero point} \qquad (7b)$$

Thus τ decreases as $1/v^2$ in this case rather than $1/v$. The additional velocity dependence of τ comes about as follows. Faster carriers can interact with lattice modes of larger P_γ. When equipartition is valid, as said before, the matrix element for scattering is the same for all modes, independent of P_γ, because the average energy of all is kT. In the zero-point lattice, however, modes of larger P_γ have larger average energy and therefore larger matrix element. This results in more effective scattering and smaller τ for faster electrons.

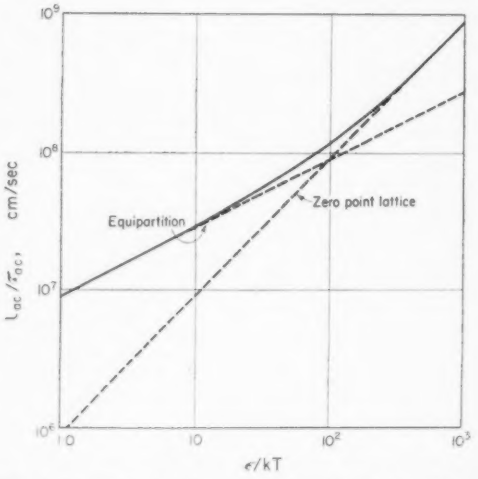

FIG. 1. Plot of l_{ac}/τ_{ac} from equation (6) as a function of energy in units of kT for a lattice temperature of 78°, effective mass of $0{\cdot}3\,m_0$, $c=5{\cdot}4\times10^5$ cm/sec. The dashed lines show the limiting cases, expressions (7a) and (7b).

A plot of l_{ac}/τ_{ac} calculated from the formula (6) is given as a function of x in Fig. 1 for the case of $m_f=0{\cdot}3m_0$, $c=5{\cdot}4\times10^5$ cm/sec, $T=78°$. The two limiting cases for expression (7a) and (7b) are shown in dashed lines. These intersect at a value of x, to be denoted by x_c, $=(25/32)(kT/mc^2)$. It can be seen that it would be a fair approximation to take $1/\tau_{ac}$ as given by expression (7a) for $x<x_c$, by expression (7b) for $x>x_c$.

In the case of optical mode scattering the square of the matrix element is of the same form as equation (2), with E_{1ac}^2 replaced by E_{1op}^2, the coupling constant to optical modes. In this case the energy of the optical phonon, cP_γ, is independent of the scattering angle, and therefore n and $|U|^2$ are also. This makes the integration required for the

calculation of the relaxation time for optical mode scattering, τ_{op}, much simpler than that for τ_{ac}. The result, for either intra- or interband case is:

$$\frac{1}{\tau_{op}} = \frac{\sqrt{(2kT/m_f)}}{l_{ac}} B\{\sqrt{(x+\theta/T)} + [\exp(\theta/T)]\sqrt{(x-\theta/T)}\} \quad (8)$$

where

$$B = \frac{b(\theta/T)}{2[\exp(\theta/T)-1]} \quad (9)$$

and

$$b = E_{1op}^2/E_{1ac}^2 \quad (10)$$

Here again, the notation and form are those of Ref. (1) except for substitution of x for ϵ/kT.

It has been seen from expressions (6) and (8) that the ratio of τ for scattering into the heavy hole band to τ for scattering into the light hole band is the 3/2 power of the ratio of heavy hole mass to light hole mass. As a consequence, in calculating μ we can neglect the scattering into the light hole band of carriers originating in either the heavy or light hole bands.

If the distribution function of the hot carriers is approximated by a Maxwell–Boltzmann distribution, the mobility is given by[3] $\mu = (e/m)\langle v^2\tau\rangle / \langle v^2\rangle$. For the τ obtained by combining expressions (6) and (8), this gives for the mobility of carriers of the ith type:

$$\mu_i = \frac{m_f}{m_i} \mu_{ac_0(m_f)} \beta^{1/2} I(\beta) \quad (11)$$

where $\beta = T/T_e$, the ratio of lattice temperature to electron temperature and

$$I(\beta) = \int_{y=0}^{\infty} \frac{ye^{-y}\,dy}{\left[\left(\frac{kT}{m_f c^2}\right)^2 \frac{\beta^2}{y^2} \int_{u=0}^{(2m_f c^2 y/\beta kT)^{1/2}} u^4 \coth u\, du + B\{\sqrt{(1+\beta\theta/Ty)} + [\exp(\theta/T)]\sqrt{(1-\beta\theta/Ty)}\}\right]} \quad (12)$$

The quantity $\mu_{ac_0(m_f)}$ is the low-field acoustical lattice mobility for intraband scattering, given by:[3]

$$\mu_{ac_0(m_f)} = \frac{4}{3} \frac{el_{ac}}{\sqrt{(2\pi m_f kT)}} \quad (13)$$

For n-germanium the ratio of the observed mobility at a field E to the low-field mobility, μ_0, is then:

$$\frac{\mu}{\mu_0} = \beta^{1/2} \frac{I(\beta)}{I(1)} \quad (14)$$

For p-germanium, if we use the subscript 1 for heavy holes, 2 for light holes and f_i for the fraction of the holes which are of the ith type, we can express the observed mobility as $f_1\mu_1 + f_2\mu_2$. Under the assumption that the two types of hole have the same temperature at all fields,[1] this leads to the ratio μ/μ_0 for p-germanium:

$$\frac{\mu}{\mu_0} = \left\{\frac{f_1(\beta) + f_2(\beta)\, m_1/m_2(\beta)}{f_1(1) + f_2(1)\, m_1/m_2(1)}\right\} \beta^{1/2} \frac{I(\beta)}{I(1)} \quad (15)$$

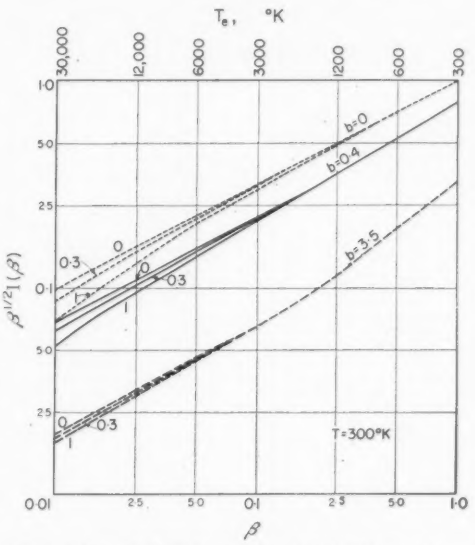

FIG. 2. Plots of $\beta^{1/2}I(\beta)$, equal to $(\mu/\mu_0)I(1)$, as a function of β and T_e for a lattice temperature of 300°. The b-value of 0 (dotted lines) represents the case of acoustical mode scattering only; 0·4 (solid lines) electrons in germanium; 3·5 (dashed lines) holes in germanium. The numbers at the left are m_f-values in units of the free electron mass, $m_f = 0$ indicating that equipartition has been assumed for the acoustical lattice oscillators.

The factor in braces varies with β from a value of unity at low fields to about 3/4 in the limit of such fields, probably over 20,000 V/cm at 300°,[1] that the masses of the two holes are essentially the same. Since this factor is of the order of unity and slowly varying, we shall generally assume it to be unity in what follows. In any case, this error is probably smaller than that arising from the use of an incorrect distribution function.

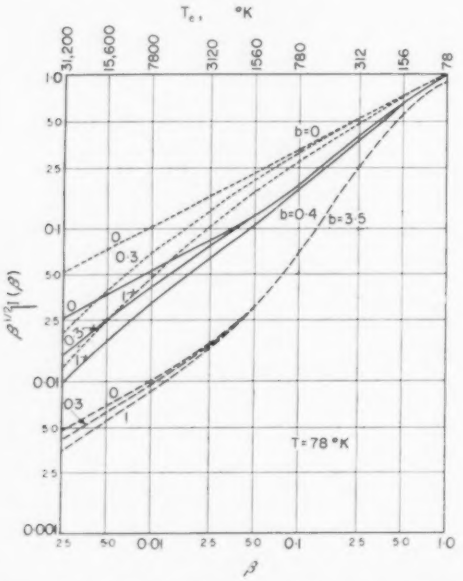

FIG. 3. Plots of $\beta^{1/2}I(\beta)$, equal to $(\mu/\mu_0)I(1)$, as a function of β and T_e for a lattice temperature of 78°K. The b-value of 0 (dotted lines) represents the case of acoustical mode scattering only; 0·4 (solid lines) electrons in germanium; 3·5 (dashed lines) holes in germanium. The numbers at the left are m_f-values in units of the free electron mass, $m_f = 0$ indicating that equipartition has been assumed for the acoustical lattice oscillators.

3. CALCULATED RESULTS FOR GERMANIUM

In order to show the variation with carrier temperature of the mobility and the relative importance of acoustical and optical mode scattering, plots were made of the quantity $\beta^{1/2}I(\beta)$ as a function of β for various values of the parameters. These constitute Figs. 2–6. To obtain μ/μ_0 from these plots, the plotted quantity must be divided by the intercept at $\beta = 1$ of the curve to which it belongs. The quantity $I(\beta)$ was evaluated by computer. For all plots the parameter θ was taken as 430°.[5] The values of b, defined by equation (10), required to give the observed temperature dependence of low-field lattice mobility can be calculated from expressions (11) and (12) with $\beta = 1$. These are 0·4 and 3·5 for n- and p-germanium, respectively.* The calculations were carried out for these values of b and also for $b = 0$ in order to show the effect of acoustical mode scattering alone. For each curve the b value is indicated at the right of the plot. The

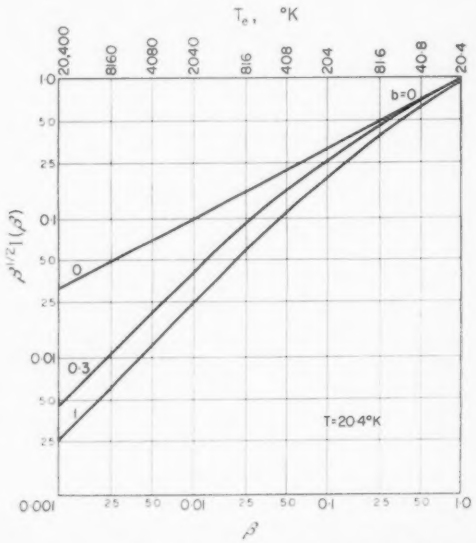

FIG. 4. Plots of $\beta^{1/2}I(\beta)$ as a function of β and T_e for the case of acoustical mode scattering only and a lattice temperature of 20·4°. The numbers at left are m_f-values in units of the free electron mass, $m_f = 0$ indicating that equipartition has been assumed for the acoustical lattice oscillators.

numbers associated with each curve at the left of the plot are the m_f values in units of the free electron mass. To show the effect of the departure from equipartition, curves have also been included for which equipartition was assumed to hold for all β. The effect of assuming equipartition is the replacement of the first term in the denominator of $I(\beta)$ by

* For plots which show the agreement between the experimentally observed lattice mobility vs. temperature and these calculated results see CONWELL E. M., *Sylv. Tech.* XII, 30 (1959). These plots also show, in dashed lines, the lattice mobility that would be observed if b were zero, which for electrons is μ_{ac_0}, for holes $[f_1+f_2(m_1/m_2)]\mu_{ac_0}(m_1)$.

unity. Since this is what the first term becomes in the limit of vanishing m_f, these curves have been labelled $m_f = 0$. For heavy holes the appropriate value of m_f is $0{\cdot}3\ m_0$, and, as noted previously, this serves as an adequate approximation for the light holes also. The case of electrons is unfortunately much more complicated. The factor m_f appears in $I(\beta)$ mainly as a result of the operation of expressing P_1 in terms of ϵ. Due to the ellipsoidal

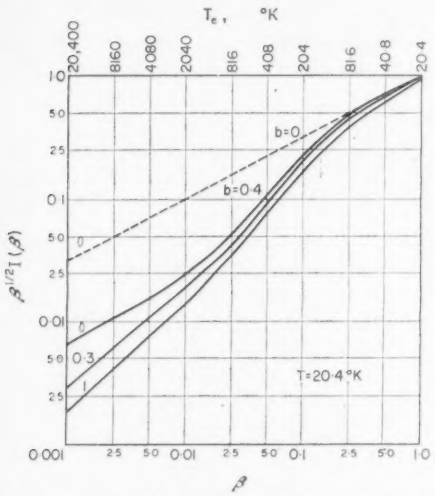

FIG. 5. Plots of $\beta^{1/2}I(\beta)$, equal to $(\mu/\mu_0)I(1)$, as a function of β and T_e for a lattice temperature of 20·4°. The b-value of 0 (dotted line) represents the case of acoustical mode scattering only; 0·4 (solid lines) electrons in germanium. The numbers at the left are m_f-values, $m_f = 0$ indicating that equipartition has been assumed for the acoustical lattice oscillators.

larger than the average. For β values close to 1, even as low as 0·1, whatever the value chosen for m_f (in the range 0–1 m_0) the first term in the denominator of $I(\beta)$ is still well approximated by unity. Thus the choice of m_f does not have a significant influence on $I(\beta)$ until β-values less than 0·1 are reached. This can be seen from the various plotted curves. It suggests that good over-all results

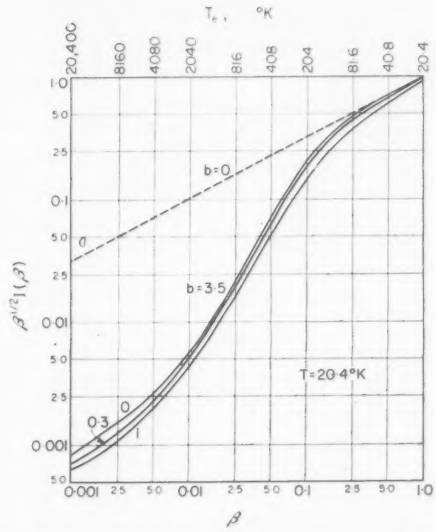

FIG. 6. Plots of $\beta^{1/2}I(\beta)$, equal to $\mu/\mu_0 I(1)$, as a function of β and T_e for a lattice temperature of 20·4°. The b-value of 0 (dotted line) represents the case of acoustical mode scattering only; 3·5 (solid lines) holes in germanium. The numbers at the left are m_f-values in units of the free electron mass, $m_f = 0$ indicating that equipartition has been assumed for the acoustical lattice oscillators.

constant energy surfaces there is not a unique energy but a range of energy correlated with a given P_1, and correspondingly a range of P_1 associated with a given energy. Thus for a given energy some of the carriers—e.g. the ones of larger P_1—may interact with larger phonons than the others, and may be affected by the departure from equipartition more than the others. For this reason, choosing for m_f the value which relates P_1 to the average energy for a carrier with momentum P_1 would probably result in an underestimate of the effect of the deviation from equipartition. Rather arbitrarily, the values of $0{\cdot}3\ m_0$ and $1\ m_0$, both larger than the average, were chosen for the calculations. There is another reason also for calculating with m_f values would be obtained if the m_f value chosen represented the mass of hot carriers rather than thermal ones. To indicate what the effect would be of larger m_f for the hot carriers plots have been included for all cases with $m_f = 1\ m_0$.

It has, of course, been assumed that the same parameters are valid throughout the range of β plotted, and that no new scattering processes appear in this range. These assumptions must be valid, to the extent that the model on which the calculation is based is valid, through at least a small range of β's below $\beta = 1$. They will almost certainly not be valid over the whole range of β's plotted. Where the assumptions cease to be valid, the calculations are, of course, not expected to be

applicable. They may still have value, however, in such ranges, precisely to help show that changes in the parameters or scattering processes have occurred.

We shall consider now the various plotted curves in more detail, starting with those for acoustical scattering only, i.e. those for which $b = 0$. When $b = 0$ and equipartition is assumed, $I(\beta) = 1$ and the quantity plotted is μ/μ_0, which is of course expected for this case to equal $\beta^{1/2}$.[2] When equipartition is not assumed the acoustical lattice mobility is lower, the more so the larger the m_f value. The reason for this is that for given $\langle\epsilon\rangle$ or T_e, the larger m_f means larger carrier momenta, on the average, and therefore interaction with phonons of larger momentum. As discussed before, when equipartition does not hold the modes of larger P_γ have larger matrix element and thus scatter more effectively. Comparing the $b = 0$ curves of Figs. 2, 3 and 4, one sees that the effects of the departure from equipartition increase when the lattice temperature goes down, as expected. In the limit of high enough T_e, or low enough β, according to equations (7b) or (12), when $b = 0$, μ/μ_0 should be proportional to β. This is seen to be the case for 20·4° from about $\beta = 0{\cdot}01$ to 0·001, the slope of the log–log plots being unity in this region. At 78° the region where μ is proportional to β is approached at the smallest β's plotted, but it is not found at all at 300°.

So far as optical modes are concerned, it has been commented for the case of thermal carriers, that the lattice temperature must be $\theta/4$ or higher for their scattering effect to be perceptible. Consistent with this, only for 300° does $I(1)$ differ appreciably from unity. According to the plots for 78° and 20·4°, the statement made above for thermal carriers can be extended to say that for a lattice temperature less than $\theta/4$, the carrier temperature must be $\theta/4$ or higher for the optical modes to affect the mobility appreciably. As T_e increases beyond $\theta/4$, the importance of optical mode scattering increases, the extent of the increase being determined by the values of b and m_f as well as β. At the smaller β's, for $b = 0{\cdot}4$ optical and acoustical mode scattering are more or less comparable in magnitude, with the latter being somewhat more important, while for $b = 3{\cdot}5$ optical mode scattering is considerably more important than acoustical.

In the limit where $T_e \gg \theta$, $\langle\epsilon\rangle \gg k\theta$, and $(1/\tau_{op}) \propto \sqrt{\epsilon}$. Thus, when both types of scattering are present and equipartition is assumed for the acoustical modes it is expected that at high enough T_e or small enough β, $(\mu/\mu_0) \propto \beta^{1/2}$. This limiting behavior of the $m_f = 0$ curves is found at 300°K below $\beta = 0{\cdot}1$, at 78°K below $\beta = 0{\cdot}01$, and is only approached for the smallest β's at 20·4°. When equipartition is not assumed, simple behavior—i.e. $\beta^{1/2}\, I(\beta)$ proportional to β to some power—in the limit of small β is not expected. It might be added that, as will be shown shortly, when simple behavior of this sort is predicted, it has significance for distributions other than the Maxwell–Boltzmann, even though it was derived assuming the latter.

It is of some interest to consider the theoretical predictions for the dependence of μ on electric field intensity when the assumption of equipartition is dropped. It is worthwhile to do this in fairly general fashion, and we shall consider first the case where $\tau \propto v^n$ where n is a constant. To obtain μ from τ requires taking the appropriate weighted average of τ over the correct distribution. Under the assumption that the scattering is approximately elastic, which is true at high enough fields even when optical mode scattering is present, it can be shown[6] that $\mu = K_1\langle v^n\rangle$, where K_1 is a constant depending on the distribution function, but not explicitly on E. Assume now that the distribution function is such that $K_1\langle v^n\rangle = K_2\langle v\rangle^n$, where K_2 is independent of E. This is true for the Maxwell–Boltzmann distribution, and for the Druyvestyn distribution, which is the correct one for the case of high electric field intensity under the conditions of the simple model of the band structure and equipartition for acoustical modes.[2,7] It is also true, for example, for any distribution of the form $f = A(E)\exp[-\epsilon^a g(E)]$, where a is a constant and A and g are arbitrary functions of E. Thus, for all distributions that satisfy the specified conditions if $\tau \propto v^n$ then $\mu \propto \langle v\rangle^n$ and $\langle\epsilon\rangle^{n/2}$. As a corollary, if it has been found that $\mu \propto \beta^m$ or $\mu \propto \langle\epsilon\rangle^{-m}$, using the Maxwell–Boltzmann distribution, the same dependence of μ on $\langle\epsilon\rangle$ would be found for all distributions that satisfy the specified conditions.

To determine the dependence of μ on E it is convenient to use the steady state condition: $q\mu E^2 + \langle d\epsilon/dt\rangle = 0$.[1] We shall consider the case

where $d\epsilon/dt \propto v^m$, where m is a constant. For distributions that satisfy the specified conditions we can then write $\langle d\epsilon/dt \rangle = -K_3 \langle v \rangle^m$, where K_3 is not a function of E. The steady-state condition then gives

$$qK_2 \langle v \rangle^n E^2 - K_3 \langle v \rangle^m = 0$$

from which we obtain

$$\langle v \rangle = \left(\frac{qK_2}{K_3} \right)^{1/(m-n)} E^{2/(m-n)} \qquad (16)$$

and

$$\mu = K_2 \left(\frac{qK_2}{K_3} \right)^{n/(m-n)} E^{2n/(m-n)} \qquad (17)$$

For interaction with acoustical modes only and equipartition assumed, $n = -1$, $m = 3$ and this leads to the familiar prediction of $E^{-0.5}$ dependence for μ.[2] For the zero point lattice and no optical mode scattering, $n = -2$, $m = 3$[1] and this leads to $\mu \propto E^{-0.8}$. This result was obtained by PARANJAPE[8]. It is seen, however, that the result is more generally valid than shown by him, in that it applies to a wide class of distribution functions rather than only to the one obtained when inter-electronic equilibrium is established faster than electron–lattice equilibrium.

The results, expressions (16) and (17), have been derived for the case in which $\tau \propto v^n$ and $(d\epsilon/dt) \propto v^m$ where n and m are constants over the range of electron energies important for the conductivity. In general, such simple relationships with n and m constant do not hold. It can then be expected that the behavior of μ vs. $\langle \epsilon \rangle$ and vs. E will depend on the detailed nature of the distribution function. It is not useful to consider such cases further without use of the correct distribution function.

It was found by MENDELSON and BRAY[9] that $\mu \propto E^{-0.8}$ for high resistivity p-germanium at 78° in the range of fields 600–10,000 V/cm. Since this is the dependence of μ on E predicted for interaction with a zero point lattice, PARANJAPE has suggested that that is the origin of the observed dependence. Even apart from the question of the role of the optical modes, this explanation appears quite unlikely. At 78° for a mass of $0.3\ m_0$, according to Fig. 1, the region where $\tau \propto 1/v^2$ does not start until ϵ is several hundred kT. For a mass of $0.04\ m_0$ much larger ϵ's still would be required before the $1/v^2$ dependence is reached. The observed mobility change at the fields where the 0·8 dependence begins is approximately a factor 3. If μ were proportional to $1/\sqrt{\langle \epsilon \rangle}$ at the lower fields, this μ change would indicate an increase in $\langle \epsilon \rangle$ of no more than a factor 10. It is hard to imagine that $\langle \epsilon \rangle$ could have changed by a factor much greater than 10 at these fields. It can only be concluded that it is very unlikely that the carriers are hot enough in the range of fields where the -0.8 dependence has been observed for the zero point lattice explanation to be correct. In addition to this objection, of course, there is the one that PARANJAPE's explanation requires that there be no interaction with any scattering mechanism having different velocity dependence for τ, such as optical modes. Eliminating the optical mode scattering would leave, at least at present, no satisfactory explanation for the observed $T^{-2.3}$ dependence of the lattice mobility.

4. SCATTERING BY IMPURITIES

It has been predicted that when the mobility is determined primarily by impurity scattering it should increase upon application of electric fields beyond the ohmic range.[10] Measurements of Hall mobility vs. E on n-germanium samples at 5°K[11] and on an n-silicon sample at 20°K[12] have shown an increase attributable to this source. An increase that might arise at least partly from this source has also been found in measurements of σ vs. E for compensated p-germanium samples with ionized impurity concentration of about $10^{17}/\text{cm}^3$ at 78°K.[13] Unfortunately, the theory in Ref. (10) is not directly applicable to any of these cases because ionization of the impurities was incomplete, with the consequences that neutral impurity scattering may have been considerable, and ionization and perhaps excitation of impurities were also taking place at these fields. It seems, however, that the observed increases, particularly in the case of MENDELSON and BRAY, were less than might have been expected, even allowing for the complications mentioned.

Two major reasons can be presented for a discrepancy between the theory in Ref. (10) and experimental results for samples of high impurity concentrations at low temperature. First, it was

assumed in the theoretical treatment that $\tau_I \propto v^3$, dependence of the log term on v being neglected. This is a good approximation only for lightly doped samples and high temperatures; it would not be a good approximation for the germanium samples in question at 78°. The effect of the log term in τ_I is to make the exponent of v smaller, and therefore the amount of the expected increase in μ smaller. According to the Conwell–Weisskopf theory of impurity scattering, for germanium samples with $N_I = 10^{17}/\text{cm}^3$, taking into account the log term would make the exponent of v lie between 1 and 2. This theory is, of course, based on the Born approximation, the validity of which is somewhat doubtful for samples with such doping at 78°K.[14,15] According to the treatment of impurity scattering based on the method of partial waves, which should be more valid for the case in question, the exponent should be smaller than that obtained from the Born approximation. It is clear that for the samples in question the increase in mobility in the impurity scattering range should be considerably smaller than that calculated on the assumption $\tau_I \propto v^3$.

On the basis of the Born approximation, as the temperature decreases the effective exponent of v in τ_I decreases monotonically, going through zero and ultimately assuming a value of -1. In the latter region the effect of applying a high field would be to decrease μ_I. Actually, the dependence of τ_I on v for very low velocity carriers should be more complicated than predicted by the treatment based on the Born approximation, but regions of τ_I independent of v and τ_I decreasing with v could still be expected to occur. Judging from BLATT's calculations,[14] for an ionized impurity concentration N_I of $10^{16}/\text{cm}^3$ in silicon, τ_I should be approximately independent of v in the temperature region 20–50°K, and below this τ_I should decrease with increasing v. It should be emphasized that this means $N_I = 10^{16}$ at the temperature in question which in turn means much larger N_I at room temperature since the degree of ionization would be much smaller at the low temperature.

A second effect that would cut down the increase in μ due to the increase of μ_I with T_e is the increasing interaction with optical modes as T_e goes up. As can be seen from Fig. 3, this would be particularly effective in counteracting the increase in μ at 78°, and for p-type samples. At 20° and lower, it would be much less effective because carrier temperature must go up quite considerably before the carriers can interact much with optical modes. The presence of neutral impurity scattering, with τ independent of v, would also tend to cut down the possible increase of μ.

It is not felt that the theory of impurity scattering is reliable enough at present for the high impurity concentration and low temperature region to make quantitative calculations of μ vs. E incorporating μ_I worthwhile. Neglect of impurity scattering, however, makes the present calculations invalid at low temperature only for low and intermediate fields. When the carriers are hot enough, both ionized and neutral impurities should be relatively ineffective scatterers compared to the lattice vibrations. Thus, within the framework of the calculation set up here, at high field all samples should come to the same mobility independent of impurity content. This was found to be the case for a set of uncompensated p-germanium samples with carrier concentration ranging from $3\times10^{12}/\text{cm}^3$ to $4\times10^{15}/\text{cm}^3$ at 78°,[13] all samples of the set showing the same $\mu(E)$ above 10^3 V/cm.*

In conclusion, it should be remarked that, despite the simplifications in treating band structure and distribution function, the calculations in this paper should serve to give a good idea of the variation with lattice and carrier temperature of the relative importance of acoustical and optical mode scattering, and of the carrier temperature to be associated with a given μ/μ_0. This is to be expected particularly for n-germanium because of the good agreement with experiment of μ vs. E for 300° calculated on the same model with the same approximations.[1] For p-germanium, of course, the agreement with experiment of the calculated μ vs. E was not good. It is felt, however, that the main source of error there was not in the determination of μ/μ_0 as a function of T_e, but rather in the calculation of T_e as a function of E. Thus it is expected that the present results provide a fairly good approximation for the average hole mobility as a function of the average hole temperature.

* SEEGER K., *Phys. Rev.* **114**, 476 (1959) found, using microwave excitation, that samples of high ρ did not show as large mobility changes as samples of lower ρ, but this result has been questioned by ZUCKER J., *J. Phys. Chem. Solids*, in press.

REFERENCES

1. CONWELL E. M., *J. Phys. Chem. Solids* **8,** 234 (1959).
2. SHOCKLEY W., *Bell Syst. Tech. J.* **30,** 990 (1951).
3. SHOCKLEY W., *Electrons and Holes in Semiconductors* Chapter 11. Van Nostrand, New York (1950).
4. KANE E. O., *J. Phys. Chem. Solids* **1,** 82 (1956).
5. BROCKHOUSE B. N. and IYENGAR P. K., *Phys. Rev.* **111,** 747 (1958).
6. CONWELL E. M., *Phys. Rev.* **88,** 1379 (1952).
7. YAMASHITA J. and WATANABE M., *Prog. Theor. Phys.* **12,** 443 (1954).
8. PARANJAPE B. V., *Proc. Phys. Soc., Lond.* B**70,** 628 (1957). This result was also obtained earlier by SHOCKLEY W., then at Bell Laboratories.
9. MENDELSON K. S. and BRAY R., *Proc. Phys. Soc., Lond.* B**70,** 899 (1957).
10. CONWELL E. M., *Phys. Rev.* **90,** 769 (1953).
11. KOENIG S. H. and GUNTHER-MOHR G. R., *J. Phys. Chem. Solids* **2,** 268 (1957).
12. KAISER W. and WHEATLEY G. H., *Phys. Rev. Letters* **3,** 334 (1959).
13. MENDELSON K. S. and BRAY R., Purdue University, unpublished. These results were kindly communicated by Prof. BRAY.
14. BLATT F. J., *J. Phys. Chem. Solids* **1,** 262 (1957).
15. SCLAR N., *Phys. Rev.* **104,** 1548 (1956).

VOL.
15
1960

J. Phys. Chem. Solids Pergamon Press 1960. Vol. 15. pp. 218–224. Printed in Great Britain.

THE RADIATION INDUCED DECOMPOSITION OF POTASSIUM NITRATE*

J. FORTEN and E. R. JOHNSON

Stevens Institute of Technology, Hoboken, New Jersey

(*Received* 28 *July* 1959; *revised* 19 *November* 1959)

Abstract—Measurements of the heats of solution of irradiated KNO_3 indicate that a transition resembling a lambda transition is induced in the solid at about 1 mol per cent decomposition. It is believed that this transition can account for the sharp decrease in the decomposition yield which occurs at about 1 mol per cent decomposition. In addition evidence is presented which indicates that the mechanism for the decomposition is molecular rather than by means of free radicals or other reactive species.

SOLID potassium nitrate when exposed to ionizing radiation undergoes decomposition to yield nitrite ion and oxygen in equivalent amounts.[1,2,3,4,5]

$$KNO_3 = KNO_2 + 1/2\ O_2 \qquad (1)$$

The oxygen apparently remains trapped in the lattice as oxygen molecules[1] up to about 22 per cent decomposition[2] when the salt is decomposed at room temperature. CUNNINGHAM and HEAL[2], have shown that the G value (molecules decomposed per 100 eV absorbed) for the decomposition of potassium nitrate changes with temperature, and at some temperature ranges, with per cent decomposition. At room temperature they find that the slope of a plot of the yield of nitrite ion as a function of dose changes abruptly at some point below 2 per cent decomposition. Further they find that the decomposition yield is independent of the intensity, and dependent only upon the amount of nitrate present up to about 22 per cent decomposition. Above this amount of decomposition oxygen diffuses out of the lattice. There is no doubt that the radiation decomposition of KNO_3 is very complex as is probably the decomposition of other nitrates,[2,4] and as yet there is no clear evidence for the support of any particular reaction mechanism.

It has been determined that an explanation for some of the phenomena observed by CUNNINGHAM and HEAL can be found by measurements of the heats of solution of irradiated KNO_3. In addition some evidence is presented to indicate a molecular rather than a free radical mechanism.

EXPERIMENTAL

The radiation source was a cylinder of Co^{60} of about 250 curies. The source is so arranged that both the center and outside of the cylinder may be used.[6] Dose was determined by ferrous sulfate dosimetry using a G value of 15·5 molecules of Fe^{++} oxidized per 100 eV absorbed. True absorption coefficients were not used in calculating dose. It was assumed that the mass absorption coefficient of solid KNO_3 was sufficiently similar to that of a 1 mM solution of $FeSO_4$ in 0·8N H_2SO_4, so that differences in absorption could be neglected.

Nitrite ion was determined by the color developed with n-(1-naphthyl)-ethylenediamine dihydrochloride, sulfanilamide reagent.[7] The molar extinction at 5380 Å was 420×10^2.

Heats of solution were determined by well established methods.[8,9,10] A twin differential calorimeter (Fig. 1) using exactly two-gram samples was used. Temperatures were determined using carefully calibrated thermistors. The apparatus was checked by observing zero heat differential when identical samples were compared.

* Research supported by the AEC Contract No. AT(30–1)1824.

VOL. 15 1960

The heat of solution determined was for the reaction

$$KNO_3(2\text{ g}) + H_2O(280\text{ g}) = KNO_3\text{ aq.}$$

For the non-irradiated salt the value of ΔH_{298} for the above reaction was $82{\cdot}31 \pm 0{\cdot}05$ cal/g. This may be compared with the interpolated value from

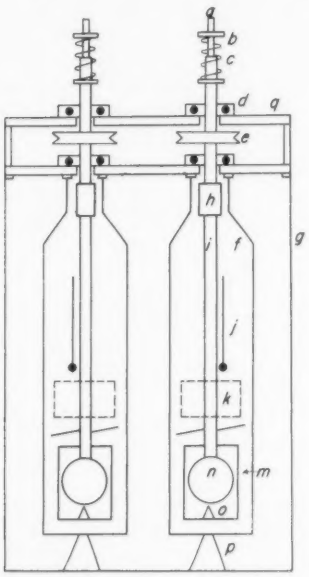

FIG. 1. Schematic of Twin Differential Calorimeter. Electrical circuits not shown.

a Pyrex tube
b spring retainer
c sample release spring
d ball bearing
e stirrer drive pulley
f narrow-neck Dewar flask
g copper submarine
h Bakelite section of stirrer shaft
i Monel tube stirrer shaft
j thermistor
k heater
l stirrer blades
m sample release stirrup
n Pyrex sample bulb
o sample release spike
p rubber support cone
q Masonite cover and supporting framework.

circular 500 N.B.S.[11] of 82·39 cal/g. The differences in our heats of solution could possibly be attributed to the fact that the potassium nitrate used was Bakers C.P. containing 99·3 per cent KNO_3. No correction was made for the impurities. During the dissolution of the irradiated salt[1] there arises the question of whether or not the oxygen liberated in equation (1) dissolves in the solvent. Experiments were performed where the irradiated salt was dissolved under conditions identical with those used in determining the heats of solution except that provision was made to collect any liberated gas. Although no strictly quantitative determinations were possible the experiments indicated that more than 80 per cent of the oxygen liberated in equation (1) does not dissolve in the solvent. A small fraction of oxygen may dissolve, but certainly the major fraction of the liberated oxygen does not.

C.P. potassium nitrate previously ground to a uniform mesh was used in all the experiments. Irradiation was done by filling a small medicine vial with sample and irradiating at room temperature. Air was not excluded from the samples during irradiation.

Densities were determined in the presence of n-nonane. A weighed quantity of the powdered salt was added to a pycnometer and then soaked for several days in nonane. The densities determined at 27°C were reproduced to $\pm 0{\cdot}0016$.

RESULTS AND DISCUSSIONS

Figure 2 shows a plot of the nitrite ion yield vs. dose for the decomposition of KNO_3. At a dose of about 40×10^{20} eV/g there is a sharp break in the slope of the yield vs. dose curve which is equivalent to a change in the G value (molecules converted per 100 eV absorbed). CUNNINGHAM and HEAL observed a similar change in the G value of KNO_3 as well as of several other nitrates. This change in G value with dose for KNO_3 has been found by CUNNINGHAM and HEAL to occur over the temperature range of −19°C–200°C except in the vicinity of the transition temperature (85°C–128°C). There is a relatively large dispersion in experimental points above an absorbed dose of about 50 eV/g. We cannot offer an explanation for this but apparently others[2] have experienced the same difficulty.

In Fig. 3 is shown a plot of the heat absorbed when irradiated KNO_3 is dissolved in water as explained under Experimental. Since a twin differential calorimeter was used, the values shown represent the difference between the heats of solution of equal weights of the irradiated and non-irradiated salts. Heats of solution of both potassium nitrate and nitrite are endothermic while that of oxygen is exothermic.

Above an absorbed dose of about 27×10^{20} eV/g there is a sharp decrease in the amount of

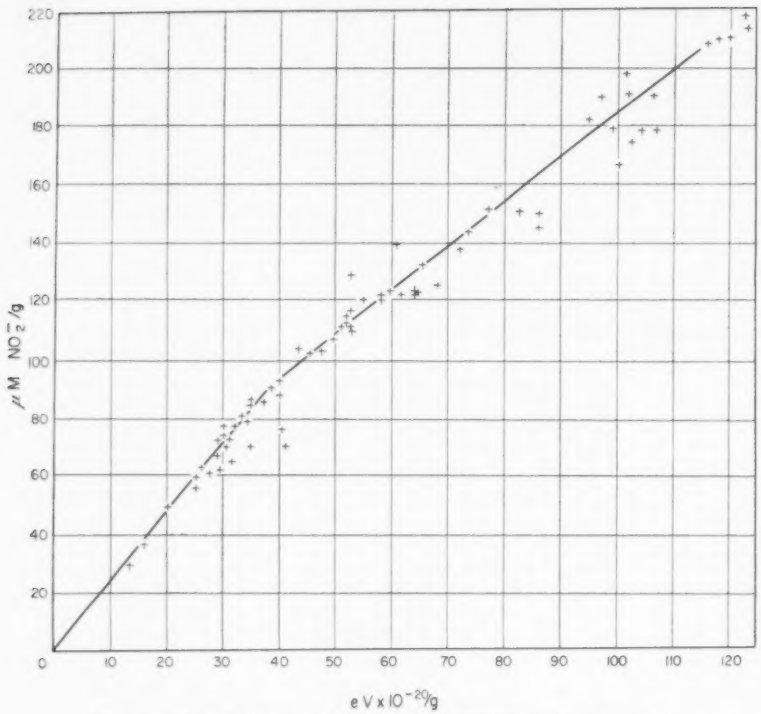

FIG. 2. Yield of nitrite ion in irradiated KNO_3 as function of dose.

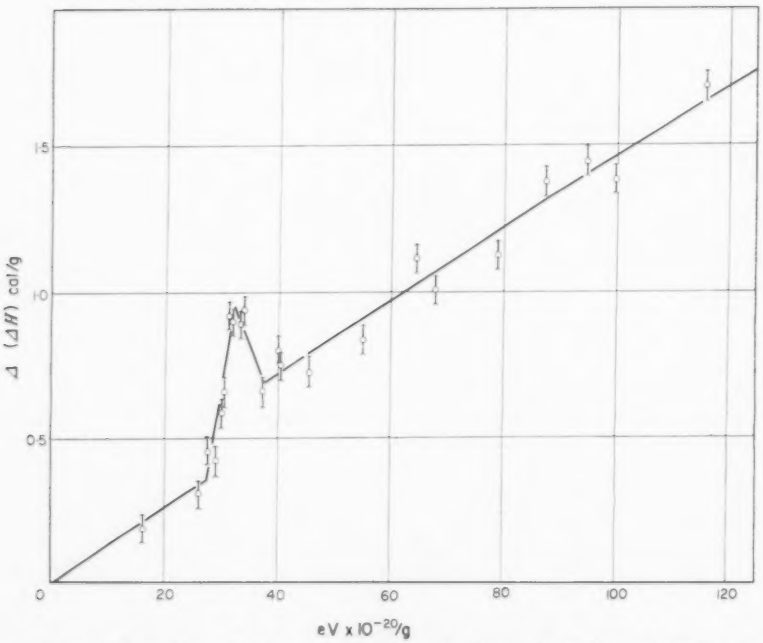

FIG. 3. Experimentally determined change in heat of solution of irradiated KNO_3 as function of dose.

heat absorbed upon dissolution of the irradiated salt. The experimental points shown prior to this discontinuity in the heat of solution and during the apparent discontinuity, are averages of quadruplicate results to insure maximum precision. For a dose of about 40×10^{20} eV/g and higher, the heats of solution appear to be linear. The point of discontinuity represents about 0·95 mol per cent decomposition, and the total curve shown, represents about 3 mol per cent decomposition.

particular dose, on a per gram basis. The calculated curves represent the difference between the theoretical heat of solution and 82·31 cal/g, which is the heat of solution of one gram of pure KNO_3 under the experimental conditions.* Curve A is the experimentally determined curve. Curve B is a calculated curve based on the nitrite yield for the particular dose involved and assuming oxygen dissolves in the solvent. Curve C is also a calculated curve identical with B except we assume that the

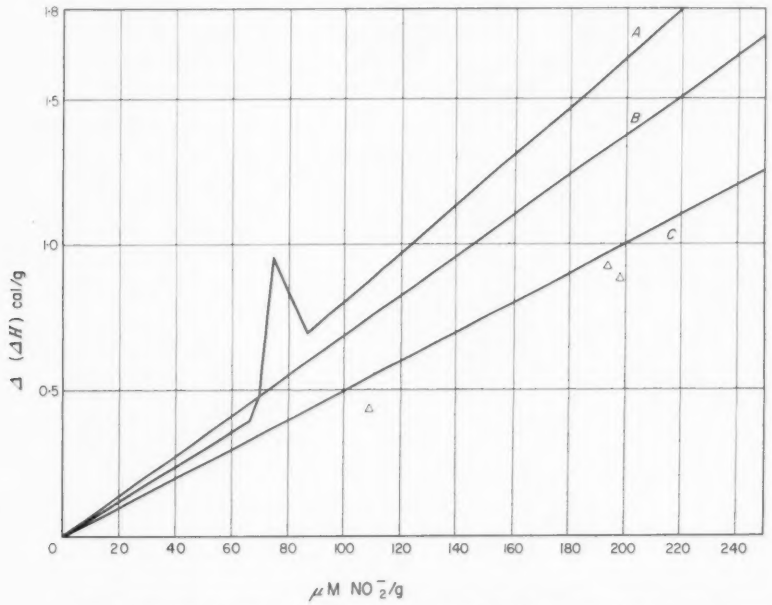

FIG. 4. Change in heat of solution of irradiated KNO_3 as function of nitrite ion yield.

A Experimental curve
B Calculated curve, assuming O_2 dissolves
C Calculated curve, assuming O_2 does not dissolve
Δ Experimental values for fused mixtures KNO_3–KNO_2

Fig. 4 shows a comparison between the experimental curve (Fig. 3) and two calculated curves for the heats of solution of irradiated potassium nitrate as a function of nitrite ion concentration. The calculated curves involved the use of the heat of solution value of $82{\cdot}31 \pm 0{\cdot}05$ cal/g for potassium nitrate and the N.B.S. values of 38·77 cal/g for potassium nitrite and $-118{\cdot}75$ cal/g for oxygen. The theoretical heat of solution was obtained from the above values and the calculated amount of nitrate ion, nitrite ion and oxygen present, for a oxygen liberated from equation (1) does not dissolve in the solvent.

The validity of Curve C (and therefore Curve B) was established by determining the heats of solution of both fused and mixed samples of KNO_3 and KNO_2. These points are appropriately indicated on Curve C.

* It should be noted that the theoretical curve as calculated is only a close approximation, since the initial and final thermodynamic states do not correspond strictly to the ones for which the N.B.S. values are given.

As explained under Experimental the oxygen liberated in equation (1) does not appear to dissolve in the solvent,* therefore Curve A (beyond the discontinuity) should be compared with Curve C. However since exact quantitative data on the amount of oxygen dissolved were not obtained, Curve B for comparative purposes may be considered as a low limit of the difference between the experimentally determined and calculated heats. The differences between the slopes of Curves A and C is 0·00309 cal/μM NO_2^- and this represents the stored energy per μM of nitrite ion formed.

The nature of the stored energy is in a large part due to the apparent transition, and the remainder possibly to some lattice strain. We do not believe it can be due to presence of oxygen atoms in the lattice.

Since the oxygen is apparently released during the solution process the only plausible reaction of the oxygen atoms would be with themselves to form molecules. This reaction is highly exothermic ($\Delta H = -119$ kcal/mol) and would easily be detected by our measurements. These results support the findings of HENNIG *et al.*[1] that the oxygen formed in equation (1) exists in the lattice as molecules not atoms.

MECHANISM OF THE DECOMPOSITION

The G value for nitrite production below 1 per cent decomposition was 1·33 and above 1 per cent decomposition the G value was found to be 1·17. CUNNINGHAM and HEAL found 1·94 and 1·4 respectively. The discrepancy between these results and ours may possibly be accounted for on the basis of experimental error. There does not appear to be any other explanation at this time.

Referring to Fig. 3 we see that the irradiated salt appears to have undergone some sort of transition above about one mol per cent decomposition. Above this transition solution of the irradiated salt is less endothermic by about 0·21 cal/g. Powdered X-ray patterns do not reveal a new lattice or any new lattice points. However, with the small amount of energy involved one would not expect a real lattice transition.

The transition which is observed appears to bear a resemblance to the lambda transitions observed in many ionic solids.[12,13,14,15] KRACEK[13] and his colleagues[14] have firmly established the existence of a gradual transition in crystalline sodium nitrate in the vicinity of 150–180°C. The property studied in greatest detail was volume expansion. AUSTIN and PIERCE[15] showed later that the volume expansion during this transition in sodium nitrate, occured in a preferred crystal orientation, notably the *c*-axis. Gradual changes in volume and heat capacity are characteristic of lambda transitions.

Irradiated KNO_3 definitely undergoes a lattice expansion. Density measurements which are summarized in Table 1 show a sharp decrease in the density following the apparent transition. Our measurements are not sufficiently accurate to decide whether or not a small decrease in density occurs prior to the transition, but they are sufficiently accurate to show that immediately following the transition an appreciable decrease in density occurs. The results also suggest that the density might be decreasing slowly after the transition. The density change observed following the transition is less than 1 per cent which is about the same amount found for the lambda transition, induced by heat, at about 240°K for the ammonium halides.

Table 1. *Comparison of densities in irradiated* KNO_3

Dose ($eV \times 10^{20}$/gm)	Density	Av. Deviation
—	2·0947	±0·0016
—	2·0934	
13·39	2·0919	
20·07	2·0929	
25·3	2·0929	
33·97	2·0729	
41·23	2·0796	
65·43	2·0716	
85·98	2·0704	

The energy involved in lambda transitions is usually quite small, which is what was found in the transition observed with irradiated KNO_3, i.e. about 21 cal/mol.

* It is interesting to note the difference in dissolution between a sample of irradiated KNO_3 and normal KNO_3. The irradiated salt appears to burst apart rather violently during dissolution, while the non-irradiated salt behaves normally. This may be caused by the internal pressure of the trapped oxygen in the lattice.

VOL. 15 1960

Some lambda transitions, especially those occuring in solids, are believed to involve a change from torsional rotation to comparatively free rotation of ions, which in this case would be the nitrate ion. However, BECK[16] has observed rotation in ammonium halides both before and after the so-called lambda transition. We do not know the origin of this transition or exactly what is involved in it. CUNNINGHAM and HEAL found a new vibration band in the spectra of irradiated KNO_3 at 1250 cm^{-1}. They first show the appearance of this new band after about 4 per cent decomposition. Fig. 5 shows the spectra of irradiated KNO_3 at about 1 per cent decomposition. At this low percentage decomposition the 1250 cm^{-1} band is barely visible. This band is very close to the 1270 cm^{-1} band of the nitrite ion. The results of CUNNINGHAM and HEAL show that the 1250 cm^{-1} band increases in intensity up to about 12 per cent decomposition where it ceases to grow noticeably. The band disappears at about 24 per cent decomposition which is the point where the crystal lattice begins to deteriorate (i.e. this is the point where the oxygen diffuses out of the lattice).

CUNNINGHAM and HEAL believe the band to be due to single nitrite ions originally dispersed in the nitrate lattice, and after pelleting dispersed in a modified lattice of nitrate with the KBr spacing. We believe this band to be due to nitrite ions in a nitrate lattice modified by the transition referred to above. No other changes in the spectra of irradiated KNO_3 were observed. It is probably very unlikely, however, that one could observe a small change in vibration rotation spectra in nitrate ion with our present techniques.

The mechanism for the transition could be free rotation of nitrate ions at decomposition sites* resulting in an increase in symmetry in its own field of force. This weakens its orientating influence on neighboring nitrate ions facilitating their rotation. The continued slight decrease in density, if real, we believe due to the pressure exerted by the trapped oxygen in the lattice.

The decrease in density which is observed above about 1 mol per cent decomposition is not sufficient in itself to account for the decrease in G value. However, if the apparent transition which we observe is due to either increased rotation or simply rotation of the nitrate ion group, then it is possible that this could account for the decrease in decomposition yield.

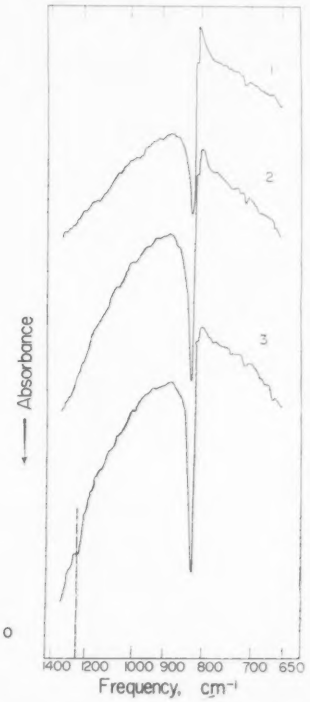

FIG. 5. Infrared spectra of irradiated and non-irradiated KNO_3 determined in KBr pellets. (1) Non-irradiated. (2) Irradiated for a total dose of 16×10^{20} eV/g. (3) Irradiated for a total dose of 86×10^{20} eV/g.

The mechanism for the decomposition of potassium nitrate and other nitrates we believe is essentially molecular, i.e. the oxygen and the nitrite are produced simultaneously without going through any reactive intermediates such as free radicals or free radical ions. Support for a molecular mechanism is found in the heats of solution and magnetic susceptibility measurements both of which indicate that oxygen is present in the lattice as molecules, not as atoms. Furthermore the results of CUNNINGHAM and HEAL show that there is no intensity dependence on nitrite yield and that the rate of decomposition of potassium nitrate at

* It is also possible that this could occur at displacement sites. Displacement sites in ionic crystals are undoubtedly few, but it has been clearly established that atom displacement occurs both in alloys and semiconductors under bombardment with cobalt 60 gamma rays.

constant dose is dependent only on the amount of nitrate present.

REFERENCES

1. HENNIG G., LEES R. and MATHESON M. S., *J. Chem. Phys.* **21,** 664 (1953).
2. CUNNINGHAM J. and HEAL H. G., *Trans. Faraday Soc.* **54,** 1335–69 (1958).
3. HOCHANADEL C. J. and DAVIS T. W., *J. Chem. Phys.* **27,** 333 (1957).
4. JOHNSON E. R., *J. Amer. Chem. Soc.* **80,** 4460 (1958).
5. LA MAR L. E., U.S. Atomic Energy Report, AECU-3047 (1955).
6. JOHNSON E. R., BRUCE R. A., STEINMANN R. and CAGNATI V., *Nucleonics* 14, No. 11, 119 (1956).
7. SHINN M. B., *Indstr. Engng. Chem.* Analytic Ed. **13,** 33 (1941).
8. WHITE W. P., *The Modern Calorimeter,* Chem. Catalog Co. N.Y. (1928).
9. GUCKER F. T. Jr., PICKARD H. B. and PLANCK R. W., *J. Amer. Chem. Soc.* **61,** 463 (1939).
10. WEISSBERGER A., *Physical Methods of Organic Chemistry,* Vol. I, Chapt. XIV Interscience, New York (1949).
11. *Selected Values of Chemical Thermodynamics Properties.* Circular of the National Bureau of Standards 500 U.S. Dept. of Commerce.
12. STAVELEY L. A. K., *Quarterly Reviews* **3,** 65 (1949).
13. KRACEK F. C., *J. Amer. Chem. Soc.* **53,** 2609 (1931).
14. KRACEK F. C., POSNJAK E. and HENDRICKS S. B., *J. Amer. Chem. Soc.* **53,** 3339 (1931).
15. AUSTIN J. B. and PIERCE R. H. H., *J. Amer. Chem. Soc.* **55,** 661 (1933).
16. BECK C., *J. Chem. Phys.* **12,** 71 (1944).

J. Phys. Chem. Solids Pergamon Press 1960. Vol. 15. pp. 225–233. Printed in Great Britain.

FERROELECTRIC DOMAIN DELINEATION IN TRIGLYCINE SULPHATE AND DOMAIN ARRAYS PRODUCED BY THERMAL SHOCKS

A. G. CHYNOWETH and W. L. FELDMANN

Bell Telephone Laboratories, Inc., Murray Hill, New Jersey

(*Received* 28 *December* 1959)

VOL. 15 1960

Abstract—The ferroelectric domains in single crystals of triglycine sulfate can be delineated with high resolution simply by etching the crystal in a water bath for a few seconds at room temperature. Both the ends and sides of domains can be revealed where they intersect planes perpendicular and parallel to the ferroelectric axis, respectively. With these techniques many totally internal cigar-shaped domains, with their long axes parallel to the ferroelectric axis, have been discovered.

It has also been shown that a very regular array of domains is introduced into the crystal when it is subjected to a thermal shock. A cooling shock gives rise to many small spike-shaped nuclei extending into the crystal from the surfaces. A warming shock results in a regular array of considerably larger domains. It seems that in both cases, the driving force that creates these new domains is the field arising from the polarization discontinuities which, in turn, are caused by the transient thermal gradients set up in the crystal when subjected to the thermal shock. The shapes of the spike-shaped domains introduced by the cooling shock agree with those predicted by a, necessarily, idealized model.

PREFACE

THE WORK described in this paper falls naturally into two parts. The first part describes new etching techniques which have been developed for delineating domain configurations in the ferroelectric crystal, triglycine sulfate, and the results of the new etching technique are compared with methods used previously for revealing domain structures. During this work, intriguing fine detail was frequently observed in the domain patterns. The study of this fine detail forms the subject of the second part of the paper where it is concluded that the fine domain detail is generated when the crystal is subjected to a thermal shock.

PART I. DOMAIN DELINEATION TECHNIQUES–1

Introduction

HOOTON and MERZ[1] showed that ferroelectric domains in barium titanate could be revealed simply by etching the crystal with acid. These techniques have been exploited by many authors, and particularly by MILLER[2], in studies of the polarization reversal process. Recently, PEARSON and FELDMANN[3] described techniques for delineating domains that were applicable to various ferroelectrics, including triglycine sulfate. One method, somewhat analogous to Bitter patterns, was to place a colloidal suspension of a suitable powder on the surface of the crystal; the powder settles out preferentially along the domain walls and on domain ends of appropriate sign. This technique is admirable for studying large domains but it does not have the resolving power of good etching techniques. Another technique, which was shown to be useful for triglycine sulfate and had somewhat greater resolving power than the powder method, was to rub the crystal surface briefly on wet cloth (twill jean was usually used) and then to dry it by rubbing it on a dry portion of the same cloth. However, while one sign of domain end etches fairly smoothly, domain ends of the opposite sign develop a highly pebbled surface thereby making it difficult to discern fine structure within these domains. This objection has now been overcome for triglycine sulfate by using etch baths.

For convenience, the two etching techniques will be referred to as the rub technique (described above) and the dip technique. For the dip technique to reveal a maximum of detail, it was usually preferable to polish the cleavage slice defined by the (010) cleavage planes—the polishing method has been described previously.[4] The etch pattern is then brought out simply by immersing the crystal in water (at any desired temperature) for a sufficient period. At the end of the etching period the crystal is quickly transferred to a bath of ethyl alcohol, rinsed and dried.

Unfortunately, the water dip technique is extravagant with material because of the high solubility of triglycine sulfate in water. Fig. 1 shows the etching rate on an (010) face as a function of temperature. Thus the dip technique with water is not suitable where many successive domain patterns are required, as in polarization reversal studies, for example.

Unless noted otherwise, the thicknesses of the crystals used for the etch studies ranged between 0·5 and 3·0 mm, the actual thickness being not too critical for most purposes.

Results

(1) *Etch patterns produced by rub technique*

Typical etch patterns produced by the rub method are shown for the top and bottom faces of a crystal slice in Fig. 2. Clearly the major domains, generally lenticular in shape, correlate in the two photographs showing that the domains run right through the crystal thickness. The pebbled appearance of one sign of domain end is also apparent. On closer examination it always appears that the pebbled areas consist of large numbers of "pebbles", roughly equi-spaced, and each with a flat top which is lenticular in shape with its major axis running parallel to those of the larger domains. (This direction lies in or close to the optic plane.[4]) Fine structure can also be discerned in the smooth domain areas though here it appears as an array of very fine dots, again regularly spaced.

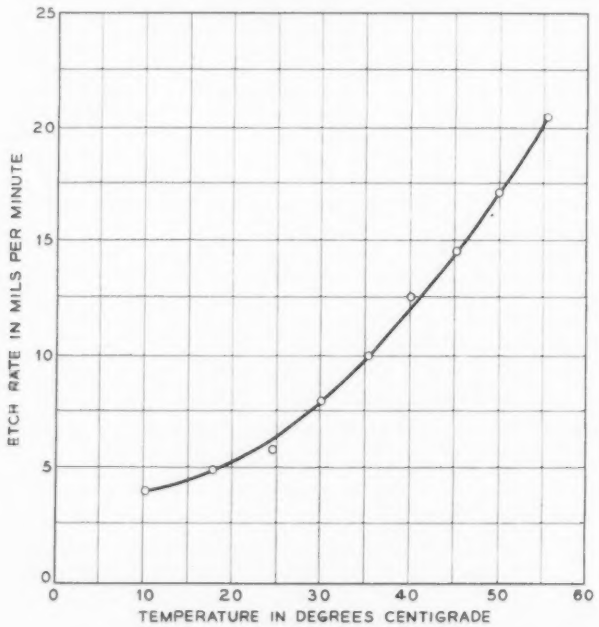

FIG. 1. The etching rate (for one surface) of triglycine sulfate in water as a function of temperature.

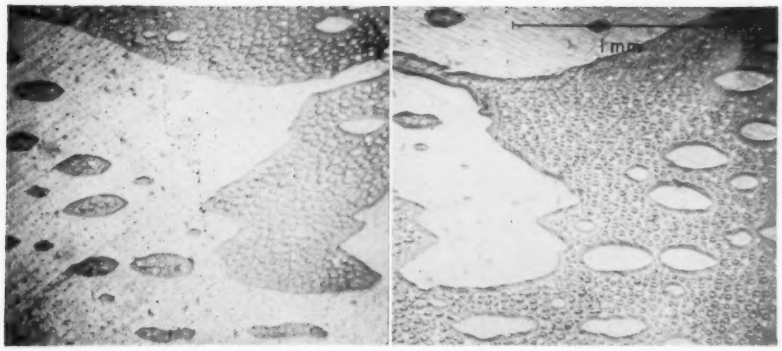

(a) (b)

FIG. 2. Opposite matching surfaces of a crystal that has been rub etched to bring out the domain structure.

VOL.
15
1960

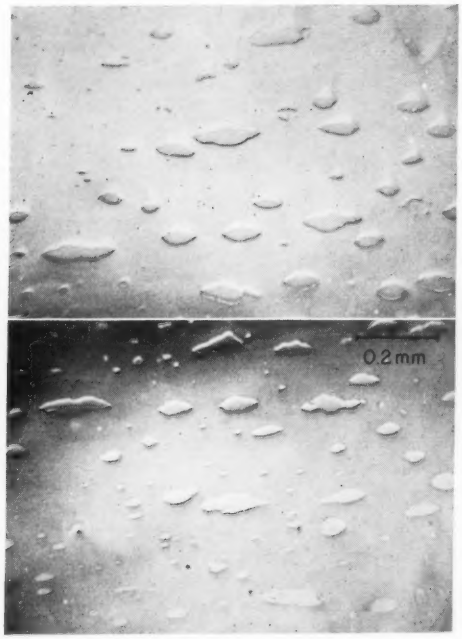

(a)

(b)

FIG. 3. Opposite matching surfaces of a crystal that has been dip etched to bring out the domain structure.

[*facing p.* 226

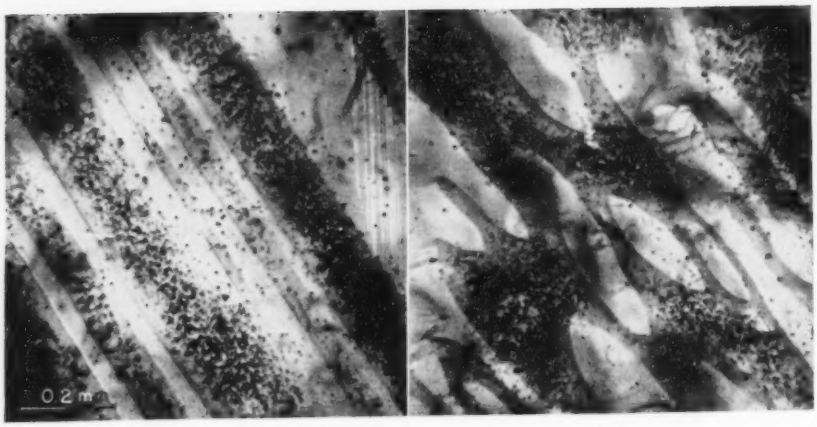

(a) (b)

FIG. 4. Showing two examples of the correspondence between dip etch domain patterns and powder deposition patterns.

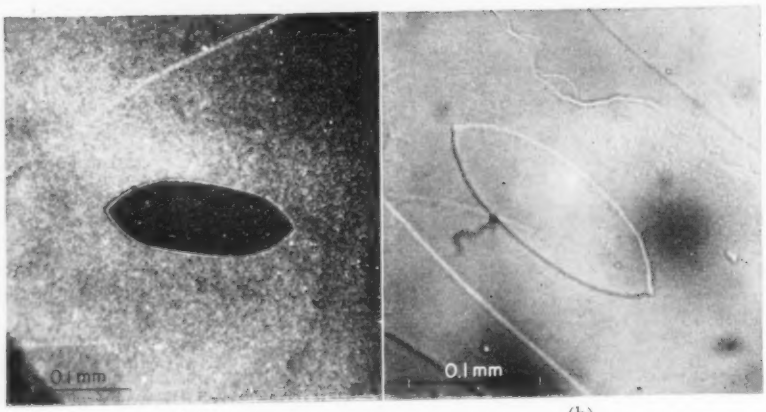

(a) (b)

FIG. 5. Two examples showing the high resolution attainable with the dip etch.

VOL.
15
1960

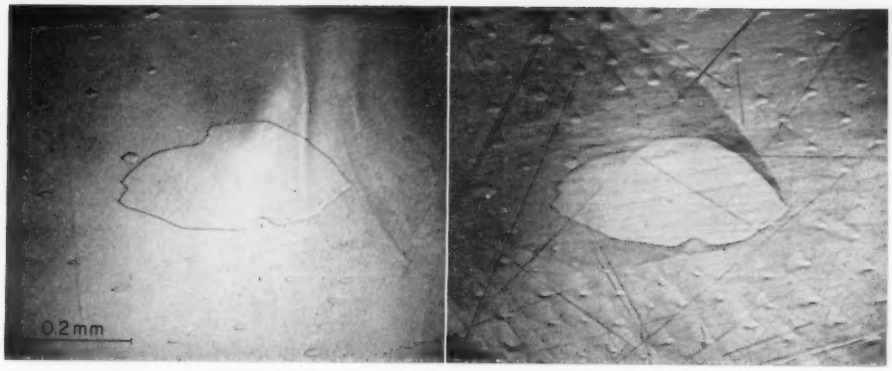

(a) (b)

FIG. 6. Comparison of (a) dip etch and (b) rub etch patterns on the same area of a crystal. The rub etch pattern was obtained after the dip etch pattern.

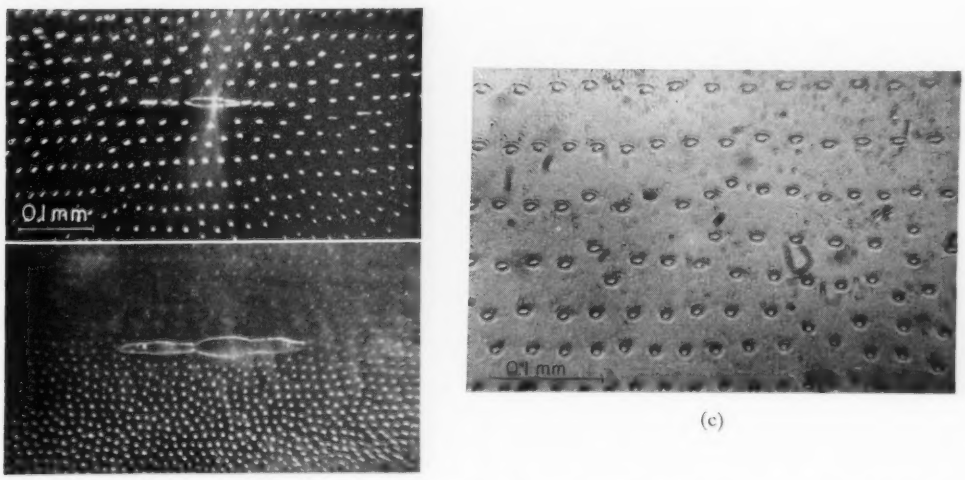

(a)

(b)

(c)

FIG. 7. Fine detail in the domain structure that results when the crystal is subjected to a cooling shock, as revealed by the dip etch. Figs. (a) and (b) are of opposite faces of a crystal while (c) shows a typical array at higher magnification.

(a)

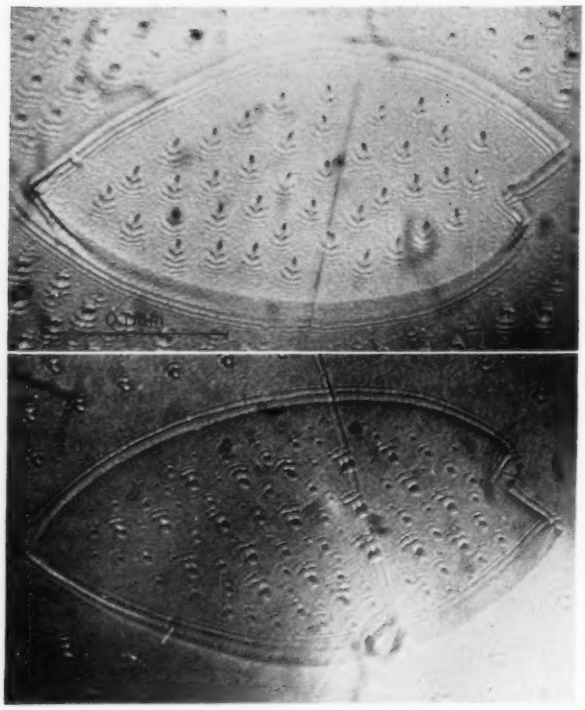

(b)

FIG. 8. Domain structure on opposite faces of a crystal showing the matching major domain outlines and the lack of correlation of the fine detail on the two faces.

VOL.
15
1960

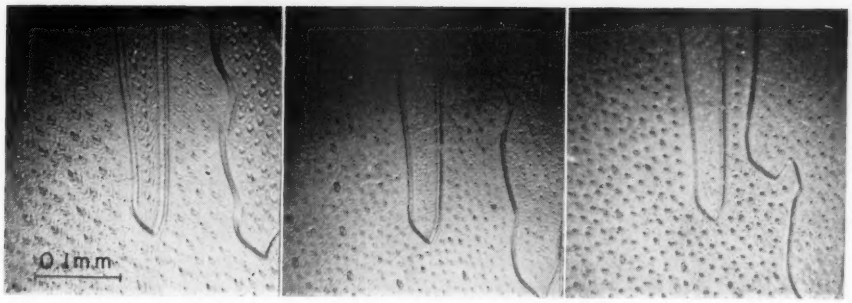

(a) (b) (c)

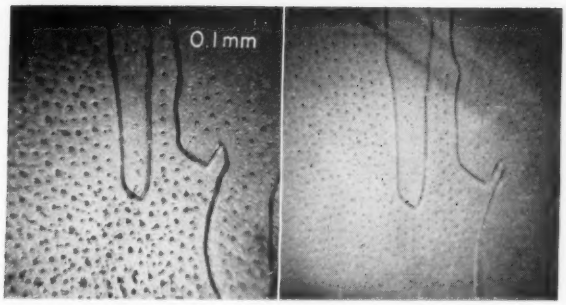

(d) (e)

FIG. 9. Fine detail dip etch patterns on the same face of a crystal after repeated dip etches. During each dip, the crystal thickness was reduced by about $2{\cdot}5 \times 10^{-2}$ cm. The figures show that the density of the fine detail does not change noticeably with crystal thickness or etching time.

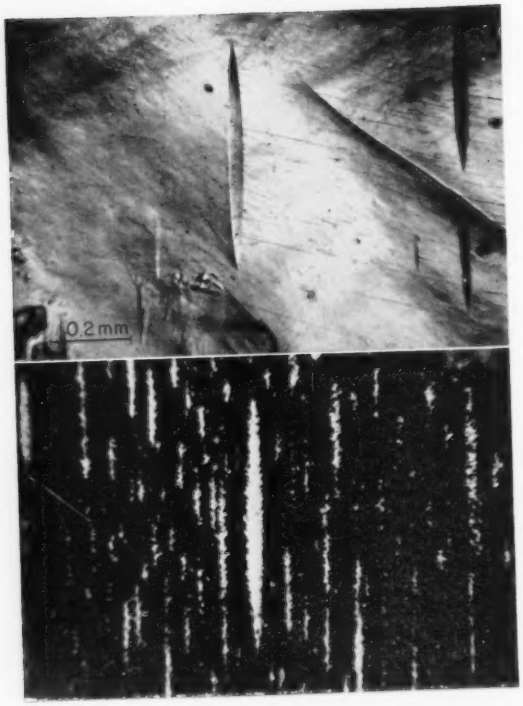

FIG. 10. Domains revealed on a side of the crystal parallel to the ferroelectric axis (a) by the dip etch method and (b) by the powder deposition method. Note that each of the domains in (a) correlates with a domain in (b) but there are also many others in (b) which do not show in (a). This demonstrates the ability of the powder technique to reveal domains submerged below the crystal surface.

VOL
15
196

VOL.
15
1960

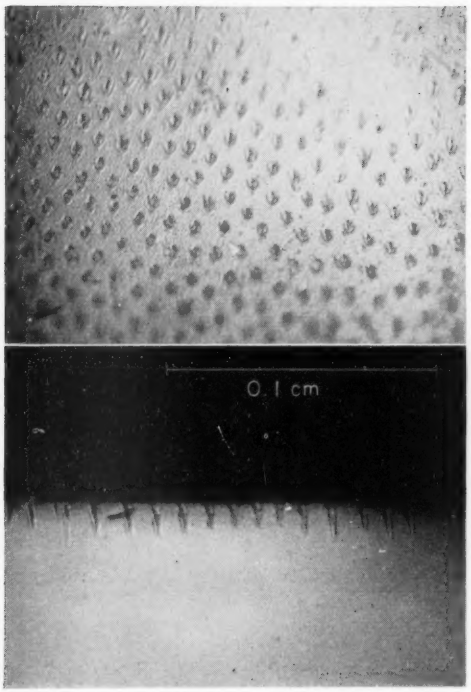

FIG. 11. Fine detail revealed by the dip etch method on (a) the face perpendicular and (b) the face parallel to the ferroelectric axis. These photographs show that the fine dots in (a) represent the bases of small spike-shaped domains.

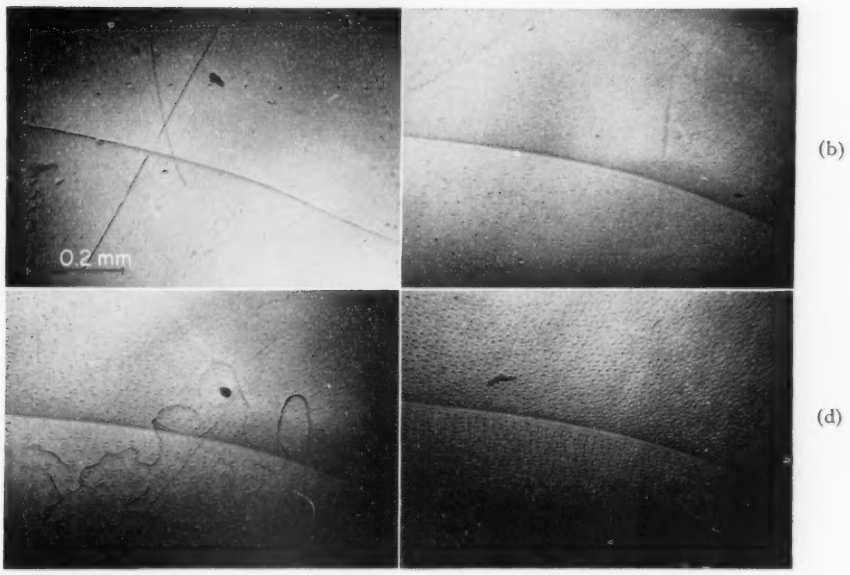

FIG. 12. Fine dot patterns revealed after transferring a crystal to an alcohol bath at 23°C from water baths at (a) 25°C; (b) 30°C; (c) 35°C; (d) 40°C.

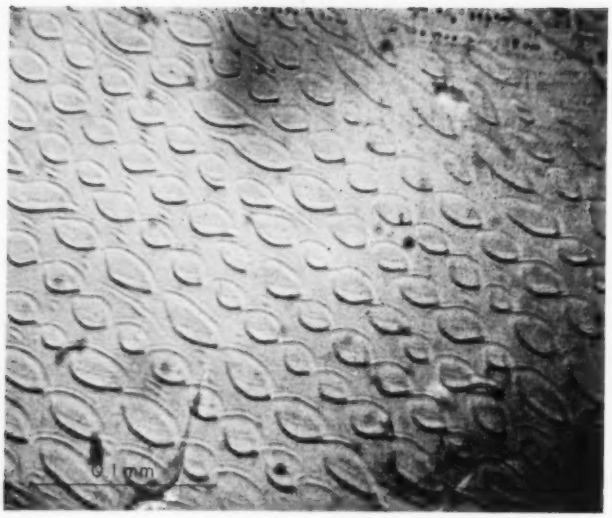

FIG. 13. A typical domain array as revealed by transferring a crystal from a water bath at 23°C to an alcohol bath at 36°C.

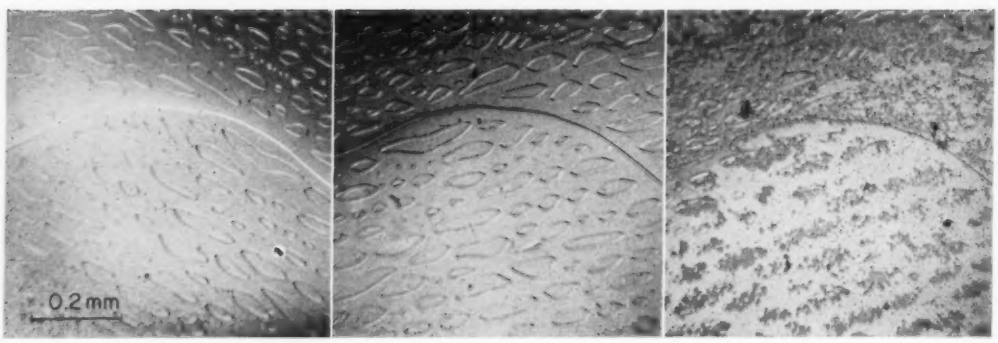

(a) (b) (c)

FIG. 14. Figs. (a) and (b) show matching opposite faces of a crystal that has been subjected to a warming shock. Fig. (c) shows a superposition of a powder pattern on that of (b).

From such photographs it was established that the average number of dots per unit unpebbled area was equal to the average number of pebbles (or miniature lenticular shapes—lentils) per unit pebbled area.

With thin crystals (e.g. about 0·5 mm thick) rub etched on both faces it was sometimes possible to establish a one-to-one correlation between the dot pattern on one face and the pebble pattern on the opposite face. This was done simply by focussing the microscope on the two faces in turn or by using an intermediate focus where the two patterns appeared superimposed. It seems certain that the dots and lentils represent domains which are long in the direction of the ferroelectric axis and narrow in directions at right angles to it. These domains have been observed to extend through crystals of up to a millimeter in thickness. In thick crystals, however, there is frequently a lack of correlation showing that the domains can terminate within the crystal interior.

VOL. 15 1960

(2) *Etch patterns produced by dip techniques*

Dip etch patterns, such as those shown in Figs. 3(a) and 3(b) for opposite crystal faces, are free from the disadvantage of a pebbled surface and it is clear that the domains are brought out with good resolution. Again there is a good correlation between the two photographs for the larger domains showing that they extend right through the crystal. However, from further comparisons between Figs. 3(a) and 3(b) as well as between Figs. 2(a) and 2(b), many of the smaller domains present in one photograph do not have their counterpart in the companion photograph and furthermore, even the larger domains which do correlate have slightly different sizes. Thus, the domain walls do not necessarily lie parallel to the ferroelectric axis and it is necessary to conclude that the smaller domains terminate within the crystal slice in the form of spikes.

Both the rub and dip patterns can be compared with the domain pattern revealed using the powder deposition technique. Good correlation was found for the former by PEARSON and FELDMANN[3] and the same is true also for the dip technique, as shown in Fig. 4. Here, after having been dip-etched, the crystal was lightly powdered (so as not to hide the etch pattern) and it is clear that the powder has settled virtually completely on one sign of domain end, thus confirming the correspondence between dip etch patterns and the domain configurations.

Some idea of the resolution possible with the dip technique is given by Figs. 5(a) and (b), these being photographs of typical, undeformed, isolated domains.

(3) *Comparison between rub and dip etch patterns*

A crystal was first dip etched and a particular domain selected for comparison with a rub etch. The dip etch pattern, Fig. 6(a), shows this domain, which is somewhat irregular in shape, surrounded by a fairly uniform array of small lentils. The pattern obtained subsequently with the rub etch, shown in Fig. 6(b), shows the same domain reproduced exactly as with the dip technique, again establishing the validity of these etches for showing up gross domain features. However, while the major domain is again surrounded by a more or less regular array of small lentils, the density of this array is somewhat greater than with the dip etch. Evidence will be given in Part II of this paper which suggests that this difference results from different amounts of thermal shock received by the crystal in the two etch methods.

Conclusions to Part I

It has been shown that etching triglycine sulfate crystals in a water bath at room temperature is a satisfactory way of revealing domain structures with high resolution for *both* signs of domain end. The technique suffers from the disadvantage, however, that the water usually dissolves a considerable amount of material, thereby making the technique less desirable than others when a series of domain delineations is needed on the same crystal (as in switching studies, for example).

PART II. DOMAIN ARRAYS CAUSED BY THERMAL SHOCK—II

(1) *Fine detail arrays in dip etch patterns*

As mentioned above, when using either the rub etch or the dip etch method it is frequently found that the whole crystal surface is covered by an array of fine dots (lentils), either etch pits or hillocks. Figs. 7(a) to 7(c) show typical examples of these patterns and the tendency for these etch dots to form into a regular array is very striking. It will be noted that in the crystal shown in Fig. 7, both

faces of the crystal show dot arrays but of somewhat different densities, showing that if the dots represent the ends of long thin domains, these domains can terminate within the crystal. (Also, note the different sizes of the corresponding larger domains on the two surfaces.) It was usual, however, for the dot densities to be comparable on the two faces.

In particularly good etchings the dots usually appear as very small lentils [Fig. 7(c)], again with their major axes aligned parallel to those of large lenticular domains. Also, the small lentils tend to form chains lying along this same direction. More often, however, the dots do not have a distinct lenticular shape, but appear as small multi-wrinkled areas. Typical examples of these are shown in Figs. 8(a) and (b). A clue to the cause of these indistinct dots is given by the wall of the major domain—it appears as if the domain jerked its position during etching at least seven times, thus giving rise to a series of slightly displaced outlines. A series of small sideways jerks of the whole domain structure in unison, both the dots and domains, could give rise also to the observed wrinkles around the dots. Such jerking of the domain structure as envisaged here is conceivable if the etching process serves to relieve stresses within the crystal, for example.

Figure 8 also show that the dots occur in regions of either polarization but again there is not an exact correlation between the top and bottom faces. Also, though not too apparent in the figures, the dots appear as hillocks in one sign of domain and as pits in the other sign of domain. This is consistent with the view that the dots represent the ends of long, thin, spike-shaped domains. It can also be seen that in the immediate vicinity of a major domain wall there is a relative dearth of dots.

(2) *Dot arrays vs. etching time*

Figures 9(a) to 9(e) show several etch patterns of the same area of a crystal, all the etches having been carried out at the same temperature, 35°C. Each etch period between the photographs was about 1 minute, each etch thereby reducing the total crystal thickness by about $2{\cdot}5 \times 10^{-2}$ cm. By counting, it was established that the dot density remained constant to within ± 10 per cent; thus the dot density is essentially independent of the etching time and the crystal thickness, at least, for thicknesses greater than about 5×10^{-2} cm. Slight changes in the outlines of the major domains again prove that the domain walls have appreciable slopes.

Fig. 9(b) is unusual in that it shows two grades of fine detail. In addition to the background dot lattice, a "superlattice" of intermediate size lentils can be discerned.

(3) *Etch patterns on sides of crystal*

That the etch dots on the face perpendicular to the ferroelectric axis represent spike shaped regions was verified by etching a side of the crystal that was roughly parallel to the ferroelectric axis. (That domains can be revealed in this way is a surprising fact since the polarization for either sign of domain is supposedly parallel to the surface. It suggests that the atomic configurations in at least some planes parallel to the ferroelectric axis depend on the direction of the polarization). Dip-etching the side of the crystal reveals both major domains running right through the crystal and domains which are completely internal. The latter appear as long, thin, cigar-shaped domains, pointed at both ends, lying along the ferroelectric axis and are, no doubt, lenticular in cross-section. Fig. 10(a) shows some typical internal domains while Fig. 10(b) shows their delineation using the powder deposition technique. The latter also reveals many more similar domains which are, presumably, slightly below the crystal surface. The fields surrounding these submerged domains give rise to the powder patterns whereas it seems necessary that the domain should intersect the surface if it is to be revealed by etching. It should be noted also that the crystal face used for Figs. 10(a) and 10(b) must have been very close to parallel with the ferroelectric axis since the domain patterns revealed by both the etch and powder techniques are of the same length.

In addition to the large domains, side-etches also usually reveal small spike-shaped domains of roughly uniform size with their bases lying at the crystal face perpendicular to the ferroelectric axis. Fig. 11 shows a typical spike array as partially revealed on the side of the crystal. (As the sides of the crystal were usually not sufficiently plane and parallel to the ferroelectric axis, it was rarely possible to see the whole length of the spikes simultaneously.) It can be seen that the spikes are very regularly spaced and it was established that the

spacing of the spikes was equal to that of the dots on the major surface. It is therefore concluded that the dots do represent the bases of spike-shaped domains. As will be discussed below, these spikes appear when the crystal is suddenly cooled by taking the crystal from a water bath to a cooler alcohol bath. It was established that the spikes that appeared when the crystal was taken from water at 36°C to alcohol at 23°C had a length-to-radius ratio of 12 ± 4.

(4) *Production of domain arrays by thermal shock*

It was discovered that the density of the dots depended very much on the *temperature difference* between the water bath and the alcohol bath. If the crystal was first allowed to reach thermal equilibrium in the water bath (immersion period $\gtrsim 10$ sec) and then quickly transferred to the alcohol bath for rinsing, very few dots would be visible, no matter what the temperatures of the two baths were as long as they were equal. This was true no matter how long the crystal was kept in the water bath. On the other hand, if the water bath was *warmer* than the alcohol, dots were readily produced. Furthermore, the density of dots increased with the temperature difference. From many such experiments it was established that it was the magnitude of the thermal shock that was operative rather than the absolute temperature of either bath or the time for which the crystal was in it. Figs. 12(a) to 12(e) show typical dot patterns produced on a crystal by various magnitudes of thermal shock. From such photographs it was possible to obtain quantitative data on the dot density versus the thermal shock. (In all this work with cooling shocks, the alcohol bath was kept at room temperature, 23°C.) Such data were relatively reproducible (to within a factor of about 2) not only on the same crystal, but also for different crystals.

It should be emphasized that no dot arrays could be seen while the crystal was still in the water bath. The arrays appeared immediately when the crystal was transferred to the alcohol bath. Yet, alcohol baths alone will not etch a crystal so as to reveal a domain structure, at least for immersion periods of up to a few minutes. It is believed that the domain structure which results from the thermal shock of the transfer between the two baths is revealed because the crystal carries over enough water on its surfaces to perform the etching before the water gets displaced by the alcohol.

Having determined the effect of cooling shocks it was of interest to investigate the effect of heating shocks. When a crystal was transferred from a water bath to a warmer alcohol bath a domain pattern immediately became apparent. But it was a very different pattern from that produced by a cooling shock. Fig. 13 is a typical example of the regular array of domains produced by a warming shock. In their regularity they resemble the dot arrays but there is no sign of any dots present in the patterns produced by a warming shock. Also, any dots initially present in a crystal (from a previous cooling shock) rapidly disappear in the warming shock but there is no obvious correlation between the original dot patterns and the new domain patterns. In particular, it was established that the dots (spikes) do not provide nuclei from which the larger domains grow. Furthermore, the density of the new regular domain arrays was also found to depend on the magnitude of the thermal shock and had no relation to the initial dot density.

Figures 14(a) and 14(b) show the etch patterns on opposite faces of a crystal subjected to a warming shock from water at 23°C to alcohol at 36°C. By superimposing a tracing of one photograph on the other it was found that there was almost 100 per cent correspondence in the etch patterns showing that the domains run right through the crystal. The line curving across the picture represents a domain wall pre-existing in the crystal; the regions on either side of this wall had opposite polarizations initially but it is apparent that in both regions the domain array has appeared in the same way.

The freshly formed domains are stable as they can be subsequently delineated using the powder deposition method, as shown in Fig. 14(c). On the other hand, it was found to be impossible to delineate the dots with the powder method; this negative result could arise if the external fields of the spikes are too weak and the powder lacks sufficient resolving power, or if the spike-shaped domains are unstable and disappear. The latter seems to be the case as no dot arrays persisted when a cold-shocked crystal was re-etched at room temperature.

(5) *Transient studies*

The formation of the domain arrays can be

VOL. 15 1960

observed, though crudely, by the following technique: with the crystal immersed in an alcohol or water bath, its top surface that is being viewed through the microscope is subjected to squirts of warmer or colder water from an eye-dropper. The dot arrays appear suddenly when subjected to a cooling shock. On the other hand, the arrays produced by a warming shock show a growth period; they appear immediately but only as an array of small dots. These dots then expand sideways to the regular dot and domain arrays is caused by the thermal shock received by the crystal in transferring it between different temperature baths. This causes us to examine the effects of rapid changes in the spontaneous polarization brought about by the thermal shock and the following model is proposed to account for the phenomena. (It should be emphasized that no external electric fields were applied to the crystals in any of these experiments.)

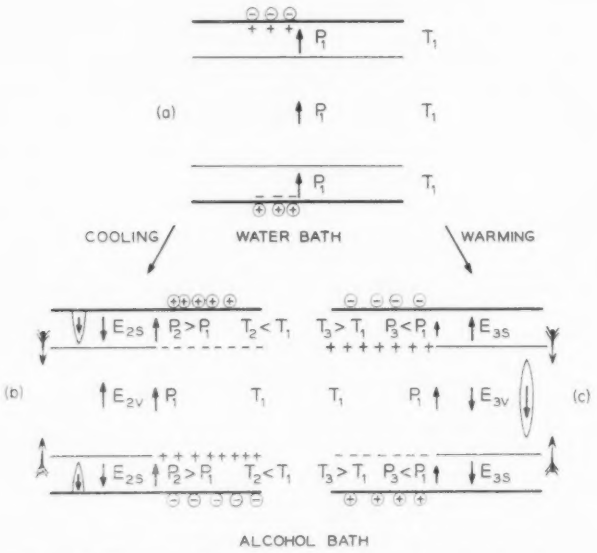

FIG. 15. Diagrams illustrating the proposed mechanism for the production of the spikes in the cooling shock and the large domains in the warming shock.

their maximum inflated sizes after which they shrink back and disappear as the crystal temperature drops back to that of the bath. It is fortuitous that the water etches at a rate sufficient to make visible the expanding domains.

When the side of a crystal is viewed while it is subjected to warming shocks, domains can be seen to nucleate internally and they appear like those in Fig. 11(a). These domains grow rapidly and soon intersect the crystal surfaces where, as they continue to grow, they give rise to the expanding domain patterns.

Discussion of regular dot and domain arrays

It has been well established that the formation of

Consider a crystal initially in thermal equilibrium in a water bath at temperature T_1 and imagine the crystal divided into three regions, as shown in Fig. 15(a); two surface regions of equal thicknesses and the interior. (The purpose in dividing the crystals into these three regions is to make clearer the role of thermal gradients and the surface regions are not to be confused with the ferroelectrically inactive surface layers that are also thought to be present in these crystals.[5]) When the crystal is plunged into a cooler alcohol bath the surface regions of the crystal are the first to attain the bath temperature, T_2. Fig. 15(b) represents the highly idealized situation of sharp boundaries between the regions of different temperature. These

VOL. 15 1960

boundaries will be moving rapidly into the interior of the crystal as indicated by the tailed arrows. Because of the temperature difference across the boundary there will be a discontinuity in the spontaneous polarization. The polarization discontinuities give rise to bound charges which will be compensated to some extent by free charges external to the crystal. These charges give rise to fields E_{2s} and E_{2v} in the surface layers and the interior, respectively. The fields E_{2s} oppose the polarization and so will cause domains to nucleate at the crystal surfaces; it is believed that the spikes are formed in this way. The field E_{2v} is in the same direction as the polarization and so will not give rise to reverse polarized domains.

In the warming shock by a similar argument, the fields in the surface layers will be in the same direction as the polarization but in the interior, the field will oppose the polarization and so can cause the nucleation of internal domains [Fig. 15(c)]. Under the influence of the interior field these domains will tend to grow though it is not obvious why they should grow as far as the surface (as has been shown to be the case). However, other experiments in this laboratory have indicated that such domain growth into the region beyond the range of the driving field can occur.[6]

The model thus provides a qualitative explanation for the production of dots by a cooling shock and the larger domains from a warming shock. It might also be noted that the spikes introduced by a cooling spike are not likely to be stable. When the crystal reaches a new thermal equilibrium their own depolarizing fields will tend to make them collapse.

The above model, while believed to be basically correct, is not susceptible to any sophisticated analysis on account of the numerous uncertainties involved. There will be some cooling of the crystal during its transfer between baths, and it is not very satisfactory to assume an abrupt temperature change at the inwardly moving boundaries. Furthermore, all attempts at predicting the spike density, n, as a function of ΔT require a knowledge of the values of various parameters in the surface layer, such as ϵ, the permittivity, and σ, the wall energy. These quantities will be expected to be highly dependent on the actual (average) temperature of the surface layer at the instant of nucleation.

A comparison can be made, however, between the expected and observed shapes of the spikes. It is reasonable to suppose that the spikes etched on the side of the crystal have a *shape* (length-to-radius ratio) appropriate to the field, E, produced in the surface layer by the shock, ΔT. Their *sizes*, on the other hand, are not necessarily meaningful. They probably represent the spikes at the moment the etchant was used up or removed rather than the minimum or maximum sizes.

The field in the surface region, thickness l, will be given by

$$E = 4\pi(P_1 - P_2)(1 - l/d)/\epsilon_l,$$

where d is the crystal thickness, P_1 and P_2 are the initial and final spontaneous polarizations, corresponding to temperatures T_1 and T_2, respectively, with $P_2 > P_1$, and ϵ_l is the dielectric constant in the b direction in the surface region. A criterion previously used in connection with Barkhausen pulses[7] may be used here; that the depolarizing field within the spike cannot be greater than the driving field. This can be expressed as,

$$\epsilon_l E > 2LP_2,$$

where P_2 is the value of the polarization both inside and outside the spike. (The particular permittivity, ϵ_l, enters as a consequence of the dielectric anisotropy of the crystal. Previously, ϵ_t, the transverse permittivity was used which is in error. Replacing $\epsilon_t = \epsilon_a$ by ϵ_c for the barium titanate work leads to much better agreement between the expected and observed sizes of the Barkhausen pulses.) The depolarizing factor, L, is expressed by,

$$L = 4\pi/m^2(-1 + ln\, 2m),$$

for a prolate spheroid of roughly circular cross-section, and $m = (\epsilon_t/\epsilon_l)^{1/2}\,(l/r)$, where l, r are the length and radius of the spike, respectively. It is a reasonable approximation to put $\epsilon_t = (\epsilon_a \cdot \epsilon_c)^{1/2}$. Using the published values[8] for ϵ_a, ϵ_b, ϵ_c, $(\epsilon_t/\epsilon_l)^{1/2} \simeq 0{\cdot}4$. Experimentally, $l/r = 12 \pm 4$. Thus $m \simeq 5 \pm 2$ for $T_1 = 36°\text{C}$, $T_2 = 23°\text{C}$. From the above relations, we thus have,

$$\Delta P/P_2 > (2/m^2)(-1 + ln\, 2m)$$

or

$$\Delta P/P_2 > 0{\cdot}12 \pm 0{\cdot}05, \text{ approximately,}$$

where

$$\Delta P = P_1 - P_2.$$

At 23°C, $P_2 = 2{\cdot}64\ \mu C\ cm^{-2}$. Thus $\Delta P > 0{\cdot}32 \pm 0{\cdot}13\ \mu C\ cm^{-2}$, which is in satisfactory agreement with the known value for ΔP, approximately $0{\cdot}48\ \mu C\ cm^{-2}$.

The empirical dependence of n on ΔP is shown in Fig. 16 where it is apparent that to within experimental error, the results can be expressed by n varying exponentially with ΔP. (On the other hand, again to within experimental error, n could vary as some power, between 1·0 and 1·5 of ΔP.)

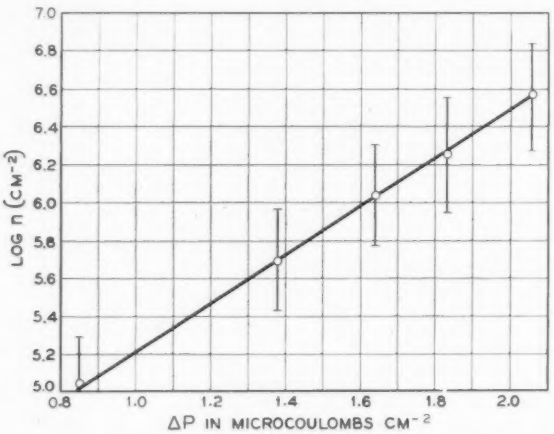

FIG. 16. Density of spikes introduced by a cooling shock (final temperature at 23°C) plotted against the change in the spontaneous polarization.

However, when the idealized model is analyzed on the basis that either charge or energy (principally wall energy or spike-interaction energy) is conserved in the surface layer at the moment the spikes are nucleated, all approaches seem to predict that n varies as $(\Delta P)^3$. The discrepancy possibly arises from the uncertainties mentioned earlier. It should be noted that the problem is not completely analogous to those cases of equilibrium domain arrays in magnetic materials that have been solved[9] since there it is supposed at the outset that the net magnetic moment of the material is zero so as to avoid free poles.

Conclusions to Part II

When ferroelectric crystals are subjected to thermal shocks there is immediately created a temperature boundary which moves inwards from the surfaces. This temperature boundary results in a polarization discontinuity which in turn gives rise to an electric field. In general, cooling shocks result in electric fields that oppose the polarization in the surface regions while the fields resulting from warming shocks oppose the polarization in the interior. The energies of these fields are compensated for by introducing domain structure in the parts of the crystal on which they act. Triglycine sulfate has only one "easy" axis of polarization so that reverse spike-shaped domains are to be expected. On the other hand, thermal shocks applied to crystals with more than one easy axis, such as barium titanate, might be expected to give rise to closure domain structures, by analogy with magnetic materials. The fact that there is only one easy axis in triglycine sulfate is also consistent with the negative results of lateral field experiments—lateral fields of up to $10^4\ V\ cm^{-1}$ fail to produce any noticeable change in the reversible polarization, in contrast to the situation with barium titanate.[10]

The thermal shock experiments show that freshly nucleated domains can be spike-shaped (with lenticular cross-section) in triglycine sulfate and that they can nucleate either at the crystal surfaces or in the interior of the crystal. The regularity of the spacings of these spikes suggests that

nucleation can occur in uniform material and does not require particular types of defect unless they are there in great density. It should be emphasized, however, that these observations on domain nucleation apply strictly to high applied fields ($> 10^4$ V cm^{-1}, arising from the polarization discontinuity) and are not necessarily appropriate for low fields.

It seems that the spikes introduced by cooling shocks are not stable and so cannot be regarded as evidence for residual domain cores. On the other hand, the stable, cigar-shaped domains revealed within the interior of the crystals by side-etchings and powderings perhaps act as domain cores or nuclei during polarization reversal by an applied field, thus obviating the need for specific domain nucleation events. It would be of interest to examine this hypothesis with further experiments.

Finally, it is to be expected that rather analogous domain arrays will result from mechanical shocks through the agency of the piezo-electric effect.

VOL. 15 1960

REFERENCES

1. Hooton J. A. and Merz W. J., *Phys. Rev.* **98,** 409 (1955).
2. Miller R. C., *Phys. Rev.* **111,** 736 (1958); **112,** 755 (1958).
3. Pearson G. L. and Feldman W. L., *J. Phys. Chem. Solids* **9,** 28 (1959).
4. Chynoweth A. G. and Abel J. L., *J. Appl. Phys.* **30,** 1073 (1959).
5. Chynoweth A. G. (unpublished work).
6. Chynoweth A. G. and Feldmann W. L. (unpublished work).
7. Chynoweth A. G., *Phys. Rev.* **110,** 1316 (1958).
8. Hoshino S., Mitsui T., Jona F. and Pepinsky R., *Phys. Rev.* **107,** 1255 (1957).
9. Kittel C., *Rev. Mod. Phys.* **21,** 541 (1949); Goodenough J. B., *Phys. Rev.* **102,** 356 (1956); Fox M. and Tebble R. S., *Proc. Phys. Soc. Lond.* **72,** 765 (1958).
10. Stadler H. L. (private communication); Chynoweth A. G. (unpublished work).

J. Phys. Chem. Solids Pergamon Press 1960. Vol. 15. pp. 234–239. Printed in Great Britain.

ON THE EXISTENCE OF A CRITICAL POINT FOR THE PHASE TRANSITION IN CERIUM*

R. I. BEECROFT* and C. A. SWENSON

Institute for Atomic Research and Department of Physics, Iowa State University, Ames, Iowa

(*Received* 10 *December* 1959)

Abstract—A piston-displacement technique has been used to examine the phase transition in cerium to 20,000 atm and 575°K. The results are in agreement with previous thermal data, and show that the volume change decreases with increasing temperature, extrapolating to zero somewhere near 630°K and 20,000 atm. Above roughly 500°K and 15,000 atm, however, the transition becomes increasingly spread out in pressure at constant temperature, and it becomes quite difficult to assign values to the transition pressures, and the volume changes. Although there are definite indications that the nature of the transition is changing at these pressures and temperatures, the possibility that the transition is merely becoming sluggish cannot be ruled out.

INTRODUCTION

THE PHASE transition in cerium has been the subject of several investigations in recent years,[1–6] the main attraction being the rather large volume effect (nearly 15 per cent in $\Delta V/V_0$) which is associated with the transition. This volume change has been attributed to an alteration in the electronic configuration of the ions[1] (a $4f$ electron moving into the conduction band), an explanation which is made the more plausible by the fact that both phases are face-centered-cubic, and that cerium ions are known to exist chemically in both trivalent and quadrivalent states.[1] In a recent paper, PONYATOVSKII[6] reported results on the temperature and pressure dependence of the cerium transition which were obtained using a thermal arrest (or "differential thermal analysis") technique. These data showed a gradual disappearance of the latent heat of the transition as the temperature was increased. This was in good agreement with qualitative observations by LIKHTER *et al.*[4], that the volume change (as obtained with a piston-displacement method) appeared to decrease with increasing temperature. PONYATOVSKII[6] suggested that his relatively insensitive thermal measurements should be verified by other techniques, and results of piston-displacement measurements which do this are given below.

EXPERIMENTAL DETAILS

The piston-displacement method which was used was identical with that described by HERMAN and SWENSON[5], with certain refinements in detail.[7] The sample itself was used as the pressure transmitter, and, hence, the pressures were only approximately hydrostatic. Briefly, a sample of cerium,‡ roughly 6 mm dia. by 3·5 mm long, was placed in a thick-walled Carboloy (type 55B) cylinder, 0·250 in. i. d. The ends of the cylinder were closed by Kennametal (type K-6) pistons, also 0·250 in. dia., and the resulting assembly was placed in the lower end of a ten ton press which had long stainless steel tension and compression members. This lower end of the press was inserted into a cylindrical furnace, while the upper end of the press, where the force was generated by a Blackhawk hydraulic ram, was maintained at room temperature.

The changes in the volume of the sample with

* Contribution No. 818. This work was performed in the Ames Laboratory of the U.S. Atomic Energy Commission.

† Present Address: Naval Ordnance Laboratory, Corona, California.

‡ The analysis of the cerium which was used is as follows: Ca, 0·06; Ta, 0·1; Si, 0·5; Fe, 0·06; Mg, 0·06; La, 0·05; Pr, ⩽ 0·02; Nd, ⩽ 0·02; Cr, 0·06; Gd, trace; all in per cent.

VOL. 15 1960

pressure were assumed to be directly proportional to the observed variations in length with applied force. These changes in sample length were measured by means of a commercial dial indicator (10^{-4} in. division, 0·020 in. travel) which was at room temperature and which was located physically above the ram. The body of the indicator was supported by two quartz feeler rods which were mounted in contact with the top of the upper piston, while the pin of the dial indicator was attached by similar feeler rods to the base of the lower piston. The oil pressure in the ram (and, hence, the force on the sample) was changed in discrete steps (as low as 200 atm sample pressure) through the direct use of a dead-weight gauge. Friction in various parts of the apparatus was compensated for by taking runs at both increasing and decreasing pressure for a given temperature. The temperature of the sample was measured with a copper–constantan thermocouple which was attached directly to the sample holder. The thermocouple voltage was used to control the sample temperature through the use of a recording potentiometer (100 microvolts full scale) which was attached to the galvanometer terminals of a Rubicon Type B potentiometer, the pointer on the recorder being used to vary the current through the furnace which surrounded the lower end of the press. The maximum temperature fluctuations were of the order of 0·3° peak to peak, while the absolute temperatures were accurate to perhaps 1° at the highest temperatures due to uncertainties in the thermocouple calibration.

The feeler rod holders and pads which supported the pistons were manufactured initially from hardened tool steel, and as a result, two catastrophic failures occurred at temperatures near 300°C due to the softening of the steel. These parts were rebuilt from high speed steel, with no further difficulties on this score. The Carboloy and Kennametal appeared to hold up extremely well under these rather severe (300°C and 20,000 atm) conditions. Extrusion of the sample through the gap between the piston sides and cylinder wall was prevented through the use of triangular steel extrusion rings, 0·030 in. on a side.[7] In the final experiments, these softened after some time at high temperature so that the ring material extruded and caused a large friction. Since our major interest was in the transition itself, and not in a detailed analysis of the compression of the cerium, these experiments were not repeated. In future work at these temperatures and pressures, hardened high-speed steel rings should be used.

EXPERIMENTAL RESULTS

Data were taken on two samples of roughly the same dimensions (0·250 in. dia. by 0·136 in. long). The first sample was lost in an early catastrophe, but data were obtained on it to roughly 505°K. The second sample survived runs at eight different temperatures from room temperature to 575°K and back to room temperature again. Typical results which were obtained for this second sample are given in Fig. 1, where the numbers refer to the order in which the runs were made. These curves have been corrected for friction by taking the mean of the increasing and decreasing pressures for a given displacement. The hysteresis in the transition (e.g. at 402°K and 475°K) may or may not be real, since it appears as excess friction in this pressure region as compared with the parts of the curve where the transition was not found. The transition region was always marked by time effects in the length data, the motion of the dial indicator ceasing only after periods of up to ten minutes after the pressure was increased by a small amount. These effects were not noticed at higher or lower pressures where the dial gauge readings indicated the small changes indicative of the normal compression of the solid.

The data taken at 505°K and 575°K (as well as at 545°K in a run not shown) were strictly reversible and showed no hysteresis, while the asymmetry in the transition in the 475°K isotherm is undoubtedly associated in some way with the extrusion of the anti-extrusion rings. The raw data implied that this extrusion did not become important until just before this (the sixth) run on the second sample.

The curves of Fig. 1 have also been corrected for the compression of the pistons and the feeler rod holders. This correction was obtained at room temperature by measuring the compression of an indium sample of the same dimensions, and making the assumption that Bridgman's data for indium are correct. An additional assumption was made that the elastic modulus of the piston and cylinder material (and, hence, this correction) did not vary with temperature. Finally, an attempt was

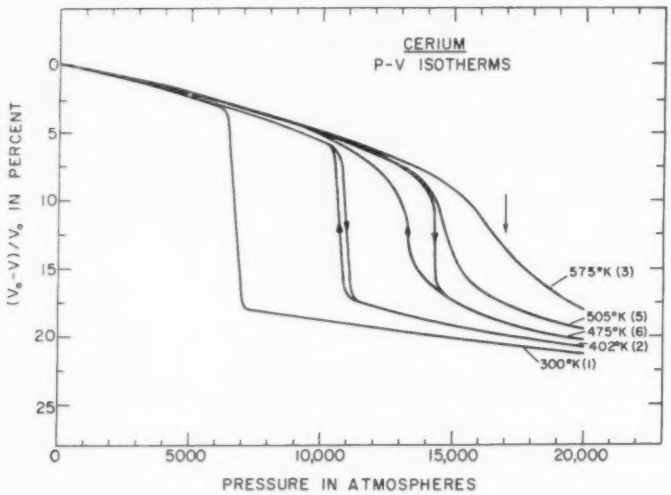

FIG. 1. Several typical pressure–volume isotherms which were obtained for the second cerium sample, corrected for sample holder distortion and friction as described in the text. The thermal expansion at zero pressure was assumed to be very small and effectively zero, so that these curves are equivalent to molar volume vs. pressure curves for various temperatures. The arrow on the 575°K isotherm indicates the pressure which was plotted as the transition pressure for this temperature in Fig. 2. The numbers indicate the order in which the isotherms were obtained, the intervening isotherms not being plotted for the sake of clarity.

made to correct the length of the sample for thermal expansion both from our data and the data of BARSON *et al.*[8] The net correction was so small that to the accuracy of Fig. 1 the thermal expansion at zero pressure in 275 centigrade degrees could be neglected and all the isotherms could be shown as originating from the same point. The method of evaluating these corrections and their relative magnitudes will be discussed in another paper.[7] The relatively high thermal expansion at high pressures (about 10^{-4}/°C) is believed to be real and at least an order of magnitude greater than at zero pressure.[8]

The transition data for both samples are collected in Fig. 2, where the transition pressures and the volume changes are plotted as functions of temperature. The data at 300°K represent the mean of five different determinations on the two samples. The average transition pressure is 6750 ($\pm$100) atm and the volume change 14·1 ($\pm$ ·2) per cent of the original volume. A transition pressure was estimated (see Fig. 1) as the point of inflection in the 575°K and 545°K (not shown) isotherms where the transition was well smeared out. The 475°K and 505°K isotherms (Fig. 1) illustrate the increasing difficulties in the determination of volume changes as the temperature is increased. Nevertheless, the variations with temperature of the volume changes and the transition pressures are quite definite.

DISCUSSION

Some qualitative observations about the equation of state, which supplement similar observations by BRIDGMAN[2], can be made from an inspection of Fig. 1. The rather large difference in the compressibility between the two phases which is found at room temperature ($k_T = -(\partial \ln V/\partial P)_T$ being roughly 5×10^{-6} for the low pressure cubic phase and $3{\cdot}5 \times 10^{-6}$ for the high pressure condensed-cubic phase) seems to become less pronounced with increase of temperature, while the increase of compressibility with pressure for the low pressure phase and the opposite behavior for

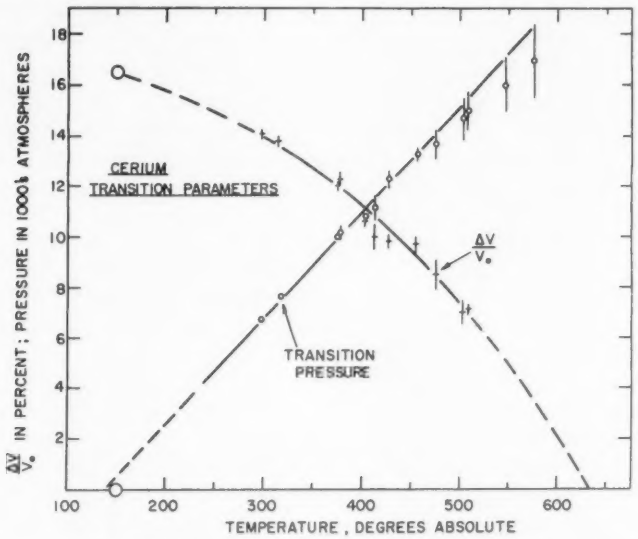

FIG. 2. The transition parameters for the cerium phase transition. The open circle at zero pressure and 150°K represents a mean transition temperature as observed in various zero pressure experiments,[5] while the similar circle at the same temperature on the $\Delta V/V_0$ curve represents the difference in the molar volumes as determined in X-ray measurements.[1,9]

the high pressure phase are apparent at all temperatures. Also, the thermal expansion at 20,000 atm is a factor of ten or more greater than at zero pressure, a behavior which is anomalous when compared with that of other metals. No attempt will be made to discuss these effects quantitatively, primarily because of uncertainties in both the method and the temperature dependence of the corrections which were applied to the data.

The transition parameters (P and $\Delta V/V_0$) which can be deduced from data similar to those given in Fig. 1 depend only slightly on the corrections which have been applied, and the estimated errors are illustrated by the error bars in Fig. 2. The current data (Fig. 2) and earlier work are in quantitative agreement as regards the temperature dependence of the transition pressure[4,5,6], while there is only qualitative agreement in the magnitudes of the $\Delta V/V_0$ data.[2,4,5,6] One puzzling factor involves the absence of appreciable hysteresis in our room temperature transitions, while HERMAN and SWENSON[5], using this same method and cerium from the same source, observed considerable hysteresis. The average transition pressures (corresponding to increasing and decreasing pressures) given in Ref. (5) agree well with Fig. 2, however, The scatter (of up to 20 per cent) which was found in the $\Delta V/V_0$ data in this earlier work was also in contrast with the very reproducible results (a few per cent) observed here. The various papers which have been published concerning cerium contain many such discrepancies, with the worst involving the appearance at times of the room temperature transition at 13,000 atm,[1,2] 6000 atm above the pressure at which it now seems to occur.

The slope of the transition line ($41{\cdot}8 \pm 1{\cdot}8$ atm/deg) and the volume change at the room temperature transition ($14{\cdot}1 \pm 0{\cdot}2$ per cent) can be combined with the molar volume (20·7 cm^3/mol) to give a latent heat of transition at room temperature of 880 (± 50) cal/mol, in good agreement with the thermal analysis value of 880 cal/mol.[3] The calculated latent heat remains roughly constant to 500°K, decreasing very slightly to 840 (± 70) cal/mol at this temperature. The observations of PONYATOVSKII[6] that the latent heat of transition decreases in the region of these temperatures

undoubtedly was associated with the smearing out of the transition. The apparent concave-downwards shape of the transition pressure curve (Fig. 2) would seem to be only slightly outside experimental error, and to depend on the definition of the transition pressure.

The major purpose of these experiments was to investigate PONYATOVSKII's conclusions that the equilibrium line for this cerium transition terminates in a critical point, in analogy with the behavior of the liquid–vapor line. Such a critical point has not been observed for a solid–solid or a fluid–solid transition, and the existence of such a phenomenon is generally believed to be highly improbable, primarily because the widely different symmetries of the states involved precludes their properties gradually approaching each other. Cerium would seem to offer a possibility for an exception, however, since both phases are face-centered-cubic, and differ only in ionic radii.[1,9]

From a purely experimental viewpoint, the data which are plotted in Figs. 1 and 2 do not allow a clear-cut decision to be made as to whether or not a critical point exists. The gradual smearing out of the transition above 500°K (Fig. 1) makes it impossible to speak of a phase transition in the ordinary sense in this region. Our experiments were limited by the available pressures, and even at our highest temperature (575°K), the transition did not appear to be complete at 20,000 atm. With the basic limitation being due to the pressure, no attempt was made to work at higher temperatures, desirable though this might have been.

One can attempt to give a qualitative explanation of the behavior of cerium along the transition line as follows. The cerium ions in the normal (f.c.c.) metal are believed to be trivalent, and to contain a $4f$ electron. The transition to the condensed lattice (also f.c.c.) has been postulated as being due to the formation of a quadrivalent ion through the loss of the $4f$ electron to a $5d$ orbital, or, more precisely, to the valence band.[1] Such a change in the ion would be expected to result in a smaller ionic radius (as is observed), both due to the decreased shielding of the nuclear charge upon the loss of a core ($4f$) electron, and the increased bonding caused by the addition of an electron to the valence band. In addition, investigations at zero pressure on alloys of cerium and other metals (in particular with thorium)[10,11] have shown that the apparent size of the cerium ion depends strongly on its environment. The thorium alloy experiments,[10] in particular, indicated a gradual increase in cerium ion size with increased cerium concentration, implying that a smooth variation in ion size is possible. For a given thorium concentration, the ionic size of the cerium was found to be also a function of temperature. The interpretation was given that the wave function for one of the cerium electrons contains a mixture of $4f$ and $5d$ character, with the degree of mixing being quite sensitive to both temperature and composition. The relative amounts of the $4f$ and $5d$ contributions were assumed to be decisive in determining the size of the ion, and, hence the density of the alloy.[10]

The behavior of the transition in pure cerium also may be interpreted in these terms. The wave function for the cerium ions in the metal may be considered as containing varying degrees of $4f$ character, the precise amount depending rather strongly on the temperature and pressure. Thus, figuratively speaking, one may consider that a smaller fraction of a $4f$ electron is associated with each ion in the condensed-cubic phase than in the normal cubic phase. As the temperature is increased along the equilibrium line, the degrees of $4f$ character in the wave functions of the two states would appear to approach each other, with the two phases becoming identical above 500°K. It has been suggested that even after the two phases become identical, the amount of $4f$ character which is associated with the wave function of the cerium ion may be a strong function of pressure and temperature, and that this is what is observed above 500°K, the true critical point being near this temperature.[12] In this case, the influence of the transition on the equation of state would be apparent along the extrapolated transition line well beyond the critical point. Such an effect is observed in the behavior of the heat capacity at constant pressure of argon above the critical point.[13] One cannot rule out the possibility that the smearing of the transition above 500°K is merely due to the need for subcooling in order to make the transition take place, although the reversible nature of the experimental isotherms makes this seem unlikely.

These experiments offer no clue as to the nature of the high temperature-high pressure state of

cerium; that is, as to whether or not the wave functions of the ions have an appreciable amount of 4*f* character. Magnetic susceptibility or, possibly, electrical resistivity measurements, would be necessary to obtain this information. The pressures (up to 25,000 atm) and temperatures (700°K) involved would seem to offer some difficulty in the carrying out of these measurements.

Acknowledgements—The authors are indebted to Dr. F. H. SPEDDING and Dr. A. H. DAANE for supplying the cerium which was used in these experiments. They also wish to express their appreciation to Mr. J. R. PACKARD who took and analyzed much of the data on the second cerium sample. Ref. (6) was first called to our attention by Dr. K. GSCHNEIDNER, and the authors appreciate a conversation with him in which some of the basic ideas expressed in this paper were discussed. We are also indebted to Dr. B. BERNSTEIN, Dr. S. LEGVOLD and Dr. R. E. RUNDLE for stimulating discussions.

VOL. 15 1960

REFERENCES

1. LAWSON A. W. and TANG T. Y., *Phys. Rev.* **76,** 301 (1949).
2. BRIDGMAN P. W., *Proc. Amer. Acad. Arts Sci.* **79,** 149 (1951); **81,** 165 (1952).
3. GONIKBERG M. G., SHAKOVSKII G. P. and BUTUZOV V. P., *Zh. fiz. khim.* **3,** 350 (1957).
   This paper is available in English translation from Office of Technical Services, Department of Commerce, Washington 25, D.C.
4. LIKHTER A. I., RYABININ YU. N. and VERESHCHAGIN L. F., *Zh. eksp. teor. fiz.* **33,** 610 (1957); *Soviet Physics, JETP* **6,** 469 (1958).
5. HERMAN R. and SWENSON C. A., *J. Chem. Phys.* **29,** 398 (1958).
6. PONYATOVSKII E., *Dokl. Akad. Nauk SSSR* **120,** 1021 (1958); *Soviet Physics, Doklady* **3,** 498 (1958).
7. BEECROFT R. I. and SWENSON C. A., to be published.
8. BARSON F., LEGVOLD S. and SPEDDING F. H., *Phys. Rev.* **105,** 418 (1957).
9. SCHUCH A. F. and STURDIVANT J. H., *J. Chem. Phys.* **18,** 145 (1950).
10. BATES L. F. and NEWMANN M. H., *Proc. Phys. Soc., Lond.* **72,** 345 (1958).
11. WERNICK J. H. and GELLER S., *Acta Cryst., Camb.* **12,** 662 (1959).
12. RUNDLE R. E., private communication.
13. JONES G. O. and WALKER P. A., *Proc. Phys. Soc., Lond.* B **69,** 1348 (1956).

J. Phys. Chem. Solids Pergamon Press 1960. Vol. 15. pp. 240–248. Printed in Great Britain.

NUCLEAR RESONANCE STUDY OF ELECTRONIC MAGNETISM IN COPPER–NICKEL*

D. L. WEINBERG† and N. BLOEMBERGEN

Gordon McKay Laboratory, Harvard University, Cambridge, Massachusetts

(*Received* 7 *August* 1959)

Abstract—Alloying with 27, 38 or 43 per cent nickel is found to produce extreme broadening and asymmetry of the NMR of copper. Almost every observable copper nucleus appears to undergo a decrease in magnetic field. The width between derivative peaks is increased by as much as twelve times. It is satisfactorily proportional to or independent of applied field, according as electronic paramagnetism (in the 27 per cent alloy) or weak ferromagnetism is expected to be involved, but the central portion of the line expands in proportion to the field. The concentration dependences are much slower than that of the macroscopic magnetization.

Isotropic indirect exchange coupling between the copper nuclei and the time average magnetic moments of the nickel atoms, and inhomogeneity of the Knight shift account for the measurements approximately. It is necessary to include large contributions from copper nuclei in noncubic environments. The field and concentration dependences are interpreted in terms of inhomogeneous electronic magnetism in the ferromagnetic alloys.

The nickel paramagnetism cannot be identified in alloys of up to 15 per cent nickel because of quadrupole effects.

1. INTRODUCTION

ELECTRONIC magnetism associated with transition metal solutes in copper naturally suggests study by NMR. It has already been fruitfully applied to Cu–Mn.[1–5] In that case there are enough *d*-holes so that the exchange energy of parallel spins predominates over the tendency to form a band. Each manganese atom has a localized moment, whose mean value is given by a Brillouin function. Chromium, iron and cobalt in copper show similar behavior.[5]

Two NMR investigations of Cu–Ni have been published,[4,5] but the less than 10 per cent nickel used was insufficient for magnetic effects of alloying to be distinguished. Band-wave functions are expected to be appropriate for copper rich Cu–Ni. Although the rigid band model predicts a full *d*-band up to about 40 per cent nickel, near the composition at which ferromagnetism is known to set in, there is abundant evidence for *d*-holes even in the dilute alloys.[6,7] Their electronic state has been uncertain for many years, but the recent susceptibility measurements by PUGH and RYAN, eliminating almost all of the $1/T$ contributions, seem to be decisive in favor of a band description. The question is not easily settled for the ferromagnetic alloys, but considerable *d*-band character is certainly present there, too. GOLDMAN[8,9] and FRIEDEL[10] have pointed out how a few nickel atoms in copper can distort the bands to produce *d*-holes. The positive potential energy of an itinerant electron near a nickel atom pushes the top of the *d*-band above the Fermi level locally. This also shields the extra negative charge. It is not clear why the *d*-shell of the solute is relatively less stable in Cu–Ni than in Ag–Pd,[11] which seems to have no *d*-holes up to high concentrations.[6]

The present experiments include measurements of intensity, line width, shape and frequency of the steady state resonance of ^{63}Cu at 4·2°K, 77°K and

* This paper is based on a thesis presented to Harvard University by D. L. WEINBERG in partial fulfillment of the requirements for the degree of Doctor of Philosophy. The work was supported jointly by the Office of Naval Research, Signal Corps, and the Air Force Office of Scientific Research.

† Present address: Corning Glass Works, Research and Development Division, Corning, New York.

VOL. 15 1960

room temperature, and 2640 G, 4310 G and 6220 G. At 4·2°K the resonance was detectable at all the compositions used, up to 43 per cent nickel. This contrasts with the strong magnetism of manganese in copper, of which less than 1 per cent makes the copper resonance unobservable at 4·2°K.

The intensity measurements have been reported in another paper[12] in order to consider separately the quadrupole effects of alloying. Nuclear quadrupole interaction with a single solute atom in copper broadens the near neighbor copper resonances. For nickel in copper at 6200 G, approximately the first two neighbor shells become unobservable at low concentrations. However, a copper nucleus has appreciable probability at high concentrations of being surrounded by such a configuration of nickel atoms that it experiences only a small electric field gradient. As a result, the resonances of some copper nuclei which are close to nickel atoms, and therefore strongly affected by their electronic magnetism, can be observed.

2. EXPERIMENTAL RESULTS

The ingots were made by Alloyd Research Corporation with nickel containing 0·03 per cent iron (typical analysis), the only impurity that might affect the results. The 38 per cent Ni alloy showed 0·03 per cent iron spectrophotometrically, after filing, cleaning with a magnet and grinding. Considerable static broadening would be expected, from the measurements on Cu–Fe,[5] but NMR is much less sensitive to magnetic impurities than the susceptibility. The iron introduced by filing is

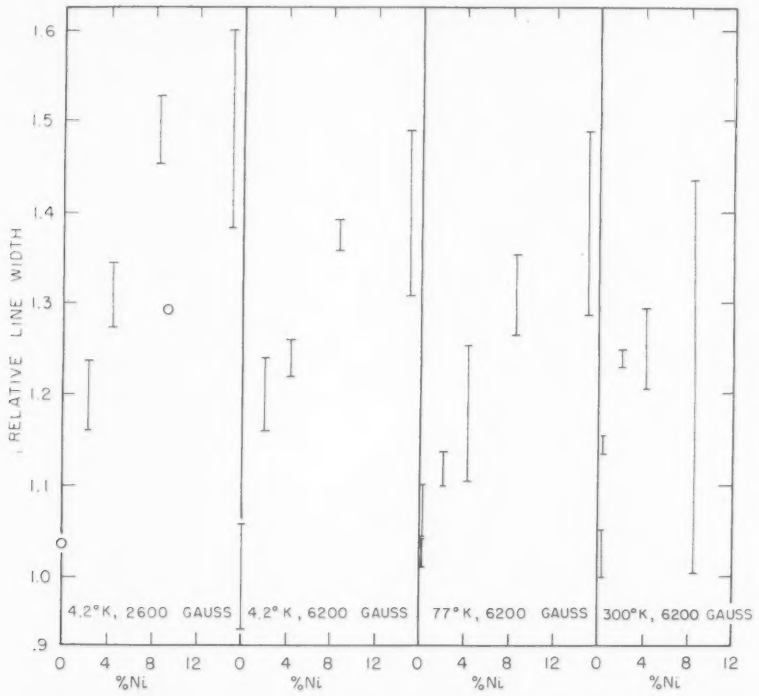

FIG. 1. Width between peaks of the ^{63}Cu absorption derivative in dilute Cu–Ni, relative to the 7·0 kc/s width in pure copper. The circles in the left hand box show CHAPMAN and SEYMOUR's data, at unspecified H_0 and T, but presumably independent of both. SUGAWARA found that the width increases by about 1 kc/s on alloying with 3·5 per cent nickel, independently of temperature.

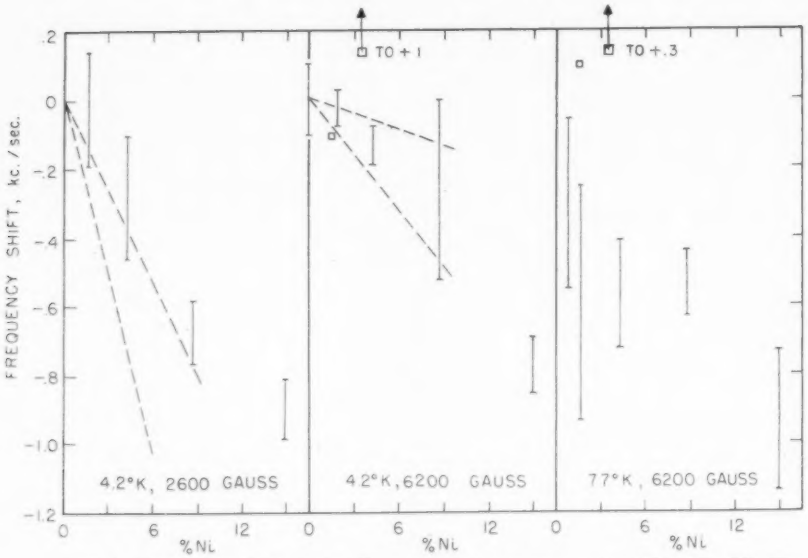

FIG. 2. Frequency shift of the ^{63}Cu absorption maximum in dilute Cu–Ni. The dashed lines are the limits of error of CHAPMAN and SEYMOUR's data, at the same fields, and independently of temperature. The squares are approximately SUGAWARA's best values, at about the same temperatures, and fields not definitely specified, but adjusted to 6200 G.

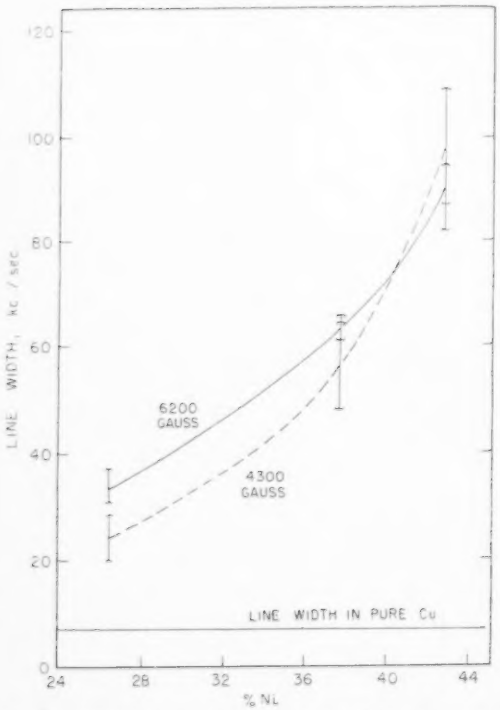

FIG. 3. Width between peaks of the ^{63}Cu absorption derivative in high concentration Cu–Ni alloys at 4·2°K.

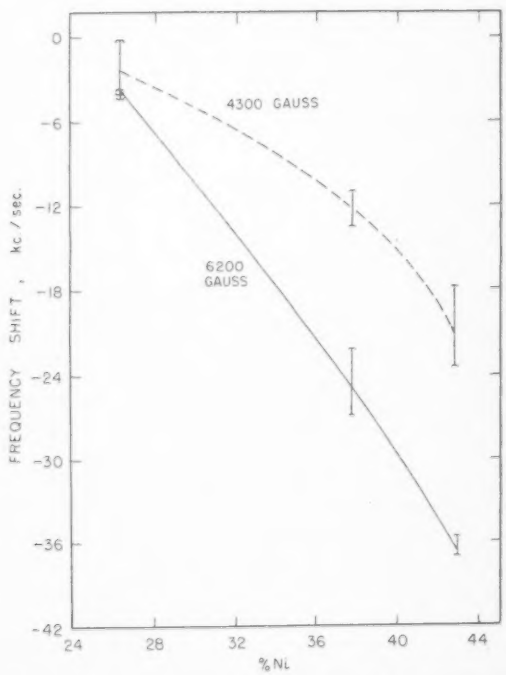

FIG. 4. Frequency shift of the ^{63}Cu absorption maximum in high concentration Cu–Ni alloys at 4·2°K.

superficial and should have little effect. The impurity broadening will be seen to be dominated in magnitude by the observed broadening and incapable of explaining the line shape. Impurity effects in the paramagnetic alloys should show temperature dependence.

The absorption derivatives were observed with a conventional Pound spectrometer. Line width and concentration alloys. In other words, all but a negligible fraction of the shifts are negative.

The line width data for high concentrations are inaccurate because of the extreme flatness of the low frequency peak. Fig. 5 compares the central portions of the line, between the peaks, at 4300 G and 6200 G at 4·2°K. They have a common frequency scale with origin at the high frequency

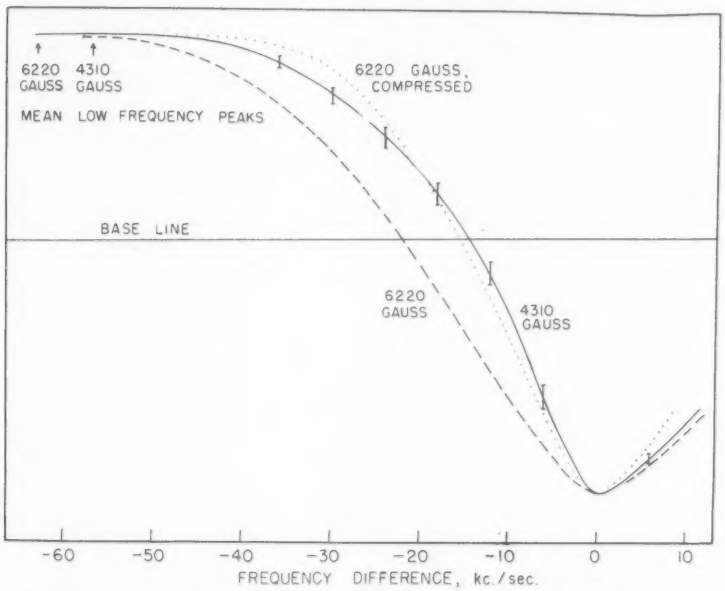

FIG. 5. Central part of the ^{63}Cu absorption derivative in the Cu–Ni alloy of 38 per cent nickel, at 4·2°K and two different fields. The signals are normalized and drawn on a common frequency scale measured from the high frequency peak. The dotted curve compresses the frequency scale of the high field resonance by 0·70. R.M.S. deviations are shown for the 4310 G line. They are smaller at 6220 G.

shift measurements at low concentrations are shown in Figs. 1 and 2, and at high concentrations in Figs. 3 and 4. The measurements refer to the frequency interval between peaks of the derivative, and the frequency shift of the absorption maximum or zero of the derivative. At low concentrations the changes in width and frequency, and the asymmetry, are slight. The line shapes at high concentrations are illustrated in Fig. 5 for $c = 0{\cdot}38$. That part of the line at higher frequencies than the high frequency peak remains practically unbroadened and unshifted relative to the low peak, and normalized peak-to-peak meter deflections. Each curve is the average of a large number of experimental traces. When the 6200 G line is compressed in frequency by a factor 0·70 it agrees well with the 4300 G line on the negative side of the origin, except for a possible small change in shape. Near the low frequency peak the derivative is too flat to be much affected by a change of frequency scale. The same analysis has been applied to the 27 per cent and 43 per cent alloys. The best average agreement is obtained with scale factors 0·71 and 0·68 for the two alloys, respectively. The

ratio of the applied fields is 0·69. The difference in shape is not consistent among the three alloys. It may be concluded that the width of the central portion of the line is proportional to H_0. The shifts of the absorption maxima are also approximately proportional to H_0 (Fig. 4). The resonances at high concentrations are too weak at 2600 G for the long, flat, low frequency ends of the lines to be distinguished. The only higher temperature resonance found in these alloys was at 27 per cent nickel, 77°K and 6200 G.

3. THEORY

(a) *General*

Internuclear interactions determine the line width in pure copper. The spin–lattice relaxation time is already so short, yet with so little effect on the line width, that lifetime broadening on alloying is not likely to be observed. Quadrupole interaction has been discussed elsewhere.

In addition to the dipolar interaction of their *d*-holes with the copper nuclei, the nickel atoms scatter electrons of the *s*-band by Coulomb and spin dependent interactions. The influence of the nickel atoms is manifested in second order in the magnetic fields of contact and dipolar type produced by the *s*-band electrons at the copper nuclei. The magnetic effects of electronic orbits will be neglected, as is usual.

A convenient approximation, in many cases, is that the contribution of the i^{th} nickel atom to the internal field at the j^{th} copper nucleus depends only on their relative positions, and not on the presence of other nickel atoms.

$$\Delta\nu_j = \sum_{\substack{i \\ \text{Ni sites}}} f_{ij} \qquad f_{ij} = f(\mathbf{r}_{ij})$$

For a random distribution the average shift is

$$\langle \Delta\nu \rangle = c \sum_i{}' f_{ij}$$

Here the sum extends over all sites except the central one.

$$(\Delta\nu_j)^2 = \left(\sum_{\substack{i \\ \text{Ni}}} f_{ij}\right)^2 = \sum_{\substack{i \\ \text{Ni}}} f_{ij}^2 + \sum_{\substack{i \\ \text{Ni}}} f_{ij} \sum_{\substack{k \neq i \\ \text{Ni}}} f_{kj}$$

$$\langle (\Delta\nu)^2 \rangle = c \sum_i{}' f_{ij}^2 + c^2 \sum_i{}' f_{ij} \sum_{k \neq i} f_{kj}$$

if the number N of atoms is infinite. The second moment is

$$\langle \delta\nu^2 \rangle = \langle (\Delta\nu - \langle \Delta\nu \rangle)^2 \rangle = c(1-c) \sum_i{}' f_{ij}^2$$

Similarly,

$$\langle (\Delta\nu - \langle \Delta\nu \rangle)^n \rangle = [c(1-c)^n + + (-)^n c^n (1-c)] \sum_i{}' f_{ij}^n \qquad n = 2, 3 \ldots$$

The limiting behavior of the moments at large n indicates that the extreme tails are intermediate between the Gaussian and Lorentzian types. This method could be generalized to multiple scattering of the *s*-band electrons by nickel atoms. It contributes terms in higher powers of c, but will not be considered further.

The time dependent part of the magnetization was found to vary too rapidly in Cu–Mn[13,5] to affect the copper resonance observably. The nickel magnetization should fluctuate even faster than that of manganese, leaving only an average component parallel to the applied field. The static magnetization associated with the *d*-holes in the paramagnetic alloys can be determined from the susceptibility measurements.[6]

$$M_d = (\chi_c - \chi_0) H_0 \qquad (\chi \text{ in volume units})$$

since the concentration dependence of the uniform magnetization is much slower. At low temperatures only the temperature independent part of $\chi_c - \chi_0$ should be retained, to eliminate the probable impurity contributions. ARROTT[14] has measured the zero field intra-domain magnetization and parasitic paramagnetic susceptibility at 37 per cent and 42 per cent nickel, and many investigations are available for higher nickel content. The interpolated M_d at some of the concentrations

Table 1. *Magnetization of the d-band at* 4·2°K *and* 6200 G

per cent Ni*	M_d(G)	per cent Ni*	M_d(G)
2·162	0·0022	26·52	0·049
4·316	0·0050	37·85†	5·3
8·604	0·011	42·93	27
14·98	0·020		

* By synthesis.
† 38·7 per cent by analysis.

VOL. 15 1960

used here, and 4·2°K and 6200 G, are listed in Table 1. The parasitic paramagnetism is assumed to represent the increase of M_d with field within a single domain.[15] Then the field induced part is only 1·5 G at 38 per cent nickel and 2·1 G at 43 per cent nickel.

An average magnetic moment $\mu_z = M_d V/Nc$ at the site of each nickel atom is used in the calculations, but this is a poor approximation in Cu–Ni, in contrast to dilute Cu–Mn. It represents another, more serious deviation from the assumption $\Delta\nu_{jl} = f(\mathbf{r}_{ij})$. In paramagnetic Cu–Ni the bands are probably pushed up by amounts depending on the nickel content in regions containing more than one atomic cell.[8] This is in accord with the rapid increase of g_{Fd}, the density of d-states at the Fermi level, with concentration.[7] The even more rapid increase of n_d, the number of d-holes (as g_{Fd}^3, in a parabolic band approximation) can account for the apparent decrease of the exchange parameter θ'.[6] In the ferromagnetic alloys, M_d has the inhomogeneity of n_d if all the d-holes in a large region are oriented at once. More probably, small independent groups of neighboring atoms become ferromagnetic whenever their nickel concentrations are high enough. Then M_d is even more inhomogeneous.

The central part of the line is narrower if M_d is inhomogeneous, than it would be if the same total magnetization were more uniformly distributed among the nickel atoms. This is especially clear if the nearest neighbor interaction is dominant.

(b) *Inhomogeneity of the Knight shift*

BLANDIN and DANIEL[16] have calculated the changes in electron density from Coulomb scattering by solute atoms, using the partial-wave method for scattering of plane waves by a spherically symmetric potential. They obtain for the fractional change in the Knight shift

$$\frac{\Delta K_j}{K_0} = \frac{(\Delta\nu_j)K}{K_0\nu_0} = \sum_{l=0}^{\infty}(2l+1)\{[n_l(k_m r_{ij})^2 - j_l(k_m r_{ij})^2]\times \sin^2\delta_l - j_l(k_m r_{ij}) n_l(k_m r_{ij}) \sin 2\delta_l\}$$

$K_0 \cong 2{\cdot}35\times10^{-3}$ is the Knight shift in pure copper, j_l and n_l are spherical Bessel and Neumann functions, and k_m is the wave number at the Fermi level. The variation of g_{Fs} with concentration is ignored. Remarkable agreement between theory and experiment has been obtained in the NaK and NaRb systems.[17] In Cu–Ni the phase shifts δ_l depend on how the shielding charge of one extra hole around the nickel atom is partitioned between the s- and d-bands, i.e. on n_d. Lacking this information, BLANDIN and DANIEL considered the two extreme cases of shielding by the plane waves of the s-band, or entirely by holes of d-symmetry around the foreign atom. For plane waves, calculations of the same kind lead to $\delta_0 = -0{\cdot}7673$, $\delta_1 = -0{\cdot}2126$, $\delta_2 = -0{\cdot}0294$ and $\delta_3 = -0{\cdot}0021$, with $k_m = 0{\cdot}2444/r_s$ inside the square well scattering potential. For exclusively d-shielding, $\delta_2 = -\pi/10$ is the only non-zero phase shift.

(c) *Isotropic indirect exchange*

A scattering method might also be applied to the spin dependent interaction of the s-band electrons with the d-holes, but it would be difficult to evaluate the phase shifts. The indirect exchange interaction of copper nuclei with nickel spins has been obtained from the zero order spin independent wave functions by perturbation theory. HUND's rule implies that the s–d exchange constant $-2J$ has a ferromagnetic sign. ZENER's[18] prediction $J = 0{\cdot}48$ eV for metallic nickel will be adopted. The hyperfine coupling with the copper nuclei may be expressed in terms of the Knight shift. From the calculation of YOSIDA for Cu–Mn[3]

$$(\Delta\nu_j)_{ex} = \tfrac{3}{2}\pi Z J\gamma\mu_z\beta^{-2}(K_0 + \sum_{i}^{N1}\Delta K_{jl})\sum_{i}^{N1}F(2k_m r_{ij})$$

$\gamma = 2\pi\nu_0/H_0$. β is the Bohr magneton. $Z \cong 1-c$ is the number of s-band electrons per atom. $F(x) = x^{-4}(x\cos x - \sin x)$ embodies the localization of the s-band magnetization. Taking the volume of the Fermi sphere proportional to Z determines k_m.

This expression is not of the form discussed previously, because of the correlation between the two summations, but the methods of Section 3(a) can be applied to evaluate the moments. In the second and higher moments there is additional interference through the cross terms between $(\Delta\nu_j)_K$ and $(\Delta\nu_j)_{ex}$. The indirect exchange is dominant in

the ferromagnetic alloys, but $(\Delta\nu_j)_K$ is important at paramagnetic concentrations.

The summations over all lattice sites need modification to allow for the quadrupole interaction. In addition to the cubic arrangements of nickel atoms, sixty-four configurations of the first shell containing six nickel atoms each, and eight configurations of the second shell with three nickel atoms each, lead to $\nabla\epsilon = 0$ at the central nucleus, when the configurations with $\nabla\epsilon$ small, are more important. They may correspond a little more closely to 50 per cent of nickel atoms in the first two shells.

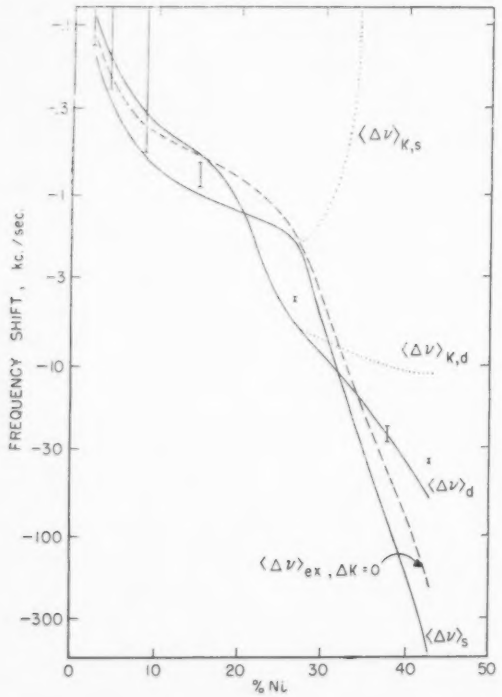

FIG. 6. Theoretical average shifts for 6200 G and 4·2°K: inhomogeneity of the Knight shift K in the two limits of plane-wave and d-wave scattering, isotropic exchange with $\Delta K = 0$, and the combined effect in the s- and d-limits. Experimental shifts of the absorption maximum are shown for comparison.

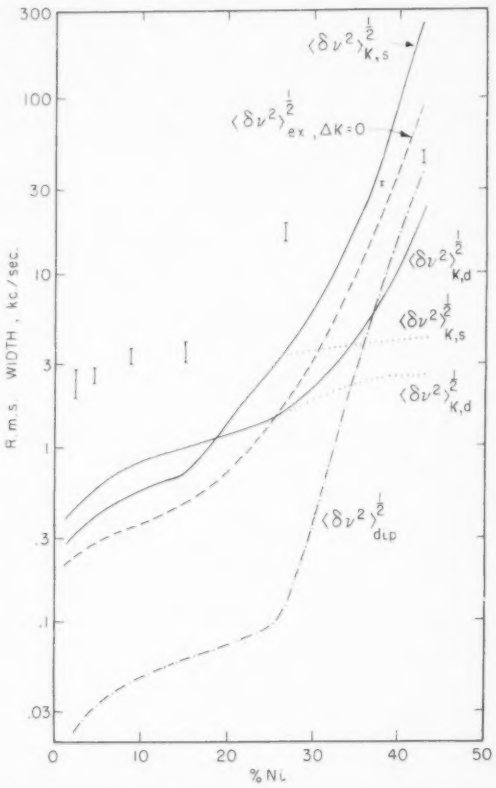

FIG. 7. Theoretical r.m.s. widths for 6200 G and 4·2°K: inhomogeneity of the Knight shift K in the two limits of plane-wave and d-wave scattering, isotropic exchange with $\Delta K = 0$, the combined effects in the s- and d-limits, and direct dipolar interaction with the nickel spins.

The measurements of the half width between derivative peaks are shown for comparison in the form $\frac{1}{2}(\Delta\nu^2_{exp} - \Delta\nu^2_{Cu})^{1/2}$, in order to correct for the width in pure copper, $\Delta\nu_{Cu} = 7{\cdot}0$ kc/s.

atoms are treated as point charges on the lattice sites.[12] If these are the observable configurations, as is assumed here, then the average numbers of first and second neighbor nickel atoms of observable copper nuclei are coincidentally about 12 c and 6 c at $c = 0{\cdot}38$ and $0{\cdot}43$, but are very small for $c \leqq 0{\cdot}15$. The intensity measurements imply that the contributions from the other, undetermined

The predictions are shown in Figs. 6 and 7 for the inhomogeneity of the Knight shift in the limits of plane-wave and pure d-wave scattering, and for the isotropic exchange with $\Delta K_{jl} = 0$. The approximate combined results of the two effects are also given. The interference terms in the ferromagnetic alloys were calculated in the nearest neighbor approximation.

VOL. 15 1960

(d) *Dipolar and pseudo-dipolar interaction*

Pseudo-dipolar indirect exchange[19] between the copper nuclei and nickel spins has the same angular dependence as the classical dipolar interaction. The pseudo-dipolar terms arise as the second order cross products between the dipolar and contact interactions of the *s*-band electrons with the nickel atoms and copper nuclei. A crude estimate, using the criterion of BLOEMBERGEN and ROWLAND with free electron wave functions, indicates that it also has the same order of magnitude as the classical effect. They should lead to similar results, and perhaps partially cancel.

In first order the dipolar fields of the nickel atoms lead to a shift

$$(\Delta\nu_j)_{\mathrm{dip}} = \mu_z(\gamma/2\pi)\sum_{\substack{i\\ \mathrm{Ni}}}(1-3\cos^2\theta_{ij})r_{ij}^{-3}$$

θ_{ij} is the angle between $\boldsymbol{H}_0$ and the radius vector $\boldsymbol{r}_{ij}$. For a powder an average is taken over all orientations of $\boldsymbol{H}_0$. $\langle\Delta\nu\rangle_{\mathrm{dip}}$ vanishes for a cubic lattice or for any polycrystalline specimen. In a face centered cubic powder

$$\langle\delta\nu^2\rangle_{\mathrm{dip}}^{1/2} = 0{\cdot}522\mu_z\gamma c^{1/2}(1-c)^{1/2}a^{-3}$$

a is the cube edge. The sum over the first two shells has been excluded, multiplying the result by 0·341. The sum in $(\Delta\nu_j)_{\mathrm{dip}}$ is also a factor in $(\nabla\epsilon)_{zz}$, so that for almost all orientations of $\boldsymbol{H}_0$, the observable copper nuclei at 6200 G are just those which have no contribution to $(\Delta\nu_j)_{\mathrm{dip}}$ from the first two shells. The r.m.s. width is plotted in Fig. 7. The second moment is additive to that of the isotropic effects.

4. DISCUSSION

The experimental shifts and half widths are compared with the theoretical average shifts and r.m.s. widths in Figs. 6 and 7. For the very asymmetric line shapes the experimental quantities would underestimate the magnitudes of the average shifts and r.m.s. widths. The isotropic interactions lead to results of about the correct magnitude. They appear capable of explaining the predominance of negative shifts, at least in the ferromagnetic alloys. There $(\Delta\nu_j)_{\mathrm{ex}}$ is the only important contribution to the frequency shifts. Calculation shows that it can account for the negative shifts, but only if the nearest neighbor contribution is dominant and the Coulomb scattering is principally of plane-wave type. The nearest neighbor contribution is, in fact, of overwhelming importance if there is a sufficient fraction of plane-wave scattering. In the 27 per cent specimen, $(\Delta\nu_j)_K$ cannot be neglected, and a nearest neighbor approximation may be inadequate. There are again many negative shifts, but it would be more complicated to understand the shape completely. Since $K_0+\Delta K_j$ must be non-negative, variation of the Knight shift alone cannot shift any nucleus downward from its frequency in pure copper by more than $\nu_0 K_0 = 17$ kc/s at 6200 G. The calculations violate this condition at high c, because multiple scattering is neglected.

The widths are approximately field independent in the ferromagnetic alloys (Fig. 3) as would be expected. The field dependence of the central parts of the lines probably occurs because the nuclei involved are those whose local fields are small. Internal fields at these nuclei may be produced primarily by paramagnetic nickel atoms. The field dependence measurements confirm that the broadening at high concentrations is of magnetic, not quadrupolar, origin.

M_d increases by a factor of 5 from $c = 0{\cdot}38$ to $c = 0{\cdot}43$, but the observed width and shift increase comparatively little. Even more striking is the similarity of these widths to those in the 27 per cent alloy. An increase in observable broadening less than in proportion to M_d is in accord with the idea of magnetic inhomogeneity. This interpretation of the concentration dependence requires that the calculated widths in the ferromagnetic alloys be reduced relative to those at $c = 0{\cdot}27$. Inhomogeneity of the magnetization also breaks down the simple relations between the magnetic and quadrupole effects in the first two shells. A rapid increase in nonrandom segregation, instead of other sources of magnetic inhomogeneity, would have much the same effect on the exchange and dipolar interactions. It would be difficult to understand the intensity measurements[12] or the line shape on this basis alone.

The predicted magnetic broadening is too small at low concentrations (Fig. 7), and adds quadratically to the mean square width, while the observed changes are approximately independent of H_0 (Figs. 1 and 2). They probably result from quadrupole

interaction, which leads to negative shifts and the right direction of asymmetry, and sometimes to increased widths.[12] The measurements of Figs. 1 and 2 are roughly consistent with those published previously, except for SUGAWARA's positive shifts.

Raising the temperature of the 27 per cent alloy from 4·2°K to 77°K changes the width and shift at 6200 G (Figs. 3 and 4) to 22 ± 2 kc/s and $-2{\cdot}2 \pm \pm 0{\cdot}3$ kc/s, respectively, without changing the shape seriously. This can be attributed to the change of magnetization of the iron impurity.

The results in the ferromagnetic alloys can be accounted for in terms of isotropic indirect exchange interaction and inhomogeneity of the Knight shift with plane-wave scattering of the *s*-band electrons by nickel atoms. The contributions of the nearest neighbor nickel atoms must be dominant, which is true if the noncubic configurations of nickel atoms make the major contribution to the observable intensity, and therefore also to the magnetic broadening. Quadrupole interaction probably plays the major role at 15 per cent nickel or less.

Acknowledgements—The help and advice of Dr. T. KUSHIDA and others in this Laboratory are gratefully acknowledged.

REFERENCES

1. OWEN J., BROWNE M. E., KNIGHT W. D. and KITTEL C., *Phys. Rev.* **102,** 1501 (1956).
2. BEHRINGER R. E., *J. Phys. Chem. Solids* **2,** 209 (1957).
3. YOSIDA K., *Phys. Rev.* **106,** 893 (1957).
4. CHAPMAN A. C. and SEYMOUR E. F. W., *Proc. Phys. Soc., Lond.* **72,** 797 (1958).
5. SUGAWARA T., *J. Phys. Soc. Japan* **12,** 309 (1957) and **14,** 643 (1959).
6. PUGH E. M. and RYAN F. M., *Phys. Rev.* **111,** 1038 (1958).
7. GUTHRIE G. L., FRIEDBERG S. A. and GOLDMAN J. E., *Phys. Rev.* **113,** 45 (1959).
8. GOLDMAN J. E., *Phys. Rev.* **82,** 339 (1951).
9. GOLDMAN J. E., *Rev. Mod. Phys.* **25,** 108 (1953).
10. FRIEDEL J., *Canad. J. Phys.* **34,** 1190 (1956).
11. HUME-ROTHERY W. and COLES B. R., *Advanc. Phys.* **3,** 149 (1954).
12. WEINBERG D. L., *J. Phys. Chem. Solids*, following paper.
13. OWEN J., BROWNE M. E., ARP V. and KIP A. F., *J. Phys. Chem. Solids* **2,** 85 (1957).
14. ARROTT A., Thesis, Carnegie Institute of Technology, unpublished (1954).
15. SATO H., ARROTT A. and KIKUCHI R., *J. Phys. Chem. Solids* **10,** 19 (1959).
16. BLANDIN A. and DANIEL E., *J. Phys. Chem. Solids* **10,** 126 (1959).
17. RIMAI L. and BLOEMBERGEN N., *J. Phys. Chem. Solids* **13,** 257 (1960).
18. ZENER C., *Phys. Rev.* **83,** 299 (1951).
19. BLOEMBERGEN N. and ROWLAND T. J., *Phys. Rev.* **97,** 1679 (1955).

J. Phys. Chem. Solids Pergamon Press 1960. Vol. 15. pp. 249–260. Printed in Great Britain.

NUCLEAR MAGNETIC RESONANCE INTENSITIES IN ALLOYS*

D. L. WEINBERG†

Gordon McKay Laboratory, Harvard University, Cambridge, Massachusetts

(*Received* 9 *September* 1959; *revised* 30 *December* 1959)

Abstract—The steady state magnetic resonances of ^{63}Cu, ^{27}Al and ^{7}Li have been studied in the majority constituents of the Cu–Ni, Cu–Au, Al–Zn and Li–Mg alloy systems, over wide ranges of composition, magnetic field and temperature. Nuclear electric quadrupole effects are most prominent. The line widths, shapes and frequencies can be qualitatively understood in simple cases, but the predictions of the general statistical problem have not been obtained. Initial intensity reductions in copper alloys are consistent with screening of excess charge by conduction electrons and enhancement by antishielding factors. The field gradients seem to be primarily of charge origin when there is a valence difference, but those arising from size differences can be comparable.

The intensity falls markedly less rapidly above about 20 per cent solute in Cu–Ni and Cu–Au, and increases very strongly at about 40 per cent Ni. The anomalous intensity is believed to arise from non-cubic configurations of solute atoms which give rise to small field gradients at the central nucleus.

The influence of order in Cu–Au on the intensity is described better by the conventional long range order than short range order, because the former distinguishes between the Cu and Au sublattices. The predictions are compared with effects of heat treatment.

1. INTRODUCTION

THE investigation of alloying by NMR has shown that striking effects occur when the resonant nucleus has a finite electric quadrupole moment.[1–6] The formal theory of nuclear quadrupole interaction in solids has been developed in many papers, notably the review by COHEN and REIF[7]. The energy levels of each nucleus in an alloy depend on the number and positions of the nearby solute atoms, and on the orientation of its crystallite relative to the applied magnetic field H_0. There may be a wide range of frequencies for different nuclei of the same species, and also for the several transitions of each. The absorption is observed to be drastically reduced on alloying, but the line widths, measured between frequencies of maximum slope, are not changed much. Admittedly, there is usually considerable intensity shifted into the observable tails. Examples have been illustrated[1,2,4] and others occur in the present work. Some nuclear transitions appear, then, to remain unperturbed, while the contributions of almost all the others are wiped out beyond observation. Since the power absorption integrated over a frequency interval $\Delta\nu \ll \nu$ is approximately conserved, the unobservable part of the intensity must have a comparatively uniform spectrum. For many other broadening mechanisms[8,9] the half width is a reasonable measure of the root second moment of the entire line.

This all or nothing model predicts the law $I(c) = (1-c)^n$ for the relative observable intensity per resonant nucleus at low solute concentrations c, if the atoms are randomly distributed. n is the number of resonances wiped out by an isolated foreign atom. Then the graph of $\log I(c)$ vs. $-\log(1-c)$ is a straight line with slope n. Use of the peak-to-peak derivative signal for $I(c)$ omits

* Most of this paper is condensed from a thesis presented to Harvard University in partial fulfillment of the requirements for the degree of Doctor of Philosophy. The work was supported jointly by the Office of Naval Research, Signal Corps, and the Air Force Office of Scientific Research.

† Present address: Corning Glass Works, Corning New York.

absorption shifted into the observable tails and the effect of a change of width. A straight line is found, within experimental error, for the intensity measurements on metallic alloys published previously.[1-3,6] Zinc in copper leads to $n = 18$ (the first two neighbor shells) for the central transition at both $H_0 = 5600$ G and 3500 G, and similarly for nickel in copper at 6200 G. Most of the other measurements on copper alloys and on the satellites in aluminum, and also those on mixed ionic crystals[10,11] satisfy straight lines with $n \geqq 35$ at small c.

The source of the all or nothing behavior, and also the dependence of the intensity decrease on the solvent and solute elements, have been the subjects of considerable discussion.

2. EXPERIMENTAL PROCEDURE

(a) *Preparation of specimens*

Alloyd Research Corp., of Watertown, Mass., made the Cu–Ni ingots from 0·9999 Cu and 0·9996 Ni containing 0·03 per cent Fe (typical analyses). The charges were melted in open graphite crucibles with an induction heater. Solidification was by air cooling from above the liquidus.

Dr. W. G. JOHNSTON of the General Electric Co. prepared the Cu–Au alloys from 0·99999 Cu and 0·99999 Au, melted together under vacuum. The solidified alloys were swaged into wires and found to be homogeneous on a macroscopic scale by measurements of the resistivity. In addition, they were annealed at high temperature.

If the particles of a specimen are not small compared to the RF skin depth, the variation of the eddy current losses—as the skin depth varies with nuclear susceptibility—is comparable to the magnetic absorption.[12] The copper alloys were subdivided with steel hand files. The steel introduced was removed with a hand magnet, as far as possible. (Spectrophotometric analysis of the 38 per cent Ni Cu–Ni powder showed 0·03 per cent Fe, as compared with 0·01 per cent by synthesis.) The copper alloys were then ground to 325 mesh with a porcelain mortar and pestle. The particles of pure copper and aluminum were thicker than the skin depth. The possibility of skin effects in the very dilute alloys had to be considered in each case.

The Al–Zn alloys were those made by ROWLAND[2,13]. Since the solubilities of zinc and manganese in aluminum are both probably less than 2 per cent at room temperature, ROWLAND quenched the ingots from above the solvus temperature, and the powdered specimens again shortly before measurement. The same procedure was followed here. ROWLAND's 200 mesh filings were principally used.

Li–Mg alloys were prepared from 0·998 Li and 0·9998 Mg, sealed in crucibles of mild steel.[14] The crucible was heated and agitated above 700°C for at least 20 min and then dropped into water. While sealed it was annealed for a day at about 5°C below the solidus. Particles of 5–20 μ diameter, dispersed in paraffin oil, were obtained by stirring[15] in a Waring Blendor.

(b) *Measurement apparatus*

Permanent magnets and Varian Associates electromagnets were used, all of negligible inhomogeneity and short time instability for the specimens used. The RF spectrometer was of the Pound-Knight-Watkins type,[16] responding to the absorption. The coil of its tuned circuit held the specimen, of the order of one gram in quantity. Spectra were usually taken by varying the RF frequency. Small amplitude sinusoidal modulation of the field permitted phase sensitive detection and display of the absorption derivative on an output recording meter. Although time constants as long as 50 sec were sometimes used, the time to sweep between derivative peaks was never appreciably less than 20 times the time constant. Up to 35 W of modulation power was used, at audio frequencies depending on H_0 and the refrigerating equipment. No corrections for finite modulation were needed, as long as the same amplitude was used for specimens compared directly. Slow passage non-saturation conditions were always satisfied.

Liquid nitrogen was held in glass dewars, and liquid helium in a metal cryostat which kept it for seven hours. Low temperatures were used partly, and for Cu–Au and Al–Zn exclusively, to improve the signal-to-noise ratio.

Intensities were compared by means of a calibrator with those of the same nuclear species, at different compositions of the same alloy system, at the same field and temperature. The experimental measure of the intensity used was the peak-to-peak derivative signal. Copper and aluminum alloys were weighed after measurement to determine the number of resonant nuclei in the coil, but Li–Mg was dissolved in water and titrated to neutrality with dilute HCl.

Field and frequency measurements were based either on crystal controlled frequency meters, adequate for small frequency differences, or on a more precise standard.[15] The accuracy was limited by the widths of the lines or poor signal-to-noise ratios. The frequency shifts refer to the absorption maximum, or zero of the derivative. The interval in frequency between the peaks of the derivative was the measure of the line width.

Each number reported is the average of two or more determinations. The errors quoted are r.m.s. deviations of the average. About 10 per cent for the intensity was usual with good signal-to-noise ratio, but with many repetitions, 5 per cent has sometimes been achieved.

3. STATISTICAL ASPECTS OF QUADRUPOLE BROADENING

(a) *Low concentrations—the all or nothing model*

The quadrupole perturbation of the central transition $m = \frac{1}{2} \rightarrow m = -\frac{1}{2}$ first occurs in second order and falls off at least as rapidly as r^{-6}. For initial cubic symmetry the nuclei in the same

spherical shell about a single solute atom have nearly the same q. $-eq = (\nabla\epsilon)_{zz}$ in principal axes. The line shape of one shell in a powder[5] has absorption spread over a continuous frequency range, so that strongly perturbed shells form a flat background relative to the unperturbed absorption. (Similar results are likely for magnetostatic dipolar broadening by impurities.) Increasing c weakens the unperturbed part of the line, so that broadened absorption should become more prominent and deviations from all or nothing behavior more readily detectable. In view of the radial variation of q^2 and the contributions of partially perturbed shells to the maximum slopes, a critical radius around a solute, separating the unobservable resonances from those unaffected, cannot reach the third neighbors in a f.c.c. lattice, when c is appreciable. Thus, the all or nothing model is plausible only for small c or n. Some detailed calculations for such cases[6,7,10] qualitatively reproduce the line shapes. Much of the increase in width in mixed NaCl–NaBr[10] seems to result from the use of single crystals, which allow peaking of the perturbed intensity. In first order the perturbation falls off comparatively slowly with distance, but the nuclei used thus far have central transitions, which obscure the weakened satellites except at $nc \ll 1$. ROWLAND[3] has also discussed the interpretation of quadrupole line shapes in alloys.

(b) *High concentrations*

A nucleus may have $\nabla\epsilon = 0$ even with foreign atoms nearby, as when identical solute atoms fill a shell in a cubic metal. With these cubic configurations, for $n = 18$ in a f.c.c. lattice,

$$I(c) = (1-c)^{18}+(1-c)^{12}c^6+(1-c)^6c^{12}+c^{18}.$$

Some shells and subshells of full cubic symmetry, such as those of more than forty-eight atoms, can be partitioned into subdivisions of full cubic symmetry. Otherwise they must have 6, 8, 12, 24 or 48 atoms. Table 1 shows how they can be further partitioned into subdivisions with lower symmetry, but

$$(\nabla\epsilon)_{ij} = \sum (3x_ix_j-\delta_{ij}r^2) = 0$$

at the center. The sum is over the lattice points of the subdivision. Each subdivision contains half the atoms of the shell. The subdivisions classified together are congruent (except at most for an inversion). The third column gives the point group of the subdivision, in the Schoenflies notation. The

Table 1. *Subdivisions of cubic shells with* $\nabla\epsilon = 0$ *at the center*

No. of atoms in a shell of full cubic symmetry	No. of ways it can be partitioned into congruent subdivisions, each with $\nabla\epsilon = 0$ at the center	Symmetry group of a subdivision	$\left\lvert\frac{\Sigma \mathbf{r}}{r}\right\rvert^2$	Example
6	8	C_3	3	100, 010, 001
8	12	T_d	0	111, 1–1–1, –11–1, –1–11
12	24	C_s	10	101, –101, 011, 0–11, –110, 110
	24	C_s	2	101, –101, 0–1–1, 0–11, –110, 110
	16	C_3	6	–10–1, –101, 011, 0–11, –110, 110
24	12	T_d	0	211, 121, 112, 2–1–1, 1–2–1, 1–1–2, –2–11, –1–21, –1–12, –21–1, –12–1, –11–2
	8	I	0	112, 1–12, 21–1, 2–1–1, –11–2, –1–1–2, –211, –2–11, 1–2–1, 121, –12–1, –1–21
48	12	T_d	0	
	8	I	0	

examples have the center as origin. KAWAMURA *et al.*[10] also mentioned such configurations. With $n = 18$ in a f.c.c. lattice their inclusion leads to

$$I(c) = (1-c)^{18}+8(1-c)^{15}c^3+$$
$$+65(1-c)^{12}c^6+512(1-c)^9c^9+$$
$$+65(1-c)^6c^{12}+8(1-c)^3c^{15}+c^{18}$$

The anomalous intensity should increase with n.

With less than full cubic symmetry the atoms will be distorted from the lattice sites. Furthermore, unless the electric field

$$\epsilon = |\epsilon_{\text{point charge}}|\frac{\Sigma r}{\gamma}$$

vanishes at the center, the central nucleus and its electrons move, with distortion of the orbits. $|\sum r/r|^2$ is listed in Table 1. Then the nucleus will ordinarily have $\nabla\epsilon \neq 0$ at its equilibrium position. FOLEY *et al.*[17] calculated $\nabla\epsilon$ thus induced at the nucleus of a Cl^- ion, by an external Na^+ ion. It first occurs in the second order of perturbation of the electron wave functions. The ratio of $q^{[2]}$ induced by ϵ to $q^{[1]}$ induced in first order by the external field gradient is 0·19[18] when the internuclear distance is 2·36 Å, as in a NaCl molecule. $q^{[1]}$ is large because of antishielding. Such a calculation may be appropriate for charge effects in solids, but quadrupole couplings in general are inadequately understood.[19] Some of the configurations of Table 1 may contribute only partially, or not at all.

Of the 2^n configurations for $n = 12, 18 \ldots$ only a small fraction have $q^{[1]} = 0$. The others have a distribution of $|q| = |q^{[1]}+q^{[2]}+\ldots|$ which are likely to take some small values, as well as large and intermediate ones. Solute atoms in more than one shell can lead to small $|q|$. The additional contributions would be difficult to determine, but they may be at least comparable to those of the configurations with $q^{[1]} = 0$. The prominence of configurations with small $|q|$ is also suggested by the line widths.

4. EXPERIMENTAL RESULTS AND DISCUSSION

(a) *Copper–nickel and copper–gold*

Intensity measurements[1,3,5,13] on copper and α-brass show that quadrupole interaction with the

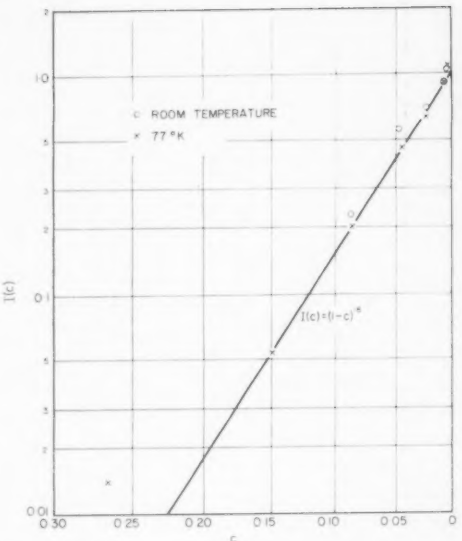

FIG. 1. Peak-to-peak absorption derivative signal of ^{63}Cu in Cu–Ni, at 6200 G, logarithmic in both $I(c)$ and $(1-c)^{-1}$.

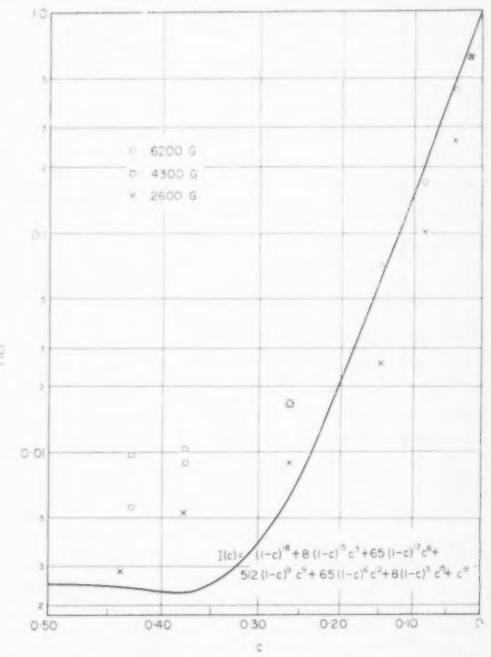

FIG. 2. Peak-to-peak absorption derivative signal of ^{63}Cu in Cu–Ni, at 4·2°K, logarithmic in both $I(c)$ and $(1-c)^{-1}$. The drawn curve is the calculated integrated observable intensity for configurations with $\nabla\epsilon^{[1]} = 0$.

VOL. 15 1960

dislocations introduced by filing wipes out the satellite transitions of ^{63}Cu almost completely. The central transitions contribute 0·4 of the total absorption in pure copper, with $I = \frac{3}{2}$, and are observed to be unaffected by filing and grinding.

Intensities in Cu–Ni are shown in Figs. 1 and 2. They are similar to the maximum absorptions of CHAPMAN and SEYMOUR with up to 9·2 per cent nickel at the same fields. The intercept of the extrapolated linear part of the experimental curve, if any, is assumed to be the intensity of the unperturbed central transition. There is satisfactory agreement with $n = 18$ from $c = 0{\cdot}005$ to $c = 0{\cdot}15$ at 6200 G, and no apparent temperature dependence. The 0·27 per cent specimen appears to retain about 5 per cent of the satellite intensity. This would correspond to $n \sim 1000$, if the effect of dislocations could be ignored.

The initial decrease of $I(c)$ is more rapid at 2600 G, as expected. There are large deviations from all or nothing behavior. The graph of $I(c)$ vs. $-\log(1-c)$ has positive curvature, and likewise at 3500 G.[20] The characteristic asymmetry (up to 15 per cent nickel) for $\gamma > 0$ in a powder, with the high frequency derivative peak stronger than the low frequency peak, becomes greater than 2 : 1. At 6200 G it ranges only up to 1·1 : 1. The asymmetry also occurs in Cu–Au, Al–Mg[2] and Li–Mg. The increase in line width and negative frequency shift in Cu–Ni[8] up to 15 per cent nickel may be quadrupole effects at both fields, but it is also possible that the smaller magnetic effects at 2600 G are compensated by prominent quadrupole broadening.

The same type of asymmetry, and also slight broadening, arise from the skin effect. The width and asymmetry in Cu–Ni are observed to go through a minimum at about 1 per cent nickel at 77°K and 6200 G, as the skin depth increases with alloying, and second order quadrupole (or magnetic) interaction sets in.

The intensities in Cu–Au (Fig. 3) are well represented at small c by $n = 35$ and 45·6, for 6200 G and 2600 G, respectively. The line width and asymmetry increase in the dilute alloys, levelling off at high concentrations at 6200 G to an increase in line width of about 25 per cent and asymmetry of about 1·5 : 1. The increase in line width is less at 2600 G. The frequencies at 6200 G are shown in Fig. 4. The shifts are negative, as for

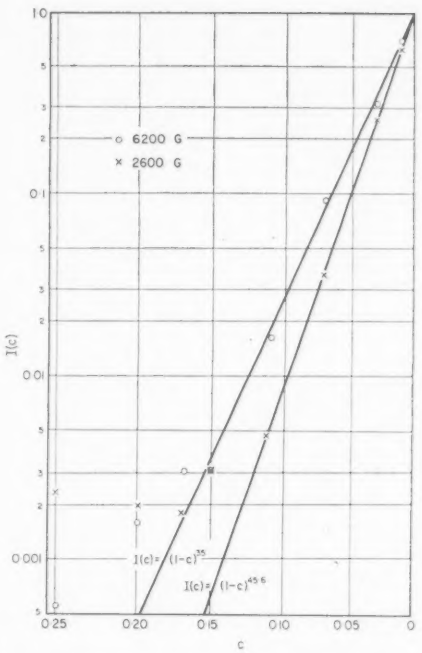

FIG. 3. Peak-to-peak absorption derivative signal of ^{63}Cu in Cu–Au, at 4·2°K, logarithmic in both $I(c)$ and $(1-c)^{-1}$.

quadrupole interaction, but of unusually large magnitude, especially up to 7·0 per cent gold. The average frequency is even lower, because of the direction of asymmetry. The shifts may be largely changes in the Knight shift.[9] Although there is

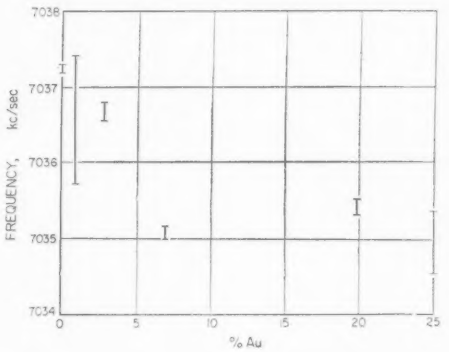

FIG. 4. Frequency of maximum absorption of ^{63}Cu in Cu–Au at 4·2°K.

no valence difference between copper and gold, the sizes and ion-cores are different. A negative shift has also been observed in Ag–Au.[9]

Skin effect may be important in the pure copper and 1·00 per cent gold specimens. The skin effect shift is negative, so that when the skin depth is increased by alloying, the observed frequency should increase. All the alloying shifts reported here are negative, which excludes skin effect as an explanation, although the true shifts may sometimes be larger in magnitude than those observed, for this reason.

(b) *Interpretation of the wipe-out numbers in copper alloys*

Experience with non-metals indicates that if the solute atom has an excess valence $Z \neq 0$, then the charge effect is likely to be the dominant source of $\nabla\epsilon$, except insofar as it is screened by conduction electrons. This interpretation is supported by the monotonic increase of n with $Z \neq 0$ in copper alloys,[3] and by RHODERICK's results on semiconductors.[4]

When a nucleus sees only one solute atom, the z principle axis of $\nabla\epsilon$ points approximately toward the solute. If in addition to the exponential conduction electron shielding, $\nabla\epsilon$ is modified by (scalar) factors β_ϵ, for the dielectric polarization, and β_0, for the distortion of the ion-core of the resonant nucleus itself, then[7]

$$q/Z\beta = 2r^{-3}[1+r/r_0+\tfrac{1}{3}(r/r_0)^2]\exp(-r/r_0).$$

$\beta = \beta_\epsilon\beta_0$ and r_0 is the shielding radius. In the Fermi–Thomas approximation $r_0 = 0{\cdot}640(a_0 r_s)^{1/2}$, where $4\pi r_s^3/3$ is the volume per conduction electron and a_0 is the first Bohr radius. The measurements are in better agreement with the improved result of PINES:[21] $r_0 = 1{\cdot}474(a_0 r_s)^{1/2} = 0{\cdot}500R_1$ (Cu), $0{\cdot}576R_1$ (Li), $0{\cdot}392R_1$ (Al, with three conduction electrons per atom). R_1 is the nearest neighbor distance. This will be used here, although r_0 may be smaller for fixed ionic charges than for PINES' mobile electrons. Nickel atoms in copper may be shielded by electrons of two different bands.[8]

The splitting between the two peaks of the averaged second order perturbed central transition of a single shell[5] is $\Delta\nu^{[2]} = 3{\cdot}4\times10^{-39}q^2/H_0$ sec^{-1} (q in cm^{-3}) for $I = \frac{3}{2}$. The line is 7·0 kc/s wide in pure copper. For $nc \ll 1$ a splitting of at least $\Delta\nu^{[2]}{}_{\min} = 12$ kc/s is required to eliminate all but 25 per cent of the shell's contribution to the maximum derivatives, while a splitting less than $\Delta\nu^{[2]}{}_{\max} = 4$ kc/s does not reduce its contribution by more than 25 per cent. Then the formula for $\Delta\nu^{[2]}$ leads to $|q|_{\max}{}^2/H_0$ and $|q|_{\min}{}^2/H_0$. The $|q|$ values are so small that fourth order effects are negligible. $Z\beta|q|_{\min}/q$ and $Z\beta|q|_{\max}/q$ in Table 2 are then the minimum values of $|Z\beta|$ to almost wipe out the resonance (at particular distances from the solute) and the maximum values of $|Z\beta|$ which will scarcely reduce the intensity, respectively, for the charge effect.

For zinc in copper, $n = 18$,[3] so that β must be at least 8·7, from Table 2, to wipe out the second neighbor resonance at 5600 G, and at most 9·4 to avoid reducing the third neighbor contribution at 3500 G. Similarly, for nickel in copper at 6200 G, $9{\cdot}2 \leqq \beta \leqq 13$. To eliminate part of the third shell at 2600 G, $8 \leqq \beta \leqq 14$. There is satisfactory

Table 2. Charge effect calculations for copper alloys

Shell	n_{fcc}	$10^{-22}\dfrac{q}{Z\beta}$	$\dfrac{\lvert q\rvert_{\max}}{q/Z\beta}$, $\dfrac{\lvert q\rvert_{\min}}{q/Z\beta}$ at H_0 =			
			2600	3500	5600	6200
1	12	7·1	0·77, 1·3	0·90, 1·6	1·1, 2·0	1·2, 2·1
2	18	1·6	3·4, 5·9	4·0, 6·9	5·0, 8·7	5·4, 9·2
3	42	0·68	8·1, 14	9·4, 16	12, 21	13, 22
4	54	0·29	19, 33	22, 38		
5	78	0·15		43, 74		

VOL. 15 1960

agreement with $|q_2|$ deduced elsewhere.[6] Indium, with $Z = 2$, affects the fourth shell at 3500 G,[3] so that $\beta \geqq 11$. $\beta \geqq 14$ for silicon, which affects the fifth shell,[3] and similarly for germanium and tin. The derived values of β are nearly the same, so that the observations are consistent with the formulation given here of the charge effect. When the charge effect is screened out and the unscreened strain effect becomes dominant, the derived values of β should increase. The values of β are close to that calculated for the free ion Cu^+, viz. $1-\gamma_\infty = 16{\cdot}0$,[18] but β_0 is larger if $\beta_\epsilon < 1$.[7]

Since $Z = 0$ for silver[1] or gold in copper, $\nabla\epsilon$ at the "critical radius" must result from strain. In the elastic continuum approximation it would have an r^{-3} dependence,[22] which with the measured n values for gold,[3] and $|q|_{\max}$, $|q|_{\min}$ at the fields used leads to $|q_3| \cong 10\times 10^{22}$ cm^{-3}. Indium and tin in copper have even larger size factors, but to determine how the charge and strain effects interfere, at least the sign of the gradient-strain component $S^{(23)}_{1111}$ would be needed.

(c) *Anomalous intensity at high concentrations*

Figure 2 shows the intensity expected for the configurations (of Table 1) with $\nabla\epsilon^{[1]} = 0$, if $n = 18$, and also $I(c)$ observed in Cu–Ni. The line widths increase by more than a factor of 10 at high concentrations,[8] which seems to be a magnetic, rather than a quadrupole effect. Therefore the relative intensity at high concentrations, obtained by integration over all the observable absorption, would be as much as two orders of magnitude larger than the experimental peak-to-peak intensity $I(c)$ of Fig. 2. $I(c)$ at high concentrations in Cu–Au also lies far above its initial straight lines (Fig. 3). The fractional increase of intensity above $(1-c)^n$ from the other configurations with $\nabla\epsilon^{[1]} = 0$ is much smaller for $c \leqq 0{\cdot}25$ than at the higher concentrations of Fig. 2. At $c = 0{\cdot}25$ they add 41 per cent for $n = 42$ and 53 per cent for $n = 54$.

The very large extra integrated intensity in both alloy systems, beyond that from configurations with $\nabla\epsilon^{[1]} = 0$, may arise from the configurations hypothesized in Section 3(b) which have $\nabla\epsilon$ small, but finite in first order. Their total probability is likely to increase as $c \to 0{\cdot}50$. Additional experimental evidence has been obtained for contributions from non-cubic configurations.[8] Considering the increase in width, the anomalous integrated intensity becomes much larger in Cu–Ni than in Cu–Au, as is plausible because of the higher concentrations used in Cu–Ni. The only other comparable experiments have been done on mixed NaCl–NaBr.[10] The intensity at high concentrations was not reported, but it was probably unexpectedly high since segregation was considered a dominant factor.

The high integrated intensities may arise partly from segregation, but it would need to be extreme to explain the rise in integrated intensity in Cu–Ni. Either a decrease of dissolved nickel with increasing c, or accumulation of undissolved copper would be required. Neither is consistent with the behavior of other resonance parameters,[8] although segregation is not altogether precluded. The Cu–Au alloys, carefully prepared to avoid segregation, show an even larger anomalous intensity at given c.

$I(c)$ in Cu–Zn, which also has $n = 18$, but not much broadening by electronic magnetism, would be expected to go through a deep minimum, and return near 50 per cent Zn to a value comparable to $I(0)$. No anomaly is apparent up to $c = 0{\cdot}20$, as in Cu–Ni, but a large positive deviation should occur at the phase limit, about 30 per cent Zn.

(d) *Aluminum alloys*

The satellites in pure aluminum are unaffected by cold work alone, in contrast to copper.[2,5,13] The principal effect of alloying is to wipe them out. Solution heat treatment of the field alloys also serves to remove dislocations.

In Fig. 5 new intensity measurements on Al–Zn at three fields are shown, and compared with ROWLAND's data at 5600 G on Al–Zn and Al–Mg. In Al–Mg the intensity continues to decrease with c to $I(0{\cdot}14) \cong 0{\cdot}14$. The two sets of measurements on Al–Zn at 5600 G are consistent, considering the uncertainties. It is difficult to determine the field dependence of the satellite intensity if the mean relative intensity has a r.m.s. deviation of more than 5 per cent. The most striking aspect of the new data is the absence of a decrease in intensity with decreasing field at the higher concentrations. The central transitions contribute 9/35 of the total intensity, with $I = 5/2$. A graph of $\log(I-9/35)$ vs. $\log(1-c)$ for $c \leqq 0{\cdot}02$ does not always lead to straight lines, but the best n values are about 90, 100 and 170 for the present work at successively lower fields, and 120 and 130 for ROWLAND's measurements on Al–Zn and Al–Mg, respectively. The integrated observable intensity has also been evaluated for Al–Zn at 5600 G. Relative to that of pure aluminum, it decreases to $0{\cdot}4 \pm 0{\cdot}02$ at $c = 0{\cdot}028$

and levels off, confirming that additional zinc scarcely increases the broadening.

It was originally concluded from the results at 5600 G that a nearest neighbor zinc atom does not broaden the central transition. However, the absence of a second order quadrupole effect, and the continued presence of

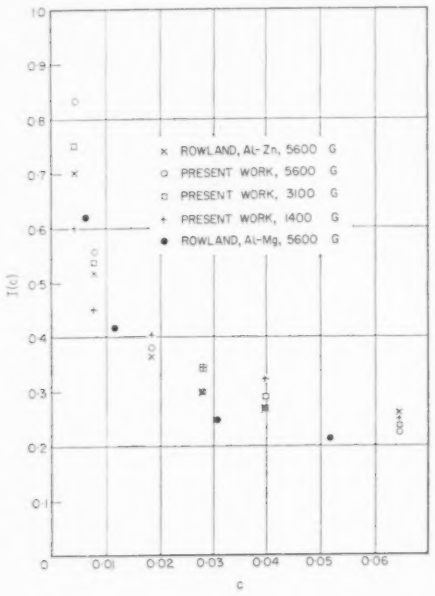

FIG. 5. Peak-to-peak absorption derivative signal of ^{27}Al in Al–Zn and Al–Mg. The 1400 G work was done at 77°K and the rest at room temperature.

satellite absorption at $c > 0{\cdot}03$, seem to be the results of precipitation of a Zn-rich phase. The early metallographic examinations of Al–Zn alloys did not provide definite evidence of precipitation, but RUDMAN and AVERBACH[24], who used diffuse X-ray scattering, state "precipitation was detected immediately on cooling to room temperature". They dealt with 10 per cent zinc or more, but AVERBACH has confirmed[25] that the effect extends to lower c. If the precipitation occurs after the quench, these experiments might be done successfully by quenching to a lower temperature and keeping the specimens cold during measurement.[26] Al–Mg solid solutions appear to be more stable.

The broadening of distance satellites is likely to be a strain effect. S_{1111} is much smaller than in copper, probably because both antishielding and ion overlap are reduced. The strain effects of zinc and magnesium in aluminum seem to be quite similar, although Z is the same and the size factor is much larger for magnesium.[27] It has been suggested[28] that the ionic radii may be important for solutes in aluminum.

ROWLAND assumed that the outer peaks of the seventh neighbor Al nuclei are shifted by $\gtrsim 5$ kc/s (the unperturbed width is 9·3 kc/s), and that q varies as r^{-3}. Then $|q_1| \gtrsim 11\times10^{22}$ cm^{-3}, and $\Delta\nu^{[2]}$ is only about 2 kc/s at 5600 G. This is consistent with experiment in Al–Zn, but not in Al–Mg. The r^{-3} variation may break down at atoms adjacent to a solute. $|q_1| \cong 30\times10^{22}$ cm^{-3}, corresponding to $\Delta\nu^{[2]} \cong 13$ kc/s at 5600 G, is a likely value for Al–Mg. From Section 4(b), $q/z\beta\times10^{-22} = 3{\cdot}9$, 0·70, 0·23 ... is the charge effect for the first few shells. It drops off too quickly to affect distant shells, but may rival the strain effect at $r = R_1$. At 1400 G even $|q_1| = 11\times10^{22}$ cm^{-3} should produce broadening of the central transition. Its absence is understandable if precipitation occurs at 2 per cent zinc. ANDERSON[29] has applied the method of RAMSEY and POUND, and concludes tentatively[30] that the zero field splittings at an Al nucleus adjacent to a Zn atom are at least 60 kc/s and 120 kc/s, for which $|q_1| \geqq 7\times10^{22}$ cm^{-3}.

The largest fractional variations of $I(c)$ with field in Al–Zn occur below 1 per cent zinc, but are barely significant. They cannot represent broadening of the central transition, unless as c increases the amount of zinc in solution decreases. The second moments of the outer satellites are

$$\langle(\Delta\nu-\langle\Delta\nu\rangle)^2\rangle/\nu_0^2 = 9\Omega^2/500 \pm$$
$$\pm 9\Omega^3/3500 - 6039\Omega^4/14{,}000{,}000 + \ldots$$
$$\Omega = e^2Qq/h\nu_0 = 0{\cdot}7 \text{ for } q = 20\times10^{22}\text{ cm}^{-3},$$
$$H_0 = 1400\text{ G}.$$

A clearly detectable field dependence evidently cannot be expected.

Alloying with zinc reduces the line width by up to 20 per cent, in consistency with ROWLAND's width of 8 kc/s at $c = 0{\cdot}064$.[13] No field dependence can be distinguished. The line width might decrease in a quadrupole line shape in a coincidental case, or by elimination of skin effect broadening or dilution of the nuclear dipolar broadeners. Inhomogeneity of the quadrupole splitting in Al–Zn causes an 18 per cent decrease of the dipolar second moment by obstructing mutual spin flips,[31] which may be pertinent here.

(e) *Lithium–magnesium*

The quadrupole studies have been extended to ^{7}Li in b.c.c. Li–Mg, at 77°K. This temperature avoids both diffusion narrowing[32] and the spontaneous transformation to a hexagonal structure.[33] Since the particles were not cold worked, the resonance in pure lithium almost certainly includes satellite absorption. $I(c)$, in Fig. 6, falls well below 0·4, so that, with $I = \frac{3}{2}$, broadening of the central transition must enter. Since $I(c)$ does not fall much below 0·1, some of the absorption is unaffected, independently of field. The width increases, but by less than 10 per cent of the 10 kc/s width in pure lithium. As usual, the tails are emphasized. The integrated observable intensity at 6200 G is $0{\cdot}39\pm0{\cdot}03$ times as large at 4·8 per cent magnesium as in pure lithium, indicating that the central transitions remain observable, while the satellites are wiped out. The frequency at 6200 G was found to decrease with c, levelling off at a negative shift

of 2·6 kc/s, or 0·025 per cent, for 7·9 per cent and 10·7 per cent magnesium. This is the value of the Knight shift in lithium,[34] so that the asymptotic frequency is that characteristic of an insulator. KNIGHT also found a frequency decrease on alloying with magnesium.[35]

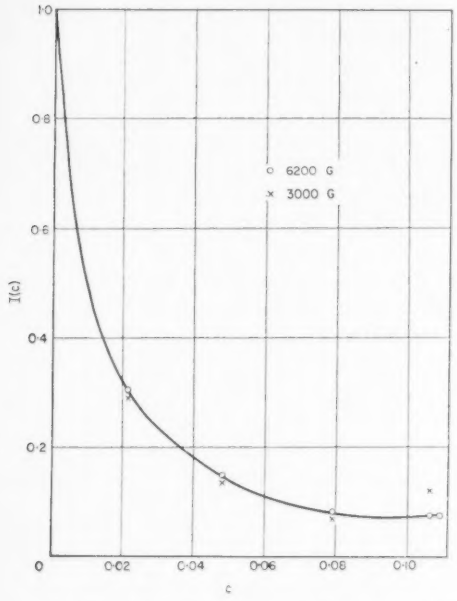

FIG. 6. Peak-to-peak absorption derivative signal of ^{7}Li in Li–Mg at 77°K.

The intensity and frequency measurements together imply that the specimens contain non-metallic lithium compounds. Their contribution to the intensity becomes dominant as the alloy resonances are weakened. The compounds may have formed by reaction with impurities in the commercial paraffin oil. Apparently the incompletely broadened central transition of the alloy masks the line width in the compound. For non-cubic configurations of magnesium atoms to explain the anomalous intensity they would have to be much more prominent than in the copper alloys.

The size factor[36,37] and initial strain broadening, with $n \cong 60$ the best value, are comparable to those in the aluminum alloys. With an analysis like ROWLAND's[2], $|Qq_1| \gtrsim 0{\cdot}005$ cm^{-1}. For a charge effect in the near shells $q/Z\beta \times 10^{-22} = 8{\cdot}7, 5{\cdot}0, 1{\cdot}1 \ldots$ Then $Q = -0{\cdot}12 \times 10^{-24}$ cm^2[38] leads to $|Qq_1| = 0{\cdot}01\beta$ cm^{-1} and $\Delta\nu^{[2]} = 1{\cdot}5\beta^2$ kc/s. From $I(c)$ and the integrated intensity at $c = 0{\cdot}048$, the absorption in question, but not the satellites, is in the observable wings of the line. It appears to have $\Delta\nu^{[2]} \sim \sim 20$ kc/s. Thus the experiment suggests a rather large value of $|Q\beta|$. Other studies of ^{7}Li in solids[29, 39] have shown comparatively weak quadrupole effects.

5. ORDER IN COPPER–GOLD

(a) *Description of the state of order*

Since NMR is sensitive to the local environments of the nuclei it may register effects of order in alloys. In Cu–Au the Cu resonance can be observed in a single phase from pure copper to compositions at which order is important. Furthermore, it orders slowly enough so that the state of order can be varied within wide limits by heat treatment.

Neither long range nor short range order describes the atomic positions completely. Short range order specifies only the (average) composition of the ith shell of neighbors, e.g. in terms of the X-ray diffraction parameters $\alpha_i = 1-\beta_i$.[40] It makes no distinction between atoms of the same shell which lie on different sublattices. If the atoms of the ith shell were independent the probability that δ_i of the n_i ith neighbors of a copper atom are copper atoms would be

$$\binom{n_i}{\delta_i}(c\beta_i)^{n_i-\delta_i}(1-c\beta_i)^{\delta_i}$$

For perfect order in Cu_3Au the correct probabilities for $i = 1$ are 1 if $\delta_1 = 8$ and 0 otherwise. The binomial formula gives

$$\binom{12}{8}(1/3)^4(2/3)^8 = 0{\cdot}24$$

for $\delta_1 = 8$, and is similarly finite for other values of δ_1. The correct results are predicted when $\delta_i = n_i$ or 0.

The β_i are defined as averages over all atoms taken as center in turn. The binomial formula gives, for the contribution from the configurations of a copper atom with all copper atoms in its first shell and all gold atoms in its second shell, when $n = 18$,

$$\begin{aligned} I(c) = {} & (1/19)(1-c)^{-1}\{(1-c)(1-c\beta_1)^{12}(c\beta_2)^6 + \\ & + 12(1-c)(1-c\beta_1)^5(c\beta_1)^2(1-c\beta_2)^2(1-c\beta_3)^4(c\beta_3)^2(1-c\beta_4)(c\beta_5)^2 + \\ & + 6c[(1-c)\beta_1]^4(1-c)\beta_2[(1-c)\beta_3]^4[1-(1-c)\beta_4]^4[(1-c)\beta_5]^4[1-(1-c)\beta_8]\}. \end{aligned}$$

The exponents are the numbers of atoms in the jth shell which are mth neighbors of an atom in the lth shell, for the appropriate j, m and l. The numerical results have been examined for the configurations with $\nabla\epsilon^{[1]} = 0$, with $c \leqq 0{\cdot}25$ and $n = 18$ or 42, assuming $\beta_1 = 1+\frac{4}{3}c$ and all other $\beta_l = 1$. This corresponds to rather strong nearest neighbor order. The wipe-out numbers are qualitatively applicable to the measurements in Cu–Au. All-copper configurations are less probable than for randomness. The other configurations are emphasized, but less at large n, since an average of at most a quarter of the atoms are gold. The total intensity is decreased slightly, by 20 per cent and 40 per cent for $n = 18$ and 42, respectively, at $c = 0{\cdot}25$. Second neighbor order would scarcely change the intensity. The effect of short range order on other observable configurations has not been ascertained, but it is probably also relatively small.

Long range order involves only the sublattices, without reference to the local influence of a copper (or gold) atom. In terms of the parameters r_a, r_b, w_a and w_b,[41] of which only one is independent, long range order for arbitrary compositions may be defined as

$$S = (r_a - c)/[(r_a)_{\max} - c]. \qquad 0 \leqq S \leqq 1.$$

r_a is the fraction of a (Au) sites occupied by right atoms etc. In Cu–Au, $(r_a)_{\max} = 1$ for $c > \frac{1}{4}$ and $4c$ for $c < \frac{1}{4}$. If $n = 12$

$$I(c) = \tfrac{3}{4}r_b^9 w_a^4 + \tfrac{1}{4}r_b^{12} w_a + \tfrac{3}{4}r_b w_b^8 r_a^4 + \tfrac{1}{4}w_a w_b^{12} + \\ + 64(\tfrac{3}{4}r_b^5 w_b^4 r_a^2 w_a^2 + \tfrac{1}{4}r_b^6 w_b^6 w_a).$$

The first four terms are from the two cubic configurations, and the bracketed terms represent the configurations from Table 1. $S = 0$ is the random limit. BLOEMBERGEN[5] gave a graph of $I(c)$ for $n = 18$, $S = 1$ and cubic configurations only. A finite S produces considerable increases in intensity, which become even greater for $n = 42$, 54 .... In a polycrystalline specimen there is no long range order, but these intensities apply for either an infinite single crystal, or a crystallite with the same S, provided the crystallite surface has no effect.

The failure of short range order to describe the large increases in intensity in Cu–Au predicted for long range order has nothing to do with distance, but simply with atoms being right or wrong. By allowing for this, a given value of S assigns a higher probability to a right or nearly right configuration than do the β_l which apply to the same configuration.

The short range order may be different from that prevailing if the a and b atoms are distributed randomly on the appropriate sublattices, consistent with a given S.[42] The description could be generalized to additional short range order by expressing r_{al}, etc., in terms of both S and the β_l.

(b) *Effects of heat treatment*

The measurements of Section 4 used Cu–Au cooled in a few minutes from far above the transformation temperature of about 389°C, and then filed and ground. It does not seem possible to deduce from studies of the kinetics of ordering[43] and the effect of cold work[44] whether the order was sufficient to account for the anomalous intensity.

It was proposed to order the alloys in known ways, and to compare the effects on $I(c)$ with the calculations. This procedure is illogical if the intensity comes chiefly from unknown configurations. The effect of ordering on their contributions is not apparent. From Section 5(a)

$$I(c) \cong \tfrac{1}{4}r_b^{36} w_a r_a^6 + 8(\tfrac{1}{4}r_b^{36} r_a^3 w_a^4)$$

for $n = 42$ and $c \cong 0{\cdot}25$. Fig. 7 shows the predictions. Maximizing $I(c)$ seems to offer the best hope of an observable change. The 25·0 per cent Au and 20·0 per cent Au powders were heat treated for $S = 0{\cdot}9$ and $S = 1$, respectively, measured by NMR, disordered for 1 hr above 500°C, quenched from about 600°C and then remeasured. For ordering Cu_3Au was cooled from 370°C to 335°C in 140 hr, and Cu_4Au was cooled from 330°C to 322°C in 157 hr, on the assumption that the X-ray data on $S(T)$[45,46] are pertinent. The water bath cracked the evacuated Pyrex tubes used, insuring fast quenches.

The measurements were at 6200 G. In Cu_3Au $I(c)$ increased on ordering by a factor $2{\cdot}1 \pm 0{\cdot}1$, and returned on quenching to $0{\cdot}98 \pm 0{\cdot}02$ of the original value. The averages of two such cycles for Cu_4Au were $0{\cdot}9 \pm 0{\cdot}1$ after ordering, and $0{\cdot}5 \pm 0{\cdot}1$ after quenching. From Figs. 3 and 7, the maximum increase, for $n = 42$, is a factor of 10 in each alloy if only the configurations with $\nabla\epsilon^{[1]} = 0$ are

applicable. The ordered phase may not extend much below $c = 0{\cdot}20$. The anomalous intensities after quenching are comparable to those of Fig. 3. If order is responsible, it must be the local order persisting above T_c.[47]

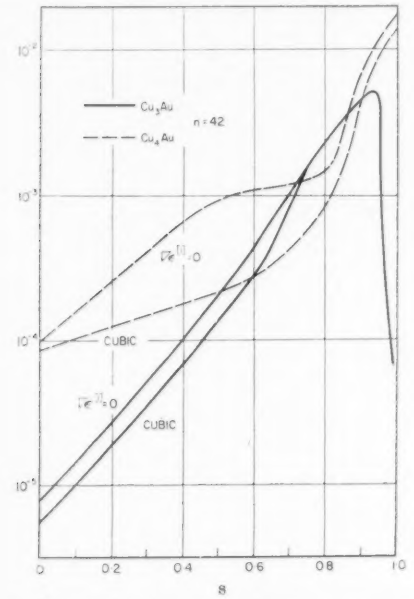

FIG. 7. Observable intensity of copper resonance in Cu–Au, calculated for long range order, with wipe-out number $n = 42$.

No change in width or shape was apparent on heat treatment. The shifts relative to the original state were $1{\cdot}7 \pm 0{\cdot}4$ kc/s after ordering and $0{\cdot}6 \pm 0{\cdot}5$ after quenching, in Cu_3Au, and in Cu_4Au $1{\cdot}7 \pm 0{\cdot}4$ kc/s and $0{\cdot}5 \pm 0{\cdot}4$ kc/s, respectively. Reduction of quadrupole broadening, as on ordering in Cu_3Au, would lead to a positive shift. Hydrostatic pressure decreases the frequency in Cu,[15] and Cu_3Au contracts slightly on ordering,[48] so that it is unlikely to be a volume effect. The electron density P_F[34] at a copper nucleus depends on the distribution of nearby gold atoms.[9] The present work has some implications for the effect of gold atoms in the various shells, but the complications of the expected oscillations of P_F and of unknown configurations prevent a prediction of even the sign of the ordering shift. As pointed out by SLATER, and used also by GOLDMAN[49], ordering superimposes a periodicity of larger unit cell on that of the monatomic lattice, so that energy discontinuities appear at the faces of the new zones in k space. The density of states at the Fermi surface may thereby be increased.

The copper resonance has recently been studied in β-brass.[50]

Acknowledgements—The author wishes to thank Professor N. BLOEMBERGEN, who suggested most of these measurements. The help and advice of Dr. A. G. REDFIELD and Dr. T. KUSHIDA, and of many others in this Laboratory, have been very valuable. Thanks also go to Dr. T. J. ROWLAND and Dr. W. G. JOHNSTON, who prepared some of the specimens, and to those investigators who made available their unpublished or not yet published results.

Note added in proof: The ideas expressed here about the charge contribution to the field gradient near a solute atom should be modified in view of new experimental and theoretical results submitted to *Phys. Rev.* by T. J. ROWLAND and by W. KOHN and S. H. VOSKO. (See *Bull. Amer. Phys. Soc.* (ser. 2) **5,** 176 (1960)).

REFERENCES

1. BLOEMBERGEN N. and ROWLAND T. J., *Acta Met.* **1,** 731 (1953).
2. ROWLAND T. J., *Acta Met.* **3,** 74 (1955).
3. ROWLAND T. J., *Progr. Met. Phys.* **9,** in press.
4. RHODERICK E. H., *Phil. Mag.* **3,** 545 (1958); *J. Phys. Chem. Solids* **8,** 498 (1959).
5. BLOEMBERGEN N., *Rept. Conf. on Defects in Crystalline Solids, Bristol,* 1954, p. 1. Physical Society, London (1955).
6. CHAPMAN A. C. and SEYMOUR E. F. W., *Proc. Phys. Soc. Lond.* **72,** 797 (1958).
7. COHEN M. H. and REIF F., *Solid State Physics* (edited by SEITZ F. and TURNBULL D.) Vol. 5, p. 321. Academic Press, New York (1957).
8. WEINBERG D. L. and BLOEMBERGEN N., *J. Phys. Chem. Solids,* preceding paper.
9. BLANDIN A. et DANIEL E., *J. Phys. Chem. Solids* **10,** 126 (1959).
10. KAWAMURA H., OTSUKA E. and ISHIWATARI K., *J. Phys. Soc. Japan* **11,** 1064 (1956).
11. OTSUKA E. and KAWAMURA H., *J. Phys. Soc. Japan* **12,** 1071 (1957).
12. CHAPMAN A., RHODES P. and SEYMOUR E. F. W., *Proc. Phys. Soc. Lond.* B**70,** 345 (1957).
13. ROWLAND T. J., unpublished Thesis, Harvard University (1954).
14. BRIDGMAN P. W., *Proc. Amer. Acad. Arts Sci.* **83,** 149 (1954).
15. BENEDEK G. B. and KUSHIDA T., *J. Phys. Chem. Solids* **5,** 241 (1958).
16. WATKINS G. D., unpublished Thesis, Harvard University (1952).
17. FOLEY H. M., STERNHEIMER R. M. and TYCKO D., *Phys. Rev.* **93,** 734 (1954).

VOL. 15 1960

18. STERNHEIMER R. M. and FOLEY H. M., *Phys. Rev.* **102,** 731 (1956).
19. DAS T. P. and KARPLUS M., *J. Chem. Phys.* **30,** 848 (1959).
20. ROWLAND T. J., private communication of unpublished work.
21. PINES D., *Solid State Physics* (edited by SEITZ F. and TURNBULL D.) Vol. 1, p. 367. Academic Press, New York (1955).
22. ESHELBY J. B., *Solid State Physics* (edited by SEITZ F. and TURNBULL D.) Vol. 3, p. 79. Academic Press, New York (1956).
23. TAYLOR E. F. and BLOEMBERGEN N., *Phys. Rev.* **113,** 431 (1959).
24. RUDMAN P. S. and AVERBACH B. L., *Acta Met.* **2,** 576 (1954).
25. AVERBACH B. L., private communication.
26. CHALMERS B., private communication.
27. AXON H. J. and HUME-ROTHERY W., *Proc. Roy. Soc.* **A193,** 1 (1948).
28. RAYNOR G. V., *Progr. Met. Phys.* **1,** 1 (1949).
29. ANDERSON A. G., *Phys. Rev.* **115,** 863 (1959).
30. ANDERSON A. G., private communication of unpublished work.
31. KAMBE K. and OLLOM J. K., *J. Phys. Soc. Japan* **11,** 50 (1956).
32. HOLCOMB D. F. and NORBERG R. E., *Phys. Rev.* **98,** 1074 (1955).
33. BARRETT C. S. and TRAUTZ O. R., *Trans. Amer. Inst. Min. (Metall.) Engrs.* **175,** 579 (1948).
34. KNIGHT W. D., *Solid State Physics* (edited by SEITZ F. and TURNBULL D.) Vol. 2, p. 93. Academic Press, New York (1955).
35. KNIGHT W. D., private communication of unpublished work.
36. LEVINSON D. W., *Acta Met.* **3,** 294 (1955).
37. HERBSTEIN F. H. and AVERBACH B. L., *Acta Met.* **4,** 407 (1956).
38. STERNHEIMER R. M. and FOLEY H. M., *Phys. Rev.* **92,** 1460 (1953).
39. HON J. F. and BRAY P. J., *Phys. Rev.* **110,** 624 (1958).
40. COWLEY J. M., *Phys. Rev.* **77,** 669 (1950).
41. PEIERLS R., *Proc. Roy. Soc.* **A154,** 207 (1936).
42. CHIPMAN D. R., *J. Appl. Phys.* **27,** 739 (1956).
43. MUTO T. and TAKAGI Y., *Solid State Physics* (edited by SEITZ F. and TURNBULL D.) Vol. 1, p. 193. Academic Press, New York (1955).
44. NIX F. C. and SHOCKLEY W., *Rev. Mod. Phys.* **10,** 1 (1938).
45. KEATING D. T. and WARREN B. E., *J. Appl. Phys.* **22,** 286 (1951).
46. JAUMOT F. E., Jr., and SUTCLIFFE C. H., *Acta Met.* **2,** 63 (1954).
47. GERMER L. H., HAWORTH F. E. and LANDER J. J., *Phys. Rev.* **61,** 614 (1942).
48. NIX F. C. and MACNAIR D., *Phys. Rev.* **60,** 320 (1941).
49. GOLDMAN J. E., *Rev. Mod. Phys.* **25,** 108 (1953).
50. SAGALYN P. L. and HOFFMAN J. A., *Bull. Amer. Phys. Soc.* (ser. 2) **4,** 166 (1959).

J. Phys. Chem. Solids Pergamon Press 1960. Vol. 15. pp. 261–269. Printed in Great Britain.

COLOUR CENTRES IN X-IRRADIATED ALKALI METAL AZIDES*

H. G. HEAL† and J. P. S. PRINGLE

(*Received* 20 *October* 1959; *revised* 17 *December* 1959)

Chemistry Department ,University of British Columbia, Vancouver, Canada.

VOL. 15 1960

Abstract—Sodium, potassium, rubidium and cesium azides X-irradiated at liquid nitrogen temperature develop *F* bands, other absorption bands at longer wavelength, ascribed to electron surplus centres, and *V* bands in the ultraviolet. At room temperature, sodium azide gives a broad band in the ultraviolet ascribed to photoemission by sodium metal; potassium develops two bands in the red ascribed to *R* centres. Cesium and rubidium azides develop broad structured bands in the ultraviolet of undetermined origin.

INTRODUCTION

SINCE the azide ion, N_3^-, is univalent and similar in volume to the bromide ion, it is not unexpected that absorption bands resembling the well-known *F*, *V* etc. bands of the alkali halides develop in the axides when these are exposed to ultraviolet light or X-rays. However, as TOMPKINS and YOUNG first showed,[1] the resemblance only appears when the crystals are irradiated, and the spectra observed, at low temperatures; on warming to room temperature, the azide *F* and *V* bands disappear. (In the alkali halides, by contrast, the *F* band and some types of *V* bands are stable for long periods at room temperature.) Consequently, earlier work by ROSENWASSER, DREYFUS and LEVY[2] in which sodium azide was irradiated with gamma rays and pile radiation at room temperature or above failed to reveal the *F* band.

The object of the work reported here has been to examine qualitatively the bands produced in the alkali azides by X-irradiation at room and liquid nitrogen temperatures, to study the changes of the low temperature bands on warming, and as far as possible, to identify the centres responsible for the bands on the basis of the alkali halide models. All the alkali azides readily obtainable as good single crystals, viz. those of sodium, potassium, rubidium and cesium have been studied.

While the present report was being written, CUNNINGHAM and TOMPKINS published a paper on the coloration of sodium and potassium azides by ultraviolet light and X-rays.[3] This work and our own to some extent overlap; the results obtained are partly at variance, as will be noted below. The present paper, however, is the first to describe colour centres in rubidium and cesium azides.

EXPERIMENTAL

Sodium azide (Eastman Kodak practical grade) was recrystallized by slow cooling from 90°C of a solution in 3 per cent hydrazoic acid.[4] Platelets about 0·1 mm thick and up to 30 mm² in area were obtained.

Potassium azide was made by neutralizing hydrazoic acid with reagent grade potassium hydroxide. The solution was concentrated by evaporation and allowed to cool, when very small platelets were obtained. These were grown by laying them on the bottom of a beaker containing a hot saturated solution and letting this cool. Plates up to 0·35 mm thick and 45 mm² in area were obtained.

Rubidium azide (A.D. Mackay Inc.) was recrystallized by slow evaporation of an aqueous

* Contribution from the Department of Chemistry, University of British Columbia, Vancouver 8, B.C., Canada. Taken in part from a thesis presented to the Faculty of Graduate Studies of the University of British Columbia by J. P. S. Pringle in partial fulfilment of the requirements for the M.Sc. degree.

† Present address: Chemistry Department, Queen's University, Belfast, N. Ireland.

solution in a vacuum desiccator; excellent transparent plates up to 0·3 mm thick and 20 mm^2 in area were obtained.

Cesium azide (A.D. Mackay Inc.) was recrystallized from hot aqueous solution, which gave good transparent plates up to 0·15 mm thick and 40 mm^2 in area.

All the azides thus purified, except sodium azide, gave within 0·1 per cent of the theoretical weight of chloride when evaporated with hydrochloric acid. The chloride residue from sodium azide was 0·4 per cent too heavy, perhaps because sodium chloride crystals occlude water tenaciously.

The *X-ray generator*, (a Machlett AEG-50T with tungsten target operating at 50 PkV and 28 mA) and arrangements for holding the crystals in the X-ray beam and in the spectrophotometer, have been described elsewhere.[5] The X-ray beam was filtered to reduce the soft components which are preferentially absorbed in the surface layers of the samples, thus giving rise to uneven rates of energy absorption. Suitable filtration was calculated by the method previously described[6] using VICTOREEN's[7] X-ray absorption data; 62·5 mg/cm^2 of aluminium was used for NaN_3 and 84 mg/cm^2 of copper for all the other azides. The samples were about 5 cm from the X-ray target.

The *spectrophotometer* was a Cary Model 14 recording instrument, in which, for the "UV" and "VIS" ranges, the light beam passes first through the monochromator and then through the sample. In the "IR" range the path is reversed, the light beam passing through the sample first and the monochromator afterwards. It was found that exposure of the crystals to the wide range of wavelengths received from the "IR" lamp resulted in bleaching effects at liquid nitrogen temperatures. Consequently, the "UV" and "VIS" spectra were measured first, then the "IR" was scanned twice; the second time to investigate bleaching effects in this region which were, in fact, slight. Finally, the "UV" and "VIS" spectra were measured to investigate the bleaching in those regions; separate tests showed that the monochromatic "UV" and "VIS" beams had no effect on the absorption bands for the times involved in measuring the spectra. To obtain the spectra due to the irradiation, the spectrum of the unirradiated crystal was subtracted from that of the same crystal after irradiation. In most cases it was found that the change in optical absorption for wavelengths greater than 1000 mμ was very small, so the zero adjustment of the spectrophotometer was set, at any convenient wavelength exceeding 1000 mμ, to equalize the optical density readings before and after irradiation.

RESULTS AND DISCUSSION

The *absorption edges* of the unirradiated crystals obtained in this work agree approximately with those of CUNNINGHAM and TOMPKINS[3]* for sodium and potassium azides. These authors quote 242 mμ and 254 mμ respectively for the points at which no detectable transmission occurs. In the present work, absorption edge optical densities of 0·5 were obtained for crystals of thickness 0·1 to 0·35 mm at 249, 259, 263 and 280 mμ for sodium, potassium, cesium and rubidium azides respectively. The anomalous position for rubidium is unlikely to be due to crystal defects since these crystals appeared the best of all. CUNNINGHAM and TOMPKINS found that for "less perfect" crystals of potassium azide the absorption tail extended to 350 mμ with a shoulder at 310 mμ, resolved in one crystal at 312 mμ. Traces of a shoulder on the absorption tail at 310 mμ were obtained in the present work, and we agree this is probably due to an impurity. CUNNINGHAM and TOMPKINS attributed the absorption tail in relatively imperfect crystals "*inter alia*, to the deformation potential associated with dislocations". In our opinion, some, at least, of this absorption may be an artifact of the optical system arising as follows. The refractive index of any crystal rises steeply as the absorption edge is approached from the long wavelength side. In some experimental arrangements, such as that used in the present work where the detector is some distance from the sample, the direction of the light ray leaving the crystal must lie within a rather narrow angle if it is to reach the photocell. If the crystal is imperfect, with facets at irregular angles, an increasing proportion of the incident light is refracted out of this critical solid angle as the absorption edge is approached. This possibility arises especially with sodium azide, the samples of which were crystalline aggregates (in contrast with the

* It is assumed that the legend "absorbance" on CUNNINGHAM and TOMPKINS' Fig. 2 should read "percentage transmittance".

VOL. 15 1960

fairly good single crystals of the other azides), and which, in fact, showed a much longer "absorption" tail than the latter.

The absorption bands produced *by irradiation at liquid nitrogen temperature* are shown in Figs. 1a, 2a, 3a and 4a.* All four azide spectra show similar features: a prominent narrow band in the visible, with a small shoulder on the long wavelength side, and a broad band in the near ultraviolet.

Table 1 gives data on the first of these bands. In agreement with TOMPKINS and co-workers, we identify this as an *F* band, on the evidence of its shape and position in the spectrum. In sodium azide it occurs at nearly the same wavelength as the *F* band in KBr (609 mμ) and RbCl (605 mμ), which have the same interionic spacing as sodium azide (3·29 Å) and similar 6-co-ordinated lattices. The *F* maxima in the other azides which have 8-co-ordinate lattices occur at somewhat shorter wavelengths than in sodium azide; a similar effect is observed in passing from 6-co-ordinate RbCl to 8-co-ordinate CsCl, and also from RbBr to CsBr. The wavelengths of the *F* maxima in the three 8-co-ordinated azides increase with interionic spacing, as in series of alkali halides with like lattices.[8] The widths of the azide *F* bands at half-height exceed those of alkali halide *F* bands (e.g. NaN_3 0·32 eV, KBr 0·22 eV).[9,10] The broadening of the *F* centre transition in the alkali halides arises from interaction with the lattice vibrations, and we attribute the extra broadening in the azides to interaction with the internal vibrations of the azide ion.

Table 1. Wavelengths of the F band in the alkali metal azides

	Co-ordination number	Lattice interionic distance (Å)	λ_{max} (millimicrons)	(Full) Bandwidth (eV)
NaN_3	6 rhombohedral	3·29	612 (610)	0·32
KN_3	8 body-centre tetragonal	3·52	568 (572)	0·60
RbN_3	8 body-centre tetragonal	3·68	578	0·50
CsN_3	8 body-centre tetragonal	3·92	592	0·43

Figures in parentheses are taken from CUNNINGHAM and TOMPKINS[2] for comparison.
(Full) Bandwidth measured at half peak height.
Irradiations performed, and spectra plotted, at −196°C.

Table 2. Wavelength of presumed V band in the alkali azides (millimicrons)

	Short wavelength shoulder	Peak	Long wavelength shoulder
NaN_3	—	330	420
KN_3	340	361 (360 UV)	390
RbN_3	350	374	400
CsN_3	365	390	420

Figure in parentheses from CUNNINGHAM and TOMPKINS[2]
Irradiation performed, and spectra plotted, at −196°C.

Table 2 gives data on the broad band in the near ultraviolet. In sodium azide, this band is much weaker than the *F* band and indistinct. CUNNINGHAM and TOMPKINS[3], irradiating sodium azide to about the same optical density, obtained a band in this region of comparable magnitude to the *F* band. The explanation of this difference is not clear. In our spectra of potassium, rubidium and

* In all the spectra shown in Figs. 1–4, optical densities are equal to $\log_{10} I_0/I$, where I_0 = intensity transmitted through unirradiated crystal, and I = intensity transmitted at the same wavelength through the same crystal after irradiation. All spectra were plotted with the crystal at −196°C, unless otherwise indicated in the caption. The abscissa is linear in energy for all these spectra. On each figure spectra from irradiation at −196°C are shown in section "a", spectra from irradiation at room temperature, or irradiation at −196°C followed by warming to room temperature, in section "b".

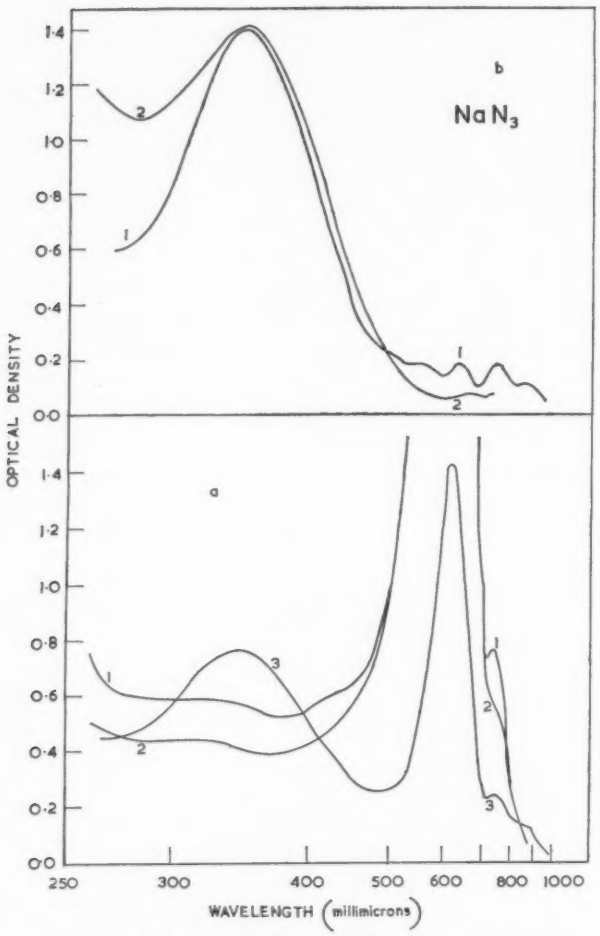

FIG. 1. Spectra of irradiated sodium azide.

a. Curve 1. Irradiated 9 hr at −196°C.
Curve 2. Irradiated 9 hr at −196°C, then exposed to "IR" lamp for 18 minutes.
Curve 3. As curve 2, then warmed until *F* band partially bleached, as determined visually.
b. Curve 1. Irradiated 28 hr at room temperature.
Curve 2. As curve 1, but spectrum plotted at room temperature.

cesium azides, however, the band is nearly as strong as the *F* band, and triple, the shoulders on each side of the main peak becoming increasingly distinct in the order given. The main peak and the shoulders probably arise from different transitions in the same type of centre, since they decrease in proportion during bleaching (Curves 1 and 2 of Fig. 4a). This band is in the same spectral region as the trapped hole bands in the alkali halides (H, V_1, and halogen molecule-ion). In view of its complex structure we are inclined to attribute it to absorption in the molecule-ion $N_3-N_3^-$, but the evidence is not decisive.[11,12]

Table 3 summarizes our data, and those of

VOL. 15 1960

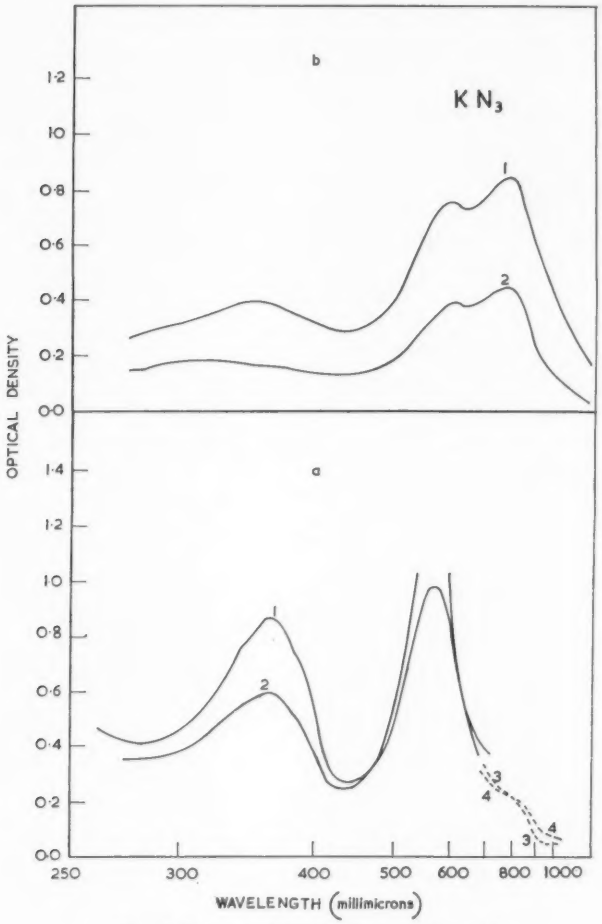

FIG. 2. Spectra of irradiated potassium azide.

a. Curve 1. Irradiated 1¼ hr at −196°C.
Curve 2. Irradiated 1¼ hr at −196°C, then exposed to "IR" lamp for 14 min.
Curve 3. Long wavelength tail of curve 1 plotted on "IR" range of spectrophotometer (plotting took first 5 of 14 min).
Curve 4. Re-trace of curve 3 taken 7 min later in one min.

b. Curve 1. Irradiated 1 hr at room temerature.
Curve 2. Irradiated 1¼ hr at −196°C, then warmed to room temperature.

CUNNINGHAM and TOMPKINS[3], on the small bands lying to the long-wavelength side of the *F* band. The partial lack of agreement suggests that some, at least, of these bands may arise from impurity centres, and it cannot be taken for granted that the same type of centre is responsible in all four azides. Considering the 740 mμ band in sodium azide, this band is too narrow (width at half-height 0·15 eV) to be an *F'* band (width in KCl, for example, 0·9 eV),[13] and CUNNINGHAM and

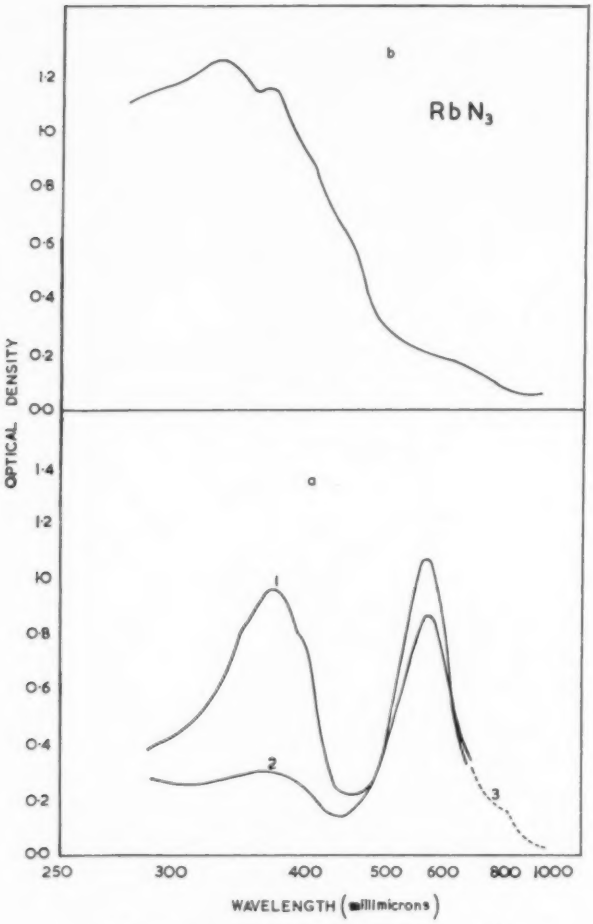

FIG. 3. Spectra of irradiated rubidium azide.

a. Curve 1. Irradiated 19¼ min at −196°C.
Curve 2. Irradiated 19¼ min at −196°C, then exposed to "IR" lamp for 16 min.
Curve 3. Long wavelength tail of curve 1, plotted on "IR" range of spectrophotometer. Retracing 7 min later produced no change.

b. Irradiated 37 min at room temperature.

TOMPKINS' model of it as an R_2 band is unsatisfactory in that it involves the diffusion of vacancies at −183°.[3] However, we consider that it and the corresponding bands in our spectra of the other azides most probably arise from trapped electron centres of *R*, *M* or *N* type.

The bleaching effects observed when the X-irradiated crystals were exposed at liquid nitrogen temperatures to the whole range of wavelengths (about 320 mμ to above 2500 mμ) from the "IR" lamp, are indicated in Figs. 1a–4a. In all cases the *V* and long wavelength absorption decreased, while the *F* band increased and, in cesium azide only, subsequently decreased. The absence of any pronounced decrease in the F_2^+ band absorption indicates that the *V* centre holes are not primarily being

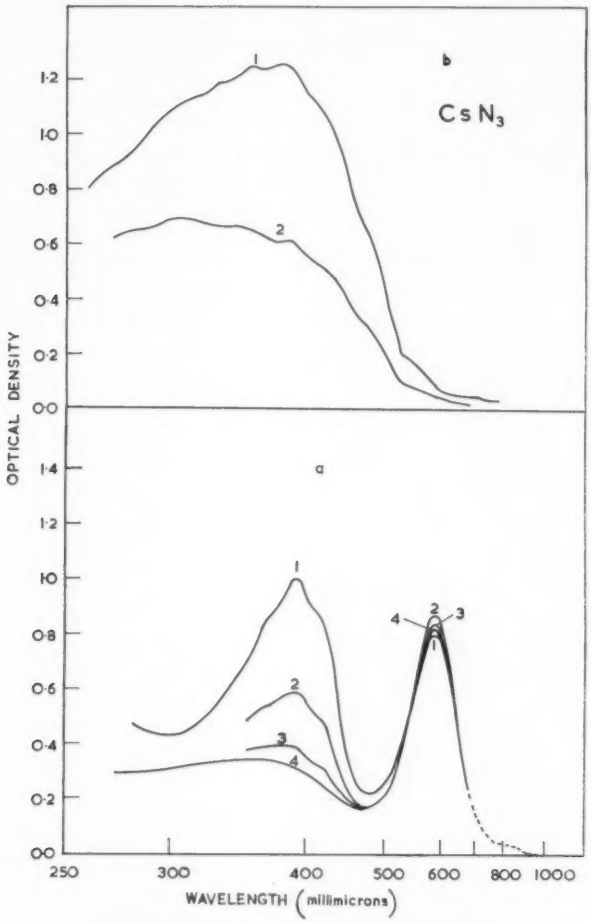

FIG. 4. Spectra of irradiated cesium azide.

a. Curve 1. Irradiated 32 min at −196°C.

Curves 2, 3, 4. Irradiated 32 min at −196°C, then exposed to "IR" lamp for $3\frac{1}{2}$, $15\frac{1}{2}$ and $45\frac{1}{2}$ min respectively.

Curve 5. Long wavelength tail of curve 1, plotted on "IR" range of spectrophotometer.

b. Curve 1. Irradiated $51\frac{1}{2}$ min at room temperature.

Curve 2. Irradiated 32 min at −196°C, and warmed to room temperature.

annihilated by electron tunnelling from F centres. Probably a variety of reactions are in competition, for example:

$$\left.\begin{matrix} N_3 \cdot N_3^- \\ N_3 + N_3^- \end{matrix}\right\} \rightarrow 3N_2 + e^- + 2 \text{ anion vacancies}$$

$$N_3 \cdot N_3^- + e^- \rightarrow 2N_3^-$$

$$N_3 + e^- \rightarrow N_3^-$$

(Destruction of V centres)

$$\text{Anion vacancy} + e^- \rightarrow F \text{ centre}$$

(Formation of F centres)

Table 3. Bands on red side of F Band

	Wavelength (millimicrons)
NaN_3	740 (740 UV; 670, 750 X-rays)
KN_3	790 (770 UV; 690, 705, 770 X-rays)
RbN_3	820
CsN_3	850

Bands reported by CUNNINGHAM and TOMPKINS[2], as produced by UV and X-irradiation respectively, are given in parentheses.

Irradiation performed, and spectra plotted, at −196°C.

$$N_3 \cdot N_3^- + F \text{ centre} \xrightarrow{\text{tunnelling}} 2N_3^- + \text{anion vacancy}$$

$$N_3 + F \text{ centre} \xrightarrow{\text{tunnelling}} N_3^- + \text{anion vacancy}$$

(Destruction of both F and V centres)

The *absorption bands developed on X-irradiation at room temperature* are shown in Figs. 1b, 2b, 3b, 4b. With the possible exception of potassium azide, the F band is completely missing. The electrons set free by the radiation are therefore trapped at other types of centres, or aggregated with cations to form particles of metal of colloidal or larger dimensions; there is chemical proof of their presence in sodium azide.[14] As photochemical decomposition of the azide ion has been observed in potassium azide at room temperature,[15] trapped hole centres are unlikely to be present, and the system resembles additively coloured alkali halides. All the spectra except that of potassium azide show a broad band in the ultraviolet. For sodium azide, at least, the peak does not change markedly in shape with temperature (Fig. 1b). This eliminates any simple type of trapped electron centre. TOMPKINS and co-workers have given evidence that this band, and a similar one in potassium azide irradiated and warmed to 60°C, arise from selective photoemission from filaments of alkali metal distributed along the dislocation network.[1,3] It is tempting to ascribe the ultraviolet bands in the spectra of rubidium and cesium azides to the same cause, but we do not wish to put forward a definite opinion on this in the absence of information on photoconductivity. If they are, indeed, photoemission bands, it is difficult to see why they should be structured (when the NaN_3 and KN_3 bands are not), why their maxima fall at shorter wavelengths than the photoemission maximum of potassium azide (440 mμ), and why the two curves for cesium azide (Fig. 4b) should differ in shape from one another.

Potassium azide at room temperature develops two well marked peaks at 590 mμ and 770 mμ; the ratio of the peak heights is, perhaps fortuitously, about the same in the two spectra shown. This behaviour resembles that observed in the alkali halide R_1 and R_2 bands.[16] The 590 mμ and 770 mμ bands are therefore tentatively ascribed to R centres; the latter may be identical with the 790 mμ band obtained at low temperatures.

Sodium azide also shows additional absorption bands at room temperature. ROSENWASSER, DREYFUS and LEVY[13] obtained two weak bands, always associated, at 660 mμ and 760 mμ from the reflection spectra at room temperature of pile irradiated material. Transmission absorption spectra in Fig. 1b, curve 2, at room temperature, confirm these observations, the bands peaking at 660 mμ and greater than 740 mμ. At liquid nitrogen temperatures, the resolution is much improved and four bands can be distinguished at 560, 630, 730 and 820 mμ; the 630 and 730 mμ corresponding to the room temperature 660 and 760 mμ bands. This 730 mμ band differs from the 740 mμ band mentioned earlier (under "Irradiation at −196°") which is unstable at −183°C and to white light at liquid nitrogen temperature, in that it is stable under both conditions and therefore definitely arises from a different centre. All four bands may be associated, since the ratio of the peaks height is fairly constant. They obviously interact strongly with the lattice vibrations. Simple centres of the R, M, N type are suggested.

In conclusion, spectra obtained by irradiating at liquid nitrogen temperatures and allowing the samples to warm up to room temperature are shown in Figs. 2b, curve 2, and 4b, curve 2. In both cases, and in sodium azide (not shown), the final result of warming to room temperature appears to be very similar to that obtained by irradiating at room temperature. Fig. 1a, curve 3, shows an intermediate stage of thermal bleaching where the crystal was warmed to the point at which the F

band started to bleach (determined visually), and then rapidly recooled to liquid nitrogen temperature for measurement. The *F* band is much diminished, the photoemission band developed and the 730 and 860 mμ peaks in evidence.

Acknowledgement—The authors thank the Defence Research Board of Canada for its support of this project with equipment, and a maintenance grant to J. P. S. PRINGLE.

REFERENCES

1. TOMPKINS F. C. and YOUNG D. A., *Proc. Roy. Soc.* A**236,** 10 (1956).
2. ROSENWASSER H., DREYFUS R. W. and LEVY P. W., *J. Chem. Phys.* **24,** 184 (1956).
3. CUNNINGHAM J. and TOMPKINS F. C., *Proc. Roy. Soc.* A**251,** 27 (1959).
4. *Inorganic Syntheses* Vol. I, p. 78 McGraw-Hill, New York and London (1939).
5. HEAL H. G., *Canad. J. Chem.* **37,** 979 (1959).
6. HEAL H. G., *Canad. J. Chem.* **31,** 91 (1953).
7. VICTOREEN J. A., *J. Appl. Phys.* **20,** 1141 (1949).
8. IVEY H. F., *Phys. Rev.* **72,** 341 (1947).
9. JACOBS I. S., *Phys. Rev.* **93,** 993 (1954).
10. *Landolt–Bornstein Tables*, (6th Ed.) I, 4, p. 981 Springer Verlag, Berlin, (1955).
11. CASTNER J. G. and KANZIG W., *J. Phys. Chem. Solids* **3,** 178 (1957).
12. DELBECQ C. J., SMALLER B. and YUSTER P. H., *Phys. Rev.* **111,** 1235 (1958).
13. SEITZ F., *Rev. Mod. Phys.* **18,** 384 (1946).
14. HEAL H. G., *Trans. Faraday Soc.* **53,** 210 (1957).
15. JACOBS P. W. M. and TOMPKINS F. C., *Proc. Roy. Soc.* A**215,** 254 (1952).
16. HERMAN R., WALLIS M. C. and WALLIS R. F., *Phys. Rev.* **103,** 87 (1956).

VOL. 15 1960

J. Phys. Chem. Solids Pergamon Press 1960. Vol. 15. pp. 270–290. Printed in Great Britain.

ION SIZE EFFECT AND MECHANISM OF ELECTROLYTIC RECTIFICATION

P. F. SCHMIDT,* F. HUBER and R. F. SCHWARZ

Philco Corporation, Research Div., Philadelphia, Pa.

(*Received* 26 *October* 1959; *revised* 22 *December* 1959)

Abstract—A review is given of previous theories of electrolytic rectification and it is shown that none of them are able to account for all of the phenomena observed.

Experimental results are then presented which show that both the magnitude of the cathodic current at a given applied field, and the activation energies for cathodic current flow are controlled by the size of the cation in solution, and by specific adsorption under applied cathodic bias. The existence of a surface barrier, height about 1 volt, thickness about 250 Å, has been proven.

The proposed band scheme for anodic oxide layers thus includes a steep surface barrier at the outer oxide interface, an ohmic contact at the valve metal/oxide interface, and traps in the oxide.

1. FORMULATION OF THE PROBLEM

ANODIC oxide films are known as excellent insulators, both when used as capacitors in an electrolyte under anodic bias, or when sandwiched between another metal contact.[1] In this latter case the polarity of the applied bias does not play a very important role.[1a]

Why then does the oxide layer become a much better conductor under cathodic bias when an electrolyte is used as the other contact?

The answer to this question will provide a better understanding of such important parameters as: the barrier at the metal/oxide interface; density and depth of trapping levels in the oxide; barrier at the oxide/metal contact interface.

2. PREVIOUS WORK ON THE MECHANISM OF CATHODIC CURRENT FLOW THROUGH OXIDE LAYERS

Any explanation of the mechanism of electrolytic rectification is rendered difficult by the large number of parameters which must be taken into account simultaneously. This is not surprising in view of the composite nature of the system (valve metal† /anodic oxide film/electrolyte), of the poor crystal structure and the exceedingly small thickness of the oxide film (10^{-6} to 3×10^{-5} cm), the high field strength in the film (close to or above the breakdown strength of the bulk dielectric) and the fact that the current changes from electronic to ionic at the oxide/electrolyte interface.

A review of previous theories is included not only in order to familiarize the reader with the complexity of the problem but also because the experimental results presented afterwards become much more meaningful when seen against this background.

It may be useful to first summarize pertinent information previously published in the literature:

(1) The system valve metal/anodic oxide/metal contact is electrically highly insulating, irrespective of the applied polarity.[1a] The currents are larger with cathodic bias (i.e. valve metal negative) than with anodic bias, but they remain in the $\mu A/cm^2$ range up to field strengths at which dielectric breakdown occurs. The work function of the metal contact does not play an important role,‡ the mechanical properties of the metal contact probably being of greater importance (e.g. high local fields at sharp points etc.).

* Present Address: Westinghouse Electric Corporation, Research Laboratories, Pittsburgh 35, Pa.

† Metals like Ta, Zr, Nb, Ti, Al are referred to as valve metals.

‡ This statement includes our own experiments with Na or K metal pressure contacts.

VOL. 15 1960

(2) If an aqueous electrolyte is used instead of a metal contact, then the cathodic current at field strengths of the order of 10^5 V/cm increases by many orders of magnitude over the cathodic current in the valve metal/anodic oxide/metal system; the anodic current remains small.[1e,2]

(3) The dielectric breakdown strength of these very thin films is considerably higher than that of the bulk material;[3] it is difficult for avalanches to reach critical size.

(4) Carefully prepared anodic oxide films do not show any pores even under the high magnification obtainable with an electron microscope.[4] They have also been found to be completely vacuum tight. Al_2O_3 windows 0·2 cm^2, 2800 Å thick, can withstand a pressure difference of 0·14 atm without leaking.

(5) Capacitance measurements[5] have shown that there is at least one region of increased conductivity in the oxide.

(6) Illumination of anodic oxide films with light of suitable wave length (u.v. on Ta, visible light on Nb and InSb) produces an open circuit photovoltage of $\sim$ 1 V,* the valve metal being the negative pole.[6] A potential hill for electrons in the oxide film sloping down from the outer surface of the oxide towards the metal must therefore be postulated.

(7) Any very wide gap materials known to date contain numerous (electron or hole) traps; there is no reason to postulate their absence in anodic oxide films.

(8) The anodic leakage currents of all electrolytic rectifiers tested so far obey a log $i \propto \sqrt{(F)}$ relationship, as first pointed out by VERMILYEA[7].

(9) The photocurrent on Ta/Ta_2O_5, and also on other valve metal/anodic oxide systems, shows a considerable inertia, i.e. it increases resp. decreases slowly with time; this points to trapping effects.[6a,b]

Previous theories

(a) VAN GEEL[8] postulated that oxygen ions are removed from the oxide lattice under cathodic bias, thus converting the oxide into an *n*-type semiconductor with increased conductivity.

This mechanism clearly involves migration of oxygen ions from lattice positions, and over a considerable distance.

VAN GEEL's conclusions are in part based upon a.c. experiments, in which the oxide showed rectification up to frequencies of 5000 c/s. It seems hardly possible that the large oxygen ions of such refractory materials as Al_2O_3 or SiO_2 could be sufficiently mobile at room temperature for this mechanism to apply, even when allowing for the large electric fields usually applied in a.c. experiments (under d.c. cathodic bias the current becomes excessively large already at a few per cent of the forming voltage, whereas it is usually assumed that ionic current flow is quite negligible at 90 per cent of the forming voltage). A further difficulty of this model is that if the large oxygen ions can move towards the electrolyte side under cathodic bias, then the small metal ions should move towards the metal side, still leaving most of the oxide in a stoichiometric state.

Further convincing arguments against VAN GEEL's model are provided by the experiments described below. It was found that the passage or blocking of cathodic current in liquid SO_2 solutions depends on the size of the cation present. Particularly striking is the fact that if both small and large cations are present in solution simultaneously, the current is determined by the larger one, i.e. it remains small.

(b) DECKER and URQUHART[9] in explaining the current hysteresis effects observed in a.c. experiments, suggested collision ionization in the oxide, causing formation of bound holes located mostly at the oxide/electrolyte interface. A steady state is reached when the number of recombinations equals the number of holes generated by collision ionization.

It is known from other experiments by VAN GEEL[10] that light flashes occur under large a.c. bias both during the cathodic and during the anodic cycle.

Broad area luminescence of anodic oxide films under full forming voltage, as well as tiny sparks in the oxide above a certain critical anodic voltage are well known phenomena.[11] No steady state luminescence during cathodic current flow, even at very large current densities, has ever been observed,

* Actually, the magnitude of the photovoltage is a function of time passed since the anodic bias was applied.

provided an aqueous electrolyte is used as the other contact. One may therefore conclude that collision ionizations under d.c. cathodic bias in aqueous solution are not numerous enough to produce perceptible luminescence in the visible. This is in agreement with the fact that the field in the oxide in this case is much lower.

(c) VERMILYEA[12] communicated results of probing a Ta/Ta_2O_5 film with a fine needle; he found large variations in resistance depending on the position and size of the needle. He also claimed that at the spots of low resistance hydrogen bubbles formed during cathodic current flow, and hence concluded that rectification occurs at singularities in the oxide film, which were identified with impurities originally present in the Ta metal at the same position. However, no evidence was presented to show that only the cathodic, and not also the anodic leakage current, is flowing through these weak spots. They may define the active area of the oxide film, but they do not necessarily constitute a mechanism of rectification. The method of investigation—with a fine needle—is unreliable in view of the high fields at a sharp point.[13] It can also be shown that the hardness of the underlying metal or the mechanical stress in the oxide are of great importance.*

Evolution of hydrogen bubbles at certain spots also occurs on an oxide film thermally prepared in pure oxygen on highest purity Si, where agglomeration of impurities is known not to occur. Furthermore, the number of sites at which hydrogen bubble evolution occurs increases with increasing current density. These spots may be locations at which formation of hydrogen bubbles from molecular hydrogen can occur easily. They are not necessarily related to the mechanism of electronic current flow through the oxide. These objections have also been raised by Dutch authors.[14]

Finally, cathodically sputtered Ta, in which the impurities are presumably statistically dispersed, behaves in just the same manner as a Ta sheet with regard to cathodic current flow (compare below).

* It is possible to press a steel needle with considerable force against a Si/SiO_2, or Ge/GeO_2 electrode formed to 100 V with 100 V applied across the oxide film, without causing a large current to flow. Substitution of Ta/Ta_2O_5 electrode under the same conditions would result in immediate dielectric breakdown.

(d) SMITH[15] proposed a mechanism according to which the electrolyte injects holes into the valence band of the oxide; these holes are supposed to flow all the way across to the metal interface, the Fermi level of the metal being half way between valence and conduction band of the oxide.

This mechanism is not in agreement with the fact that cathodic current flow of the system (5Λ cm) p-Si/SiO_2/aqueous electrolyte is greatly impeded compared to the system n-Si/SiO_2/aqueous electrolyte. With negative bias applied to the p-type Si, the band at the surface can swing down, but by not more than $\sim$ 1 eV. If the swinging down of the band on p-Si were to block the injection of holes from the valence band of the oxide one would have to postulate that the tops of the valence bands in the oxide and in the p-Si are originally separated by not more than 1 eV.

The gap of Si is $\sim$ 1·1 eV, the gap of SiO_2 about 10 eV. Postulating that the curvature of the bands inside the p-Si blocks the current therefore places the conduction band of the SiO_2 about 9 eV above the Fermi level in the Si. This is in disagreement with the fact that the SiO_2 film at the Si/SiO_2 interface must be assumed to be either an intrinsic semiconductor (i.e. insulator) or an n-type semiconductor due to excess metal in the film near the Si/SiO_2 interface.

One could, however, postulate that the bands inside the oxide swing down, i.e. that there is an ohmic contact between the two conduction bands. This curvature of the bands in the oxide would block hole transfer from the oxide to the p-Si (or to a metal), but would allow for current flow by recombination between holes which have arrived near the interface, and electrons injected by the metal (or by n-Si) into the oxide. The difficulty with this model is to explain the absence of visible luminescence by electron-hole recombination in such wide gap materials even at large current densities.

SMITH's model also does not provide an obvious explanation for the experiments with the system Ta/Ta_2O_5/electrolyte, in which the cathodic current increases by a factor of $\sim 10^3$ after etching off a thin surface layer (250 Å) of the oxide film. (Compare below.)

(e) KOBAYASHI[16] postulated the existence of a p–i–n junction inside the oxide from the similarity in variation of capacitance with applied bias to that

VOL. 15 1960

of a *p–i–n* junction in silicon. However, it is not necessary to postulate the existence of a (well conductive) *p*-region in order to explain the results; an *i–n* transition would yield very similar *Cf*(V) curves.

Furthermore, this model does not explain the difference between the Ta/Ta_2O_5/electrolyte and the Ta/Ta_2O_5/metal contact system.

(f) YOUNG[17] postulated that microfissures develop in a Ta_2O_5 film under cathodic bias due to H_2 evolution and that the so-called "after-effect" (i.e. the increase of current with time at constant voltage) is due to cracking of the oxide. Microfissures are thus supposed to contribute to the magnitude of the cathodic current, but are not claimed to be necessarily the mechanism of rectification.

Cracking of the oxide is probably limited to a few systems only. A Ta_2O_5 film prepared under certain conditions can be peeled off the metal very easily. Other oxide films (SiO_2, TiO_2) adhere very tenaciously to the valve metal. We have also seen a Ta/Ta_2O_5 film formed to 300 V which did not show any hysteresis at all.

(g) Based on preliminary experiments with valve metal/anodic oxide film systems in liquid SO_2, SCHMIDT[18] postulated that in aqueous solution protons penetrate into the oxide film, converting it in one way or the other into a semiconductor. Further work has now shown that penetration of cations into the oxide film is unlikely but that the size of the cation adsorbed onto the oxide surface controls the magnitude of the cathodic current.

3. SOME GENERAL REMARKS

The problem of electronic current flow through insulating oxide layers will be treated here using the same concepts as are applied to semiconductors or dielectrics of good crystal perfection. Anodic oxide films are either amorphous or very poorly crystalline. Enough work on glasslike semiconductors,[19] however, is now available to show that general semiconductor concepts apply also to amorphous materials, even if quantities like mobility, activation energies for conduction, lifetimes of minority carriers, etc., must be given statistical significance only. Applying these terms to anodic oxide films should therefore not be regarded as unusual.

During the course of this work it became clear that the cathodic current flow is a co-operative phenomenon, the conductance of the oxide depending on the size of the cation in the solution. In aqueous solution the large effects due to the smallest cation—the proton—masks the effects due to other cations. No protons are present in liquid SO_2 and the effect of ion size can be conveniently studied in this solvent by going through the series LiI–NaI–KI–RbI (only the iodides and thiocyanates of the alkali metals are sufficiently soluble in liquid SO_2).

The different polarization of the surrounding medium by ions of different size and/or different electron shell configuration is a well known effect in crystal chemistry; it is also effective in determining the stability of multiply charged cations in a given solvent. The presence of this effect in surface chemistry or surface physics is not really surprising but seems not to have been studied before except in some work on photoelectric cathodes.[20]

When considering surface effects due to the electrostatic field of the individual ions it is clearly necessary to use an atomistic point of view. The lack of relationship between applied voltage and field acting across the interface can otherwise become quite confusing.

4. EXPERIMENTAL

Fig. 1 is a schematic of the apparatus used for the measurements taken in liquid SO_2 (or NH_3). The SO_2 gas is first dried by passing over silica gel, and then condensed in a Pyrex glass vessel immersed in a alcohol/dry ice cold bath. The SO_2 is then re-distilled into the measuring cell. Tests for H_2O in the cell with cobalt thiocyanate were negative.[21]

Addition on purpose of small quantities of H_2O to the SO_2 did not affect the electric measurements; the water is apparently not ionized under the given conditions.

The different alkali iodides used were dried by heating for 1 hr at 150°C in the measuring cell under reduced pressure ($\sim 0{\cdot}1$ mm Hg). Sufficient SO_2 was then condensed into the measuring cell to arrive at a $0{\cdot}01$ N concentration of the alkali iodides. One side arm of the measuring cell was constructed in such a way as to serve as a conductivity cell, and the (relative) conductivities of the solutions could be measured before and during the course of an experiment. The resistivities of the various solutions at the indicated temperature are shown in Table 1. The potential of the cathode (e.g. Ta/Ta_2O_5 or Zr/ZrO_2) was measured against an Ag/AgI reference electrode* placed in close proximity to the sample; no effect on the potential of the distance between the reference electrode and the oxide coated cathode was noticed.

* We are indebted to Dr. P. RUETSCHI, Electric Storage Battery Co., Yardley, Pa., for this suggestion.

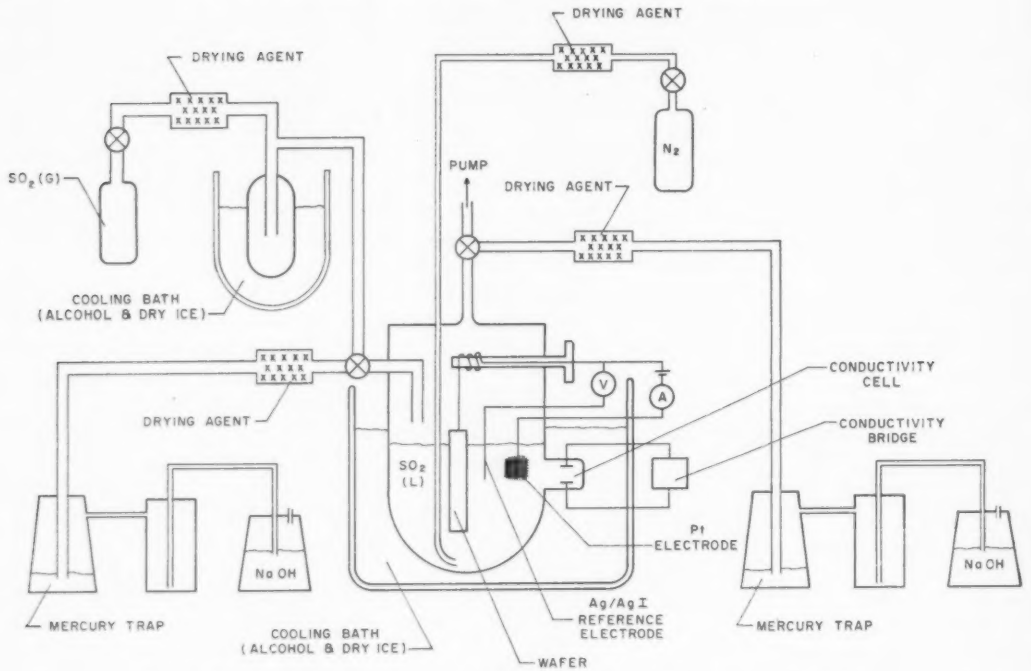

FIG. 1. Sketch of the apparatus used for measurements in liq. SO_2 (or liq. NH_3).

Table 1. *Resistivity of liquid* SO_2 *and liquid* NH_3 *electrolytes measured at* $-40°C$; *of* N, N-*dimethylformamide*: $+25°C$

Electrolyte	Specific resistivity ($k\Omega$cm)
liquid SO_2+0·01 N LiI	2·5
liquid SO_2+0·01 NaI	8·0
liquid SO_2+0·01 KI	2·5
liquid SO_2+0·01 RbI	2·5
liquid SO_2+0·01 NaSCN	20·0
liquid SO_2+0·01 KSCN	4·0
liquid NH_3+0·1 N NH_4NO_3	0·3
N, N-dimethylformamide +0·1 N $NaNO_3$	0·4

The potential of the sample during experiments in aqueous solution was measured against a H_2/platinized Pt electrode dipping into the same electrolyte in a separate vessel, kept at the same temperature, and connected to the sample via a Haber–Luggin capillary. Oxygen was carefully excluded from the cathode compartment in the measurements. In the few experiments performed in liquid NH_3 the potential was measured vs. a Pt reference electrode.

Platinum gauze was used as the auxiliary electrode in all experiments.

The temperature of the cooling bath for the SO_2 experiments (alcohol and dry ice contained in a Dewar flask) was kept constant to $\pm 1°C$ by adding CO_2 or alcohol. The temperature inside the measuring cell varied even less due to thermal dampening by the glass cell.

The samples were suspended from a Pt wire and could be lowered into the electrolyte by means of a glass spindle.

Materials

All valve metals with the exception of transistor grade *n*-type Si (produced at Philco) were supplied by A. D. Mackay, Inc., New York.

The spectroscopic analysis of the metals was as shown in Table 2.

The Li, Na, and K iodides were reagent grade, supplied by Merck & Co.; RbI, reagent grade, supplied by Fisher Scientific Co. Metal sheet, 10 mils thick, was mostly used for the electrodes. The edges of the wafers were smoothed by chemical etching, and the anodic leakage current was found to be proportional to the area exposed to the electrolyte.

The electric power was supplied by commercial 45 V

Table 2

	Ta	Zr*	Ti	Nb
Al			0·0X high	
Cu		0·000X high	0·00X	0·00X low
Fe		0·X low	0·X low	
Mn			0·0X high	
Mo			0·X high	
Si	not detected		0·X low	
Ti			major	
Zr		major		
Ta	major			
Nb				major

* Hf was detected but no estimate was made because of lack of sensitivity values.

batteries, and the voltage was varied by means of a potential divider. Voltages were measured with a Keithley electrometer, model 210, and currents with a RCA ultrasensitive microammeter WV-84B.

Reproducibility

Because the magnitude of the cathodic current at a given potential is a function of the anodic leakage current[22] to which the sample has been formed, the reproducibility of the cathodic J–V curves depends on the reproducibility of the anodic leakage current; the latter is rather poor (perhaps ± 10 per cent from one sample to the next*). This inaccuracy, however, does not seem to affect the characteristic shape of the curves much but only introduces a parallel shift along the current axis.

The reproducibility of the activation energies, i.e. of the slope of the line drawn through a large number of points, was quite satisfactory (about ± 5 per cent). The individual points, on the other hand, showed considerable scatter.

At large current densities or large applied voltages there occurs a slow drift of the current (usually to large values). The activation energies were therefore measured at current levels where this phenomenon is not too disturbing, and the J–V curves at the largest current densities were taken rapidly.

5. RESULTS

(1) In liquid SO_2 the cathodic current of all valve metal/anodic oxide systems tested, i.e. Ta/Ta_2O_5, Zr/ZrO_2, Nb/Nb_2O_5, Si/SiO_2, and Ti/TiO_2† depends on the size of the cation, the smaller cation giving the larger current at elevated field strengths. At low field strengths the picture is reversed, the larger cation then giving the larger current.

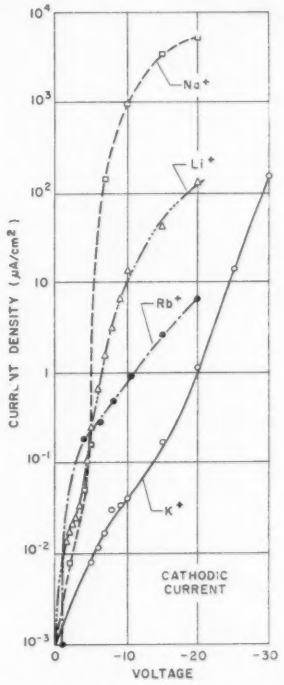

FIG. 2. Cathodic I–V characteristics of a Ta/Ta_2O_5 electrode in liq. SO_2 at $-60°C$, going through the series LiI–NaI–KI–RbI. Ta/Ta_2O_5 formed to 50 V.

Fig. 2 shows the cathodic I–V characteristic of Ta/Ta_2O_5 (formed to 50 V) in liquid SO_2 at $-60°C$ going through the series LiI–NaI–KI–RbI. The current with Na^+ ions is 4–5 orders of magnitude larger in the high field region than with K^+ ions. There is a double inversion as to cation size; the curve for Li^+ lies between that for Na^+ and K^+, and the Rb^+ curve lies above the K^+ curve. At low field strengths, however, both the Na^+ and the Li^+ curve are crossed by the Rb^+ curve. This crossover is seen more clearly in Fig. 3 where only

* Stopping the forming at the same leakage current but after different lengths of time for different samples is not a justified procedure.

† Al/Al_2O_3 is very quickly attacked by liquid SO_2 and cannot be tested reliably.

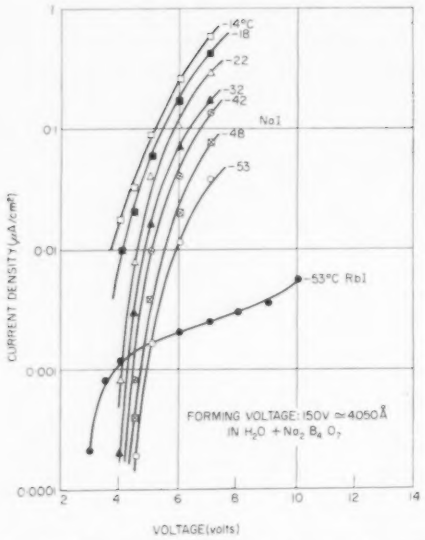

FIG. 3. Cathodic *I–V* characteristics of a Zr/ZrO_2 electrode in liq. SO_2+0·01 N NaI as a function of temperature, and in liq. SO_2+0·01 N RbI at −53°C. Zr/ZrO_2 formed to 150 V.

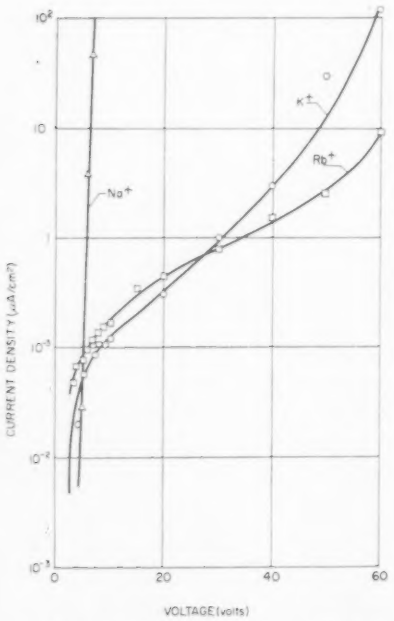

FIG. 4. Cathodic *I–V* characteristics of a Ta/Ta_2O_5 electrode in liq. SO_2 at −40°C with different cations present (Na^+, K^+, Rb^+). Ta sputtered and formed to 60 V at 105°C, oxide thickness ~ 2000 Å.

the Na^+ and the Rb^+ curves are shown, and where the scale is larger. In Fig. 4 the crossover of the K^+ and Rb^+ curves at high field strengths is shown.

It must be stressed, however, that the cathodic *I–V* characteristic as shown in Fig. 2 is valid only for a certain temperature region. As will be shown in the next paragraph, the cathodic current flow with small cations present has a higher apparent activation energy, so that at very low temperatures

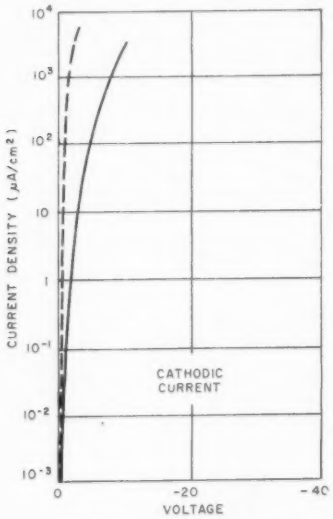

———— *n*-Si, Solvent liquid NH_3, electrolyte HN_4NO_3 (−50°C).
– – – – –Ta, solvent liquid NH_3, electrolyte NH_4NO_3 (−40°C).

FIG. 5. Cathodic *I–V* characteristics of valve metal electrodes in liq. $NH_3+NH_4NO_3$. Left curve: Ta/Ta_2O_5 formed to 200 V in N-methylacetamide+0·04 N KNO_3; measured in liq. NH_3+0·1 N NH_4NO_3 at −40°C. Right curve: *n*-Si/SiO_2 formed to 200 V in N-methylacetamide+0·04 N KNO_3; measured in liq. NH_3+0·1 N NH_4NO_3 at −50°C.

the picture would be reversed, unless there were a change in the slope of the log i–$1/T$ curves at the very low temperatures. Due to the limitation imposed by the freezing point of the SO_2 this question could not be investigated experimentally.

Fig. 5 shows the cathodic *I–V* characteristics of Ta/Ta_2O_5 and of *n*-Si/SiO_2 in liquid ammonia. The currents are decidedly larger than in SO_2+NaI and begin to approach those observed in aqueous solution at the same field strength. The difference

between the Ta/Ta_2O_5 and the n-Si/SiO_2 curves is, at least in part, due to voltage drops across the base contact and across the bulk of the n-Si. If p-Si instead of n-Si had been used, the current would have been blocked by the absence of free electrons in the p-Si; the higher the resistivity of the p-Si, i.e. the thicker the surface space charge region, the higher

$$\text{Rate} \propto \text{current} = A \exp -\left(\frac{W-BF}{kT}\right)^{*}$$

is large in the case of small cations (Li^+, Na^+), and small in the case of large cations (K^+, Rb^+). The same trend (i.e. small cation = H^+, large E, large current) continues to aqueous solutions.

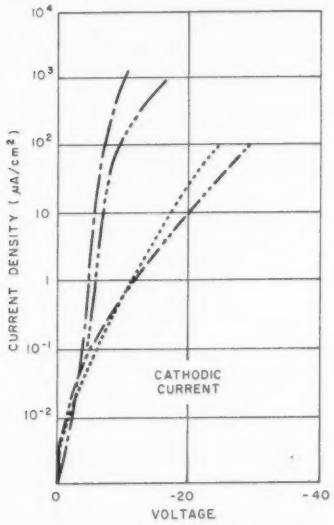

—— · —— Ta, solvent liquid SO_2, Electrolyte NaI
—— -- —— Ta, solvent liquid SO_2, electrolyte NaSCN
..... Ta, solvent liquid SO_2, KI.
— — · — · — Ta, SO_2, KSCN.

FIG. 6. Cathodic I–V characteristics of a Ta/Ta_2O_5 electrode in liq. SO_2 with different anions (I^- resp. SCN^-) present, measured at −40°C. Ta/Ta_2O_5 formed to 50 V.

the voltage that can be applied without causing current to flow.

Fig. 6 shows that there is a small effect due to the anions; the curves for NaI and NaSCN, and for KI and KSCN do not coincide. The effect is not very large, however, and has not been investigated in more detail. It is probably caused by competition of the various ions and molecules for adsorption sites on the Ta_2O_5.

(2) The apparent activation energies for cathodic current flow in liquid SO_2 (i.e. the quantity $E = W-BF$ in the Arrhenius equation)

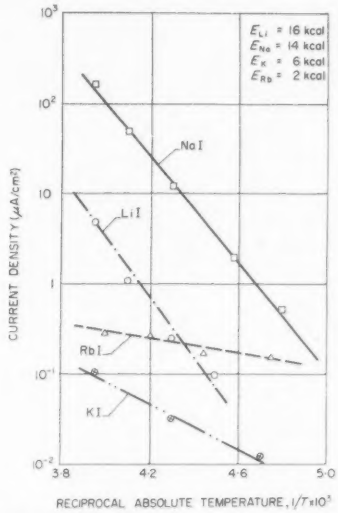

FIG. 7(a). Apparent activation energy for cathodic current flow of a Ta/Ta_2O_5 electrode in liq. SO_2 with cations of different size. Ta/Ta_2O_5 formed to 50 V. Cathodic field strength $9{\cdot}0 \times 10^5$ V/cm.

Fig. 7(a) shows the apparent activation energies in the series Li^+–Na^+–K^+–Rb^+. The graph shows convincingly that much higher activation energies are connected with much larger rates. Something unusual must therefore have happened in the frequency factor "A" of the Arrhenius equation. It is known that the "compensation law"[23] applies in the case of electron emission; however, this would only yield a current more or less independent of activation energy W, not a current larger by several orders of magnitude in spite of a much larger activation energy.

The only factors lumped into the constant "A" which could account for such an increase of rate with increase in W are the change in entropy ΔS,

* A = Frequency factor; W = Activation energy at zero applied field; B = Constant; F = Field; k = Boltzmann constant; T = abs. temperature.

and the change in the activity of the reacting species. For electrochemical reactions it is known that ΔS in a series of similar reactions (e.g. current with small and with large cations) does not change by more than 3–4 units, whereas a very much larger value of ΔS would be required to explain the phenomenon. One is thus led to assume a

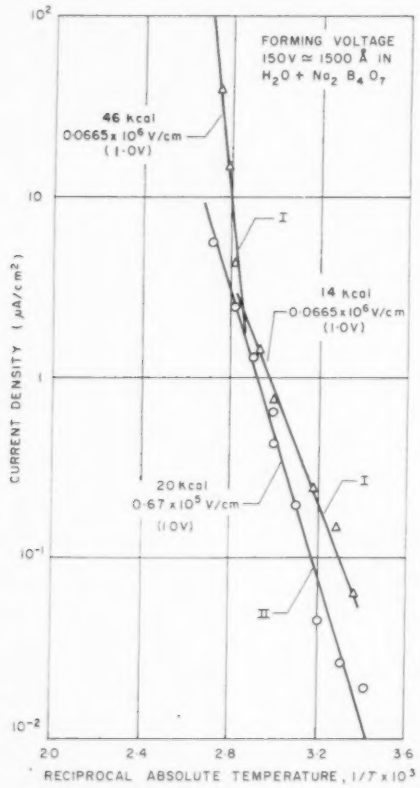

FIG. 7(b). Apparent activation energy for cathodic current flow of a Ta/Ta_2O_5 electrode in (I) alkaline and in (II) acidic solution.

change in the activity of the reacting species, i.e. of the electron.

The apparent activation energies in aqueous solution are larger than those in liquid SO_2. It is, however, very remarkable that there is a pronounced difference in the log i vs. $1/T$ curve of the Ta/Ta_2O_5 system in alkaline and in acidic solution. At elevated temperatures the apparent activation energy in acidic solution is less than in alkaline solution, and there is no break in the curve in acidic solution, as is observed in alkaline solution (see Fig. 7b); in N, N-dimethylformamide (Table 3, No. 8) and with aquadag (Table 3, No. 9) or MnO_2 (Table 3, No. 10) contact (compare below).

(3) At high field strength a constant activation energy independent of F, is reached. The small cations again have a larger value of the field independent activation energy than do the large cations. The limiting value of the activation energy in aqueous solutions cannot be observed because the current increases too much, damaging the oxide.

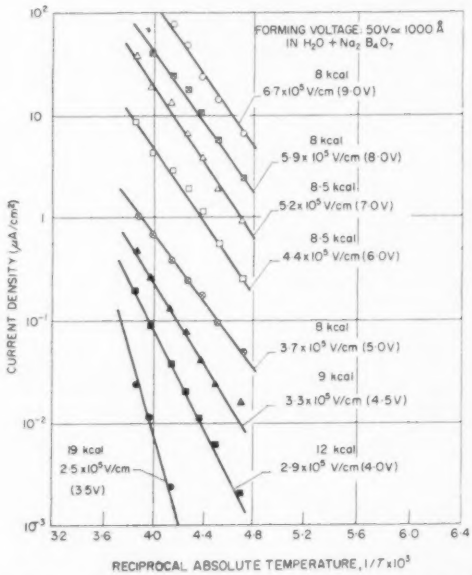

FIG. 8. Apparent activation energies for cathodic current flow in the system Zr/ZrO_2/liq. SO_2+0·01 NaI as a function of field strength. Zr/ZrO_2 formed to 50 V.

Figs. 8 and 9 show the effect for the system Zr/ZrO_2/liquid SO_2+0·01 N NaI. It can be seen that the (apparent) activation energy becomes independent of field strength the sooner the thicker the oxide film (i.e. the higher the original forming voltage). In fact it seems that the dependence on field strength stops at about the same applied bias, independent of oxide thickness.

Exactly the same effect is observed on Ta/Ta_2O_5, (in Table 3, No. 1) on Nb/Nb_2O_5 (in Table 3, No. 2) and on Ti/TiO_2 (Table 3, No. 3).

(4) Sputtered and then anodically formed

Table 3. Apparent activation energies of cathodic current flow

No.	System	Oxide thickness d (cm)	Temperature range ($1000/T$°K)	Cathodic field strength (V/cm)	Apparent activation energies (kcal/mole)	Current density at the field strength shown (μA/cm^2)	
						Smallest	Largest
(1a)	Ta/Ta_2O_5/liq. SO_2+0·01 N NaI. Oxide formed in sat. borate solution	5×10^{-6}	4·27–3·96	$7{\cdot}0\times10^5$	25	$2{\cdot}7\times10^{-4}$ at $1000/T=f=4{\cdot}69$	
		5×10^{-6}	4·69–3·96	$8{\cdot}0\times10^5$	17		
		5×10^{-6}	4·69–3·96	$9{\cdot}0\times10^5$	14		
		5×10^{-6}	4·69–3·96	$1{\cdot}0\times10^6$	12		
		5×10^{-6}	4·69–3·96	$1{\cdot}6\times10^6$	12		
		5×10^{-6}	4·69–3·96	$2{\cdot}0\times10^6$	11		2·0 at $f=3{\cdot}96$
(1b)	Same as (1a)	$1{\cdot}5\times10^{-5}$	4·07–3·89	$2{\cdot}0\times10^5$	37	$1{\cdot}2\times10^{-4}$ at $f=4{\cdot}41$	
		$1{\cdot}5\times10^{-5}$	4·41–3·89	$2{\cdot}4\times10^5$	31		
		$1{\cdot}5\times10^{-5}$	4·62–3·89	$2{\cdot}6\times10^5$	22		
		$1{\cdot}5\times10^{-5}$	4·80–3·89	$3{\cdot}0\times10^5$	17		
		$1{\cdot}5\times10^{-5}$	4·80–3·89	$3{\cdot}3\times10^5$	13		
		$1{\cdot}5\times10^{-5}$	4·80–3·89	$3{\cdot}6\times10^5$	12		
		$1{\cdot}5\times10^{-5}$	4·80–3·89	$4{\cdot}0\times10^5$	11·5		
		$1{\cdot}5\times10^{-5}$	4·80–3·89	$4{\cdot}6\times10^5$	11·5		5·8 at $f=3{\cdot}89$
(1c)	Oxide formed at 98°C in 2 per cent aqueous HNO_3. 20 Å/V forming voltage assumed. Oxide is still amorphous	2×10^{-5}	4·53–3·96	$1{\cdot}5\times10^5$	20	$1{\cdot}5\times10^{-4}$ at $f=4{\cdot}53$	
		2×10^{-5}	4·80–3·96	$2{\cdot}0\times10^5$	14·5		
		2×10^{-5}	4·80–3·96	$2{\cdot}5\times10^5$	12		
		2×10^{-5}	4·80–3·96	$4{\cdot}0\times10^5$	11		
		2×10^{-5}	4·80–3·96	$5{\cdot}0\times10^5$	11		8×10^{-1} at $f=3{\cdot}96$
(1d)	Same as (1a)	3×10^{-5}	4·62–3·89	$0{\cdot}7\times10^5$	24	$2{\cdot}0\times10^{-4}$ at $f=4{\cdot}62$	
		3×10^{-5}	4·80–3·89	$1{\cdot}0\times10^5$	21		
		3×10^{-5}	4·89–3·89	$1{\cdot}3\times10^5$	20		
		3×10^{-5}	4·89–3·89	$2{\cdot}3\times10^5$	15		
		3×10^{-5}	4·89–3·89	$2{\cdot}6\times10^5$	13		
		3×10^{-5}	4·89–3·89	$3{\cdot}3\times10^5$	12·5		
		3×10^{-5}	4·89–3·89	$5{\cdot}0\times10^5$	11·5		
		3×10^{-5}	4·89–3·89	$6{\cdot}6\times10^5$	12·0		10 at $f=3{\cdot}89$
(2)	Nb/Nb_2O_5/liq. SO_2+0·01 N RbI. Oxide formed in sat. borate solution	3×10^{-5}	4·69–4·02	8×10^3	13	$1{\cdot}2\times10^{-2}$ at $f=4{\cdot}69$	
		3×10^{-5}	4·69–4·02	$1{\cdot}7\times10^4$	11		
		3×10^{-5}	4·69–4·02	$3{\cdot}0\times10^4$	10		
		3×10^{-5}	4·69–4·02	$5{\cdot}0\times10^4$	9		
		3×10^{-5}	4·69–4·02	$1{\cdot}0\times10^5$	8		
		3×10^{-5}	4·69–4·02	$1{\cdot}7\times10^5$	8		
		3×10^{-5}	4·69–4·02	$2{\cdot}66\times10^5$	8		$3{\cdot}0\times10^2$ at $f=4{\cdot}02$
(3)	Ti/TiO_2/liq. SO_2+0·01 N NaI	$\sim6{\cdot}6\times10^{-6}$ (formed to 22 V)	4·69–4·02	4×10^4	16	$1{\cdot}5\times10^{-2}$ at $f=4{\cdot}69$	
			4·69–4·02	7×10^4	13		
			4·69–4·02	$1{\cdot}5\times10^5$	10		
			4·69–4·02	3×10^5	6·5		
			4·69–4·02	$4{\cdot}5\times10^5$	6·5		
			4·69–4·02	$6{\cdot}0\times10^5$	6·5		
			4·69–4·02	$7{\cdot}5\times10^5$	6·5		$7{\cdot}0\times10^2$ at $f=4{\cdot}02$

[*Continued overleaf*

Table 3. (Contd.)

No.	System	Oxide thickness d (cm)	Temperature range (1000/T°K)	Cathodic field strength (V/cm)	Apparent activation energies (kcal/mole)	Current density at the field strength shown (μA/cm^2)	
						Smallest	Largest
(4)	Ta/Ta_2O_5/liq. SO_2+0·01 N NaI. Ta sputtered and formed at 105°C in a mixture 1 : 2 : 3 by weight of oxalic acid, water and ethylene glycol	$1·2\times10^{-5}$ (formed to 60 V)	4·69–4·02	$4·2\times10^5$	18	3×10^{-2} at $f=4·35$	
			4·69–4·02	$5·0\times10^5$	15		
			4·69–4·02	$5·8\times10^5$	14		
			4·69–4·02	$6·6\times10^5$	12		
			4·69–4·02	$8·3\times10^5$	12		$1·4\times10^3$ at $f=4·02$
(5)	Ta/Ta_2O_5/liq. SO_2+0·01 N KI. Ta sputtered and formed as in No. 4	$\sim1·2\times10^{-5}$ (formed to 60 V)	4·74–3·97	$3·3\times10^5$	10	2×10^{-3} at $f=4·74$	
			4·74–3·97	$4·2\times10^5$	7		
			4·74–3·97	$8·4\times10^5$	5		
			4·74–3·97	$1·7\times10^6$	4		$5·5\times10^{-1}$ at $f=3·97$
(6a)	Ta/Ta_2O_5/liq. SO_2+0·01 N RbI. Ta sputtered and formed as in No. 4	$\sim6\times10^{-6}$ (formed to 30 V)	4·95–3·94	$1·7\times10^5$	6	$1·0\times10^{-3}$ at $f=4·95$	
			4·95–3·94	$3·3\times10^5$	5		
			4·95–3·94	$5·0\times10^5$	5		
			4·95–3·94	$8·3\times10^5$	5		
			4·95–3·94	$1·0\times10^6$	5		
			4·95–3·94	$1·3\times10^6$	4·5		
			4·95–3·94	$1·7\times10^6$	4·5		5 at $f=3·94$
(6b)	Same as (6a)	$\sim1·2\times10^{-5}$ (formed to 60 V)	4·70–3·95	$8·3\times10^4$	11	$1·0\times10^{-3}$ at $f=4·70$	
			4·70–3·95	$1·7\times10^5$	7		
			4·95–3·95	$4·2\times10^5$	6		
			4·95–3·95	$8·3\times10^5$	5		
			4·95–3·95	$1·7\times10^6$	4		
			4·95–3·95	$3·4\times10^6$	4		4 at $f=3·95$
(7a)	Ta/Ta_2O_5/saturated aqueous solution of $Na_2B_4O_7$. Oxide formed in saturated aqueous solution of $Na_2B_4O_7$	$1·5\times10^{-5}$	3·60–3·20	$0·1\times10^6$	11	6×10^{-3} at $f=3·60$	$4·1\times10^{-2}$ at $f=3·20$
		$1·5\times10^{-5}$	3·20–2·86	$0·1\times10^6$	40	$4·1\times10^{-2}$ at $f=3·20$	$5·2\times10^1$ at $f=2·86$
(7b)	Same as (7a), but oxide formed in 0·1 N aqueous H_2SO_4. (Anodic leakage current larger than in (7a))	$1·5\times10^{-5}$	3·60–3·20	$0·1\times10^6$	8	2·7 at $f=3·60$	11·5 at $f=3·20$
		$1·5\times10^{-5}$	3·20–2·98	$0·1\times10^6$	38	11·5 at $f=3·20$	$1·0\times10^3$ at $f=2·98$
(7c)	Same as (7a)	$1·5\times10^{-5}$	3·25–2·87	$6·7\times10^4$	14	$1·3\times10^{-1}$ at $f=3·25$	2·0 at $f=2·87$
		$1·5\times10^{-5}$	2·87–2·73	$6·7\times10^4$	46	2·0 at $f=2·87$	$4·0\times10^1$ at $f=2·73$
(7d)	Same as (7c)	$1·5\times10^{-5}$	3·41–3·18	$1·3\times10^5$	32	$1·3\times10^2$ at $f=3·41$	7×10^3 at $f=3·18$
(8)	Ta/Ta_2O_5/0·1 N solution of $NaNO_3$ in N, N-dimethylformamide. Oxide formed in sat. aqueous solution of $Na_2B_4O_7$	$1·5\times10^{-5}$	4·13–2·89	$6·6\times10^4$	6	$1·5\times10^{-1}$ at $f=4·13$	4·2 at $f=2·89$
		$1·5\times10^{-5}$	2·89–2·53	$6·6\times10^4$	34	4·2 at $f=2·89$	$1·2\times10^3$ at $f=2·53$
		$1·5\times10^{-5}$	4·49–3·45	$1·3\times10^5$	5	$6·3\times10^{-1}$ at $f=4·49$	7·0 at $f=3·45$
		$1·5\times10^{-5}$	3·45–2·93	$1·3\times10^5$	24	7·0 at $f=3·45$	$2·6\times10^3$ at $f=2·93$

VOL. 15 1960

No.	System	Oxide thickness d (cm)	Temperature range (1000/T°K)	Cathodic field strength (V/cm)	Apparent activation energies (kcal/mole)	Current density at the field strength shown (μA/cm^2)	
						Smallest	Largest
(9)	Ta/Ta_2O_5/aquadag; oxide formed in sat. aqueous solution of $Na_2B_4O_7$	$1{\cdot}5\times10^{-5}$	4·11–3·66	$6{\cdot}6\times10^{5}$	5·5	$4{\cdot}5\times10^{-4}$ at $f=4{\cdot}11$	$1{\cdot}4\times10^{-3}$ at $f=3{\cdot}66$
		$1{\cdot}5\times10^{-5}$	3·66–3·34	$6{\cdot}6\times10^{5}$	15·0	$1{\cdot}4\times10^{-3}$ at $f=3{\cdot}66$	$1{\cdot}5\times10^{-2}$ at $f=3{\cdot}34$
		$1{\cdot}5\times10^{-5}$	4·32–3·66	$1{\cdot}0\times10^{6}$	6·5	$1{\cdot}7\times10^{-3}$ at $f=4{\cdot}32$	$1{\cdot}4\times10^{-2}$ at $f=3{\cdot}66$
		$1{\cdot}5\times10^{-5}$	3·66–3·34	$1{\cdot}0\times10^{6}$	11·5	$1{\cdot}4\times10^{-2}$ at $f=3{\cdot}66$	$8{\cdot}4\times10^{-2}$ at $f=3{\cdot}34$
(10)	Ta/Ta_2O_5/MnO_2 commercial solid electrolytic capacitor. (Sprague Electric Co.) Method of fabrication unknown.	max. permissible d.c. anodic bias 35 V	4·57–3·55	6 V	4	$1{\cdot}2\times10^{-2}$ at $f=4{\cdot}57$	$8{\cdot}7\times10^{-2}$ at $f=2{\cdot}55$
			3·55–2·67	6 V	19	$8{\cdot}7\times10^{-2}$ at $f=3{\cdot}55$	$5{\cdot}7\times10^{2}$ at $f=2{\cdot}67$
				Anodic bias			
			4·57–3·92	35 V	4	$5{\cdot}2\times10^{-3}$ at $f=4{\cdot}57$	$2{\cdot}1\times10^{-2}$ at $f=3{\cdot}92$
			3·92–2·67	35 V	9	$2{\cdot}1\times10^{-2}$ at $f=3{\cdot}92$	4·1 at $f=2{\cdot}67$
(11)	Zr/ZrO_2/0·1 N solution of $NaNO_3$ in N, N-dimethyl formamide Oxide formed in sat. aqueous solution of $Na_2B_4O_7$.	$2{\cdot}0\times10^{-5}$	3·74–2·90	$5{\cdot}0\times10^{4}$	7	$2{\cdot}4\times10^{-3}$ at $f=3{\cdot}74$	$4{\cdot}2\times10^{-2}$ at $f=2{\cdot}90$
		$2{\cdot}0\times10^{-5}$	2·90–2·61	$5{\cdot}0\times10^{4}$	27	$4{\cdot}2\times10^{-2}$ at $f=2{\cdot}90$	1·9 at $f=2{\cdot}61$
		$2{\cdot}0\times10^{-5}$	3·74–2·96	$7{\cdot}5\times10^{4}$	7	$4{\cdot}0\times10^{-2}$ at $f=3{\cdot}74$	$5{\cdot}0\times10^{-2}$ at $f=2{\cdot}96$
		$2{\cdot}0\times10^{-5}$	2·96–2·61	$7{\cdot}5\times10^{4}$	27	$5{\cdot}0\times10^{-2}$ at $f=2{\cdot}96$	6·0 at $f=2{\cdot}61$
(12)	Ta/Ta_2O_5/liq. SO_2+0·01 N RbI+0·001 N NaI. Oxide formed in sat. aqueous solution of $Na_2B_4O_7$	$1{\cdot}5\times10^{-5}$	4·72–3·95	$2{\cdot}7\times10^{5}$	9	$1{\cdot}0\times10^{-4}$ at $f=4{\cdot}72$	
		$1{\cdot}5\times10^{-5}$	4·72–3·95	$5{\cdot}3\times10^{5}$	7		
		$1{\cdot}5\times10^{-5}$	4·72–3·95	$1{\cdot}0\times10^{6}$	7		
		$1{\cdot}5\times10^{-5}$	4·72–3·95	$1{\cdot}3\times10^{6}$	7		
		$1{\cdot}5\times10^{-5}$	4·72–3·95	$2{\cdot}0\times10^{6}$	5		
		$1{\cdot}5\times10^{-5}$	4·72–3·95	$2{\cdot}7\times10^{6}$	5		1·3 at $f=3{\cdot}95$
(13)	Ta/Ta_2O_5/liq. SO_2+0·01 N NaI. Oxide formed in 2 per cent aqueous HNO_3 at 98°C and is *crystalline*.	$\sim 2\times10^{-5}$	4·47–3·82	$1{\cdot}5\times10^{5}$	21	3×10^{-4} at $f=4{\cdot}72$	
		$\sim 2\times10^{-5}$	4·72–3·82	$2{\cdot}0\times10^{5}$	16		
		$\sim 2\times10^{-5}$	4·72–3·82	$2{\cdot}5\times10^{5}$	12		
		$\sim 2\times10^{-5}$	4·72–3·82	$4{\cdot}0\times10^{5}$	12		
		$\sim 2\times10^{-5}$	4·72–3·82	$5{\cdot}0\times10^{5}$	11		1·7 at $f=3{\cdot}82$
(14)	Ta/Ta_2O_5/sat. aqueous solution of $Na_2B_4O_7$. Oxide formed in the same solution	$1{\cdot}5\times10^{-5}$ Sample formed to an anodic leakage current of 0·2μA/cm^2	3·29–2·80	$1{\cdot}3\times10^{5}$	29	5·0 at $f=3{\cdot}29$	$4{\cdot}0\times10^{3}$ at $f=2{\cdot}80$
		$1{\cdot}5\times10^{-5}$ Sample formed to an anodic leakage current of 25·0μA/cm^2	3·60–3·21	$1{\cdot}3\times10^{5}$	30	16·0 at $f=3{\cdot}60$	$3{\cdot}6\times10^{3}$ at $f=3{\cdot}21$

Notes: All forming of the oxide films was done at room temperature, unless otherwise stated.

The following oxide thicknesses per volt forming voltage have been assumed in order to calculate the cathodic field strength from the relation V applied/d : Ta_2O_5 : 10 Å/V; ZrO_2 : 27 Å/V; SiO_2 : 4 Å/V; Nb_2O_5 : 22 Å/V; TiO_2 : 30 Å/V. The value for TiO_2 is open to doubt.

Ta/Ta_2O_5 electrodes behave in exactly the same manner as Ta sheet with regard to cathodic current flow. Sputtering should disperse any impurity agglomerations present in the original Ta sample. Thus no significant effect appears to exist which could be attributed to agglomeration in the Ta sheet (at least, so far as cathodic current flow with electrolyte contacts is concerned).

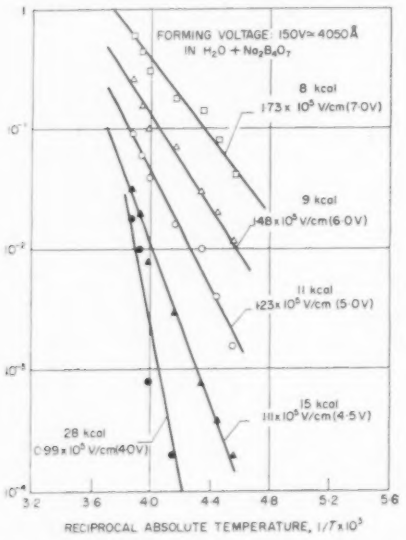

FIG. 9. Same as Fig. 8, but Zr/ZrO_2 formed to 150 V.

Table 3, Nos. 4, 5, 6 show the apparent activation energies for sputtered Ta/Ta_2O_5 in liquid SO_2 with cation size and film thickness as parameters.*

(5) The limiting cathodic activation energies are different for different metals in the same electrolyte. At lower field strengths the activation energies depend slightly on the solvent used for forming a given valve metal.†

Comparison of Figs. 8 and 9 and Table 3, No. 1 shows that the limiting activation energy in liquid SO_2+0·01 N NaI is 8 kcal for Zr/ZrO_2, and 11–12 kcal for Ta/Ta_2O_5.

(6) Ta/Ta_2O_5 shows a pronounced break in the slope of the log i vs. $1/T$ plot, the position of the break depending on the applied field strength. This effect was observed with aqueous electrolytes, N, N-dimethylformamide, and with MnO_2 or aquadag contacts. This break in the log i–$1/T$ curves is shown in Table 3, Nos. 7, 8, 9 and 10. It also shows up in the anodic log i–$1/T$ curve as shown in Table 3, No. 10. Zr/ZrO_2 shows a similar break at about the same temperature, as seen in Table 3, No. 11.

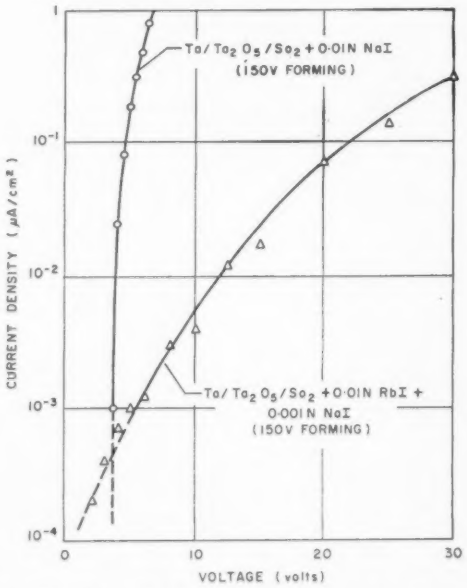

FIG. 10. Cathodic I–V characteristics of a Ta/Ta_2O_5 electrode in liq. SO_2 at −40°C with 0·01 N NaI (○) and with 0·01 N RbI+0·001 N NaI (△).

(7) With large cations in liquid SO_2 *at high applied fields*, violent current fluctuations and even light flashes can be observed if the oxide thickness exceeds a certain limit (about 2000 Å for Ta_2O_5); thinner oxide films do not show these fluctuations. With small cations in liquid SO_2 fluctuations are observed only at the largest current densities, and they are considerably damped as compared to the fluctuations with large cations. Apparently a fluctuating current component (of the avalanche type) is superimposed on a large non-fluctuating current component. No strong fluctuations occur in aqueous solutions.

* Sputtered Ta samples by courtesy of D. A. McLEAN, Bell Telephone Labs., Murray Hill, N.J.

† Since the oxide thickness at a given forming voltage can depend slightly on the electrolyte, this could also be a field effect.

VOL. 15 1960

(8) If both large and small cations are simultaneously present in liquid SO_2 (e.g. Na^+ and Rb^+), then the current as well as the activation energy are determined by the larger cation.

Fig. 10 and Table 3, No. 12 show this effect for a solution of 0·01 N RbI+0·001 N NaI in liquid SO_2.

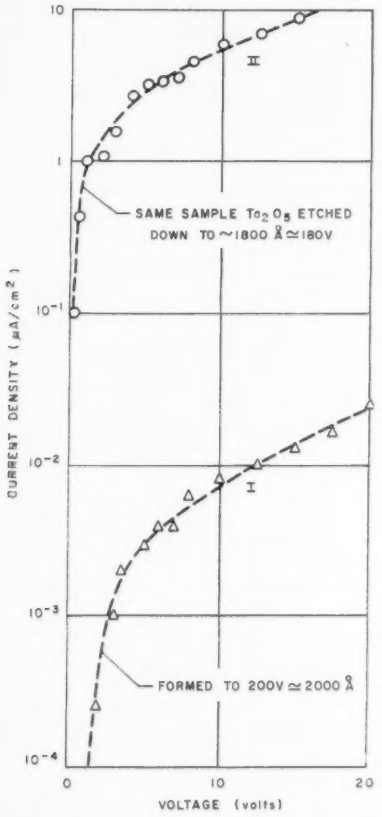

FIG. 11. Cathodic I–V characteristics of a Ta/Ta_2O_5 electrode in liq. SO_2+0·01 N RbI (I) before and (II) after slight etching of the electrode in HF. Etching removed an oxide layer ~ 200 Å thick, Ta/Ta_2O_5 formed originally to 200 V = 2000 Å.

For the comparison, the curve for 0·01 N NaI is also shown in Fig. 10.

If the RbI acted as an inert carrier electrolyte, the currents for 0·01 N NaI and 0·001 N NaI could certainly not be different by three powers of ten at the same field strength, as is actually the case. If RbI and NaI are present in equal concentration—0·01 N—then the current still follows the RbI curve, except that there are sudden violent current bursts, suggestive of desorption and adsorption phenomena. It must be concluded that the Rb^+ is preferentially adsorbed to the Ta_2O_5 surface and prevents Na^+ ions from coming in contact with the Ta_2O_5 surface.

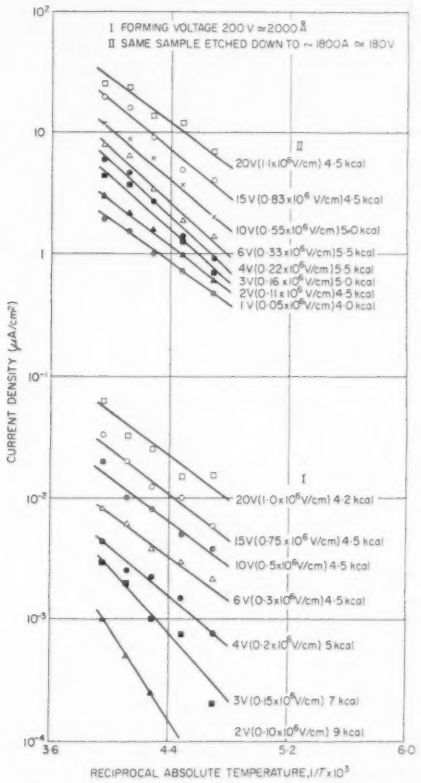

FIG. 12. Apparent activation energy for cathodic current flow in the system Ta/Ta_2O_5/liq. SO_2+0·01 N RbI (I) before and (II) after slight etching of the electrode in HF. Etching removed an oxide layer ~ 200 Å thick. Ta/Ta_2O_5 originally formed to 200 V = 2000 Å.

(9) As shown in paragraphs (1) and (8) of this Section, blocking of the cathodic current up to very large applied voltages occurs in the systems valve metal/anodic oxide/liquid SO_2+RbI.

The current increases by a factor of ~ 10^3 if a thin surface layer of the oxide is etched off in HF, but the characteristic shape of the curve does not

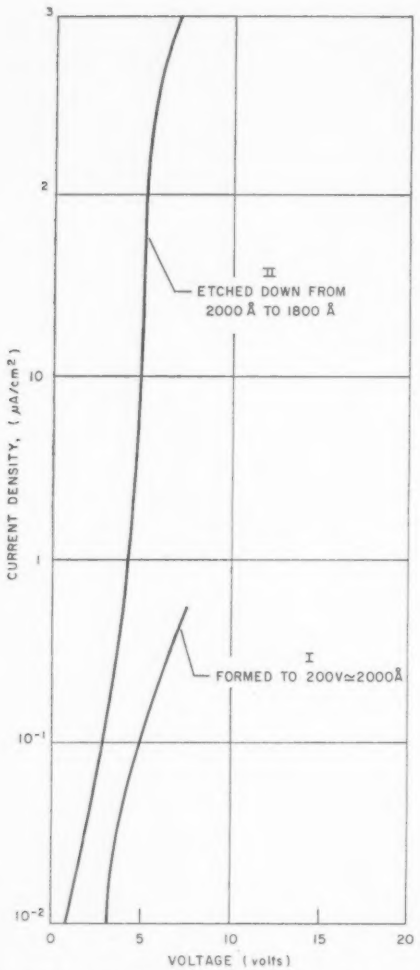

FIG. 13. Cathodic *I–V* characteristics of a Ta/Ta_2O_5 electrode in liq. SO_2+0·01 N NaI at −40°C (I) before and (II) after slight etching in HF (200 Å). Ta/Ta_2O_5 formed to 200 V.

change. The same effect is observed also in the case of Na^+ ions, or in aqueous solution.

Fig. 11 shows that the cathodic current in the system Ta/Ta_2O_5/liquid SO_2+0·01 N RbI increases by a factor of 10^3 in the flat region of the curves if the original oxide thickness of 2000 Å is reduced to 1800 Å by etching in dilute HF.* From the flatness of both curves it follows that the 10 per cent increase in field strength at the same applied bias does not play a significant role in this voltage range. At the very low voltages the field strength will be more important, and the change in shape of the upper curve in the low voltage region may at least in part be due to the reduced thickness of the oxide, i.e. to the higher field at the same applied voltage.

* After etching in HF, the sample was rinsed in water, then in alcohol, and then dried in air. The interference colors after etching were completely homogeneous.

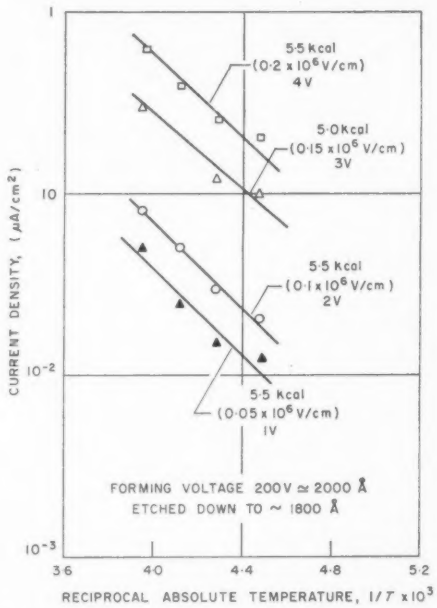

FIG. 14. Activation energy for cathodic current flow in the system Ta/Ta_2O_5/liq. SO_2+0·01 N NaI after slight etching in HF (200 Å). Ta/Ta_2O_5 formed to 200 V.

Fig. 12 shows the activation energies for cathodic current flow (I) before and (II) after removing an oxide layer of 200 Å with HF. The etched sample shows no field dependence of the activation energy.

Fig. 13 shows the cathodic *I–V* characteristic of the system Ta/Ta_2O_5/liquid SO_2+0·01 N NaI (I) before and (II) after removing an oxide layer of 200 Å with HF.

Fig. 14 shows the activation energy in the system Ta/Ta_2O_5/liquid SO_2+0·01 N NaI after etching (200 Å) in HF. Just as with Rb^+ ions, the activation energy has become independent of the field and has about the same numerical value as with

Rb^+ ions, but differs greatly from the value of the limiting activation energy of an unetched Ta/Ta_2O_5 electrode in liquid $SO_2+0{\cdot}01$ N NaI. Fig. 14 should be compared to Fig. 12 and Table 3, No. 1.

Fig. 15 shows the cathodic *I–V* characteristic of a Ta/Ta_2O_5 electrode in saturated borate solution

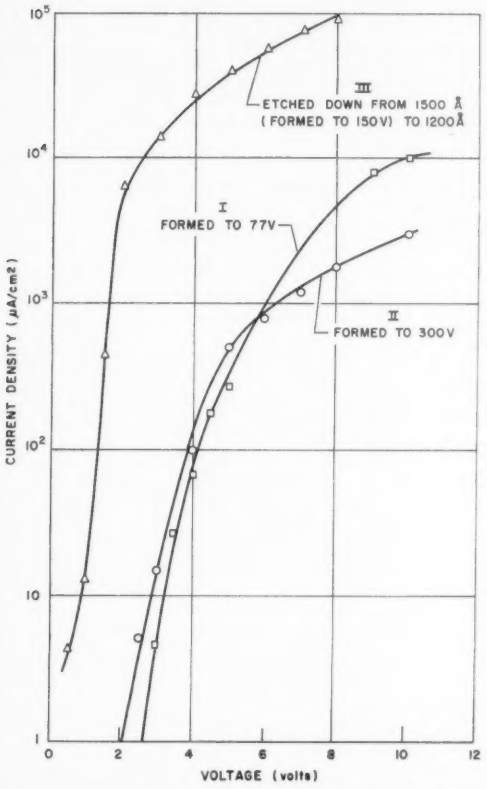

FIG. 15. Cathodic *I–V* characteristics of Ta/Ta_2O_5 electrodes in saturated borate solution. Samples I and II unetched, sample III slightly etched in HF (300 Å). Forming voltages: I = 77 V; II = 300 V; III = 150 V.

(formed to 150 V) after removing 300 Å of the oxide by etching in HF. For comparison, the cathodic *I–V* curves of two other Ta/Ta_2O_5 electrodes in saturated borate solution (forming voltages 77 and 300 V) are also shown in this graph. Also after slight etching in HF no visible luminescence is observed during d.c. cathodic current flow.

Fig. 16 shows the activation energies for cathodic current flow in the system $Ta/Ta_2O_5/0{\cdot}1$ N aqueous H_2SO_4 (I) before and (II) after etching in HF (300 Å). The activation energy after etching has decreased from 23 kcal to 8 kcal. Both curves do not show a break in the slope, as already pointed out in connection with Fig. 7(b).

The change in activation energy after etching in HF was determined only on Ta/Ta_2O_5 electrodes

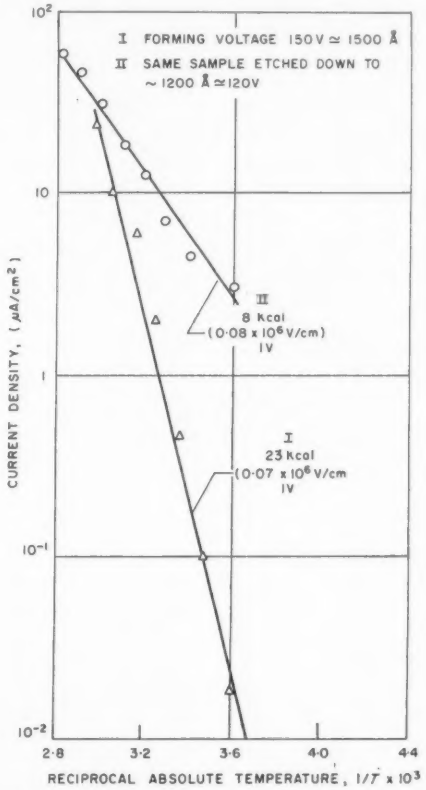

FIG. 16. Activation energies for cathodic current flow of a Ta/Ta_2O_5 electrode in $0{\cdot}1$ N H_2SO_4 (I) before and (II) after slight etching in HF (300 Å).

because the slopes of the log i vs. $1/T$ curves before etching are already rather low in the other systems (Zr/ZrO_2, Nb/Nb_2O_5, Ti/TiO_2), and because the currents after etching increase by a factor of $\sim 10^3$, which fact is less disturbing for the measurements if the initial leakage current is very low, as it is on Ta/Ta_2O_5.

(10) A photoeffect of 0·87 V at room temperature is observed with the system Ta/Ta_2O_5/electrolyte, the Ta being the negative pole. This

photo-effect disappears completely if a thin surface layer of the Ta_2O_5 is etched off with HF. Nb/Nb_2O_5 behaves in the same manner.

The Ta electrode in this experiment had been formed to 150 V, i.e. the film thickness was originally 1500 Å; etching with HF removed 300 Å, as shown by the interference colors. This result thus shows that the thickness of the surface barrier region is $\leqq$ 300 Å.

About 50 per cent of the photoeffect persists if only 150 Å are etched off.

(11) The open circuit potential in liquid SO_2 prior to cathodic current flow is independent of the cation size. The potential shifts somewhat after passage of current. Sodium ions give the largest current (at a given applied cathodic bias) and the largest subsequent shift in open circuit potential, as shown in Table 4.

Ta/Ta_2O_5 (formed to 50 V) in liquid SO_2+0·01 N NaI. Also on Ta/Ta_2O_5 in liquid SO_2+0·01 N RbI stirring (by means of bubbling He through the solution from directly underneath the sample) has practically no effect on the magnitude of the cathodic current; if the smallness of the current with Rb^+ ions present were due to a very small number of spots through which current can flow, then a large though very localized, i.r. drop should occur in the electrolyte, and stirring of the solution should produce an appreciable effect.

The current saturation at higher field strengths is therefore most likely due to phenomena inside the oxide, not in the Nernst diffusion layer in the electrolyte.

(14) We have had some samples of Ta/Ta_2O_5 formed to e.g. 300 V, Fig. 17, which in aqueous solution showed not the slightest trace of hysteresis

Table 4. Potentials before and after cathodic current flow of a sputtered Ta *sample anodized to* 60 V_f *at* 105°C*

Electrolyte	0·01 N NaI in liq. SO_2		0·01 N KI in liq. SO_2		0·01 N RbI in liq. SO_2	
Highest current density reached during passage of cathodic current	1 mA/cm²		1 μA/cm²		5 μA/cm²	
	Before	*After*	*Before*	*After*	*Before*	*After*
Potential (V)	0·55	0·55 (−60°C)	0·51	0·52 (−60°C)	0·54	0·52 (−60°C)
Potential (V)	0·56	0·60 (−50°C)	0·53	0·55 (−50°C)	0·54	0·54 (−50°C)
Potential (V)	0·56	0·61 (−40°C)	0·52	0·54 (−40°C)	0·52	0·52 (−40°C)
Potential (V)	0·56	0·60 (−30°C)	0·54	0·55 (−30°C)	0·53	0·53 (−30°C)
Potential (V)	0·56	0·66 (−20°C)	0·54	0·56 (−20°C)	0·53	0·53 (−20°C)

* Potentials were measured by means of a Ag/AgI reference electrode. The potentials were more positive with regard to the Ag/AgI reference electrode; the accuracy is about ±0·01 V.

It appears therefore that the preferential adsorption of Rb^+ occurs only under applied cathodic bias.

(12) The open circuit potential of the system Ta/Ta_2O_5 in aqueous solution is strongly but erratically influenced by the Na^+ concentration at constant pH. Potassium ions give a smaller effect. This effect resembles the alkaline error of the glass electrode. The adsorbed species are thus different in aqueous solution and in liq. SO_2.

(13) Vigorous stirring of the solution caused no change in the shape of the cathodic *I–V* curve of in the cathodic *I–V* characteristic on increasing and decreasing the current; the well known effect that the cathodic current in aqueous electrolytes increases with time at constant applied field is thus not always present.[24]

In liquid SO_2 the increase of cathodic current with time at constant applied field is less pronounced than in aqueous solutions, and only occurs on exceeding some critical field strength, resp. current density.

(15) In liquid SO_2+0·01 N NaI with appreciable fields applied in the cathodic direction an increase

of current with illumination by means of an incandescent bulb was observed on Nb/Nb_2O_5. This is suggestive of immobile holes (otherwise the photocurrent may be expected to buck the field current).

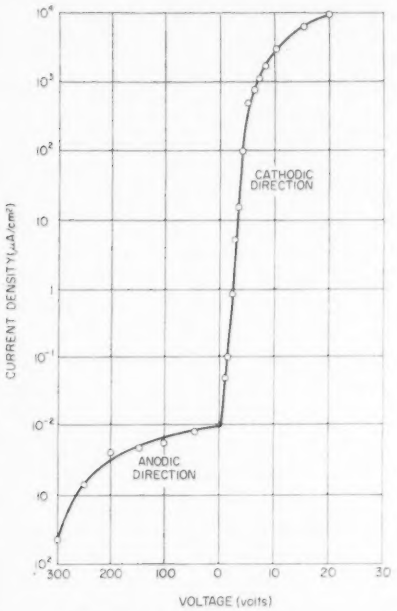

FIG. 17. Cathodic *I–V* characteristics of a Ta/Ta_2O_5 electrode in a dilute aqueous solution of $Na_2B_4O_7$. Ta/Ta_2O_5 formed to 300 V.

(16) Field induced crystallization of an amorphous Ta_2O_5 film[25] does not change the cathodic current characteristics (i.e. the magnitude of the current at a given field strength, and the activation energy for cathodic current flow) as shown in Table 3, No. 1c and Table 3, No. 13.

(17) A thin Al_2O_3 film, non-porous,[4a] with aqueous electrolyte contacts applied to both sides, transmits only a small current, somewhat larger than the anodic leakage current (by a factor of 10–100) even at quite large applied fields ($5{\cdot}3 \times 10^5$ V/cm).

(18) The degree of anodic forming, i.e. the amount of the anodic leakage current, affects only the magnitude of the cathodic current (i.e. the frequency factor); it does not affect the apparent activation energy, as shown in Table 3, No. 14.

The limiting value of the activation energy for cathodic current flow in liquid SO_2 is not affected by the degree of anodic forming.

(19) The system Ta/Ta_2O_5/evaporated Pt contact shows increased conductance in hydrogen atmosphere; the effect is more pronounced under cathodic than under anodic bias. It increases slowly with time in H_2, and disappears slowly when the H_2 is replaced by He or by air. Gold or aluminum electrodes do not show this effect.

(20) Under continuous cathodic current flow in aqueous solution a Ta/Ta_2O_5 electrode becomes embrittled to such an extent that it can be crumbled to pieces between the fingers. Thus hydrogen diffuses through Ta_2O_5. While it appears not very likely that this diffusion occurs by direct transfer of protons from the solution into the Ta_2O_5, it is rather likely that the atomic hydrogen formed as the cathodic reaction product diffuses into the Ta_2O_5; it further appears rather likely that hydrogen can be electrically active at least in some oxide films, in analogy to the donor action of H in ZnO,[26] H in BaO,[27] and on oxide covered Ge surfaces.[28] The slow deforming under cathodic bias in aqueous solutions may in part be due to this effect.

The increased conductance of the system $Ta/Ta_2O_5/Pt$ in a hydrogen atmosphere may very well be due to a donor action of adsorbed or absorbed hydrogen.

6. DISCUSSION

(1) *The Surface Barrier.* The existence of a surface barrier has been proven by the disappearance of the open circuit photoeffect and the increase in cathodic current after slight etching of the oxide film in HF. The photoeffect is equal to or less than the height of this barrier; the width of the barrier can be estimated by the disappearance of the photoeffect as a function of surface layer thickness removed.

The positive end of the dipole is almost certainly due to the field induced emission of electrons from traps under full anodic forming voltage, which creates net positive charges. Under reduced anodic bias, resp. at zero applied bias, some of these electron traps will become filled again. However, the net positive charges located near the outer oxide surface evidently cannot easily recapture electrons; electrons entering the oxide from the metal side

will be trapped already a short distance from the metal interface.

The negative end of the dipole will be constituted by oxygen ions adsorbed on the outer surface of the oxide. Conditions for chemisorption of oxygen are, of course, ideal during forming at constant voltage. As pointed out by HUETTIG[29] the strength of chemisorption increases with the bond strength of the solid, and with the charge on the cations. The bond strengths of all electrolytically rectifying oxides are quite high, and the cations are multiply charged (+3 to +5). In addition to chemisorbed oxygen ions, there may also be a deficit of cations in the surface layer of the oxide (it has recently been shown that even ZrO_2 can exist with cation deficit.[30]) The exact shape of the barrier will depend on whether or not a cation deficit is realized in the outermost layer of the oxide.

While this may be only a minor point with regard to the electrostatic field of the barrier, it may perhaps be of importance if the conduction in the oxide is by very slow electrons, i.e. by transfer of an electron from one atom to the next, requiring a considerable activation energy (as in very narrow 3*d* bands of the transition metal oxides, cf. Ref. 31). In this case a change in the cation–cation distance near the surface could have a considerable influence on the activation energies required for current flow.

The assumption of formation of net positive charges directly underneath the oxide surface by field emission from traps is in agreement with the experimental work of BOER *et al.*[32] It was shown by ADIROVITCH[33], that the distance between the cathode interface and the location of the emptied traps depends on the emissive or blocking properties of the cathode. Since the electrons are tightly bound to the chemisorbed oxygen ions on the surface (i.e. because under anodic bias the electrolyte-cathode is a blocking electrode), it may be deduced that the net positive charge will be located very near the outer oxide surface.

Charge neutralization in the barrier region by internal leakage will lead to a decrease of the barrier height; this is presumably the reason why ability to block anodic current slowly decreases with time under zero applied bias.* This internal leakage is apparently small on some oxides (Ta_2O_5), and more appreciable on others (Al_2O_3, SiO_2) which therefore require some reforming before they can be used as current blocking electrodes. This may also be the reason why Al_2O_3 windows with electrolyte contacts applied to both sides, showed no electric dissymetry; a long time had passed between anodization of the Al, and testing of the Al_2O_3 windows, due to the slow process of producing the windows.

(2) *The Ion Size Effect.* It has been shown that much larger rates are associated with much larger activation energies. One possibility of explaining this anomaly lies apparently in assuming that the high local field of the small cations can lower the barrier height more than the lesser field of the larger cations, or can extract electrons from deeper surface traps than can the large cations. The effect is also observed after the surface barrier has been etched off with HF, but in this case the activation energies for all cations are of the same magnitude (4–6 kcal on Ta/Ta_2O_5, the only system which could be conveniently tested), and are independent of field strength in the voltage range investigated. The higher rates should again be associated with an increased activity of the electrons in the case of small cations. This increased activity of the electrons could be due to a more frequent emptying of surface traps by the stronger field of the small cations. The field dependence of the activation energy of the unetched valve metal electrodes indicates a surface barrier which at least in part limits the current flow. Only a small part of the applied cathodic bias appears to be effective in reducing the height of this barrier. The reason for this is not understood at present.

(3) *The Change in Slope of the Log i vs. 1/T Curves.* The upward "curvature" of this change in slope points to the fact that current flow can apparently occur by two parallel mechanisms of which the one with the larger activation energy becomes activated only at higher temperatures. This might e.g. be tunneling through a barrier and electron emission over the barrier.

(4) *Adsorption Phenomena.* The blocking of the cathodic current in liq. SO_2 if both Na^+ and Rb^+ are present simultaneously points to specific adsorption of Rb^+ under applied cathodic bias, which excludes Na^+ ions from the interface.

This specific adsorption may also be the

* Also the photoeffect decreases slowly with time; it was shown by etching in HF that the photoeffect arises in a thin surface layer ~ 300 Å thick.

explanation for the fact that the larger cations give the larger current at very small applied bias, i.e. for the cross-over of the curves with the various alkali cations in liq. SO_2.

(5) *Penetration of Cations into the Oxide Film does not Occur.* The various facts mentioned below: high resistance of Al_2O_3 windows with aqueous electrolyte contacts applied to both sides; the identical behavior of amorphous and crystalline Ta_2O_5 films; the blocking of the current if both Rb^+ and Na^+ ions are present simultaneously in liq. SO_2, all tend to rule out penetration of cations into the oxide lattice. Considerations of ion size and lattice parameters lead to the same result for the system ZrO_2–Na^+ ions (compare Appendix).

Penetration of atomic hydrogen appears definitely to occur, at least into Ta_2O_5.

VOL. 15 1960

APPENDIX

Structure of ZrO_2

The stable form of ZrO_2 possesses a structure that is a distortion of the fluorite (CaF_2) arrangement, the symmetry being monoclinic with four ZrO_2 molecules in a unit cell of dimensions*:

$a_0 = 5{\cdot}21$Å, $b_0 = 5{\cdot}26$Å, $c_0 = 5{\cdot}37$Å, $\beta = 80^0 32'$

This structure can be referred to an idealized cubic structure consisting of a free-centered cubic lattice of Zr^{4+} ions. In this ideal fluorite form the O^{2-} ions would then be placed so as to lie midway between center of the unit cell and each of the eight corners. In the true monoclinic structure the O^{2-} ions are appreciably displaced from these sites. Each Zr^{4+} ion is coordinated by eight O^{2-} arranged at the corners of a distorted cube. The Zr–O bond lengths range between about 1·95 Å and 2·65 Å, the shorter of these distances being significantly less than the sum of the Goldschmidt ionic radii for Zr^{4+} (0·87 Å) and O^{2-} (1·32 Å).

The unit cell is characterized by an empty cage site at its center which possess the same oxygen coordination as the Zr^{4+} ions occupying the corners and face centered positions in the unit cell. Each face of the cage is defined by edges formed by Zr–O bonds.

If current flow were to occur in such a lattice by a mechanism involving the movement of interstitial cations such as Li^+ or Na^+, these carriers would have to slip through holes in the faces of the cages. A simple calculation based on the monoclinic structure of ZrO_2 shows that the maximum radius for such holes formed between the Zr^{4+} and O^{2-} ions comprising the cage faces is about 0·3 Å. It must therefore be concluded that Li^+ or Na^+ ions would not be mobile in a ZrO_2 lattice at room temperature even in the presence of a field of 10^5 V/cm.

* *Wyckoff Crystal Structures*, Vol. I, Chapter 4, Interscience, New York (1948).

SUMMARY

The two more important facts established by this work are: the ion size effect, which is present both in the presence and in the absence of a surface barrier and the existence of a surface barrier, or, more strictly speaking, the extreme thinness of this barrier ($\sim$ 300 Å). The fact that the bands slope down from the outer surface of the oxide towards the metal was known previously.

The ion size effect is thought to be a result of field emission of electrons from surface traps, due to the high local field of the cations in the electrolyte, but it is not clear whether the differences in the resulting cathodic currents are due to the different depths of the traps affected (i.e. their number), or to a different frequency of trap emptying.

The surface barrier has been shown to be due to a non-thermodynamic-equilibrium situation produced by the extremely strong fields during anodic forming.

The fact that the surface barrier does not disappear under application of a cathodic voltage equal to or larger than the height of the barrier probably means that no appreciable concentration of *free* electrons inside the oxide can be realized. The slow neutralization of positive charges in the surface barrier region by electrons emitted into the oxide by the metal may explain, at least in part, the gradual increase of cathodic current with time at constant applied bias.

Too little, however, is known about the exact distribution of the potential in the oxide under cathodic bias to attempt a mathematical description of the cathodic current flow at this stage.

The experimental results presented appear not to be in contradiction to any well established facts known previously, rather, they appear to establish a connection between the various theories of

cathodic current flow proposed hitherto by other authors.

In particular, the well known difference in the behavior of electrolytic rectifiers under a.c. bias and under d.c. cathodic bias becomes understandable as due to slow desorption and adsorption processes at the oxide/electrolyte interface.

It also appears likely that the poor saturation of the cathodic current on *p*-type Ge electrodes in aqueous solution and in the absence of an oxide layer[34] is due to the field emission of electrons from the valence band.

Acknowledgements—The authors are indebted to Mr. J. WALSH for many valuable discussions, to Dr. M. FRANCOMBE for an analysis of the ZrO_2 lattice in connection with the question of possible penetration of Na^+ ions into this lattice, and to Mr. W. HAAS for help with several of the experiments. They are also indebted for discussions and advice to Prof. J. O'M. BOCKRIS and Dr. E. BLOMGREN (University of Pennsylvania, Chemistry Dept.) and to Dr. P. RUETSCHI (Electric Storage Battery Co., Yardley, Pa.).

This work was supported by the Bureau of Ships Electronics Division, Department of the Navy, under Contract No. NObsr 72770, Index No. NE–081400.

Mr. JOSEPH WALSH died on 27 November, 1959, at the age of thirty-two. To his memory we wish to dedicate this work. We shall always miss his friendship and advice.

REFERENCES

1. (a) BERRY R. and SLOAN D., *Proc. Inst. Radio Engrs.* **47,** 1070 (1959).
   (b) VAN GEEL W., *Philips Res. Rep.* **13,** 265 (1958).
   (c) ANSBACHER F. and EHRENBERG W., *Proc. Phys. Soc.* A **64,** 362 (1951).
   (d) STOERMER R., *Z. Tech. Phys.* p. 508 (1935).
   (e) BURNHAM J. and ROBINSON P., Conference on Electrical Insulation, Annual Report p. 68 National Research Council, Wash., D.C. (1948).
2. STOERMER R., *Z. Tech. Phys.* p. 508 (1935).
3. (a) LOMER P., *Proc. Phys. Soc.* **63,** 818 (1950).
   (b) LOMER P., *Nature, Lond.* **166,** 191 (1950).
   (c) AUSTIN A. and WHITEHEAD S., *Proc. Roy. Soc.* A **176,** 33 (1940).
   (d) KAWAMURA A. and AZUMA K., *J. Phys. Soc. Japan* **8,** 797 (1953).
4. (a) HAUSER U. and KERLER W., *Rev. Sci. Instrum.* **29,** 380 (1958).
   (b) POLITICKY A. and FUCHS E., *Z. Naturf.* **14 a,** 211 (1959).
5. (a) VAN GEEL W., *Halbleiterprobleme I*, p. 299. Vieweg & Sohn, Braunschweig (1954).
   (b) YOUNG L., *Trans. Faraday Soc.* **51,** 1250 (1955). (Compare, however, also WINKEL P. and DE GROOT D., *Philips Res. Rep.* **13,** 489 (1958).
6. (a) DE BOER J. and VAN GEEL W., *Physica* **1,** 449 (1934).
   (b) YOUNG L., *Trans. Faraday Soc.* **50,** 164 (1954).
   (c) VAN GEEL W., PISTORIUS C. and WINKEL P., *Philips Res. Rep.* **12,** 465 (1957); *ibid.* **13,** 265 (1958).
   (d) VENABLES J. and BROUDY R., *J. Appl. Phys.* **30,** 1110 (1959).
7. VERMILYEA D., *Acta. Met.* **2,** 346 (1954).
8. VAN GEEL W., *Halbleiterprobleme I* p. 299 Vieweg & Sohn, Braunschweig (1954).
9. DECKER A. and URQUHART H., *J. Appl. Phys.* **21,** 708 (1950).
10. VAN GEEL W., PISTORIUS C. and BOUMA B., *Philips Res. Rep.* **12,** 465 (1957).
11. GUENTHERSCHULZE A. and BETZ H., *Elektrolytkondensatoren*, (2nd Ed.) Herbert Cram, Berlin (1952).
12. VERMILYEA D., *J. Appl. Phys.* **27,** 963 (1956).
13. MUELLER E., *Ergebn. Exakt. Naturw.* **27,** 290 (1953).
14. WINKEL P. and VERKERK B., *Philips Res. Rep.* **13,** 501 (1958).
15. SMITH A., *Canad. J. Phys.* **35,** 1151 (1957).
16. KOBAYASHI M., Extended Abstract, IRE Convention, Philadelphia, May 1959.
17. YOUNG L., *Trans. Faraday. Soc.* **55,** 842 (1959).
18. SCHMIDT P., *J. Appl. Phys.* **28,** 278 (1957).
19. BAYNTON P., RAWSON H. and STANDWORTH J., *J. Electrochem. Soc.* **104,** 237 (1957); MOSS T., *Photoconductivity in the Elements* Butterworth, London (1952); GORIUNOVA N., KOLOMIETS B. and SHILO V., *Zh. Tech. Fiz.* **28,** 981 (1958).
20. DE BOER J., *Electron Emission and Adsorption Phenomena*, Cambridge University Press (1935).
21. JANDER G., *Die Chemie in Wasserähnlichen Loesungsmitteln*, p. 230. Springer Verlag, Berlin (1949).
22. VAN GEEL W. and PISTORIUS C., *Philips Res. Rep.* **14,** 123 (1959).
23. RUETSCHI P., *Z. Phys. Chem.*, **14,** 708 (1958).
24. (a) DECKER A. and URQUHART H., *J. Appl. Phys.* **21,** 708 (1950).
   (b) STOERMER R., *Z. Tech. Phys.*, p. 508 (1935).
   (c) DECKER A. and VAN GEEL W., *Philips Res. Rep.* **5,** 303 (1950).
25. VERMILYEA D., *J. Electrochem. Soc.* **102,** 207 (1955).
26. HEILAND G., *Z. Phys.* **148,** 15 (1957).
27. RUDOLPH J., *Z. Naturf.* **13 a,** 757 (1958).
28. HEILAND G. and HANDLER P., *J. Appl. Phys.* **30,** 446 (1959).
29. HUETTIG F., *Mh. Chem.* **86,** 699 (1955); GRIMLEY T. and TRAPNEL B., *Proc. Roy. Soc.* A **234,** 405 (1956).
30. RUDOLPH J., *Z. Naturf.* **14 a,** 727 (1959).
31. MORIN F. J., *Bell. Syst. Tech. J.* **37,** 1047 (1958).
32. (a) BOER K., HANSCH H. and KUMMEL U., *Z. Phys.* **155,** 170 (1959).
   (b) BOER K., *Z. Phys.* **155,** 184 (1959).
33. ADIROVITCH E., *Z. Phys.* **155,** 195 (1959).
34. FLYNN J., *J. Electrochem. Soc.* **105,** 715 (1958); GERISCHER H. and BECK F., *Z. Phys. Chem.* **13,** 389 (1957).

J. Phys. Chem. Solids Pergamon Press 1960. Vol. 15. pp. 291–305. Printed in Great Britain.

ROTATIONAL PROPERTIES OF PARAMAGNETIC RESONANCE SPECTRA OF NON-CUBIC CRYSTALS

M. SACHS

Lockheed Missiles and Space Division, Research Laboratory, Palo Alto, California

(*Received* 16 *November* 1959)

VOL. 15 1960

Abstract—The complete symmetry group for each of the twenty-seven non-cubic point groups is exploited in a derivation of the rotational properties of paramagnetic resonance spectra of non-cubic crystals. The energy eigenvalues for the magnetic substates of the ground state energy level of the paramagnetic crystal (in a uniform magnetic field) are derived as a function of the polar and azimuthal angles which locate the direction of the applied magnetic field with respect to the crystal coordinate system. The theory, which gives the line positions to second order in $|\langle e\varphi_c\rangle|/|\langle \mu \cdot \boldsymbol{H}\rangle|$, is applicable to an analysis of microwave spectra in which the non-cubic part of the electrostatic potential energy of the crystal ($e\varphi_c$) is small compared with the magnetic energy term ($-\mu \cdot \boldsymbol{H}$).

The results of the general formulation are applied explicitly to the case in which the local electrostatic crystalline potential field at the magnetic ion site is any of the trigonal or hexagonal symmetry types.

1. INTRODUCTION

THE DISCOVERY by ZAVOISKY[1,2] of the paramagnetic resonance technique for the investigation of the properties of paramagnetic salts provided an extremely precise method for determining, in an unambiguous way, many important properties of paramagnetic salts. In particular, paramagnetic resonance spectroscopy of single crystals of magnetic salts reveals data which lead, in a less ambiguous way than do the results of other experimental techniques, to the symmetry which characterizes the local electrostatic field at the magnetic ion sites, and the magnitudes of the associated crystalline field coefficients.

A general survey of the theoretical and experimental work which has been done in paramagnetic resonance studies in crystals is given by BLEANEY and STEVENS[3] and by BOWERS and OWEN[4]. The treatment discussed by these authors is based on the formulation of the so-called "effective spin" Hamiltonian. Also, some recent work by KOSTER and STATZ[5] provides an alternative method to the effective spin formalism. It is the purpose of this paper to supplement the previous theoretical work by providing an explicit formulation for the rotational properties of the energy eigenvalues of magnetic ions which are subjected to a uniform magnetic field and also a crystalline electrostatic potential field which is characterized by any of the twenty-seven non-cubic point group symmetries.

The assumption will be made that the Zeeman energy term is greater in magnitude than is the effect of the crystalline potential. (This assumption is generally valid in the analysis of the microwave spectroscopy of paramagnetic salts.) On the other hand, it will not be assumed, as it frequently has been done in the past, that the non-axial parts of the crystalline potential are small or can be neglected, in comparison with the axial terms. Thus, the aim of this paper is to exploit the totality of elements of the symmetry groups in providing a formalism to be used in the analysis of the magnetic resonance spectra of non-cubic crystals. The non-axial terms have already been shown to be important in special cases. A particular case is the rare earth ethylsulfate group of salts, which have been studied by ELLIOTT and STEVENS[6,7].

The contribution of the nuclear hyperfine interaction to the paramagnetic resonance spectrum will not be treated here. This subject has been discussed by ABRAGAM and PRYCE[8]; their results are readily adaptable to the present theory, should it

become necessary to consider the effect of the nuclear spin of the constituent magnetic ion on the magnetic resonance spectrum. Also, all internal electric and magnetic interactions between the constituent magnetic ions themselves will be neglected.

In Section 2, a discussion of the general form of the crystalline electrostatic potential, will be given. A formalism is provided which leads to a unique expression for this potential as a function of the corresponding point group symmetry. In Section 3, the crystalline potential is derived in terms of the angles $(\theta_0\phi_0)$ which locate an external magnetic field with respect to the crystalline c-axis and the energy eigenvalues of the magnetic states are then determined up to second order in the ratio $|e\varphi_c/\mu \cdot \boldsymbol{H}|$ (the ratio of the crystalline potential energy to the magnetic energy term).

The results are applied in Section 4 to an explicit determination of the energy eigenvalues of magnetic ions in a uniform magnetic field and electrostatic environments with trigonal and hexagonal symmetries.

2. THE CRYSTALLINE ELECTROSTATIC POTENTIAL FIELD

Consider now the electrostatic potential field of a host paramagnetic crystal at the site of a constituent magnetic ion, in the absence of that ion. This potential is, according to Maxwell's field equations, a solution of Laplace's equation. The most general solution is given by the multipole expansion

$$\varphi_c(\theta'\phi') = \sum_{i=1}^{n}\sum_{\lambda=0}^{\infty}\sum_{\mu=-\lambda}^{\lambda} N_{\lambda\mu}^{1/2}\Lambda_{\lambda\mu}r_i^{\lambda}Y_\lambda^\mu(\theta_i'\phi_i') \tag{1}$$

where n is the number of constituent unpaired electrons of the magnetic ion, r_i is the radius of the ith electron shell, (with the nucleus taken at the origin), Y_λ^μ is taken to be the normalized spherical harmonic*

$$Y_\lambda^\mu(\theta'\phi') = (-1)^\mu N_{\lambda\mu}^{-1/2}P_\lambda^\mu(\cos\theta')e^{i\mu\phi'} \tag{2}$$

where

$$N_{\lambda\mu} = \left[\frac{4\pi(\lambda+\mu)!}{(2\lambda+1)(\lambda-\mu)!}\right] \tag{3}$$

* Henceforth the subscript i will be implied.

and

$$P_\lambda^\mu(\cos\theta') = (-1)^\mu\frac{(\lambda+\mu)!}{(\lambda-\mu)!}P_\lambda^{-\mu}(\cos\theta')$$

is the associated Legendre function:

$$P_\lambda^\mu(x) = \frac{(1-x^2)^{\mu/2}}{2^\lambda\lambda!}\frac{d^{\lambda+\mu}}{dx^{\lambda+\mu}}(x^2-1)^\lambda \tag{4}$$

The crystalline field coefficients

$$\Lambda_{\lambda\mu} = \Lambda_{\lambda\mu}^{(r)} + i\Lambda_{\lambda\mu}^{(i)} \tag{5}$$

are complex and independent of the electron coordinates $(r,\ \theta',\ \phi')$. These coefficients may be readily determined in terms of the lattice geometry in those cases in which the surrounding nonmagnetic ions or molecules may be approximated by point charges. This assumption is, however, not always a good one; since we are only interested in the rotational properties of the spectrum (which are unaffected by the magnitudes of $\Lambda_{\lambda\mu}$) these coefficients will be treated as parameters to be extracted from the data. Imposing the restriction that the potential energy function be real, it is found that φ_c may be expressed in terms of the following expansion

$$\varphi_c = \sum_{\lambda=0}^{\infty}\sum_{\mu=0}^{\lambda}(\varphi_{\lambda\mu}+\bar{\varphi}_{\lambda\mu}) \tag{6}$$

where

$$\varphi_{\lambda\mu} = N_{\lambda\mu}^{1/2}\Lambda_{\lambda\mu}^{(r)}r^\lambda[Y_\lambda^\mu+(-1)^\mu Y_\lambda^{-\mu}] \tag{7a}$$

$$\bar{\varphi}_{\lambda\mu} = iN_{\lambda\mu}^{1/2}\Lambda_{\lambda\mu}^{(i)}r^\lambda[Y_\lambda^\mu+(-1)^{\mu+1}Y_\lambda^{-\mu}] \tag{7b}$$

If one now imposes the further restriction that φ_c be invariant under the transformations of the crystallographic symmetry group which characterizes a particular ion site, then the potential φ_c is further restricted to moments which are characterized by specific values of λ and μ. The possible types of symmetry elements which are contained in the point groups are as follows:

(1) The identity element (E).
(2) n-fold rotations about the c-axis (C_n).
(3) A horizontal reflection (i.e. the reflection plane is perpendicular to the c-axis) (σ_h).
(4) Vertical reflections (σ_v).

VOL. 15, 1960

Table 1. *Invariance requirements imposed by point group transformations on the crystal electrostatic potential moments.* ($m = 0, 1, 2 \ldots$) (*The moments* $\varphi_{\lambda\mu}$ *and* $\bar{\varphi}_{\lambda\mu}$ *are defined by equation* 7.)

	Point group transformations						
	E	C_n	σ_h	σ_v	$\sigma_d(n)$*	$U_2(n)$*	S_n†
$(\theta, \phi) \rightarrow$	(θ, ϕ)	$(\theta, \phi+2\pi/n)$	$(\pi-\theta, \phi)$	$(\theta, -\phi)$	$(\theta, -\phi+\pi/n)$	$\left(\pi-\theta, -\phi+\frac{2\pi}{n}\right)$	$\left(\pi-\theta, \phi+\frac{2\pi}{n}\right)$
$\varphi_{\lambda\mu} \rightarrow$	$\varphi_{\lambda\mu}$	$(-1)^{2\mu/n}\varphi_{\lambda\mu}$	$(-1)^{\lambda+\mu}\varphi_{\lambda\mu}$	$\varphi_{\lambda\mu}$	$(-1)^{\mu/n}\varphi_{\lambda\mu}$	$(-1)^{\lambda+2\mu/n}\varphi_{\lambda\mu}$	$(-1)^{\lambda+\mu+2\mu/n}\varphi_{\lambda\mu}$
Invariance requirement	none	$\mu = nm$	$\lambda+\mu = 2m$	none	$\mu = 2nm$	$\lambda+\frac{2\mu}{n} = 2m$	$\lambda+\mu+\frac{2\mu}{n} = 2m$
$\bar{\varphi}_{\lambda\mu} \rightarrow$	$\bar{\varphi}_{\lambda\mu}$	$(-1)^{2\mu/n}\bar{\varphi}_{\lambda\mu}$	$(-1)^{\lambda+\mu}\bar{\varphi}_{\lambda\mu}$	$-\bar{\varphi}_{\lambda\mu}$	$(-1)^{\mu/n+1}\bar{\varphi}_{\lambda\mu}$	$(-1)^{\lambda+2\mu/n+1}\bar{\varphi}_{\lambda\mu}$	$(-1)^{\lambda+\mu+2\mu/n}\bar{\varphi}_{\lambda\mu}$
Invariance requirement	none	$\mu = nm$	$\lambda+\mu = 2m$	$\bar{\varphi}_{\lambda\mu} = 0$	$\mu = n(2m-1)$	$\lambda+\frac{2\mu}{n} = 2m-1$	$\lambda+\mu+\frac{2\mu}{n} = 2m$

* The value of n refers to the minimum n-fold rotation about the c-axis which is contained in the same group.
† Note that $S_2 = I$ (the inversion element).

(5) Diagonal reflections (σ_d).

(6) Two-fold rotations about axes perpendicular to the c-axis (U_2).

(7) n-fold rotary-reflections (S_n).

The transformations of the angles ($\theta\phi$) under these operations are listed below in Table 1, together with the corresponding invariance requirement on the electrostatic potential moments.

The combination of the invariance requirements given in Table 1 with the particular transformation elements which constitute a specific point group* will determine the electrostatic potential φ_c in terms of an expansion (6) which is unique to this set of transformation elements. (This procedure will be illustrated below in Section 4.) A tabulation of the sets of transformations which define the different point groups may be found in many texts.[9]

3. THE PARAMAGNETIC RESONANCE SPECTRUM

The usual assumption will be made that the constituent magnetic ions of the crystal are energetically uncoupled so that the energy levels of each individual magnetic ion determine the energy levels of the entire crystal. The free ion energy levels are split due to the presence of an effective magnetic field in the crystal (caused by the application of an external magnetic field) and the electrostatic potential of the environment of the magnetic ion. The interaction Hamiltonian is

$$\mathcal{H}_{\text{int}} = -\mu \cdot \boldsymbol{H} + e\varphi_c \tag{8}$$

where $\boldsymbol{H}$ is the external magnetic field and φ_c is given by equation (6), subject to the restrictions imposed by the crystal symmetry (Table 1). The discussion will be restricted to those cases in which the inequality

$$|\mu \cdot \boldsymbol{H}| \gg |\langle e\varphi_c \rangle| \tag{9}$$

is valid.

In accordance with the methods of perturbation theory, the assumption is made that the zero order problem has already been solved. Our aim is then to diagonalize the perturbation operator $\mathcal{H}_{\text{int}}$. In view of (9), the calculation is carried out by first considering a lifting of all of the degeneracy of the system by the Zeeman energy term $-\mu \cdot \boldsymbol{H}$, and then calculating the shift of the magnetic energy levels by the electrostatic potential energy $e\varphi_c$. This calculation is carried out most conveniently by taking the axis of quantization to lie along the direction of magnetization in the crystal.

The magnetization direction in the crystal

The magnetization direction in a paramagnetic crystal is not, in general, parallel to the direction of the applied magnetic field. This effect is due primarily to the distorting effect of the crystalline field on the electronic structure of the constituent magnetic ions. The expectation values of the magnetic moment of a magnetic ion in a crystal is generally a function of the relative angle between the magnetic moment and the c-axis. These results show up in the g factors which differ with the direction of the applied magnetic field. We shall refer to the angles between the magnetization direction and the c-axis of the crystal as ($\theta\phi$) and to the angles between the applied magnetic field and the c-axis of the crystal as ($\theta_0\phi_0$). In order to compare theory with experiment, the angles ($\theta\phi$) must be related to the "laboratory angles" ($\theta_0\phi_0$).

If the unit vector $\boldsymbol{\epsilon}_3$ denotes the axis of quantization (i.e. the magnetization direction), then the expectation values of the magnetic moment of the ion in this coordinate system and in the crystal (primed) coordinate system, are related according

* In special cases, the purity of the single point group description of the local crystalline field at the magnetic ion site can break down. First, neighboring ions beyond the nearest neighbors, which may be described by a different symmetry group than the group which describes the immediate surroundings, may be in close enough proximity to the magnetic ion so as to have an observable effect on its spectrum. Second, an extended charge distribution on the surrounding neighbors can destroy the single point group description.

A typical example is that of the rare earth salt, cerium ethylsulfate ($Ce(C_2H_5SO_4)_3 \cdot 9H_2O$). In this case, the local electrostatic field at the Ce^{3+} ion site is predominantly of the C_{3h} type and arises primarily from the surrounding water molecules. ELLIOTT and STEVENS[6] have found, however, that in order to account for the cerium spectrum, it is necessary to also consider the charge distributions on the surrounding ethylsulfate radicals. The latter give rise to a slight deviation in the local C_{3h} electrostatic field of C_{3v} character. Thus, it becomes necessary, in this case, to consider the crystalline field in terms of an admixture of C_{3h} and C_{3v} symmetry fields.

In cases such as this, it may be more convenient to refer to a characteristic set of point group transformations without reference to any one particular point group.

to the following vector equation

$$\begin{aligned}\boldsymbol{\epsilon}_3\langle M|\mu_3|M\rangle = {} & \boldsymbol{\epsilon}_1' a_{13}\langle M|\mu_1'|M\rangle \sin\theta_0\cos\phi_0 + \\ & + \boldsymbol{\epsilon}_2' a_{23}\langle M|\mu_2'|M\rangle \sin\theta_0\sin\phi_0 + \\ & + \boldsymbol{\epsilon}_3' a_{33}\langle M|\mu_3'|M\rangle \cos\theta_0\end{aligned} \tag{10}$$

where the coefficients a_{13}, a_{23}, a_{33} are different from unity only when the direction of magnetization $\boldsymbol{\epsilon}_3$ differs from the direction of the applied magnetic field. If we now define the g factors in terms of expectation values of μ as follows

$$\begin{aligned}&\langle M|\mu_3|M\rangle = g\mu_0 M \\ &a_{i3}\langle M|\mu_i'|M\rangle = g_i'\mu_0 M\end{aligned} \qquad (\mu_0 = e\hbar/2mc) \tag{11}$$

then equation (10) takes the form

$$\begin{aligned}\boldsymbol{\epsilon}_3 g = {} & \boldsymbol{\epsilon}_1' g_1' \sin\theta_0\cos\phi_0 + \\ & \boldsymbol{\epsilon}_2' g_2' \sin\theta_0\sin\phi_0 + \boldsymbol{\epsilon}_3' g_3' \cos\theta_0\end{aligned} \tag{12}$$

The vector equation (12) leads to the relation

$$\begin{aligned}g^2 = {} & (g_1')^2 \sin^2\theta_0\cos^2\phi_0 + \\ & + (g_2')^2 \sin^2\theta_0\sin^2\phi_0 + (g_3')^2\cos^2\theta_0\end{aligned} \tag{13a}$$

which in turn reduces, in the case of cylindrical symmetry (i.e. when $g_1' = g_2' = g_\perp$, $g_3' = g_\parallel$) to the well-known equation

$$g^2 = g_\perp^2 \sin^2\theta_0 + g_\parallel^2 \cos^2\theta_0 \tag{13b}$$

The relation between the angle subtended by the axis of quantization $(\theta\phi)$ and the angle subtended by the applied magnetic field $(\theta_0\phi_0)$, with respect to the c-axis, is then obtained by successively taking the scalar product of both sides of equation (12) with the unit vectors $\boldsymbol{\epsilon}_3'$, $\boldsymbol{\epsilon}_\perp'$ and $\boldsymbol{\epsilon}_\simeq'$. This gives the following relations

$$\begin{aligned}\cos\theta &= (g_3'/g)\cos\theta_0 \\ \tan\phi &= (g_2'/g_1')\tan\phi_0\end{aligned} \tag{14}$$

The actual magnitudes of the g' factors depend on the detailed behavior of the wave functions of the magnetic ion in the crystal. Since we are only concerned here with rotational properties, these factors will be treated, along with the crystalline field coefficients as parameters to be determined by experiment.

Rotation of φ_c into the magnetization direction

The task which remains, before the perturbation Hamiltonian (equation 8) can be diagonalized, is to express the crystalline potential φ_c (equation 6) in terms of the new coordinate system in which the x_3 axis lies along the direction of magnetization (i.e. the axis of quantization).

For this purpose, the relations between functions of three sets of angles must be determined. These angles are (1) $(\theta\phi)$ which locates the axis of quantization with respect to the c-axis, (2) $(\theta'\phi')$ which locates the magnetic electron radius vector $\boldsymbol{r}$, with respect to the c-axis and (3) $(\theta''\phi'')$ which locates $\boldsymbol{r}$ with respect to the axis of quantization. Thus, the transformation required is

$$\varphi_c(\theta'\phi') \rightarrow \varphi_c[(\theta\phi), (\theta''\phi'')] \tag{15}$$

The matrix elements of φ_c may then be readily determined since the unperturbed wave functions depend on $(\theta''\phi'')$, and $(\theta\phi)$ are fixed and are related to the "laboratory angles" between the applied magnetic field $\boldsymbol{H}$ and the c-axis $(\theta_0\phi_0)$ according to equation (14).

The transformation (15) may be carried out by recognizing the relation between the spherical harmonics Y_λ^μ and the matrix elements of the irreducible representations of the rotation group $\mathscr{D}^{(\lambda)}_{\mu'\mu}(\alpha, \beta, \gamma)$. The general form for $\mathscr{D}^{(\lambda)}_{\mu'\mu}$ as a function of the three Eulerian angles (α, β, γ) is as follows[10]

$$\mathscr{D}^{(\lambda)}_{\mu'\mu}(\alpha, \beta, \gamma) = e^{i\mu'\alpha}\, d^{(\lambda)}_{\mu'\mu}(\beta) e^{i\mu\gamma} \tag{16}$$

where

$$d^{(\lambda)}_{\mu'\mu}(\beta) = \left[\frac{(\lambda+\mu')!(\lambda-\mu')!}{(\lambda+\mu)!(\lambda-\mu)!}\right]^{1/2} \sum_\nu \binom{\lambda+\mu}{\lambda-\mu-\nu}\binom{\lambda-\mu}{\nu} \cdot (-1)^{\lambda-\mu'-\nu}(\cos(\beta/2))^{2\nu+\mu'+\mu}(\sin(\beta/2))^{2\lambda-2\nu-\mu'-\mu} \tag{17}$$

In the case where $\mu' = 0$

$$\mathscr{D}^{(\lambda)}_{0\mu}(\alpha, \beta, \gamma) = \left[\frac{4\pi}{2\lambda+1}\right]^{1/2} Y^{\mu}_{\lambda}(\beta, \gamma) \quad (16')$$

The summation indicated in equation (17) is carried out over all positive integer values of ν, which make the factors a, b and $(a-b)$ in the binomial coefficient

$$\binom{a}{b} \equiv \frac{a!}{(a-b)!b!}$$

positive.

Next, considering the transformation (15) to be made up of the successive application of two Eulerian rotations, use can be made of the following properties of $\mathscr{D}^{(\lambda)}_{\mu'\mu}$. A rotation, defined by the three Eulerian angles $(\alpha', \beta', \gamma')$, which is a result of the successive application of the rotations (α, β, γ) and $(\alpha'', \beta'', \gamma'')$ (in that order), is described by the matrix representation

$$\mathscr{D}^{(\lambda)}_{\mu'\mu}(\alpha', \beta', \gamma') = \sum_{\mu''} \mathscr{D}^{(\lambda)}_{\mu'\mu''}(\alpha'', \beta'', \gamma'')\mathscr{D}^{(\lambda)}_{\mu''\mu}(\alpha, \beta, \gamma) \quad (18)$$

This equation is a generalization of the spherical harmonic addition theorem, as can be seen by setting $\mu' = \mu = 0, \lambda =$ integer, and making use of the identification of $\mathscr{D}^{(\lambda)}_{0\mu}$ with Y^{μ}_{λ}, according to equation (16').

Identifying the Eulerian angles as follows

$$\begin{aligned}(\beta'\gamma') &= (\theta'\phi') \\ (\beta''\gamma'') &= (\theta''\phi'') \\ (\beta\gamma) &= (\theta\phi)\end{aligned} \quad (19)$$

and setting $\mu' = 0$, equation (18) takes the form

$$Y^{\mu}_{\lambda}(\theta'\phi') = \sum_{\mu''=-\lambda}^{\lambda} Y^{\mu''}_{\lambda}(\theta''\phi'')\mathscr{D}^{(\lambda)}_{\mu''\mu}(0, \theta, \phi) \quad (20)$$

In equation (20), the Eulerian angle α has been arbitrarily set equal to zero. Since the specification of α only serves the purpose of orienting the x_1' axis in the (x_1', x_2') plane, this choice of α cannot affect physical observables, so long as there is a consistency with the original choice of the orientation of the x_1' axis throughout the measurements. Thus, the coefficients g_1' and g_2' will refer to the magnetization directions in the plane perpendicular to the c-axis of the crystal and along the directions ϵ_1' and ϵ_2' which had been specifically chosen in the experiment. Also, the azimuthal angle ϕ is defined as that angle in the (x_1', x_2') plane which is measured from the x_1' axis.

Combining equations (6), (7), (16) and (20), the following expressions for the electrostatic potential energy are obtained.

$$e\varphi_c[(\theta''\phi''), (\theta\phi)] = e\sum_{\lambda=0}^{\infty}\sum_{\mu=0}^{\lambda}(\varphi_{\lambda\mu}+\bar{\varphi}_{\lambda\mu}) \quad (21a)$$

---

where

$$\varphi_{\lambda\mu} = N^{1/2}_{\lambda\mu}\Lambda^{(r)}_{\lambda\mu}r^{\lambda}\left\{\left(\frac{4\pi}{2\lambda+1}\right)^{1/2} Y^{0}_{\lambda}(\theta''\phi'')[Y^{\mu}_{\lambda}(\theta\phi)+(-1)^{\mu}Y^{-\mu}_{\lambda}(\theta\phi)]+\right.$$
$$+\sum_{\mu'=1}^{\lambda}\left[Y^{\mu'}_{\lambda}(\theta''\phi'')[d^{(\lambda)}_{\mu'\mu}(\theta)e^{i\mu\phi}+(-1)^{\mu}d^{(\lambda)}_{\mu'-\mu}(\theta)e^{-i\mu\phi}]+\right.$$
$$\left.\left.+Y^{-\mu'}_{\lambda}(\theta''\phi'')[d^{(\lambda)}_{-\mu'\mu}(\theta)e^{i\mu\phi}+(-1)^{\mu}d^{(\lambda)}_{-\mu'-\mu}(\theta)e^{-i\mu\phi}]\right]\right\} \quad (21b)$$

$$\bar{\varphi}_{\lambda\mu} = iN^{1/2}_{\lambda\mu}\Lambda^{(i)}_{\lambda\mu}r^{\lambda}\left\{\left(\frac{4\pi}{2\lambda+1}\right)^{1/2} Y^{0}_{\lambda}(\theta''\phi'')[Y^{\mu}_{\lambda}(\theta\phi)+(-1)^{\mu+1}Y^{-\mu}_{\lambda}(\theta\phi)]+\right.$$
$$+\sum_{\mu'=1}^{\lambda}\left[Y^{\mu'}_{\lambda}(\theta''\phi'')[d^{(\lambda)}_{\mu'\mu}(\theta)e^{i\mu\phi}+(-1)^{\mu+1}d^{(\lambda)}_{\mu'-\mu}(\theta)e^{-i\mu\phi}]+\right.$$
$$\left.\left.+Y^{-\mu'}_{\lambda}(\theta''\phi'')[d^{(\lambda)}_{-\mu'\mu}(\theta)e^{i\mu\phi}+(-1)^{\mu+1}d^{(\lambda)}_{-\mu'-\mu}(\theta)e^{-i\mu\phi}]\right]\right\} \quad (21c)$$

The desired expression for the perturbation Hamiltonian operator which describes a paramagnetic crystal (of a particular symmetry type) in a uniform field, is then

$$\mathscr{H}_{\text{int}} = -\boldsymbol{\mu}\cdot\boldsymbol{H}+e\varphi_c[(\theta''\phi''),(\theta\phi)]$$
$$= -\boldsymbol{\mu}\cdot\boldsymbol{H}+e\sum_{\lambda=0}^{\infty}\sum_{\mu=0}^{\lambda}(\varphi_{\lambda\mu}+\bar{\varphi}_{\lambda\mu}) \quad (22)$$

where the general expression for $\varphi_{\lambda\mu}$ and $\bar{\varphi}_{\lambda\mu}$ is given by equation (21) and the particular moments of the potential are determined according to the crystalline symmetry type from Table 1.

The rotational properties of the paramagnetic resonance spectrum clearly depend on the parts of $\varphi_{\lambda\mu}$ and $\bar{\varphi}_{\lambda\mu}$ which depend on the angles $(\theta\phi)$ (and thereby, according to equation (14), depend on the laboratory angles $(\theta_0\phi_0)$). Once the crystal symmetry type has picked out the proper terms (λ, μ), the angular functions $d^{(\lambda)}_{\mu'\mu}(\theta)$ are thereby determined according to equation (17).

The energy eigenvalues

It is assumed that the zero order Hamiltonian $\mathscr{H}_0$, commutes with the square (J^2) and with the third component $(J_3 = M)$ of an angular momentum operator **J**, which is otherwise unspecified. Thus, **J** may refer below to the operator, which is almost void of orbital angular momentum due to the quenching effect of the crystalline field or it may refer to the ground state of a rare earth ion in which the surrounding crystal environment has little influence in quenching its orbital momentum. (This operator is frequently referred to as the effective spin.) The usual procedure is then to diagonalize $\mathscr{H}_{\text{int}}$ in the $|n\,JM\rangle$ basis of representation (where n represents all good quantum numbers other than the angular momentum quantum numbers), and then to compare the paramagnetic resonance spectrum with the energy differences $E(JM)-E(J, M-1)$, while treating the parameters depending on the detailed coupling which determines the total angular momentum, as constants. The latter is only possible due to a factorization of the matrix elements of the spherical harmonics, which is a consequence of the Wigner–Eckart theorem.[11,12]

The shifts of the (Zeeman) magnetic energy levels, caused by the crystalline potential, are calculated by evaluating the matrix elements of the spherical harmonics. According to the Wigner–Eckart theorem, these matrix elements may be factored into two terms, one independent of the magnetic quantum number M, and the other dependent on M. The M-dependent factor of the matrix element is the Clebsch–Gordan (vector-coupling) coefficient (and is the term whose variation with M is compared with the observations of paramagnetic resonance spectra). Thus, the matrix element of the spherical harmonic Y^{μ}_{λ} is

$$\langle n'J'M'|\,Y^{\mu}_{\lambda}|nJM\rangle$$
$$= (-1)^{\lambda-J+J'}\frac{\langle\lambda\mu JM|\lambda JJ'M'\rangle}{(2J'+1)^{1/2}}\langle n'J'||\,Y^{0}_{\lambda}||\,nJ\rangle \quad (23)$$

where

$$\langle\lambda\mu JM|\lambda JJ'M'\rangle$$

is the Clebsch–Gordan coefficient.[13]

In those cases where the constants of the motion are clearly defined the reduced matrix elements $\langle n'J'||\,Y^0_\lambda||nJ\rangle$ may be readily evaluated. Such a calculation has been carried out for the rare earth group of ions by STEVENS[14].

The eigenvalues of $\mathscr{H}_{\text{int}}$ (equation 22) may then be expressed in the form

$$E(J, M) = -g\mu_0HM+E^{(1)}_c(J, M)+$$
$$+E^{(2)}_c(J, M)+\mathrm{O}(|e\varphi_c/g\mu_0H|^2) \quad (24)$$

where $E^{(1)}_c(J, M)$ and $E^{(2)}_c(J, M)$ are respectively the first and second order energy shifts of the Zeeman levels, caused by the presence of the electrostatic potential φ_c. The portions of $\varphi_{\lambda\mu}$ and $\bar{\varphi}_{\lambda\mu}$ which are diagonal (and therefore contribute to $E^{(1)}_c$) are those terms which are proportional to Y^0_λ.

In view of the inequality (9), the remainder term $\mathrm{O}(|e\varphi_c/g\mu_0H|^2)$ will be neglected. Also, we shall assume below that only the magnetic substates of a constant J-manifold need be considered. This assumption is generally valid since the separation between the ground state level $E(J)$ and the next excited level $E(J')$ is normally much greater than the magnetic energy term, which is by assumption, much greater than $|\langle e\varphi_c\rangle|$.

Combining equations (21), (22) and (23), the first order energy shift is expressed in the general form

$$E_c^{(1)}(J,M)=\sum_{\lambda\,\text{even}}2\left(\frac{4\pi}{2\lambda+1}\right)^{1/2}F_\lambda(J)\langle\lambda,0\rangle_{JM}\times$$

$$\times\sum_{\mu=0}[\Lambda_{\lambda\mu}^{(r)}P_\lambda^\mu(\cos\theta)\cos\mu\phi+\Lambda_{\lambda\mu}^{(i)}P_\lambda^\mu(\cos\theta)\sin\mu\phi] \tag{25}$$

where

$$F_\lambda(J)\equiv\langle nJ||Y_\lambda^0||nJ\rangle\langle r^\lambda\rangle \tag{26}$$

$\langle\lambda,\mu\rangle_{JM}$ is defined in terms of the Clebsch–Gordan coefficient which is diagonal in J, i.e.

$$\langle\lambda,\mu\rangle_{JM}=\langle\lambda\mu JM|\lambda JJM+\mu\rangle(2J+1)^{-1/2} \tag{27}$$

$P_\lambda^\mu(\cos\theta)$ is the associated Legendre function (equation (4), and $(\theta\phi)$ the angle between the quantization direction and the c-axis of the crystal. The term $\langle r^\lambda\rangle$ is the mean value of the λth power of the radius of the magnetic electron shell of the paramagnetic ion. In view of the current usage of the term "effective spin," the coefficient $\langle\lambda,\mu\rangle_{JM}$ will be referred to as the effective spin moment.

The second order energy shift $E_c^{(2)}$, which is of the order of $|e\varphi_c/g\mu_0H|$ times smaller than $E_c^{(1)}$, is calculated according to standard second order perturbation theory, and has the following functional form

$$E_c^{(2)}(J,M)=-e\sum_{\lambda\,\text{even}}\frac{N_{\lambda\mu}}{g\mu_0H}|F_\lambda(J)|^2\sum_{\mu'=\mu1}^{\lambda}\{[|\langle\lambda,\mu'\rangle_{JM}|^2+|\langle\lambda,-\mu'\rangle|^2](\mu')^{-1}\times$$

$$\times[|\Lambda_{\lambda\mu}^{(r)}|^2\Upsilon_{\mu'\mu}^{(\lambda)}(\theta\phi)+|\Lambda_{\lambda\mu}^{(i)}|^2\Upsilon_{\mu'\mu}^{(i)}(\theta\phi)]\} \tag{28}$$

where

$$\Upsilon_{\mu'\mu}^{(r)}(\theta\phi)=|d_{\mu'\mu}^{(\lambda)}(\theta)|^2+|d_{\mu'-\mu}^{(\lambda)}(\theta)|^2+(-1)^\mu 2\,d_{\mu'\mu}^{(\lambda)}(\theta)\,d_{\mu'-\mu}^{(\lambda)}(\theta)\cos2\mu\phi \tag{29}$$

$$\Upsilon_{\mu'\mu}^{(i)}(\theta\phi)=|d_{\mu'\mu}^{(\lambda)}(\theta)|^2+|d_{\mu'-\mu}^{(\lambda)}(\theta)|^2+(-1)^\mu 2\,d_{\mu'\mu}^{(\lambda)}(\theta)\,d_{\mu'-\mu}^{(\lambda)}(\theta)\sin2\mu\phi \tag{29b}$$

exhibit the rotational properties of the second order shift of the paramagnetic energy level spectrum. In deriving equation (29), use was made of the following symmetry property of $d_{\mu'\mu}^{(\lambda)}(\theta)$

$$d_{\mu'\mu}^{(\lambda)}(\theta)=(-1)^{\mu'-\mu}d_{-\mu'-\mu}^{(\lambda)}(\theta) \tag{30}$$

4. APPLICATION TO TRIGONAL AND HEXAGONAL SYMMETRY GROUPS

The general results obtained in the preceding section will now be applied to a calculation of the explicit functional form for the line position H_{res} in a paramagnetic resonance spectrum of a crystal whose local symmetry at the magnetic ion site is characterized by any of the trigonal or hexagonal space groups.

Since the magnetic resonance technique entails the observation of an absorption of microwave energy (at a fixed frequency ν_0) as a function of the external magnetic field, the line position H_{res} is given (to second order) by the following expression

$$H_{\text{res}}(M-1\to M)=H_0-(g\mu_0)^{-1}[\Delta E_c^{(1)}+\Delta E_c^{(2)}]\quad\text{gauss} \tag{31}$$

where

$$H_0=h\nu_0/g\mu_0$$

The first and second order crystalline field shifts of the Zeeman line position, $(\Delta E_c^{(1)}+\Delta E_c^{(2)})$, may now be determined from $E_c^{(1)}$ and $E_c^{(2)}$, (equations (25) and (28)).

In problems of practical interest, the unpaired electrons which give rise to the paramagnetic properties are in the d shell or f shell of the parent ion. The atomic wave functions transform under rotations like the matrix representations of the rotation group $\mathscr{D}_{qm}^{(l)}$. Thus the matrix elements of the moments $\varphi_{\lambda\mu}$ and $\bar{\varphi}_{\lambda\mu}$ involve an integration of a product function of which one factor transforms as the direct product

$$\mathscr{D}^{(l)}\times\mathscr{D}^{(l)}=\sum\mathscr{D}^{(L)}$$

where $0<L<2l$. Consequently, due to the

orthogonality of the $\mathscr{D}^{(l)}$ functions, the matrix elements of the electrostatic potential moments will vanish when $\lambda > 6$ for f-shell electrons and when $\lambda > 4$ for d-shell electrons. For this reason, the only moments considered below will refer to $\lambda \leqslant 6$.

One further restriction which has been imposed above, in the calculation of the energy shifts, was the neglect of those moments with λ odd. The contribution of the odd moments arises from the coupling of the ground state orbital to higher orbital states with the opposite parity. This influence is of negligible importance because the energy separation between the orbital states of the ion is many orders of magnitude greater than the magnetic energy level separations in the microwave spectrum.

(a) *The trigonal C_3 and C_{3i} symmetry groups*

The C_3 point group contains the elements E, C_3 and C_3^2. According to Table 1, the most restrictive invariance requirement imposed on the moments of the corresponding crystalline potential is

$$\varphi_{\lambda\mu}(C_3) \text{ and } \bar{\varphi}_{\lambda\mu}(C_3): \quad \lambda = n,\ \mu = 3m \quad (n, m = 0, 1, 2 \ldots) \quad (\mu \leqslant \lambda) \tag{32}$$

The C_{3i} point group is the direct product of C_3 with the inversion group I, i.e.

$$C_{3i} = C_3 \times I$$

($I \equiv S_2$). The introduction of the inversion element (and its product with the elements of C_3) leads to the following requirement on the potential moments

$$\varphi_{\lambda\mu}(C_{3i}) \text{ and } \bar{\varphi}_{\lambda\mu}(C_{3i}): \quad \lambda = 2n,\ \mu = 3m \tag{33}$$

In view of the approximation that the odd moments may be neglected, the functional form for the potential moments of C_3 and C_{3i} become identical. Combining the general expression for the first and second order energy shifts (equations (25) and (28)) with the definitions of $\Delta E_c^{(1)}$ and $\Delta E_c^{(2)}$ (equation 31) and the requirement (33), the following functional form for $\Delta E_c^{(1)}$ and $\Delta E_c^{(2)}$ for the C_3 and C_{3i} potentials is obtained. (It should be understood henceforth that when the magnetic properties arise from d-shell electrons only, the coefficients $\Lambda_{6\mu}^{(r)}$ and $\Lambda_{6\mu}^{(i)}$ must be set equal to zero.)

$$\begin{aligned}\Delta E_c^{(1)} = e\Big\{&\left(\frac{4\pi}{5}\right)^{1/2}\Lambda_{20}^{(r)}F_2(J)P_2^0(\cos\theta)[\langle 2,0\rangle_{J,M}-\langle 2,0\rangle_{J,M-1}]+\\ &+\left(\frac{4\pi}{9}\right)^{1/2}F_4(J)[\Lambda_{40}^{(r)}P_4^0(\cos\theta)+\Lambda_{43}^{(r)}P_4^3(\cos\theta)\cos 3\phi+\Lambda_{43}^{(i)}P_4^3(\cos\theta)\sin 3\phi][\langle 4,0\rangle_{J,M}-\langle 4,0\rangle_{J,M-1}]+\\ &+\left(\frac{4\pi}{13}\right)^{1/2}F_6(J)[\Lambda_{60}^{(r)}P_6^0(\cos\theta)+\Lambda_{63}^{(r)}P_6^3(\cos\theta)\cos 3\phi+\Lambda_{63}^{(i)}P_6^3(\cos\theta)\sin 3\phi+\Lambda_{66}^{(r)}P_6^6(\cos\theta)\cos 6\phi+\\ &+\Lambda_{66}^{(i)}P_6^6(\cos\theta)\sin 6\phi][\langle 6,0\rangle_{J,M}-\langle 6,0\rangle_{J,M-1}]\Big\}\end{aligned} \tag{34}$$

$$\begin{aligned}\Delta E_c^{(2)} = -e(h\nu_0)^{-1}\{&N_{20}|F_2(J)|^2|\Lambda_{20}^{(r)}|^2\sum_{\substack{\mu'=-2\\ \neq 0}}^{2}\Upsilon_{\mu'0}^{(r)}(\theta\phi)[|\langle 2,\mu'\rangle_{J,M}|^2-|\langle 2,\mu'\rangle_{J,M-1}|^2]|\mu'|^{-1}+\\ &+|F_4(J)|^2\sum_{\substack{\mu'=-4\\ \neq 0}}^{4}[N_{40}|\Lambda_{40}^{(r)}|^2\Upsilon_{\mu'0}^{(r)}(\theta\phi)+N_{43}(|\Lambda_{43}^{(r)}|^2\Upsilon_{\mu'3}^{(r)}(\theta\phi)+|\Lambda_{43}^{(i)}|^2\Upsilon_{\mu'3}^{(i)})]\times\\ &\times[|\langle 4,\mu'\rangle_{J,M}|^2-|\langle 4,\mu'\rangle_{J,M-1}|^2]|\mu'|^{-1}+|F_6(J)|^2\sum_{\substack{\mu'=-6\\ \neq 0}}^{6}N_{60}|\Lambda_{60}^{(r)}|^2\Upsilon_{\mu'0}^{(r)}(\theta\phi)+\\ &+N_{63}(|\Lambda_{63}^{(r)}|^2\Upsilon_{\mu'3}^{(r)}(\theta\phi)+|\Lambda_{63}^{(i)}|^2\Upsilon_{\mu'3}^{(i)}(\theta\phi))+N_{66}(|\Lambda_{66}^{(r)}|^2\Upsilon_{\mu'6}^{(r)}(\theta\phi)+\\ &+|\Lambda_{66}^{(i)}|^2\Upsilon_{\mu'6}^{(i)}(\theta\phi))][|\langle 6,\mu'\rangle_{J,M}|^2-|\langle 6,\mu'\rangle_{J,M-1}|^2]|\mu'|^{-1}\}\end{aligned} \tag{35}$$

Table 2. Effective spin moments $\langle\lambda, \mu\rangle_{JM}$ *for* $\lambda = 2, 4, 6$. *For purposes of brevity, the following notation is used below:* $\binom{a}{c}^{b} = (a+b)(a+b-1) \ \ldots \ (a+c) = (a+b)!/(a+c-1)!$ *(The effective spin moment is defined by equation 27)*

λ	μ	$\langle\lambda, \mu\rangle_{JM}$
2	± 2	$[6(J\mp M)(J\mp M-1)(J\pm M+2)(J\pm M+1)]^{1/2}/[(2J_{-1}^{+3})]^{1/2}$
2	± 1	$-(1\pm 2M)[6(J\mp M)(J\pm M+1)]^{1/2}/[(2J_{-1}^{+3})]^{1/2}$
2	0	$2[3M^2-J(J+1)]/[(2J_{-1}^{+3})]^{1/2}$
4	± 4	$[70(J\mp M_{-3}^{0})(J\pm M_{+1}^{+4})]^{1/2}/[(2J_{-3}^{+5})]^{1/2}$
4	± 3	$-(3\pm 2M)[140(J\mp M_{-2}^{0})(J\pm M_{+1}^{+3})]^{1/2}/[(2J_{-3}^{+5})]^{1/2}$
4	± 2	$[3(2J_{-3}^{-2})-14(2J-3)(J\mp M-2)+14(J\mp M_{-3}^{-2})]\left[\dfrac{10(J\mp M_{-1}^{0})(J\pm M_{+1}^{+2})}{(2J_{-3}^{+5})}\right]^{1/2}$
4	± 1	$-[(2J_{-3}^{-1})-9(2J_{-3}^{-2})(J\mp M-1)+21(2J-3)(J\mp M_{-2}^{-1})-14(J\mp M_{-3}^{-1})]\times$ $\times[20(J\mp M)(J\pm M+1)]^{1/2}/[(2J_{-3}^{+5})]^{1/2}$
4	0	$2[35M^4-30J(J+1)M^2+25M^2-6J(J+1)+3J^2(J+1)^2]/[(2J_{-3}^{+5})]^{1/2}$
6	± 6	$[(77)(12)(J\mp M_{-5}^{0})(J\pm M_{+1}^{+6})]^{1/2}/[(2J_{-5}^{+7})]^{1/2}$
6	± 5	$-(5\pm 2M)[(99)(28)(J\mp M_{-4}^{0})(J\pm M_{+1}^{+5})]^{1/2}/[(2J_{-5}^{+7})]^{1/2}$
6	± 4	$[5(2J_{-5}^{-4})-22(2J-5)(J\mp M-4)+22(J\mp M_{-5}^{-4})]\times[(14)(9)(J\mp M_{-3}^{0})(J\pm M_{+1}^{+4})]^{1/2}/[(2J_{-5}^{+7})]^{1/2}$
6	± 3	$-[2(2J_{-5}^{-3})-15(2J_{-5}^{-4})(J\mp M-3)+33(2J-5)(J\mp M_{-4}^{-3})-22(J\mp M_{-5}^{-3})]\times$ $\times[(35)(12)(J\mp M_{-2}^{0})(J\pm M_{+1}^{+3})]^{1/2}/[(2J_{-5}^{+7})]^{1/2}$
6	± 2	$[(2J_{-5}^{-2})-12(2J_{-5}^{-3})(J\mp M-2)+45(2J_{-5}^{-4})(J\mp M_{-3}^{-2})-66(2J-5)(J\mp M_{-4}^{-2})+33(J\mp M_{-5}^{-2})]\times$ $\times[(30)(14)(J\mp M_{-1}^{0})(J\pm M_{+1}^{+2})]^{1/2}\times[(2J_{-5}^{+7})]^{-1/2}$
6	± 1	$-[(2J_{-5}^{-1})-20(2J_{-5}^{-2})(J\mp M-1)+120(2J_{-5}^{-3})(J\mp M_{-2}^{-1})-300(2J_{-5}^{-4})(J\mp M_{-3}^{-1})+$ $+330(2J-5)(J\mp M_{-4}^{-1})-132(J\mp M_{-5}^{-1})]\times[42(J\mp M)(J\pm M+1)]^{1/2}/[(2J_{-5}^{+7})]^{1/2}$
6	0	$4[231M^6-315J(J+1)M^4+735M^4+105J^2(J+1)^2M^2-525J(J+1)M^2+294M^2-5J^3(J+1)^3+$ $+40J^2(J+1)^2-60J(J+1)]/[(2J_{-5}^{+7})]^{1/2}$

The effective spin moments $\langle \lambda, \mu \rangle_{JM}$ (defined by equation 27) which appear in equations (34) and (35) are given explicitly in Table 2. The angular functions $\Upsilon^{(r)}_{\mu'\mu}(\theta\phi)$ and $\Upsilon^{(i)}_{\mu'\mu}(\theta\phi)$ are defined by equation (29) in terms of the θ-dependent part $d^{(\lambda)}_{\mu'\mu}(\theta)$ of the representations of the rotation group. The angular functions $d^{(\lambda)}_{\mu'\mu}(\theta)$ $(\mu \neq 0)$ which are pertinent to this calculation are given explicitly in Table 3. The angular functions with $\mu = 0$ (i.e. $\Upsilon^{(r)}_{\mu'0}$) are related to the associated Legendre functions as follows

$$\Upsilon^{(r)}_{\mu'0} = 4\frac{(\lambda-\mu')!}{(\lambda+\mu')!}|P^{\mu'}_{\lambda}(\cos\theta)|^2 \tag{36}$$

The coefficients $N_{\lambda\mu}$ are defined by equation (31) and $F_\lambda(J)$ by equation (26).

All of the other trigonal and hexagonal point groups are more symmetric than the C_3 point group. Thus, the functional forms for the remaining energy shifts may be obtained from (34) and (35) by eliminating particular terms contained there.

(b) *The trigonal C_{3v} symmetry group*

The C_{3v} point group contains the elements E, C_3 and σ_v. According to Table 1, the most restrictive invariance requirement imposed on the moments of the crystalline potential is

$$\varphi_{\lambda\mu}(C_{3v}) : \lambda = n,\ \mu = 3m \quad \bar{\varphi}_{\lambda\mu}(C_{3v}) = 0 \tag{37}$$

Thus, the functional forms for $\Delta E_c^{(1)}$ and for $\Delta E_c^{(2)}$ are obtained from equations (34) and (35) by setting

$$\Lambda^{(i)}_{43} = \Lambda^{(i)}_{63} = \Lambda^{(i)}_{66} = 0 \tag{38}$$

(c) *The trigonal D_3 and D_{3d} symmetry groups*

The D_3 point group contains the elements E, C_3 and U_2. Thus, according to Table 1, the most restrictive invariance requirement on the corresponding potential moments are as follows

$$\begin{aligned} \varphi_{\lambda\mu}(D_3) &: \begin{cases} \lambda = 2n,\ \mu = 6m \\ \lambda = 2n+1,\ \mu = 6m-3 \end{cases} \\ \bar{\varphi}_{\lambda\mu}(D_3) &: \begin{cases} \lambda = 2n+1,\ \mu = 6m \\ \lambda = 2n,\ \mu = 6m-3 \end{cases} \end{aligned} \tag{39}$$

The D_{3d} point group is the direct product of D_3 with the inversion group

$$D_{3d} = D_3 \times I$$

Thus, the moments of the corresponding potential are restricted to the even moments of D_3

$$\begin{aligned} &\varphi_{\lambda\mu}(D_{3d}) : \lambda = 2n,\ \mu = 6m \\ &\bar{\varphi}_{\lambda\mu}(D_{3d}) : \lambda = 2n,\ \mu = 6m-3 \end{aligned} \tag{40}$$

In view of our approximation in which the odd moments are neglected, (39) and (40) become identical. The energy shifts $\Delta E_c^{(1)}$ and $\Delta E_c^{(2)}$ are then obtained from equations (34) and (35) by setting

$$\Lambda^{(r)}_{43} = \Lambda^{(r)}_{63} = \Lambda^{(i)}_{66} = 0 \tag{41}$$

(d) *The hexagonal D_{3h} and C_{6v} symmetry groups*

The elements of the D_{3h} group are E, σ_h, C_3, S_3, U_2 and σ_v. Using Table 1, the most restrictive invariance requirements on the corresponding potential moments are as follows

$$\varphi_{\lambda\mu}(D_{3h}) : \begin{cases} \lambda = 2n,\ \mu = 6m \\ \lambda = 2n+1,\ \mu = 6m-3 \end{cases} \qquad \bar{\varphi}_{\lambda\mu}(D_{3h}) = 0 \tag{42}$$

The elements of the C_{6v} group are E, C_2, C_3, C_6 and σ_v. The moments of the corresponding electrostatic potential are then

$$\varphi_{\lambda\mu}(C_{6v}) : \lambda = n,\ \mu = 6m \qquad \bar{\varphi}_{\lambda\mu}(C_{6v}) = 0 \tag{43}$$

Once again, (42) and (43) become equivalent in the approximation that odd moments can be neglected.

The functional form for $\Delta E_c^{(1)}$ and $\Delta E_c^{(2)}$ is then obtained from equations (34) and (35) by setting

$$\Lambda^{(r)}_{43} = \Lambda^{(i)}_{43} = \Lambda^{(r)}_{63} = \Lambda^{(i)}_{63} = \Lambda^{(i)}_{66} = 0 \tag{44}$$

(e) *The hexagonal C_{3h}, C_6 and C_{6h} symmetry groups*

The C_{3h} group is the direct product

$$C_{3h} = C_3 \times \sigma_h$$

Thus, the addition of the horizontal reflection element leads, according to Table 1, to the following corresponding potential moments

$$\varphi_{\lambda\mu}(C_{3h}) \text{ and } \bar{\varphi}_{\lambda\mu}(C_{3h}) : \begin{cases} \lambda = 2n,\ \mu = 6m \\ \lambda = 2n+1,\ \mu = 6m-3 \end{cases} \tag{45}$$

Table 3. The $d^{(\lambda)}_{\mu'\mu}(\theta)$ functions appropriate to the trigonal and hexagonal symmetry groups

	$d^{(4)}_{\mu'\mu}(\theta)$	
μ' \ μ	3	-3
± 4	$\pm[\sqrt{(2)/8}]\sin\theta(1\pm\cos\theta)^3$	$\pm[\sqrt{(2)/8}]\sin\theta(1\mp\cos\theta)^3$
± 3	$(1/8)(1\pm\cos\theta)^3(4\cos\theta\mp 3)$	$(1/8)(1\mp\cos\theta)^3(4\cos\theta\pm 3)$
± 2	$\pm[\sqrt{(14)/8}](1\pm\cos\theta)^2\sin\theta(1\mp 2\cos\theta)$	$\pm[\sqrt{(14)/8}](1\mp\cos\theta)^2\sin\theta(1\pm 2\cos\theta)$
± 1	$[\sqrt{(7)/8}]\sin^2\theta(1\pm\cos\theta)(4\cos\theta\mp 1)$	$[\sqrt{(7)/8}]\sin^2\theta(1\mp\cos\theta)(4\cos\theta\pm 1)$
	$d^{(6)}_{\mu'\mu}(\theta)$	
± 6	$\pm[\sqrt{(55)/32}]\sin^3\theta(1\pm\cos\theta)^3$	$\pm[\sqrt{(55)/32}]\sin^3\theta(1\mp\cos\theta)$
± 5	$[\sqrt{(165)/32}]\sin^2\theta(1\pm\cos\theta)^3(2\cos\theta\mp 1)$	$[\sqrt{(165)/32}]\sin^2\theta(1\mp\cos\theta)^3(2\cos\theta\pm 1)$
± 4	$\pm[\sqrt{(30)/32}](1\pm\cos\theta)^3\sin\theta(2\mp 11\cos\theta+11\cos^2\theta)$	$\pm[\sqrt{(30)/32}](1\mp\cos\theta)^3\sin\theta(2\pm 11\cos\theta+11\cos^2\theta)$
± 3	$(1/32)(1\pm\cos\theta)^3(110\cos^3\theta\mp 165\cos^2\theta+60\cos\theta\mp 1)$	$(1/32)(1\mp\cos\theta)^3(110\cos^3\theta\pm 165\cos^2\theta+60\cos\theta\pm 1)$
± 2	$\pm(3/8)\sin\theta(1\pm\cos\theta)^2(-3\mp 5\cos\theta\pm 55\cos^2\theta\mp 55\cos^3\theta)$	$\pm(3/8)\sin\theta(1\mp\cos\theta)^2(-3\pm 5\cos\theta\mp 55\cos^2\theta\pm 55\cos^3\theta)$
± 1	$\pm[\sqrt{(90)/32}]\sin^2\theta(1\pm\cos\theta)(1\mp 4\cos\theta-11\cos^2\theta\pm 22\cos^3\theta)$	$\mp[\sqrt{(90)/32}]\sin^2\theta(1\mp\cos\theta)(1\pm 4\cos\theta-11\cos^2\theta\mp 22\cos^3\theta)$

VOL. 15 1960

Table 3. (Contd.)

μ / μ'	6	$d^{(6)}_{\mu'\mu}(\theta)$	−6
±6	$(1/64)(1 \pm \cos\theta)^6$		$(1/64)(1 \mp \cos\theta)^6$
±5	$\mp[\sqrt{(3)}/32] \sin\theta(1 \pm \cos\theta)^5$		$\mp[\sqrt{(3)}/32] \sin\theta(1 \mp \cos\theta)^5$
±4	$[\sqrt{(66)}/64] \sin^2\theta(1 \pm \cos\theta)^4$		$[\sqrt{(66)}/64] \sin^2\theta(1 \mp \cos\theta)^4$
±3	$\mp[\sqrt{(55)}/32] \sin^3\theta(1 \pm \cos\theta)^3$		$\mp[\sqrt{(55)}/32] \sin^3\theta(1 \mp \cos\theta)^3$
±2	$[3\sqrt{(55)}/64] \sin^4\theta(1 \pm \cos\theta)^2$		$[3\sqrt{(55)}/64] \sin^4\theta(1 \mp \cos\theta)^2$
±1	$\mp[3\sqrt{(22)}/32] \sin^5\theta(1 \pm \cos\theta)$		$\mp[3\sqrt{(22)}/32] \sin^5\theta(1 \mp \cos\theta)$

The C_6 group contains the elements E, C_6, $C_6^2 \ldots C_6^5$. The corresponding potential moments are then restricted to

$$\varphi_{\lambda\mu}(C_6) \text{ and } \bar{\varphi}_{\lambda\mu}(C_6) : \lambda = n,\ \mu = 6m \qquad (46)$$

The C_{6h} group is formed by taking the direct product of C_6 with the inversion

$$C_{6h} = C_6 \times I$$

Thus, (as in (33) and (40)), the potential moments of C_{6h} are restricted to the even moments of the subgroup C_6.

$$\varphi_{\lambda\mu}(C_{6h}) \text{ and } \bar{\varphi}_{\lambda\mu}(C_{6h}) : \lambda = 2n,\ \mu = 6m \qquad (47)$$

The moments (45), (46) and (47) become functionally equivalent in the approximation where odd moments are neglected. The corresponding energy shifts are then obtained from equations (34) and (35) by setting

$$\Lambda^{(r)}_{43} = \Lambda^{(i)}_{43} = \Lambda^{(r)}_{63} = \Lambda^{(i)}_{63} = 0 \qquad (48)$$

(f) *The hexagonal D_6 and D_{6h} symmetry groups*

The D_6 point group contains the elements E, C_2, C_3, C_6, U_2. According to Table 1, the corresponding potential moments are as follows

$$\varphi_{\lambda\mu}(D_6) : \lambda = 2n,\ \mu = 12m$$
$$\bar{\varphi}_{\lambda\mu}(D_6) : \lambda = 2n+1,\ \mu = 12m \qquad (49)$$

The D_{6h} point group is the direct product of D_6 with the inversion

$$D_{6h} = D_6 \times I$$

and as before, the corresponding moments are restricted to the even moments of the subgroup D_6.

$$\varphi_{\lambda\mu}(D_{6h}) : \lambda = 2n,\ \mu = 12m \quad \bar{\varphi}_{\lambda\mu}(D_{6h}) = 0 \qquad (50)$$

Since practical problems always require $\lambda \leqslant 6$ and since $\mu \leqslant \lambda$, the condition that $\mu = 12m$ reduces, in the approximation used here, to the axial case ($\mu = 0$). Thus, the energy shifts due to potentials of D_6 and D_{6h}, obtained from equations (34) and (35) by setting

$$\Lambda^{(r)}_{43} = \Lambda^{(i)}_{43} = \Lambda^{(r)}_{63} = \Lambda^{(i)}_{63} = \Lambda^{(r)}_{66} = \Lambda^{(i)}_{66} = 0 \qquad (51)$$

is equivalent to the approximation in which the $\boldsymbol{D}_6$ and $\boldsymbol{D}_{6h}$ groups are replaced by a cylindrical symmetry (i.e. invariance with respect to infinitesimal rotations about the c-axis). Thus, this approximation which is frequently made when analyzing the spectra of crystals of *any* of the non-cubic symmetry types, is, strictly speaking, only valid when the symmetry is described by the $\boldsymbol{D}_6$ or $\boldsymbol{D}_{6h}$ groups.

Summarizing, the paramagnetic resonance spectrum of a magnetic ion, subjected to a uniform magnetic field and an electrostatic potential (which is due to a local crystal symmetry of any of the trigonal or hexagonal types), is completely described to second order in $(|e\varphi_c/g\mu_0 H|)$ by equations (31) through (51). The rotational properties of the spectrum are exhibited in (31) in both the g factor (according to equation 13) and in the functions

$$P_\mu^\lambda(\cos\theta)\begin{cases}\cos\mu\phi\\ \sin\mu\phi\end{cases}$$

and $\Upsilon_{\mu'\mu}(\theta\phi)$ which appear in the energy shifts $\Delta E_c^{(1)}$ and $\Delta E_c^{(2)}$ (given by equations (34) and (35) respectively). The paramagnetic resonance spectrum for the other non-cubic crystals may be readily derived by following the same procedure as above.

It should be emphasized once more that the angles $(\theta\phi)$ in equations (34) and (35) are related to the laboratory angles $(\theta_0\phi_0)$ (which orient the applied magnetic field with respect to the crystalline c-axis) according to equation (14). Thus

$$P_2^0(\cos\theta) = \tfrac{1}{2}(3\cos^2\theta - 1) = \frac{1}{2}\left[3\left(\frac{g_3'}{g}\right)^2\cos^2\theta_0 - 1\right], \qquad (52)$$

etc.

and

$$\cos 3\phi = \cos 3\left[\tan^{-1}\left(\frac{g_2'}{g_1'}\tan\phi_0\right)\right] = g_1'\cos\phi_0[(g_1')^2\cos^2\phi_0 - 3(g_2')^2\sin^2\phi_0]/[(g_1')^2\cos^2\phi_0 + (g_2')^2\sin^2\phi_0]^{3/2} \qquad (53)$$

$$\cos 6\phi = \cos 6\left[\tan^{-1}\left(\frac{g_2'}{g_1'}\tan\phi_0\right)\right] = [(g_1')^6\cos^6\phi_0 - 15(g_1')^4(g_2')^2\cos^4\phi_0\sin^2\phi_0 + 15(g_1')^2(g_2')^4\cos^2\phi_0\sin^4\phi_0 - (g_2')^6\sin^6\phi_0]/[(g_1')^2\cos^2\phi_0 + (g_2')^2\sin^2\phi_0]^3 \qquad (54)$$

$$\sin 3\phi = \sin 3\left[\tan^{-1}\left(\frac{g_2'}{g_1'}\tan\phi_0\right)\right] = (g_2')\sin\phi_0[3(g_1')^2\cos^2\phi_0 - (g_2')^2\sin^2\phi_0]/[(g_1')^2\cos^2\phi_0 + (g_2')^2\sin^2\phi_0]^{3/2} \qquad (55)$$

$$\sin 6\phi = \sin 6\left[\tan^{-1}\left(\frac{g_2'}{g_1'}\tan\phi_0\right)\right] = 2g_1'g_2'\sin\phi_0\cos\phi_0[3(g_1')^4\cos^4\phi_0 - 10(g_1')^2(g_2')^2\sin^2\phi_0\cos^2\phi_0 + 3(g_2')^4\sin^4\phi_0]/[(g_1')^2\cos^2\phi_0 + (g_2')^2\sin^2\phi_0]^3 \qquad (56)$$

It should also be restated here that while the c-axis of the crystal uniquely defines the polar angle θ_0, the azimuthal angle ϕ_0 must be measured with respect to an axis x_1', which is initially chosen (arbitrarily, at the Eulerian angle α) in the plane perpendicular to the c-axis. The values which are then obtained (from the experiment) for g_1' and g_2' then refer to the initial choice of the x_1' axis.

REFERENCES

1. Zavoisky E., *Zh. fiz. Mosk.* **9,** 211 (1945).
2. Zavoisky E., *Zh. fiz. Mosk.* **10,** 197 (1946).
3. Bleaney B. and Stevens K. W. H., *Reports on the Progress of Physics.* **16,** 108 (1953).
4. Bowers K. D. and Owens J., *Rep. Progr. Phys.* **18,** 304 (1955).
5. Koster G. F. and Statz H., *Phys. Rev.* **113,** 445 (1959).
6. Elliott R. J. and Stevens K. W. H., *Proc. Roy. Soc.* A **215,** 437 (1952).
7. Elliott R. J. and Stevens K. W. H., *Proc. Roy. Soc.* A **218,** 553 (1953).

8. ABRAGAM A. and PRYCE M. H. L., *Proc. Roy. Soc.* A **205,** 135 (1952).
9. See, for example, KOSTER G. F., *Solid State Physics*, Vol. V (edited by SEITZ F. and TURNBULL D.) Academic Press, New York (1957).
10. See, for example, EDMONDS A. R., *Angular Momentum in Quantum Mechanics*, Chapter 4. Princeton University Press, Princeton, New Jersey (1957).
11. WIGNER E. P., *Z. Phys.* **43,** 624 (1927).
12. ECKART C., *Rev. Mod. Phys.* **2,** 305 (1930).
13. Ref. 10, Section 3.6.
14. STEVENS K. W. H., *Proc. Phys. Soc. Lond.* A **65,** 209 (1952).

VOL.
15
1960

J. Phys. Chem. Solids Pergamon Press 1960. Vol. 15. pp. 306–310. Printed in Great Britain.

THE PREPARATION AND THE ELECTRICAL AND OPTICAL PROPERTIES OF SnS CRYSTALS

W. ALBERS, C. HAAS and F. van der MAESEN

Philips Research Laboratories, N. V. Philips' Gloeilampenfabrieken, Eindhoven, Netherlands

(*Received* 10 *December* 1959)

Abstract—SnS crystals were prepared by melting the components in an evacuated quartz tube at about 900°C. The observed melting point is 880 ± 5°C. The crystals were *p*-type with a hole density between 10^{17} and 10^{18} cm^{-3} and $\mu_p = 65$ cm^2/V sec at room temperature. One of the crystals showed an anomalous behaviour of the Hall-coefficient with temperature similar to what was found recently in SnSe.

Preliminary measurements show that the conductivity in the direction of the *c*-axis is about six times smaller than in the direction perpendicular to the *c*-axis at room temperature. Analysis of infrared transmission measurements at room temperature on cleavage plates perpendicular to the *c*-axis reveal the energy gap to be 1·07 ± 0·04 eV. The free carrier absorption part of the transmission curve shows a dependence of $\alpha \sim \lambda^2$; analysis of this curve leads to an effective mass $m = 0{\cdot}4\ m_0$ for the holes.

INTRODUCTION

THE OPTICAL and photoconductive properties of PbS, PbSe and PbTe have been studied intensively, especially in view of the application of these compounds as sensitive infrared detectors. The corresponding stannous salts have attracted much less attention. In recent years some papers have been published on the electrical and optical properties of SnSe crystals.[1,2,3]

Whereas PbS, PbSe and PbTe, as well as SnTe, crystallize in the sodium chloride structure, SnS and the isomorphous SnSe show a more complicated rhombic structure.[4,5] This structure, which is pseudotetragonal, may be thought of as a rather strongly distorted sodium chloride structure. The crystal consists of double layers perpendicular to the *c*-axis in which the Sn and S atoms are tightly bound. The bonding between these layers is much weaker as shown by larger interatomic distances, and by a (001) cleavage plane.

ANDERSON *et al.* have studied the electrical conduction[6,7,8] and the thermoelectric power[9] of SnS pellets. He found *p*-type conductivity and a band gap of approximately 1·2 eV. BRAITHWAITE[10] found photoconductivity in SnS powder, with a long wavelength threshold of 1·1 μ. GOBRECHT and BARTSCHAT[11] measured the infrared transmission, photoconductivity and rectifying properties of layers of SnS, and estimated a band gap of 1·25 eV.

PREPARATION OF THE CRYSTALS

Crystals of SnS were prepared by melting stoichiometric amounts of the component materials* at a temperature of about 900°C in an evacuated quartz tube. Since the maximum vapour pressure of sulphur at this temperature can be expected to be approximately 100 atmospheres, part of the tube was kept at 400°C to avoid explosion. The gray mass obtained in this way was powdered and placed in a silica boat. In order to avoid the sticking of the product to the quartz the surface of the boat was roughened by sandblasting, then covered with a layer of graphite by pyrolysis of butane at 1000°C and next with a soot layer. The silica boat was placed inside an evacuated quartz tube which was heated at 420°C. Finally a molten zone of about 900°C was passed through the sample at a rate of

* Stannum pulvis purissimum ST442 from Brocades-Stheeman & Pharmacia, Amsterdam, Holland; Sublimed Sulphur 7982 from E. Merck A.G., Darmstadt, Germany.

about 1 cm per hr in order to obtain single crystals.

In this way a bar of the composition SnS was obtained as shown by an X-ray powder diagram and by chemical analysis (Table 1). The observed

Table 1. *Chemical analysis of* SnS *crystals prepared by fusion of the constituent elements.*

Specimen	Sn (wt%)	S (wt%)
A	79·2 ± 0·5	
B	78·5 ± 0·5	21·5 ± 0·5
C	79·7 ± 0·5	20·9 ± 0·5
D	78·8 ± 0·5	
theoretical	78·7	21·3

melting point was 880 ± 5°C. Spectrochemical analysis showed the presence of various impurities (Fe, Pb, Al, Sb, Ni, Mn, Cu) with a total concentration of the order of 10^{18} to 10^{19} cm^{-3}, which is comparable with the impurity concentrations in the starting materials.

It was possible to cut neat-looking crystals of considerable size (dimensions up to $2 \times 0{\cdot}5 \times 0{\cdot}3$ cm^3) from the bar. The crystals have a metallic appearance. They can be cleaved very easily along the cleavage plane; slices of a thickness down to 20μ can be prepared in this way.

The electrical and optical experiments were all done on apparently single crystals. X-ray Laue diagrams of the crystals show single crystals of considerable size. It must be noted, however, that twinning may occur rather frequently in these crystals as earlier pointed out by HOFMANN[4].

ELECTRICAL PROPERTIES

The resistivity and Hall coefficient of SnS crystals were measured as a function of temperature. Most of the measurements were done on cleavage plates perpendicular to the crystallographic *c*-axis. The crystals showed *p*-type conductivity. From an analysis of the results both the number and the mobility of the charge carriers were determined in the usual way.

Fig. 1 shows the number of holes present in three typical samples of SnS as a function of temperature. For the crystals I and II the hole

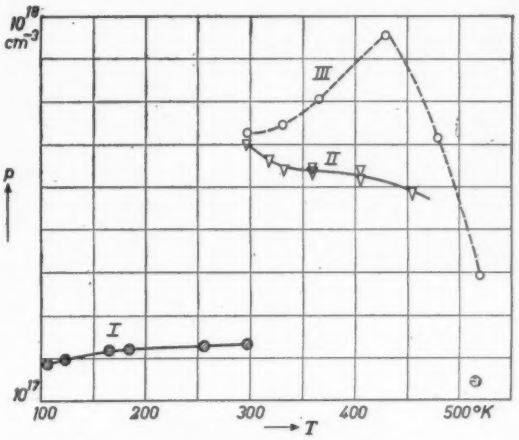

FIG. 1. Concentration of holes p as a function of temperature for three different crystals.

concentration does not depend strongly on T in the ranges measured and has values of 2 and 7×10^{17} cm^{-3} respectively. Crystal III, however, shows a rather anomalous behaviour of a decreasing hole

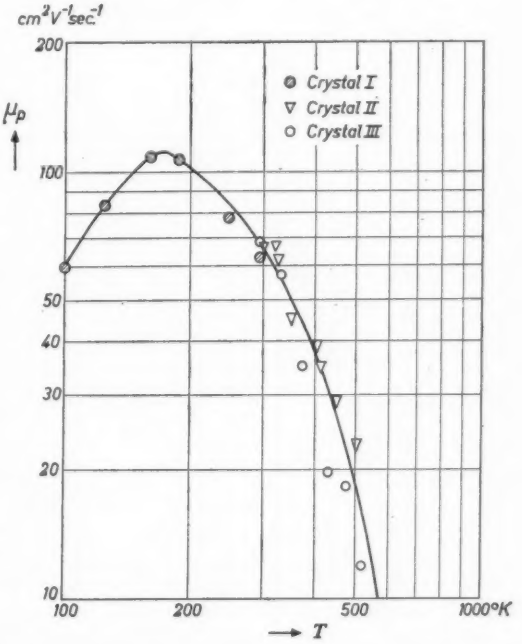

FIG. 2. Hole mobility μ_p perpendicular to the *c*-axis as a function of temperature for three different crystals.

concentration (increasing Hall-coefficient) with temperature in the range of 430–520°K.

Fig. 2 gives the corresponding experimentally determined mobilities perpendicular to the *c*-axis, the points are seen to scatter within a rather narrow region about the drawn curve. The mobility is about 65 cm^2/V sec at room temperature. For SnSe a hole mobility of the same order of magnitude was recently reported.[1,2] Between 100°K and 175°K the mobility changes approximately with $T^{3/2}$, indicating that ionic impurity scattering dominates in this temperature region. Between 175°K and 350°K the mobility varies roughly as $T^{-3/2}$, a behaviour characteristic of lattice scattering.

At still higher temperature the mobility decreases more strongly with temperature.

The mobility deduced from the measurements on crystal III does not show an anomalous behaviour. This suggests that the decreasing hole concentration mentioned is probably due to irreversible changes in the number of acceptors or donors or both during measuring. Similar changes are reported in SnSe crystals[2] and might be caused by the diffusion of impurities. Preliminary measurements on crystals with suitable dimensions ($0{\cdot}25 \times 0{\cdot}25 \times 0{\cdot}25$ cm^3) reveal an anisotropy of the electrical properties. It was found that at room temperature the mobility of the holes parallel to the *c*-axis is approximately six times smaller than the mobility perpendicular to the *c*-axis.

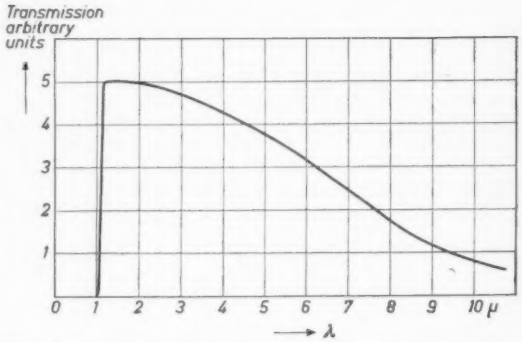

FIG. 3. Transmission (arbitrary units) of SnS cleavage plate thickness 0·037 cm, as a function of wavelength.

OPTICAL PROPERTIES

The infrared transmission of cleavage plates (perpendicular to the crystallographic *c*-axis) of SnS single crystals was measured at room temperature using a Perkin Elmer double beam spectrometer with NaCl and LiF prisms. Because of the poor optical quality of the surface, the absolute value of the observed transmission is not reliable. The form of the transmission curve, however, was quite reproducible and essentially the same for all specimens.

A typical transmission curve is shown in Fig. 3. For wavelengths shorter than 1μ the crystal is strongly absorbent. Absorption in this region is presumably intrinsic, corresponding to transitions

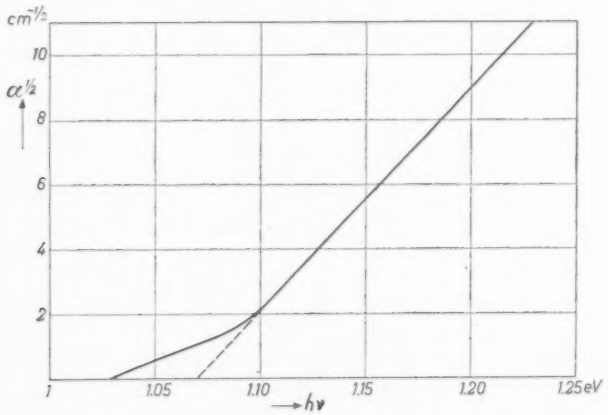

FIG. 4. Absorption edge: square root of the absorption coefficient α as a function of photo energy.

of electrons from the valence to the conduction band. The absorption at longer wavelengths is characteristic of free carrier absorption.

The absorption edge at 1μ was analyzed more carefully, using a LiF prism which has a higher resolving power in this spectral region. It was found that, if the square root of the absorption coefficient α* is plotted as a function of photon energy, a straight line is obtained between 1·10 and 1·25 eV (see Fig. 4). A rather small residual absorption remains at lower photon energy. The straight line portion of the curve indicates that absorption in this region is due to indirect transitions. Consequently the maximum of the valence band and the minimum of the conduction band occur at different values of the crystal momentum vector k. Theory[12] predicts for the absorption coefficient in this case:

$$\alpha = A(h\nu - E_G \pm \hbar\omega)^2$$

where $h\nu$ is the photon energy, E_G the band gap and $\hbar\omega$ the energy of the phonon which makes the indirect transition possible. The plus sign in the equation applies if the indirect transition involves the absorption of a phonon, the minus sign if the transition involves the emission of a phonon.

From our preliminary results an extensive analysis is not possible; this would require measurements at low temperature with a higher spectral resolution.[13] We may conclude, however, that the extrapolated straight line intersects the abscissa at $E_G \pm \hbar\omega$. Estimating the phonon energy to SnS to be equal to or smaller than 0·04 eV we obtain for the band gap of SnS at room temperature: $E_G = 1{\cdot}07 \pm 0{\cdot}04$ eV.

The absorption coefficient for free carrier absorption was found to be proportional to the square of the wavelength λ in a large spectral region (Fig. 5). This result is in agreement with the classical Drude theory for free carrier absorption. At shorter wavelengths ($\lambda < 6\mu$) some additional absorption is present. It should be noted that, because the absolute value of the transmission is not accurately known, only the change of the absorption coefficient with wavelength is reliable. Therefore the fact that the straight line in Fig. 5 does not pass through the origin is not significant.

* The absorption coefficients were not corrected for reflection.

According to the simple Drude theory,[14] the absorption coefficient is given by

$$\alpha = \frac{Ne^3\lambda^2}{\pi C^3 \mu n (m^*)^2}$$

where N is the number of carriers, C the velocity of light in vacuum, n the refractive index, μ the mobility, e the charge and m^* the effective mass of the carriers. A reasonable value for the refractive index of a semiconductor with a band gap of about 1 eV is $n = 3{\cdot}5$ (compare silicon with $E_G = 1{\cdot}15$ eV and $n = 3{\cdot}4$). Substituting this value, and $\mu = 65$ cm²/V sec and $N = 5{\cdot}10^{17}$ holes/cm³ obtained from the Hall measurements at room temperature we find for the effective mass of holes $m^* = 0{\cdot}4\ m_0$ (m_0 is the free electron mass). Because the Drude theory gives an oversimplified description of the scattering mechanism responsible for free carrier absorption,[15] we may at best hope that the value obtained here for the effective mass is of the correct order of magnitude.

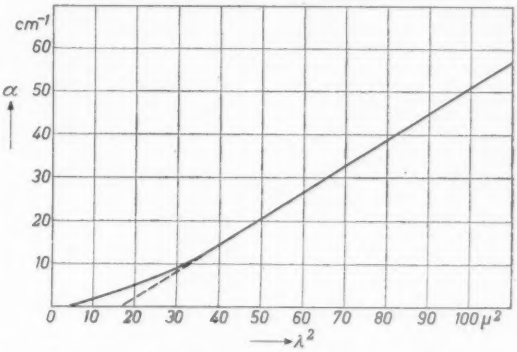

FIG. 5. Free carrier absorption: absorption coefficient α as a function of the square of the wavelength.

REFERENCES

1. ASANABE S. and OKAZAKI A., *Proc. Phys. Soc., Lond.* **73**, 824 (1959).
2. ASANABE S., *J. Phys. Soc., Japan* **14**, 281 (1959).
3. MITCHELL O. L. and LEVINSTEIN H., *Bull. Amer. Phys. Soc.* (ser. 2), **6**, 133 (1959).
4. HOFMANN W., *Z. Kristall.* **92**, 161 (1935).
5. OKAZAKI A., *J. Phys. Soc., Japan* **11**, 470 (1956).
6. ANDERSON J. S. and CLARK M. C., *Nature, Lond.* **152**, 75 (1943).
7. ANDERSON J. S. and MORTON M. C., *Nature, Lond.* **155**, 112 (1945).

VOL. 15 1960

8. ANDERSON J. S. and MORTON M. C., *Proc. Roy. Soc.* A**184**, 83 (1945).
9. ANDERSON J. S. and MORTON M. C., *Trans. Faraday Soc.* **43**, 185 (1947).
10. BRAITHWAITE J. G. M., *Proc. Phys. Soc., Lond.* B**64**, 274 (1951).
11. GOBRECHT H. and BARTSCHAT A., *Z. Phys.* **149**, 511 (1957).
12. BARDEEN J., BLATT F. J. and HALL L., *Photoconductivity Conference* 1954–1956, John Wiley, New York.
13. MACFARLANE G. G., MCLEAN T. P., QUARRINGTON J. E. and ROBERTS V., *Phys. Rev.* **108**, 1377 (1957).
14. MOSS T. S., *Optical Properties of Semiconductors*, Butterworths, London (1959).
15. MEYER H. J. G., *Phys. Rev.* **112**, 298 (1958).

J. Phys. Chem. Solids Pergamon Press 1960. Vol. 15. pp. 311–323. Printed in Great Britain.

DISLOCATIONS, STACKING FAULTS AND TWINS IN THE SPINEL STRUCTURE

J. HORNSTRA

Philips Research Laboratories, N. V. Philips Gloeilampenfabrieken
Eindhoven, Netherlands

(*Received* 1 *December* 1959)

VOL. 15 1960

Abstract—The slip plane in crystals of the spinel type is assumed to be the (111) plane in analogy with the basal slip of corundum. This is also in agreement with experimentally observed deformation twinning, which may be explained as a mechanism involving partial dislocations with a (111) slip plane. Dislocations with a (111) slip plane may consist of four partial dislocations separated by three stacking faults. The detailed structure of these stacking faults is compared with the perfect spinel lattice. During slip the cations move in a direction different from that of the oxygen ions. This process, the synchro-shear process, is discussed for the case that cations with fourfold coordination take part in it. Another type of stacking fault shows relationship to the olivine lattice. Two possible configurations of the (111) twin boundary are discussed.

1. INTRODUCTION

RECENTLY many authors have studied the plastic deformation of ceramic oxides, e.g. α-Al_2O_3 (KRONBERG[1]) and MgO, α-Al_2O_3 and rutile (WACHTMAN and MAXWELL[2]).

In this laboratory much work has been done on spinels of different compositions by GORTER and co-workers (reviewed by GORTER[3]). It therefore seemed desirable to investigate the plastic behaviour of these mixed oxides, the more so because dislocations may play an important role in sintering, which is the usual method of preparing these materials. It is difficult to study the plasticity experimentally, as the equilibrium oxygen pressure of most spinels is rather high at the temperature required for these experiments. In this paper the structure of dislocations is studied theoretically as was done for corundum by KRONBERG[1].

The first problem to be solved is the choice of the slip plane. In corundum, which has a slightly distorted hexagonal close-packed oxygen lattice, the predominant slip plane is the basal plane (0001). The corresponding planes in the spinel lattice, which has a slightly distorted cubic close-packed oxygen lattice, are the {111} planes. In this case dislocations can dissociate into four partial dislocations separated by stacking faults as in the case of corundum.[1] This slip plane would be in agreement with the experiments on deformation twinning by GRÜN[4], who found that {111} twinning could be induced by high pressure. The mechanism of deformation twinning is usually the passage of partial dislocations along the twin plane.

However, not all face centered cubic (f.c.c.) lattices show the slip plane {111}. Metals like copper do, but NaCl and several other halides with the same structure have the slip plane {110}, although they contain an f.c.c. lattice of anions. An examination of the difference between the structure of these halides and the spinel structure may explain this behaviour. In NaCl the number of cations is equal to the number of anions, whereas in spinels the proportion of cations is smaller. Moreover, most cations in spinels have a higher valency than the anions and are therefore smaller compared with the anions than in the case of NaCl, where cations and anions have the same valency. In spinels the oxygen ions do not form a perfect cubic close-packed lattice; hence their packing is less dense than that of the chloride ions in NaCl. The tetrahedral interstices appear to be of almost

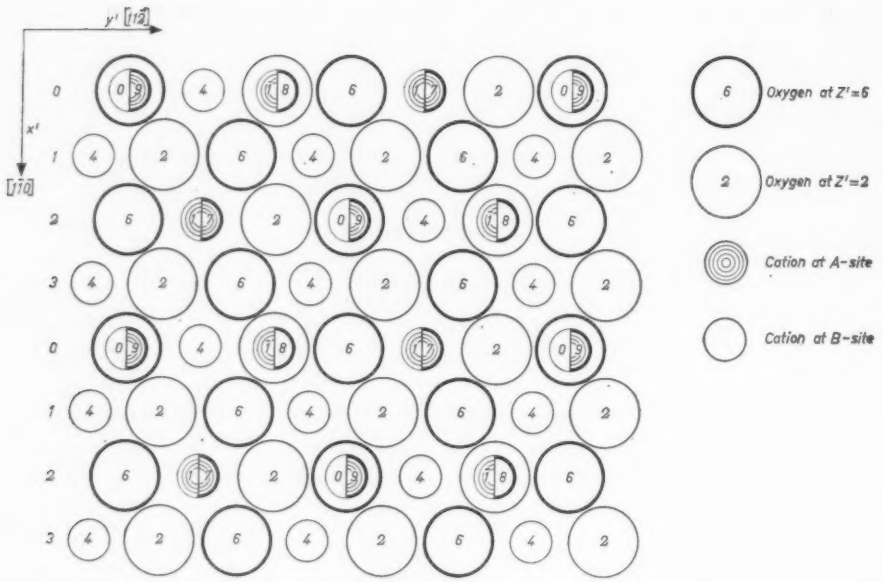

(a)

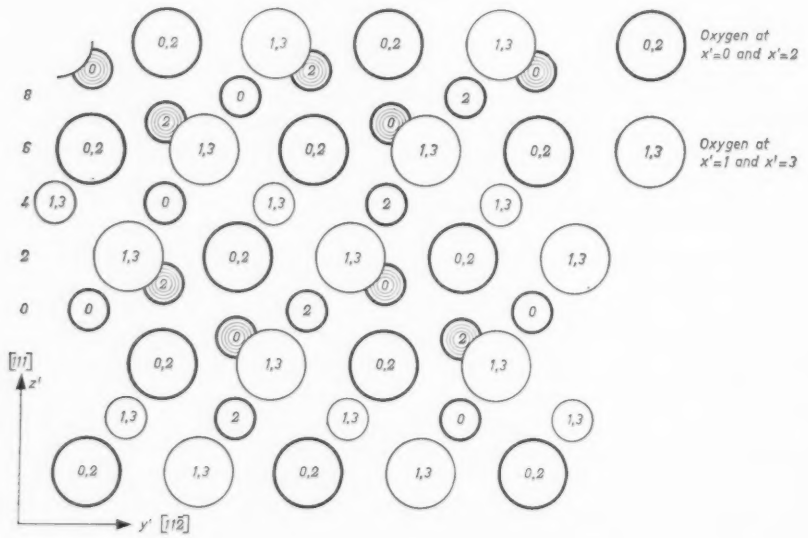

(b)

FIG. 1. (a) Projection of the idealized spinel lattice on the (111) plane; the height z' is given in multiples of $1/24\ a_0\sqrt{3}$, where a_0 is the edge of the unit cell. Oxygen ions at $z' = 2$ and 10 are omitted. (b) Projection on the $(1\bar{1}0)$ plane; the height x' is given in multiples of $\frac{1}{8}a_0\sqrt{2}$. Ions are drawn in thick lines when x' is an even number and in thin lines when x' is an odd number. The figures at the left side of Fig. 1(b) correspond with the figures in the ions of Fig. 1(a) and the figures at the left of Fig. 1(a) with those in the ions of Fig. 1(b).

the same size as the octahedral interstices. Not only the regular tetrahedral interstices will be enlarged by this deviation, but the tetrahedral interstices that are temporarily occupied during the slip process, as will be discussed later on, may also be large enough to accommodate both kinds of cations. Because of these three effects the cations will hinder slip along {111} planes in spinels to a much smaller extent than in NaCl. Therefore in this paper only the {111} slip plane will be considered. By a similar reasoning one finds that corundum will slip on the basal plane rather than on $\{1\bar{1}00\}$ planes, in agreement with experiment.[1]

VOL. 15 1960

2. THE SPINEL LATTICE

In Fig. 1(a) the lattice of spinel ($MgAl_2O_4$) is projected on the (111) plane. For the sake of clearness and simplicity the ions are drawn smaller than the distances between them and the structure is idealized so that the oxygen ions occupy a perfect f.c.c. lattice. The height z' of the ions above the plane of projection is expressed in multiples of $1/24\ a_0\sqrt{3}$, where a_0 is the lattice constant, in order to obtain whole numbers. Only part of the structure is shown since the layer at $z' = 0$ is not repeated until $z' = 24$. Of the six oxygen layers only those at $z' = 2$ and $z' = 6$ are given, the projections of the oxygen ions at $z' = -2$ and $z' = 10$ falling in the open spaces between them. In Fig. 1(b) the idealized spinel lattice is projected on the $(1\bar{1}0)$ plane. The layer at $x' = 4$ is a repetition of the layer at $x' = 0$.

In Fig. 1(a) the zero-point of height has been chosen as lying in a layer of cations at *B*-sites, with sixfold coordination (octahedral ions), so that all these ions and the oxygen ions are at even heights, and the cations at *A*-sites, with fourfold coordination (tetrahedral ions) are at odd heights. For instance, the tetrahedral ion at $z' = 7$ is surrounded by four oxygen ions, one at $z' = 10$ and three at $z' = 6$.

Of all octahedral interstices at $z' = 4$ only three quarters are occupied. The cations at this height form a layer structure which has been called a kagome-structure by IIDA[5]. This layer consists of hexagons and triangles, as may be seen in Fig. 1(a). Between the oxygen layers at $z' = 6$ and $z' = 10$, cations of both kinds are found. Although these cations are at different heights ($z' = 7$, 8 and 9) and therefore do not, strictly speaking, form a layer, we will call this composite layer a mixed cation layer. Between the oxygen layers in a $\langle 111 \rangle$ direction are found alternately kagome layers and mixed layers.

The tetrahedral ions (at $z' = 7$ and $z' = 1$) nearest to a kagome layer ($z' = 4$) occupy sites above and below the empty sites at the centres of the hexagons of the kagome layer. In all directions there is always an empty octahedral site between two neighbouring tetrahedral cations. The projections of the cations at $z' = 8$ and $z' = 9$ (Fig. 1(a)) coincide with the centres of the triangles of the kagome layer at $z' = 4$.

In Fig. 1(a) as well as in Fig. 1(b) one can see that every oxygen ion in the spinel lattice is surrounded by four cations, one at a tetrahedral site and three at octahedral sites. This is in agreement with Pauling's rule that the valency of an anion is equal to the sum of the valencies of the surrounding cations divided by the corresponding coordination numbers. If there are divalent cations at the tetrahedral sites and trivalent cations at the octahedral sites (normal spinel), the equation reads $2/4+3\times 3/6 = 2$.

3. EXTENDED *abc*-NOTATION

In discussions about close-packed lattices it is customary to denote the stacking order in the $\langle 111 \rangle$ direction of a cubic close-packed lattice by . . . *abcabc* . . . and that in the [0001] direction of a hexagonal close-packed lattice by . . . *ababab* . . . or . . . *bcbc* . . . etc. This notation can be directly applied to the oxygen ions of the spinel lattice, as may be seen in the (111) projection of Fig. 1(a). Let us assume that the oxygen ions at $z' = 2$ occupy *a*-sites, those at $z' = 6$ occupy *c*-sites and those at $z' = -2$ and $z' = 10$ occupy *b*-sites. Since the projections of all cations coincide with the projections of oxygen ions, the cation sites can also be described by this notation. The octahedral cations at $z' = 4$ occupy *b*-sites like the oxygen ions at $z' = -2$ and $z' = 10$. The tetrahedral cations at $z' = 9$ occupy *c*-sites like the oxygen ions at $z' = 6$, etc.

However, not all octahedral and tetrahedral interstices are occupied by cations, but only three quarters of the sites at $z' = 4$ and one quarter of the sites at $z' = 7$, 8 and 9. Therefore, the sites of each layer have to be divided into four groups, as is shown in Fig. 2. A similar subdivision was made

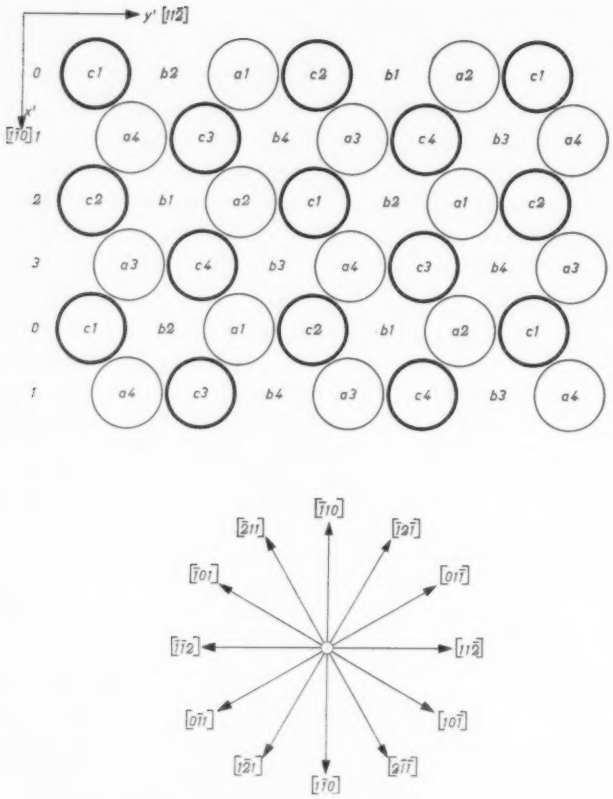

FIG. 2. Extended *abc*-notation and directions of all possible Burgers vectors of perfect and partial dislocations.

by IIDA[5], who used a slightly different notation.* Comparing Fig. 1(a) with Fig. 2, one can see that the spinel lattice can be represented schematically as is shown in Table 1. The subdivision of the three layers has been chosen in such a way that the occupied positions at $z' = 7$, 8 and 9 and the unoccupied site of the cation layer at $z' = 4$ are given the same figure.

4. DISLOCATIONS AND PARTIAL DISLOCATIONS

The Burgers vector of a dislocation is equal to

* IIDA used capitals A, B, C where we use small letters to exclude confusion with *A*- and *B*-sites, which are sites with fourfold and sixfold coordination. It is also to be noted that figures preceded by a small letter refer to the subdivision mentioned above and not to height.

Table 1. *The spinel lattice in extended abc-notation*

z'	occupied position	kind of ion
10	*b* 1, 2, 3, 4	oxygen ion
9	*c* 1	*A*-cation
8	*a* 1	*B*-cation
7	*b* 1	*A*-cation
6	*c* 1, 2, 3, 4	oxygen ion
5	—	
4	*b* 2, 3, 4	*B*-cation
3	—	
2	*a* 1, 2, 3, 4	oxygen ion
1	*b* 1	*A*-cation
0	*c* 1	*B*-cation
−1	*a* 1	*A*-cation
−2	*b* 1, 2, 3, 4	oxygen ion

the distance between two equivalent sites, e.g. c 1-sites in Fig. 2. For instance, when a dislocation between the oxygen layers at $z' = 2$ and $z' = 6$ passes a certain point and we suppose the lower part of the crystal ($z'<3$) to be fixed, then the upper half must slip $\frac{1}{2}\, a_0\sqrt{2}$ in a $\langle 110\rangle$ direction. This will not take place in one step; in the case of a Burgers vector $\frac{1}{2}\,[01\bar{1}]$ the oxygen ion at c 1 will go by way of the intermediate positions b 2, c 4 and b 3. The behaviour of the cations at $z' = 4$ during the slip process will be discussed in Section 5.

Because the oxygen ions fit quite well in the intermediate positions, there will be certain regions

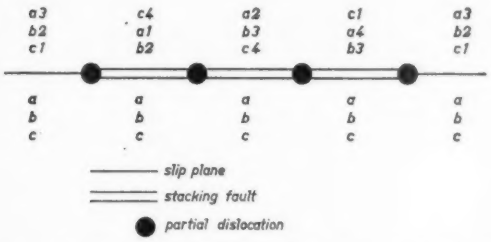

FIG. 3. Extended dislocation. The letters denote the stacking of the oxygen ions. In the top half one of the four oxygen ions in each layer is selected and for each stacking fault the position of the corresponding ion is given to show the Burgers vectors of the partial dislocations.

in the slip plane where they occupy these wrong positions. These regions are called stacking faults, and the boundaries between two stacking faults or between a stacking fault and the perfect lattice are called partial dislocations (here: quarter dislocations). Therefore, a dislocation with a {111} slip plane may consist of four partials and three stacking faults as is shown in Fig. 3 together with the stacking of the oxygen ions.

The Burgers vector of each quarter dislocation has the length $1/12\, a_0\sqrt{6}$ and the direction $\langle 112\rangle$. It is possible, although unlikely, that the free energy of one or more of these stacking faults is so high that the width of the faulted region becomes very small, so that two quarter dislocations nearly coincide and almost form one half dislocation with Burgers vector $\frac{1}{4}\, a_0\sqrt{2}$ in a $\langle 110\rangle$ direction.

5. SYNCHRO-SHEAR

When two oxygen layers slip along each other, the octahedral cations between them cannot remain in their original positions with respect to one of the oxygen layers, but have to move to a new octahedral site. This mechanism was described by KRONBERG[1] for the corundum lattice and was called synchro-shear. The direction in which the cations move differs by 60° from the direction in which the oxygen ions move. When, in the notation of Fig. 2, the oxygen ion at c 1 goes to b 2, the octahedral ion at b 2 must find its new position at c 3 or c 4, which now become octahedral sites. The new position c 1 would require motion in a sense opposite to that of the oxygen ions, whereas position c 2 is too far off.

All octahedral ions of the kagome layer at $z' = 4$ (Fig. 1(a)) have to move in the $[\bar{1}\ 2\ \bar{1}]$ or the $[2\ \bar{1}\ \bar{1}]$ direction and the empty octahedral cation site will also move in one of these directions. All empty sites will move in the same direction, because otherwise a new type of cation layer would be formed and this will be prevented by the electrostatic repulsion between the cations.

Now we shall discuss the case of the slip plane coinciding with a mixed layer instead of with a kagome layer. In this case tetrahedral cations take part in the synchro-shear process. In Fig. 4 it is shown that again all cations can move in directions that are parallel in the (111) projection, so that the layer structure is restored. Since the cations at $z' = 3$ and $z' = 5$ have their heights interchanged by the slip process, the new layer is a mirror image of the original one, or, which comes to the same thing, is rotated by 60° or 180° about [111]. The new layer has to be a mirror image of the original one, because the stacking of the oxygen ions now corresponds to that of a (111) twin.

In the intermediate position of Fig. 4(b) all cations are assumed to occupy deformed tetrahedral interstices. Four oxygen neighbours (H, K, L and M) of the octahedral ion in this position remain its neighbours all the way from the initial to the final state. The tetrahedral ion has only two neighbours which are common to the initial and the final state (C and D); the neighbours of this ion change from $A\,B\,C\,D$ via $B\,C\,D\,E$ to $C\,D\,E\,F$. In the synchro-shear process the path of the octahedral ions is straight, whereas that of the tetrahedral ions is kinked.

If the cations can change freely from an octahedral to a tetrahedral position and vice versa, as

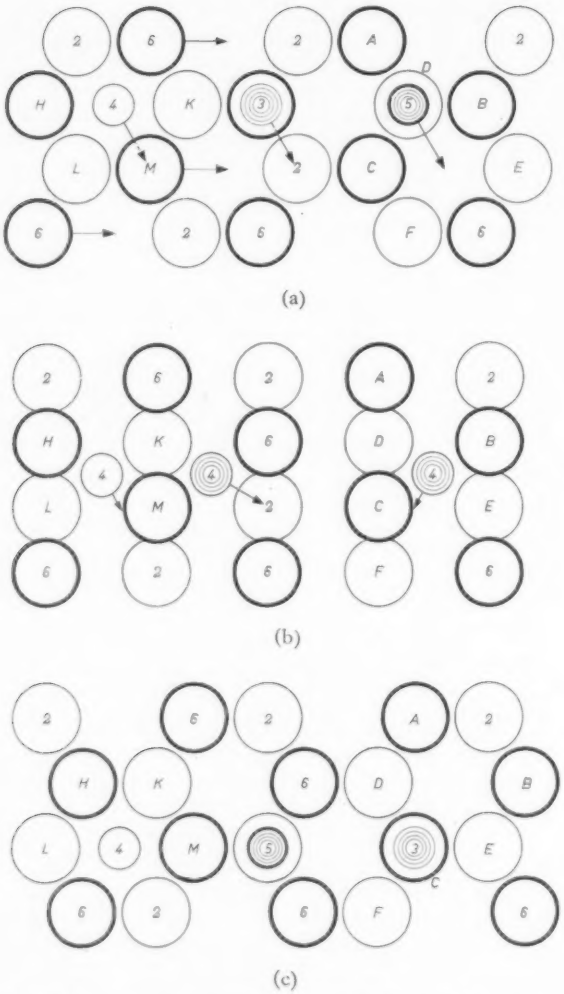

FIG. 4. Synchro-shear with one octahedral ion (left) and two tetrahedral ions (middle and right) projected on to (111). (a) Initial state; (b) intermediate state; (c) final state. All arrows end at the final position. The figures denote height above the plane of projection as in Fig. 1(a).

for instance in Fe_3O_4, then several other final states are possible. This possibility will not be discussed in detail on account of its complexity, although it might lead to more favourable stacking faults in some cases.

6. STACKING FAULTS

With the synchro-shear mechanism discussed in the preceding section it is possible to construct models of the stacking faults occurring in dislocations. After the passage of one quarter dislocation the central cation layer is shifted with respect both to the upper and the lower part of the crystal. In other stacking faults the central layer may be shifted with respect to one part of the crystal only; therefore we shall speak of double

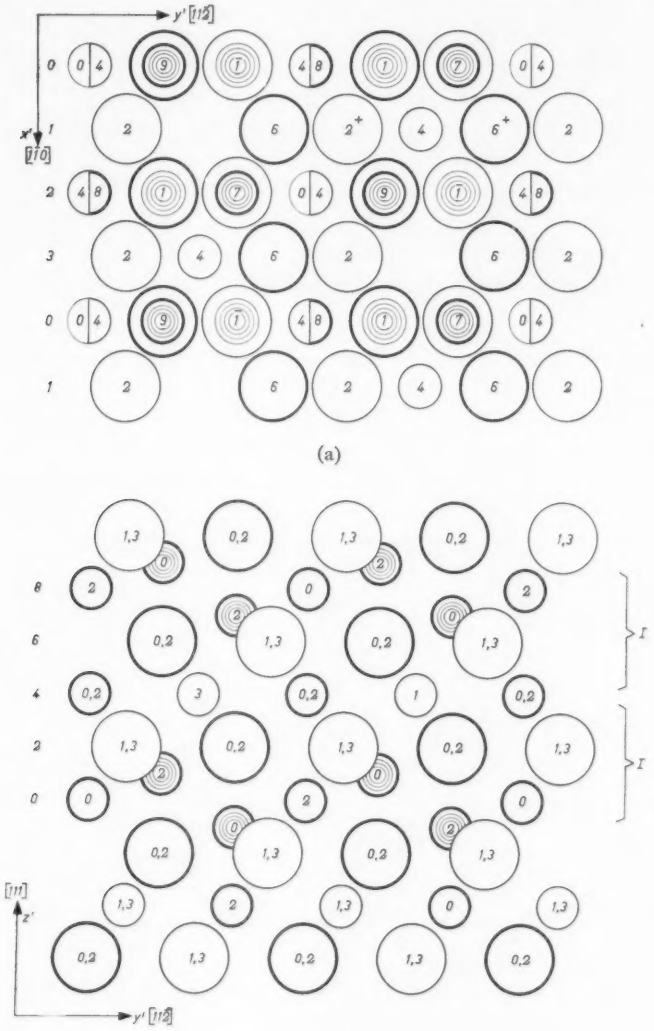

FIG. 5. Stacking fault of type I–I. (a) Projection on the (111) plane; (b) projection on the (1$\bar{1}$0) plane. The heights are indicated in the same way as in Fig. 1.

and single stacking faults in these cases. Since every double stacking fault is a combination of two single ones, it is only necessary to discuss the single stacking faults in detail; their combination does not usually present difficulties. Of the three stacking faults shown in Fig. 3 the middle one may be single, the other two must be double. This is because the middle stacking fault has a cubic stacking of the oxygen ions, whereas the outer ones have a hexagonal stacking.

The two outer stacking faults are similar; the detailed structure of the left one is presented in Fig. 5. It consists of two stacking faults which will be called type I. Characteristic for this type is the

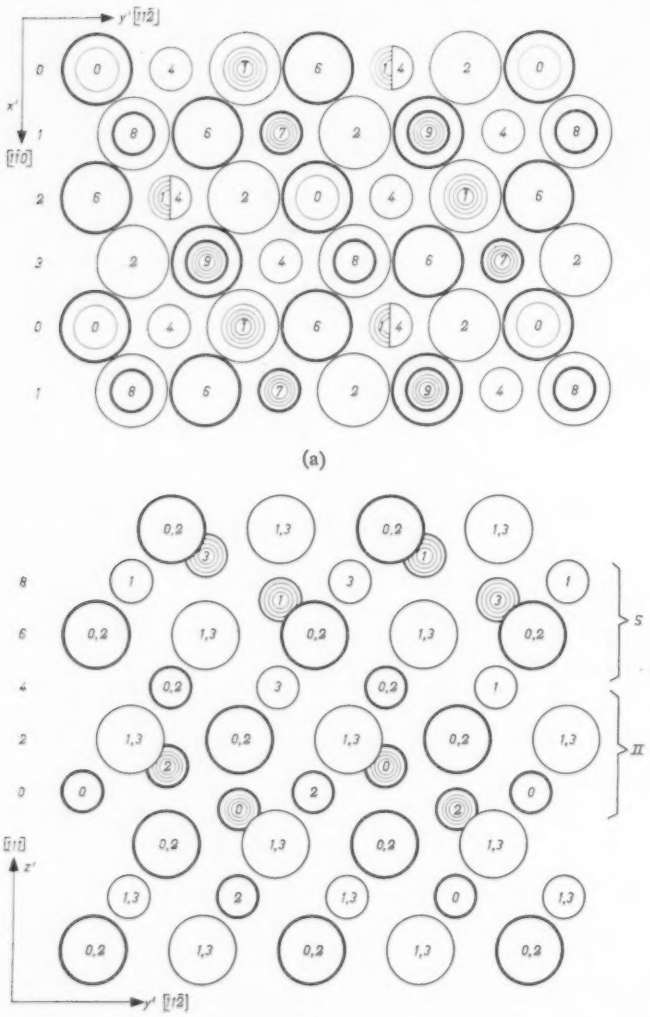

FIG. 6. Stacking fault of type *S*–II. (a) Projection on the (111) plane; (b) projection on the (1$\bar{1}$0) plane.

occurrence of octahedral ions at short distances from each other, namely in octahedra with one face in common (in Fig. 5(a) at $z' = 0$ and 4, $z' = 4$ and 8). The same configuration is found in the structure of some hexagonal ferromagnetic oxides.[6] The octahedral cations at $z' = 4$ never have one neighbour at $z' = 0$ and one at $z' = 8$ simultaneously. This would be an unfavourable combination I–I, although a similar configuration does occur in the structure of the compounds $Ba_2Zn_2Fe_{12}O_{22}$ and $Ba_3Co_2Fe_{24}O_{41}$ described by BRAUN[6].

The structure of the stacking fault found in the middle of the dislocation is given in Fig. 6. This type of misfit is called type II, the normal stacking of the spinel lattice is denoted by *S*. It is assumed that type II occurs only once, because the cations prefer positions which correspond with at least

Table 2. The entire dislocation of Fig. 3 in the abc-notation of Fig. 2. The ion layers are given in the same order as in Table 1. At the top of each column the type of stacking fault is given.

z'	S	I–I	S–II	I–I	S
10	*b* 1, 2, 3, 4	*a* 1, 2, 3, 4	*b* 1, 2, 3, 4	*a* 1, 2, 3, 4	*b* 1, 2, 3, 4
9	*c* 1	*b* 2	*c* 4	*b* 3	*c* 1
8	*a* 1	*c* 2	*a* 4	*c* 3	*a* 1
7	*b* 1	*a* 2	*b* 4	*a* 3	*b* 1
6	*c* 1, 2, 3, 4	*b* 1, 2, 3, 4	*c* 1, 2, 3, 4	*b* 1, 2, 3, 4	*c* 1, 2, 3, 4
5	—	—	—	—	—
4	*b* 2, 3, 4	*c* 1, 2, 4	*b* 1, 2, 3	*c* 1, 3, 4	*b* 2, 3, 4
3	—	—	—	—	—
2	*a* 1, 2, 3, 4	*a* 1, 2, 3, 4	*a* 1, 2, 3, 4	*a* 1, 2, 3, 4	*a* 1, 2, 3, 4
1	*b* 1	*b* 1	*b* 1	*b* 1	*b* 1
0	*c* 1	*c* 1	*c* 1	*c* 1	*c* 1
−1	*a* 1	*a* 1	*a* 1	*a* 1	*a* 1
−2	*b* 1, 2, 3, 4	*b* 1, 2, 3, 4	*b* 1, 2, 3, 4	*b* 1, 2, 3, 4	*b* 1, 2, 3, 4

VOL. 15 1960

one part of the crystal and this is possible here. Characteristic of this stacking fault is the occurrence of cations in tetrahedra ($z' = 1$) and octahedra ($z' = 4$) with one face in common.

In both stacking faults Pauling's rule is not obeyed for some oxygen ions. In Fig. 5(a) the two oxygen ions at $x' = 1$ marked with a plus sign have one neighbour too many, the oxygen ions below the cations at $z' = 9$ and above the cations at $z' = -1$ have one too few. In Fig. 6(a) the oxygen ions below the cations at $z' = 8$ have one neighbour too many and those above the cations at $z' = -1$ have one too few. The deviation from Pauling's rule is here 1/2 or 1/3; the same deviation occurs in unfaulted spinels which contain some monovalent or tetravalent ions and also in the complicated compounds mentioned above. Therefore, this deviation is no reason for considering stacking faults as very unfavourable configurations.

In Table 2 the entire dislocation of Fig. 3 is shown in the extended *abc*-notation. With the aid of Fig. 2 one finds that the first three columns correspond with Figs. 1, 5 and 6 respectively.

The two stacking faults discussed so far are sufficient to describe the extended dislocation, but still another type is possible (type III). This type will be discussed in Section 7 (Fig. 7); it has a hexagonal close-packed oxygen lattice like type I, but it cannot be formed from the spinel lattice by the passage of one quarter dislocation, except when the slip plane coincides with a mixed cation layer and free interchange of octahedral and tetrahedral cations is possible. Usually three appropriate quarter dislocations are necessary; the stacking thereby changes as follows $S \rightarrow$I$\rightarrow$II$\rightarrow$III. Whereas stacking fault II can occur alone, I and III are always found in pairs or in the combination I–III. If I and III occur alone, the lattice is changed to the twin orientation. Therefore I and III represent two possible structures of the (111) twin plane, as will be discussed in the following section.

7. SPINEL TWINS

The spinel structure is well known for its (111) twins. These twins are so common that (111) twins occurring in other cubic crystals are also called spinel twins. Macroscopically this twinning may be described either as a reflection with respect to a (111) plane or as a rotation about [111] by 60° or 180°, or even as a rotation of 180° about a $\langle 112 \rangle$ axis. Microscopically the mirror plane may be a glide plane and the twin axis need not coincide with a threefold axis. There is a close relation between stacking faults and twins as stacking faults may often be considered as extremely thin twin lamellae. This is not true for the stacking fault of type II, but only for those of type I and III. Type I has already been described in Section 6 as part of an extended dislocation, type III is shown in Fig. 7 as forming a twin plane. In the projection on the

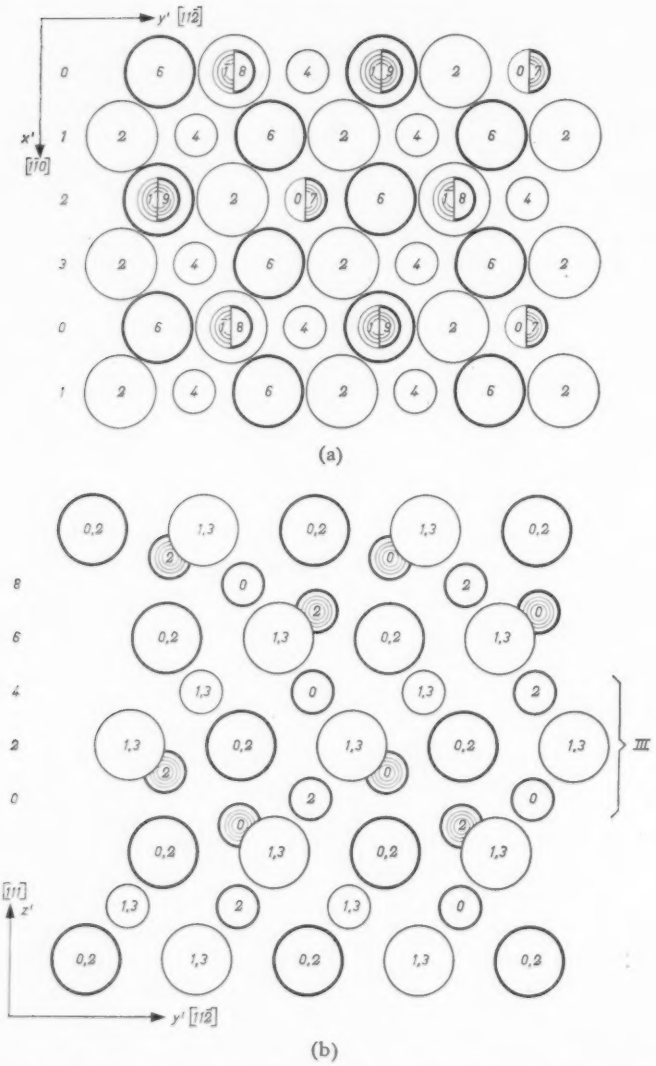

FIG. 7. Stacking fault of type III forming a twin boundary. Explanation as in Fig. 1.

(111) plane (Fig. 7a) the octahedral cations at $z' = 0$ coincide with the centres of the hexagons of the kagome layer at $z' = 4$, whereas in the unfaulted spinel lattice the centres of these hexagons coincide with the projection of the nearest tetrahedral cations. The projections of the tetrahedral ions at $z' = 1$ and $z' = -1$ are found in the triangles of the kagome layer.

In this type of stacking fault Pauling's rule is obeyed, all oxygen ions having four cation neighbours. In addition, there are no cations very close to one another in polyhedra with one face in common as there are in stacking faults I and II. The energy difference between this structure and the perfect spinel lattice will therefore be small and it is not surprising that a lattice similar to that of

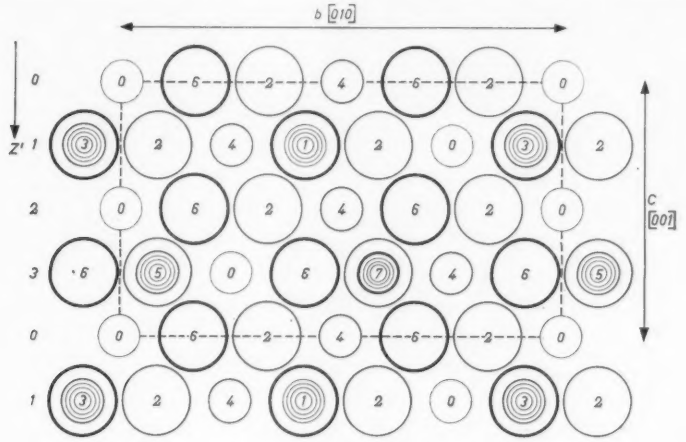

(a)

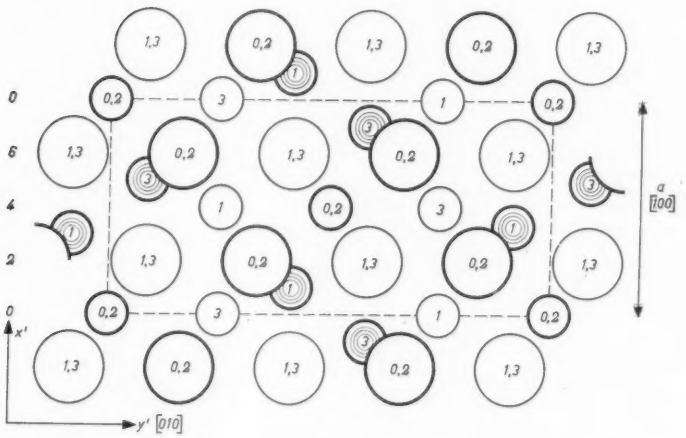

(b)

FIG. 8. Lattice of olivine, Mg_2SiO_4; large circles represent O-ions, small open circles Mg-ions and small circles with concentric circles Si-ions. (a) Projection on the (100) plane; the height x' above the plane of projection is expressed in multiples of $a/8$, where a is the unit distance in the x'-direction. (b) Projection on the (001) plane; the height z' is expressed in multiples of $c/4$ where c is the unit distance in the z'-direction.

stacking fault III occurs in nature: the olivine lattice.

The olivine lattice (Mg_2SiO_4) is given in Fig. 8 in an idealized form; the data were taken from the paper by BRAGG and BROWN[7]. Olivine has a slightly distorted hexagonal close-packed oxygen lattice; the Mg-ions have sixfold coordination (octahedral sites), while the Si-ions have fourfold coordination (tetrahedral sites). The successive cation layers parallel to (100) in olivine are similar whereas in the spinel lattice (111) layers with and without tetrahedral ions alternate. The tetrahedral ions ($z' = 3$ and 5) lie between triangles of octahedral cations at $z' = 0$ and 8. Stacking faults in the olivine lattice will be discussed in a subsequent paper on a possible mechanism for the olivine–

spinel transition. This transition is assumed to take place at the high pressure occurring in the interior of the earth,[8, 9, 10, 11] because the spinel structure is denser than the olivine structure.

Up till now no experiments have been done on the plastic deformation of spinels to test the hypotheses presented in this paper, but there is a paper about deformation twinning by GRÜN[4]. In that paper a description is given of the formation of twin lamellae in magnetite crystals by high pressure. Deformation twinning is known to be related to plastic deformation; it takes place when a partial dislocation (in this case a quarter dislocation) passes between every pair of successive oxygen layers.

This mechanism of twin formation is illustrated in Table 3. The left column shows the original oxygen layers at $z' = 10$ and $z' = 14$. In this way the width of the twin lamella is increased.

The motion of the ions during the twinning process is shown in Fig. 9, where a part of Fig. 2 is reproduced. The figures beside the arrows refer

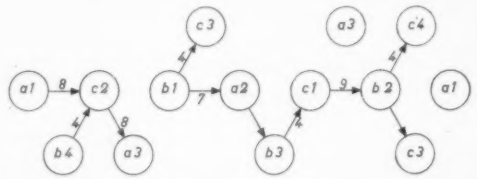

FIG. 9. Part of Fig. 2 to explain deformation twinning given in Table 3. The figures beside the arrows correspond with z' from Table 3. Only the motion of the cations is shown. In both steps the oxygen ions move to the right, as do the cations at $z' = 7$, 8 and 9 in the first step.

Table 3. *Mechanical twinning by partial dislocations*

z'	Spinel	After first step	After second step	
14	*a* 1, 2, 3, 4	*c* 1, 2, 3, 4	*b* 1, 2, 3, 4	
13	—	—	—	
12	*c* 2, 3, 4	*b* 1, 3, 4	*a* 2, 3, 4	
11	—	—	—	
10	*b* 1, 2, 3, 4	*a* 1, 2, 3, 4	*c* 1, 2, 3, 4	I
9	*c* 1	*b* 2	*b* 3	
8	*a* 1	*c* 2 ——→	*a* 3	
7	*b* 1	*a* 2	*c* 3	
6	*c* 1, 2, 3, 4	*b* 1, 2, 3, 4	*b* 1, 2, 3, 4	*T*
5	—	—	—	
4	*b* 2, 3, 4 ——→	*c* 1, 2, 4	*c* 1, 2, 4	
3	—	—	—	
2	*a* 1, 2, 3, 4	*a* 1, 2, 3, 4	*a* 1, 2, 3, 4	I
1	*b* 1	*b* 1	*b* 1	
0	*c* 1	*c* 1	*c* 1	

spinel lattice. A quarter dislocation (denoted by an arrow) between the oxygen layers at $z' = 2$ and $z' = 6$ changes it into the configuration of the second column, which was presented in Table 2 as stacking fault I–I. After the passage of a quarter dislocation with the same Burgers vector between the oxygen layers at $z' = 6$ and $z' = 10$ the configuration of the last column is obtained. Now a narrow twinned region T is separated from the bulk of the crystal by two stacking faults I forming the twin planes. The next step (not shown) will be the passage of a quarter dislocation between the

to the height z' of the corresponding ions. Because the cations at $z' = 7$ and $z' = 9$ change their heights, the corresponding arrows have not been marked with a figure. It may be noted that the direction of synchro-shear at $z' = 4$ differs from that at $z' = 8$. Although the partial dislocations have the same Burgers vector, they are clearly different. Apparently, in the case of synchro-shear partial dislocations are not completely determined by their Burgers vector alone, but the direction of synchro-shear should also be given.

By the twinning mechanism just described, only

twins with twin planes of type I can be formed. A twin plane of type III, which is more favourable, may be formed afterwards by the passage of two quarter dislocations with appropriate Burgers vectors along the twin plane. When twins are formed during crystal growth, a twin plane of type III is most likely.

8. CONCLUSIONS

All stacking faults that are possible in the spinel lattice are combinations of only three types of "single stacking faults", namely type I, II, and III. When interchange of the tetrahedral and octahedral cations is impossible, only types I and II occur in extended dislocations. A {111} twin boundary may be of type I or of type III. The former type is more easily formed by deformation twinning, whereas from the energy point of view the latter type is more favourable, because all oxygen ions are surrounded by four cations and no cations are very close to each other. In stacking faults of types I and II some oxygen ions have three or five cation neighbours and at some places two cations are so close that the oxygen polyhedra surrounding them have a face in common. These unfavourable configurations will not prevent the existence of stacking faults, since similar configurations are found in some hexagonal ferromagnetic oxides.

In a paper on the plastic deformation of sapphire, KRONBERG[1] has introduced the name "synchro-shear" for the simultaneous motion of cations and anions in different directions during the slip process. He discussed the mechanism in detail for the case of cations with sixfold coordination. In the present paper the case of cations with fourfold coordination is considered in detail. It is shown that, in the (111) projection, it looks as if all cations move in parallel directions, but that the tetrahedral cations undergo a change of their height above the plane of projection.

The ferrimagnetism of crystals of the spinel type is determined by super-exchange causing the magnetic moments of all tetrahedral ions to be parallel in one direction and the magnetic moments of all octahedral ions to be parallel in the opposite direction. These interactions are disturbed by each kind of stacking fault, so that twin planes are favourable sites for certain types of domain walls. The free energy of a domain wall at a twin plane will depend on the type of stacking fault present. It might therefore be possible to distinguish between the two twin plane configurations because of their different magnetic properties, but the difference is probably too small.

Acknowledgement—The author wishes to thank Dr. E. W. GORTER for suggesting the problem and for valuable discussions about the subject of the present paper.

REFERENCES

1. KRONBERG M. L., *Acta Met.* **5,** 507 (1957).
2. WACHTMAN J. B. and MAXWELL L. H., *J. Amer. Ceram. Soc.* **37,** 291 (1954); **40,** 377 (1957).
3. GORTER E. W., *Advanc. Phys.* **6,** 336 (1957).
4. GRÜN A., *Neues Jahrbuch für Mineralogie*, p. 99 (1918).
5. IIDA S., *J. Phys. Soc., Japan* **12,** 222 (1957).
6. BRAUN P. B., *Philips Res. Rep.* **12,** 491 (1957).
7. BRAGG W. L. and BROWN G. B., *Z. Kristallogr.* **63,** 538 (1926).
8. BERNAL J. D., *Observatory* **59,** 268 (1936).
9. RINGWOOD A. E., *Nature, Lond.* **178,** 1303 (1956).
10. VENING MEINESZ F. A., *Proc. Kon. Ned. Akad. Wet., Amsterdam* **B60,** 409 (1957).
11. MEIJERING J. L. and ROOYMANS C. J. M., *Proc. Kon. Ned. Akad. Wet., Amsterdam* **B61,** 333 (1958).

VOL. 15 1960

J. Phys. Chem. Solids Pergamon Press 1960. Vol. 15. pp. 324–334. Printed in Great Britain.

REACTIONS OF LITHIUM AS A DONOR AND AN ACCEPTOR IN ZnO

J. J. LANDER

Bell Telephone Laboratories, Incorporated, Murray Hill, New Jersey

(*Received* 7 *January* 1960)

Abstract—Reactions of oxidized lithium with ZnO have been investigated by means of conductivity measurements. Donors are formed in ZnO if the atmosphere surrounding the crystal is reducing. The donor centre is probably the molecular ion $LiO^{=}$. Oxidizing conditions favor an acceptor center presumably obtained by displacement of a lattice zinc atom by lithium. Solubilities and diffusion coefficients were measured and some results are reported for the kinetics and equilibria of the displacement reaction. High temperatures favor displacement. In one atmosphere of oxygen the Fermi level, which is normally near the top of the 3·0 eV band gap, can be pushed down to the centre of the band gap. Impractically high oxygen pressures would be required to produce strongly *p*-type material. The precipitation of lithium on dislocations and their decoration were also studied.

1. INTRODUCTION

IT HAS been found in earlier work that reactions of ZnO with hydrogen,[1,2] zinc,[3] and indium[4] produce *n*-type conductivity. Since *p*-type material has not been reported and would have properties of considerable interest, a study has been made of reactions which might be expected to produce such material. The substitution of an alkali atom for a lattice zinc atom should yield an acceptor center and reactions with lithium are the subject of this report. Some properties of sodium reactions with ZnO were also studied and found to be similar to those of lithium.

A qualitative understanding of the reactions of lithium with zinc oxide was obtained from the following experiments carried out on single crystals of needle form with diameters of the order of 0·01 cm and initial conductivity of the order of 0·1 $(\text{ohm cm})^{-1}$ (donor concentration about 4×10^{15} per cm^3) at room temperature.

(1) When crystals of ZnO are exposed at moderate temperatures (300°C to 600°C) to Li vapor at low pressures (10^{-5} mm of Hg) or dipped in dilute solutions (0·1 per cent) of Li in Zn or Hg, reaction occurs. Conductivity is observed to increase at a rate which depends on temperature, activity of lithium and size of the crystal. High values may be obtained.

It is apparent that in this stage of the reaction donors diffuse into ZnO, though they may be interstitial zinc.[3]

(2) After prolonged reaction under the above conditions it is found on cooling that the crystals have darkened and lost strength (some disintegrate) and that they contain a high concentration of lithium (greater than 10^{19} atoms per cm^3).

Thus under these conditions:

(a) Lithium has diffused into the crystal.

(b) The resulting *n*-type solutions are too concentrated for accurate study by semiconductor techniques.

(c) The reaction proceeds to the internal precipitation of lithium which produces darkening and severe strains in the crystal. The major part of this precipitation presumably takes place during cooling.

(3) If reaction is interrupted in a preliminary stage and the crystal is quenched to room temperature it is found that:

(a) The donor concentration is maintained (the donor is a "hydrogen-like" centre with an ionization energy near 0·050 eV).[5]

(b) The crystal remains strong.

(4) If the crystal is etched (so that there will be no subsequent reaction with surface contamination) and heated in air at 300°C or higher,

conductivity decreases and ultimately may reach a value as low as 10^{-9} (ohm cm)$^{-1}$ at 300°C but p-type conductivity is not observed. This low conductivity once attained is not changed much by heat treatment in air at higher temperatures (800°C).

It is concluded that under these conditions:

(a) Lithium at low concentrations reacts further to produce acceptor centers.
(b) This reaction proceeds readily at temperatures above 300°C.
(c) The acceptor centers are probably immobile at moderate temperatures.
(d) The diffusion rate of lithium in the donor form is relatively high.

VOL. 15 1960

2. MODEL

In order to account for the above results and to set up a basis for quantitative work the following assumptions are made:

(1) The donor and mobile form of lithium in zinc oxide is interstitial lithium, which may form a molecular ion with oxygen.

(2) Interstitial lithium becomes an acceptor by displacing a lattice zinc ion. Since the maximum charge on the lithium ion is $+1$ the center has a charge of -1 if surrounding oxygen ions have their normal charge. The charged acceptor center will be described by the symbol Li^-, according to a convention which indicates only the excess charge of the center.

(3) Local reversibility of this displacement reaction can be attained at moderate temperatures. This assumption will be valid for a sufficiently large crystal.

(4) The displaced zinc ion becomes an interstitial and as such must play an important role in subsequent kinetics and equilibria. THOMAS[3] has studied the behavior of interstitial zinc in ZnO and has reported values for the solubility as a function of temperature and zinc pressure and for the diffusion coefficient.

According to this model the minimum system of solute species in an n-type crystal contains Li_i^+, Li_s^-, Zn_i^+ and e^-.* The simplest reactions which can be written to represent the system in equilibrium with its enviroment (assumed gaseous) are:

(1) The solution of lithium at pressure P_{Li} in the gaseous environment to produce interstitial lithium in the solid

$$Li(v) \rightleftarrows Li(s) \qquad K_1 = [Li]/P_{Li} \tag{1}$$

(2) The ionization of interstitial lithium

$$Li(s) \rightleftarrows Li^+ + e^- \qquad K_2 = [Li^+][e^-]/[Li] \tag{2}$$

(3) The solution of zinc at pressure P_{Zn} in the environment to produce interstitial zinc.

$$Zn(v) \rightleftarrows Zn(s) \qquad K_3 = [Zn]/P_{Zn} \tag{3}$$

(4) The ionization of interstitial zinc

$$Zn(s) \rightleftarrows Zn^+ + e^- \qquad K_4 = [Zn^+][e^-]/[Zn] \tag{4}$$

In addition there is the homogeneous reaction in which interstitial lithium displaces a lattice zinc ion to produce the acceptor center

$$Zn(l) + Li_i^+ + e^- \rightleftarrows Zn_i^+ + Li_s^-$$
$$K_5 = [Li^-][Zn^+]/[Li^+][e^-] \tag{5}$$

where $Zn(l)$ is a lattice zinc atom. This will be called the displacement reaction and it is similar to reactions proposed for copper and nickel in silicon and germanium.[6,7]

Note that the equilibrium of Reaction (5) is shifted to the right by the removal of interstitial zinc, for example by oxidation at the surface. This results in an increasing relative concentration of acceptors.

In addition one expects the production of ion pairs and more complex centers under appropriate conditions. For example the molecule Li_2O may be formed within the crystal by the reaction of Li^+, Li^- and an oxygen atom. The energy of the electrons in this molecule may lie below the top of the valence band. Similarly a variety of reactions may occur between foreign imperfections and lithium.

3. THE SOLUBILITY AND DIFFUSION COEFFICIENT OF INTERSTITIAL LITHIUM IN ZnO

It was noted above that the reaction between ZnO and lithium even in dilute solution in Zn and at the lowest practical temperatures, produces lithium concentrations which are too high to be studied by semiconductor techniques. The activity of lithium in the external phase must be

* The subscripts i and s will be dropped in succeeding equations.

reduced drastically to obtain solutions of the proper dilution.

Consider a crystal of ZnO coated with the stable product of reaction between Li_2O and ZnO, for example Li_2ZnO_2, and heated in zinc vapor. Since zinc is much less active than lithium, the reaction

$$Li_2ZnO_2 + Zn(v) \rightleftarrows 2ZnO + 2Li(v)$$
$$K_6 = P_{Li}^2/P_{Zn} \qquad (6)$$

should provide a source of lithium with low activity. The dependence of interstitial lithium concentration in ZnO on zinc pressure, obtained from equations (6), (1) and (2) and their equilibrium constants, is given by

$$Li_2ZnO_2 + Zn(v) \rightleftarrows 2Li^+ + 2\epsilon^- + 2ZnO$$
$$K_7 = [Li^+]^2[e^-]^2/P_{Zn} = K_2^2K_1^2K_6 \qquad (7)$$

When interstitial lithium is the dominating solute species $[Li^+] = [e^-]$ and, since practically all interstitial lithium is ionized at reaction temperatures, lithium concentration should vary with $P_{Zn}^{1/4}$. Similarly if oxygen pressure is varied one obtains from

$$ZnO \rightleftarrows Zn + \tfrac{1}{2}O_2 \qquad K_8 = P_{O_2}^{1/2}P_{Zn} \qquad (8)$$

and (7), a dependence of interstitial lithium concentration on the reciprocal one-eighth power of oxygen pressure. One can thus hope to control the activity of lithium over a very wide range without adding a new component to the system.

This scheme was found to be practical, though the coatings applied were actually Li evaporated in thin films onto crystals and subsequently oxidized, or LiOH (which dissociates to the oxide when heated to about 300°C in a sufficiently dry atmosphere free of CO_2). The latter method is the most convenient and was introduced by D. G. THOMAS. Very similar results were obtained with each.

Note that equation (7) defines a solubility product for Li^+ and e^-, but does not define their concentrations unless other interacting solute species are present in negligible quantity. In particular the concentration of the acceptor form, Li^-, must be negligible. This was found to be the case at temperatures below about 400°C if the pressure of zinc is high.

The diffusion coefficient of lithium and the solubility of lithium in ZnO coated with Li_2ZnO_2(?) were obtained as a function of temperature and zinc pressure from conductivity data obtained in the apparatus shown in Fig. 1. The part most relevant to the experiment is the closed quartz

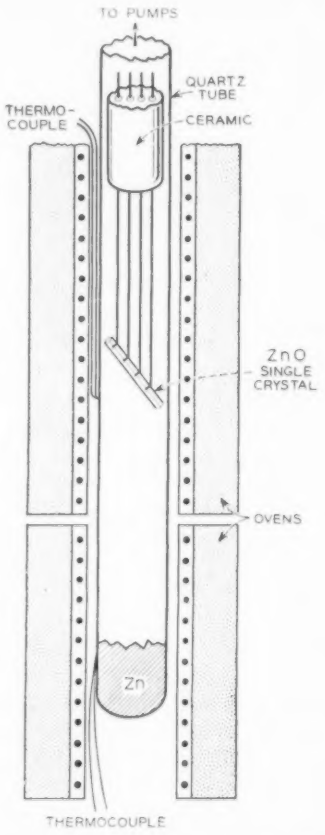

FIG. 1. Apparatus for studying changes in conductivity of ZnO in Zn vapor and coated with LiOH.

tube containing zinc and crystal surrounded by separate ovens. The crystal is held by four spring tungsten leads (forming a four probe circuit) running through a four holed rod of alumina up to a four lead stem. A vacuum of the order of 10^{-5} was maintained above the ceramic during most of the tests. Temperatures were obtained from two Pt/Pt-Rh thermocouples pressed at appropriate spots against the quartz tube by sprung tungsten rings.

VOL. 15 1960

The parameters measured in these experiments were conductivity, time, temperature of zinc and temperature of the crystal. Conductivity, σ, was reduced to carrier concentration by means of the equation

$$[e^-] = \sigma/e\mu = 9{\cdot}6 \times 10^{12}\sigma T^{3/2} \qquad (9)$$

Data for the mobility, μ, are those reported by HUTSON[5] and e is the electronic charge. Donors will be confined for the moment to the rates of solution.

The diffusion of lithium into the hexagonal shaped needles of ZnO was observed to obey simple cylindrical diffusion theory and diffusion coefficients were calculated from the equation

$$D = 0{\cdot}060 r_0^2/t(1/2) \qquad (\text{cm}^2/\text{sec}) \qquad (10)$$

where r_0 is half the average diameter and $t(1/2)$ is

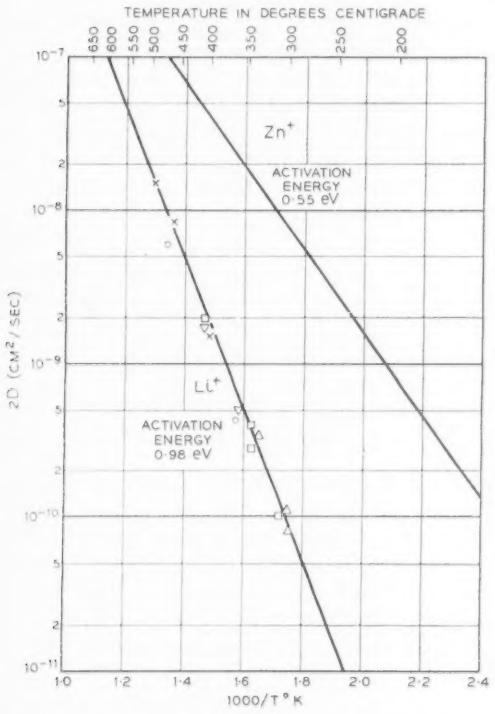

FIG. 2. Diffusion coefficients of Li^+ and Zn^+ in ZnO as a function of temperature.

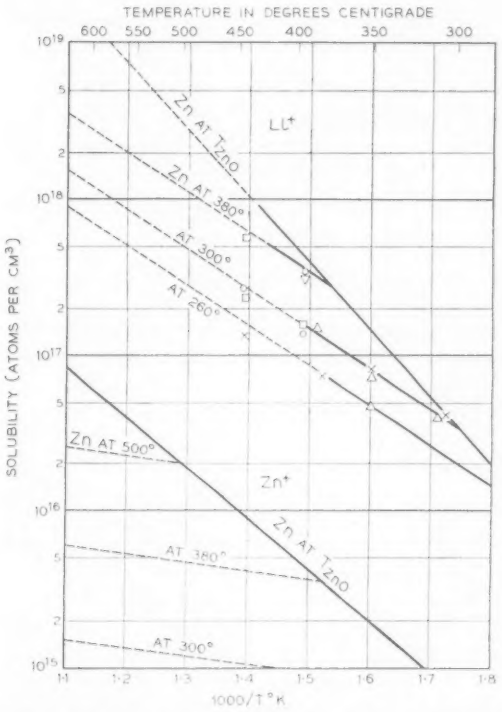

FIG. 3. Solubility of Li^+ and Zn^+ in ZnO as a function of temperature.

are nearly all ionized in the range of measurement and conditions under which electron concentration $[e^-]$ is equal to donor concentration $[Li^+]$ have been mentioned above. Assuming that these conditions have been met, diffusion coefficients may be obtained from rates of increase of electron concentration, and solubility from the saturation values. Under some conditions decreasing conductivity may not be a measure of the diffusion of lithium out of the sample and therefore attention the time taken to reach 50 per cent saturation. Data are given in Fig. 2 together with the curve obtained by THOMAS[3] for interstitial zinc which will be used later. The curve drawn through the experimental points for Li^+ has the equation

$$2D = 0{\cdot}040 \exp(-0{\cdot}98/kT) \qquad (11)$$

The factor of 2 indicates that the ambipolar nature of the diffusion process has been taken into account. The results are not greatly different from those

obtained for H^+ which diffuses about ten times faster than Li^+ in the 300°C to 400°C range (and is far less soluble at the same pressure).

Several tests with sodium were also made. The results indicated a diffusion coefficient about one order of magnitude less than that of lithium.

Values for the solubility of lithium are given in Fig. 3. Most of the data were obtained with the source of zinc vapor at 300°C. Additional data for the conditions zinc source at 260° and at 380° yield a one-quarter power dependence on zinc pressure within experimental error. The equation for the concentration of lithium (zinc source at T_{ZnO}) is

$$[Li^+] = (K_7 P_{Zn})^{1/2}/[e^-] = 1{\cdot}3 \times 10^{24} \exp(-0{\cdot}86/kT) \quad (12)$$

Data for the vapor pressure of zinc over solid zinc can be obtained from the equation

$$P_{Zn} = 1{\cdot}5 \times 10^9 \exp(-1{\cdot}365/kT) \quad (13)$$

which is assumed sufficiently accurate through a moderate range above the melting point of zinc (420°C).

THOMAS[3] gives the equation

$$[Zn^+] = 3{\cdot}4 \times 10^{20} \exp(-0{\cdot}65e/kT) = K_3 K_4 P_{Zn}/[e^-] \quad (14)$$

for the solubility of interstitial zinc when ZnO and Zn are at the same temperature.

It has been proposed[2] that hydrogen reacts with lattice oxygen in zinc oxide to form the molecular ion $OH^=$. It is expected that the bond will be stable and that the odd electron, being spread over a large volume in a medium of high dielectric constant, will be easily ionized. Diffusion then proceeds by jumps from oxygen to oxygen with alternate breaking and formation of bonds. Similar molecular ions are expected in the case of lithium and zinc, the ion $LiO^=$ probably being much more stable than $ZnO^=$. The values of the diffusion coefficients (cm^2/sec) for these donors at 500°C are

$$2D_{Li^+} = 2 \times 10^{-8}, \qquad 2D_{H^+} = 7 \times 10^{-8}$$
$$2D_{Zn^+} = 2 \times 10^{-7}$$

which is the order of the expected stability of the bonds. The formation of molecular ions will also be an important factor in solubility.

Attempts were made to observe an infrared absorption to be associated with vibration of the ZnO^- ion. None was found, but the fundamental mode should be at about 10μ, which is a region obscured by strong harmonics of lattice vibrations of the zinc oxide, and therefore a sensitive test cannot be made.

4. KINETICS OF THE DISPLACEMENT REACTION

It was found that at higher temperatures and lower zinc pressures displacement of lattice zinc ions by interstitial lithium is no longer negligible. The resulting rate phenomena (an example is given in Fig. 5) have properties which are not observed in simpler diffusion processes. They are produced by the replacement of interstitial lithium by interstitial zinc. The purpose of this section is to illustrate these properties with a special case which has a relatively simple solution. The results will be used in a qualitative way in descriptions of observed phenomena.

Consider the displacement reaction:

$$Zn(\ell) + Li^+ + e^- \rightleftarrows Li^- + Zn^+$$
$$K_5 = [Li^-][Zn^+]/[Li^+][e^-] \quad (5)$$

The mobile atomic species at moderate temperatures are Li^+ and Zn^+. Changes in their concentrations in a region of a crystal are determined by their concentration gradients and by the change in concentration of Li^- produced by displacement. Neglecting field effects, they are described (in a one dimensional case) by the equations

$$\frac{\partial[Li^+]}{\partial t} = D_{Li^+}\frac{\partial^2[Li^+]}{\partial x^2} - \frac{\partial[Li^-]}{\partial t} \quad (15)$$

$$\frac{\partial[Zn^+]}{\partial t} = D_{Zn^+}\frac{\partial^2[Zn^+]}{\partial x^2} + \frac{\partial[Li^-]}{\partial t} \quad (16)$$

In the special case $D_{Li^+} = D_{Zn^+} = D$ the sum function

$$\frac{\partial[Li^+ + Zn^+]}{\partial t} = D\frac{\partial^2[Li^+ + Zn^+]}{\partial x^2} \quad (17)$$

has well known solutions. D_{Zn^+} is in fact much larger than D_{Li^+}, except at very high temperatures.

The surface boundary conditions are determined by the zinc pressure. Assuming that surface reactions are not rate limiting a fixed zinc pressure results in the conditions

$$[Li^+] = [Li^+]_0 \qquad x = 0, \text{ all } t \tag{18}$$

$$[Zn^+] = [Zn^+]_0 \qquad x = 0, \text{ all } t \tag{19}$$

Furthermore it is assumed that the crystal is initially empty.

Reaction (5), which describes the displacement process, imposes an internal constraint on the system. If local equilibrium is not attained two rate constants are required to describe the process, one for the forward and one for the reverse reaction. It was found that the reaction can be observed at temperatures below 300°C, therefore the assumption of local equilibrium at higher temperatures seems fair and one notes that its validity increases with increasing crystal size.

The neutrality condition

$$[Li^+]+[Zn^+] = [Li^-]+[e^-] \tag{20}$$

together with equations (15) and (16) ,the assumed boundary conditions, and the internal equilibrium described by K_5 completely define the system. The neutrality condition together with the expression for K_5 generally result in quadratic forms for the dependent variable. In one particular case a simple form is obtained. If $K_5 = 1$ (displacement strongly favored) the result is that everywhere

$$[Li^+] = [Li^-] \tag{21}$$

In this case equation (15) becomes

$$\frac{\partial[Li^+]}{\partial t} = \frac{D_{Li^+}}{2}\frac{\partial^2[Li^+]}{\partial x^2} \tag{22}$$

and it is possible to evaluate all concentrations as a function of time using data for simple diffusion processes.

Solutions for this special case are given in Fig. 4. They are for diffusion perpendicular to the axis of a cylinder of infinite length with radius r_0. Total amounts of each species are plotted as a function of $(Dt/r_0^2)^{1/2}$. The assumed boundary conditions are $[Li^+ + Zn^+]_0 = 1$, $[Zn^+]_0 = 0{\cdot}05$, with the crystal initially empty. Note that if everywhere $[Li^+] = [Li^-]$ then the neutrality condition requires that $[Zn^+] = [e^-]$ everywhere.

A qualitative picture of the following characteristic properties of the approach to equilibrium when displacement is not negligible is suggested by the data of Fig. 4:

(1) Since the solubility of Li^+ is much larger than that of Zn^+, the production of Zn^+ by displacement may result in total concentrations of Zn^+ higher than the equilibrium value. In the example chosen the concentration of interstitial zinc and therefore of electrons increases to a maximum which is considerably higher than the final value.

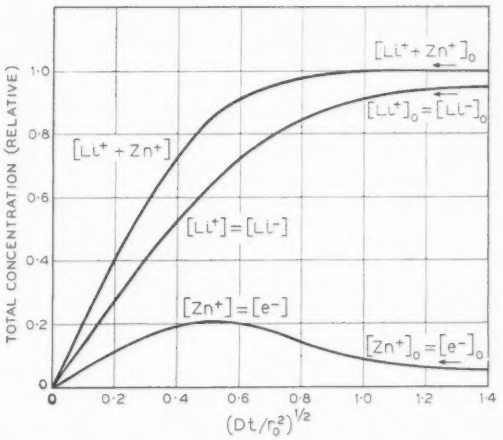

FIG. 4. Kinetics of the displacement reaction discussed in Section 4.

Since D_{Zn^+} is in fact much larger than D_{Li^+} the maximum value of Fig. 4 is an exaggeration. A ratio D_{Zn^+}/D_{Li^+} equal to 10 is approximately correct for the range 400° to 600°C. As a first approximation, the value of the difference between the maximum and the final value should be decreased by $\sqrt{(10)}$. In some cases during the initial stages of the reaction $[Zn^+]$ will be much higher than $[Li^+]$ near the center of the crystal.

(2) Displacement impedes the attainment of the final state. When displacement is negligible, the rate is determined by the diffusion rate of Li^+. When displacement is strongly favored the rate is much slower because the displaced zinc concentration must hunt for the boundary value. For example, in the case of Fig. 4, the time to attain 90 per cent of the equilibrium electron concentration is increased by a factor of about five over that for no displacement.

5. THE MEASUREMENT OF K_5, THE EQUILIBRIUM CONSTANT FOR THE DISPLACEMENT REACTION

Values of $K_5 = [Li^-][Zn^+]/[Li^+][e^-]$ are easily obtained if zinc pressure is adjusted to a range which yields an equilibrium ratio $[Li^-]/[Li^+]$ near unity. $[e^-]$ is then obtained by a measurement of conductivity and the value of $[Zn^+]$ from the data of THOMAS. This is found to be practical throughout a considerable range of interest because the ratio $[Li^-]/[Li^+]$ is near unity over a very wide range of zinc pressure.

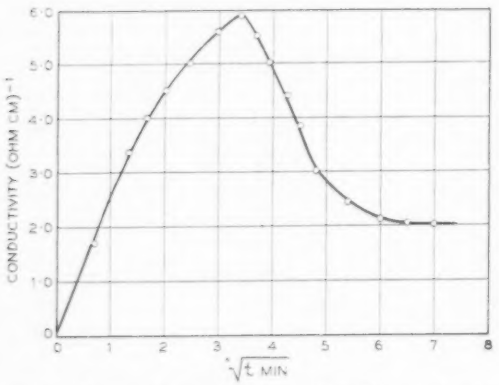

FIG. 5. Change in conductivity of ZnO coated with LiOH and held at 504°C in Zn vapor from source at 450°C.

As an example, consider the data of Fig. 5 where conductivity is plotted against time for a crystal coated with LiOH and held at 504°C in zinc vapor from a source at 450°C. The diameter of the crystal was $6{\cdot}0\times10^{-3}$ cm. Compare the maximum in conductivity with that in the curve for electron concentration in Fig. 4. Presumably the concentration of lithium continues to increase after the maximum and the degree of compensation also increases. Suppose the ratio $[Li^-]/[Li^+]$ is large, say 0·9. The equilibrium concentration of electrons obtained from the conductivity value of 2·0 (ohm cm)$^{-1}$ and an estimated mobility (at 504°C) equal to 30 is 4×10^{17} per cm^3. According to the data of Thomas $[Zn^+][e^-] \simeq 1\times10^{32}$ under these conditions.

Thus

$$K_5(504°C) \simeq 0{\cdot}9\times1\times10^{32}/16\times10^{34} = 0{\cdot}00057 \quad (23)$$

With a crystal at 600°C and the zinc source at 600°C the value of $[Zn^+][e^-]$ is $3{\cdot}6\times10^{33}$. During lithium doping a maximum and a final conductivity indicating a large amount of compensation was observed. The final conductivity was 4, which corresponds to an electron concentration equal to about 9×10^{17}. Assuming again that the ratio $[Li^-]/[Li^+]$ is about 0·9, then

$$K_5(600°C) \simeq 0{\cdot}9\times3{\cdot}6\times10^{33}/81\times10^{34} = 0{\cdot}0045$$

The above values of K_5 are to be taken as approximations. Results of repeated tests scattered by a factor of about four, but the cause of scatter was not determined.

A consequence of the assumptions made about the lithium reactions is that the equilibrium total concentration of lithium is independent of zinc pressure. This is easily seen in the region where compensation is nearly complete. Then $[Li^+] \simeq [Li^-]$ $[Zn^+] \simeq K_5[e^-]$ and equations (1) to (5) and the neutrality condition yield $[Li^+] \simeq K_1K_2/K_4K_5$, which is independent of zinc pressure. This prediction has been tested by spectrochemical analyses of crystals doped with lithium through a very wide range of zinc pressures. The results are given in Table 1.

Again considerable scatter is observed in the results, nevertheless samples treated in air contain about as much lithium as those treated at the same temperature in high zinc pressures, and the result is in agreement with the model. The cause of the scatter has not been determined. It is probably not due to variation in initial purity. The crystals were from the same lot and had initial conductivities of about 0·2, corresponding to donor concentrations of about 1×10^{-16}.

6. DIFFUSION OF Li^+ OUT OF ZnO

Consider a crystal which has been saturated with Li^+ at a moderate temperature (300–400°C) and which is in equilibrium with zinc from a source at about the same temperature. Since compensation does not dominate the conductivity behavior, conductivity is a measure of the concentration of Li^+. If the zinc pressure is abruptly decreased by about one order of magnitude conductivity is observed to decrease to a new quasi-equilibrium value. The initial and later values are proportional very nearly to the reciprocal of the one-quarter power of the ratios of the zinc pressures, as theory

Table 1

Sample No.	Doping Temperature (°C)	Pressure of Zn (mm of Hg)	Total Lithium (atoms per cm³)	Average
J(6)	390	0·09	$2{\cdot}9\times10^{17}$	3×10^{17}
J(1)	500	1·5	$4{\cdot}8\times10^{17}$	
J(10)	500	1·5	$6{\cdot}5\times10^{17}$	8×10^{17}
J(2)	500	0·1	$1{\cdot}4\times10^{18}$	
J(9)	500	10^{-23} (air)	$7{\cdot}0\times10^{17}$	
J(5)	600	13	$1{\cdot}4\times10^{19}$	
J(3)	600	0·1	$1{\cdot}1\times10^{18}$	5×10^{18}
J(4)	600	10^{-20} (air)	$2{\cdot}1\times10^{18}$	
J(7)	600	10^{-20} (air)	$3{\cdot}2\times10^{18}$	

VOL. 15 1960

predicts. A subsequent slow and small decrease in conductivity which is produced by the formation of Li^- ends at a true equilibrium value.

Diffusion coefficients calculated from the first change in conductivity agree very well with those given for Li^+ in Fig. 2.

The diffusion rate of Li^+ out of ZnO can not be obtained simply from the change in conductivity produced by an abrupt lowering of temperature. The reason will be given in the next section.

7. INTERNAL NUCLEATION, PRECIPITATION AND DECORATION

An extreme case of internal precipitation was described in the introduction. It was observed that crystals of ZnO containing very high concentrations of Li^+ ($\gg 1\times10^{19}$) disintegrate on cooling. A similar process, which does not weaken the crystal seriously, has been observed where concentrations are lower. The basis for the interpretation of the effect of precipitation on conductivity in zinc oxide has been discussed by THOMAS[4] who studied the precipitation of indium.

Data are given in Fig. 6 for the change in conductivity of a crystal which was saturated with Li^+ at 440°C (with the Zn vapor also at 440°C), quenched to room temperature, then heated to the indicated temperatures in air. The changes in conductivity were observed at the temperatures indicated and the run at 317°C is a continuation of that at 286°C, etc. The lines do not meet at a point at $t = 0$ because of the correction for the change of mobility with temperature. Note the change of time scale with change in temperature.

Theory for nucleation and precipitation along non-interacting line dislocations leads to the expression

$$x = 1/0{\cdot}36\pi D\tau \text{ (cm)}$$

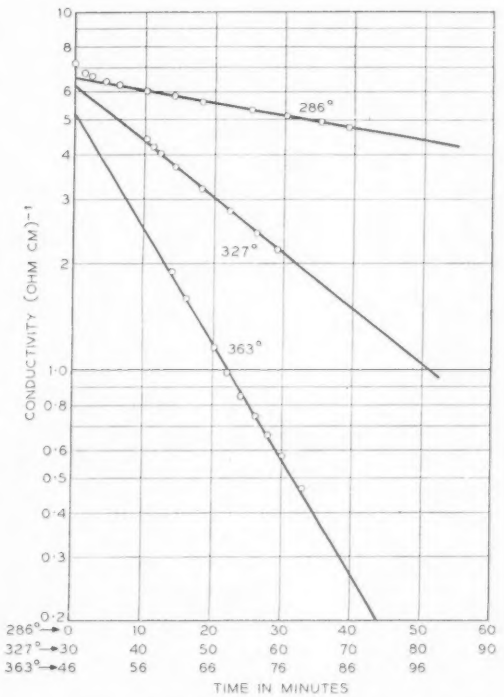

FIG. 6. Change in conductivity in ZnO with precipitation of Li at temperatures indicated.

and a linear relation between log σ and time. x is the length of the cylinder of precipitated material (total length of dislocations), τ is the time required

for σ to drop to $\sigma_0/2{\cdot}72$ and D is the diffusion coefficient for the rate limiting transport process. The data of Fig. 6 fit a linear log σ vs. t relation very well. Two numbers can be obtained from these data; the activation energy for the rate limiting process and the total length of dislocations. A comparison of the temperature coefficient of the time constants with that for the diffusion coefficients of Li^+ indicates that the rate limiting factor is the diffusion rate of Li^+. A total length of line dislocations was therefore calculated using the values of D for Li^+. The results are given in Table 2.

Table 2

Temp. (°C)	τ (sec.)	D (cm^2/sec)	x (cm)
286	7600	$5{\cdot}0\times10^{-11}$	$2{\cdot}3\times10^{6}$
327	1700	$2{\cdot}2\times10^{-10}$	$2{\cdot}4\times10^{6}$
363	810	$6{\cdot}4\times10^{-10}$	$1{\cdot}7\times10^{6}$

The value for x corresponds to a high dislocation density and is similar to that observed by THOMAS[4] for some crystals in a more extensive study of nucleation of an In_2O_3+ZnO phase in ZnO. The precipitation of 1×10^{18} atoms of metallic Li (corresponding to the initial conductivity equal to 7) as cylinders with a total length of 2×10^{6} cm yields cylinders with average diameter equal to about 150 Å, and average distance apart equal to about 60,000 Å.

Precipitation of lithium from much higher concentrations obtained by doping in the neighborhood of 700°C results in a darkening which is due to decoration of the dislocations. This is observable under the high power of a microscope. The decorated dislocations were seen, in the crystals studied, to be fine dark lines running perpendicular to the axis of the needle shaped crystals with hexagonal cross section. Their density varied by a factor of about three and counts gave an average value of about 2×10^{6} cm per cm^3 in agreement with the values given in Table 2. Crystals decorated in this fashion are extremely fragile.

8. INTRINSIC BEHAVIOR

The lowest conductivity so far observed in ZnO was obtained by doping a crystal with Li^+ to a concentration of about 1×10^{18} (atoms/cm^3), quenching to room temperature, then heating the crystal in air to about 700°C for a few minutes. During this treatment the conductivity at 700°C dropped to $2{\cdot}0\times10^{-5}$ and the value at 400°C was found to be $1{\cdot}2\times10^{-8}$. The activation energy computed from this temperature dependence is about 1·5 eV which is half the band gap for this temperature range. The concentration of electrons calculated from the conductivity at 400°C is $1{\cdot}4\times10^{9}$. The formula for intrinsic ionization (neglecting holes) yields

$$[e^-] = N_c \exp(-3{\cdot}0/2kT)$$
$$= 1\times10^{20}\times10^{-11{\cdot}2} = 6\times10^{8} \qquad (24)$$

where the value of N_c, the density of states in the conduction band, is that given by HUTSON[5]. Thus material which is practically intrinsic has been produced by doping with lithium.

9. CONCENTRATION OF SOLUTE SPECIES AS A FUNCTION OF ZINC PRESSURE

The solute species of the system have been assumed to be Li^+, Li^-, Zn^+ and e^-. In a p-type range e^+ must also be considered. Their concentrations are determined by the pressures of oxygen and zinc above the sample and can be calculated using data now available.

The pressures of oxygen and zinc are related by equation (8). Values for K_8 can be obtained from data given by KITCHENER and IGNATOWICZ[8] for the reduction of ZnO by carbon monoxide in the range 500°–800°C. They recommend for the free energy of dissociation of ZnO the equation $\Delta F = -114{,}640+5165T$ and this agrees well with effusion data obtained by us in the range from 900°–1100°C.

The following system of equations with K's evaluated at 500°C is obtained from data given above. Logarithms are to the base 10. The pressure of zinc over metallic zinc at 500°C is 0·0017 atm, and this is the limit of the experimentally accessible region on the high zinc pressure side.

$$\log P_{Zn}+\tfrac{1}{2}\log P_{O_2} = \log K_8 = -21{\cdot}22 \qquad (26)$$

$$\log[Zn^+]+\log[e^-]-\log P_{Zn} = \log K_3K_4 = 35{\cdot}37 \qquad (27)$$

$$2\log[Li^+]+2\log[e^-]-\log P_{Zn} = \log K_7 = 76{\cdot}68 \quad (28)$$

$$\log[Li^-]+\log[Zn^+]-\log[Li^+]-\log[e^-] = \log K_5 = -3{\cdot}37 \quad (29)$$

$$\log[e^-]+\log[e^+] = \log K_i = 20{\cdot}4 \quad (30)$$

$$\log([Li^+]+[Zn^+]+[e^+])-\log([Li^-]+[e^-]) = 0 \quad (31)$$

The last equation is obtained from the neutrality condition. The value of K_i has been obtained assuming an energy gap equal to 3·0 eV, and a value of $N_cN_v = 1\times10^{40}$.

The significant feature of the results is the very large range of nearly perfect compensation. The predicted pressures of oxygen which will drive the system significantly p-type are impractically large. Thus the chemistry of the system is such that substantial p-type behavior is not expected under equilibrium conditions near the temperature and pressures considered. The band gap is too wide. Practically, one can drive the Fermi level through a range of about 1·5 eV by treatments ranging from strongly reducing to strongly oxidizing. The results are shown in Fig. 7.

This calculation has ignored ion pairing and the formation of other complex solutes about which no information is available. If in fact they occur in quantities which are not negligible a reinterpretation of the above data is in order.

10. THE RATE OF COMPENSATION IN AIR

The solutions to the rate equations given in Fig. 4 describe a process with two characteristic stages; a first stage dominated by the influx of Li^+ which attains a substantial fraction of its final value, and a second stage dominated by Zn^+ which is generated by displacement and which flows out of the crystal with a concurrent increase in compensation. Experimental data for crystals heated in zinc vapor follow this pattern.

The process in crystals compensated by heat treatment in air is found to be quite different. The results, though not understood, are given here because of the need for high resistivity zinc oxide in some investigations and applications. A study of partially compensated crystals showed that such crystals contain an outer highly compensated region separated by a sharp boundary from an inner unaffected region.* The process proceeds as if the interface between compensated and non-compensated material is a sink for Li^+. But this is expected when conditions are adjusted to maintain the conductivity of the surface region at relatively low values. The region between low and high conductivity material then contains a large potential gradient opposing diffusion of Li^+ inwards and aiding the diffusion of Zn^+ outwards and also an increasing electron concentration which favors the displacement reaction. In a special case reaction might proceed with the neutralization of an amount $[D^+]dx$ of immobile donors by an influx $D_{Li}{}^+[Li^+]dt/x$ of Li^+ in the time interval dt. This has the solution

$$t = [D^+]x^2/2D_{Li}{}^+[Li^+] \quad (32)$$

The experimental data do in fact have the form of equation 32. Data for three runs are given in Fig. 8 in which conductivity is plotted against the square root of time. The linear relationship holds

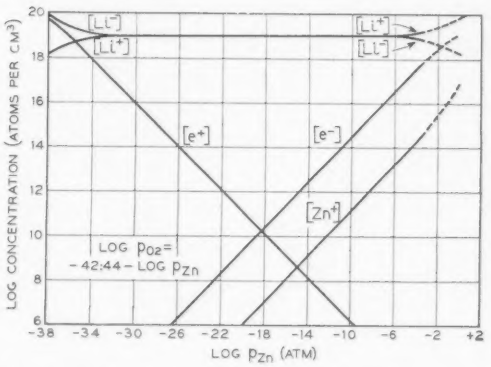

FIG. 7. Data for concentrations of indicated solute species as a function of zinc pressure for the problem discussed in Section 9. The right hand limit corresponds to data given in Fig. 3, the center to data obtained in one atmosphere of oxygen, and the left hand limit to p-type behavior expected at impractically high oxygen pressures.

* This was determined by successive etches and measurements of conductivity. The etch was 10 per cent HF. In the case of partially compensated crystals etching produced no change in conductance until the outer compensated region was removed. Subsequent etching then produced changes in conductance proportional to the amounts of crystal removed.

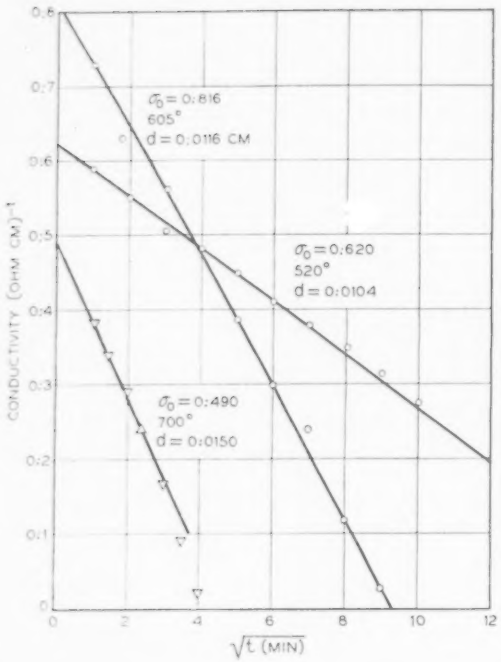

Fig. 8. Change in conductivity with time of ZnO crystals coated with LiOH and heated in air to the indicated temperatures.

to quite low values of conductivity, whereas in normal diffusion a breaking away from the straight line would be observed after conductivity dropped by about 30 per cent. However, values of $[Li^+]$ computed using equation (32) and the data given in Fig. 8 are low by about three orders of magnitude, therefore, the model considered cannot be correct. A satisfactory model has not been found. The experimental results are also of interest because they describe a process for obtaining abrupt changes of potential within a crystal.

Acknowledgements—During the course of this work the author has profited very much from discussions of the subject matter with D. G. THOMAS and A. R. HUTSON. The analytical results given in Table 1 are the contribution of E. K. JAYCOX.

REFERENCES

1. MOLLWO E., *Z. Phys.* **138,** 478 (1954).
2. THOMAS D. G. and LANDER J. J., *J. Chem. Phys.* **25,** 1136 (1956).
3. THOMAS D. G., *J. Phys. Chem. Solids* **3,** 229 (1957).
4. THOMAS D. G., *J. Phys. Chem. Solids* **9,** 31 (1959).
5. HUTSON A. R., *Phys. Rev.* **108,** 222 (1957).
6. VAN DER MAESEN F. and BRENKMAN J. A., *J. Electrochem. Soc.* **102,** 229 (1955).
7. FRANK F. C. and TURNBULL D., *Phys. Rev.* **104,** 617 (1956).
8. KITCHENER J. A. and IGNATOWICZ S., *Trans. Faraday Soc.* **47,** 1278 (1951).

J. Phys. Chem. Solids Pergamon Press 1960. Vol. 15. pp. 335–353. Printed in Great Britain.

ORIGIN OF MAGNETOELASTIC EFFECTS IN COBALT–IRON FERRITE

J. C. SLONCZEWSKI

International Business Machines Corporation, Research Laboratory, Poughkeepsie, New York

(*Received* 14 *October* 1959; *revised* 13 *January* 1960)

VOL. 15 1960

Abstract—The dependence of magnetostrictive strain and elastic coefficients on temperature and orientation of spontaneous magnetization is calculated for the special case of a cubic crystal containing an orbitally degenerate transition ion in a trigonal crystal field. The functional dependence of strain on orientation has a special form which cannot be expressed by means of standard phenomenological formulas. The strain is an order of magnitude larger than that which TSUYA calculated for certain ferrites not involving orbital degeneracy. The temperature dependence of strain agrees partially with measurements in cobalt–iron ferrite. By fitting theory to experiment a trigonal-field splitting of about 1600 cm^{-1} for the ground state of the cobalt ion is inferred.

An orbitally degenerate transition ion should have a large electrical polarizability because its first excited state is separated from the ground state by only spin-orbit energy. This polarizability is shown to give rise to elastic energy which depends on orientation of magnetization. This energy should be appreciable in cobalt–iron ferrite.

1. INTRODUCTION

ALTHOUGH magnetoelastic phenomena have been studied for a long time,[1] little has been done to relate them to electron structure. Recently, however, some progress has been made in antiferromagnetic oxides[2] and in ferrites.[3] We will consider here magnetoelastic effects associated with the presence of Co^{2+} in the ferrite composition $Co_xFe_{3-x}O_4$. This compound is interesting because the effects are amenable to fairly explicit calculation and are relatively large. Its magnetic anisotropy was discussed earlier.[4]

Two magnetoelastic phenomena will be considered. The first is the well known effect of magnetostriction. This refers to the spontaneous strain which a ferromagnetic crystal undergoes when its magnetization is saturated. The strain is a function of the orientation of the magnetic moment $\boldsymbol{M}$ with respect to the crystal axes. We may think of it as being caused by an internal magnetoelastic stress.

The second effect we will consider is the morphic effect which refers to the dependence of the elastic coefficients on the orientation of $\boldsymbol{M}$. MASON[5] has given a phenomenological treatment of the morphic effect. It is rarely discussed in the literature and where measured it has been found to be very small.[5,6]

It is instructive to compare the physical origin of magnetostriction in several magnetic compounds. CoO is an antiferromagnetic compound having a rock-salt structure with a small tetragonal distortion. According to KANAMORI's[2] explanation of this distortion the Co^{2+} ion is in an effective P-state. The cubic crystal field of an undistorted rock-salt structure allows the expectation value of the orbital momentum $\langle \boldsymbol{L} \rangle$ to orient itself freely in any direction. Therefore, at the absolute zero of temperature, spin–orbit coupling aligns $\langle \boldsymbol{L} \rangle$ with the net spin $\boldsymbol{S}$ of the ion so that the electron charge distribution is concentrated near an equatorial plane perpendicular to $\boldsymbol{S}$. (The spin–orbit interaction mixes orbital states so that $|\langle \boldsymbol{L} \rangle|$ is less than the largest value it could attain in the absence of spin-orbit coupling. However, this does not affect the essential nature of the physical picture.) This charge distribution repels the neighboring O^{2-} ions and expands the crystal in directions perpendicular to the spin axis more than in the direction parallel to the spin axis. If we imagine

the common spin axis of CoO to be variable by external means then we may say that this system has a large "magnetostriction". In practice, of course, CoO has no net moment and the spin axis cannot be oriented by means of an external field of reasonable magnitude. The crystal is in equilibrium when the common spin axis is parallel to ⟨100⟩. Consequently the natural crystal structure is tetragonal with the four-fold axis slightly shorter[7] (1·2 per cent, extrapolated to 0°K) than the two-fold axes.

In the case of ferrites containing cobalt TSUYA[3] has taken the view that the crystal field acting on Co^{2+} is unsymmetric because of the disordered arrangement of different cations on octahedral sites. We will make the assumption, found applicable to $Co_xFe_{3-x}O_4$ for small x[4], that the effect of disorder may be neglected. The Co^{2+} ion lies on an octahedral site. It experiences a moderately large trigonal crystal field in addition to the large cubic field. This aligns $\langle \boldsymbol{L} \rangle$ of the effective P-state parallel, in either sense, to the trigonal axis. Spin–orbit energy is much smaller than the trigonal field energy. Therefore, for an arbitrary orientation of $\boldsymbol{S}$, $\langle \boldsymbol{L} \rangle$, in each state, is deflected only slightly from the trigonal axis, and at 0°K $\langle \boldsymbol{L} \rangle$ assumes whichever orientation is closer to $\boldsymbol{S}$. The distribution of electron charge varies only slightly with spin direction and therefore the magnetostrictive effect of cobalt is much weaker than in CoO. According to the calculation to be given here it is reduced by a factor of order $\mathcal{H}_s/E_t$ where $\mathcal{H}_s$ is spin-orbit energy and E_t is the trigonal splitting of the effective P-state.

Magnetostriction is reduced even further in order of magnitude if the ground state does not have orbital degeneracy, in which case $\langle \boldsymbol{L} \rangle$ vanishes in first order. This is the most common situation. TSUYA[3] finds in certain cases (Ni^{2+} and Fe^{2+} in ferrites) that, unless the ground state of the free ion is an S-state, spin–orbit coupling is the predominant mechanism for magnetostriction with magnetic dipole interactions contributing substantial corrections. He shows that the magnetostrictive action of these cations is smaller than that of Co^{2+} in CoO by a factor of the order $(\mathcal{H}_s/\Delta \boldsymbol{E})^2$ where ΔE is an appropriate crystal field splitting. If all the cations in the compound occupy S-states in the free condition, then the effect of magnetic dipole interactions predominates.[3]

These remarks are illustrated in Table 1. As one proceeds down the Table, quenching of orbital momentum increases. As quenching increases, the order of perturbation theory required to calculate magnetostriction due to spin–orbit coupling increases. The last column lists experimental values of the magnetostrictive constant λ_{100}, showing how the order of magnitude of magnetostriction correlates with the order of the perturbation calculation. Placing $Co_{0.8}Fe_{2.2}O_4$ in the second row of this table may be disputed on the grounds that the crystal field does not have

Table 1. *Magnetostriction of selected compounds. Measurements were made at room temperature unless indicated otherwise.*

Number of orbital states	Order in $\mathcal{H}_s/\Delta E$	Compound	Effective cations	Experimental λ_{100}
3	0[b]	CoO	Co^{2+}	-8×10^{-3} [d]
2	1	$Co_{0.8}Fe_{2.2}O_4$	Co^{2+}	$-7{\cdot}4\times10^{-4}$ [a, e]
		$Co_{0.04}Fe_{2.96}O_4$	Co^{2+}	$-7{\cdot}0\times10^{-4}$ [a, b]
1	2[c]	$Ni_{0.8}Fe_{2.2}O_4$	$Ni^{2+}_{0.8}\ Fe^{2+}_{0.2}$	$-3{\cdot}6\times10^{-5}$ [f]
		Fe_3O_4	Fe^{2+}	$-2{\cdot}3\times10^{-5}$ [g]

a—These values are adjusted to one Co^{2+} ion per M Fe_3O_4 molecule (see Section 5)
b—Reference 2
c—Reference 3
d—Reference 7, value extrapolated to 0°K
e—Reference 16
f—SPAIN R., private communication
g—BICKFORD, PAPPIS and STULL, *Phys. Rev.* **99**, 1210 (1955).

trigonal symmetry because of disorder on octahedral sites. However, the value of λ_{100} adjusted for cobalt concentration is consistent with that for $Co_{0.04}Fe_{2.96}O_4$. This point is discussed in Section 5.

The relationship between magnetostriction and the degree of degeneracy is not as general as Table 1 would suggest. Often special considerations are involved, as in the case of Cu^{2+}. For detailed discussion of many other experimental and theoretical results the original work of TSUYA[3] should be consulted.

Explicit calculations of the morphic effect are not found in the literature. The morphic effect which we find to be appreciable in $Co_xFe_{3-x}O_4$ is caused by the electric polarization of the Co^{2+} ion. Straining the crystal produces a change in the crystal electric field. This produces electric polarization of the ground state of the Co^{2+} ion. Since the crystal field has inversion symmetry the lowest order multipole induced is a quadrupole. The energy of polarization is quadratic in strain and therefore is part of the elastic energy. The presence of an excited orbital state, separated from the ground state by only the spin-orbit splitting causes this effect to be much larger than in the more common case where the lowest excited state is separated from the ground state by a crystal-field splitting.

The calculations are based on the well-established crystal-field model. They take into account symmetry restrictions more explicitly than is usual in problems of this sort. This was done in order to demonstrate clearly that magnetostriction vanishes in first order and to write the results in a form sufficiently general to allow numerical estimates to be corrected easily as our knowledge of the energy levels and wave functions of the cobalt ion improves.

In Section 2, forms are derived for the matrix elements of the spin–orbit operator and the strain-dependent part of the crystal-field operator by means of symmetry arguments. In Section 3, a first-order effective Hamiltonian is used to calculate the contribution of an orbitally degenerate magnetic ion to the elastic energy. In Section 4, a second-order effective Hamiltonian is used to calculate the magnetostrictive strain caused by an orbitally degenerate magnetic ion. In Section 5, the results of these calculations are used to discuss magnetostriction and elasticity of cobalt–iron ferrite. Section 6 summarizes the results of the paper.

2. THE HAMILTONIAN

In this section we consider some formal properties of the Hamiltonian for a localized $\mathcal{N}$-electron system in a trigonal crystal field. We will factor some of its terms into forms useful in later calculations.

The Hamiltonian has the form

$$\mathcal{H} = \mathcal{H}_0+\mathcal{H}_e+\mathcal{H}_s+\mathcal{V}. \tag{2.1}$$

Here $\mathcal{H}_0$ represents the internal energy of the $\mathcal{N}$-electrons including their kinetic energy, coulomb interaction with the nucleus, mutual coulomb interaction, and electrostatic energy in the crystalline potential for vanishing strain. The exchange energy $\mathcal{H}_e$ of interaction between the total spin $\boldsymbol{S}$ of the local system and the other unpaired spins in the magnetic crystal is assumed to have the phenomenological form

$$\mathcal{H}_e = 2\beta \boldsymbol{H}\cdot\boldsymbol{S} \tag{2.2}$$

where β is the Bohr magneton and $\boldsymbol{H}$ is the molecular field. We assume that $\boldsymbol{H}$ is a vector operator function of electron positions and is parallel to the saturation magnetization $\boldsymbol{M}$ of the crystal. The spin-orbit energy $\mathcal{H}_s$ has the form

$$\mathcal{H}_s = \textstyle\sum_i \boldsymbol{u}(i)\cdot\boldsymbol{\sigma}(i) \tag{2.3}$$

where $\boldsymbol{\sigma}(i)$ is the Pauli spin operator

$$\left(\textstyle\sum_i \boldsymbol{\sigma}(i) = 2\boldsymbol{S}\right)$$

for the i-th electron and

$$\boldsymbol{u}(i) = (\hbar/4m^2c^2)\nabla V'(\boldsymbol{r}_i)\times\boldsymbol{p}_i \tag{2.4}$$

Here V' is the self-consistent one electron potential including the crystal field potential. The term $\mathcal{V}$ in equation (2.1) represents the change in the crystal field energy caused by elastic strain in the crystal. It is a function of the elastic strain tensor $A_{pq}(p,q = x,y,z)$.

We let the basic wave functions ψ_{nSM_slm} satisfy the eigenvalue equation

$$\mathcal{H}_0\psi_{nSM_slm} = E_{nS}\psi_{nSM_slm} \tag{2.5}$$

Each of these functions is anti-symmetric with respect to simultaneous interchange of any pair of

$\mathbf{r}_i$ and the respective spin variables $m_s(i) = \pm\frac{1}{2}$ which appear in its argument. The term $\mathscr{H}_0$ is invariant with respect to the trigonal group $\mathscr{G}$ of coordinate transformations. We let $\psi_{nSM_sl m}$ transform according to the m-th row of the l-th irreducible representation of $\mathscr{G}$ when the transformations are applied to all of the $\mathbf{r}(i)$, but none of the $\boldsymbol{\sigma}(i)$. Also, $\mathbf{S}^2$ has the diagonal value $S(S+1)$ in units of $\hbar^2$ and S_ζ, the spin component in an arbitrary fixed direction ζ, has the diagonal value M_s. The index n is an additional quantum number which serves to distinguish states having identical sets of values for the remaining quantum numbers.

where f is any function of x, y, z. Thus the proper rotations of the trigonal group are: (xyz) (identity); (yzx), (zxy) ($\pm 120°$ rotations about [111]); $(\bar{x}\bar{z}\bar{y})$, $(\bar{z}\bar{y}\bar{x})$, and $(\bar{y}\bar{x}\bar{z})$ (180° rotations about $[01\bar{1}]$, $[\bar{1}01]$, and $[1\bar{1}0]$ respectively). In this notation $\bar{x} \equiv -x$, etc. If improper rotations also exist, as in the spinel, they may be taken into account by classifying the wave functions according to parity. Since it is not necessary to take it into explicit account we may consider parity to be included in the quantum number n of $\psi_{nSM_sl m}$.

There are three irreducible representations of $\mathscr{G}$; two of one dimension each ($l = 1, 2$) and one of two dimensions ($l = 3$). When there is no ambiguity we may write $\psi_{\nu\mu}$ for the basic functions. Here ν represents the set nSM_s and $\mu(=1, 2, +,$ or $-)$ represents the set $lm(=11, 21, 31,$ or 32 respectively). Convenient representations are given in Table 2, which shows the effect of an operator listed in the first column on a wave function listed in the first row. The fact that these representations are irreducible may be verified by well known methods.

Table 2. Irreducible representations of the trigonal group. A symmetry element listed in the column at the left operates on a wave function of the top row to produce the result in the body of the table. Here $\omega = e^{2\pi i/3}$

	Γ_1	Γ_2	Γ_3	
	$\psi_{\nu 1}$	$\psi_{\nu 2}$	$\psi_{\nu +}$	$\psi_{\nu -}$
$(x\ y\ z)$	$\psi_{\nu 1}$	$\psi_{\nu 2}$	$\psi_{\nu +}$	$\psi_{\nu -}$
$(y\ z\ x)$	$\psi_{\nu 1}$	$\psi_{\nu 2}$	$\omega^*\psi_{\nu +}$	$\omega\psi_{\nu -}$
$(z\ x\ y)$	$\psi_{\nu 1}$	$\psi_{\nu 2}$	$\omega\psi_{\nu +}$	$\omega^*\psi_{\nu -}$
$(\bar{x}\ \bar{z}\ \bar{y})$	$\psi_{\nu 1}$	$-\psi_{\nu 2}$	$\omega^*\psi_{\nu -}$	$\omega\psi_{\nu +}$
$(\bar{z}\ \bar{y}\ \bar{x})$	$\psi_{\nu 1}$	$-\psi_{\nu 2}$	$\omega\psi_{\nu -}$	$\omega^*\psi_{\nu +}$
$(\bar{y}\ \bar{x}\ \bar{z})$	$\psi_{\nu 1}$	$-\psi_{\nu 2}$	$\psi_{\nu -}$	$\psi_{\nu +}$

Exchange energy is assumed to be diagonal in these basic functions. We have then

$$\mathscr{H}_e\psi_{nSM_sl m} = 2\beta H_{nSl}M_s\psi_{nSM_sl m} \qquad (2.6)$$

Here the ζ-axis of spin quantization is parallel to $\mathbf{H}$ and H_{nSl} is an eigen-value of H_ζ. It seems inconsistent with the general idea of a molecular field model to let $\mathscr{H}_e$ have a more general form than that expressed by equation (2.6).

Our discussion of $\mathscr{H}_0$ is restricted to the case of a crystal field of trigonal symmetry such as that which occurs on octahedral sites in ferrimagnetic spinels.[8] It is convenient to let the three-fold axis of the crystal field be the [111]-direction relative to the xyz axes. For a cubic crystal such as the spinel these are the cubic axes. The symbol (rst) will represent the transformation operation defined by the equation

$$(rst)f(x, y, z) = f(r, s, t) \qquad (2.7)$$

Since $\mathscr{H}_0$ is a real differential operator, it has the same eigenvalue for $\psi_{\nu\mu}$ as for the complex conjugate function $\psi_{\nu\mu}{}^*$. Now let $\xi\eta\zeta$ be a set of cartesian axes. Also let the conventional phases be chosen in defining the spin operators, namely such that $\sigma_\xi(i) \pm i\sigma_\xi(i)$ have real matrix elements. Also, let the relative phases of $\psi_{nSM_sl m}$ for different M_s be so chosen that the representation of $S_\xi \pm iS_\eta$ in this basis have the conventional, real matrix

elements. Then one can easily see that the representation of $\boldsymbol{S}$ in these basic functions is unchanged when each is replaced by its complex conjugate. (In general, complex conjugation has the effect of time-reversing the orbital state and leaving the spin state unchanged.) It follows that

$$\psi^*_{nSM_s lm} = \sum_{m'} C_{nSlm',m}\psi_{nSM_s lm'} \qquad (2.8)$$

where the coefficients C remain to be determined.

It is seen from equation (2.8) that a suitable choice of phase constant makes the one-dimensional bases $\psi_{\nu 1}$ and $\psi_{\nu 2}$ real. According to Table 2 the pair $\psi_{\nu-}{}^*$, $\psi_{\nu+}{}^*$ transforms like the pair $\psi_{\nu+}$, $\psi_{\nu-}$ respectively so that, from equation (2.8)

$$\psi_{\nu+} = e^{i\delta}\psi_{\nu-}, \qquad (2.9)$$

where δ is a real phase angle. Now we adjust the phase constants of these functions so that

$$\psi^*_{\nu+} = -\psi^*_{\nu-}. \qquad (2.10)$$

These phase conventions agree with those used in crystal field treatments based on the concept of "effective P-states".

Matrix elements of $\mathscr{H}_s$ may be written in the factored form

$$(nSM_s lm|\mathscr{H}_s|n'S'M'_s l'm') = (nSlm|\boldsymbol{U}|n'S'l'm') \times \times (SM_s|\boldsymbol{Q}|S'M'_s). \qquad (2.11)$$

Here $\boldsymbol{U}$ is a hermitean operator which transforms under $\mathscr{G}$ applied to spacial coordinates just like the vector $\boldsymbol{u}(i)$. It is likewise imaginary:

$$\boldsymbol{U}^* = -\boldsymbol{U} \qquad (2.12)$$

The matrix elements of the vector operator $\boldsymbol{Q}$ appearing in equation (2.11) are determined by the condition that the operator $\boldsymbol{\sigma}(i)$ appearing in $\mathscr{H}_s$ is of type $\boldsymbol{T}$ with respect to $\boldsymbol{S}$ in the language of CONDON and SHORTLEY[9]. The matrix elements of $\boldsymbol{Q}$ are given on page 63 of the same reference. In particular, for $S = S'$

$$(SM_s|\boldsymbol{Q}|SM_s') = (SM_s|\boldsymbol{S}|SM_s'). \qquad (2.13)$$

Thus equation (2.11) is a generalization of the form $\lambda\boldsymbol{L}\cdot\boldsymbol{S}$ for spin-orbit energy in the Russell–Saunders approximation.

We may separate each matrix element of $\boldsymbol{U}$ into one factor determined by the crystal field symmetry and a second factor requiring explicit calculation. For example, by applying in order, each of the operations listed in Table 2, we obtain

$$\begin{aligned}(nS+|U_x|n'S'-) &= \omega^*(nS+|U_y|n'S'-)\\ &= \omega(nS+|U_z|n'S'-) = -\omega^*(nS-|U_x|n'S'+)\\ &= -\omega(nS-|U_z|n'S'+) = -(nS-|U_y|n'S'+)\end{aligned} \qquad (2.14)$$

The complex conjugate operation provides another relation. From equations (2.9) and (2.12) we have

$$(nS+|U_z|n'S'-)^* = -(nS-|U_z|n'S'+) \qquad (2.15)$$

From equations (2.14) and (2.15) it follows that the parameter defined by

$$U(nS3,n'S'3) \equiv 3^{1/2}(nS+|U_z|n'S'-) \qquad (2.16)$$

is real. All of the matrix elements appearing in equations (2·14) are proportional to $U(nS3, n'S'3)$.

Table 3. Matrix elements of the operator (U_x,U_y,U_z). The coefficients $U(nSl,n'S'l)$ and $U'(nS3,n'S3)$ are real.

	Γ_1 $n'S'1$	Γ_2 $n'S'2$	Γ_3	
			$n'S'+$	$n'S'-$
$nS1$	0	$iU(nS1,n'S'2)(1,1,1)$	$iU(nS1,n'S'3)(\omega,\omega^*,1)$	$-iU(nS1,n'S'3)(\omega^*\omega,1)$
$nS2$	$-iU(nS2,n'S'1)(1,1,1)$	0	$U(nS2,n'S'3)(\omega,\omega^*,1)$	$U(nS2,n'S'3)(\omega^*,\omega,1)$
$nS+$	$-iU(nS3,n'S'1)(\omega^*,\omega,1)$	$U(nS3,n'S'2)(\omega^*,\omega,1)$	$3^{-1/2}U'(nS3,n'S'3)(1,1,1)$	$U(nS3,n'S'3)(\omega,\omega^*,1)$
$nS-$	$iU(nS3,n'S'1)(\omega,\omega^*,1)$	$U(nS3,n'S'2)(\omega,\omega^*,1)$	$-U(nS3,n'S'3)(\omega^*,\omega,1)$	$-3^{-1/2}U'(nS3,n'S3)(1,1,1)$

By further applications of symmetry and complex conjugate operations the matrix elements of $\boldsymbol{U}$ may be placed in the form given in Table 3. In Table 3 each matrix element is a given multiple of the real parameter $U(nSl,n'S'l')$ or $U'(nS3,n'S'3)$. Apart from the restrictions imposed by the Hermiticity of $\boldsymbol{U}$, nothing may be determined about these parameters without employing explicit wave functions.

Matrix elements of $\mathscr{V}$ may be factored in a similar way. The elements of the strain tensor $A_{pq}(p,q = x, y, z)$ are defined by equations of the types

$$A_{xx} = \frac{\partial R_x}{\partial x},$$

$$A_{yz} = \frac{1}{2}\left(\frac{\partial R_y}{\partial z} + \frac{\partial R_z}{\partial y}\right), \ldots \qquad (2.17)$$

where $\boldsymbol{R}$ is the macroscopic displacement of a point in the crystal initially at (x, y, z). The transformation properties of the A_{pq} under $\mathscr{G}$ may be determined from those for $x\,y\,z$ and one finds that only simple interchanges occur. We may expand $\mathscr{V}$ in powers of A_{pq}:

$$\mathscr{V}(\boldsymbol{r}(1), \ldots \boldsymbol{r}(\mathscr{N}); A_{xx}, A_{yz}, \ldots) = \sum_{p \leqslant q} \mathscr{V}_{pq}(\boldsymbol{r}(1), \ldots \boldsymbol{r}(\mathscr{N})) A_{pq} + \ldots \qquad (2.18)$$

Since $\mathscr{V}$ is invariant with respect to simultaneous transformations in $\mathscr{G}$ of $\boldsymbol{r}(i)$ and A_{pq}, it follows from equation (2.18) that V_{pq} transforms just like A_{pq}.

Matrix elements of V_{pq} may be factored as before. Table 4 shows how real parameters of the type $V_e(nSl,n'Sl')$ and $V'_e(nS3,n'S3)$ factor out of matrix elements of V_{xx}, V_{yy}, and V_{zz}, related to *extension* strains. A precisely similar table applies to matrix elements of V_{yz}, V_{zx}, and V_{xy}, related to *shear* strains with the difference that V_e and V'_e must be replaced by different parameters V_s and V'_s respectively. All such parameters are mutually independent except for restrictions imposed by Hermiticity of $\mathscr{V}$.

3. MORPHIC EFFECT

The dependence of the elastic coefficients of a crystal on the orientation of its magnetic moment is known as the morphic effect. In the particular case under consideration, a first order calculation of the morphic effect requires only the use of a first order effective Hamiltonian. First order calculation of the more familiar magnetostriction, or spontaneous distortion of the crystal, requires the use of a second-order effective Hamiltonian. Therefore, the morphic effect is the easier to calculate and will be discussed first. Magnetostriction will be considered in a separate section.

We are interested in the case where the lowest multiplet, with spin S_0, belongs to the two-dimensional representation (Γ_3) of $\mathscr{G}$. In order to calculate the sub-matrix of $\mathscr{H}_s$ in this multiplet we note that since $\boldsymbol{U}$ is Hermitian, it follows from Table 3 that for any n

$$U(nS3, nS3) = 0 \qquad (3.1)$$

Then from Table 2 the submatrix of $\boldsymbol{U}$ is

$$\boldsymbol{U} = U_0 \boldsymbol{k} \begin{pmatrix} 1 & 0 \\ 0 & -1 \end{pmatrix} \qquad (3.2)$$

where we have let $U_0 = U'(0S_03,0S_03)$ and where $\boldsymbol{k}$ is a unit vector parallel to [111]. From equations (2.11) and (3.2) the submatrix of $\mathscr{H}_s$ is diagonal in the orbital quantum numbers. To

Table 4. Non-vanishing matrix elements of (V_{xx}, V_{yy}, V_{zz}). The same table with V_e and V'_e replaced by V_s and V'_s respectively holds for (V_{yz}, V_{zx}, V_{xy}).

	Γ_1	Γ_2	Γ_3	
	$n'S1$	$n'S2$	$n'S+$	$n'S-$
$nS1$	$V_e(nS1,n'1)(1,1,1)$	0	$iV_e(nS1,n'3)(\omega,\omega^*,1)$	$iV_e(nS1,n'3)(\omega^*,\omega,1)$
$nS2$	0	$V_e(nS2,n'2)(1,1,1)$	$V_e(nS2,n'S3)(\omega,\omega^*,1)$	$-V_e(nS2,n'3)(\omega^*,\omega,1)$
$nS+$	$-iV_e(nS3,n'1)(\omega^*,\omega,1)$	$V_e(nS3,n'2)(\omega^*,\omega,1)$	$V_e'(nS3,n'3)(1,1,1)$	$V_e(nS3,n'3)(\omega,\omega^*,1)$
$nS-$	$-iV_e(nS3,n'1)(\omega,\omega^*,1)$	$-V_e(nS3,n'2)(\omega,\omega^*,1)$	$V_e(nS3,n'3)(\omega^*,\omega,1)$	$V_e'(nS3,n'3)(1,1,1)$

VOL. 15 1960

first order, we may replace $\mathscr{H}_s$ by its diagonal parts $\pm U_0\boldsymbol{k}\cdot\boldsymbol{S}$.

Then from equations (2.1), (2.5) and (2.6) the effective Hamiltonian to first-order approximation becomes

$$\mathscr{H}_{\text{eff}} = E_0 + 2\beta\boldsymbol{H}\cdot\boldsymbol{S} \pm U_0\boldsymbol{k}\cdot\boldsymbol{S} + \mathscr{V} \qquad (3.3)$$

where the sign of the third term depends on the direction of "pseudo-momentum" $\pm\boldsymbol{k}$. For the sake of brevity some subscripts have been dropped from $E_{0S_0 3}$ and $\boldsymbol{H}_{0S_0 3}$. The diagonal values of $\mathscr{H}_{\text{eff}}$ for vanishing $\mathscr{V}$ are given by

$$\epsilon = E_0 + |2\beta\boldsymbol{H} \pm U_0\boldsymbol{k}|M_s \qquad (3.4)$$

$$= E_0 + [4\beta^2H^2 \pm 4\beta HU_0\cos\theta + U_0^2]^{1/2}M_s \qquad (3.5)$$

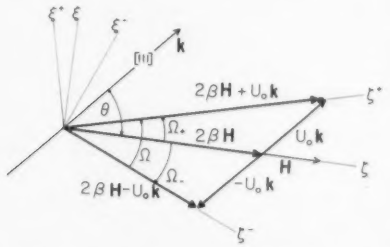

FIG. 1. Orientation of axes of spin quantization. The η^-, η and η^+-axes are normal to the plane of the diagram.

where the $\zeta^\pm$-axis of spin quantization is parallel to $2\beta\boldsymbol{H} \pm U_0\boldsymbol{k}$ and θ is the angle between $\boldsymbol{H}$ and $\boldsymbol{k}$ (see Fig. 1). We had shown previously[4] how these energy levels account for the effect of small substitutions of cobalt on the anisotropy of magnetite. The constant U_0 was $-\alpha\lambda$ in the earlier notation. The eigenstates corresponding to the eigenvalues (3.4) are denoted by $\phi_{M_s\pm}$ with spin quantized in the direction $2\beta\boldsymbol{H} \pm U_0\boldsymbol{k}$ respectively. According to equation (2.18) and Table 4 the submatrix of $\mathscr{V}$ in this representation is given by

$$(M_s+|\mathscr{V}|M'_s+) = (M_s-|\mathscr{V}|M'_s-) = \mathscr{V}_{++}\delta_{M_s,M_s'} \qquad (3.6)$$

where

$$\mathscr{V}_{++} = V'_e(A_{xx}+A_{yy}+A_{zz}) + V'_s(A_{yz}+A_{zx}+A_{xy}), \qquad (3.7)$$

and

$$(M_s+|\mathscr{V}|M_s'-) = \mathscr{V}_{+-}|S_0M_s|_+\,|S_0M_s')_- \qquad (3.8)$$

where

$$\mathscr{V}_{+-} = V_e(\omega A_{xx}+\omega^*A_{yy}+A_{zz}) + V_s(\omega A_{yz}+\omega^*A_{zx}+A_{xy}) \qquad (3.9)$$

Here we have let $V_e = V_e(0S_03,03)$, etc. The ket vector $|S_0M_s)_\pm$ appearing in equation (3.8) is the spin state with quantization axis $\zeta^\pm$. An explicit formula for $(S_0M_s|_+\ |S_0M_s')_-$ is given by EDMONDS[10]. For cobalt in magnetite $2\beta H$ ($= 640\ \text{cm}^{-1}$) is about 5 times U_0 ($= 132\ \text{cm}^{-1}$)[4] so that the angle Ω between the ζ^+-axis and the ζ^--axis is small and $(S_0M_s|_+\ |S_0M_s')_-$ is nearly $\delta_{M_s,M_s'}$.

Magnetoelastic energy, which gives rise to magnetostriction, is linear in strain. In the present approximation it should appear in the diagonal part of $\mathscr{V}$ given in equations (3.6) and (3.7). Since $(M_s\pm|\mathscr{V}|M_s\pm)$ turns out to be independent of the orientation of $\boldsymbol{H}$ and of the energy level occupied, magnetostriction vanishes in this approximation. The remaining, non-magnetostrictive terms represent permanent stresses caused by the electrostatic forces of the trigonally symmetric charge distribution of the magnetic ion which act on the surrounding ions. We will neglect these terms in what follows.

Calculation of energy to second order in strain yields non-vanishing results which depend on the orientation of $\boldsymbol{H}$. This energy is the cause of the morphic effect. We assume that kT is small compared to βH but not necessarily small compared to U_0. Let $\epsilon_\pm$ be the lowest energy levels of equation (3.5) with $M_s = -S_0$. Then the free energy per atom is given by

$$f = -kT\ln[\exp(-\epsilon_+/kT)+\exp(-\epsilon_-/kT)] \qquad (3.10)$$

For small increments $\Delta\epsilon_\pm$ due to strain, the increment in f is

$$w \equiv \Delta f = \frac{\Delta\epsilon_+\exp(-\epsilon_+/kT)+\Delta\epsilon_-\exp(-\epsilon_-/kT)}{\exp(-\epsilon_+/kT)+\exp(-\epsilon_-/kT)} \qquad (3.11)$$

Calculation of $\Delta\epsilon_\pm$ to second order in strain may be carried out exactly in our manifold of $2(2S_0+1)$ states. Owing to the complexity of the general formula for $(S_0M_s|_+\ |S_0M_s')_-$ the resulting expressions for $\Delta\epsilon_\pm$ would be very long. We will calculate

only terms up to order Ω^2 or, what is equivalent $(U_0/\beta H)^2$. Since $|S_0M_s)_+$ is obtained by rotating $|S_0M_s)_-$ through Ω about the η-axis we may write

$$|S_0M_s)_+ = \exp(-i\Omega S_\eta|S_0M_s)_- \quad (3.12)$$

Expanding the exponential, one finds

$$(S_0-S_0|_+\,|S_0-S_0)_- = 1-S_0\Omega^2/4+\ldots \quad (3.13)$$

Applying second order perturbation theory one finds that only connections between the two lowest states give energy terms up to order Ω^2, the result being

$$\Delta\epsilon_\pm = \pm\frac{|\mathscr{V}_{+-}|^2}{(\epsilon_+-\epsilon_-)}(1-S_0\Omega^2/2) \quad (3.14)$$

By expressing Ω in terms of θ and retaining terms up to order $(U_0/\beta H)^2$ we obtain

$$\Delta\epsilon_\pm = \mp\frac{|\mathscr{V}_{+-}|^2}{2S_0U_0\cos\theta}\times \times\left[1-\frac{(S_0-\tfrac{1}{4})U_0^2}{2\beta^2H^2}\sin^2\theta\right] \quad (3.15)$$

From equation (3.11) and the fact that $\Delta\epsilon_+ = -\Delta\epsilon_-$ in this approximation the elastic energy per atom is given by

$$w = \Delta\epsilon_+\tanh[(\epsilon_--\epsilon_+)/2kT] \quad (3.16)$$

in combination with equations (3.9) and (3.15). This expression is valid if either kT or $|\epsilon_+-\epsilon_-|$ is much greater than $|\mathscr{V}_{+-}|$. When both of these inequalities are violated higher order terms become important.

We may apply this result to a cubic crystal having sites with trigonal symmetry. For the above case in which [111] is the trigonal axis,

$$\cos\theta = 3^{-1/2}(\alpha_x+\alpha_y+\alpha_z) \quad (3.17)$$

where α_x, α_y and α_z are the direction cosines of $\boldsymbol{M}$ or $\boldsymbol{H}$ with respect to the cubic axes, we have from equations (3.5), (3.15), (3.16) and (3.17).

$$w(\alpha_x\alpha_y\alpha_z) = |\mathscr{V}_{+-}|^2 g(\alpha_x\alpha_y\alpha_z) \quad (3.18)$$

where

$$g(\alpha_x\alpha_y\alpha_z) = \frac{-3^{1/2}}{2S_0U_0(\alpha_x+\alpha_y+\alpha_z)}\left[1-\frac{(S_0-\tfrac{1}{4})U_0^2}{3\beta^2H^2}(1-\alpha_x\alpha_y-\alpha_y\alpha_z-\alpha_z\alpha_x)\right]\times$$

$$\times\tanh\left\{\frac{S_0U_0(\alpha_x+\alpha_y+\alpha_z)}{3^{1/2}kT}\left[1-\frac{U_0^2}{12\beta^2H^2}(1-\alpha_x\alpha_y-\alpha_y\alpha_z-\alpha_z\alpha_x)\right]\right\}. \quad (3.19)$$

In the argument of tanh powers of U_0 higher than fourth are neglected.

The elastic energy of orbitally degenerate atoms lying on a site whose trigonal axis is different from [111] may be obtained by transforming coordinates in equation (3.18). The total elastic energy arising in this way becomes, for a cubic crystal,

$$W_m = N_{111}|\mathscr{V}_{+-}(xyz)|^2 g(\alpha_x\alpha_y\alpha_z)+ +N_{\bar{1}11}|\mathscr{V}_{+-}(\bar{x}yz)|^2 g(\bar{\alpha}_x\alpha_y\alpha_z)+ +N_{1\bar{1}1}|\mathscr{V}_{+-}(x\bar{y}z)|^2 g(\alpha_x\bar{\alpha}_y\alpha_z)+ +N_{11\bar{1}}|\mathscr{V}_{+-}(xy\bar{z})|^2 g(\alpha_x\alpha_y\bar{\alpha}_z) \quad (3.20)$$

where N_i is the number of such atoms having i for its trigonal axis. The transformations on the "arguments" xyz of $\mathscr{V}_{+-}$ indicated in equation (3.19) are to be applied to the tensor A_{pq} appearing in equation (3.9). Substituting equation (3.9)

in (3.20) we have

$$\begin{aligned} W_m = {} & k_{11}(A_{xx}^2 - A_{xx}A_{yy} - A_{xx}A_{zz}) + 2k_{14}A_{xx}A_{yz} - k_{25}A_{xx}A_{zx} - k_{36}A_{xx}A_{xy} \\ & k_{11}(A_{yy}^2 - A_{yy}A_{zz}) - k_{14}A_{yy}A_{yz} + 2k_{25}A_{yy}A_{zx} - k_{36}A_{yy}A_{xy} \\ & + k_{11}^2 A_{zz} - k_{14}A_{zz}A_{yz} - k_{25}A_{zz}A_{zx} + 2k_{36}A_{zz}A_{xy} \\ & + k_{44}A_{yz}^2 + k_{45}A_{yz}A_{zx} + k_{46}A_{yz}A_{xy} \\ & + k_{44}A_{zx}^2 + k_{56}A_{zx}A_{xy} \\ & + k_{44}A_{xy}^2 \end{aligned} \tag{3.21}$$

where

$$\begin{aligned} k_{11} &= Ve^2(p_0+p_1+p_2+p_3) \\ k_{44} &= V_s^2(p_0+p_1+p_2+p_3) \\ k_{14} &= V_eV_s(p_0+p_1+p_2+p_3) \\ k_{25} &= V_eV_s(p_0+p_1+p_2+p_3) \\ k_{36} &= V_eV_s(p_0-p_1-p_2+p_3) \\ k_{45} &= V_s^2(-p_0+p_1+p_2-p_3) \\ k_{46} &= V_s^2(-p_0+p_1-p_2+p_3) \\ k_{56} &= V_s^2(-p_0-p_1+p_2+p_3) \end{aligned} \tag{3.22}$$

and

$$\begin{aligned} p_0 &= N_{111}g(\alpha_x\alpha_y\alpha_z) \\ p_1 &= N_{\bar{1}11}g(\bar{\alpha}_x\alpha_y\alpha_z) \\ p_2 &= N_{1\bar{1}1}g(\alpha_x\bar{\alpha}_y\alpha_z) \\ p_3 &= N_{11\bar{1}}g(\alpha_x\alpha_y\bar{\alpha}_z) \end{aligned} \tag{3.23}$$

For a given total concentration N of orbitally degenerate atoms the values of N_i may be varied, within limits, by magnetic annealing.[4] Suppose we consider the symmetric case where $N_i = N/4$ for all i. For a general orientation of $\boldsymbol{M}$ the k-coefficients appearing in equation (3.20) do not vanish and the elastic symmetry is no higher than that of a triclinic crystal. If $\boldsymbol{M}$ is parallel to [100] phenomenological considerations demand that the elastic symmetry be as high as that of a tetragonal crystal. In this case we have from equations (3.19) and (3.23),

$$p_0 = p_1 = p_2 = p_3. \tag{3.24}$$

From equation (3.22) we see that all k-coefficients vanish except k_{11} and k_{44} so that the symmetry of W_m is cubic.[11] The reason for this result is that in the approximation used here the energy levels depend on θ but not on the azimuthal angle of $\boldsymbol{M}$ with respect to $\boldsymbol{k}$. Since θ is the same for all $\langle 100 \rangle$ -directions the elastic energy is the same for all $\langle 100 \rangle$-directions and therefore must have the symmetry of a cube. If $\boldsymbol{M}$ is parallel to $\langle 111 \rangle$, the elastic symmetry is trigonal as expected.

We may say that the crystal exhibits a Jahn–Teller effect of a second order. The first order Jahn–Teller effect occurs when a system has a precise coincidence in orbital energy. The nuclear configuration of the system deforms spontaneously and removes the degeneracy. A second order effect occurs here because there is only a near-coincidence of orbital energy. There is no energy term which is first order in strain (in the present approximation) so that the crystal does not deform spontaneously. Since $p_i<0$ we have $k_{11}<0$ and $k_{44}<0$, so that if a single component of A_{pq} is non-vanishing W_m is negative. Therefore, we may say that the second-order Jahn–Teller effect merely weakens the resistance of the crystal to distortion. This effect might, in principle, be so strong as to reverse the sign of elastic coefficients and cause the undeformed crystal to be in a state of unstable equilibrium. It is also interesting to note that the contribution to bulk modulus

$$\tfrac{1}{3}(\partial^2 W_m/\partial A_{xx}^2 + 2\partial^2 W_m/\partial A_{xx}^2 \partial A_{yy})$$

vanishes.

The morphic effect has been described as a secondary effect,[5] intimately connected with magnetostriction. It has been supposed that elastic coefficients change as a consequence of the

magnetostrictive distortion of the crystal structure. We find, in this instance, that the morphic effect is primary in that it appears even when magnetostriction is neglected.[12] The magnitude of the effect in cobalt–iron ferrite will be considered in a later section.

4. MAGNETOSTRICTION

In order to calculate magnetostrictive strains it is necessary first to calculate magnetostrictive stresses. These are given by the first derivative of free energy with respect to the components of strain, evaluated at zero strain. They vanished in the first-order approximation of the previous section. We will obtain here a non-vanishing second-order effect. Consider the pair of states $\phi_{-S_0\pm}$ with energy values (3.4). We may obtain an effective 2×2 Hamiltonian for these states by "removing" the perturbing effect of the terms $\mathscr{H}_s$ and $\mathscr{V}$ through excited states.

A general method of constructing an effective Hamiltonian is to separate a complete set of states into a class A, containing a finite number of states, and a class B, containing all other states. The effective Hamiltonian $\mathscr{U}_{mn}$ for the states of class A is given by[13]

$$\mathscr{U}_{mn}=\mathscr{H}_{mn}+\sum_{\alpha}^{\mathrm{B}}\frac{\mathscr{H}_{m\alpha}\mathscr{H}_{\alpha n}}{E-\mathscr{H}_{\alpha\alpha}}+$$

$$+\sum_{\substack{\alpha\beta\\ \alpha\neq\beta}}^{\mathrm{B}}\frac{\mathscr{H}_{m\alpha}\mathscr{H}_{\alpha\beta}\mathscr{H}_{\beta n}}{(E-\mathscr{H}_{\alpha\alpha})(E-\mathscr{H}_{\beta\beta})}+\ldots \quad (4.1)$$

where m and n refer to states in class A, E is the eigenvalue of $\mathscr{H}$ to be found, and the summations are carried over states in class B. A necessary condition for convergence of eigenvalues of $\mathscr{U}$ to eigenvalues of $\mathscr{H}$ is that

$$|\mathscr{H}_{mn}|/(E-\mathscr{H}_{mm})|\ll|$$

for m and n ($\neq m$) in class B. In this formulation of perturbation theory $\mathscr{H}$ is not partitioned explicitly into an unperturbed part and a perturbation. The partition is implied by the representation used.

Let class A contain two states $\phi_{-S_0\pm}$ written simply as $|+)$ and $|-)$. Class B contains the remaining states $\phi_{M_s\pm}$ of the orbital doublet and all states ψ_{nSM_slm} not belonging to this doublet. Note that each of the functions ϕ_{M_s+}, ϕ_{M_s-} and ψ_{nSM_slm} has a different axis of spin quantization. The quadratic secular equation has the solutions

$$\epsilon=\mathscr{A}\pm[\mathscr{B}^2+|\mathscr{U}_{+-}|^2]^{1/2} \quad (4.2)$$

where

$$\mathscr{A}=\tfrac{1}{2}(\mathscr{U}_{++}+\mathscr{U}_{--}) \quad (4.3)$$

and

$$\mathscr{B}=\tfrac{1}{2}(\mathscr{U}_{++}-\mathscr{U}_{--}). \quad (4.4)$$

If only the states $|+)$ and $|-)$ are appreciably populated, the free energy per ion is

$$f=\mathscr{A}-kT\ln\{2\cosh[(\mathscr{B}^2+|\mathscr{U}_{+-}|^2)^{1/2}/kT]\} \quad (4.5)$$

The energy associated with magnetostrictive stress is the differential of f with respect to strain, given by

$$df=d\mathscr{A}-[\mathscr{B}d\mathscr{B}+\mathscr{R}e(\mathscr{U}_{+-}d\mathscr{U}^*_{+-})]\times$$

$$\times(\mathscr{B}^2+|\mathscr{U}_{+-}|^2)^{-1/2}\tanh[(\mathscr{B}^2+|\mathscr{U}^*_{+-}|^2)^{1/2}/kT] \quad (4.6)$$

where $d\mathscr{A}$, $d\mathscr{B}$, $d\mathscr{U}_{+-}$ are first order differentials with respect to strain. They come in through the term $\mathscr{V}$ in $\mathscr{H}$. The quantities $\mathscr{B}$ and $\mathscr{U}_{+-}$ appearing in equation (4.6) are evaluated at zero strain.

The approximation used in calculating df will be applicable to the case $|\mathscr{H}_s|\ll|\mathscr{H}_e|$, ΔE, where ΔE is characteristic of crystal field splitting. It will develop that df is of the order $\mathscr{H}_s d\mathscr{V}/\Delta E$. The calculation will include terms of this order and terms of order $\mathscr{H}_s{}^2 d\mathscr{V}/\Delta E\mathscr{H}_e$.

Equation (4.6) may be simplified. In calculating $\mathscr{U}_{+-}$, $\mathscr{V}$ is set equal to zero. Also, the off-diagonal elements of the remaining part of $\mathscr{H}$ connecting the states $\phi_{M_s\pm}$ to each other vanish. Therefore, $\mathscr{U}_{+-}$ is second order in $\mathscr{H}$. Since the only non-diagonal part of $\mathscr{H}$ besides $\mathscr{V}$ is $\mathscr{H}_s$, $\mathscr{U}_{+-}$ is of the order $\mathscr{H}_s{}^2/\Delta E$. On the other hand $\mathscr{B}$ is of the order $\mathscr{H}_s$. Therefore, in our approximation, $|\mathscr{U}_{+-}|$ may be neglected in the term $(\mathrm{B}^2+|\mathscr{U}_{+-}|^2)^{1/2}$. Also, $d\mathscr{U}_{+-}$ may be replaced by $d\mathscr{V}_{+-}$ obtained from equation (3.9). Since V_e and V_s are real we then have

$$f_{zz}=\frac{\partial f}{\partial A_{zz}}=\frac{\partial\mathscr{A}}{\partial A_{zz}}-$$

$$-\left[\frac{\partial\mathscr{B}}{\partial A_{zz}}+\frac{V_e\mathscr{R}e(\mathscr{U}_{+-})}{\mathscr{B}}\right]\tanh(\mathscr{B}/kT) \quad (4.7)$$

$$f_{xy} = \frac{\partial f}{\partial A_{xy}} = \frac{\partial \mathscr{A}}{\partial A_{xy}} - \left[\frac{\partial \mathscr{B}}{\partial A_{xy}} + \frac{V_s \mathscr{R}_e(\mathscr{U}_{+-})}{\mathscr{B}}\right]\tanh(\mathscr{B}/kT) \quad (4.8)$$

We will now calculate the second order quantities appearing in equations (4.7) and (4.8).

Matrix element $\mathscr{U}_{+-}$

From equations (4.1), (2.1), (2.5) and (2.6),

$$\mathscr{U}_{+-} = -\sum_{nSM_s lm} (+|\mathscr{H}_s|nSM_s lm)\times \times (nSM_s lm|\mathscr{H}_s|-)/E'_{nSM_s l}, \quad (4.9)$$

$$E'_{nSM_s l} = -E_0 + E_{nSl} + 2\beta(HS_0 + H_{nl}M_s) \quad (4.10)$$

Connections among $\phi_{M_s\pm}$ vanish and are omitted in equation (4.9). Terms in equation (4.10) due to $\mathscr{H}_x$ have been neglected. Matrix elements of $\mathscr{H}_s$ may be evaluated from equation (2.17), which we write for brevity in the form

$$\mathscr{H}_s = \boldsymbol{U}\cdot\boldsymbol{Q} \quad (4.11)$$

Note that the product in this equation is not a matrix product. This is just a shorthand expression for equation (2.11). Let $\alpha_{rs}(r = xyz;\ s = \xi,\ \eta,\ \zeta)$ be the coefficients of an orthogonal transformation between the $x\ y\ z$ axes and the $\xi\ \eta\ \zeta$ axes. Then

$$\mathscr{H}_s = \sum_{rs} U_r \alpha_{rs} Q_s$$

We may let

$$Q_\pm = Q_\xi \pm iQ_\eta,\ \alpha_{r\pm} = \tfrac{1}{2}(\alpha_{r\xi} \pm i\alpha_{r\eta}) \quad (4.12)$$

to obtain

$$\mathscr{H}_s = \sum_r \sum_{i=+-\zeta} U_r \alpha^*_{ri} Q_i = \sum_r \sum_{i=+-\zeta} U_r \alpha_{ri} Q_i^\dagger \quad (4.13)$$

where the superscript $\dagger$ means adjoint.

Substituting equation (4.13) in equation (4.9), we obtain

$$\mathscr{U}_{+-} = -\sum_{nSM_s lm}\sum_{ri} \alpha^*_{ri}(0S_0+|U_r|nSlm)\times \times (S_0 - S_0|_+ Q_i|SM_s)\cdot\sum_{gj}\alpha_{gj}(0S_0-|U_g|nSlm)^*\times \times (S_0 - S_0|_- Q_j|SM_s)^*/E'_{nSM_s l} \quad (4.14)$$

Carrying out the sum over lmr and g with the aid of Table 3 we get

$$\mathscr{U}_{+-} = \sum_{nSM_s ij}(S_0 - S_0|_+ Q_i|SM_s)(S_0 - S_0|_- Q_j|SM_s)^*\{-\sum_{l=1,2}(-1)^l[U(0S_03, nSl)]^2\times \times(\omega^*\alpha^*_{xi} + \omega\alpha^*_{yi} + \alpha^*_{zi})(\omega^*\alpha_{xj} + \omega\alpha_{yj} + \alpha_{zj})/E'_{nSM_s l} + 3^{-1/2}U'(0S_03, nS3)U(0S_03, nS3)\times \times[(\alpha^*_{xi} + \alpha^*_{yi} + \alpha^*_{zi})(\omega\alpha_{xj} + \omega^*\alpha_{yj} + \alpha_{zj}) + (\omega\alpha^*_{xi} + \omega^*\alpha^*_{yi} + \alpha^*_{zi})\times \times(\alpha_{xj} + \alpha_{yj} + \alpha_{zj})]/E'_{nSM_s 3}\} \quad (4.15)$$

Since the state $|S_0 - S_0)_\pm$ is obtained by rotating $|S_0 - S_0)$ through an angle $\Omega_\pm$ about η-axis, we may write

$$|S_0 - S_0)_\pm = \exp(-i\Omega_\pm S\eta)|S_0 - S_0) \cong |S_0 - S_0) - \Omega_\pm(S_0/2)^{1/2}|S_0 - S_0 + 1) \quad (4.16)$$

To first order in U_0, from Fig. 1,

$$\Omega_+ = -\Omega_- = (U_0/2\beta H)\sin\theta \quad (4.17)$$

To order $U_0/2\beta H$ we have

$$(S_0 - S_0|_+ Q_i|SM_s)(S_0 - S_0|_- Q_j|SM_s)^* = (S_0 - S_0|Q_i|SM_s)(S_0 - S_0|Q_j|SM_s) + +(S_0/2)^{1/2}(U_0/2\beta H)\sin\theta(S_0 - S_0|Q_i|SM_s)(S_0 - S_0 + 1|Q_j|SM_s) - -(S_0 - S_0 + 1|Q_i|SM_s)(S_0 - S_0|Q_j|SM_s)] \quad (4.19)$$

Equation (4.19) may be substituted in equation (4.15) and the result simplified by noting which matrix elements of Q_i vanish. By means of algebraic manipulation and the vector cross-product relation

$$\sin\theta(\alpha_{x\eta}, \alpha_{y\eta}, \alpha_{z\eta}) = (\alpha_x, \alpha_y, \alpha_z)\times\frac{1}{\sqrt{3}}(1,1,1) \quad (4.20)$$

$\mathscr{R}_e\mathscr{U}_{+-}$ may be reduced to the form

$$\mathscr{R}_e\mathscr{U}_{+-} = B(\alpha_x + \alpha_y + \alpha_z)\times \times(2\alpha_z - \alpha_x - \alpha_y) + B'(3\alpha_z^2 - 1) \quad (4.21)$$

VOL. 15 1960

where

$$B = \sum_{nSM_s} \{(C_{S,M_s} - C'_S\delta_{M_s,-S_0}) \sum_{l=1,2} (-1)^l [U(0S_03, nSl)]^2 / E'_{nSM_sl} + (C_{S,M_s} + \tfrac{1}{2}C'_S\delta_{M_s,-S_0}) \times$$
$$\times U'(0S_03, nS3) U(0S_03, nS3) / 3^{1/2} E'_{nSM_s3}\} \tag{4.22}$$

$$B' = \tfrac{1}{2} \sum_{nSM_s} (-C_{S,M_s} + C'_S\delta_{M_s,-S_0}) \sum_{l=1,2} (-1)^l [U(0S_03, nSl)]^2 / E'_{nSM_sl} \tag{4.23}$$

and where

$$C_{S,M_s} = (S_0 - S_0|Q_\xi|SM_s)^2 - \tfrac{1}{4}(S_0 - S_0|Q_+|SM_s)^2 - \tfrac{1}{4}(S_0 - S_0|Q_-|SM_s)^2,$$
$$C'_s = U_0(S_0/2)^{1/2}(2\beta H)^{-1}[(S_0 - S_0|Q_-|S - S_0 + 1)(S_0 - S_0 + 1|Q_\xi|S - S_0 + 1) +$$
$$+ (S_0 - S_0|Q_\xi|S - S_0)(S_0 - S_0 + 1|Q_+|S - S_0)].$$

Terms of order $\mathscr{H}_s^3 / E'^2_{nSM_sl}$ and higher appearing in C'_s have been neglected.

Matrix elements $d\mathscr{U}_{++}$ and $d\mathscr{U}_{--}$

To obtain the quantities dA and dB we calculate the second order contribution $d\overset{(2)}{\mathscr{U}}{}^{(++)}_{(--)}$ to $d\mathscr{U}^{(++)}_{(--)}$ arising from the first order in $\mathscr{H}_s$ and the first order in dV.

$$d\overset{(2)}{\mathscr{U}}{}^{(++)}_{(--)} = -\sum_{nSM_slm} [(\pm|\mathscr{H}_s|nSM_slm)(\pm|d\mathscr{V}|nSM_slm)^* + c.c.] / E_{nSM_sl} \tag{4.24}$$

where *c.c.* means complex conjugate of the preceding term and where the summation is over all states except $nSl = 0S_03$. Substitution of equation (4.13) in equation (4.24) yields

$$d\overset{(2)}{\mathscr{U}}{}^{(++)}_{(--)} = -\sum_{nSM_slmri} [(0S_0 \pm |U_r|nSlm)\alpha_{ri}(S_0 - S_0|_\pm \quad \overset{\dagger}{Q}_i|SM_s) \times$$
$$\times (0S_0 \pm |d\mathscr{V}|nSlm)^*(S_0 - S_0|_\pm|SM_s)^* + c.c.] / E'_{nSM_sl} \tag{4.25}$$

Substitution of equations (4.16) and (4.17) yields to first order in $U_0\beta H$

$$d\overset{(2)}{\mathscr{U}}{}^{(++)}_{(--)} = S_0 \sum_{nlmr} (0S_0 \pm |U_r|nS_0lm) \times$$
$$\times (0S_0 \pm |d\mathscr{V}|nS_0lm)^* \times$$
$$\times [\alpha_r \pm (U_0/2\beta H)\sin\theta\alpha_{r\xi}] / E'_{nS_0 - S_0l} + c.c. \tag{4.26}$$

Application of the vector relation

$$\sin\theta(\alpha_{x\xi}, \alpha_{y\xi}, \alpha_{z\xi}) = [(\alpha_x, \alpha_y, \alpha_z) \times 3^{-1/2}(1,1,1)] \times (\alpha_x, \alpha_y, \alpha_z) \tag{4.27}$$

and of Tables 3 and 4 yields the result

$$\partial\overset{(2)}{\mathscr{U}}{}^{(++)}_{(--)} / \partial A_{zz} = \pm A_e(2\alpha_z - \alpha_x - \alpha_y) \pm$$
$$\pm A'_e(\alpha_x + \alpha_y + \alpha_z) - \epsilon A_e(\alpha_x + \alpha_y + \alpha_z) \times$$
$$\times (2\alpha_z - \alpha_x - \alpha_y) + \epsilon A'_e \times$$
$$\times [3 - (\alpha_x + \alpha_y + \alpha_z)^2] \tag{4.28}$$

where

$$\epsilon = U_0/2{\cdot}3^{1/2}\beta H, \tag{4.29}$$

$$A_e = S_0 \sum_{nl} U(0S_03, nS_0l) \times$$
$$\times V_e(0S_03, nl) / E'_{nS_0 - S_0l}, \tag{4.30}$$

$$A'_e = 2{\cdot}3^{-1/2}S_0 \sum_n U'(0S_03, nS_03) \times$$
$$\times V'_e(0S_03, n3) / E'_{nS_0 - S_0l} \tag{4.31}$$

We have, finally, from equations (3.7), (4.3), (4.4) and (4.28)

$$\frac{\partial\mathscr{A}}{\partial A_{zz}} = V'_s - \epsilon A_e(\alpha_x + \alpha_y + \alpha_z)(2\alpha_z - \alpha_x - \alpha_y) +$$
$$+ \epsilon A'_e[3 - (\alpha_x + \alpha_y + \alpha_z)^2] \tag{4.32}$$

$$\frac{\partial \mathscr{B}}{\partial A_{zz}} = A_e(2\alpha_z-\alpha_x-\alpha_y)+A'_e(\alpha_x+\alpha_y+\alpha_z) \quad (4.33)$$

Magnetostriction

To the order of our approximation we have from equations (4.4) and (3.5)

$$\mathscr{B} = -3^{-1/2}U_0S_0(\alpha_x+\alpha_y+\alpha_z) \quad (4.34)$$

Substituting equations (4.21), (4.32), (4.33) and (4.34) in equation (4.7) we find for the magnetoelastic stress per atom having [111] for its axis of trigonal symmetry:

$$f_{zz}(\alpha_x\alpha_y\alpha_z) = V'_e+G_e[3-(\alpha_x+\alpha_y+\alpha_z)^2]-K_e(2\alpha_z-\alpha_x-\alpha_y)(\alpha_x+\alpha_y+\alpha_z)+ +[A'_e(\alpha_x+\alpha_y+\alpha_z)+D_e(z\alpha_z-\alpha_x-\alpha_y)-F_e(3\alpha_z^2-1)/(\alpha_x+\alpha_y+\alpha_z)]\times \times\tanh[U_0S_03^{-1/2}k^{-1}T^{-1}(\alpha_x+\alpha_y+\alpha_z)] \quad (4.35)$$

where

$$G_e = U_0A'_e/(2\cdot3^{1/2}\beta H) \quad (4.36)$$

$$K_e = \tfrac{1}{4}U_0A_e/(2\cdot3^{1/2}\beta H) \quad (4.37)$$

$$D_e = A_e-3^{1/2}V_eB/U_0S_0 \quad (4.38)$$

$$F_e = 3^{1/2}V_eB'/U_0S_0 \quad (4.39)$$

From the fact that V_{xy} has the same symmetry as V_{zz}, it follows that f_{xy} has precisely the same form as equation (4.35) except that the subscript e appearing in equations (4.30), (4.31) and (4.35)–(4.39) is replaced by s.

The magnetostrictive stress of an atom with some other orientation of its trigonal axis is obtained from equation (4.35) by transforming co-ordinates. If N_k (k = 111, $\bar{1}11$, $1\bar{1}1$, $11\bar{1}$) is the number of atoms per unit volume, the total magnetostrictive stress $\mathscr{F}_{ij} = \partial\mathscr{F}/\partial A_{ij}$($\mathscr{F}$ = free energy per unit volume) is given by formulas of the sort

$$\mathscr{F}_{zz}(\alpha_x\alpha_y\alpha_z) = N_{111}f_{zz}(\alpha_x\alpha_y\alpha_z)+N_{\bar{1}11}f_{zz}(\bar{\alpha}_x\alpha_y\alpha_z)+ +N_{1\bar{1}1}f_{zz}(\alpha_x\bar{\alpha}_y\alpha_z)+N_{11\bar{1}}f_{zz}(\alpha_x\alpha_y\bar{\alpha}_z) \quad (4.40)$$

and

$$\mathscr{F}_{xy}(\alpha_x\alpha_y\alpha_z) = N_{111}f_{xy}(\alpha_x\alpha_y\alpha_z)-N_{\bar{1}11}f_{xy}\times \times(\bar{\alpha}_x\alpha_y\alpha_z)-N_{1\bar{1}1}f_{xy}(\alpha_x\bar{\alpha}_y\alpha_z)+N_{11\bar{1}}f_{xy}\times \times(\alpha_x\alpha_y\bar{\alpha}_z) \quad (4.41)$$

We will now obtain the magnetostrictive strain. If we neglect the magnetoelastic coefficients describing the morphic effect of Section 3, the elastic energy of a cubic crystal is[11]

$$\mathscr{W} = \tfrac{1}{2}C_{11}(A_{xx}^2+A_{yy}^2+A_{zz}^2)+ +C_{12}(A_{yy}A_{zz}+A_{zz}A_{xx}+A_{xx}A_{yy})+ +2C_{44}(A_{yz}^2+A_{zx}^2+A_{xy}^2) \quad (4.42)$$

To find the equilibrium strain, minimize the quantity $\mathscr{F}+\mathscr{W}$. Dilation is given by

$$\Delta = A_{xx}+A_{yy}+A_{zz} = -(C_{11}+2C_{12})^{-1}(\mathscr{F}_{xx}+\mathscr{F}_{yy}+\mathscr{F}_{zz}) \quad (4.43)$$

By performing reflection operations which leave [111] invariant we find the relations

$$f_{xx}(\alpha_x\alpha_y\alpha_z) = f_{zz}(\alpha_z\alpha_y\alpha_x) \quad (4.44)$$

and

$$f_{yy}(\alpha_x\alpha_y\alpha_z) = f_{zz}(\alpha_x\alpha_z\alpha_y) \quad (4.45)$$

which facilitate the calculation of $\mathscr{F}_{xx}$ and $\mathscr{F}_{yy}$ in terms of the function f_{zz}. If the N atoms per unit volume are distributed equally, then $N_i = \frac{1}{4}N$ and the dilation is

$$\Delta = -N(C_{11}+2C_{12})^{-1}\{3V'_e+6G_e+ +q(\alpha_x\alpha_y\alpha_z)+q(\bar{\alpha}_x\alpha_y\alpha_z)+q(\alpha_x\bar{\alpha}_y\alpha_z)+ +q(\alpha_x\alpha_y\bar{\alpha}_z)\} \quad (4.46)$$

where

$$q(\alpha_x\alpha_y\alpha_z) = \tfrac{3}{4}A'_e(\alpha_x+\alpha_y+\alpha_z)\times \times\tanh[U_0S_0(3^{1/2}kT)^{-1}(\alpha_x+\alpha_y+\alpha_z)] \quad (4.47)$$

The term in V'_e does not depend on orientation.

The remaining terms depend on orientation and describe volume magnetostriction. The magnetostrictive "pressure" giving rise to this effect originates from the dependence of the spin-orbit parameter of the ground state multiplet on dilation. For extensions we have

$$A_{zz} = -(C_{11}-C_{12})^{-1}[\mathscr{F}_{zz}+C_{12}\Delta] \quad (4.48)$$

For shear magnetostriction,

$$A_{xy} = -\mathscr{F}_{xy}/4C_{44} \quad (4.49)$$

The magnetostrictive strain embodied in equations (4.48), (4.49), (4.35), (4.40), (4.41) and (4.46) may be compared to the phenomenological power series in α_r, of which the leading terms are, in the two-constant form,[1]

$$A_{zz} = \text{const.}+\tfrac{3}{2}\lambda_{100}\alpha_z^2+\ldots \quad (4.50)$$

$$A_{xy} = \tfrac{3}{2}\lambda_{111}\alpha_x\alpha_y+\ldots \quad (4.51)$$

To describe shear magnetostriction we define

$$\lambda_\varepsilon = (1/3)[A(011,011)-A(011,01\bar{1})] = (4/3)A_{xy}(110) \quad (4.55)$$

and

$$\lambda'_\varepsilon = (3/8)[A(111,111)-A(111,11\bar{1})] = zA_{xy}(111) \quad (4.56)$$

The quantities λ_ε and λ'_ε reduce to λ_{100} when the strain obeys the two-constant law, as it does in the present case at high temperatures. The quantities λ_ε and λ'_ε reduce to λ_{111} under the same condition. The quantities λ_ε and λ_ε may conveniently be measured with strain gauge and saturating field lying in the (100)-plane. Similarly, λ'_ε and λ'_ε may be measured in the $(1\bar{1}0)$-plane.

Substitution of equations (4.48), (4.49), (4.35), (4.40), (4.41) and (4.46) into these expressions yields the equations

$$\lambda_\varepsilon = 2N(C_{11}-C_{12})^{-1}\{K_\varepsilon+(F_\varepsilon-D_\varepsilon)\tanh(U_0S_0/3^{1/2}kT)\}, \quad (4.57)$$

$$\lambda_\varepsilon = -(N/6C_{44})\{-2G_\varepsilon+2K_\varepsilon+2^{1/2}[A'_\varepsilon-D_\varepsilon+\tfrac{1}{2}F_\varepsilon]\tanh(2^{1/2}U_0S_0/3^{1/2}kT)-F_\varepsilon U_0S_0/3^{1/2}kT\}. \quad (4.58)$$

$$\lambda'_\varepsilon = [N/3(C_{12}-C_{11})]\{-6K_\varepsilon+4(D_\varepsilon-F_\varepsilon)\tanh(U_0S_0/3^{1/2}kT)+2^{1/2}(D_\varepsilon-\tfrac{1}{2}F_\varepsilon)\tanh[2^{1/2}U_0S_0/3^{1/2}kT]- -U_0S_0F_\varepsilon/3^{1/2}kT\}-[2NA'_\varepsilon/3(C_{11}+2C_{12})][\tanh(U_0S_0/3^{1/2}kT)-2^{-1/2}\tanh(2^{1/2}U_0S_0/3^{1/2}kT)] \quad (4.59)$$

$$\lambda'_\varepsilon = (N/2C_{44})\{\tfrac{2}{3}(G_\varepsilon-K_\varepsilon)-(3^{1/2}/4)A'_\varepsilon\tanh(U_0S_0/kT)+3^{-1/2}(A'_\varepsilon/4+2D_\varepsilon)\tanh(U_0S_0/3kT)\} \quad (4.60)$$

An expansion of the function (4.35) in powers of α_r results in strains having the phenomenological form but it does not converge for small T.

When comparing our results with experiment it is useful to define special quantities to describe magnetostriction. For extension-strains these quantities are

$$\lambda_\varepsilon = (2/3)[A_{zz}(001)-A_{zz}(010)] \quad (4.52)$$

and

$$\lambda'_\varepsilon = (2/3)[A_{zz}(001)-A_{zz}(110)] \quad (4.53)$$

Let $A(\boldsymbol{\beta},\boldsymbol{\alpha})$ be the extension-strain in the direction $\boldsymbol{\beta}$ when M is parallel to $\boldsymbol{\alpha}$. It is given by

$$A(\boldsymbol{\beta},\boldsymbol{\alpha}) = \sum_{ij} A_{ij}(\boldsymbol{\alpha})\beta_i\beta_j \quad (4.54)$$

The T^{-1} terms appearing in some of these equations arise when the limit $(\alpha_x+\alpha_y+\alpha_z)\to 0$ is taken in equation (4.35). The calculation fails at $T=0$ because the quantity $\mathscr{W}_{+-}$ was neglected in the term $[\mathscr{B}^2+|\mathscr{W}_{+-}|^2]^{1/2}$ which appears in equation (4.6). For $\alpha_x+\alpha_y+\alpha_z=0$, $\mathscr{B}$ vanishes and this neglect is not proper. Owing to this fact, the results apply only to temperatures greater than $|\mathscr{W}_{+-}|/k$. From our discussion of cobalt substitutions in Fe_3O_4 one can show that this condition is $T\gtrsim 20°K$.

5. APPLICATION TO COBALT-IRON FERRITE

We may apply our formulas for magnetostriction and morphic effect to Co^{2+} ions in the mixed spinel ferrite $Co_xFe_{3-x}O_4$. Here Co^{2+} occupies octahedral

sites which have trigonal symmetry.[8] For basic states in the trigonal field we use the eigenstates of the crystal field Hamiltonian for cubic symmetry. This approximation is justified if the splitting of energy levels due to the trigonal field is much smaller than that due to the cubic field. Estimates of cubic splitting are available in the literature. The trigonal splitting of the ground state will be inferred from experimental data to show the consistency of the approximation.

The energy levels of Co^{2+} in a cubic field have been given by several authors. A very complete calculation by Low[14] gives the energy of seventeen levels arising from the configuration $3d^7$. The ground state is an effective P-state ($^4\Gamma_4$). Let the real, normalized, ground orbital states be ϕ_r ($r = x, y, z$); the subscripts indicate that these wave functions transform like x, y and z under proper rotations of the cubic group. Their parity under inversion is even rather than odd as for x, y and z. The trigonal field splits this level into a doublet ($r = 3$) and a singlet ($l = 2$). Basic states for the representations given in Table 2 are

$$\psi_+ = 3^{-1/2}(\omega\phi_x + \omega^*\phi_y + \phi_z)$$
$$\psi_- = -3^{-1/2}(\omega^*\phi_x + \omega\phi_y + \phi_z)$$
$$\psi_2 = 3^{-1/2}(\phi_x + \phi_y + \phi_z) \qquad (5.1)$$

where $\psi_\pm$ belong to the ground level and ψ_2 to the first excited level for a small trigonal field of appropriate sign.

We may now relate the spin–orbit coefficients of Table 3 connecting these two levels. Since U is imaginary and Hermitian we have

$$(\phi_y|U_z|\phi_x) = -(\phi_x|U_z|\phi_y) \qquad (5.2)$$

By applying symmetry operations of the cube to $(\phi_r|U_z|\phi_{r'})$ we find that all elements except those appearing in equation (5.2) vanish. From Table 3 we have

$$U_0 \equiv U'(0S_03, 0S_03) = 3^{1/2}(\psi_+|U_z|\psi_+) \qquad (5.3)$$

and

$$U(0S_03, 0S_02) = (\psi_+|U_z|\psi_2) \qquad (5.4)$$

Substituting equations (5.1) and (5.2) in (5.3) and (5.4) we find

$$U(0S_03, 0S_02) = -3^{-1/2}U_0 \qquad (5.5)$$

Applying a similar procedure to the crystal-field coefficients in Table 4 we find

$$V_e(0S_03, 02) = -V_e(0S_03, 03) = -V_e \qquad (5.6)$$

and

$$V_s(0S_03, 02) = \tfrac{1}{2}V_s(0S_03, 03) = \tfrac{1}{2}V_s \qquad (5.7)$$

The parameters V_e and V_s are related to parameters b_1 and b_2 appearing in the magnetoelastic Hamiltonian (corresponding to our $\mathcal{V}$) of Kanamori[2] given by

$$\mathcal{H}_{ME} = b_1[A_{xx}l_x^2 + A_{yy}l_y^2 + A_{zz}l_z^2 - (2/3)\times$$
$$\times(A_{xx}+A_{yy}+A_{zz})] + b_2[A_{xy}(l_xl_y+l_yl_x)+$$
$$+A_{yz}(l_yl_z+l_zl_y)+A_{zx}(l_zl_x+l_xl_z)] \qquad (5.8)$$

where l_x, l_y and l_z are components of pseudo-momentum in the effective P-state. One can readily show that

$$V_e = (1/3)b_1,\ V_s = (2/3)b_2 \qquad (5.9)$$

In his theory of CoO, Kanamori[2] estimated directly

$$b_1 = 1{\cdot}95\times10^4\ \text{cm}^{-1} \qquad (5.10)$$
$$b_2 = 1{\cdot}0\times10^3\ \text{cm}^{-1} \qquad (5.11)$$

Comparing his theory with measurements of tetragonal distortion in CoO he finds that the value

$$b_1 = 1{\cdot}2\times10^4\ \text{cm}^{-1} \qquad (5.12)$$

would produce agreement. We shall adopt this value instead of (5.10).

Other numerical values needed are $S_0 = 3/2$ and $N = 1{\cdot}35\times10^{22}\text{cm}^{-3}$, where x is the composition variable appearing in $Co_xFe_{3-x}O_4$. From earlier work we have the empirical values $U_0 = 132\ \text{cm}^{-1}$ and $\beta H = 320\ \text{cm}^{-1}$. For mineral specimens of Fe_3O_4 Doraiswami finds the average elastic constants $C_{11} = 2{\cdot}73\times10^{12}$, $C_{12} = 1{\cdot}06\times10^{12}$, $C_{44} = 0{\cdot}97\times10^{12}$ in dyne/cm^2.

Our effective-P approximation takes into account a single excited state ψ_2. Applying equations (5.5), (5.6) and (5.7) to the results of the previous section, one finds for the parameters of the magnetostriction formulas

$$G_e = 0, \quad K_e = S_0U_0^2V_e/6\beta HE_t, \quad A_e' = 0$$
$$D_e = \{[2(1+2\beta H/E_t)]^{-1} - (S_0-\tfrac{1}{2})U_0/\beta H\}\times$$
$$\times U_0V_e/3^{1/2}E_t$$

$$F_\varepsilon = -3^{1/2}\{S_0+(S_0-\tfrac{1}{2})U_0/\beta H- -[2(1+2\beta H/E_t)]^{-1}\}U_0V_\varepsilon/2E_t \quad (5.13)$$

in the case of extensions, and

$$G_s = 0, \quad K_s = -S_0U_0^2V_s/12\beta HE_t, \quad A_s' = 0$$

$$D_s = -\{\tfrac{3}{2}S_0+(S_0-\tfrac{1}{2})U_0/\beta H- -[2(1+2\beta H/E_t)]^{-1}\}U_0V_s/3^{1/2}E_t$$

$$F_s = -3^{-1/2}\{S_0+(S_0-\tfrac{1}{2})U_0/\beta H- -[2(1+2\beta H/E_t)]^{-1}\}U_0V_s/2E_t \quad (5.14)$$

in the case of shears. Here E_t is the energy difference between ψ_2 and $\psi_\pm$, and the exchange field for ψ_2 and $\psi_\pm$ is assumed to have the same value H.

This calculation is best compared with experiments on only small concentrations of cobalt because cobalt ions which are nearest neighbors may interact strongly to disturb the symmetry of the crystal field.[4] Magnetostriction of synthetic crystals of $Co_xFe_{3-x}O_4$ with small values of x has been measured in the interval $148<T<273$°K by the strain gauge technique.[15] Part of this magnetostriction is due to iron and part is due to cobalt. TSUYA's calculations[3] indicate that the magnetostrictive effect of S-state ions is much smaller than that of ions not in S-states. Since the Fe^{3+} ion occupies an S-state, we neglect it and write

$$\lambda_\varepsilon'(Co_x^{2+}) = \lambda_\varepsilon'(Co_xFe_{3-x}O_4)- -(1-x)\lambda_\varepsilon'(Fe_3O_4) \quad (5.15)$$

for the part of the magnetostriction attributable to x cobalt ions per molecule of ferrite. The dashed curve in Fig. 2 shows the experimental results for $\lambda_\varepsilon'(Co_{0.04}^{2+})$ from measurements on $Co_{0.04}Fe_{2.96}O_4$ and Fe_3O_4 taken in a (110)-plane.[15] At room temperature SPAIN finds

$$\lambda_\varepsilon'(Fe_3O_4) = -11\times10^{-6}$$

and

$$\lambda_\varepsilon'(Co_{0.04}Fe_{2.96}O_4) = -39\times10^{-6};$$

BOZORTH *et al*[16] find

$$\lambda_{100}(Co_{0.8}Fe_{2.2}O_4) = -590\times10^{-6}.$$

Approximating λ_{100} by λ_ε', we may compare the ratios

$$\lambda_\varepsilon'(Co_{0.8}^{2+})/0{\cdot}8 = -7{\cdot}4\times10^{-4},$$
$$\lambda_\varepsilon'(Co_{0.04}^{2+})/0{\cdot}04 = -7{\cdot}0\times10^{-4} \quad (5.16)$$

to see that the measurements are reasonably consistent in spite of probable pair-interactions for large x. The ratios (5.16) were entered in Table 1.

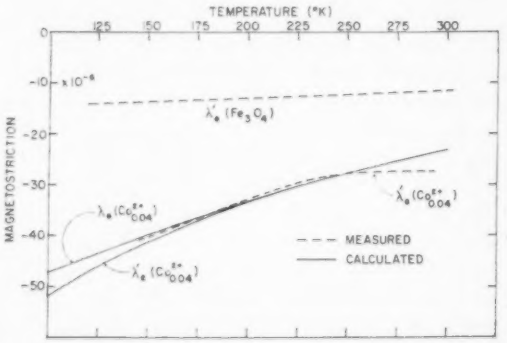

FIG. 2. Temperature dependence of magnetostriction, illustrating the effect of Co^{2+} in $Co_{0.04}Fe_{2.96}O_4$. The quantities λ_ε and λ_ε', defined by equations (4.52) and (4.53), involve only diagonal components of the strain-tensor and correspond approximately to the conventional λ_{100}. The measurements are due to R. SPAIN (private communication).

These results are also consistent with those for

$$Co_{0.3}Zn_{0.2}Fe_{2.2}O_4(\lambda_{100} = -2{\cdot}1\times10^{-4})$$

and

$$Co_{0.3}Mn_{0.4}Fe_2O_4(\lambda_{100} = -2{\cdot}0\times10^{-4})^{[16]}$$

We have given above estimates of all the constants required to calculate $\lambda_\varepsilon'(Co_x^{2+})$ from equations (4.59) and (5.13) except E_t. The value $E_t = 1{\cdot}6\times10^3$ cm^{-1} produces the fit shown in Fig. 2. (The expression for λ_ε' and the numerical value for E_t given here differ slightly from our previous results[4] because of improved approximations. To illustrate the difference between calculated λ_ε and λ_ε', λ_ε (equation 4.57) is also shown in Fig. 2.

An estimate of cubic splitting may be obtained from the work of LOW[14] on Co^{2+} in MgO. Optical absorption of this crystal shows a first excited state, Γ_5, 8470 cm^{-1} above the ground state, Γ_4. Since the oxygen-to-cation distances in MgO

(2·10 Å)[17] and Fe_3O_4 (2·06 Å)[18] are similar this is a good estimate of the cubic splitting of Co^{2+} in cobalt–iron ferrite. Since this is considerably greater than the trigonal splitting of 1600 cm^{-1} the effective-P approximation is reasonably consistent. However, this consistency may be fortuitous because the large number of highly excited levels may produce an effect which is similar to that of one low-lying state ψ_2.

In Fig. 3 are shown the theoretical curves of λ_s/xV_s and λ_s'/xV_s using equation (4.58), equation (4·59), and the numerical values mentioned above.

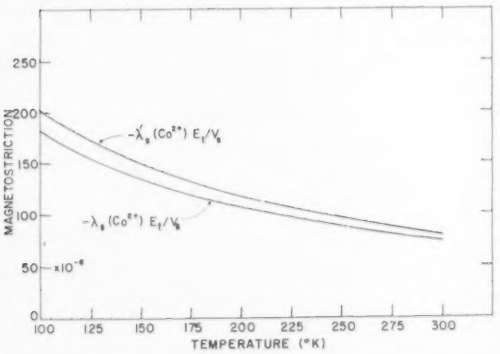

FIG. 3. Calculated temperature dependence of magnetostriction arising from the presence of Co^{2+} in $Co_xFe_{3-x}O_4$, normalized to $x = 1$. The quantities λ_s and λ_s', defined by equations (4.55) and (4.56), involve only off-diagonal components of the strain-tensor and correspond approximately to the conventional λ_{111}. Here V_s is a matrix element of strain-dependent crystal field energy and E_t is the trigonal splitting of the ground state.

Preliminary measurements[15] of $\lambda_s(Co_x^{2+})$ disagree with the calculation. They are peaked rather than monotonic in temperature and are an order of magnitude larger than predicted from KANAMORI's estimate of b_2 (or V_s). The cause of these discrepancies is not understood. Approximating λ_{111} by λ_s' we find that the measured λ_{111} $(Co_{0.8}^{2+}) = 1{\cdot}0\times10^{-4}$ [16] is consistent with $V_s = -2500\ cm^{-1}$ which may be compared with KANAMORI's estimate $V_s = 700\ cm^{-1}$.

Our partial agreement with measurements on $Co_{0.8}Fe_{2.2}O_4$ is surprising in view of other evidence[4] for the inadequacy of the trigonal-field approximation at high cobalt concentrations. When TSUYA assumes that the doublet is split by a field of lower symmetry, his calculation does not reproduce the signs or the orders of magnitude of λ_{100} or λ_{111} for $Co_{0.8}Fe_{2.2}O_4$. He does find agreement in sign and order of magnitude by assuming that the singlet ψ_2 is lowest. However, it seems implausible that the sign of the trigonal splitting should depend on cobalt concentration because the distribution of cation charges among octahedral and tetrahedral sites does not change and the lattice parameters change imperceptibly.[19]

According to equations (4.46), (4.47) and (5.13) the volume magnetostriction Δ vanishes in the effective-P approximation. Volume magnetostriction is caused by the dependence of cubic anisotropy energy on volume. The change in the crystal field caused by a change in volume without change in shape is trigonal and therefore it connects the ground level only to other levels with $l = 3$ and $S = S_0$. Therefore, the change in cubic anisotropy appears only as a result of the change in the ground state spin–orbit constant U_0 due to admixture of these excited states. Since they lie higher than ψ_2 one expects Δ to be smaller than volume-conserving forms of magnetostriction.

It has been suggested that the morphic effect might be appreciable in ferrites which contain cobalt because of the decrease in crystal symmetry caused by magnetostriction.[1] We explained in Section 3 that this reasoning does not apply literally to the present case. However, we will now show that the morphic effect should in fact be appreciable in cobalt–iron ferrite. If C_i' represents the "magnetic" part of the elastic coefficient, then from equations (3.21)

$$C_{11}' = 2k_{11}, \quad C_{12}' = -k_{11}. \tag{5.12}$$

Letting $N_i = N/4$ and neglecting quantities of order $(U_0/\beta H)^2$, we have from Section 3, for special orientations of $\boldsymbol{M}$,

$$\begin{aligned}
k_{11}(100) &= -(3^{1/2}NV_e^2/2S_0U_0)\tanh(S_0U_0/3^{1/2}kT)\\
k_{11}(110) &= -(NV_e^2/4)\times\\
&\quad\times[(3^{1/2}/2^{1/2}S_0U_0)\tanh(2^{1/2}S_0U_0/3^{1/2}kT)+\\
&\quad\quad+(kT)^{-1}]\\
k_{11}(111) &= -(NV_e^2/8S_0U_0)\times\\
&\quad\times[\tanh(S_0U_0/kT)+9\tanh(S_0U_0/3kT)]
\end{aligned} \tag{5.13}$$

The temperature curves of k_{11} given in Fig. 4 were obtained using the numerical values given earlier. At $T = 150°K$ the "anisotropy" (variation of C_{11} and C_{12} with orientation of M) is about $x\%$. The morphic effect is indeed small, especially since equations (5.13) may be accurate only for small x. However, the fact that our calculation is consistent with the magnetostriction (λ_{100}) of $Co_{0.8}Fe_{2.2}O_4$ suggests that our estimates of C_{11}' and C_{12}' may be of the correct order of magnitude

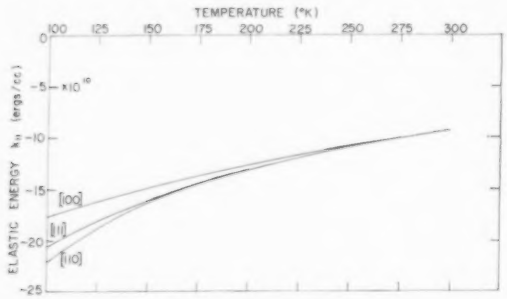

FIG. 4. Calculated temperature dependence of elastic energy arising from the presence of Co^{2+} in $Co_xFe_{3-x}O_4$, normalized to $x = 1$. Contributions to elastic coefficients are given by $C_{11}' = 2k_{11}$ and $C_{12}' = -k_{11}$, with k_{11} plotted for representative orientations of magnetization.

for large x as well. If this is the case then the morphic effect is larger than any values given for Ni (up to 0·3 per cent),[5, 6] the only substance which has been investigated.

The value of V_s estimated by KANAMORI, as well as that estimated from λ_{111} ($Co_{0.8}{}^{2+}$) is an order of magnitude smaller than V_e. From equations (3.21) and (3.22) we expect the non-cubic elastic coefficients to be at least an order of magnitude smaller than C_{11}' and C_{12}'.

It is possible that the differences between the elastic coefficients of $Co_{0.32}Z_{0.22}Fe_{2.2}O_4$($C_{11} = 2{\cdot}66$, $C_{12} = 1{\cdot}53$, $C_{44} = 0{\cdot}78$)[20] and of Fe_3O_4 (see above) may be due, in part, to this effect of Co^{2+}. The signs of the differences are borne out by our calculation. However, the relation (from equation 5.12) $C_{11}' = -2C_{12}'$ is not satisfied, which suggests that other effects are important as well.

Spin–orbit coupling is the only type of interaction between spin and orbital motion which we have taken into account. Since the magnetostriction calculated in this way is a second-order effect it is possible that some smaller energy term will produce a significant effect if it appears in a lower order of approximation. Such a term is dipolar spin–spin coupling which may be written in the form[21]

$$-\rho[(\boldsymbol{L}\cdot\boldsymbol{S})^2+\tfrac{1}{2}(\boldsymbol{L}\cdot\boldsymbol{S})-\tfrac{1}{3}LS(L+1)(S+1)]$$

for a given multiplet of a free ion. Since this makes a first order contribution to $\mathcal{H}_{+-}$ appearing in equation (4.6), it contributes terms of order $\rho V_e/U_0$ to the magnetoelastic energy. This is to be compared with the calculated terms of order U_0V_e/E_t. Analyses of spectra of transition elements indicate that ρ may be of the order of 1 cm^{-1}[21, 22]. Therefore, the correction to magnetostriction should be on the order of 10 per cent and may be worth investigating.

6. SUMMARY

We have calculated the influence of orbitally degenerate ions on the magnetostrictive strain and elastic energy of a ferrimagnetic crystal. The treatment was restricted to the case of a trigonal crystal field and a cubic structure. The general results for elastic energy, embodied in equations (3.21)–(3.23) show that (1) the resistance of the crystal to change in shape is decreased by the presence of the orbitally degenerate ion, (2) the elastic coefficients depend on the orientation of the magnetic moment (morphic effect), and (3) for a general orientation of the moment all of the elastic coefficients are non-vanishing and the crystal has no elastic symmetry.

The general results for magnetostriction, embodied in equations (4.48), (4.49), (4.40), (4.41), (4.46) and (4.35) show that (1) the magnetostrictive strain is large, being of first order in spin–orbit energy rather than second or higher order as in the case of a non-degenerate ion, and (2) the functional dependence of strain on orientation has a special form which is not readily expressed in the usual phenomenological terms because the expansion in powers of direction cosines of magnetization does not converge at sufficiently low temperatures. To facilitate comparison of theory with experiment, certain measurable quantities, somewhat analogous to the phenomenological λ_{100} and

λ_{111} were defined in equations (4.52)–(4.56). Theoretical formulas for these quantities are given in equations (4.57)–(4.59).

In order to make numerical predictions from the general formulas, it is necessary to make explicit assumptions concerning wave functions and energy levels. In Section 5 we considered the case of cobalt substitutions in Fe_3O_4, using a simple "effective-P" approximation which employs eigenfunctions of a cubic rather than trigonal crystal field Hamiltonian. The perturbing effect of only the lowest of several excited orbital levels was considered.

Our results for the magnetostrictive effect of cobalt substitutions were found to be in partial agreement with experimental data for cobalt–iron ferrite. The calculated extension-strain is fairly consistent with experiment over a range of temperatures. The calculated shear-strain, however, has the wrong sign, seems too small and has a temperature dependence which is qualitatively different from that given by experiment. Perhaps more excited states must be taken into account to obtain satisfactory agreement.

We have estimated that the effect of cobalt substitutions on the elastic coefficients of a ferrite should amount to about a 10 per cent change per mole of cobalt. The existing data on elastic coefficients of Fe_3O_4 and $Co_{0.32}Zn_{0.22}Fe_{2.2}O_4$ tend to support this prediction. Also, the predicted variation of elastic coefficients with orientation of moment is of the order of 1 per cent per mole of cobalt. Experimental data bearing on this effect are not available.

VOL. 15 1960

REFERENCES

1. For a review of magnetoelastic effects see LEE E. W., *Reports on the Progress of Physics* **18**, 184–229 (1955).
2. KANAMORI J., *Progr. Theor. Phys., Osaka* **17**, 177, 197 (1957).
3. TSUYA N., *Sci. Rep. RITU, (Japan)* B. **8**, 161 (1957).
4. SLONCZEWSKI J. C., *J. Appl. Phys.* **29**, 448 (1958); *Phys. Rev.* **110**, 1341 (1958). A preliminary report of the present work appears in *J. Appl. Phys.*, Suppl. to Vol. **30**, No. 4, p. 310S (April, 1959).
5. MASON W. P., *Phys. Rev.* **82**, 715 (1951).
6. ALERS G. A., NEIGHBOURS J. R. and SATO H., *J. Phys. Chem. Solids* **9**, 21 (1959).
7. ROOKSBY H. P. and TOMBS N. C., *Nature, Lond.* **167**, 364 (1950); GREENWALD S. *Acta Cryst., Camb.* **6**, 396 (1953).
8. The structure and magnetic properties of spinel ferrites are discussed by GORTER E. W., *Philips Res. Rep.* **9**, 295, 321, 403 (1954).
9. CONDON E. U. and SHORTLEY G. H., *The Theory of Atomic Spectra*, Chapter 3. Cambridge University Press, New York and London (1935).
10. EDMONDS A. R., *Angular Momentum in Quantum Mechanics*, Chapter 4. Princeton University Press (1957).
11. See, for example LOVE A. E. H., *Mathematical Theory of Elasticity* (4th Ed.), p. 160. Dover, New York (1944).
12. This agrees with a general comment of SATO H., *J. Appl. Phys.* **29**, 456 (1958).
13. LÖWDIN P-O., *J. Chem. Phys.* **19**, 1396 (1951).
14. LOW W., *Phys. Rev.* **109**, 256 (1958).
15. SPAIN R., private communication.
16. BOZORTH R. M., TILDEN E. F. and WILLIAMS A. J., *Phys. Rev.* **99**, 1788 (1955).
17. *International Critical Tables* Vol. I, p. 344. McGraw-Hill, New York and London (1933).
18. HAMILTON W. C., *Phys. Rev.* **110**, 1050 (1958).
19. For a tabulation of lattice parameters see VERWEY E. J. W. and HEILMANN E. L., *J. Chem. Phys.* **15**, 174 (1947).
20. MCSKIMIN H. J., WILLIAMS A. J. and BOZORTH R. M., *Phys. Rev.* **95**, 616 (1954).
21. PRYCE M. H. L., *Phys. Rev.* **80**, 1107 (1950).
22. TREES R. E., *Phys. Rev.* **82**, 683 (1951); ABRAGAM A. and PRYCE M. H., *Proc. Roy. Soc.* A**205**, 135 (1951).

LETTERS TO THE EDITOR

Further experimental evidence on majority carrier injection in CdS single crystals

(*Received* 23 *December* 1959; *revised* 25 *January* 1960)

INVESTIGATIONS of the d.c. characteristics of CdS single crystals have led SMITH and ROSE to the assumption that under certain conditions majority carriers can be injected into CdS crystals, resulting in space-charge-limited currents ("S.C.L.C.").[1,2] In accord with this assumption, the effects explained as S.C.L.C. occurred only if the electrodes were ohmic (indium or gallium contacts).[3] The theory developed on S.C.L.C.[2, 4] accounted well for the observed phenomena. ROSE[2] and his co-workers[5] pointed out that the investigation of S.C.L.C. could serve as a sensitive experimental tool for the study of imperfections in a pure crystal.

BÖER and KÜMMEL interpreted similar experimental results very differently.[6, 7, 8]. They agree with SMITH and ROSE only on the assumption that moderate fields cause an increase of the free carrier concentration in CdS crystals, but they attribute this phenomenon to field-release of electrons from defect states and pre-breakdown avalanches. BÖER and KÜMMEL also employed indium electrodes mostly. According to the theory of BÖER and KÜMMEL such electrodes should not be essential for the process of electron multiplication; ohmic electrodes merely ensure that the internally liberated electrons may leave the crystal. Ohmic electrodes thus facilitate convenient investigation of the phenomena.

In the course of one of the recent experiments[9] designed to prove their assumptions, BÖER and KÜMMEL applied four electrodes to a CdS single crystal. Two of the electrodes were not in actual contact with the crystal but were insulated by thin mica sheets. The other two electrodes were made of vacuum evaporated indium film. In their first experiment, the crystal was irradiated by 5400 Å light at liquid air temperature. After six minutes at liquid air temperature in the dark, the crystal was slowly warmed and the "conduction glow curve" recorded. For this measurement, a small direct potential (10 V) was applied to the indium electrodes. The second experiment was similarly performed, the only difference being that they applied during the "waiting period" an alternating potential difference (2 kV, 50 cycles) across the insulated electrodes. In this case the area under the "conduction glow curve" was smaller by a factor of about three than in the case when no high alternating field acted during the waiting period. BÖER and KÜMMEL infer from this that the high alternating field releases trapped electrons. Their experiment thus proves that the concentration of free carriers in a CdS crystal can be increased by a high field even if there is no possibility of majority carrier injection.

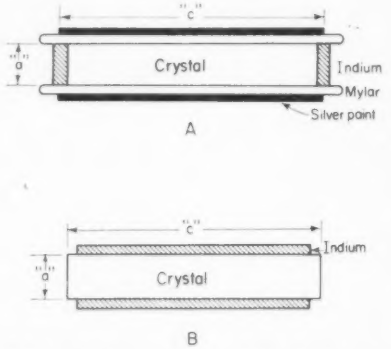

FIG. 1. Schematic diagram of the electrode arrangements. Not drawn to scale.

On the other hand, the experiments to be described in this letter show that the results of SMITH and ROSE can be explained only on the assumption of majority carrier injection and cannot be accounted for by bulk liberation of carriers.

We utilized a method previously used for the investigation of electroluminescent ZnS crystals.[10] A thin rectangular CdS crystal (dimensions: $a = 0{\cdot}05$ mm, $b = 0{\cdot}2$ mm, $c = 1{\cdot}5$ mm) was selected. On the faces perpendicular to "c", indium electrodes were soldered. Mylar insulators (thickness: 0·01 mm) were placed on the two faces perpendicular to "a". The insulators were covered with silver paint on their backs (Fig. 1A). The dimensions of the condenser plates thus formed were larger than those of the corresponding crystal face. Flat phosphor bronze springs pressed

the mylar sheets to the crystal and served as leads to the silvered backs of the insulators.

We applied 15 volts d.c. between the indium electrodes and measured the current with an electrometer amplifier. The dark resistance of the crystal was of the order of $10^{13}\Omega$. The crystal was highly photosensitive; exposure to room light decreased its resistance by a factor of about 10^6. While keeping the crystal in the dark, alternating voltages up to 200 V r.m.s. (600 cycles) were applied to the "insulated" electrodes from a balanced amplifier. The reading of the electrometer amplifier was not changed by the presence of the alternating voltage. (The amplifier did not record a.c.). With the experimental arrangement used, a change of 10 per cent in the direct component of the current could have been easily detected.

As the alternating voltage did not influence the crystal resistance, we inferred from this that at these voltages no substantial release from traps or pre-breakdown avalanches could have taken place.

The crystal was now tested for space-charge-limited currents. The soldered indium electrodes were removed. On the crystal faces perpendicular to "*a*" the mylar sheets were changed to indium electrodes (Fig. 1B). To these new indium electrodes alternating voltages up to 60 V r.m.s. (50 cycles) were applied. The a.c. characteristics of the crystal were displayed on an oscilloscope. The characteristics obtained were very similar to those recorded by SMITH and ROSE[1]. The changes in the characteristics with time, previous history, and infrared illumination also corresponded closely with SMITH and ROSE's observations. It should be emphasized that the average current in this experiment was about 10^{-7} A. Had the alternating field caused the appearance of a similar large average conductance in the previous experment (with blocking a.c. electrodes) as well, we ought to have discovered this easily by means of the d.c. test potential.

These experiments prove that in the field range where SMITH and ROSE's observations were made, the use of ohmic electrodes is a prerequisite for the creation of excess carrier concentration in the crystal and does not merely facilitate the detection of the excess concentration. This conclusion is in full accord with the S.C.L.C. theory, but seems to be incompatible with theories based on internal liberation of carriers.

Comparing our results with those of BÖER and KÜMMEL one concludes that different physical conditions caused the difference in the results. S.C.L.C. could be expected to be prominent in thin and approximately perfect crystals, equipped with ohmic electrodes. Release from defect levels and pre-breakdown avalanches should appear normally only at higher voltages. If the conditions during the crystal growth were such as to favour formation of internal barriers, the latter processes might appear at comparatively low voltages as well, because of the increase of the local fields in the barrier regions.

Acknowledgements—The author would like to express his thanks to Professor E. ALEXANDER and Dr. E. HARNIK for helpful discussions, and to Mr. G. LERMAN for technical assistance.

Department of Physics,
The Hebrew University,
Jerusalem,
Israel.

I. T. STEINBERGER

References

1. SMITH R. W. and ROSE A., *Phys. Rev.* **97,** 1531 (1955).
2. ROSE A., *Phys. Rev.* **97,** 1538 (1955).
3. SMITH R. W., *Phys. Rev.* **97,** 1525 (1955).
4. LAMPERT M. A., *Phys. Rev.* **103,** 1648 (1956).
5. LAMPERT M. A., ROSE A. and SMITH R. W., *J. Phys. Chem. Solids* **8,** 464 (1959).
6. BÖER K. W. and KÜMMEL U., *Z. Naturf.* **9a,** 177 (1954).
7. BÖER K. W. and KÜMMEL U., *Ann. Phys. Lpz.* **14,** 341 (1954).
8. BÖER K. W. and KÜMMEL U., *Ann. Phys. Lpz.* **20,** 303 (1957).
9. BÖER K. W. and KÜMMEL U., *Z. Naturf.* **13a,** 698 (1958).
10. STEINBERGER I. T., *Symposium on Solid State Physics, Brussels* 1958. Academic Press, London (1959).

Nuclear magnetic resonance in metallic potassium*

(*Received* 11 *January* 1960)

THE SHIFT of the NMR frequency in Li, Na, Rb,

* This work has been partly supported by the U.S. Atomic Energy Commission and the U.S. Office of Naval Research.

and Cs is known.[1, 2] We report here the observation of the NMR in metallic potassium (K^{39}) relative to the diamagnetic salt KCl. The result is $\Delta H/H = 0\ 261 \pm 0\ 002$ per cent.

This quantity may be expressed[1] in terms of the hyperfine coupling constant for the 4*s* electron in the atom, P_F/P_A, the ratio of probability densities of the wave function in the metal to that in the atom, and χ_p, the spin susceptibility of the conduction electrons. Since direct measurements[3] of χ_p are available only for Li and Na, we use the theoretical estimate, kindly provided by Professor BROOKS. This value, $\chi_p = 0{\cdot}875 \times 10^{-6}\text{gm}^{-1}$, is based on a Wigner–Seitz radius of 4·8 Bohr units, a modified electron mass of 1·02, and includes a correction which is the ratio of the directly measured value to the theoretical estimate in sodium. This is to be compared with $0{\cdot}70 \times 10^{-6}$, derived from recent measurements of the electronic specific heat by Phillips, and $0{\cdot}60 \times 10^{-6}$ for free electrons with an effective mass of unity.

We calculate from equation (16·1) of Ref. (1) a value $P_F/P_A = 0{\cdot}905$, which is to be compared with BROOKS' theoretical estimate of 0·82. It appears that the behavior of potassium is consistent with that of the other alkalis.[2]

The sample was prepared by exposing the metal to intense ultrasonic radiation. The resonance was observed at 2·58 Mc in an applied field of 13,000 oersteds. The line width was approximately 0·7 kc, and, with an integrating time constant of 1 sec, a signal-to-noise ratio of 50 was obtained.

The frequency shift was measured at 25°C relative to a saturated aqueous solution of KCl, to which no paramagnetic impurities had been added.

Acknowledgements—We wish to thank Professor H. BROOKS and Dr. N. E. PHILLIPS for supplying us with their unpublished results. The apparatus was a Varian V-4200 Nuclear Induction Spectrometer, for the use of which we wish to thank Dr. J. VIVO ACRIVOS.

Lawrence Radiation Laboratory, Livermore, California. M. P. KLEIN

Department of Physics, University of California, Berkeley. W. D. KNIGHT

References

1. KNIGHT W. D., *Solid State Physics* **2,** 93 (1956).
2. BENEDEK G. B. and KUSHIDA T., *J. Phys. Chem. Solids* **5,** 241 (1958).
3. SCHUMAKER R. T. and SLICHTER C. P., *Phys. Rev.* **101,** 58 (1956).

Phenomenology of impurity conduction in semiconductors*

(*Received* 11 *January* 1960; *revised* 19 *February* 1960)

IN THIS letter, the phenomenological behavior of semiconductors in the impurity-conduction region is discussed with reference to the available experimental literature on shallow impurity states in Ge, Si, InSb, SiC, CdS, and Mg_2Sn. The phenomenological relation

$$N_c = (2{\cdot}2a_H)^{-3} \exp -(\epsilon - 1)$$

is presented, where a_H is the hydrogenic Bohr

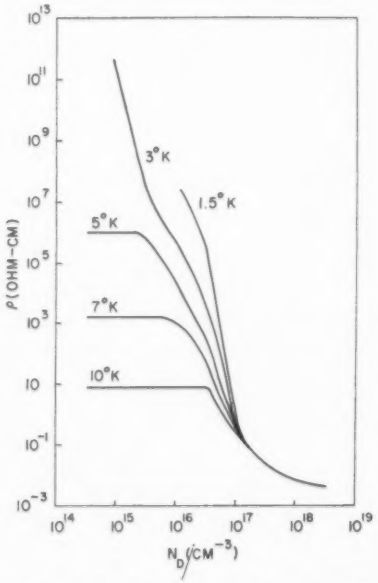

FIG. 1. Electrical resistivity as a function of donor concentration for *n*-type germanium at different temperatures; the compensation ratio is essentially the same for all samples.

* This research was sponsored by the Advanced Research Projects Agency under Bureau of Ships Contract NObs–77144.

radius. This expression relates ϵ, the static dielectric constant of the pure host material, to N_c, the critical impurity concentration above which temperature-independent impurity conduction is observed.

FRITZSCHE has extensively investigated antimony-doped germanium to determine its low-temperature electrical properties.[1, 2, 3] The characteristics which were found give a general picture

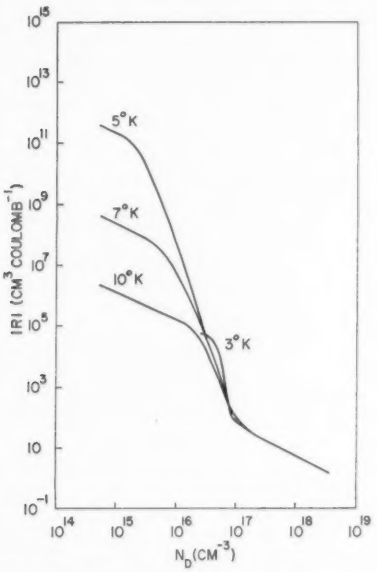

FIG. 2. Hall coefficient as a function of donor concentration for n-type germanium at different temperatures.

of a conduction-band conductivity, a temperature-dependent impurity conductivity for intermediate impurity concentrations at low temperatures, and a temperature-independent impurity-band conductivity for high impurity concentrations. These impressions are substantiated by plotting as a function of donor concentration the electrical resistivity (see Fig. 1) and the Hall coefficient (see Fig. 2) of a number of samples having approximately the same compensation ratio. At impurity concentrations above $1{\cdot}3\times10^{17}$, these data show no temperature dependence in the low-temperature region. For n-type germanium, then, $N_c = 1{\cdot}3\times10^{17}$.

In a similar fashion, the available literature on p-type germanium,[1, 2] n- and p-type silicon,[4,5,6] and p-type indium antimonide[7] has been analyzed. The data on these materials are extensive and allow a rather good determination of N_c, although the possibility that N_c depends upon the impurity element does exist. Since temperature-independent impurity conduction has not been observed in n-InSb, N_c could not be evaluated, but it must be very low, indicating a possible effective-mass dependence. The low-temperature behavior of silicon carbide,[8] cadmium sulfide,[9] and magnesium stannide[10] has also been investigated. The available data are meager, and in the case of magnesium stannide there is some evidence that surface conduction may be playing a role, but tentative values of N_c may be assigned to these materials. The results are presented in Table 1, along with the theoretically predicted value of N_c for metallic hydrogen. The latter value is predicted by MOTT[11] on the basis of BALTENSPERGER's cellular calculation of a cubic lattice[12] of hydrogen atoms.

Table 1. *Critical impurity concentration for a number of semiconductors**

Material	$N_c(\text{cm}^{-3})$	ϵ
p–Mg_2Sn	$\sim10^{16}$	19
p–InSb	$1{\cdot}3\times10^{17}$	16·0
n–Ge	$1{\cdot}3\times10^{17}$	15·8
p–Ge	$1{\cdot}4\times10^{17}$	15·8
n–Si	$1{\cdot}6\times10^{19}$	11·7
p–Si	$6{\cdot}5\times10^{18}$	11·7
n–CdS	$\sim10^{18}$	11·6
n–SiC	$\sim10^{20}$	10·0
metallic H (theory)	$6{\cdot}0\times10^{23}$	1·0

* For concentrations of majority impurities above N_c, the Hall coefficient and resistivity are temperature-independent.

If the shallow-impurity-state picture is correct, the results of the metallic-hydrogen calculation should be scaled by a factor $(m^*/m\epsilon)^3$ to be applicable to a real material, since the radius of Wannier orbitals would go as $(\epsilon m/m^*)$. It will be noticed from Table 1 that

1. n-Ge, p-Ge, and p-InSb all have the same experimental N_c, despite the difference in their effective masses;

2. N_c for n-Si is larger than that for p-Si, although effective-mass arguments would predict the opposite order.

If differences in effective mass are ignored, and if the empirical values of N_c are plotted logarithmically as a function of the known dielectric constants ϵ, the result fits remarkably well to a straight line (see Fig. 3). The surprising thing is that the slope of this line is $-1{\cdot}0$, so that the empirically determined relation is the simple expression

$$N_c = (2{\cdot}2a_H)^{-3} \exp-(\epsilon-1),$$

or, numerically,

$$N_c = (1{\cdot}6\times 10^{24}) \exp-(\epsilon).$$

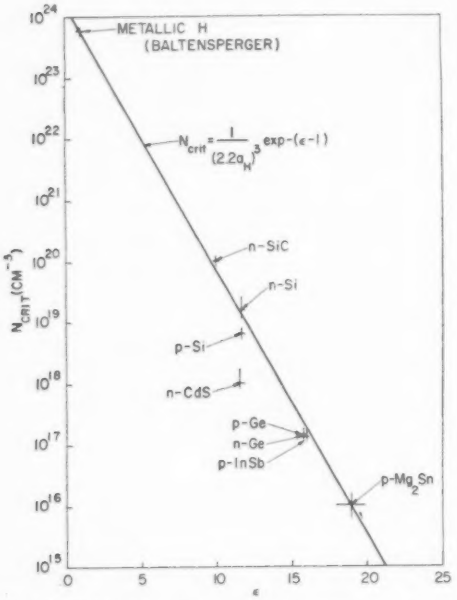

FIG. 3. Critical impurity concentration as a function of dielectric constant for various materials showing impurity conduction.

John Jay Hopkins Laboratory for Pure and Applied Science,
General Atomic Division,
General Dynamics Corporation,
San Diego,
California

E. C. MCIRVINE*

References

1. FRITZSCHE H. and LARK-HOROVITZ K., *Physica* **20,** 834 (1954).
2. FRITZSCHE H., *Phys. Rev.* **99,** 406 (1955).
3. FRITZSCHE H., *J. Phys. Chem. Solids* **6,** 69 (1958).
4. MORIN F. J. and MAITA J. P., *Phys. Rev.* **96,** 28 (1954).
5. CARLSON R. O., *Phys. Rev.* **100,** 1075 (1955).
6. SWARTZ G., *J. Phys. Chem. Solids* **12,** 245 (1960).
7. FRITZSCHE H. and LARK-HOROVITZ K., *Phys. Rev.* **99,** 400 (1955).
8. BUSCH G., *Helv. Phys. Acta* **19,** 167 (1946).
9. KROGER F. A., VINK H. J. and VOLGER J., *Physica* **20,** 1095 (1954).
10. FREDERIKSE H. P. R., HOSLER W. R. and ROBERTS D. E., *Phys. Rev.* **103,** 67 (1956).
11. MOTT N. F., *Canad. J. Phys.* **34,** 1356 (1956).
12. BALTENSPERGER W., *Phil. Mag.* **44,** 1355 (1953).

* Present address: Scientific Laboratory, Ford Motor Company, Dearborn, Michigan.

BOOK REVIEW

J. M. ZIMAN: **Electrons and Phonons.** Clarendon Press, Oxford, 1960. 554 pp., 84s.

THIS BOOK provides an interesting and generally excellent account of those ubiquitous elementary particles of solid state physics, electrons and phonons. Essentially a selection of theoretical resumés, it serves both to expound the important ideas and to introduce the reader to the extensive literature concerning electrons and phonons in solids. The book is organized into twelve chapters discussing separately electrons and phonons alone, electron–electron, phonon–phonon, and electron–phonon interactions, interactions of both electrons and phonons with various crystalline imperfections and various transport phenomena involving electric and magnetic fields, temperature and concentration gradients. To adequately cover so much material in a single volume, Mr. ZIMAN has needed to be both selective and concise; in giving such a satisfactory treatment within that limitation of space he has demonstrated an unusual ability to get right to the heart of the matter he has to discuss.

In surveying theoretical work on a variety of subjects, a reviewer meets with special difficulties in connection with the choice of mathematical notation. Clearly, some minimum amount of mathematical notation is essential for quantitative discussion. The reviewer would like to choose notation that is economical, unified and adapted to his taste and point of view; at the same time, for convenience in commenting on the work he is surveying, he often needs to use the notation of the authors of the principal works he is surveying; finally, his exposition will be much easier to apprehend if he can use a notation that is as conventional as possible. Since he cannot ordinarily satisfy any two of these criteria with a single notation, he may be hard put to avoid bloating his text with very lengthy explanations of terminology. Mr. ZIMAN has made an uncompromising choice among these critera; he has chosen a notation primarily to satisfy his own taste. I found Mr. ZIMAN's notation more than a little bizarre, and failed to see the advantage of its numerous unconventional features. On the other hand, I like his handling of notation; he has managed to express his mathematical ideas clearly without getting involved in notational intricacies, and when the chips were down he has adopted a casual attitude about notation which I found very gratifying.

The overwhelming emphasis throughout is on theory, so the book contains discussions of a number of calculations. The calculations are treated in such a way as to indicate the elements that entered them, rather than to explain how the computational difficulties were surmounted. Theory is approached largely in terms of concepts and schematic procedures rather than detail. I thought the balance between mathematical and qualitative discussions just right for a theoretical survey.

It is not feasible to review the individual treatments of even broad subjects, except to say they are generally quite good and, in view of space limitations, quite thorough. The illustrations are very good and make an important contribution to the success of the text. A number of treatments given are previously unpublished. One, perhaps minor, point of especial interest is Mr. ZIMAN's careful distinction between the terminology "Brillouin zone" and what he calls the "Jones' zone". This distinction has been needed for many years; it should serve to emphasize that Jones' theories of "higher zones" in metals and alloys are really theories of intraband energy level structure rather than interband energy structure, and it may perhaps reduce some of the confusion in the minds of beginning students, who often wonder, e.g. how a "Brillouin zone" can contain an irrational fraction of an electron per atom.

There were a few things about the book I disliked or thought distinctly below average. I thought the discussion of the fundamentals of transport theory somewhat poor, and the treatment of the equivalent Hamiltonian (p. 94 et seq.) subtly wrong and entirely misleading as to what the theoretical problem is. The discussion of dielectric breakdown would probably leave the reader with the erroneous impression that e.g. breakdown effects are much less than would be expected from theory. I thought the discussion of the polaron inadequate in view of the importance of the subject. Finally, I felt that a number of the

plausibility arguments and summarizing comments were not formulated carefully enough to be really useful, and in the worst cases, represented hit-and-run thinking.

According to the preface, this book is intended to be useful both to the graduate student and to the professional research worker in Solid State Physics. However, in virtue of the considerable condensation of material and somewhat informal style, it will be a difficult book for graduate students, who will generally lack the sophistication to see the implications of what is and is not said and will probably find the mathematical discussion unduly brief. However, for the professional research worker in solid state, who typically has at least a garbled acquaintance with most of the theory, this book should be of great value both in clarifying concepts and in enlarging his acquaintance with the most important detailed developments of the theory.

E. N. ADAMS

VOL.
15
1960